OBSERVATOIRE DE PARIS

SYSTÈMES DE RÉFÉRENCE TEMPS-ESPACE

UMR8630 / CNRS

Scientific developments from highly accurate space-time reference systems

Développements scientifiques à partir de systèmes de référence de haute exactitude

JOURNÉES 2013 ☆

SYSTÈMES DE RÉFÉRENCE SPATIO - TEMPORELS

☆ PARIS, 16-18 SEPTEMBER

OBSERVATOIRE DE PARIS

SYSTÈMES DE RÉFÉRENCE TEMPS-ESPACE

UMR 8630 / CNRS

61 avenue de l'Observatoire, F-75014 Paris, FRANCE

Scientific developments from highly accurate space-time reference systems

Développements scientifiques à partir de systèmes de référence de haute exactitude

Edited by

Actes publiés par

N. CAPITAINE

JOURNÉES 2013 ☆

SYSTÈMES DE RÉFÉRENCE SPATIO - TEMPORELS

☆ PARIS, 16-18 SEPTEMBER

Participants in the Journées 2013 in the indoor garden of Ecole Normale Supérieure

ISBN 978-2-901057-69-7

TABLE OF CONTENTS

PREFACE

The Journées 2013 "Systèmes de référence spatio-temporels", with the sub-title "Scientific developments from highly accurate space-time reference systems", were organized from 16 to 18 September 2013 at Paris Observatory and Ecole Normale Supérieure in Paris, France. These Journées and their proceedings have been sponsored by Paris Observatory scientific council, the CNRS Institut des Sciences de l'Univers-GRAM, the SYRTE Department, the Labex FIRST-TF and the Ministry of Education and Research (Programme ACCES). They were the twenty-second conference in this series whose main purpose is to provide a forum for researchers in the fields of Earth rotation, reference frames, astrometry and time. The Journées were organized in Paris each year from 1988 to 1992, and then, since 1994, alternately in Paris (in 1994, 1996, 1998, 2000, 2004, 2007 and 2010) and other European cities, namely Warsaw in 1995 and 2005, Prague in 1997, Dresden in 1999 and 2008, Brussels in 2001, Bucharest in 2002, St. Petersburg in 2003 and Vienna in 2011. Such an organization has been the result of an active and continuing cooperation between the "Systèmes de Référence Temps Espace" (SYRTE) Department of Paris Observatory and other institutions in Europe. The Journées 2013 have been co-sponsored by the International Astronomical Union (IAU)and the International Association of Geodesy (IAG)

The scientific programme of the Journées 2013 was focused on the scientific developments in geodesy, astronomy and astrophysics, etc. based on highly accurate reference frames and time scales. In addition, there have been presentations and discussions related to the new IAU Division A Working Groups that have been established at the 28th IAU GA, with WG meetings organized in association with the Journées. For the first time, tutorial lectures have been held the day before the beginning of the Journées with the goal of making our discipline more broadly accessible.

There were 101 participants, coming from 18 different countries. The scientific programme included 10 invited papers, 41 oral communications and 32 posters; it was composed of the following sessions:
Session 1: Theoretical aspects of reference systems;
Session 2: The next ICRF - Progress and developments;
Session 3: Atomic and pulsar-based time scales - Progress and developments;
Session 4a: Earth rotation - Theory;
Session 4b: Earth rotation - Modelling and observations;
Session 5: Solar system dynamics - Theory, modelling and numerical standards .

In addition to these scientific activities, the participants met for a cocktail and a conference dinner on Monday and Tuesday evening September 16 and 17, respectively. On Wednesday afternoon, there was the possibility to visit a small exhibition at Paris Observatory on Nicolas Louis de Lacaille (author of the star catalogue, called *Coelum Australe Stelliferum*, which is relevant to the Journées 2013 topics) from the archives of Paris Observatory.

These Proceedings are divided into six sections corresponding to the sessions of the meeting. The Table of Contents is given on pages iii to v, the list of participants on pages vii and viii, the scientific programme and list of posters on pages ix to xiii. The Postface on page 281 gives the announcement of the "Journées" 2014 that will be organized from 22 to 24 September 2014 at Pulkovo Observatory (Russia), with the sub-title "Recent developments and prospects in ground-based and space astrometry"'.

We thank here all the participants in the Journées 2013. We are very grateful to the Scientific Organizing Committee for its active role in the elaboration of the scientific programme and to all the authors of the papers for their valuable contributions. On behalf of the SOC, we thank the Local Organizing Committee, and especially its Chair, Noël Dimarcq, for the very efficient preparation of the meeting and the very good local conditions and organization. We are also very grateful to O. Becker for the invaluable technical help for the preparation of the meeting and the publication of the Proceedings.

Nicole CAPITAINE
Chair of the SOC
September 2014

List of Participants

ANDREI Alexandre, *Observatorio Nacional / MCTI*, Brazil
ANGONIN Marie-Christine, *SYRTE - Observatoire de Paris, CNRS/UPMC*, France
ARMINJON Mayeul, *Lab. 3SR (CNRS and Universités de Grenoble: UJF, Grenoble-INP)*, France
BACHMANN Sabine, *Federal Agency for Cartography and Geodesy (BKG), Germany*, Germany
BARACHE Christophe, *SYRTE - Observatoire de Paris, CNRS/UPMC*, France
BERTARINI Alessandra, *Inst. of Geodesy and Geoinformation, Bonn Univ. & MPIfR Bonn*, Germany
BERTHIER Jérôme, *IMCCE - Observatoire de Paris*, France
BERTONE Stefano, *SYRTE - Observatoire de Paris, CNRS/UPMC*, France
BISE Penelope, *Universität Oldenburg*, Germany
BIZOUARD Christian, *SYRTE - Observatoire de Paris, CNRS/UPMC*, France
BOEHM Johannes, *Vienna University of Technology*, Austria
BONNEFOND Pascal, *GéoAzur - Observatoire de Côte d'Azur*, France
BOURGOIN Adien, *SYRTE - Observatoire de Paris, CNRS/UPMC*, France
BRZEZINSKI Aleksander, *Space Research Centre, Polish Academy of Sciences*, Poland
CAPITAINE Nicole, *SYRTE - Observatoire de Paris, CNRS/UPMC*, France
CHAPANOV Yavor, *National Institute of Geophysics, Geodesy and Geography, BAS*, Bulgaria
CHARLOT Patrick, *Laboratoire d'Astrophysique de Bordeaux*, France
CHOLIY Vasyl, *Kyiv Shevchenko University*, Ukraine
CHUPIN Baptiste, *SYRTE - Observatoire de Paris, CNRS/UPMC/LNE*, France
DAMLJANOVIC Goran, *Astronomical Observatory*, Serbia
DE WITT Aletha, *Hartebeesthoek Radio Astronomy Observatory (HartRAO)*, South Africa
DEFRAIGNE Pascale, *Royal Observatory of Belgium*, Belgium
DEHANT Véronique, *Royal Observatory of Belgium*, Belgium
DÉBARBAT Suzanne, *SYRTE - Observatoire de Paris, CNRS/UPMC*, France
DIMARCQ Noël, *SYRTE - Observatoire de Paris, CNRS/UPMC*, France
ESCAPA Alberto, *Department of Applied Mathematics, University of Alicante*, Spain
FEDOROVA Elena, *National Taras Shevchenko University of Kyiv, Astronomical Observatory*, Ukraine
FERRÁNDIZ José, *University of Alicante*, Spain
FIENGA Agnès, *GéoAzur - Observatoire de Côte d'Azur*, France
FILIPPOVA Alexandra, *Moscow Aviation Institute*, Russia
FILIPPOVA Elena, *Moscow Aviation Institute*, Russia
GAMBIS Daniel, *SYRTE - Observatoire de Paris, CNRS/UPMC*, France
GATTANO César, *SYRTE - Observatoire de Paris, CNRS/UPMC*, France
GIRDIUK Anastasiia, *Saint Petersburg State University*, Russia
GROSS Richard, *Jet Propulsion Laboratory*, USA
GUO Li, *Shanghai Astronomical Observatory, Chinese Academy of Sciences*, China
HAN Wen-Biao, *Shanghai Astronomical Observatory, Chinese Academy of Sciences*, China
HEES Aurélien, *Jet Propulsion Laboratory (postdoc)*, USA
HEINKELMANN Robert, *Helmholtz Centre Potsdam, GFZ*, Germany
HESTROFFER Daniel, *IMCCE - Observatoire de Paris*, France
HOBBS George, *CSIRO*, Australia
HOHENKERK Catherine, *HM Nautical Almanac Office*, United Kingdom
HUANG Chengli, *Shanghai Astronomical Observatory, Chinese Academy of Sciences*, China
IDDINK Andreas, *Institute of Geodesy and Geoinformation, University of Bonn*, Germany
IVANOVA Tamara, *Institute of Applied Astronomy, Russian Academy of Sciences*, Russia
JACOBS Christopher, *Jet Propulsion Laboratory*, USA
KHELIFA Sofiane, *Centre of Space Techniques*, Algeria
KOVALEVSKY Jean, *Observatoire de Côte d'Azur*, France
KRASNA Hana, *Vienna University of Technology*, Austria
KUDRYAVTSEV Sergey, *Sternberg Astronomical Institute of Lomonosov Moscow State Univ.*, Russia
LAMBERT Sébastien, *SYRTE - Observatoire de Paris, CNRS/UPMC*, France
LAZARUS Patrick, *Max-Planck-Institut fuer Radioastronomie*, Germany
LEPONCIN-LAFITTE Christophe, *SYRTE - Observatoire de Paris, CNRS/UPMC*, France

LIU Jia-Cheng, *Nanjing University*, China
LOPES Pedro, *SYRTE - Observatoire de Paris, CNRS/UPMC*, France
MALKIN Zinovy, *Pulkovo Observatory*, Russia
MARCO Francisco J., *Universidad Jaume I*, Spain
MARTINEZ Maria J., *Universidad Politecnica de Valencia*, Spain
MCCARTHY Dennis, *U.S. Naval Observatory (retired)*, USA
METIVIER Laurent, *IGN - LAREG*, France
METRIS Gilles, *GéoAzur - Observatoire de Côte d'Azur*, France
MEYNADIER Frédéric, *SYRTE - Observatoire de Paris, CNRS/UPMC*, France
MIGNARD Francois, *Observatoire de la Côte d'Azur*, France
NAGALSKI Tomasz, *Space Research Centre, Polish Academy of Sciences*, Poland
NASTULA Jolanta, *Space Research Centre, Polish Academy of Sciences*, Poland
NELMES Susan, *HM Nautical Almanac Office*, United Kingdom
NICOLAIDIS Efthymios, *SYRTE - Observatoire de Paris, CNRS/UPMC*, France
NOTHNAGEL Axel, *Institute of Geodesy and Geoinformation, University of Bonn*, Germany
PASHKEVICH Vladimir, *Pulkovo Observatory*, Russia
PAVLOV Dmitry, *Institute of Applied Astronomy, Russian Academy of Sciences*, Russia
PEREPELKIN Vadim, *Moscow Aviation Institute*, Russia
PETIT Gérard, *Bureau international des poids et mesures (BIPM)*, France
PITJEVA Elena, *Institute of Applied Astronomy, Russian Academy of Sciences*, Russia
POTTIÉ Paul-Eric, *SYRTE - Observatoire de Paris, CNRS/UPMC/LNE*, France
PREMA Paresh, *HM Nautical Almanac Office*, United Kingdom
QI Zhaoxiang , *Shanghai Astronomical Observatory, Chinese Academy of Sciences*, China
RAMBAUX Nicolas, *IMCCE - Observatoire de Paris, UPMC*, France
RAPOSO-PULIDO Virginia, *Inst. GeogrÁfico Nacional (IGN) / GeoForschungsZentrum (GFZ)*, Spain/Germany
RICHARD Edouard, *SYRTE - Observatoire de Paris, CNRS/UPMC*, France
RICHARD Jean-Yves, *SYRTE - Observatoire de Paris, CNRS/UPMC*, France
ROLAND Jacques, *Institut d'Astrophysique de Paris*, France
RON Cyril, *Astronomical Institute AS CR*, Czech Republic
ROSAT Séverine, *IPGS-EOST*, France
SHEN Wenbin, *Wuhan University*, China
SKURIKHINA Elena, *Institute of Applied Astronomy, Russian Academy of Sciences*, Russia
SOFFEL Michael, *Lohrmann observatory*, Germany
SONG Yezhi, *Shanghai Astronomical Observatory, Chinese Academy of Sciences*, China
SOUAMI Damya, *SYRTE - Observatoire de Paris, CNRS/UPMC*, France
SOUCHAY Jean, *SYRTE - Observatoire de Paris, CNRS/UPMC*, France
TARIS François, *SYRTE - Observatoire de Paris, CNRS/UPMC*, France
TEYSSANDIER Pierre, *SYRTE - Observatoire de Paris, CNRS/UPMC*, France
THUILLOT William, *IMCCE - Observatoire de Paris*, France
VONDRÁK Jan, *Astronomical Institute AS CR*, Czech Republic
WIECZOREK Mark, *Institut de Physique du Globe de Paris*, France
WOLF Peter, *SYRTE - Observatoire de Paris, CNRS/UPMC*, France
XU Minghui, *Shanghai Astronomical Observatory, Chinese Academy of Sciences*, China
XU Xueqing, *Shanghai Astronomical Observatory, Chinese Academy of Sciences*, China
YAGUDINA Eleonora, *Institute of Applied Astronomy, Russian Academy of Sciences*, Russia
YATSKIV Yaroslav, *Main Astronomical Observatory NAS of Ukraine*, Ukraine
ZHAROV Vladimir, *Sternberg Astronomical Institute of Lomonosov Moscow State University*, Russia
ZOTOV Leonid, *Sternberg Astronomical Institute of Lomonosov Moscow State University*, Russia

SCIENTIFIC PROGRAMME

Scientific Organizing Commitee: A. Brzeziński, Poland; N. Capitaine, France (Chair); V. Dehant, Belgium; A.Escapa, Spain; C.Hohenkerk, UK; C.-L. Huang, China; I. Kumkova, Russian Federation; D.D.McCarthy, USA; M. Soffel, Germany; J. Souchay, France; J. Vondrák, Czech R.; Ya.Yatskiv, Ukraine

Local Organizing Commitee: P. Baudoin, O. Becker, C. Bizouard, N. Capitaine, P. Delva, N. Dimarcq (Chair), S. Lambert, M. Pailler, D. Souami, F. Taris

Monday 16 September 2013

(at ENS: amphithéâtre Dussane)

9:15-9:30: **Opening of the Journées 2013**

Welcome from N. Dimarcq, Director of Department SYRTE of Paris Observatory (Chair of the LOC)
Introduction to the Journées 2013 by N. Capitaine (Chair of the SOC)

9:30-11:00: **Session 2 - The Next ICRF - Progress and developments**
(Chair: J. Souchay, J. Vondrák)

Jacobs C.and ICRF-3 WG (invited): *Proposed Roadmap for the ICRF-3*
Mignard F. (invited): *Gaia status and early mission*

Bertarini A., Horiuchi S., Jacobs C., Jung T., Lovel J., McCallum J., Ojha R., Quick J., Sohn B.W., de Witt A.: *Extending the K-band Celestial Frame with Emphasis on the Southern Hemisphere*
Krasna H., Malkin Z., Böhm J.: *Impact of seasonal station displacement models on radio source positions*
Malkin Z.: *On systematic and random errors of radio source position catalogs*
Zharov V., Shmeleva N.V.: *Analysis of time series of the EOP and the ICRF source coordinates*

11:00-11:30: Coffee-break

11:30-13:00: Session 2 - Continuation
(Chair: C. Jacobs, Ya. Yatskiv)

Bachmann S., Engelhardt G., Thaller D.: *Source positions from VLBI combined solution*
Iddink A., Nothnagel A., Artz T.: *Development of a VLBI Intra-Technique Combination Strategy for CRF Determination*
Andrei H., Antón S., Taris F., Bourda G., Souchay J., Bouquillon J., Barache C., Pereira Osorio J.J., Charlot P., Vieira Martins R., Lambert S., Camargo J.I., da Silva Neto D.N., Assafin M., le Campion J.-F.: *The Gaia Initial Quasar Catalog*
Souchay J., Andrei A., Barache C., Taris F., Bouquillon S., Gattano C.: *The update of Large Quasar Astrometric Catalog*
Damljanovic G., Taris F., Boeva S., Latev G.: *Optical data of ERS made at 60 cm ASV and 2m Rozhen telescopes useful for the link of ICRF-future Gaia CRF*
Discussion

13:00-14:00: Lunch break

14:00-16:00: Theoretical aspects of reference systems
(Chair: N. Capitaine, M. Soffel)

Métivier L., Collilieux X., Altamimi Z., Lercier D. (invited): *The ITRF and its scientific applications*
Soffel M., Klioner S., Zschocke S. (invited): *Relativistic astrometry: status and prospects*
Fedorova E., Alexandrov A.N., Zhdanov V.I.: *Optical coordinate system for a local observer in a weak gravitational field*
Bertone S., Le Poncin-Lafitte C., Crosta M., Vecchiato A.: *Latest advances in an astrometric model based on the Time Transfer Functions formalism*
Girdiuk A., Titov O.: *Plans for VLBI observations of close approaches of Jupiter to compact extragalactic radio sources in 2014-2016*
Teyssandier P., Linet B.: *Enhanced term of order G3/c6 in the light travel time*
Roland J.: *Binary black holes in nuclei of extragalactic radio sources*
Liu J.-C., Xie Y., Zhu Z.: *Aberration in proper motions for stars in our Galaxy*

16:15-16:45: Coffee-break

16:45-18:00: POSTER SESSION

18:00-19:30: Welcome drink

Tuesday 17 September 2013

(at ENS: amphithéâtre Dussane)

9:00-10:30: Session 3 - Atomic and pulsar-based timescales - Progress and developments
(Chair: D.D. McCarthy, G. Petit)

Defraigne P. (invited): *Multi-GNSS time and frequency transfer*
Hobbs G. (invited): *A pulsar-based time scale from the International Pulsar Timing Array*

Petit G.: *Atomic time scales*
Pottié P.-E., Lopez O., Kanj A., Rovera D., Aschkar J., Chardonnet Ch., Amy-Klein A., Santarelli G.:*Time and frequency comparisons with optical fiber links*
Guo L., Zhao M., Li L.: *Some astrometric discussions on the pulsar parameters by timing*

Discussion

10:30-11:00: Coffee-break

11:00-13:00: Session 4a - Earth Rotation - Theory
(Chair: V. Dehant, C. Huang)

Ferrándiz J., Gross R. (invited): *The goal of the IAU/IAG Joint Working Group on the Theory of Earth rotation*

Dehant V., Folgueira M., Puica M., Koot L., Van Hoolst T., Trinh A.: *Next step in Earth interior modeling for nutation*
Escapa A., Getino J., Ferrándiz J.M., Baenas T. *: On the changes of IAU 2000 nutation theory stemming from IAU 2006 precession theory*
Filippova A., Markov Y., Rykhlova L.: *Rotational-oscillatory motion of the deformable Earth in the short time intervals*
Huang C., Liu C., Liu Y.: *A generalized theory of the figure of the Earth: application to the moment of inertia and global dynamical flattening*
Pashkevich V.: *Construction of the new high-precision Earth rotation series at a long time interval*
Ron, C., Vondrák J., Chapanov Y.: *Free core nutation - possible causes of changes of its phase and amplitude*
Zotov L., Bizouard C.: *Study of the prograde and retrograde excitation at the Chandler frequency*

13:00-14:00: Lunch break

14:00-16:15: Session 4b - Earth Rotation - Modelling and observations
(Chair: A. Brzeziński, R. Gross)

Thaller D. (invited): *The IERS Retreat: How to improve Earth Rotation products?*

Bizouard C.: *Comparison of geodetic and modeled excitation functions by Allan variance*
Boehm J., Schindelegger M., Salstein D.: *Analysis of atmosphere-excited intraseasonal polar motion via the torque approach*
Brzeziński A., Rajner M.:*Estimation of the Chandler wobble parameters by the use of the Kalman deconvolution filter*
Chapanov Y., Vondrák J., Ron C., Pachalieva R.: *Natural and systematic polar motion jumps*
Ding H., Shen W.-B.: *Observation of a 531-day-period polar motion*
Capitaine N., Yao K.: *Nutation determination by means of GNSS - Comparison with VLBI*
Lambert S., Capitaine N., Rosat S., Souchay J.: *The Earth's nutation: VLBI vs. IAU 2000A*

Nastula Y.: *Gravimetric excitation function of polar motion from the GRACE RL05 solution*
Xu X., Zhou Y., Liao X.: *Researches on predictions of Earth orientation parameters*
Yatskiv Y., Odynets P., Volvach O.: *The "Simeiz-Katzively" co-location site of space geodesy techniques: current state and future activity*

16:15-16:45: Coffee-break

16:45-17:30: Discussion

19:30-22:30: Conference dinner

Wednesday 18 September 2013

(at ENS: amphithéâtre Dussane)

9:00-11:00: Session 5 - Solar System Dynamics - Theory, modelling and numerical standards *(Chair: J. A.Escapa, C. Hohenkerk)*

Wieczorek M., M.T. Zuber (invited): *New results from NASA's lunar gravity mapping mission GRAIL*
Rambaux N. (invited): *Rotation/libration of solar system bodies*

Hees A., Folkner W., Park R., Jacobson R., Lamine B., Le Poncin-Lafitte C., Wolf P.: *Tests of gravitation at Solar System scale beyond PPN formalism*
Pitjeva E., Kosmodamianskiy G., Pavlov D., Pitjev N., Poroshina A., Skripnichenko V.: *Numerical ephemerides of planets (EPM) and natural satellites of IAA RAS and their uses for scientific research*
Fienga A., Verma, A.K., Laskar, J., Manche, H., Gastineau, G.: *INPOP13*
Kudryavtsev S.: *Approximation of orbital elements of telluric planets by compact analytical series*
Yagudina E., Vasiliev M.: *EPM-ERA 2013 - New Version of Lunar ephemeris Developed in IAA RAS*
Hestroffer D., Berthier J., Carry B., David P., Thuillot W., Arlot J-E., Bancelin D., Colas F., Devillepoix H., Fouchard M., Ivantsov A., Lainey V., Rambaux N., Robert V.: *Solar System dynamics with the Gaia mission and beyond*

11:00-11:30: Coffee-break

Discussion

12:30-12:45: Closing of the Journées 2013

and Announcement of the Journées 2014

13:00-14:00: Lunch break

At Observatoire de Paris

14:00-17:30: WG and task group meetings (Meeting rooms of Paris Observatory)

16:00-17:00: Possibility of a visit of the exhibition Lacaille at Paris Observatory

16:00-17:00: Possibility of a visit of the exhibition Lacaille at Paris Observatory

Or, in Paris

14:30-17:00: Possibility of a visit of the exhibition Lacaille at Paris Observatory

LIST OF POSTERS

Session 1: Theoretical aspects of reference systems

1.1 Arminjon M.: *On the definition of a reference frame and the associated space in a general spacetime*
1.2 Hees A., Bertone S., Le Poncin-Lafitte C.: *The Time Transfer Function as a tool to compute range, Doppler and astrometric observables*
1.3 Khelifa S.: *Noise characteristics in DORIS position time series derived from IGN-JPL, INASAN and CNES-CLS analysis centres*
1.4 Kudryavtsev S.: *Corrections to the IERS amplitudes of variations of the geopotential coefficients due to frequency dependence of Love numbers*
1.5 Malkin Z.: *On the Galactic aberration constant*
1.6 Nicolaïdis E., Débarbat S., Malpangotto M., Eisensdaedt J., Blay M., Toulemonde M., Dimarcq N., Delva P., Lautier J., Meynadier F., Bizouard C.: *OMIM, an interdisciplinary group at SYRTE*
1.7 Qi Z., Yu Y., Tang Z., Zhao M.: *Astrometric Support for the Lunar-based Ultraviolet Telescope*

Session 2: The Next ICRF - Progress and developments

2.1 Coelho B., Andrei A., Antón S.: *The SDSS quasars as a testbench for the Gaia fundamental reference frame grid-points*
2.2 de Witt A., Horiuchi S., Jacobs C., Jung T., Lovel J., McCallum J., Ojha R., Quick J., Sohn B.W., Bertarini A.: *Experimental plan for improving the K-band Celestial Frame*
2.3 Lambert S., Arias E. F., Souchay J.: *VLBI representations of the celestial reference system*
2.4 Marco F.J., Martinez, M.J, Lopez, J.A.: *An accurate and stable mixed method to obtain coefficients in VSH developments of residuals from ICRF2- Catalog differences*
2.5 Marco F.J., Martinez, M.J, Lopez, J.A.: *About homogeneity in combined catalogs*
2.6 Martinez, M.J, Marco F.J., Lopez, J.A.: *Problems caused by biased data in models of catalog adjustment*
2.7 Raposo-Pulido V., Heinkelmann R., Nilsson T., Karbon M., Schuh H., Gómez-Gónzalez J.: *Effects of the datum configuration of radio sources on the EOP determined by VLBI*

Session 3: Atomic and pulsar-based timescales - Progress and developments

3.1 Chupin B., Abgrall M., Bize S., Guéna J., Laurent P., Rosenbusch P., Rovera G., Uhrich P.: *The new UTC(OP) based on the LNE-SYRTE atomic fountains*
3.2 Meynadier F., Delva P., Le Poncin Lafitte C., Guerlin C., Laurent P., Wolf P.: *ACES Micro-wave Link data analysis - status update*
3.3 Song Y., Hu X., Huang Y.: *Prediction of the Atomic clock bias for COMPASS Satellites*

Session 4b: Earth Rotation - Modelling and observations

4.1 Hu H., Vondrák J., Su Y.: *Anomalies of astronomical time-latitude residuals at YAO before Wenchuan Earthquake*
4.2 Lopes P., Barache C., Richard J.Y., Bizouard C., Gambis D. *Prediction of EOPs using the artificial neural network: Revisiting the method*
4.3 Malkin Z.: *On detection of the free inner core nutation from VLBI data*
4.4 Nagalski T.: *Analysis of EWT maps from GRACE mission and land hydrology data*
4.5 Perepelkin V., Bondarenko V.V., Markov Yu.G.: *Amplitude-frequency analysis of the Earth orientation parameters and the variation of the second zonal harmonic of the geopotential*
4.6 Skurikhina E., Ipatov A., Smolentsev S., Kurdubov S., Gayazov I., Diyakov A., Schpilevsky V.: *CONT11 - High-Frequency Earth Rotations Variations from VLBI Observations*

Session 5: Solar System Dynamics - Theory, modelling and numerical standards

Session 1

THEORETICAL ASPECTS OF REFERENCE SYSTEMS

ASPECTS THÉORIQUES DES SYSTÈMES DE RÉFÉRENCE

THE ITRF AND ITS SCIENTIFIC APPLICATIONS

L. METIVIER[1], X. COLLILIEUX[1,2], Z. ALTAMIMI[1], D. LERCIER[1]
[1] IGN LAREG, Univ Paris Diderot, Sorbonne Paris Cité
5 rue Thomas Mann, 75205 Paris Cedex 13, France
e-mail: laurent.metivier@ign.fr, xavier.collilieux@ign.fr, zuheir.altamimi@ign.fr, daphne.lercier@ign.fr
[2] SYRTE, Observatoire de Paris, CNRS, UPMC,
61, avenue de l'Observatoire, 75014 Paris, France

ABSTRACT. The ability to assign accurate time-dependent coordinates to points on the Earth's surface is fundamental for many Earth observation applications. Point positions, to be meaningful and fully exploitable, have to be determined in a well-defined Terrestrial Reference Frame. All current global and regional reference frames rely on the availability of the International Terrestrial Reference Frame (ITRF), which is the most accurate realization of the International Terrestrial Reference System (ITRS). Positions and velocities in the last release of the ITRF, entitled ITRF2008, are determined with a precision better than a few millimeters and 1 mm/yr, respectively. This paper focuses on geophysical applications that benefited of the precision and stability of the ITRF. Sea level rise estimations, global plate tectonics, co/post-seismic deformation studies or the interpretation of displacements induced by postglacial rebound or recent ice melting all require an accurate reference frame. Conversely, the knowledge of the expected displacements from geophysical theories and external measurements allows providing constraints on the error budget of the ITRF defining parameters. For future releases of the ITRF, an estimation model that takes into account a more complex modeling of the seismic and loading displacements will be necessary.

1. INTRODUCTION

According to the two International Union of Geodesy and Geophysics (IUGG) resolutions 2 adopted in 1991 and 2007, the International Terrestrial Reference System (ITRS) is the recommended Terrestrial Reference System (ITRS) for Earth science applications. Twelve realizations of the ITRS, called International Terrestrial Reference Frame (ITRF), from ITRF88 to ITRF2008, have been computed since the creation of the International Earth Rotation and Reference Frames Service (IERS). They include the coordinates for several hundreds of stations derived from space geodesy measurements: Global Navigation Satellite System (GNSS), Satellite Laser Ranging (SLR), Very Long Baseline Interferometry (VLBI) and Doppler Orbitography Integrated by Satellite (DORIS). Those measurements are analyzed by National Agencies or Universities, in relation with the Technique Services of the IERS. The estimated coordinates are then averaged rigorously combined to obtain long-term coordinates in a well defined TRF that verify ITRS specifications (Petit and Luzum, 2010): see for example Altamimi et al. (2011) for a whole description process of the most recent ITRF computation.

ITRF coordinates are not intended to include all Earth's deformation contributions. Indeed, a few corrections are necessary to restore instantaneous coordinates from ITRF coordinates, see chapter 7 of the IERS conventions (Petit and Luzum, 2010). These corrections mainly include high frequency coordinate variations while the first prerequisite is that corresponding models be available with a sufficient accuracy. Up to now, solid Earth tides, tidal ocean loading, pole tide or atmospheric tides are included in this list. Thus, ITRF coordinates include all residual deformations that could be modeled with piece-wise linear functions of time.

In this paper, we will review the geophysical processes that generate these residual variations and discontinuities in the ITRF coordinates. The study of ITRF coordinate variations and global scale geodynamic processes has revealed that both geophysical model and the ITRF itself could benefit from inter-comparison (Collilieux et al., 2013). While those analyses have been successful, the current level of precision reveals significant geophysical processes that are not yet modeled in ITRF coordinates and that should be considered for next ITRS realizations to comply with the user accuracy requirement.

2. ITRF AND GEOPHYSICAL MODELS

In the previous years, several studies have highlighted how the knowledge of the geophysical processes that take place at geodetic stations help to assess the TRF coordinate accuracy. A geophysical evaluation of the ITRF can be done, either by confronting station velocity estimations at regional scales, or by assessing the consistency between the frame parameters and ITRS specifications. For instance, the frame origin has to be at the Center of Mass of the Earth (CM) at long-period, and the scale is supposed to keep the same definition over time. While an extensive review and classifications of the studies and methods can be found in Collilieux et al. (2013), we review a few relevant examples here.

A domain of applications that particularly needs ITRF accuracy is the measurement of sea level variations (Blewitt et al., 2011). The TRF coordinates are used either as a priori coordinates to compute altimeter satellite orbits or as a reference to correct tide gauges (TGs) measurements for land motion. While some potential reference frame deficiencies would map differently into sea level rise, residual errors cannot be excluded at the 0.1 mm/yr level (Collilieux and Wöppelmann, 2011). However, recent error analyses of the ITRF2008 velocity field, based on geophysical expectations, showed that the potential errors in the ITRF2008 origin motion is likely smaller than 0.5 mm/y along each component (Wu et al., 2011) and that the error in the scale rate is smaller than 0.2 mm/yr (Collilieux and Schmid, 2013). In addition, the assessment of GNSS-corrected TG series located within the same oceanographic region show much more consistent records (Santamaria et al., 2012), which informs about the quality of up to date GNSS and TRF results. In general, post-glacial rebound models are used for TG corrections instead of geodetic results when those are missing. But even for those studies, global velocity field as the one of ITRF2008 has been shown to be a valuable dataset to assess the postglacial rebound model itself. As an example, Métivier et al. (2012) showed that ITRF2008 vertical velocity comparisons with different geophysical models allow discussing some modeling issues and complements results from the GRACE mission. While the postglacial rebound signal is also present in the horizontal ITRF2008 velocity filed, it is shown not to affect drastically the determination of the global plate motion as demonstrated by Altamimi et al. (2012). See figure 1 illustrating the ITRF2008 velocity field.

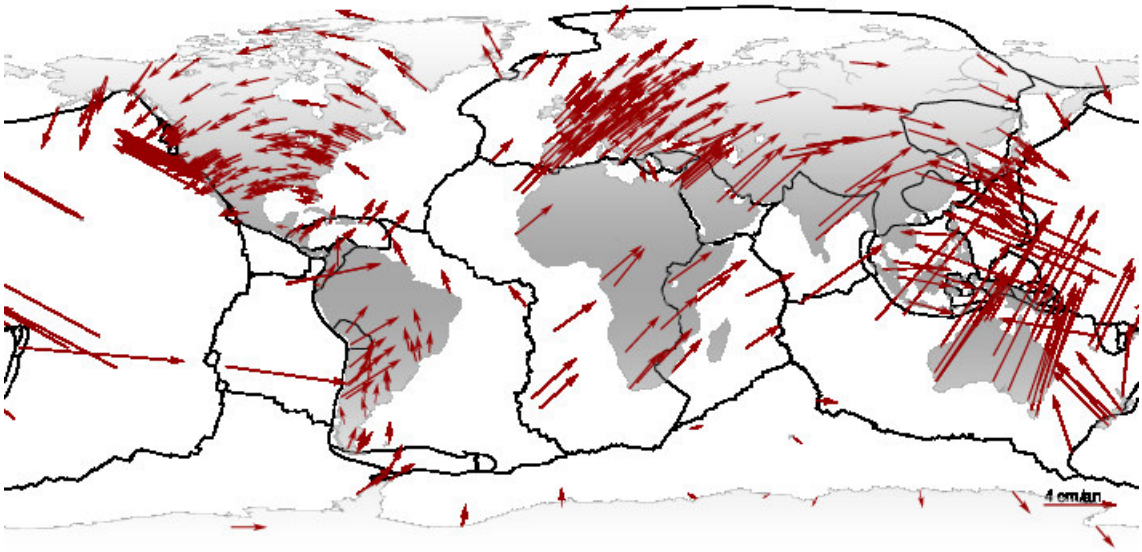

Figure 1: ITRF2008 horizontal velocities.

3. CHALLENGES

As mentioned before, the ITRF2008 is based on a piece-wise linear model for the time evolution of station coordinates. Even if the linear model has proven its efficiency for global positioning on Earth until now, the continuous improvement in the precision of geodetic techniques imposes to realize more accurate and stable reference frames, raising the question of the adequacy of the reference frame model itself. Station position residual time series in ITRF2008 show clear non-linear behaviors that can be

attributed to various geophysical phenomena, but also remaining technical systematic errors that would not need to be modeled if they were controlled.

Apart from tides, which are already corrected, the largest non-linear motions that can be observed in geodetic time series are abrupt discontinuities. They are typically due to equipment changes or earthquake ruptures and are generally taken into account in the pre-processing of terrestrial reference frame constructions. However the discontinuity detection remains usually empirical, i.e. mostly based on visual assumptions, which is today a limitation. For instance, it appears that co-seismic deformations may impact significantly GPS positions thousands of kilometers away from the earthquake epicenters, considering the current precision in GPS measurements (Tregoning et al., 2013). Unfortunately, small discontinuities are not always visible in time series due to the level of station seasonal displacements and due to the noise level in geodetic solutions, yet their presence in time series may affect the estimations of the station velocities. This issue calls for more investigations on the systematic treatment of discontinuities in geodetic time series. In addition, after a great earthquake, some of the geodetic stations impacted by the earthquake show non-linear relaxation motions during a few years due to post-seismic deformations. This non-linear behavior is today modeled in reference frame constructions as a piece-wise linear function, which is not accurate enough. At a shorter time scale, geodetic stations are affected by non-tidal loading deformations induced by the atmosphere, the oceans, the ice sheets and continental hydrology. They typically generate annual and semi-annual motions of geodetic stations up to 15 mm but also significant inter-annual displacements as a function of the regional climate (Valty et al., 2014). In addition, the last decade has shown a new class of station non-linear behavior in the form of global station accelerations in different regions. Fig. 2 shows the case of the GPS and DORIS stations located in Thule, in Greenland. These stations all present a net acceleration in their vertical components, probably due to the Greenland ice sheet retreat induced by recent global climate changes (Khan et al., 2010). The climate evolution also impact the position of the CM (Métivier et al., 2010, 2011), which might be a future issue for the determination of the ITRF origin if the effect is significant.

Considering the necessity today to gain one order of magnitude in reference frame precision, a major challenge will be to incorporate those non-linearity behaviors in the ITRF model for the time evolution of station coordinates and/or frame parameters. Different approaches may be investigated: either correcting the geodetic time series from geophysical models before the construction of the ITRF, which raises the issue of the models quality and their evaluation, or incorporating new degrees of freedom in the ITRF model in the form of non-linear parametric functions.

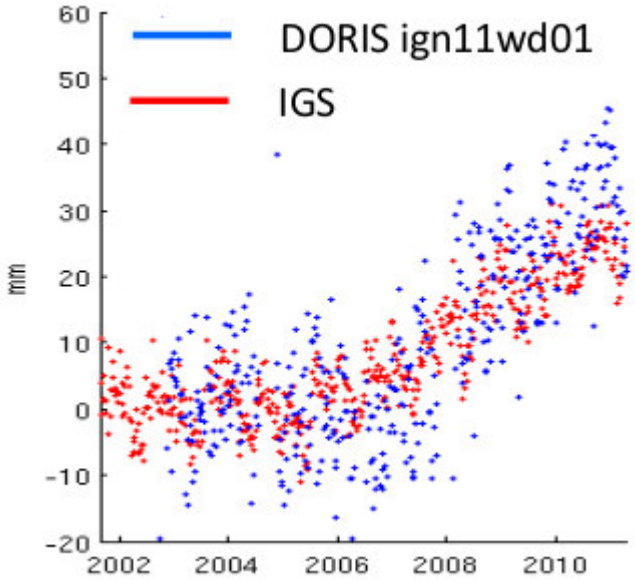

Figure 2: Thule GPS and DORIS Height displacements. The acceleration is related to recent ice melting as observed by (Khan et al., 2010).

Acknowledgements. This work was partly funded by the Centre National d'Etudes Spatiales (CNES) through a TOSCA grant.

REFERENCES

Altamimi, Z., Collilieux, X., Métivier, L., 2011, "ITRF2008: an improved solution of the International Terrestrial Reference Frame", J. Geodesy, 85(8), pp. 457-473, doi: 10.1007/s00190-011-0444-4.

Altamimi, Z., Métivier, L., Collilieux, X., 2012, "ITRF2008 plate motion model", J. Geophys. Res.(Solid Earth), 117(B07402), doi: 10.1029/2011JB008930.

Blewitt, G., Altamimi, Z., Davis, J. L., Gross, Richard S., Kuo, C., Lemoine, F.G., Neilan, R.E., Plag, H.P., Rothacher, M., Shum, C.K., Sideris, M.G., Schöne, T., Tregoning, P., Zerbini, S., 2011, "Geodetic observations and global reference frame contributions to understanding sea level rise and variability", In T. Aarup, J. Church, S. Wilson, and P. Woodworth editors, "Understanding Sea level Rise and Variability, A World Climate Research Programme Workshop and a WCRP contribution to the Global Earth Observation System of Systems", UNESCO, pp. 127-143.

Collilieux, X.,Altamimi, Z., 2012, "External Evaluation of the Origin and the Scale of the International Terrestrial Reference Frame", in Z. Altamimi and X. Collilieux editors, Proceedings of the IAG Symposium REFAG2010, International Association of Geodesy Symposia, 138, pp. 27-31, doi: 10.1007/978-3-642-32998-2_5

Collilieux X., Altamimi Z., Argus, D.F., Boucher, C., Dermanis, A., Haines, B.J., Herring, T.A., Kreemer, C., Lemoine, F.G., Ma,C., MacMillan, D.S., Makinen, J., Métivier, L., Ries, J.C., Teferle, F. N., Wu. X., 2013, "External evaluation of the terrestrial reference frame: report of the task force of the iag sub-commission 1.2" In P. Willis editor, Proceedings of the XXV IUGG General Assembly 139 of International Association of Geodesy Symposia, 139, doi: 10.1007/978-3-642-37222-3_25.

Collilieux, X., Altamimi, Z., Coulot, D., van Dam, T., Ray, J., 2010, "Impact of loading effects on determination of the International Terrestrial Reference Frame", Adv. Space Res., 45, pp. 144-154, doi:10.1016/j.asr.2009.08.024.

Collilieux, X., Altamimi, Z., Ray, J., van Dam, T., Wu, X., 2009, "Effect of the satellite laser ranging network distribution on geocenter motion estimation", J. Geophys. Res.(Solid Earth), 114(B04402), doi: 10.1029/2008JB005727.

Collilieux, X., Schmid, R., 2013, "Evaluation of the ITRF2008 GPS vertical velocities using satellite antenna z-offsets", GPS Solutions, 17(2), pp. 237-246, doi: 10.1007/s10291-012-0274-8.

Collilieux, X., Wöppelmann, G., 2011, "Global sea-level rise and its relation to the terrestrial reference frame", J. Geodesy, 85(1), pp. 9-22, doi: 10.1007/s00190-010-0412-4.

Khan, S. A., Wahr, J., Bevis, M., Velicogna, I. Kendrick, E., 2010, "Spread of ice mass loss into northwest Greenland observed by GRACE and GPS", Geophys. Res. Lett., 37(L06501), pp. 6501, doi:10.1029/2010GL042460.

Métivier, L., Collilieux, X., Altamimi, Z., 2012, "ITRF2008 contribution to glacial isostatic adjustment and recent ice melting assessment", Geophys. Res. Lett., 39(L01309), doi: 10.1029/2011GL049942.

Métivier, L., Greff-Lefftz, M., Altamimi, Z., 2010, "On secular geocenter motion: The impact of climate changes", Earth Planet. Sc. Lett., 296, pp. 360-366, doi: 10.1016/j.epsl.2010.05.021.

Métivier, L., Greff-Lefftz, M., Altamimi, Z., 2011, "Erratum to "On secular geocenter motion: The impact of climate changes" [Earth Planet. Sci. Lett. 296 (2010) 360-366]", Earth Planet. Sc. Lett., 306, pp. 136, doi: 10.1016/j.epsl.2011.03.026.

Petit G., Luzum B. (eds.), 2010, "IERS conventions (2010) (iers technical note 36)", Frankfurt am Main: Verlag des Bundesamts fr Kartographie und Geodsie, 179 pp., ISBN 3-89888-989-6.

Tregoning, P., Burgette, R., Mc Clusky, S. C., Lejeune, S., Watson, C. S., Mc Queen, H., 2013, "A decade of horizontal deformation from great earthquakes", J. Geophys. Res.(Solid Earth), 118(5), pp. 2371-2381.

Valty, P. and de Viron, O. and Panet, I. and Collilieux, X., 2014, "Impact of the North Atlantic Oscillation on Southern Europe water distribution: insights from geodetic data", Geophys. Res. Lett., in review.

Wu, X.,Collilieux, X., Altamimi, Z., Vermeersen, B., Gross, R.S., Fukumori, I., "Accuracy of the International Terrestrial Reference Frame origin and Earth expansion", Geophys. Res. Lett., 38(L13304), doi: 10.1029/2011GL047450.

TOWARDS SUB-MICROARCSECOND MODELS FOR RELATIVISTIC ASTROMETRY

S. ZSCHOCKE, S.A. KLIONER, M.H. SOFFEL
Lohrmann Observatory
Helmholtzstrasse 10, D-01062 Dresden, Germany
e-mail: michael.soffel@tu-dresden.de

ABSTRACT. Astrometric space missions like Gaia have stimulated a rapid advance in the field of relativistic astrometry. Present investigations in that field aim at accuracies significantly less than a microarcsecond. We review the present status of relativistic astrometry. As far as the problem of light propagation is concerned we face two problems: the form of the BCRS metric and solutions to the light-ray equation. Finally, work in progress in that field is briefly mentioned.

1. INTRODUCTION

The Hipparcos astrometric space mission has determined positions (proper motions) of some 120000 stars with a precision of a milliarcsecond (mas/y). The forthcoming mission Gaia is expected to reach a level of up to some μas for one billion stars depending on stellar brightness. Proposed missions like the 'Nearby Earth Astrometric Telescope' (NEAT) envisage an accuracy of 50 nanoarcseconds (nas). This stunning progress in astrometry implies the necessity to formulate appropriate relativistic astrometric models with an intrinsic accuracy of 1 nas. One is still far from that goal but there has been a lot of work in that direction.

Any relativistic astrometric model based on Einstein's theory of gravity employs one or several different reference systems (4-dimensional coordinate systems) to describe the location and motion of gravitating bodies and the light trajectory from the emitter to the observer. In one of these well related coordinate systems one has to formulate the astrometric observable as a coordinate independent quantity (i.e., as a scalar). A model for a concrete astrometric mission will contain a certain set of coordinate-dependent parameters that have to be fitted from observational data. The reference system then becomes the corresponding reference frame, materialized e.g., by a stellar (or quasar) catalog.

If physically relevant local coordinates, co-moving with the observer are introduced, then it might be possible to derive observables from coordinate quantities as it is the case in the Gaia Relativistic Model (GREM) developed by Klioner (2003a). An astrometric model thus involves the following constructions: i) one or several space-time reference systems, i.e., space-time coordinates and the corresponding metric tensor, ii) the trajectories of light-rays, iii) the trajectories of the observer and gravitating bodies, and iv) the calculation of astrometric observables. This contribution focuses on the first two aspects i) and ii).

2. APPROXIMATION METHODS FOR REFERENCE SYSTEMS

To construct a space-time reference system with a metric tensor as solution of Einstein's field equations for real high precision astrometric observations one resorts to approximation schemes, either to a post-Newtonian hierarchy (weak field, slow motion) or to the post-Minkowskian approximation (weak field). For light rays the post-Newtonian (PN) metric is of the form

$$g_{00} = -1 + \frac{2w}{c^2}\,, \qquad g_{0i} = 0\,, \qquad g_{ij} = \left(1 + \frac{2w}{c^2}\right)\delta_{ij}\,, \tag{1}$$

where w is the gravitational potential. The corresponding post-post Newtonian (2PN) metric for light rays can be written in the form

$$g_{00} = -1 + \frac{2w}{c^2} - \frac{2w^2}{c^4}\,, \quad g_{0i} = -\frac{4w^i}{c^3}\,, \quad g_{ij} = \left(1 + \frac{2w}{c^2} + \frac{2w^2}{c^4}\right)\delta_{ij} + \frac{4}{c^4}q_{ij}\,, \tag{2}$$

where w^i is the gravito-magnetic potential induced by moving or rotating masses. For one body at rest (rotating, vibrating, with arbitrary shape and decomposition) the exterior metric is known for both the post-Newtonian (Blanchet & Damour, 1989) and the post-Minkowskian case (Damour & Iyer, 1991), and it has been demonstrated that the metric in both cases is determined by only two families of multipole moments, M_L (mass-moments) and S_L (spin-moments).

In what follows we will give an overview of the present status of the theory of light propagation.

3. LIGHT PROPAGATION IN THE FIELD OF MASS MONOPOLES

Light propagation in the field of mass monopoles with constant velocity: Explicit post-Newtonian solutions for the light propagation in the case of uniformly moving bodies, where the position of the body is given by $\boldsymbol{x}_A(t) = \boldsymbol{x}_A^{\rm eph}(t_A^0) + \dot{\boldsymbol{x}}_A^{\rm eph}(t_A^0)\left(t - t_A^0\right)$, were derived by Klioner (1989); here $\boldsymbol{x}_A^{\rm eph}$ and $\dot{\boldsymbol{x}}_A^{\rm eph}$ are the actual position and velocity of body A taken from an ephemeris for some instant of time t_A^0. Following a suggestion by Hellings (1986), Klioner & Kopeikin (1992) have argued that in order to minimize the errors in the light propagation the free parameter t_A^0 should be chosen to coincide with the moment of closest approach between the body and the light ray. Furthermore, Klioner (2003b) has suggested a straightforward way to calculate the effect of uniform translational motion of a body on the light propagation by a Lorentz transformation of the light trajectory in a reference system where the body is at rest. In this way Klioner (2003b) has derived a post-Minkowskian solution for the light propagation in the field of a mass monopole moving with constant velocity. It has been demonstrated that the more general solution of Kopeikin & Schäfer (1999) can be reproduced in the limiting case of uniform motion.

Light propagation in the field of arbitrarily moving mass monopoles: A rigorous solution of the problem in the first post-Minkowskian approximation has been found by Kopeikin & Schäfer (1999), where the geodetic equations for photons are integrated using retarded potentials. The numerical accuracy of various approaches has been investigated by Klioner & Peip (2003). Especially, Klioner & Peip (2003) have numerically compared various available solutions for the light propagation for observations made within the Solar system. The authors used both artificial orbits for deflecting bodies as well as planetary trajectories taken from JPL solar system ephemerides. It has been demonstrated that the simple solution obtained in (Klioner, 1991) and (Klioner & Kopeikin, 1992) is sufficient for an accuracy of about 2 nas, provided that $\boldsymbol{x}_A^{\rm eph}$ and $\dot{\boldsymbol{x}}_A^{\rm eph}$ are taken in the optimal way.

2-PN Light propagation in the field of mass monopoles at rest: The light trajectories in the Schwarzschild field, that means in the field of a single mass monopole at rest, can be found in an analytically closed form as it has been demonstrated at the first time by Hagihara (1931); for a re-derivation we refer to Chandrasekhar (1983). However, this exact analytical solution is not convenient for data reduction of astrometric observations, since the light curve is not given by an explicit time dependence of the coordinates of the photon $x(t), y(t)$ but only implicitly in terms of $y(x)$.

From a practical point of view, post-post-Newtonian effects in the light propagation in the Schwarzschild field have been considered by many authors. An important progress has been made by Brumberg (1991) who has found an explicit post-post-Newtonian solution for light trajectories in the Schwarzschild field as function of coordinate time in a number of coordinate gauges. Generalizations of that solution for the case of the parametrized post-post-Newtonian metric have been given by Klioner & Zschocke (2010). The latter authors have investigated in great detail the numerical magnitudes of various post-post-Newtonian terms and formulated practical algorithms for highly-effective computation of the post-post-Newtonian effects. It has been demonstrated that the so-called enhanced post-post-Newtonian terms are due to a physically inadequate choice of the parametrization of the light rays; see also Bodenner & Will (2003).

Two alternative approaches to the calculation of propagation times and directions of light rays have been formulated recently. Both approaches allow one to avoid explicit integration of the geodetic equations for light rays. The first approach (Le Poncin-Lafitte, Linet & Teyssandier, 2004; Teyssandier & Le Poncin-Lafitte, 2008) is based on the use of Synge's world function. Several applications of this approach have been published: higher post-Newtonian approximations in spherically symmetric gravitational fields and post-Newtonian effects in the gravitational field with multipole moments. Another approach based on the eikonal concept has been developed by Ashby & Bertotti (2010) to investigate the light propagation in the field of a spherically symmetric body. All the results of these authors confirm the conclusions and formulas obtained in Klioner & Zschocke (2010).

2-PN Light propagation in the field of moving mass monopoles: There are only very limited results dealing with moving deflecting bodies in the post-post-Newtonian approximation. Especially, Brügmann (2005) has investigated some effects of the light propagation in the post-post-Newtonian gravitational field of a system of two bodies, where two important approximations are used. First, both the light source and the observer are assumed to be located at infinity in an asymptotically flat space. Second, some of the results were obtained in form of an expansion in powers of the ratio between the distance between two bodies and the impact parameter of the light ray with respect to the center of mass of the two-body system. These assumptions imply, however, that the results are not applicable to observations in the solar system.

4. LIGHT PROPAGATION IN THE FIELD OF MASS QUADRUPOLES

Light propagation in the quadrupole field of bodies at rest: Analytical solutions of light deflection in a quadrupole gravitational field have previously been investigated by many authors. However, for the first time the full analytical solution for the light trajectory in a quadrupole field has been obtained by Klioner (1991), where an explicit time dependence of the coordinates of a photon and the solution of the boundary value problem for the geodetic equation has been obtained. These results were confirmed by a different approach in Le Poncin-Lafitte & Teyssandier (2008), while a simplified expression with μas accuracies has been derived in Zschocke & Klioner (2011).

Light propagation in the quadrupole field of arbitrarily moving bodies: The light-deflection at moving massive bodies, having monopole and quadrupole structure, has been investigated by Kopeikin & Makarov (2007), where the quadrupole term is taken into account in local coordinates of the body in Newtonian approximation. Using the harmonic gauge, the linearized Einstein equations are inhomogeneous wave equations and a general solution is given in terms of a multipole expansion (Thorne, 1980; Blanchet & Damour, 1986). In Kopeikin & Makarov (2007) the geodesic equation is rewritten into a considerably simpler form. Using a special integration method, they succeeded to integrate analytically the geodesic equation by neglecting all terms that contribute by less than 1 μas.

5. LIGHT PROPAGATION IN THE FIELD OF BODIES WITH SPIN

Light propagation in the field of bodies at rest with a spin-dipole: The first explicit post-Newtonian solution of the light trajectory in the gravitational field of massive bodies at rest possessing a spin dipole has been obtained by Klioner (1991). This solution provides all the details of light propagation, especially the explicit time dependence of the coordinates of the photon and the solution of the corresponding boundary value problem. Kopeikin (1997) has generalized the solution for the case of motionless bodies possessing any set of time-independent spin (and mass) moments, and it has been shown that the expression in Klioner (1991) and Kopeikin (1997) agree with each other.

Light propagation in the field of arbitrarily moving bodies with spin-dipole: Kopeikin & Mashhoon (2002) have derived formulas for the case of light propagation in the field of arbitrarily moving bodies possessing mass monopole and spin dipole.

6. LIGHT PROPAGATION IN THE FIELD OF HIGHER MASS AND SPIN MULTIPOLE MOMENTS

Mass and spin multipole moments at rest: A systematic approach to the integration of light geodesic equation in the stationary post-Newtonian gravitational field of an isolated system of N bodies having a complex but time-independent multipole structure has been worked out in Kopeikin (1997) and Kopeikin et al. (1999). Especially, the work of Kopeikin (1997) represents a generalized solution for the case of motionless bodies possessing any set of time-independent mass and spin moments, that is M_L and S_L, respectively. Later, in Kopeikin, Korobkov & Polnarev (2006) and Kopeikin & Korobkov (2005), the propagation of light rays in the field of localized sources which are completely characterized by time-dependent mass and spin multipoles, $M_L(t)$ and $S_L(t)$, respectively, has been investigated. Kopeikin, Korobkov & Polnarev (2006) and Kopeikin & Korobkov (2005) have found an analytical solution for the light propagation in such gravitating systems.

7. WORK IN PROGRESS

Presently several groups try to extend relativistic astrometry to still higher accuracies. Our group presently concentrates on the 2PN field of arbitrarily moving bodies endowed with arbitrary mass- and spin multipole moments where the metric in harmonic gauge is given by (2). There have been first attempts to tackle this problem (e.g., Xu & Wu 2003; Minazzoli & Chauvineau 2009) but they are far from being complete.

Problems, that have been ignored in these preliminary papers, are related with the internal structure of the bodies. For a single body at rest these problems are well understood for both the post-Newtonian and the post-Minkowskian case (Blanchet & Damour, 1989; Damour & Iyer, 1991) where many structure dependent terms appear in intermediate calculations that cancel exactly in virtue of the local equations of motion or can be eliminated by corresponding gauge transformations. However, for the post-linear case the situation is still unclear. In course of our studies for the general problem just mentioned we found that even for the spherically symmetric case of a single body the complete derivation of the exterior metric (the Schwarzschild metric) is interesting. In a forthcoming paper (Klioner & Soffel, 2014) we will show how such structure-dependent terms cancel and one ends up with the Schwarzschild solution in harmonic gauge.

8. REFERENCES

Ashby, N., Bertotti, B., 2010, "Accurate light-time correction due to a gravitating mass", Class. Quantum Grav. 27, 145013.

Blanchet, L., Damour, T., 1986, "Radiative gravitational fields in general relativity: I. General Structure of the field outside the source", Phil. Trans. R. Soc. London A 320, 379.

Blanchet, L., Damour, T., 1989, "Post-Newtonian generation of gravitational waves", Annales de I'lnstitut Henri Poincaré I Physique Theorique 50, 377.

Bodenner, J., Will, C.M., 2003, "Deflection of light to second order: A tool for illustrating principles of general relativity", Am. J. Phys. 71, 770.

Brügmann, M.H., 2005, "Light deflection in the post-linear gravitational field of bounded pointlike masses", Phys. Rev. D 72, 024012.

Brumberg, V.A., 1991, "Essential Relativistic Celestial Mechanics", Adam Hilger, Bristol

Chandrasekhar, S., 1983, "The mathematical Theory of Black Holes", Clarendon Press, Oxford.

Damour, T., Iyer, B.R., 1991, "Multipole analysis for electromagnetism and linearized gravity with irreducible Cartesian tensors", Phys. Rev. D 43, 3259.

Hagihara Y., 1931, "Theory of the relativistic trajectories in a gravitational field of Schwarzschild", Jap. J. Astron. Geophys. 8, 67.

Hellings, R.W., 1986, "Relativistic Effects in Astronomical Timing Measurements", AJ 91, 650.

Klioner, S.A., 1989, "Propagation of the Light in the Barycentric Reference System considering the Motion of the Gravitating Masses", Communications of the Institute of Applied Astronomy No 6, 21.

Klioner, S.A., 1991, "Influence of the quadrupole field and rotation of objects on the light propagation", Sov. Astron. 35, 523.

Klioner, S.A., 2003a, "Practical Relativistic Model of Microarcsecond Astrometry in Space", AJ 125, 1580.

Klioner, S.A., 2003b, "Light Propagation in the Gravitational Field of Moving Bodies by means of Lorentz Transformation. I. Mass monopoles moving with constant velocities", A & A 404, 783.

Klioner, S.A., Kopeikin, S.M., 1992, "Microarcsecond Astrometry in Space: Relativistic Effects and Reduction of Observations", AJ 104, 897.

Klioner, S.A., Peip, M., 2003, "Numerical simulations of the light propagation in the gravitational field of moving bodies", A & A 410, 1063.

Klioner, S.A., Zschocke, S., 2010, "Numerical versus analytical accuracy of the formulas for light propagation", Class. Quantum Grav. 27, 075015.

Klioner, S.A,. Soffel, M., 2014, to be published

Kopeikin, S.M., 1997, "Propagation of light in the stationary field of a multipole gravitational lens", J. Math. Phys. 38, 2587.

Kopeikin, S.M., Korobkov, P., 2005, "General Relativistic Theory of Light Propagation in the Field of Radiative Gravitational Multipoles", arXiv:gr-qc/0510084v1.

Kopeikin, S.M., Korobkov, P., Polnarev, A., 2006, "Propagation of light in the field of stationary and radiative gravitational multipoles", Class. Quantum Grav. 23, 4299.

Kopeikin, S.M., Makarov, V.V., 2007, "Gravitational bending of light by planetary multipoles and its measurement with microarcsecond astronomical interferometers", Phys. Rev. D 75, 062002.
Kopeikin, S.M., Mashhoon, B., 2002, "Gravitomagnetic-effects in the propagation of electromagnetic waves in variable gravitational fields of arbitrary-moving and spinning bodies", Phys. Rev. D 65, 064025.
Kopeikin, S.M., Schäfer, G., 1999, "Lorentz covariant theory of light propagation in gravitational fields of arbitrary-moving bodies" Phys. Rev. D 60, 124002.
Kopeikin, S.M., Schäfer, G., Gwinn, C.R., Eubanks, T.M., 1999, "Astrometric and timing effects of gravitational waves from localized sources", Phys. Rev. D 59, 084023.
Le Poncin-Lafitte, C., Linet, B., Teyssandier, P., 2004, "World function and time transfer: general post-Minkowskian expansions", Class. Quantum Grav. 21, 4463.
Le Poncin-Lafitte, C., Teyssandier, P., 2008, "Influence of mass multipole moments on the deflection of a light ray by an isolated axisymmetric body", Phys. Rev. D 77, 044029.
Minazzoli, O.L., Chauvineau, B., 2009, "Post-Newtonian metric of general relativity including all the c^{-4} terms in the continuity of the IAU2000 resolutions", Phys. Rev. D 79, 084027.
Teyssandier, P., Le Poncin-Lafitte, C., 2008, "General post-Minkowskian expansion of time transfer functions", Class. Quantum Grav. 25, 145020.
Thorne, K.S., 1980, "Multipole expansions of gravitational radiation", Rev. Mod. Phys. 52, 299.
Xu, C., Wu, X., 2003, "Extending the First-Order Post-Newtonian Scheme in Multiple Systems to the Second-Order Contributions to Light Propagation", Chinese Physics Letters 20, No. 2, 195.
Zschocke, S., Klioner, S.A., 2011, "On the efficient computation of the quadrupole light deflection", Class. Quantum Grav. 28, 015009.

OPTICAL COORDINATE SYSTEM FOR A LOCAL OBSERVER IN A WEAK GRAVITATIONAL FIELD

A.N. ALEXANDROV[1], E. FEDOROVA[1,2], V.I. ZHDANOV[1]
[1] Taras Shevchenko National University of Kyiv, Astronomical Observatory
Observatorna str.3, 04053 Kiev, Ukraine
[2] Institute of Astrophysics and Geophysics of Liege University
allee du 6 Aout 17, Liege 4000, Belgium
e-mail: an_alex@ukr.net; efedorova@ukr.net; ValeryZhdanov@gmail.com

ABSTRACT. We develop a method to construct the reference system (RS) of a local observer which is based on the transformation from the instant normal coordinates to the Fermi and optical ones. The main advantage of our approach is due to a direct relation of the optical coordinates with observable positions of distant objects on the celestial sphere. The method is applied to a construction of local observer RS in a weak field within the linearized gravitation theory.

1. INTRODUCTION

Outstanding perspectives of microarcsecond astrometry connected with challenging space projects such as GAIA mission, demand to construct the reference systems (RS) which would be accurate enough to deal with fine relativistic effects. On the other hand these RS must be convenient and clearly understandable as much as possible. The IAU Resolutions concerning the reference frames, adopted by the XXIVth International Astronomical Union General Assembly focus mainly on harmonic coordinates, and this direction is most developed (see Soffel et al., 2003). Harmonic coordinates are convenient to be used in the barycentric system for limited ensemble of masses with asymptotically flat metric and the space origin at the barycentre of the ensemble of bodies. In this barycentric system we can easily fix the coordinates if they are quasi-Cartesian and the metric tensor is pseudo-Euclidian at the infinity. We remind that the harmonicity conditions have the form of partial differential equations and for unique determination of harmonic coordinates additional conditions are required. For the case of geocentric coordinates or coordinates associated with a satellite this choice looks something artificial. It is not linked with any physical or geometrical preferences, but just with the method of solving the Einstein equations for metric tensor or with the particular choice of transformations to the barycentric system. Also, a genetic relationship of harmonic coordinates with Einstein's equation requires additional efforts (see, e.g., Klioner & Soffel, 2000; Klioner, 2003) when the General Relativity is compared with alternative theories of gravity.

Harmonic coordinates are not observable and are not associated with the observations. Therefore, their use does not solve directly the problem of the interpretation of observations. On the other hand, there are the well known relativistic reference frames that are based on invariant interrelations characterizing the observables. These RS are thus connected with results of observations in a direct way. Such relations are determined correctly for any kind of metric, despite the kind of field equations, and they are independent on a physical model of the reference body. As an example of such systems we can remind the local observer's frame, based on the Riemannian normal coordinates (RNC), Fermi coordinates (FC) or on optical ones (OC) (Synge, 1960). Reference systems of the local observer are based on the geodesics lines and have a clear geometric interpretation. The Fermi coordinates are the most direct relativistic generalization of the reference frame of the moving observer in Newtonian mechanics. At the same time, the optical coordinates that operate directly with the position of an object on the celestial sphere, are most closely associated with the observations. Transition to the optical coordinates can be treated as an important step in solving the problem of observables. Fermi coordinates are better known (see e.g. Ashby & Bertotti, 1986; Fukushima, 1988; Aleksandrov et al., 1990; Marzlin, 1994; Nesterov A. 1999), while the optical coordinates have not been given due attention. However, in recent years some version of optical coordinates is used in cosmology under the name "observational coordinates" (Clarkson & Maartens, 2010). Note also a possibility of introducing a generalized EC and OC, measured from the surface of the Earth, instead from its center (Zhdanov, 1994).

Here we demonstrate how the developed mathematical apparatus associated with geodesics, their deviation, and parallel transport is used to construct coordinate transformations to FC and OC, and to find the metric in these coordinates for an arbitrary weak field. Note the ideological affinity of our approach to work by Nesterov (1999). However, we achieve a significant simplification by transition from integration of the curvature tensor to the integrals of the metric perturbations.

2. BASIC RELATIONS IN GENERAL

Suppose that the observer is moving along the world line $x_c^\mu(\tau)$, τ is his proper time, and $e^\alpha_{(\mu)}$ is his proper reference frame (here, the index in parentheses indicates the number of the vector). Vector $e^\alpha_{(0)}$ coincides with observer's four-velocity, i.e. $\frac{dx_c^\alpha}{d\tau} = u^\alpha = e^\alpha_{(0)}$. Proper frame is transported along the observer's world line as follows (e.g. Misner, Thorne and Wheeler, 1973):

$$\frac{De^\alpha_{(\mu)}}{\partial\tau} = \Omega^\alpha{}_\beta e^\beta_{(\mu)}. \tag{1}$$

Here $\Omega_{\alpha\beta} = a_\alpha u_\beta - u_\alpha a_\beta + \varepsilon_{\alpha\beta\gamma\delta}u^\gamma\omega^\delta$ is the four-tensor of observer's rotation; a^α his four-acceleration, ω^β angular velocity.

Consider geodesic $x^\mu(\tau, s)$ parameterized with canonical parameter s, which passes through the observed point and $x^\mu(\tau, 0) = x_c^\mu(\tau)$. Let v^α be a tangential ort to this geodesic at the point $x_c^\mu(\tau)$. Then (instant) RNK of the point $x^\mu(\tau, s)$ adapted to the tetrad $e^\alpha_{(\mu)}$ and originated at $x_c^\mu(\tau)$ are $y^\mu = v^\mu s$, where $v^\mu = e^{(\mu)}_\alpha v^\alpha$. So, to find formulae for the transformation to normal coordinates, one needs to construct the general solution $x^\mu(\tau, s) = X^\mu(x_c^\nu(\tau), v^\alpha s)$ of Cauchy problem for the geodesic equation

$$\frac{d^2x^\mu}{ds^2} + \Gamma^\mu_{\nu\lambda}\frac{dx^\nu}{ds}\frac{dx^\lambda}{ds} = 0. \tag{2}$$

In the case of an analytic metric this solution is known in a form of the covariant Taylor series (see Pyragas et al., 1995). Also, in the weak-field approximation it is easy to present the solution in the integral form (see below).

The construction of Fermi coordinates involves only the geodesics, which are orthogonal to the world line of the observer $g_{\alpha\beta}v^\alpha u^\beta = v^0 = 0$. Then, FC z^μ are defined by the following relations:

$$z^0 = \tau, \quad z^i = y^i, \quad i = 1, 2, 3. \tag{3}$$

Similarly, the optical coordinates ζ^μ are constructed by means of light geodesics $g_{\alpha\beta}v^\alpha v^\beta = 0$ of the past $v^0 = -\sqrt{\sum_{i=1}^3 (v^i)^2}$:

$$\zeta^0 = \tau, \quad \zeta^i = y^i. \tag{4}$$

Jacobi matrices, which connect the tensor components in the FC (or OC) and RNC include solutions of the equation of geodesic deviation. The corresponding general formulae were found by Zhdanov and Alexandrov (1990) and Alexandrov and Zhdanov (1992) (see also Pyragas et al., 1995). A fundamental role is played by the matrices $S^\rho_\sigma(y^\mu)$ and $C^\rho_\sigma(y^\mu)$, which satisfy the equations:

$$D^2\mathbf{S} + D\mathbf{S} = \tilde{\mathbf{r}}\mathbf{S}, \tag{5}$$

$$D^2\mathbf{C} - D\mathbf{C} = \tilde{\mathbf{r}}\mathbf{C}. \tag{6}$$

Here $D = y^\mu\frac{\partial}{\partial y^\mu}$, $\tilde{r}^\rho_\sigma = \tilde{R}^\rho_{\mu\nu\sigma}(y^\tau)\, y^\mu y^\nu$, $\tilde{R}^\rho_{\mu\nu\sigma}$ is a result of the parallel transport of the curvature tensor along the geodesic to the reference point. Geodesic deviations and the metric tensor in normal coordinates as well as the aforementioned Jacobi matrixes are expressed through these matrices. In particular, for the metric tensor in optical coordinates $g^{Opt}_{\mu\nu}$ we have (Alexandrov & Zhdanov, 1992)

$$g^{opt}_{\mu\nu} = \eta_{\rho\sigma}G^{O\rho}_\mu G^{O\sigma}_\nu, \tag{7}$$

where

$$G^{O\rho}_0 = C^\rho{}_0 + S^\rho{}_i\Omega^i{}_k y^k, \quad G^{O\rho}_j = S^\rho{}_j + S^\rho{}_0\frac{y^j}{y^0}. \tag{8}$$

Similarly, for the metric in Fermi coordinates $g_{\mu\nu}^{Fermi}$ (Zhdanov & Alexandrov, 1990)

$$g_{\mu\nu}^{Fermi} = \eta_{\rho\sigma} G_{\mu}^{F\rho} G_{\nu}^{F\sigma}, \tag{9}$$

$$G_{0}^{F\rho} = C^{\rho}{}_{0} + S^{\rho}{}_{i} \Omega^{i}{}_{k} y^{k}, \quad G_{j}^{F\rho} = S^{\rho}{}_{j}. \tag{10}$$

It should be noted that the matrixes $G_{\mu}^{O\rho}$ and $G_{\mu}^{F\rho}$ appearing here are nothing but the operator of parallel transport along the geodesic in the corresponding coordinates. Thus, $G_{\mu}^{O\rho}$ directly describes the transfer of the wave 4-vector and the polarization from the source to the observer.

3. WEAK FIELD

In weak-field approximation the metric tensor of spacetime $g_{\mu\nu}(x^{\tau})$ is treated as a sum of Minkowski tensor $\eta_{\mu\nu}$ and a perturbation term $h_{\mu\nu}$, so that

$$g_{\mu\nu} = \eta_{\mu\nu} + h_{\mu\nu}(x^{\tau}), \tag{11}$$

where all of the components of $h_{\mu\nu}$ are much less than one (and similarly for all derivatives of $h_{\mu\nu}$). Then one ignores all products of $h_{\mu\nu}$ (or its derivatives). The Christoffel symbols can be calculated as

$$\Gamma_{\nu\lambda}^{\mu} = \frac{1}{2} g^{\mu\tau} \left(g_{\tau\nu,\lambda} + g_{\tau\lambda,\nu} - g_{\nu\lambda,\tau} \right) = \frac{1}{2} \eta^{\mu\tau} \left(h_{\tau\nu,\lambda} + h_{\tau\lambda,\nu} - h_{\nu\lambda,\tau} \right), \tag{12}$$

and Riemann tensor as

$$R_{\rho\mu\nu\sigma} = \frac{1}{2} \left(h_{\rho\sigma,\mu\nu} + h_{\mu\nu,\rho\sigma} - h_{\mu\sigma,\nu\rho} - h_{\nu\rho,\mu\sigma} \right). \tag{13}$$

A simple coordinate transformation of the form

$$x^{\mu} = x'^{\mu} - \frac{1}{2} h_{\nu}^{\mu}(x_c^{\tau}) (x'^{\nu} - x_c^{\nu}) - \frac{1}{2} \Gamma_{\nu\sigma}^{\mu}(x_c^{\tau}) (x'^{\nu} - x_c^{\nu}) (x'^{\sigma} - x_c^{\sigma}) \tag{14}$$

converts metric tensor as follows

$$g'_{\mu\nu}(x'^{\tau}) = \eta_{\mu\nu} + h_{\mu\nu}(x'^{\tau}) - h_{\mu\nu}(x_c^{\tau}) - h_{\mu\nu,\tau}(x_c^{\tau}) (x'^{\tau} - x_c^{\tau}). \tag{15}$$

In small terms differences $(x'^{\tau} - x_c^{\tau})$ are replaced with y^{τ}:

$$g'_{\mu\nu}(x'^{\tau}) = \eta_{\mu\nu} + h'_{\mu\nu}(x_c^{\tau}, y^{\mu}), \tag{16}$$

$$h'_{\mu\nu}(x_c^{\tau}, y^{\mu}) = h_{\mu\nu}(x_c^{\tau} + y^{\mu}) - h_{\mu\nu}(x_c^{\tau}) - h_{\mu\nu,\sigma}(x_c^{\tau}) y^{\sigma}. \tag{17}$$

In the case of moving reference point $x_c^{\mu}(\tau)$ this transformation depends on the parameter τ.
The transformed metric satisfies the following conditions:

$$g'_{\mu\nu}(x_c^{\tau}) = \eta_{\mu\nu}, \quad g'_{\mu\nu,\tau}(x_c^{\sigma}) = \Gamma'_{\mu\nu,\tau}(x_c^{\sigma}) = 0.$$

In order to simplify the formulae below, we shall omit the primes associated with the transformation (12).

Let's introduce three sets of integrals through which all necessary quantities can be expressed:

$$I_{\mu\nu}(x_c^{\sigma}, y^{\tau}) = \frac{1}{s} \int_0^s h_{\mu\nu}(x_c^{\sigma}, s_1 v^{\sigma}) \, ds_1, \quad J_{\mu\nu}(x_c^{\sigma}, y^{\tau}) = \int_0^s \frac{h_{\mu\nu}(x_c^{\sigma}, s_1 v^{\sigma})}{s_1} ds_1,$$

$$K_{\mu\nu}(x_c^{\sigma}, y^{\tau}) = s \int_0^s \frac{h_{\mu\nu}(x_c^{\sigma}, s_1 v^{\sigma}) \, ds_1}{s_1^2}. \tag{18}$$

Integrating the geodesic equation (2) with the expression (12), we find the transformation to RNC (cf. Marzlin, 1994)

$$x^\mu = x_c^\mu + y^\mu - y^\nu \eta^{\mu\sigma} I_{\nu\sigma} + \frac{1}{2}\eta^{\mu\sigma} y^\nu y^\lambda \left(J_{\nu\lambda} - I_{\nu\lambda}\right)_{,\sigma}. \tag{19}$$

There and below the comma denotes the partial derivative with respect to the normal coordinates. In the case of a weak field matrices $S_\sigma^\rho\left(y^\mu\right)$ and $C_\sigma^\rho\left(y^\mu\right)$ are presented in the following form:

$$S_\sigma^\rho = \delta_\sigma^\rho + \Sigma_\sigma^\rho, \quad C_\sigma^\rho = \delta_\sigma^\rho + \Delta_\sigma^\rho, \tag{20}$$

$\Sigma,\ \Delta$ being small. We linearize equations (5,6) and by integration we obtain

$$\Sigma_{\mu\nu} = \frac{1}{2}\left[h_{\mu\nu} - 2I_{\mu\nu} + 2y^\rho\left(J_{\rho(\nu,\mu)} - 2I_{\rho(\mu,\nu)}\right) + y^\rho y^\sigma\left(J_{\rho\sigma,\mu\nu} - I_{\rho\sigma,\mu\nu}\right)\right], \tag{21}$$

$$\Delta_{\mu\nu} = \frac{1}{2}\left[h_{\mu\nu} - 2y^\rho J_{\rho(\mu,\nu)} + y^\rho y^\sigma\left(K_{\rho\sigma,\mu\nu} - J_{\rho\sigma,\mu\nu}\right)\right]. \tag{22}$$

Substituting these expressions into (7-10) one can easily obtain expressions for the metric in FC and OC. Of course, the same expressions can be obtained by successive transformation of coordinates first to RNC (19) and then to the FC and OC in accordance with formulae (3) and (3).

4. SUMMARY

We developed the method to construct the reference frame of a local observer basing on geodesics, their deviation, and parallel transport. We applied it to the non-inertial observer in an arbitrary weak gravitational field, for two kinds of coordinates: optical and Fermi. We have found the transformation formulae to the new systems and the metric tensor components in the new systems via the integrals of the metric perturbations. The results can be useful for the interpretation of the most precise astrometric projects such as GAIA or future space VLBI.

5. REFERENCES

Aleksandrov A.N., Zhdanov V.I., Parnovskii S.L., 1990, "Relativistic frame of reference near the Erth and radiointerferometric observations", Kinematica i Fizika Nebesnykh Tel, **6**, pp. 3-7

Alexandrov A.N., Zhdanov V.I., 1992, "To the theory of reference frames based on the optical coordinates", Herald Taras Shevchenko Nat. Univ. Kyiv, Phys.-Math., **3**, pp. 6-11 (in Ukrainian)

Ashby N., Bertotti B. 1986, "Relativistic Effects in Local Inertial Frames", Phys. Rev. D. **34**(8), pp. 2246-2259

Clarkson C., Maartens R., 2010, "Inhomogeneity and the foundations of concordance cosmology", Class. Quantum Grav., **27**, 124008

Fukushima T. 1988, "The Fermi coordinates for weak gravitational fields", Cel. Mech., **44**, pp. 61-75

Klioner S.A., 2003. "A Practical Relativistic Model for Microarcsecond Astrometry in Space", AJ, **125** pp. 1580-1597

Klioner S.A., Soffel M.H. 2000, "Relativistic celestial mechanics with PPN parameters", Phys. Rev. D **62**, id.024019.

Marzlin K., 1994, "Fermi coordinates for a weak gravitational fields", Phys. Rev., D **50**, pp. 888-891

Misner C.W., Thorne K.S., Wheeler J.A., 1973, Gravitation, Freeman and Co, San Francisco

Nesterov A. 1999, "Riemann normal coordinates, Fermi reference system and the geodesic deviation equation" Class. Quantum. Grav., **16**, pp.465-477

Pyragas K.A., Zhdanov V.I., Alexandrov A.N., Kudrya Yu.N., Pyragas L.E., 1995, Qualitative and analytical methods in relativistic dynamics, Energoatomizdat, Moscow (in Russian)

Soffel M., Klioner S., Petit G., et al., 2003, "The IAU 2000 resolutions for astrometry, celestial mechanics and metrology in the relativistic framework: explanatory supplement", Astronomical Journal, **126,** pp. 2687-2706.

Synge J.L., 1963, General relativity, North-Holland, Amsterdam

Zhdanov V.I., 1994, "Relativistic models of reference systems in the vicinity of the Earth" In: Studying Earth as a planet by methods of astronomy, geophysics and geodesy, Ya.S. Yatskiv (ed.), MAO, Kiev, pp. 41-53 (in Russian)

Zhdanov V.I., Alexandrov A.N., 1990, "Fermi coordinates and radiointerferometric observations", Herald Taras Shevchenko Nat. Univ. Kyiv , Astronomy, **32**, pp. 24-28 (in Russian)

LATEST ADVANCES IN AN ASTROMETRIC MODEL BASED ON THE TIME TRANSFER FUNCTIONS FORMALISM

S. BERTONE[1,2], A. VECCHIATO[2], C. LE PONCIN LAFITTE[1], M. CROSTA[2], L. BIANCHI[3]
[1] SYRTE - Paris Observatory, UPMC - 77, Av. Denfert Rochereau - 75014 Paris, France
e-mail: stefano.bertone@obspm.fr
[2] Astrophysical Observatory of Torino, Strada Osservatorio 20 - 10025 Pino Torinese, Italy
[3] Eurix - Eurixgroup, Via Carcano 26 - 10100 Torino, Italy

ABSTRACT. Given the extreme accuracy of modern space astrometry, a precise relativistic modeling of observations is required. Moreover, the availability of several models formulated in different and independent ways is a security against the presence of systematic errors in the analysis of future experimental results, like in the case of the Gaia mission. In this work, we simulate a series of observations using the two models to be used for the data analysis of Gaia, the Gaia RElativistic Model (GREM) and the Relativistic Astrometric MODel (RAMOD), and we compare them with the results of our astrometric model based on the Time Transfer Functions.

1. INTRODUCTION

A large number of missions planned or proposed for the next years (Gaia, GAME, NEAT) will aim to an increasing astrometric accuracy in order to fulfill their scientific objectives. Aside of the technological capabilities, an accurate description of light propagation in a general relativistic framework will be required. Several independent approaches have been developed in the last years, which are well summarized in [Vecchiato, 2013]. Then, comparing the outcome of the different models allows for checking their physical consistency.

In particular, the space astrometry mission Gaia (Bienayme & Turon, 2002), which has been launched by the European Space Agency (ESA) at the end of 2013, will determine the astrometric parameters for a billion stars with an accuracy of some μas. The resulting catalog will set the basis for a new celestial reference frame. The catalog is built upon a kernel of up to 100 million stars whose positions and motions are reconstructed within a process called "Astrometric Sphere Reconstruction", an extremely difficult task but also a crucial one for the outcome of the mission. This solution will be performed by the Astrometric Global Iterative Solution (AGIS) software (Lindegren et al., 2012). At the same time, an independent verification unit for AGIS called Global Sphere Reconstruction (GSR) (Vecchiato et al., 2012) has been set within the Gaia Data Processing and Analysis Consortium (DPAC). Both pipelines are intended to operate on the same real data and the comparison of their results will validate the final astrometric catalog. In order to keep the two software as separate as possible, two different relativistic modelings of light propagation have been implemented: AGIS relies on GREM (Klioner, 2003), while GSR implements RAMOD (de Felice et al., 2006). Moreover, an independent approach to the modeling of the astrometric observables based on the TTF (Teyssandier et al., 2008) has been recently put in place in the GSR framework. An analysis of these three approaches and their application to astrometry has been recently given in (Bertone et al., 2013). Here, we recall the basis of the TTF approach as well as the early results of the comparison of the three models on simulated Gaia observations.

2. TIME TRANSFER FUNCTIONS IN ASTROMETRY

The goal of astrometry is to determine the position of celestial bodies from angular measurements. One way to get a relativistic (*i.e.* covariant) definition of the astrometric observable is by using the tetrad formalism (Misner et al., 1972), thus giving the direction of observation of an incoming light ray in a particular frame comoving with the observer.

Let us note $E^{\mu}_{(\alpha)}$ the components of this tetrad, where (α) corresponds to the tetrad index and μ is a normal tensor index which can be lowered and raised by using the metric. It has been shown

in (Brumberg, 1991) that we can express the direction of the light ray in the tetrad frame as

$$n^{(i)} = -\frac{E^0_{(i)} + E^j_{(i)}\hat{k}_j}{E^0_{(0)} + E^j_{(0)}\hat{k}_j} = -\frac{E^0_{(i)} + \hat{k}_j E^j_{(i)}}{u^0\left(1 + \hat{k}_j\beta^j\right)} \,, \tag{1}$$

where $\widehat{k}_i = k_i/k_0$ is the so called light direction triple with $k_\mu = g_{\mu\nu}k^\nu$ the covariant components of the tangent vectors to the light ray $k^\mu \equiv dx^\mu/d\lambda$, u^α represents the unit four-velocity of the satellite and $\beta^i \equiv v^i/c$, v^i being the coordinate velocity of the observer.

Let us suppose the existence of a unique light ray connecting the emission event of the signal $x_A = (ct_A, \boldsymbol{x}_A)$ and its reception event $x_B = (ct_B, \boldsymbol{x}_B)$. It has been shown in (Bertone & Le Poncin-Lafitte, 2012) that, under some conditions, $\widehat{k}_i$ can be expressed as the integral of the metric tensor and its derivatives along the Minkowskian straight line. Then, a generic tetrad comoving with the chosen observer and computed at the same accuracy can be used in Eq. (1) to compute the direction of light in the observer reference frame.

3. SIMULATED OBSERVATIONS IN THE GAIA CONTEXT

We implement the model presented in Section 2 in the GSR software and we use it to generate a series of simulated observations. The result is a "GSR-TTF" code well adapted to support the further development of the GSR code and to investigate the results of both AGIS and GSR. Let us illustrate how each of Gaia observations is represented in these software. Each point of the celestial sphere can be fixed in the reference system of the Gaia spacecraft by three direction cosines $n_{(i)}$. From a geometrical point of view, Gaia will measure the abscissa of such a point, *i.e.* the angle ϕ between the x-axis of the spacecraft and the projection of the point in the $x-y$ plane. This angle is related to the director cosines $n_{(i)}$ by the following relations

$$\cos\phi = \frac{n_{(1)}}{\sqrt{1 - n^2_{(3)}}} \,, \tag{2}$$

The abscissa is generally expressed as function of the astrometric parameters $(\alpha_*, \delta_*, \varpi_*, \mu_{\alpha*}, \mu_{\delta*})$ and of the satellite attitude. Eq. (2) also depends on a set of instrument parameters $\{c_l\}$ to provide a sort of long-term calibration. Moreover, when working within the PPN formalism, one should add the parameter γ to the unknowns. As consequence, each of the Gaia observations can be resumed to a non-linear function of these four classes of unknown included in a suitable model of the abscissa ϕ

$$\cos\phi \equiv \mathcal{F}\Big(\alpha_*, \delta_*, \varpi_*, \mu_{\alpha*}, \mu_{\delta*}, a^{(j)}_1, a^{(j)}_2, ..., c_1, c_2, ..., \gamma\Big) \,. \tag{3}$$

The GSR software is built so that the director cosines are provided using the RAMOD model (more precisely, the version actually implemented is PPN-RAMOD (Vecchiato et al., 2003)). Since the software is built in a modular structure, it is nevertheless possible to use other models to treat light propagation, the aberration corrections, etc.

In particular, we implemented the TTF model presented in Section 2 to compute the director cosines at the accuracy required by the Gaia mission: we modeled the gravitational light deflection within the Solar System by using a PN expansion of the direction triple and the RAMOD tetrad (Crosta & Vecchiato, 2010) for the transformation from the Barycentric Celestial Reference System (BCRS) to the Co-Moving Reference System (CoMRS) of Gaia. We used the director cosines $n_{(i)}$ so defined to build the abscissae ϕ, necessary to write the so called known-terms at the left-hand side of Eq. (3).

This completes the implementation in GSR of an abscissa ϕ based on our model. We shall now compare our results to those of PPN-RAMOD (actually implemented in GSR) and of GREM (the model implemented in AGIS). The analytical equivalence between the models has been shown in (Bertone et al., 2014): this step will then allow us to validate our implementation and explore the residual differences between the different models.

We perform a simulation over one day of observations using the three models to generate the abscissae ϕ. The results are illustrated in Fig. 1 (produced using the Gaia-tools provided by the Gaia DPAC), where the models are compared one to each other. The numbers on the left axis have a double meaning: they mark (1) the difference in μas between the two models - represented by the red plot - and (2) the distance in degrees/10 between a given planet and the observation - the blue, green and yellow plot

representing Jupiter, Saturn and Mars, respectively. In particular, the periodic oscillation of the distance planet-observation illustrated in the plots is due to the Gaia scanning law (de Bruijne et al., 2010) setting a rotation period of approximately 6 h. Let us analyze each comparison, noting that we can generally separate the observations in "near" and "far" from the planets with respect to the maximum impact parameter to get 1 μas gravitational deflection:

- (PPN-)RAMOD vs TTF - we use different models for gravitational light deflection but the same description for the motion of the observer. We get huge differences (up to 500 μas) for the observations near Jupiter. This is expected since PPN-RAMOD is an early study based on a "parametrized" Schwarzschild model of the Solar System, while our TTF model includes the contribution of all major Solar System bodies. On the other hand, the two modelings give equivalent results for most observations "far" from the planets.

- TTF vs GREM - both the modelings of gravitational light deflection and the aberration caused by the motion of the observer are different. Nevertheless, as shown in (Bertone et al., 2014), we would expect not to observe sensible differences in the results. Indeed, the results of the two models are comparable at the μas level but the signature of our results far from the Solar System planets suggests substantial differences between the two models or their implementation, while the sudden shift at the maximum approach of the observation field to Jupiter hints for some discrepancy in the treatment of the satellite attitude.

4. CONCLUSIONS

This preliminary study shall give a global overview of how the Time Transfer Functions approach can be applied to the complex task of processing the observations of a space astrometry mission. The periodic signature resulting from the comparison of the abscissae computed using the TTF and GREM approaches, even if limited to the μas level, highlights some systematic discrepancy between the two implementations. On the other hand, we observe that the differences between RAMOD and our model are centered around the conjunction with major Solar System bodies. Further investigations will then focus on the implementation of the aberration and the retarded times, which was the same for RAMOD and the TTF but a different one in GREM. It also constitutes the basis for the solution of a celestial sphere based on GSR-TTF.

Acknowledgements. S. Bertone thanks UIF/UFI (French-Italian University) for the financial support of this work. S. Bertone and C. Le Poncin-Lafitte are grateful to the financial support of CNRS/GRAM and CNES/Gaia. The work of M. Crosta and A. Vecchiato has been partially funded by ASI under contract to INAF I/058/10/0 (Gaia Mission - The Italian Participation to DPAC).

5. REFERENCES

Bertone, S. & Le Poncin-Lafitte, C. , Memorie della Società Astronomica Italiana, 2012, 83, 1020

Bertone, S.; Le Poncin-Lafitte, C.; Crosta, M.; Vecchiato, A.; Minazzoli, O. & Angonin, , SF2A-2013: Proceedings of the Annual meeting of the SF2A, 2013, 155-159

Bertone, S.; Minazzoli, O.; Crosta, M.; Le Poncin-Lafitte, C.; Vecchiato, A. & Angonin, M.-C. , Classical and Quantum Gravity, 2014, 31, 015021

Bienayme, O. & Turon, C. , EAS Publications Series, 2002, 2

Brumberg, V. A. , Bristol, England and New York, Adam Hilger, 1991, 271 p., 1991

Crosta, M. & Vecchiato, A. , Astronomy and Astrophysics, 2010, 509, A37

de Bruijne, J.; Siddiqui, H.; Lammers, U.; Hoar, J.; O'Mullane, W. & Prusti, T. Klioner, S. A. , IAU Symposium, 2010, 261, 331-333

de Felice, F.; Vecchiato, A.; Crosta, M. T.; Bucciarelli, B. & Lattanzi, M. G. , Astrophysical Journal, 2006, 653, 1552-1565

Klioner, S. A. , Space Astronomical Journal, 2003, 125, 1580-1597

Lindegren, L.; Lammers, U.; Hobbs, D.; O'Mullane, W.; Bastian, U. & Hernàndez, J. , Astronomy & Astrophysics, 2012, 538, A78

Misner, C.; Thorne, K. & Wheeler, J. Gravitation San Francisco: W. H. Freeman, 1973

Teyssandier, P. & Le Poncin-Lafitte, C. , Classical and Quantum Gravity, 2008, 25, 145020

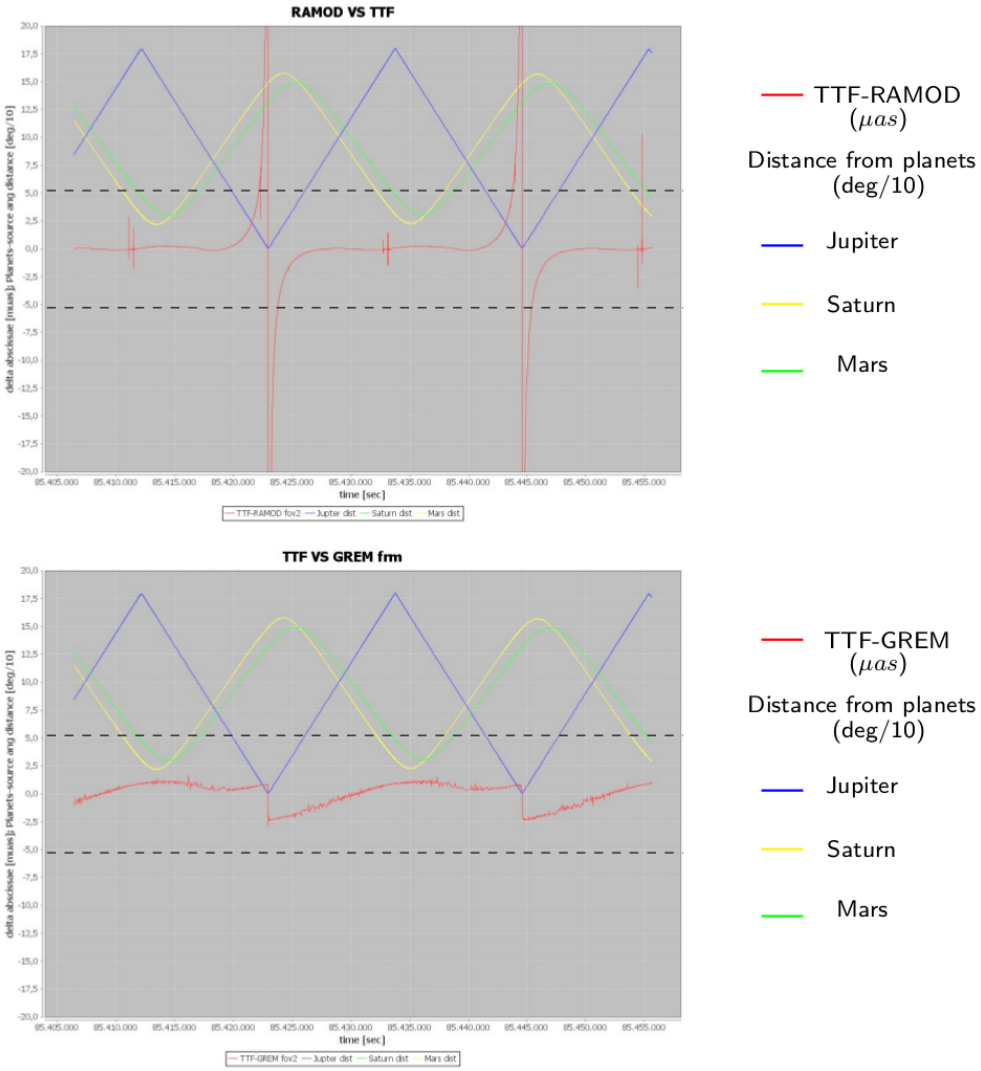

Figure 1: Difference between the abscissae resulting from the TTF and PPN-RAMOD (**top**) and GREM (**bottom**) models. The numbers on the left axis mark (1) the difference in μas between the two models - represented by the red plot - and (2) the distance in degrees/10 between a given planet and the observation. The y-axis is limited to ± 20 μas while the black dotted lines indicate a ± 5 μas difference.

Vecchiato, A.; Lattanzi, M. G.; Bucciarelli, B.; Crosta, M.; de Felice, F. & Gai, M. , Astronomy & Astrophysics, 2003, 399, 337-342

Vecchiato, A.; Abbas, U.; Bandieramonte, M.; Becciani, U.; Bianchi, L.; Bucciarelli, B.; Busonero, D.; Lattanzi, M. G. & Messineo, R. , Society of Photo-Optical Instrumentation Engineers (SPIE) Conference Series, 2012, 8451

Vecchiato, A.; Gai, M.; Lattanzi, M. G.; Crosta, M.; Becciani, U. & Bertone, S. , ArXiv e-prints, 2013

PLAN FOR VLBI OBSERVATIONS OF CLOSE APPROACHES OF JUPITER TO COMPACT EXTRAGALACTIC RADIO SOURCES IN 2014–2016

A. GIRDIUK[1], O. TITOV[2]
[1] Saint-Petersburg State University
Universitetsky prospect 28, Petrodvorets, 198504, Saint-Petersburg, Russia
e-mail: girduik@ipa.nw.ru
[2] Geoscience Australia
PO Box 378, Canberra, ACT 2601, Australia
e-mail: Oleg.Titov@ga.gov.au

ABSTRACT. Very Long Baseline Interferometry is capable of measuring the gravitational delay caused by the Sun and planet gravitational fields. The post-Newtonian parameter γ is now estimated with accuracy of $\sigma_\gamma = 2 \cdot 10^{-4}$ using a global set of VLBI data from 1979 to present (Lambert, Gontier, 2009), and $\sigma_\gamma = 2 \cdot 10^{-5}$ by the Cassini spacecraft (Bertotti et. al, 2003). Unfortunately, VLBI observations in S- and X-bands very close to the Solar limb (less than 2-3 degrees) are not possible due to the strong turbulence in the Solar corona. Instead, the close approach of big planets to the line of sight of the reference quasars could be also used for testing of the general relativity theory with VLBI. Jupiter is the most appropriate among the big planets due to its large mass and relatively fast apparent motion across the celestial sphere. Six close approaches of Jupiter with quasars in 2014-2016 were found using the DE405/LE405 ephemerides, including one occultation in 2016. We have formed tables of visibility for all six events for VLBI radio telescopes participating in regular IVS programs. Expected magnitudes of the relativistic effects to be measured during these events are discussed in this paper.

1. USING VLBI OBSERVATIONS FOR TESTING GENERAL RELATIVITY

Close approaches of the Sun and Jupiter to the apparent positions of compact extragalactic radio sources are used to estimate the PPN parameter γ by the geodetic VLBI technique. A first attempt to test the general relativity theory using the close pass of Jupiter to quasar 0201+113 has been done in 1988 (Schuh et al., 1988) at the angular distance of $3'.5$. A more famous experiment was arranged on 8 Sep 2002 (Fomalont & Kopeikin, 2003) when Jupiter approached quasar J0842+1835 at the angular distance of $3'.7$. Variations of the relative separation on the sky between this quasar and a reference radio source were measured by the VLBA network and the Effelsberg 100-meter radio telescope. Another experiment was done on 18 November, 2008 as a part of the session OHIG60 arranged by the International VLBI Service. During this session Jupiter approached quasar 1922-224 at an angular distance of $1'.2$. Four VLBI stations observed this event for about 12 hours.

2. ESTIMATION OF THE PPN-PARAMETER γ FROM THE VLBI OBSERVATIONS

Besides three classical tests, the fourth test of general relativity - the delay of a signal propagating in the gravitational field, has been proposed by Shapiro (1964) and known as the Shapiro delay. The difference between two Shapiro delays as measured with two radio telescopes gives a gravitational delay which must be considered at the standard reduction of the high-precision geodetic VLBI data. The IERS Conventions 2010 (Petit and Luzum, 2010) comprises the 'consensus' formula for the gravitational delay which is valid for the most cases unless a distant quasar and a deflecting body are too close. This formula is presented as follows

$$\bigtriangleup t_{grav} = \frac{(\gamma+1)GM}{c^3} \ln \frac{|\vec{r_1}| + \vec{s} \cdot \vec{r_1}}{|\vec{r_2}| + \vec{s} \cdot \vec{r_2}}, \quad (1)$$

where γ - the PPN-parameter of general relativity (Will, 1993), G - the gravitational constant, M - the mass of gravitational body, c - speed of light, $\vec{s}$ - the barycentric unit vector towards the radio source and

$\vec{r_i}$ - the vector between gravitating body's center of mass and i-th telescope (see i.e. Kopeikin (1990), Hellings and Shahid-Saless (1991), Klioner (1991) for more details).

An expression that links the gravitational delay and the formula for the light deflection angle (Einstain, 1916) yet to be developed. To obtain it we have expanded the gravitational delay using the Taylor times series on $o(\frac{b}{r})$. Finally, the main terms of this expansion are given by

$$\tau_{grav} = -\frac{(\gamma+1)GM}{c^3}\frac{b}{r}\cos\varphi + \frac{(\gamma+1)GM}{c^3}\frac{b}{r}\frac{\sin\varphi\sin\theta\cos A}{1-\cos\theta} + o(\frac{b^2}{r^2}), \tag{2}$$

where vectors $\vec{b}$, $\vec{r}$, and angles φ, ψ, θ and A are shown on Fig. 1 (Turyshev, 2009).

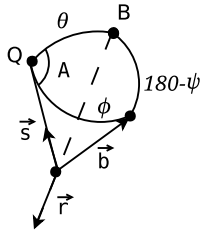

Figure 1: Schematic image shows positions of the quasar Q, deflecting body B (Jupiter), baseline vector $\vec{b}$, $\vec{r}$ - vector from Jupiter to geocenter, barycentric unit vector $\vec{s}$ to the quasar Q. Angle θ - the impact parameter, angle φ between vectors $\vec{b}$ and $\vec{s}$, angle ψ between vector $\vec{b}$ and $\vec{r}$

Surprisingly, we found the first term in (2) is equal to the term including the PPN parameter γ at the geometric delay, but with opposite sign. Keeping in mind that ($\vec{b}\cdot\vec{s} = |\vec{b}|\cos\varphi$) the formula for the total group delay recommended by the IAU (Eubanks, 1991), Petit and Luzum (2010):

$$\tau_{group} = \frac{\tau_{grav} - \frac{\vec{b}\cdot\vec{s}}{c}(1 - \frac{(\gamma+1)GM}{c^2 r} + ...)}{1 + \frac{1}{c}(\vec{s}\cdot(...))} = \frac{\tau_{\rm GR} + ...}{1 + \frac{1}{c}(\vec{s}\cdot(...))}, \tag{3}$$

where $\tau_{\rm GR}$ is the resultant contribution of the general relativity (GR) effects to the τ_{group}, includes two relativistic terms which cancel each other out. Then, $\tau_{\rm GR}$ may be written as follows

$$\tau_{\rm GR} = \frac{(\gamma+1)GM}{c^3}\ln\frac{|\vec{r_1}| + \vec{s}\cdot\vec{r_1}}{|\vec{r_2}| + \vec{s}\cdot\vec{r_2}} + \frac{(\gamma+1)GM(\vec{b}\cdot\vec{s})}{c^3 r} \tag{4}$$

or, from (2) and (4)

$$\tau_{\rm GR} = \frac{(\gamma+1)GM}{c^3}\frac{b}{r}\frac{\sin\varphi\sin\theta\cos A}{1-\cos\theta} + o(\frac{b^2}{r^2}). \tag{5}$$

Given that $\gamma = 1$ in general relativity, and ignoring $o(\frac{b^2}{r^2})$ for the sake of simplicity

$$\tau_{\rm GR} = \frac{2GM}{c^3}\frac{b\ \sin\varphi\sin\theta\cos A}{r(1-\cos\theta)}. \tag{6}$$

For the approximation of small angles (if $\theta \to 0$), (6) comes down to

$$\tau_{\rm GR} = \frac{4GM}{c^3}\frac{b\ \sin\varphi\cos A}{R}, \tag{7}$$

where $R = \theta\cdot r$ is the linear impact parameter. It is now easily to note that the term (7) corresponds to the formula of the light deflection developed by Einstein in 1916:

$$\alpha'' = \frac{4GM}{c^2 R}, \tag{8}$$

as follows

$$\tau_{\rm GR} = \alpha''\frac{b}{c}\sin\varphi\cos A. \tag{9}$$

Formula (9) proves that in the first approximation the deflection angle (8) as measured with the geodetic VLBI is independent on a baseline length. The factor $\cos A$ is individual for each baseline Fig.2, therefore, implication of the angle A in (9) is important.

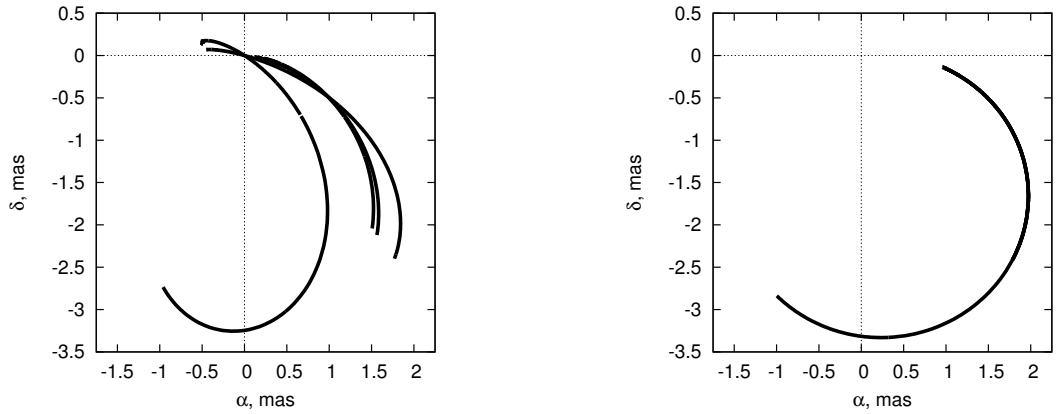

Figure 2: α''_A for baselines: Hobart26-Tsukub32, Parkes-Tsukub32, Hobart26-Parkes, Hobart26-Kokee on the left plot, and α'' on the right plot.

Fig. 2 displays the dependence of the factor $\cos A$ on the calculation of the deflection angle α'' in the plane of equatorial coordinates (α, δ). The left plot shows the angle

$$\alpha''_A = \alpha'' \cdot \cos A, \quad \alpha''_A = \frac{c\tau_{\rm GR}}{b \sin \varphi} \tag{10}$$

for four individual baselines (from the OHIG60 experiment on 18 November, 2008), where $\tau_{\rm GR}$ is calculated by (7). The right plot shows the angle as

$$\alpha'' = \frac{c\tau_{\rm GR}}{b \sin \varphi \cos A}. \tag{11}$$

All four individual curves shown on the left plot are merging to one common pathway on the right plot. Thus, it proves that the angle A must be taken into account for proper conversion from $\tau_{\rm GR}$ to α'' and vice versa as (9) and (11). This is also true for an arbitrary angle θ in (6).

3. FUTURE EVENTS AND THEIR SCHEDULING

N	quasar	date	θ''	Flux, mJy	$\frac{\alpha''}{\cos A}$, mas	small terms, pks, for b=6000 km
1	0846+184	28.08.2014	45	?	6.0	8.5
2	0918+167	09.02.2015	30	?	12.8	39.1
3	0912+171	24.05.2015	39	?	7.7	14.2
4	0920+168	08.06.2015	37	?	7.8	14.8
5	1109+070	26.03.2016	26	≈ 200	14.5	50.1
6	1101+077	09.04.2016	20(8)	≈ 150	16(46)	142(503)

Table 1: Close approaches of Jupiter to quasars in 2014-2016.

angular distance″	170	148	126	104	83	64	48	41	46	61	79	100	121	143	166
station/UT	4	5	6	7	8	9	10	11	12	13	14	15	16	17	18
Badary	+	+	+	+	+	+	+	+	+	+	+	+	+		
Svetloe, Zelenchuk				+	+	+	+	+	+	+	+	+	+	+	+
Medicina, Hartrao, Yebes						+	+	+	+	+	+	+	+	+	+
Kokee, MN-VLBA, Seshan25	+	+	+	+	+										
FD-LA-KP-OV-BR-VLBA, Pietown	+	+												+	+
SC-HN-NL-VLBA												+	+	+	+
Parkes, Tsukub32	+	+	+	+	+	+	+	+							

Table 2: Table of visibility for event on 08 June, 2015.

Six close approaches of Jupiter to quasars will happen in 2014-2016 including one occultation. Table 1 shows names of quasars, dates of event, impact parameters θ, flux densities (X-band), the maximum angles of the light deflection for the major term and the contributions of the minor terms $o(\frac{b^2}{r^2})$ in (2) for baseline length of $b = 6000$ km and $\gamma = 1$. A total occultation of the Jupiter by the quasar 1101+077 will happen on 9 April, 2016. Therefore, the numbers for the minimum angle θ and the angle θ at the limb of Jupiter are shown separately for that event. Flux densities of four quasars from Table 1 are not available presently and should be measured as soon as possible.

Table 2 presents a visibility chart for several VLBI radio telescopes for the event on 8 June, 2015. This event will last than more ten hours (when the angular distance between objects is less then $3'$). The sign '+' notes the hour when both objects will be above the level of horizon for a particular VLBI station. Due to very weak flux for the quasars in Table 1, we have preselected only large size radio telescopes to ensure a reasonable integration time (300 seconds). Thus, many small VLBI radio telescopes were discarded from Table 1 after repeated calculations of the integration time.

4. PLAN FOR VLBI OBSERVATIONS

The maximum deflection angle for the list of close approaches in Table 1 is 16 mas, or equivalent to the time delay of about 1600 pks for a baseline of 6000 km length. When the current accuracy of a single group delay as measured by VLBI is about 30 pks, the relative accuracy of γ would reach $\sigma_\gamma = 0.02$. Conservatively, it would be possible to evaluate the parameter γ with accuracy $\sigma_\gamma = 10^{-3}$ for a single VLBI experiment, if a substantial number of VLBI group delays is collected. In addition, it may be possible for one to prove existence of the minor terms from the last column of Table 1 for the two last approaches. It is necessary to organize as many large radio telescopes as possible to maximize a potential amount of observations. Therefore, we are planning to submit proposals for the large available networks (IVS, VLBA, LBA) to observe these rare events.

5. REFERENCES

Schuh, H., Fellbaum, M., Campbell, J., Soffel, M., Ruder, H., Schneider, M., 1988, "On the deflection of radio signals in the gravitational field of Jupiter", Phys. Lett. A, vol. 129, Issue 5-6, pp. 299-300.

Fomalont, E., Kopeikin, S., 2003, "The measurement of the light deflection from Jupiter: experimental results", Astronomical Journal, vol. 598, Issue 1, pp. 704-711.

Einstein, A., 1916, "Die Grundlage der allgemeinen Relativitatstheorie", Annalen der Physik, vol. 354, Issue 7, pp. 769-822

Lambert, S., Gontier, A., 2009, "On radio source selection to define a stable celestial frame", A&A , vol. 493, Issue 1, 2009, pp. 317-323

Bertotti, B., Iess, L., Tortora, P., 2003, "A test of general relativity using radio links with the Cassini spacecraft", Nature, vol. 425, Issue 6956, pp. 374-376

Shapiro, I., 1964, "Fourth Test of General Relativity", Phys. Rev. Lett., vol. 13, Issue 26, pp. 789-791

Shapiro, S., Davis, J., Lebach, D., Gregory, J., 2004, "Measurement of the Solar Gravitational Deflection of Radio Waves using Geodetic Very-Long-Baseline Interferometry Data, 1979-1999", Phys. Rev. Lett., vol. 92, Issue 12, id. 121101

Hellings, R., Shahid-Saless, B., 1991, "Relativistic Effects on VLBI Observables and Data Processing Algorithms", Proceedings of the U. S. Naval Observatory Workshop on Relativistic Models for Use in Space Geodesy, U. S. Naval Observatory, Washington, D. C., pp. 164-174.

Klioner, S., 1991, "General Relativistic Model of VLBI Observables", Proceedings of the U. S. Naval Observatory Workshop on Relativistic Models for Use in Space Geodesy, U. S. Naval Observatory, Washington, D. C., pp. 188-202.

Will, C., 1993, "Theory and Experiment in Gravitational Physics", Cambridge University Press

Eubanks, T. (ed.), 1991, Proc. of the U. S. Naval Observatory Workshop on Relativistic Models for Use in Space Geodesy, U. S. Naval Observatory, Washington, D. C.

Kopeikin, S., 1990, "Theory of relativity in observational radio astronomy", Sov. Astron., vol.34, pp. 5-9

Turyshev, S., 2009, "Relativistic gravitational deflection of light and its impact on the modeling accuracy for the Space Interferometry Mission", Astronomy Letters, vol. 35, Issue 4, pp. 215-234

Petit, G., Luzum, B. (eds.), 2010, IERS Conventions (2010), IERS Technical Note 36, Frankfurt am Main: Verlag des Bundesamts fur Kartographie und Geodasie.

ENHANCED TERM OF ORDER G^3 IN THE LIGHT TRAVEL TIME: DISCUSSION FOR SOME SOLAR SYSTEM EXPERIMENTS

P. TEYSSANDIER[1], B. LINET[2],
[1] SYRTE, Observatoire de Paris, CNRS, UPMC
61 avenue de l'Observatoire, F-75014 Paris (France)
Pierre.Teyssandier@obspm.fr
[2] Laboratoire de Mathématiques et Physique Théorique, CNRS/UMR 7350
Université François Rabelais, F-37200 Tours (France)
Bernard.Linet@lmpt.univ-tours.fr

ABSTRACT. It is generally believed that knowing the light travel time up to the post-post-Minkowskian level (terms in G^2) is sufficient for modelling the most accurate experiments designed to test general relativity in a foreseeable future. However, we have recently brought a rigorous justification of the existence of an enhanced term of order G^3 which become larger than some first-order contributions like the gravitomagnetic effect due to the rotation of the Sun or the solar quadrupole moment for light rays almost grazing the solar surface. We show that this enhanced term must be taken into account in solar system experiments aiming to reach an accuracy less than 10^{-7} in measuring the post-Newtonian parameter γ.

1. INTRODUCTION

In many experiments designed to test relativistic gravity, it is essential to calculate the light travel time $t_B - t_A$ between an emitter located at point $\boldsymbol{x}_A$ and a receiver located at point $\boldsymbol{x}_B$ as a function of $\boldsymbol{x}_A$ and $\boldsymbol{x}_B$ for a given time of reception t_B, namely the expression $\mathcal{T}_r(\boldsymbol{x}_A, t_B, \boldsymbol{x}_B)$ such that

$$t_B - t_A = \mathcal{T}_r(\boldsymbol{x}_A, t_B, \boldsymbol{x}_B). \tag{1}$$

The function $\mathcal{T}_r$ may be called the "reception time transfer function". Knowing this function enables one to model the Doppler-tracking or the gravitational bending of light involved in the determinations of the post-Newtonian parameter γ from solar system experiments (see, e.g., Le Poncin et al. 2004).

It is generally believed that projects like LATOR, ASTROD, SAGAS, ODYSSEY, GAME — designed to measure the post-Newtonian parameter γ at accuracies less than 10^{-7}— only require the determination of the light travel time up to the order G^2, with G being the Newtonian gravitational constant (see, e.g., Minazzoli & Chauvineau 2011 and refs. therein). However, this approach neglects the fact that some so-called "enhanced" term of order G^3 in the time transfer function may become comparable to the regular term of order G^2, which can be estimated as const.m^2/cr_c, with m being half the Schwarzschild radius of the central body and r_c the 0th-order distance of closest approach of the light ray. The enhancement occurs in a close superior conjunction, i.e. in the case where the emitter and the receiver are almost on opposite sides of the central body—a configuration of crucial importance in experimental gravitation (Ashby & Bertotti 2010). The third-order enhanced contribution can be recovered from the full expression of the time transfer function that we have recently obtained for a large class of static, spherically symmetric metrics generalizing the Schwarzschild solution (Linet & Teyssandier 2013). We show that this contribution must be taken into account for modelling the above-mentioned experiments.

2. TIME TRANSFER FUNCTION UP TO ORDER G^3

The relativistic contributions to the light travel time due to the non-sphericity or to the motions of the Sun and the planets have been studied within the first order in G, and may be neglected beyond the linear regime (see, e.g., Klioner 1991, Kopeikin 1997, Linet & Teyssandier 2002, Kopeikin & Schäfer 1999, Kopeikin & Mashoon 2002, Kopeikin et al. 2006, Zschocke & Klioner 2011, Bertone et al. 2014, and refs. therein). So our investigation of the higher orders of approximation is confined to the static, spherically symmetric metrics describing the gravitational field of an isolated body of mass M. Spacetime

is assumed to be covered by a single quasi-Cartesian coordinate system $x^\mu = (x^0, \boldsymbol{x})$. For convenience, we put $x^0 = ct$ and the spatial coordinates $\boldsymbol{x}$ are chosen so that the metric takes an isotropic form:

$$ds^2 = \mathcal{A}(r)(dx^0)^2 - \mathcal{B}(r)^{-1} d\boldsymbol{x}^2, \tag{2}$$

where $r = |\boldsymbol{x}|$. This metric is considered as a generalization of the Schwarzschild metric. So it is assumed that $\mathcal{A}$ and $\mathcal{B}$ may be expanded in analytical series in m/r:

$$\mathcal{A}(r) = 1 - \frac{2m}{r} + 2\beta\frac{m^2}{r^2} - \frac{3}{2}\beta_3\frac{m^3}{r^3} + \beta_4\frac{m^4}{r^4} + \sum_{n=5}^{\infty}\frac{(-1)^n n}{2^{n-2}}\beta_n\frac{m^n}{r^n}, \tag{3}$$

$$\mathcal{B}(r)^{-1} = 1 + 2\gamma\frac{m}{r} + \frac{3}{2}\epsilon\frac{m^2}{r^2} + \frac{1}{2}\gamma_3\frac{m^3}{r^3} + \frac{1}{16}\gamma_4\frac{m^4}{r^4} + \sum_{n=5}^{\infty}(\gamma_n - 1)\frac{m^n}{r^n}, \tag{4}$$

where $m = GM/c^2$ and the coefficients $\beta, \beta_3, \ldots, \beta_n, \ldots \gamma, \epsilon, \gamma_3, \ldots \gamma_n \ldots$ are generalized post-Newtonian parameters chosen so that

$$\beta = \beta_3 = \cdots = \beta_n = \cdots = 1, \quad \gamma = \epsilon = \gamma_3 = \cdots = \gamma_n = \cdots = 1 \tag{5}$$

in general relativity.

Owing to the static character of the metric, the light travel time between $\boldsymbol{x}_A$ and $\boldsymbol{x}_B$ does not depend on the time of reception t_B and equation (1) reduces to $t_B - t_A = \mathcal{T}(\boldsymbol{x}_A, \boldsymbol{x}_B)$. In what follows, it is assumed that the time transfer function is expressible in a series in powers of G having the form

$$\mathcal{T}(\boldsymbol{x}_A, \boldsymbol{x}_B) = \frac{|\boldsymbol{x}_B - \boldsymbol{x}_A|}{c} + \sum_{n=1}^{\infty}\mathcal{T}^{(n)}(\boldsymbol{x}_A, \boldsymbol{x}_B), \tag{6}$$

where $\mathcal{T}^{(n)}$ stands for the term of order G^n. Till lately, $\mathcal{T}$ was known only up to the second order in G; for $\mathcal{T}^{(1)}$, which is the well-known Shapiro time delay, see, e.g., Will 1993; for $\mathcal{T}^{(2)}$, see Le Poncin-Lafitte et al. 2004, Teyssandier & Le Poncin-Lafitte 2008 and Klioner & Zschocke 2010, which generalize the pioneering papers by John 1975, Richter & Matzner 1983 and Brumberg 1987. Very recently, however, we have proposed a new procedure enabling one to determine $\mathcal{T}$ at any order of approximation (Linet & Teyssandier 2013). Based on an iterative solution of an integro-differential equation derived from the null geodesic equations, this new procedure exclusively needs elementary integrations which may be performed with any symbolic computer program. We have obtained

$$\mathcal{T}^{(1)}(\boldsymbol{x}_A, \boldsymbol{x}_B) = \frac{(1+\gamma)m}{c}\ln\left(\frac{r_A + r_B + |\boldsymbol{x}_B - \boldsymbol{x}_A|}{r_A + r_B - |\boldsymbol{x}_B - \boldsymbol{x}_A|}\right), \tag{7}$$

$$\mathcal{T}^{(2)}(\boldsymbol{x}_A, \boldsymbol{x}_B) = \frac{m^2}{r_A r_B}\frac{|\boldsymbol{x}_B - \boldsymbol{x}_A|}{c}\left[\kappa\frac{\arccos \boldsymbol{n}_A.\boldsymbol{n}_B}{|\boldsymbol{n}_A \times \boldsymbol{n}_B|} - \frac{(1+\gamma)^2}{1 + \boldsymbol{n}_A.\boldsymbol{n}_B}\right], \tag{8}$$

$$\mathcal{T}^{(3)}(\boldsymbol{x}_A, \boldsymbol{x}_B) = \frac{m^3}{r_A r_B}\left(\frac{1}{r_A} + \frac{1}{r_B}\right)\frac{|\boldsymbol{x}_B - \boldsymbol{x}_A|}{c(1 + \boldsymbol{n}_A.\boldsymbol{n}_B)}\left[\kappa_3 - (1+\gamma)\kappa\frac{\arccos \boldsymbol{n}_A.\boldsymbol{n}_B}{|\boldsymbol{n}_A \times \boldsymbol{n}_B|} + \frac{(1+\gamma)^3}{1 + \boldsymbol{n}_A.\boldsymbol{n}_B}\right], \tag{9}$$

where

$$\boldsymbol{n}_A = \frac{\boldsymbol{x}_A}{r_A}, \qquad \boldsymbol{n}_B = \frac{\boldsymbol{x}_B}{r_B} \tag{10}$$

and κ and κ_3 are coefficients defined as

$$\kappa = 2(1+\gamma) - \beta + \frac{3}{4}\varepsilon, \qquad \kappa_3 = 2\kappa - 2\beta(1+\gamma) + \frac{1}{4}(3\beta_3 + \gamma_3). \tag{11}$$

Of course, (7) and (8) coincide with the previously known results. On the other hand, (9) is new and enables us to determine the enhancement effects appearing in a superior conjunction up to order G^3.

3. ENHANCED TERMS UP TO ORDER G^3

In the case where $\boldsymbol{x}_A$ and $\boldsymbol{x}_B$ are in almost opposite directions (superior conjunction), an elementary geometrical reasoning shows that

$$\frac{1}{1 + \boldsymbol{n}_A.\boldsymbol{n}_B} \sim \frac{2r_A r_B}{(r_A + r_B)^2}\frac{r_A r_B}{r_c^2}, \tag{12}$$

where r_c is the 0th-order distance of closest approach to the center of mass of the deflecting body, i.e. the Euclidean distance between the origin of the spatial coordinates and the line passing through $\boldsymbol{x}_A$ and $\boldsymbol{x}_B$:

$$r_c = \frac{r_A r_B |\boldsymbol{n}_A \times \boldsymbol{n}_B|}{|\boldsymbol{x}_B - \boldsymbol{x}_A|}. \tag{13}$$

It follows from (12) that the first three perturbation terms in (6) are enhanced according to the asymptotic expressions (see Ashby & Bertotti 2010 for a different method)

$$\mathcal{T}^{(1)}_{enh}(\boldsymbol{x}_A, \boldsymbol{x}_B) \sim \frac{(1+\gamma)m}{c} \ln\left(\frac{4r_A r_B}{r_c^2}\right), \tag{14}$$

$$\mathcal{T}^{(2)}_{enh}(\boldsymbol{x}_A, \boldsymbol{x}_B) \sim -2\frac{(1+\gamma)^2 m^2}{c(r_A + r_B)} \frac{r_A r_B}{r_c^2}, \tag{15}$$

$$\mathcal{T}^{(3)}_{enh}(\boldsymbol{x}_A, \boldsymbol{x}_B) \sim 4\frac{(1+\gamma)^3 m^3}{c(r_A + r_B)^2} \left(\frac{r_A r_B}{r_c^2}\right)^2. \tag{16}$$

The reliability of expansion (6) requires that inequalities

$$\left|\mathcal{T}^{(n)}(\boldsymbol{x}_A, \boldsymbol{x}_B)\right| \ll \left|\mathcal{T}^{(n-1)}(\boldsymbol{x}_A, \boldsymbol{x}_B)\right|$$

are satisfied for any n, with $\mathcal{T}^{(0)}$ being conventionally defined as $\mathcal{T}^{(0)}(\boldsymbol{x}_A, \boldsymbol{x}_B) = |\boldsymbol{x}_B - \boldsymbol{x}_A|/c$. It may be easily inferred from (14)-(16) that these inequalities are fulfilled for $n = 1, 2, 3$ as long as the distance of closest approach meets a condition as follows (see also Ashby & Bertotti 2010):

$$\frac{2m}{r_A + r_B} \frac{r_A r_B}{r_c^2} \ll 1. \tag{17}$$

Condition (17) is met in the currently designed solar system experiments. Indeed, assuming $r_B = 1$ au and $r_A \geq r_B$, we have for light rays bypassing the Sun

$$\frac{2m_\odot}{r_A + r_B} \frac{r_A r_B}{r_c^2} \leq 9.12 \times 10^{-4} \times \frac{R_\odot^2}{r_c^2}, \tag{18}$$

where $R_\odot$ is the solar radius.

4. APPLICATION TO SOLAR SYSTEM EXPERIMENTS

1. Let us examine a SAGAS-like scenario (Wolf et al. 2009) aiming to determine the post-Newtonian parameter γ at a level of accuracy reaching 10^{-8}: $r_A \approx 50$ au, $r_B \approx 1$ au. Then Shapiro's formula (7) shows that $\mathcal{T}$ must be measured with an accuracy of 0.7 ps (picosecond) in a superior conjunction configuration. Comparing this value with the contributions to the light travel time displayed in Table 1 shows that the enhanced term $\mathcal{T}^{(3)}_{enh}$ must be taken into account for rays almost grazing the Sun.

Moreover, Table 1 shows that $\mathcal{T}^{(3)}_{enh}$ can be greater than the first-order gravitomagnetic effect $|\mathcal{T}^{(1)}_S|$ due to the spinning of the Sun and than the first-order contribution $\mathcal{T}^{(1)}_{J_2}$ due to the solar mass quadrupole.

$r_c/R_\odot$	$\lvert\mathcal{T}^{(1)}_S\rvert$	$\mathcal{T}^{(1)}_{J_2}$	$\mathcal{T}^{(2)}_{enh}$	$\mathcal{T}^{(2)}_{\kappa}$	$\mathcal{T}^{(3)}_{enh}$
1	10	2	−17616	123	31.5
2	5	0.5	−4404	61.5	2
5	2	0.08	−704.6	24.6	0.05

Table 1: Numerical values in ps of the light travel time in the solar system for various values of $r_c/R_\odot$. We put $r_A = 50$ au, $r_B = 1$ au, $\gamma = 1$ and $\kappa = 15/4$. For the numerical estimates of $|\mathcal{T}^{(1)}_S|$ and $\mathcal{T}^{(1)}_{J_2}$, the light ray is assumed to propagate in the equatorial plane of the Sun. For the solar quadrupole moment, we put $J_{2\odot} = 2 \times 10^{-7}$ and for the internal angular momentum of the Sun, we take $S_\odot = 2 \times 10^{41}$ kg m^2 s^{-1} (see Komm et al. 2003). $\mathcal{T}^{(2)}_{\kappa}$ denotes the contribution due to κ in the right hand side of (8).

2. Consider now the deflection of light in a LATOR-like experiment, designed to reach an accuracy of a few 10^{-9} on γ (Turyshev et al. 2009). The propagation direction of light is determined by the gradients of the function $\mathcal{T}$ (Le Poncin-Lafitte et al. 2004). For a ray passing near the Sun, the third-order enhanced term (16) yields a contribution $\Delta\chi^{(3)}_{enh}$ to the deflection between the emitter and the receiver given by

$$\Delta\chi^{(3)}_{enh} \sim c\left|\boldsymbol{\nabla}_{\boldsymbol{x}_A}\mathcal{T}^{(3)}_{enh}(\boldsymbol{x}_A,\boldsymbol{x}_B)+\boldsymbol{\nabla}_{\boldsymbol{x}_B}\mathcal{T}^{(3)}_{enh}(\boldsymbol{x}_A,\boldsymbol{x}_B)\right| \sim \frac{16(1+\gamma)^3m^3}{r_c^3}\frac{r_Ar_B}{(r_A+r_B)^2}\frac{r_Ar_B}{r_c^2}. \tag{19}$$

This estimate gives for $r_A \approx 1$ au, $r_B \approx 1$ au and $r_c \approx R_\odot$:

$$\Delta\chi^{(3)}_{enh} \approx 3\,\mu\text{as}. \tag{20}$$

Such a contribution cannot be neglected in the discussion since determining γ at the level 5×10^{-9} requires to measure the light deflection with an accuracy about 0.01 μas.

3. The same conclusion is valid for an astrometric mission like GAME aiming to reach a 10^{-7} level, or better, in measuring γ (Gai et al., 2012). The limit of (19) when $r_A \to \infty$ yields a third-order contribution to the deflection of a light ray coming from infinity and observed at $\boldsymbol{x}_B$ given by

$$\Delta\chi^{(3)}_{enh} \sim \frac{16(1+\gamma)^3m^3}{r_c^3}\left(\frac{r_B}{r_c}\right)^2. \tag{21}$$

Taking $r_B \approx 1$ au and $r_c \approx R_\odot$, we find a contribution larger than the expected precision of 0.2 μas :

$$\Delta\chi^{(3)}_{enh} \approx 12\,\mu\text{as}. \tag{22}$$

It may be noted that (22) is in good agreement with the numerical estimate obtained in Hees et al. 2013.

5. CONCLUSION

Our explicit calculation of the time transfer function up to order G^3 for a large class of parametrized static, spherically symmetric metrics enables us to determine the enhanced contributions in the configurations of superior conjunction. It may be concluded that the third-order enhanced term given by (16) must be taken into account for modelling the future measurements of γ from solar system experiments.

6. REFERENCES

Ashby, N., Bertotti, B., 2010, Class. Quantum Grav., 27, 145013 (27 pp).
Bertone, S., et al., 2014, Class. Quantum Grav., 31, 015021 (13 pp).
Brumberg, V. A., 1987 Kinematics Phys. Celest. Bodies, 3, pp. 6-12.
Gai, M., et al., 2012, Exp. Astron., 34, pp. 165-180.
Hees, A., Bertone, S., Le Poncin-Lafitte, C., 2013, Journées 2013 "Systèmes de référence spatio-temporels".
John, R. W., 1975, Exp. Tech. Phys., 23, pp. 127-140.
Klioner, S. A., 1991, Sov. Astron., 35, pp. 523-530.
Klioner, S. A., Zschocke, S., 2010, Class. Quantum Grav., 27, 075015 (25 pp).
Komm, R., Howe, R., Durney, B. R., Hill, F., 2003, Astrophys. J., 586, pp. 650-662.
Kopeikin, S. M., 1997, J. Math. Phys., 38, pp. 2587-2601.
Kopeikin, S. M., Schäfer, G., 1999, Phys. Rev. D, 60, 124002 (44 pp).
Kopeikin, S. M., Mashhoon, B., 2002, Phys. Rev. D, 65, 064025 (20 pp).
Kopeikin, S. M., Korobkov, P., Polnarev, A., 2006, Class.Quantum Grav., 23, pp. 4299-4322.
Le Poncin-Lafitte, C., Linet, B., Teyssandier, P., 2004 Class. Quantum Grav., 21, pp. 4463-4483.
Le Poncin-Lafitte, C., Teyssandier, P., 2008, Phys. Rev. D, 77, 044029 (7 pp).
Linet, B., Teyssandier, P., 2002, Phys. Rev. D, 66, 024045 (14 pp).
Linet, B., Teyssandier, P., 2013, Class. Quantum Grav., 30, 175008 (23 pp).
Minazzoli, O., Chauvineau, B., 2011, Class. Quantum Grav., 28, 085010 (27 pp).
Richter, G. W., Matzner, R. A., 1983 Phys. Rev., D 28, pp. 3007-3012.
Teyssandier, P., Le Poncin-Lafitte, C., 2008, Class. Quantum Grav. 25, 145020 (12 pp).
Turyshev, S. G., et al., 2009, Exp. Astron., 27, pp. 27-60.
Will, C. M., 1993, Theory and Experiment in Gravitational Physics (Cambridge University Press)
Wolf, P., et al., 2009, Exp. Astron., 23, pp. 651-687.
Zschocke, S., Klioner, S. A., 2011, Class. Quantum Grav., 28, 015009 (11 pp).

RADIO QUASARS AND THE LINK WITH GAIA

J. ROLAND
Institut d'Astrophysique de Paris
98 Bis Bd Arago, 75014 Paris, France
e-mail: jacques.roland.7@gmail.com

ABSTRACT. Modeling VLBI ejections of nuclei of extragalactic radio sources, indicates that their nuclei contain a binary black hole system. One can derive the distance and the positions of the two black holes in the plane of the sky. We can also use the RMS of the time series of the ICRF2 survey to obtain an estimate of the structure and the size of the nuclei. We will discuss the possible problems to link VLBI observations and GAIA optical observations of radio quasars if they contain a binary black hole system.

1. STRUCTURE OF COMPACT RADIO SOURCES MODELING VLBI EJECTIONS

VLBI observations of compact radio sources show that the ejection of VLBI components does not follow a straight line but undulates. These observations suggests a precession of the accretion disk. To explain the precession of the accretion disk, we will assume that the nucleus of radio sources contains a binary black hole system (BBH system) .

A BBH system produces 2 main perturbations of the VLBI ejection due to:

1. the precession of the accretion disk and
2. the motion of the two black holes around the gravity center of the BBH system.

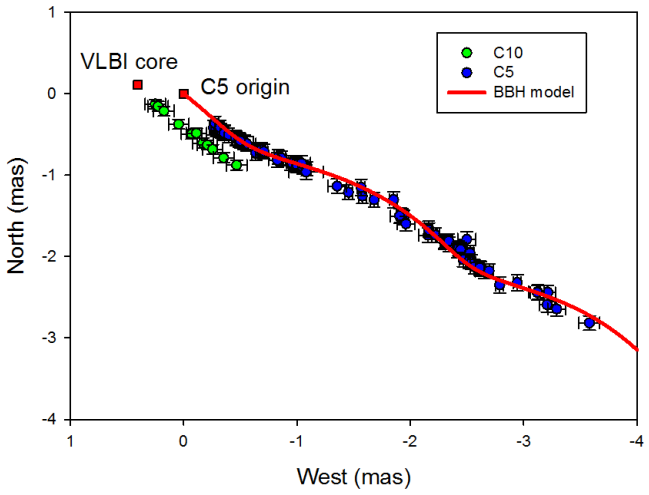

Figure 1: Using the MOJAVE data (Lister & al 2009), we plot the trajectories of C5 and C10. Component C10 is ejected by the VLBI core and component C5 is ejected with a large offset from the VLBI core. Components C5 and C10 follow two different trajectories and are ejected from different origins, indicating that the nucleus of 3C 279 contains a BBH system.

The presence of a BBH system, induces several consequences, which are:

1. the 2 black holes can have accretion disks with different angles with the plane of rotation of the BBH system and can eject VLBI components; in that case we will observe two different families of trajectories, a good example of a source showing 2 families of trajectories is 3C 279 (see Figure 1),

2. if the VLBI core is associated with one black hole and if the ejection of the VLBI component comes from the second black hole, there will be an offset between the VLBI core and the origin of the ejection of the VLBI component; this offset will correspond the radius of the BBH system.

We model the ejection of the VLBI component using a geometrical model taking into account the two main perturbations due to the BBH system. We determine the free parameters of the model comparing the observed coordinates of the VLBI component with the calculated coordinates of the model.

Modeling the ejection of VLBI components using a BBH system has been developed in previous articles, Britzen & al. 2001 modeled 0420-014, Lobanov & Roland 2005 modeled 3C 345, Roland & al. 2008 modeled 1803+784, and Roland & al. 2013 modeled 3C 279 and 1823+568.

Results concerning 3C 279 are shown in Figure 1.

2. STRUCTURE USING THE RMS OF THE TIME SERIES OF THE ICRF2 SURVEY

The ICRF2 Survey (International Celestial Reference Frame) has been obtained using about 6.5 millions of VLBI observations of about 3400 radio sources (Fey & al. 2010).

Important information concerning the structure of the nucleus can be obtained using the RMS of the time series of the ICRF2 survey (Lambert 2013 and http://ivsopar.obspm.fr/). To begin, let us take the example of the source 1803+784. The RMS time series of 1803+784 are presented in Figure 2.

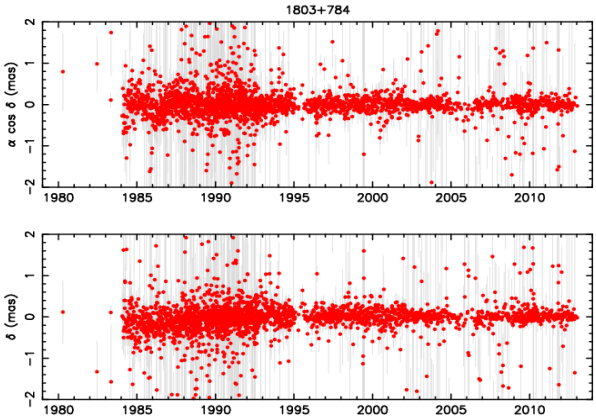

Figure 2: The RMS time series for the coordinates of 1803+784 are ≈ 0.12 *mas* and ≈ 0.12 mas. It has been shown by Roland & al 2008 that the nucleus of 1803+784 contains a BBH system of size ≈ 0.10 mas.

More generally, using the results obtained from the modeling of VLBI ejections, it can been shown that the RMS time series are correlated with the structure of the nucleus (see Table 1). Indeed, the RMS of the time series is always larger than the size of the BBH system deduced from modeling VLBI ejections.

Table 1 : Structures of compact sources and RMS time series

Source	Structure	RMS time series
PKS 0420-014	BBH system : $R_{bin} \approx 0.12$ mas (Britzen et al 2001)	0.32 * 0.47
3C 345	BBH system : (Lobanov & Roland 2005)	0.71 * 0.69
S5 1803+784	BBH system : $R_{bin} \approx 0.10$ mas (Roland et al 2008)	0.12 * 0.12
1823+568	BBH system : $R_{bin} \approx 0.06$ mas (Roland et al 2013)	0.16 * 0.21
3C 279	BBH system : $R_{bin} \approx 0.42$ mas (Roland et al 2013)	0.90 * 1.11
PKS 1741-03	BBH system : $R_{bin} \approx 0.18$ mas (Work in progress)	0.20 * 0.23
1928+738	BBH system : $R_{bin} \leq 0.23$ mas (Work in progress)	0.22 * 0.35
3C 345	3 BH or 2 BBH systems (Work in progress)	0.71 * 0.69

The ICRF survey has been done at 8 GHz and the smallest RMS time series found are ≈ 0.1 mas at this frequency. The IRCF survey is now going to be done at 22 GHz and 32 GHz and one can expect to reach for point source sources RMS time series of 0.03 mas. If the smallest RMS time series at these frequencies are, say, ≈ 0.08 mas, this will mean that the sources are not point sources but contain BBH systems which sizes are $R_{bin} \approx 0.07$ mas.

So we can use the RMS time series to look for compact radio sources.

3. LINK BETWEEN VLBI OBSERVATIONS AND GAIA

GAIA will be able to provide a very precise position but has a relatively low resolution (compared to VLBI). For point sources which magnitude is $m_v \approx 15$ the precision of the position will be ≈ 0.02 mas, but for point sources which magnitude is $m_v \approx 18$ the precision of the position will be ≈ 0.10 mas.

The optical emission from a radio quasar can be due to

- the non thermal core (optical emission of the ultra relativistic $e^- e^+$ ejected relativistically),
- the black body radiation of the central parts of the accretion disk,
- broad line region and
- the stars.

The optical emission of radio quasars is dominated by the non thermal emission (synchrotron and/or inverse Compton emissions). This result is indicated by the power law distribution of the spectrum from the radio to the Xray emission and the linear polarization of the emission (see the spectrum of 3C 273 shown in Figure 3).

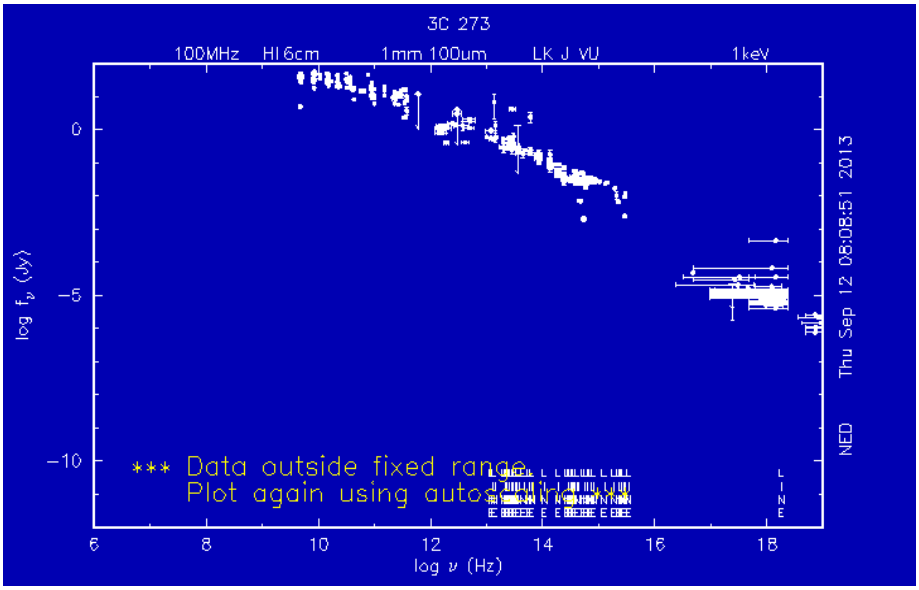

Figure 3: The spectrum of 3C 273. The spectrum shows a power law distribution between the radio to X and γ rays, indicating a non thermal origin. The radiation is linearly polarized. This caption is from the NASA/IPAC Extragalactic Data Base (http://ned.ipac.caltech.edu/)

Due to opacity effect, the optical core and the radio core positions are not the same. However, if the inclination angle of the source is very small, i.e. $i_o \leq 3^o$, opacity effect will be small. The position of the black hole emitting the VLBI jet is not the same that the positions of the optical core and the radio core.

If the nucleus of the radio quasar contains a BBH system and if the two black holes are active, three different cases can happen:

1. the radio core and the optical core are associated with the same BH, then the distance between the radio core and the optical core depends on the opacity effect which will be small if the inclination angle is small,

2. the radio core and the optical core are associated with different black holes, then the distance between the radio core and the optical core is more or less the size of the BBH system (corrected by the possible opacity effect), and

3. the two black holes are emitting in the optical, then GAIA will provide a mean position between the two optical cores ! This position will be different from the positions of the two radio cores.

as quasars are strongly and rapidly variables, during the 5 years of observations of GAIA, the 3 different cases can happen for a given source !

4. CONCLUSION

To link, with a precision of ≤ 150 μas, the Local Reference Frame obtained by GAIA and the Reference Frame provided by distant radio quasars, one has to use radio quasars which magnitude is $m_v \leq 18$ and which are a priori the most compact.

Ideally, one has to define a sample of at least 10 radio quasars characterized by:

- $m_v \leq 18$,
- a RMS of the time series $RMS \leq 200$ μas and
- a declination $-90^o \leq \delta \leq 90^o$,

which is currently not possible. Indeed, if we look for sources which have a RMS of the time series $RMS \leq 200$ μas, we find only 10 sources with a declination $\delta > 0^o$. To obtain sources with $\delta < 0^o$, one has to look to sources with a RMS of the time series $RMS \leq 500$ μas ! This is due to the lack of VLBI observations in the south hemisphere.

Modeling VLBI ejection using sources from this sample can be done if each VLBI component has been observed at least 20 times and if the component can be followed on a path long enough. It has the advantage to provide the size of the BBH system, the positions of the two black holes and the inclination of the radio source.

During the five years of GAIA observations it will be crucial to improve the number and the quality (UV coverage) of VLBI observations of radio sources with negative declinations in order to model the VLBI ejections and to reduce significantly the RMS of the time series.

5. REFERENCES

Britzen, S., Roland, J., Laskar, J., 2001, "On the origin of compact radio sources. The binary black hole model applied to the gamma-bright quasar PKS 0420-014", A&A, 374, 784

Fey, A.L., Gordon, D.G., Jacobs, C.S. & al., 2009, "International Earth Rotation and Reference Systems Service (IERS) Technical Note 35 " in Bundesamts für Kartographie und Geodäsie, Ed. Frankfurt am Main

Lambert, S., 2013, "Time stability of the ICRF2 axes", A&A, 553, 122

Lister, M. L., Aller, H. D., Aller, M. F., & al, 2009, "MOJAVE: Monitoring of Jets in Active Galactic Nuclei with VLBA Experiments. V. Multi-Epoch VLBA Images", AJ, 137, 3718-3729

Lobanov, A.P., Roland, J., 2005, "A supermassive binary black hole in the quasar 3C 345", A&A, 431, 831

Roland, J., Britzen, S., Kudryavtseva, N.A., Witzel, A., Karouzos, M., 2008, "Modeling nuclei of radio galaxies from VLBI radio observations. Application to the BL Lac Object S5 1803+784", A&A, 483, 125

Roland, J., Britzen, S., Caproni, A., Fromm, C., Glück, C., Zensus, A., 2013, "Binary black holes in nuclei of extragalactic radio sources", A&A, 557, 85

ABERRATION IN PROPER MOTIONS FOR GALACTIC STARS

J.-C. LIU, Y. XIE, Z. ZHU
School of Astronomy and Space Science, Nanjing University
22 Hankou Rd., 210093 Nanjing, China
e-mail: jcliu@nju.edu.cn

ABSTRACT. Accelerations of both the solar system barycenter (SSB) and stars in the Milky Way cause a systematic observational effect on the stellar proper motions, which was first studied by J. Kovalevsky (2003). This paper intends to extend that work and aims to estimate the magnitude and significance of the aberration in proper motions of stars, especially in the region near the Galactic center (GC). We adopt two models for the Galactic rotation curve to evaluate the aberrational effect on the Galactic plane. We show that the effect of aberration in proper motions depends on the galactocentric distance of stars; it is dominated by the acceleration of stars in the central region of the Galaxy. Then we investigate the applicability of the theoretical expressions: if the orbital period of stars is only a fraction of the light time from the star to the SSB, the expression with approximation proposed by Kovalevsky is not appropriate. With a more suitable formulation, we found that the aberration has no effect on the determination of the stellar orbits on the celestial sphere. In the future this aberrational effect under consideration should be considered with high-accurate astrometry, particularly in constructing the Gaia celestial reference system realized by Galactic stars.

1. INTRODUCTION

It is well known that the velocity of the solar system barycenter (SSB) is responsible for the first order aberration in position of about $150''$, however this value is a constant and not detectable. In addition, the acceleration of an observer produce aberrational effect in proper motions of celestial objects (Kovalevsky 2003; Kopeikin & Makarov 2006), which is a variational effect with respect to the aberration in position. Given astrometric measurements at micro-arcsecond level, the aberration in proper motions resulting from the acceleration of the SSB has impact on the celestial reference system realized by extragalactic radio sources (ICRS) and Earth rotation parameters, thus should be considered in the near future (Titov 2010; Liu et al. 2012).

In our Galaxy, the aberration in proper motions for stars can be written as the first time derivative of the aberration in positions:

$$\Delta\dot{\boldsymbol{p}}^{\rm S} = \frac{1}{c}\boldsymbol{p}\times[(\boldsymbol{a}^{\rm B}-\boldsymbol{a}^{\rm S})\times\boldsymbol{p}], \tag{1}$$

where $\boldsymbol{p}$ is the position vector of the star, and the superscript 'B' and 'S' represent the SSB and star, respectively. The proper motion (independent of distance of stars) resulting from $\boldsymbol{a}^{\rm B}$ is the same as the effect for extragalactic sources, which forms a dipolar field on the celestial sphere from the anti-Galactic center to the Galactic center (GC). The second part corresponding to the acceleration $\boldsymbol{a}^{\rm S}$ is more complicated and will be discussed in detail in the following.

Projecting Eq. (1) to the local tangential coordinate system (x, y, z) in the Galactic coordinate system, the aberrational proper motions in longitude and latitude directions can be derived as follows:

$$\Delta\mu_\ell\cos b = \frac{1}{c}\boldsymbol{p}\times[(\boldsymbol{a}^{\rm B}-\boldsymbol{a}^{\rm S})\times\boldsymbol{p}]\cdot\boldsymbol{e}_\ell\ ; \qquad \Delta\mu_b = \frac{1}{c}\boldsymbol{p}\times[(\boldsymbol{a}^{\rm B}-\boldsymbol{a}^{\rm S})\times\boldsymbol{p}]\cdot\boldsymbol{e}_b, \tag{2}$$

where $\boldsymbol{e}_\ell$, $\boldsymbol{e}_b$ are the unit vectors in the direction of increasing longitude and latitude.

For conciseness, we define following parameters in the unit of proper motions:

$$A^{\rm B} = \frac{a^{\rm B}}{c} = \frac{V_0^2}{cR_0} \simeq 5\,\mu{\rm as\,yr}^{-1}\ ; \qquad A^{\rm S} = \frac{a^{\rm S}}{c} = \frac{a^{\rm B}}{c}\frac{a^{\rm S}}{a^{\rm B}} = A^{\rm B}\frac{a^{\rm S}}{a^{\rm B}} = \gamma A^{\rm B}, \tag{3}$$

where the former quantity $A^{\rm B}$ (constant) corresponding to the SSB was called the 'Galactic aberration constant' in Malkin (2011) and the parameter γ is the ratio of the accelerations of the star and SSB.

Using the above formulas and definitions, the proper motions in Eq. (2) can be written as:

$$\Delta\mu_\ell \cos b = A^{\rm B}\boldsymbol{p} \times [(\boldsymbol{e}_{X_{\rm G}} - \gamma\boldsymbol{\rho}) \times \boldsymbol{p}] \cdot \boldsymbol{e}_\ell \ ; \quad \Delta\mu_b = A^{\rm B}\boldsymbol{p} \times [(\boldsymbol{e}_{X_{\rm G}} - \gamma\boldsymbol{\rho}) \times \boldsymbol{p}] \cdot \boldsymbol{e}_b, \tag{4}$$

in which $\boldsymbol{e}_{X_{\rm G}}$ and $\boldsymbol{\rho}$ are the unit vectors in the direction of $\boldsymbol{a}^{\rm B}$ and $\boldsymbol{a}^{\rm S}$, respectively; both pointing to the GC; R_0 and V_0 are the Galactocentric distance and rotation velocity of the SSB. For extragalactic radio sources whose accelerations are zero or too small to be detected (i.e. $\gamma = 0$), Eq. (4) degenerates into the form of the pure dipolar proper motion field.

2. ABERRATION IN PROPER MOTIONS BASED ON ROTATION CURVES

In order to evaluate the magnitude of aberrational proper motions, it is necessary to know the accelerations of stars, or equivalently the parameter γ. Since accelerations of stars are not available one by one, certain statistical models for the Galactic kinematics, such as rotation curves, are necessarily be used. For stars in the Galaxy, especially for those on the Galactic disk, every star revolves more or less around the GC. One simplified case is such that the rotation curve is completely flat throughout the Galaxy (see Fig. 1a). In this case, $\gamma = R_0/d$ (d is the distance from the star to the GC.), so that we have

$$\Delta\mu_\ell \cos b = -A^{\rm B}\left[1 - \left(\frac{R_0}{d}\right)^2\right] \sin\ell \ ; \quad \Delta\mu_b = -A^{\rm B}\left[1 - \left(\frac{R_0}{d}\right)^2\right] \cos\ell \sin b. \tag{5}$$

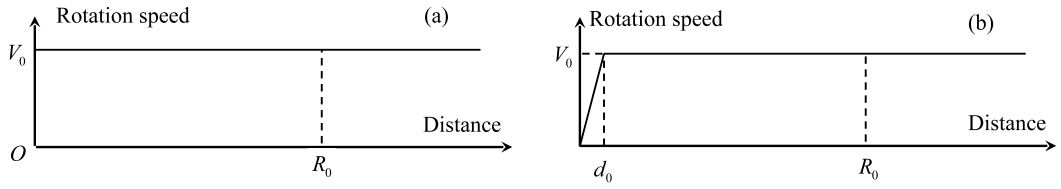

Figure 1: The simplified rotation curves of the Galaxy. The origin of both plots is the Galactic center. (a) Flat rotation curve at V_0; (b) linear rotation curve up to d_0 and then constant from d_0 at V_0.

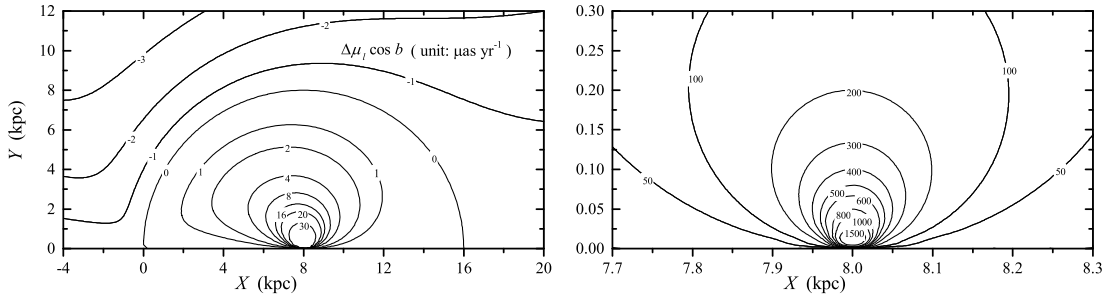

Figure 2: The amplitude of aberration in proper motions on the Galactic plane ($b = 0$, Eq. 5) corresponding to the flat rotation curve in Fig. 2(a). The Galactic center is located at (8.0, 0) and the SSB is at the (0, 0) point. The left plot covers almost the whole Galactic plane, while the right plot is the enlarged drawing for the vicinity of the Galactic center.

In the brackets of the above expressions, the second terms are inversely proportional to the squared distance of the star to the Galactic center. This means that the proper motions increase as the stars are closer to the Galactic center. Figure 2 shows the contour plot of $\Delta\mu_\ell \cos b$ for stars on the Galactic plane. The left panel is for a wider range up to 12 kpc in X and Y directions centered on the Galactic center, and the right panel is enhancement around the center up to 300 pc.

In contrast to the flat rotation curve, a more reasonable approximation of the rotation curve is the one as shown in Fig. 1b, which separate the bulge from the disk at the boundary $d = d_0$. Out of the

bulge, the rotation curve is almost flat. The expression of the rigid rotation acceleration of stars within the boundary d_0 is $\gamma = R_0 d/d_0^2$. It is proportional to the galactocentric distance of the star (d), while in the previous case it is in inverse proportion to d. Then we obtain the resulting aberrational proper motions in Galactic longitude and latitude:

$$\Delta\mu_\ell \cos b = -A^{\rm B}\left[1-\left(\frac{R_0}{d_0}\right)^2\right]\sin\ell\ ; \quad \Delta\mu_b = -A^{\rm B}\left[1-\left(\frac{R_0}{d_0}\right)^2\right]\cos\ell\sin b\ \ (d<d_0). \tag{6}$$

The term $1-(R_0/d_0)^2$ in brackets is a constant of an order of 1000 (if $R_0 = 8.0$ kpc and $d_0 = 0.3$ kpc), consequently the proper motions are independent of distance of stars in the rigid rotation mode. Adopting $d_0 = 0.3\,$kpc, the magnitude of proper motions are shown in Fig. 3 right panel. In this area, the largest proper motion is only about $150\,\mu{\rm as\,yr}^{-1}$ at $X = 8.0\,$kpc and $Y = d_0$.

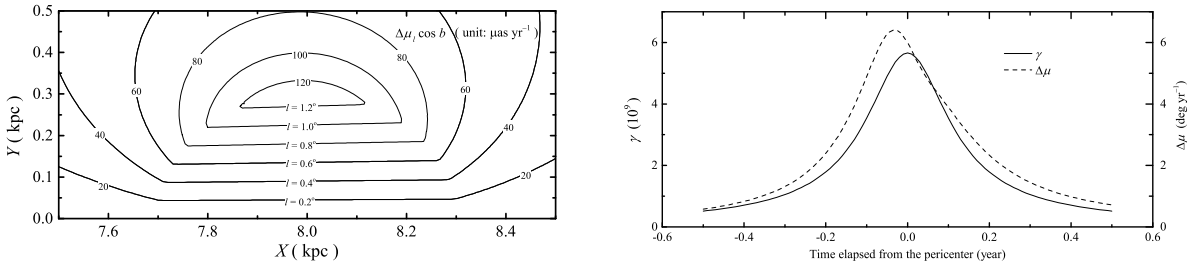

Figure 3: Left: The amplitude of aberration in proper motions on the Galactic plane ($\ell = 0$) corresponding to the rotation curve in Fig. 1b. Right: The parameter γ and the aberrational proper motions for the S0-2 star near the pericenter of the orbit. $\Delta\mu$ represents the general proper motion.

3. PROPER USE OF THE EXPRESSIONS

Conceptually, the aberration in proper motions resulting from the stellar acceleration $\boldsymbol{a}^{\rm S}$ is the variation of projected velocity on the celestial sphere during the light time from the star to the observer (SSB). Written in Eq. (1), the acceleration of the star $\boldsymbol{a}^{\rm S}$ should be a constant vector, which means that the motion of the star must be (or approximately) rectilinear during the time span of light travel. To this end, we note that Eq. (1) and follow-up expressions that describe the spurious proper motions are simplified, and should be used with caution, especially for short periodic stars.

A typical example is the S0-2 star in the central cluster of our Galaxy, the well determined orbital solutions of which has been provided by Schödel et al. (2003). We have calculated the expressions for the aberration in proper motions in the equatorial coordinate system using Eq. (1) and found

$$\Delta\mu_\alpha \cos\delta \simeq \gamma A^{\rm B}\frac{\Delta x}{d}\ ; \quad \Delta\mu_\delta \simeq \gamma A^{\rm B}\frac{\Delta y}{d}, \tag{7}$$

where Δx and Δy is the coordinates of S0-2 in the tangential coordinate system centered on GC. Shown in Fig. 3 right panel, the parameter γ for S0-2 is on the order of $10^7 - 10^9$, and the proper motions can be up to several degrees per year. This appears unrealistic because the orbital period of S0-2 is only about 15 yr, while the light time from S0-2 to the SSB is about $T_{\rm L} \simeq 8000\,{\rm pc} \times 3.26\ {\rm yr\,pc}^{-1} = 26000\,{\rm yr}$, which is about 1700 times larger than P ($\tau \simeq 1/1700$). The calculation using Eq. (1) extrapolates the acceleration at the staring point to the whole time span as if the acceleration was a constant, and this inappropriate procedure causes accumulated high proper motion corrections.

For short periodic stars, after a time span covering integer multiple of orbital periods, the star moves back to the same point on the orbit which means that its velocity is the same as it is at the beginning of that time span, and the corresponding effect of aberration resulting from the acceleration of the star is zero. Only orbital period fraction ($P_{\rm f}$ = remainder of $T_{\rm L}$ divided by P) within the light time is responsible for effective aberration in proper motions, and Eq. (1) should be written as a more suitable form:

$$\Delta\dot{\boldsymbol{p}}^{\rm S} = \frac{1}{c}\boldsymbol{p}\times\left[\left(\boldsymbol{a}^{\rm B}-\frac{\boldsymbol{v}_2^{\rm S}-\boldsymbol{v}_1^{\rm S}}{T_{\rm L}}\right)\times\boldsymbol{p}\right], \tag{8}$$

where $\boldsymbol{v}_1^{\rm S}$ and $\boldsymbol{v}_2^{\rm S}$ are the velocities of the star on its orbit at the beginning (t_1) and the end (t_2) of the effective fraction of the period, respectively. To calculate the value for Eq. (8), it would require that the accuracy of the light time be measured to an accuracy at least better than $P_{\rm f}$.

Note that most of the short periodic stars are near the Galactic center, where the influence caused by the acceleration of the SSB can be ignored, we only consider the effect resulting from the motion of the star. Projecting Eq. (8) on the celestial sphere, we obtain the aberrational proper motions in the equatorial coordinate system:

$$\Delta\mu_\alpha\cos\delta = \frac{1}{\kappa}\frac{v_{2,x}-v_{1,x}}{r}, \quad \Delta\mu_\delta = \frac{1}{\kappa}\frac{v_{2,y}-v_{1,y}}{r}, \tag{9}$$

where the subscript x, y means that the velocity vectors are decomposed in the tangential coordinate system that is established by ($\boldsymbol{e}_\alpha$, $\boldsymbol{e}_\delta$, $\boldsymbol{e}_r$) triad, and $\kappa = 4.74047$ is a constant factor for unit transformation if proper motions are in unit of $\mu{\rm as\,yr^{-1}}$, velocities in $\rm km\,s^{-1}$, and r in pc. Because the true proper motions of the star at t_1 are such that:

$$[\Delta\mu_\alpha\cos\delta]_1^{\rm true} = \frac{1}{\kappa}\frac{v_{1,x}}{r}, \quad [\Delta\mu_\delta]_1^{\rm true} = \frac{1}{\kappa}\frac{v_{1,y}}{r}, \tag{10}$$

we have the observed proper motions at t_1 by adding the corrections in Eq. (9):

$$[\Delta\mu_\alpha\cos\delta]_1^{\rm obs} = \frac{1}{\kappa}\frac{v_{2,x}}{r} = [\Delta\mu_\alpha\cos\delta]_2^{\rm true} \;\; ; \quad [\Delta\mu_\delta]_1^{\rm obs} = \frac{1}{\kappa}\frac{v_{2,y}}{r} = [\Delta\mu_\delta]_2^{\rm true}. \tag{11}$$

This shows that the effect of aberration in proper motions only changes the observed phase of the star on the stellar orbit. It does not change the shape of the orbit on the celestial sphere, although we can not measure the exact value of the correction.

4. DISCUSSION AND CONCLUSION

In this paper we have improved the results of Kovalevsky (2003) to a more concise form. Two kinds of rotation curves of the Galactic disk were adopted to examine the property of the aberrational proper motions, especially in the vicinity of the Galactic center. A flat rotation curve starting from the Galactic center leads to enlargement of the proper motions to $1000\,\mu{\rm as\,yr^{-1}}$ at $d = 0.2$ kpc, while the more realistic rotation curve rising linearly from the Galactic center to the bulge-disk boundary gives limited proper motions up to about $150\,\mu{\rm as\,yr^{-1}}$. If the period of the stellar orbit is shorter than the light time from the star to the observer, the assumption of constant acceleration in this period of time does not hold. In this circumstances, one need more basic expression as written in Eq. (8). The magnitudes of the aberration in proper motions are difficult to measure, however we have shown that there is no effect on determining the orbit of stars.

Because the amplitudes of the systematic proper motions is at some places much larger than the Gaia accuracy for the proper motion measurements, this effect should be considered to eliminate the rotation and distortion in the future Gaia celestial reference system realized by stars in optical bandpass. However, this would be possible only if the accelerations of stars are known with satisfactory precision, or we have more reliable kinematics of the Galaxy for modeling those accelerations.

5. REFERENCES

Kovalevsky, J., 2003, "Aberration in proper motions", A&A 404, 743-747

Kopeikin, S. M., Makarov, V. V., 2006, "Astrometric Effects of Secular Aberration", AJ, 131, 1471-1478

Liu, J.-C., Capitaine, N., Lambert, S. B., Malkin, Z., Zhu, Z., 2012, "Systematic effect of the Galactic aberration on the ICRS realization and the Earth orientation parameters", A&A , 548, A50

Malkin, Z. M., 2011, "The influence of galactic aberration on precession parameters determined from VLBI observations", Astronomy Report, 55, 810-815

Schödel, R., Ott, T., Genzel, R., Eckart, A., Mouawad, N., Alexander, T., 2003, "Stellar dynamics in the central arcsecond of our Galaxy", ApJ, 596, 1015-1034

Titov, O., 2010, "Secular aberration drift and IAU definition of International Celestial Reference System", MNRAS, 407, L46-L48

ON THE DEFINITION OF A REFERENCE FRAME AND THE ASSOCIATED SPACE IN A GENERAL SPACETIME

M. ARMINJON
Laboratory "Soils, Solids, Structures, Risks"
(CNRS, UJF, Grenoble-INP), Grenoble, France
e-mail: Mayeul.Arminjon@3sr-grenoble.fr

ABSTRACT. A reference frame F can be defined as an equivalence class of spacetime charts (coordinate systems) having a common domain U and exchanging by a spatial coordinate change. The associated physical space is made of the world lines having constant space coordinates in any chart of the class. This is a local definition. The data of a global 4-velocity field v defines a global "reference fluid". The associated global physical space is made of the maximal integral curves of that vector field. Assume that the local and global spaces correspond with the same three-dimensional network of observers. In that case, the local space can be identified with a part (an open subset) of the global space.

1. INTRODUCTION

A reference frame is essentially a three-dimensional network of observers equipped with clocks and meters. To any reference frame, one should be able to associate some three-dimensional *space,* in which the observers of the network are at rest (even though their mutual distances may depend on time). Clearly, both notions are fundamental ones for physics. In the relativistic theories of gravitation, the spacetime metric tensor $g_{\mu\nu}$ is a field, thus it depends in particular on time. Hence, one expects that relevant reference frames are not rigid. The relevant notion is that of a *reference fluid,* given by a 4-velocity field v on spacetime: v is the unit tangent vector field to the world lines of the observers belonging to the network (Cattaneo, 1958). In standard practice, one often admits implicitly that a reference frame can be fixed by the data of one *coordinate system* (or *chart*). The link with the definition by the 4-velocity field v tangent to a network of observers was also given by Cattaneo (1958). Any admissible chart on the spacetime, $\chi : X \mapsto (x^\mu)$ $(\mu = 0, ..., 3)$, defines a unique network of observers, whose world lines are

$$x^j = \text{Constant } (j = 1, 2, 3),\ x^0 \text{ variable}. \tag{1}$$

The corresponding four-velocity field v has the following components in the chart χ:

$$v^0 \equiv \frac{1}{\sqrt{g_{00}}}, \qquad v^j = 0 \quad (j = 1, 2, 3). \qquad [\text{signature } (+ - - -)\,] \tag{2}$$

We note, however, that this is valid only within the domain of definition U of the chart χ, thus in general not in the whole spacetime.

The notion of the space associated with a network of observers was missing in the general-relativistic literature. But in practice, one cannot dispense with some notion of a *physical space.* One needs to define the spatial positions of physical objects, even though these depend on the reference network considered. One also needs a physical space to define the quantum space of states, and spatial vectors or tensors such as the usual 3-velocity vector or the rotation rate tensor of a triad. We recall previous results (Arminjon & Reifler, 2011) that provide *local* definitions. Then we announce results of a current work, that aims at defining *global* notions and at relating them to the formerly introduced local notions.

2. LOCAL DEFINITION OF A REFERENCE FRAME AND ASSOCIATED SPACE

One may formally define a reference frame as being an *equivalence class of charts* which are all defined on a given open subset U of the spacetime V and are related two-by-two by a *purely spatial* coordinate change:

$$x'^0 = x^0, \quad x'^k = \phi^k((x^j)) \qquad (j, k = 1, 2, 3). \tag{3}$$

This does define an equivalence relation (Arminjon & Reifler, 2011). Thus a reference frame F, i.e. an equivalence class for this relation, can indeed be given by *the data of one chart* $\chi : X \mapsto (x^\mu)$ *with its domain of definition* U (an open subset of the spacetime manifold V). Namely, F is the equivalence class of (χ, U). I.e., F is the set of the charts χ' which are defined on U, and which are such that the transition map $f \equiv \chi' \circ \chi^{-1} \equiv (\phi^\mu)$ corresponds with a purely spatial coordinate change (3). The local physical space $\mathrm{M} = \mathrm{M_F}$ is defined as the set of the world lines (1), which are implicitly restricted to the common domain U of the charts $\chi \in \mathrm{F}$. Consider any given chart $\chi \in \mathrm{F}$. With any world line $l \in \mathrm{M_F}$, let us associate the triplet $\mathbf{x} \equiv (x^j)$ made with the *constant* spatial coordinates of the points $X \in l$ in the chart χ. We thus define a mapping

$$\widetilde{\chi} : \mathrm{M_F} \to \mathbb{R}^3, \quad l \mapsto \mathbf{x} \text{ such that } \forall X \in l,\ \chi^j(X) = x^j \ (j = 1, 2, 3). \tag{4}$$

We defined a structure of differentiable manifold on $\mathrm{M_F}$, for which the set of the mappings $\widetilde{\chi}$ (for $\chi \in \mathrm{F}$) is an atlas: *The spatial part of any chart* $\chi \in \mathrm{F}$ *defines a chart* $\widetilde{\chi}$ *on* $\mathrm{M_F}$ (Arminjon & Reifler, 2011).

3. THE GLOBAL SPACE ASSOCIATED WITH A TIME-LIKE VECTOR FIELD

Given a global vector field v on the spacetime V, and given an event $X \in \mathrm{V}$, let C_X be the solution of

$$\frac{dC}{ds} = v(C(s)), \qquad C(0) = X \tag{5}$$

that is defined on the *largest possible* open interval I_X containing 0 (Dieudonné, 1971). Call the *range* $l_X \equiv C_X(\mathrm{I}_X) \subset \mathrm{V}$ the "maximal integral curve at X". If $X' \in l_X$, then it is easy to show that $l_{X'} = l_X$. The *global space* N_v *associated with the vector field* v is the set of the maximal integral curves of v :

$$\mathrm{N}_v \equiv \{l_X;\ X \in \mathrm{V}\}. \tag{6}$$

A chart χ with domain $\mathrm{U} \subset \mathrm{V}$ is said "v–adapted" iff the spatial coordinates remain constant on any integral line l of v — more precisely, remain constant on $l \cap \mathrm{U}$: For any $l \in \mathrm{N}_v$, there is some $\mathbf{x} \equiv (x^j) \in \mathbb{R}^3$ such that

$$\forall X \in l \cap \mathrm{U}, \quad P_S(\chi(X)) = \mathbf{x}. \tag{7}$$

(Here $P_S : \mathbb{R}^4 \to \mathbb{R}^3, \quad \mathbf{X} \equiv (x^\mu) \mapsto \mathbf{x} \equiv (x^j)$ is the spatial projection.) For any v–adapted chart χ, the mapping

$$\bar{\chi} : l \mapsto \mathbf{x} \text{ such that (7) is verified} \tag{8}$$

is well defined on

$$\mathrm{D_U} \equiv \{l \in \mathrm{N}_v;\ l \cap \mathrm{U} \neq \emptyset\}. \tag{9}$$

Call the v–adapted chart χ "nice" if the mapping $\bar{\chi}$ is one-to-one. Assume the global vector field v on V is non-vanishing (which is true if v is time-like) and "normal" (which means that the flow of the field v is indeed non-pathological in some technical sense). Then, for any point $X \in \mathrm{V}$, there exists a nice v–adapted chart χ whose domain is a neighborhood of X. Consider the set $\mathcal{F}_v$ made of all nice v–adapted charts on the spacetime manifold V. Define the set $\mathcal{A}$ made of the mappings $\bar{\chi}$, where $\chi \in \mathcal{F}_v$, Eq. (8). We can define a structure of differentiable manifold on N_v, for which the set $\mathcal{A}$ is an atlas. The manifold structure gives a firm status to the space attached to a reference network and allows us to define spatial tensors naturally, as tensor fields on the space manifold.

Let v be a normal non-vanishing vector field on V, and let F be a reference frame as in Sect. 2, but *made of nice* v*–adapted charts,* all defined on the same open set $\mathrm{U} \subset \mathrm{V}$. We can show that the local space $\mathrm{M_F}$ is made of the intersections with the local domain U of the world lines belonging to N_v. We may identify the local space $\mathrm{M_F}$ with the subset $\mathrm{D_U}$ of the global space N_v, which is open in N_v.

4. REFERENCES

Arminjon, M., Reifler, F., 2011, "General reference frames and their associated space manifolds", Int. J. Geom. Meth. Mod. Phys. 8, pp. 155–165. [arXiv:1003.3521 (gr-qc)]

Cattaneo, C., 1958, "General relativity: relative standard mass, momentum, energy and gravitational field in a general system of reference", Nuov. Cim. 10, pp. 318–337.

Dieudonné, J., 1971, Eléments d'Analyse, Tome 4 (1st edition, Gauthier-Villars, Paris, 1971), pp. 4–7.

THE TIME TRANSFER FUNCTION AS A TOOL TO COMPUTE RANGE, DOPPLER AND ASTROMETRIC OBSERVABLES

A. HEES[1], S. BERTONE[2], C. LE PONCIN-LAFITTE[2]
[1] Jet Propulsion Laboratory - California Institute of technology
4800 Oak Grove Drive, Pasadena, CA, 91109, USA
e-mail: Aurelien.D.Hees@jpl.nasa.gov
[2] SYRTE, Observatoire de Paris, CNRS, UPMC
61 avenue de l'Observatoire, F-75014 Paris, France
e-mail: stefano.bertone@obspm.fr, christophe.leponcin@obspm.fr

ABSTRACT. In this communication, we will show how the Time Transfer Function (TTF) can be used in the relativistic modeling of range, Doppler and astrometric observables. We will present a method to compute these observables up to second post-Minkowskian order directly from the space-time metric $g_{\mu\nu}$ without explicitly solving the null geodesic. The resulting expressions involve integrals of some functions defined by the metric tensor taken along a straight line between the emitter and the receiver of the electromagnetic signal. Some examples are given within the context of future space missions.

1. MODEL

Let us consider two observers $\mathcal{O}_\mathcal{A}$ and $\mathcal{O}_\mathcal{B}$ moving along their respective worldlines. $\mathcal{O}_\mathcal{A}$ sends an electromagnetic signal received by $\mathcal{O}_\mathcal{B}$. The signal is emitted at the coordinates $(t_A, \mathbf{x_A})$ with a frequency ν_A. It is received by $\mathcal{O}_\mathcal{B}$ at the coordinates $(t_B, \mathbf{x_B})$, with a frequency ν_B. We denote by $n^{(i)}$ the incident direction of the received signal with respect to a tetrad $\lambda^\mu_{(\alpha)}$ comoving with $\mathcal{O}_\mathcal{B}$.

2. COMPUTATION OF THE OBSERVABLES FROM THE TTF

The coordinate travel time of a light ray connecting a emission and a reception point-events is given by the Time Transfer Function $\mathcal{T}_r$ (Teyssandier and Le Poncin-Lafitte, 2008a):

$$t_B - t_A = \mathcal{T}_r(\mathbf{x}_A(t_A), t_B, \mathbf{x}_B). \tag{1}$$

It has been shown that the expression for the frequency shift can be written as (Teyssandier et al. 2008b and Hees et al. 2012)

$$\frac{\nu_B}{\nu_A} = \frac{\left[g_{00} + 2g_{0i}\ \beta^i + g_{ij}\ \beta^i\beta^j\right]_A^{1/2}}{\left[g_{00} + 2g_{0i}\ \beta^i + g_{ij}\ \beta^i\beta^j\right]_B^{1/2}} \times \frac{1 - c\ \beta^i_B\ \frac{\partial \mathcal{T}_r}{\partial x^i_B} - \frac{\partial \mathcal{T}_r}{\partial t_B}}{1 + c\ \beta^i_A\ \frac{\partial \mathcal{T}_r}{\partial x^i_A}}\ , \tag{2}$$

where $\beta^i_{A/B} = \dfrac{1}{c}\dfrac{dx^i_{A/B}}{dt}$ is the coordinate velocity of $\mathcal{O}_{\mathcal{A}/\mathcal{B}}$.

The direction of the incident light ray observed by $\mathcal{O}_\mathcal{B}$ is given by the components of the spatial part of the wave vectors in the tetrad basis (Brumberg, 1991)

$$n^{(i)} = -\frac{\lambda^0_{(i)} + \lambda^j_{(i)}\hat{k}_j}{\lambda^0_{(0)} + \lambda^j_{(0)}\hat{k}_j},$$

where $\hat{k}_j \equiv k_j/k_0$ with k_μ being the covariant coordinates of the wave vector at reception (expressed in the global coordinate system). The last relation can be expressed in term of the TTF (Hees et al, 2013)

$$n^{(i)} = -\frac{\lambda^0_{(i)}\left(1 - \frac{\partial \mathcal{T}_r}{\partial t_B}\right) - c\ \lambda^j_{(i)}\frac{\partial \mathcal{T}_r}{\partial x^j_B}}{\lambda^0_{(0)}\left(1 - \frac{\partial \mathcal{T}_r}{\partial t_B}\right) - c\ \lambda^j_{(0)}\frac{\partial \mathcal{T}_r}{\partial x^j_A}}, \tag{3}$$

where the components of the tetrad $\lambda^{\mu}_{(\alpha)}$ are evaluated at reception coordinates $(t_B, \mathbf{x}_B)$.

The expression of the TTF as a post-Minkowskian series is given in Teyssandier and Le Poncin-Lafitte (2008)

$$\mathcal{T}_r(\mathbf{x}_A, t_B, \mathbf{x}_B) = \frac{R_{AB}}{c} + \frac{1}{c}\sum_n \Delta_r^{(n)}(\mathbf{x}_A, t_B, \mathbf{x}_B),$$

where the superscript (n) stands for the nth PM order (quantity of order $\mathcal{O}(G^n)$ with G the Newton gravitational constant) and $R_{AB} = |\mathbf{x}_B - \mathbf{x}_A|$.

In Hees et al. (2013), we showed how to compute the TTF and its derivatives up to the second PM approximation as *integrals of functions depending on the metric taken along the Minkowskian path* (a straight line joining the emitter and the receiver). The corresponding expressions are then used in (1), (2) and (3). This formulation is very general and well adapted to the case of numerical evaluation. In particular, it can be applied to any space-time in GR or in alternative metric theories of gravity.

3. APPLICATION TO A GAME-LIKE SCENARIO

We apply our results to simulate the angular deflection of a light ray coming from a static light source and observed by a satellite in a 1 AU orbit around the Sun during a Solar conjunction. This configuration corresponds to a GAME-like observation (Vecchiato et al. 2009) whose expected accuracy is at the μas level. In Figure 1, we present some high-order PM corrections to the direction of light. The 2PM contribution to the light deflection has been separated in two parts: the so-called enhanced term, proportional to the factor $(1+\gamma)^2$ and the contribution proportional to $\kappa = 2(1+\gamma) - \beta + 3/4\epsilon$ (with γ, β and ϵ the PPN parameters). The 3PM term has been computed analytically by extending the results of Linet and Teyssandier (2013). As can be seen from Figure 1, the complete 2PM contribution needs to be modeled for GAME-like missions and even some third order terms show amplitudes well above the desired accuracy (at least near the Sun limb).

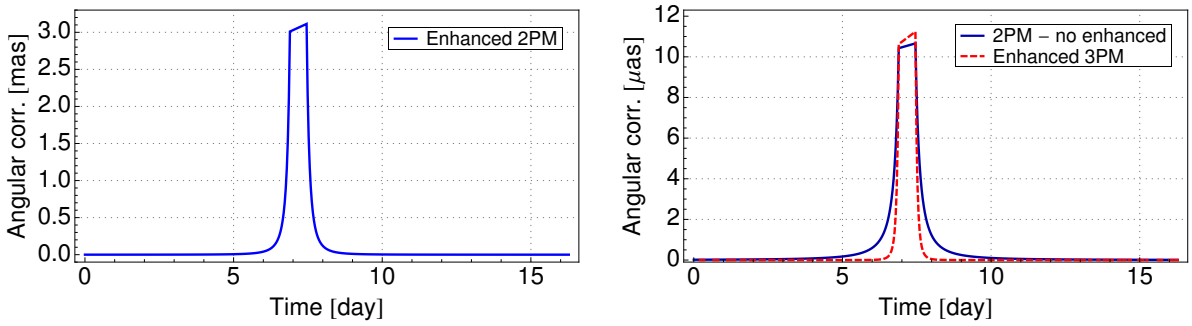

Figure 1: Contribution of the 2PM and 3PM corrections to the angular deflection of a light ray during a solar conjunction.

Acknowledgements. The research described in this poster was partially carried out at the Jet Propulsion Laboratory, California Institute of Technology, under contract with the National Aeronautics and Space Administration A. Hees thanks the BAEF for financial support.

4. REFERENCES

Brumberg, C., 1991, "Essential relativistic celestial mechanics", Adam Hilger.
Hees, A., Lamine, B., Reynaud, S., 2012, Class. and Quantum Grav. 29, 235027.
Hees, A., Bertone, S., Le Poncin-Lafitte, C., 2013, to be submitted.
Linet, B., Teyssandier, P., 2013, Class. and Quantum Grav. 30, 175008.
Teyssandier, P., Le Poncin-Lafitte, C., 2008a, Class. and Quantum Grav. 25, 145020.
Teyssandier, P., Le Poncin-Lafitte, C., Linet, B., 2008b, in Lasers, Clocks and Drag-Free Control: Exploration of Relativistic Gravity in Space, p. 153, Springer.
Vecchiato, A., Gai, M., Donati, P., et al., 2009, Advances in Space Research 44, 579.

NOISE CHARACTERISTICS IN DORIS STATION POSITIONS TIME SERIES DERIVED FROM IGN-JPL, INASAN AND CNES-CLS ANALYSIS CENTRES

S. KHELIFA
Centre of Space Techniques
PO Box 13, 31200, Arzew, Algeria
khelifa_sofiane@yahoo.fr

ABSTRACT. Using wavelet transform and Allan variance, we have analysed the solutions of weekly position residuals of 09 high latitude DORIS stations in STCD (STation Coordinate Difference) format provided from the three Analysis Centres : IGN-JPL (solution ign11wd01), INASAN (solution ina10wd01) and CNES-CLS (solution lca11wd02), in order to compare the spectral characteristics of their residual noise. The temporal correlations between the three solutions, two by two and station by station, for each component (North, East and Vertical) reveal a high correlation in the horizontal components (North and East). For the North component, the correlation average is about 0.88, 0.81 and 0.79 between, respectively, IGN-INA, IGN-LCA and INA-LCA solutions, then for the East component it is about 0.84, 0.82 and 0.76, respectively. However, the correlations for the Vertical component are moderate with an average of 0.64, 0.57 and 0.58 in, respectively, IGN-INA, IGN-LCA and INA-LCA solutions. After removing the trends and seasonal components from the analysed time series, the Allan variance analysis shows that the three solutions are dominated by a white noise in the all three components (North, East and Vertical). The wavelet transform analysis, using the VisuShrink method with soft thresholding, reveals that the noise level in the LCA solution is less important compared to IGN and INA solutions. Indeed, the standard deviation of the noise for the three components is in the range of 5-11, 5-12 and 4-9mm in the IGN, INA, and LCA solutions, respectively.

RESULTS AND DISCUSSION

After having removed the trend, the annual and semi annual signals from the original time series of North, East and Vertical components, the slopes of the Allan variance (Allan, 1966) graphs (see figure 1) show that the noise type which characterises the positions time series of DORIS stations in all three solutions is a dominant white noise. However, the white noise signature in the position residuals would comfort the basic linear motion model (Feissel-Vernier et al., 2007). As the analysed time series are affected by a dominant white noise, then we have employed the VisuShrink method (Donoho and Johnstone, 1994) which is better suited to de-noise a time series affected by a white noise. The chosen wavelet is the Meyer wavelet as in (Khelifa et al., 2012) and the wavelet coefficients are calculated from a decomposition of the time series at level 4 with a soft thresholding. The results shown in the table 1 reveal that the noise level is the smallest in the LCA solution compared to IGN and INA solutions.

Station	Site	STD (mm) - IGN			STD (mm) - INA			STD (mm) - LGA		
		North	East	Vertical	North	East	Vertical	North	East	Vertical
ADFB	Terre Adelie	6.5	8.3	7.1	6.9	7.0	5.6	5.6	5.2	4.1
BEMB	Belgrano	6.8	6.8	7.2	7.0	5.7	5.8	5.9	5.8	4.5
METB	Metsahovi	6.8	9.1	7.9	7.4	9.6	8.1	5.9	7.8	6.3
REZB	Reykjavik	7.7	10.1	10.1	8.3	10.2	8.4	6.3	8.8	6.4
ROUB	Rothera	7.8	9.0	9.0	7.5	9.8	7.4	5.8	7.0	5.9
SPJB	Ny-lesund	7.2	5.4	6.3	7.3	5.4	5.2	6.0	5.0	4.9
SYPB	Syowa	9.6	9.5	10.0	9.9	10.1	9.2	6.5	7.7	6.9
THUB	Thule	6.5	6.3	8.5	6.6	6.1	6.1	4.8	4.7	5.2
YEMB	Yellowknife	8.2	10.3	10.5	8.5	11.8	10.1	5.8	9.1	6.7

Table 1: Standard deviation (STD) of the noise determined by wavelet in the components North, East and Vertical for the three solutions IGN, INA and LCA.

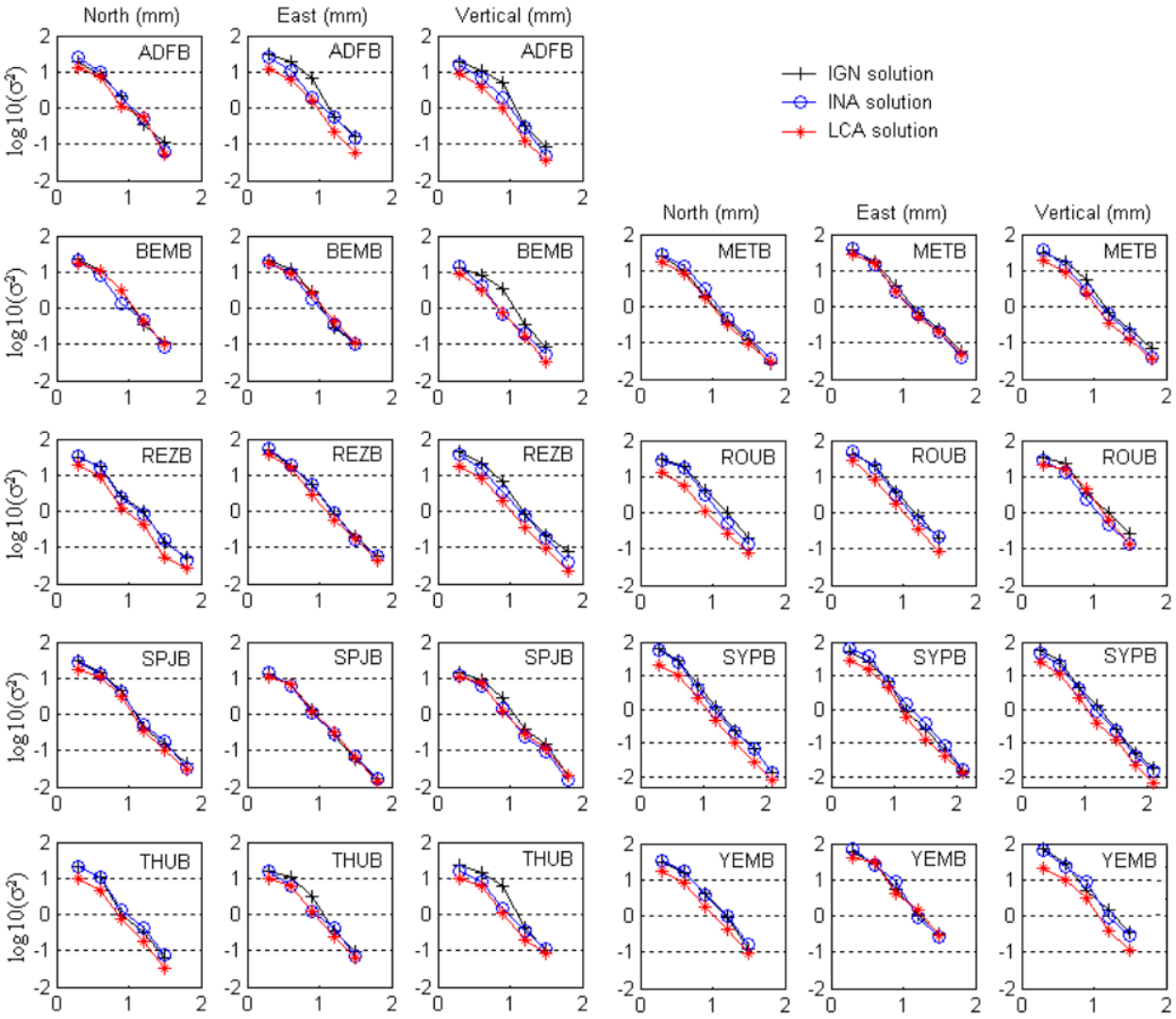

Figure 1: Allan variance (noise types) in the North, East and Vertical components for the three solutions IGN, INA and LCA

REFERENCES

Allan, D.W., 1966, "Statistics of atomic frequency standards", IEEE Trans., 54, 221-231.

Feissel-Vernier, M., de Viron, O., Le Bail, K., 2007, "Stability of VLBI, SLR, DORIS, and GPS positioning". Earth Planets Space, 59, 475-497.

Donoho, D., Johnstone, I., 1994, "Ideal spatial adaptation via wavelet shrinkage", Biometrika, 81, 425-455.

Khelifa, S., Kahlouche, S., Belbachir, M.F., 2012, "Signal and noise separation in time series of DORIS station coordinates using wavelet and singular spectrum analysis", C. R. Geosci., 344(6-7), 334-348.

CORRECTIONS TO TIDAL VARIATIONS OF THE GEOPOTENTIAL DUE TO FREQUENCY DEPENDENCE OF LOVE NUMBERS

S.M. KUDRYAVTSEV
Lomonosov Moscow State University, Sternberg Astronomical Institute
13, Universitetsky Pr., Moscow, 119992, RUSSIA
e-mail: ksm@sai.msu.ru

EXTENDED ABSTRACT[1]

[1] The research details are available in Kudryavtsev (2013)

The main effect of the solid Earth tides on the Earth gravitational potential (defined as "Step 1") can be described through variations $\Delta\bar{C}^{ST}_{nm}$, $\Delta\bar{S}^{ST}_{nm}$ in the instant values of the normalized standard geopotential coefficients of degree n and order m (Eanes et al. 1983)

$$\Delta\bar{C}^{ST}_{nm} - i\Delta\bar{S}^{ST}_{nm} = \frac{k_{nm}}{2n+1}\sum_{j=2}^{3}\frac{\mu_j}{\mu_E}\left(\frac{R_E}{r_j}\right)^{n+1}\bar{P}_{nm}\left(\sin\phi_j\right)e^{-im\lambda_j}, \tag{1}$$

where $i \equiv \sqrt{-1}$; k_{nm} are frequency-independent complex Love numbers; R_E, μ_E are, respectively, the Earth's equatorial radius and gravitational parameter; μ_j, r_j, ϕ_j and λ_j are, respectively, the gravitational parameter, geocentric distance, geocentric latitude and East longitude (from Greenwich) of the Moon ($j = 2$) and Sun ($j = 3$) at epoch t; $\bar{P}_{nm}$ is the normalized associated Legendre functions.

Anelasticity of the Earth's mantle leads to frequency dependence of Love numbers. Therefore, as "Step 2", the IERS Conventions (2010) (Petit & Luzum, 2010) recommend to calculate some additional tidal corrections to the gravitational coefficients due to deviations δk^R_{2mf}, δk^I_{2mf} of the degree 2 complex Love numbers at frequency f from their nominal values. The presently recommended by Petit & Luzum (2010) formulae use the tide height values from the Earth tide-generating potential (TGP) expansion by Cartwright and Tayler (1971), Cartwright and Edden (1973). However, tide heights are not included to the HW95 format (Hartmann and Wenzel, 1995), which is considered as a common standard for TGP catalogues now. The known factors for conversion of amplitudes of tidal terms from Hartmann and Wenzel's conventions to Cartwright-Tayler-Edden's ones (Petit & Luzum, 2010) do not take into account the phase of tidal waves. The latter is zero for all tidal terms in the TGP catalog by Cartwright and Tayler (1971), Cartwright and Edden (1973), but it is not the case in the modern TGP catalogs. In particular, the phase of some waves used in computing the tidal corrections at "Step 2" is not zero there.

The Earth TGP development in the HW95 format represents the TGP value at a surface point P as

$$V(t) = \sum_{n=2}^{n_{max}}\left(\frac{r}{R_E}\right)^n\sum_{m=0}^{n}\bar{P}_{nm}\left(\sin\varphi'\right)\sum_{f(n,m)}\left[\bar{C}^*_{nmf}(t)\cos\omega^*_{nmf}(t) + \bar{S}^*_{nmf}(t)\sin\omega^*_{nmf}(t)\right], \tag{2}$$

where

$$\bar{C}^*_{nmf}(t) = \bar{C}^*_{0nmf} + \bar{C}^*_{1nmf}t, \qquad \bar{S}^*_{nmf}(t) = \bar{S}^*_{0nmf} + \bar{S}^*_{1nmf}t, \tag{3}$$

ω^*_{nmf} are arguments based on the development frequencies f, and $\bar{C}^*_{0nmf}$, ..., $\bar{S}^*_{1nmf}$ are constants.

Then the in-phase $A^{(ip)}_{2mf}$ and out-of-phase $A^{(op)}_{2mf}$ amplitudes ($m = 0, 1, 2$) are (Kudryavtsev 2013):

$$A^{(ip)}_{20f} = \frac{R_E}{\mu_E}\left(\delta k^R_{20f}\bar{C}^*_{20f} + \delta k^I_{20f}\bar{S}^*_{20f}\right), \qquad A^{(op)}_{20f} = \frac{R_E}{\mu_E}\left(-\delta k^R_{20f}\bar{S}^*_{20f} + \delta k^I_{20f}\bar{C}^*_{20f}\right), \tag{4}$$

$$A^{(ip)}_{21f} = \frac{R_E}{\mu_E}\left(\delta k^R_{21f}\bar{S}^*_{21f} - \delta k^I_{21f}\bar{C}^*_{21f}\right), \qquad A^{(op)}_{21f} = \frac{R_E}{\mu_E}\left(\delta k^R_{21f}\bar{C}^*_{21f} + \delta k^I_{21f}\bar{S}^*_{21f}\right), \tag{5}$$

$$A^{(ip)}_{22f} = \frac{R_E}{\mu_E}\delta k^R_{22f}\bar{C}^*_{22f}, \qquad A^{(op)}_{22f} = -\frac{R_E}{\mu_E}\delta k^R_{22f}\bar{S}^*_{22f}. \tag{6}$$

Eqs. (3)–(6) give updated amplitudes of the tidal corrections to the geopotential coefficients of the second degree due to frequency dependence of Love numbers. They employ the Earth TGP development represented in the HW95 format and take into account the phases of tidal waves.

By using Eqs. (3)–(6) and the Earth TGP development by Hartmann and Wenzel (1995) we recalculated amplitudes of the "Step 2" corrections and compared them with those recommended by the IERS Conventions (2010), Tables 6.5a,b,c. Tables 1–2 show the updated in-phase amplitudes $A_{21f}^{(ip)}$ and $A_{22f}^{(ip)}$ for which the differences with the corresponding amplitudes given by the IERS Conventions (2010) have only been found.

f, deg/hr	Doodson	$A_{21f}^{(ip)}$	
	No.	IERS Conventions (2010)	This study
15.07749	166,455	0.1	0.2
15.08214	166,554	-20.6	-20.5

Table 1: Updated values for in-phase amplitudes $A_{21f}^{(ip)}$, units: 10^{-12}

f, deg/hr	Doodson	$A_{22f}^{(ip)}$	
	No.	IERS Conventions (2010)	This study
28.43973	245,655	-0.3	0.2
28.98410	255,555	-1.2	0.8

Table 2: Updated values for in-phase amplitudes $A_{22f}^{(ip)}$, units: 10^{-12}

Our further analysis proves that such relatively large corrections to $A_{22f}^{(ip)}$ values are not only due to use of either modern TGP catalogs or more accurate Eqs. (3)–(6), but also can be obtained with use of older TGP catalogs, e.g. that by Cartwright and Tayler (1971), Cartwright and Edden (1973), and present formulae from Petit & Luzum (2010). Therefore, the noticed differences in the presently recommended by the IERS values for $A_{22f}^{(ip)}$ in-phase amplitudes are likely due to some errors in the IERS Conventions (2010), Tables 6.5c, which should be corrected.

Acknowledgements. Research supported in part by the Russian Foundation for Basic Research. A travel grant provided to the author by the LOC of the Journées 2013 and the French Ministry of Education and Research in the framework of the programme ACCES* is sincerely appreciated.

REFERENCES

Cartwright, D.E., Tayler, R.G., 1971, "New computations of the tide-generating potential", Geophys. J. R. astr. Soc., 23, pp. 45–74.

Cartwright, D.E., Edden, A.C., 1973, "Corrected tables of tidal harmonics", Geophys. J. R. astr. Soc., 33, pp. 253–264.

Eanes R.J., Schutz, B., Tapley, B., 1983, "Earth and ocean tide effects on Lageos and Starlette", In: Kuo, J.T. (ed.) Proceed. of the Ninth Intern. Sympos. on Earth tides, E. Sckweizerbart'sche Verlagabuchhandlung, Stuttgart.

Hartmann, T., Wenzel, H.-G., 1995, "The HW95 tidal potential catalogue", Geophys. Res. Lett., 22, pp. 3553–3556.

Kudryavtsev, S.M., 2013, "A series expansion of the solid Earth tide effect on geopotential", Celest. Mech. Dyn. Astr. , 115, pp. 353–364, doi: 10.1007/s10569-012-9467-2.

Petit, G., Luzum, B. (eds.), 2010, "IERS Conventions (2010)", IERS Technical Note 36, Frankfurt am Main: Verlag des Bundesamts für Kartographie und Geodäsie, 179 pp.

ON THE GALACTIC ABERRATION CONSTANT

Z. MALKIN[1,2]
[1] Pulkovo Observatory, St. Petersburg, Russia
[2] St. Petersburg State University, St. Petersburg, Russia
e-mail: malkin@gao.spb.ru

ABSTRACT. In this work, we analyzed all available determinations of the Galactic rotation parameters R_0 and Ω_0 made during last 10 years to derive the most probable value of the Galactic aberration constant $A = R_0\Omega_0^2/c$. We used several statistical methods to obtain reliable estimates of R_0 and Ω_0 and their realistic errors. In result, we obtained the value of $A = 5.0 \pm 0.3$ μas/yr as the current best estimate of the GA constant. We suggest that the proposed value of the GA constant can be safely used in practice during coming years.

1. INTRODUCTION

Galactic aberration (GA) is a small effect in proper motion of about 5 μas/yr already noticeable in VLBI and other highly-accurate astrometric observations. However accounting for this effect during data processing faces difficulty caused by the uncertainty in the GA constant $A = R_0\Omega_0^2/c$, where R_0 is the Galactocentric distance of the Sun, Ω_0 is the angular velocity of circular rotation of the Sun around the Galactic center, c is speed of light.

The value of the GA constant can be derived either using the stellar astronomy methods or VLBI observations of the extragalactic radio sources. It seems that the former provide more accurate results, while the latter are still somewhat contradictory. So, we use the results of the observations of Galactic objects to improve A. Our previous estimate of the GA constant (Malkin 2011) yields the values of $R_0 = 8.2$ kpc, $\Omega_0 = 29.5$ km s^{-1} kpc^{-1}, and $A = 5.02$ μas/yr. This work is performed to check and improve if necessary this estimate taking into account more recent measurements of the Galactic rotation parameters.

2. DERIVING THE BEST VALUE OF THE GA CONSTANT

In this work, we have used 35 R_0 measurements and 30 Ω_0 measurements made during last 10 years. They are listed in Table 1. We consider the results obtained during last 5 years as the most reliable, especially for R_0 estimates, for which the direct methods, such as measurements of the parallax or stellar orbits around the massive black hole, become routine starting from 2008. So, the results published in 2008–2013 were used to derive the final estimate of the GA constant. The results of 2003–2007 were processed for control of its stability.

We have applied several statistical techniques mostly used in physics and metrology to these data, as described in Malkin (2012, 2013). Results of computation are presented in Table 2. The first line corresponds to the best current estimates of the GA constant, in our opinion. The second result obtained by using only direct R_0 measurements is practically the same. It shows that the results of the direct determinations of R_0 does not substantially differ (in average) from other estimates. The results obtained with all measurements of the Galactic rotation parameters made during last 10 years are given in the third line. We think it is less reliable than the first two ones. However, it allows one to get an impression about the stability of the GA constant in time.

For comparison, the standard weighted mean estimate yields for the main variant corresponding to the first line of Table 2 (data interval of 2008–2013, all R_0 measurements) $R_0 = 8.03 \pm 0.06$ kpc, $\Omega_0 = 29.23 \pm 0.19$ km s^{-1} kpc^{-1}, $A = 4.83 \pm 0.07$ μas/yr. Precision of these estimates seems to be too optimistic. Using combined estimate of different statistical techniques as suggested by Malkin (2012) provides more reliable A estimate with a realistic uncertainty. Further analysis has shown that error in Ω_0 prevails in the A error. Besides, published Ω_0 results are not statistically consistent, unlike R_0 measurements. So, more attention is needed to compute the best estimate of Ω_0.

R_0	σ	Reference
8.3	0.3	Gerasimenko, 2004
7.7	0.15	Babusiaux & Gilmore, 2005
8.01	0.44	Avedisova, 2005
8.7	0.6	Groenewegen & Blommaert, 2005
7.2	0.3	Bica, et al., 2006
7.52	0.36	Nishiyama, et al. 2006
8.1	0.7	Shen & Zhu, 2007
7.4	0.3	Bobylev, et al., 2007
7.94	0.45	Groenewegen, et al., 2008
8.16 *	0.5	Ghez, et al., 2008
8.07 *	0.35	Trippe, et al. 2008
8.33 *	0.35	Gillessen, et al., 2009
8.7	0.5	Vanhollebeke, et al., 2009
7.58	0.40	Dambis, 2009
8.4 *	0.6	Reid, et al., 2009
7.75	0.5	Majaess, et al., 2009
8.24	0.43	Matsunaga, et al., 2009
7.9 *	0.75	Reid, et al., 2009
7.7	0.4	Dambis, 2010
8.1	0.6	Majaess, 2010
8.3 *	1.1	Sato, et al., 2010
7.80 *	0.26	Ando, et al., 2011
8.29	0.16	McMillan, 2011
7.9	0.36	Matsunaga, et al., 2011
8.03	0.70	Liu & Zhu, 2011
8.54	0.42	Pietrukowicz, et al., 2012
7.7 *	0.4	Morris, et al., 2012
8.27	0.29	Schoenrich, 2012
8.05 *	0.45	Honma, et al., 2012
7.51	0.23	Bobylev, 2013
8.24	0.43	Matsunaga, et al., 2013
8.38 *	0.18	Reid, 2013
8.08	0.44	Zhu & Shen, 2013
8.2	0.35	Nataf, et al., 2013
7.4	0.21	Francis & Anderson, 2013

Ω_0	σ	Reference
27.6	1.7	Bedin, et al., 2003
32.8	1.2	Olling & Denhen, 2003
25.3	2.6	Kalirai, et al., 2004
28.0	0.6	Bobylev, 2004
29.45	0.15	Reid & Brunthaler, 2004
29.96	1.29	Zhu, 2006
26.0	0.3	Bobylev et al., 2007
30.7	1.0	Lepine, et al., 2008
27.67	0.61	Bobylev, et al., 2008
28.06	1.04	Ghez, et al., 2008
30.2	1.0	Dambis, 2009
30.3	0.9	Reid, et al., 2009a
29.8	1.0	Bovy, et al., 2009
31	1	Melnik & Dambis, 2009
27.27	1.04	Dambis, 2010
30.65	0.85	Macmillan & Binney, 2010
31.0	1.2	Bobylev & Bajkova, 2010
27.3	0.8	Ando, et al., 2011
28.7	1.3	Nagayama, et al., 2011
30.4	1.5	Stepanishchev & Bobylev, 2011
31.5	0.9	Bobylev & Bajkova, 2011
29.27	1.04	Liu & Zhu, 2011
28.8	0.8	Bajkova & Bobylev, 2012
27.5	0.5	Bobylev & Bajkova, 2012
28.78	1.04	Schoenrich, 2012
31.09	0.78	Honma, et al., 2012
31.63	3.31	Bobylev, 2013
28	2	Nagayama, et al., 2013
29.0	1.0	Reid, 2013
32.38	1.04	Bobylev & Bajkova, 2013

Table 1: R_0 [kpc] and Ω_0 [km s^{-1} kpc^{-1}] estimates. Direct R_0 measurements are marked with asterisk.

Interval	R_0 data	R_0	Ω_0	A
2008–2013	all	8.06 ± 0.12	29.59 ± 0.75	4.96 ± 0.26
2008–2013	direct	8.14 ± 0.15	29.59 ± 0.75	5.01 ± 0.27
2003–2013	all	8.00 ± 0.14	29.28 ± 0.66	4.83 ± 0.24

Table 2: Results of computation of R_0 [kpc], Ω_0 [km s^{-1} kpc^{-1}], and A [μas/yr.].

3. CONCLUSION

We derived the current best estimate of the GA constant using all available measurements of the Galactic rotation parameters made during last 5 years, which yields the result $A = 4.96 \pm 0.26$ μas/yr. For practical applications we suggest to use the value $A = 5$ μas/yr. Using this value of the GA constant allows one to eliminate about 90% of the GA effect. Remaining uncertainty in proper motion of about 0.5 μas/yr is negligible nowadays. Thus the proposed value of the GA constant can be safely used in practice during coming years, presumably for at least the nearest decade, until new VLBI and space observations provide substantially better result.

Acknowledgements. The author is grateful to the organizers of the conference for the travel support.

4. REFERENCES

Malkin, Z.M., 2011, Astron. Rep. 55, pp. 810–815.
Malkin, Z., 2012, arXiv:1202.6128.
Malkin, Z.M., 2013, Astron. Rep. 57, pp. 882–887.

2500 YEARS OF SPACE-TIME REFERENCES

C. Bizouard & OMIM Group
SYRTE, Observatoire de Paris, CNRS, UPMC
e-mail: christian.bizouard@obspm.fr

ABSTRACT. Time and space reference systems result from the historical developments of the observational techniques and concepts from Antiquity to nowadays. Moreover ancient observations, involving various techniques and epochs, are quite often reprocessed, because of the extension or modification of their compilations or for benefiting of the progress of the computer capabilities. These historical aspects constitute an other skill of SYRTE. For a better integration of our various researches and their achievements, and having an epistemological overview on them, we set up in 2013 an internal interdisciplinary group, assembling time and astro-geodesy competence centers with the historians. This is OMIM: "Observations, Mesures, Incertitude, Modèles" (i.e. Observations, Measurements, Uncertainties and Models). The present poster is aimed at illustrating the evolution in measuring/conceptualising space and time from the Greeks to our days.

A BRIEF HISTORY OT THE SPACE-TIME APPREHENSION

Reference of time and space is the basis of any rational knowledge of our environment and permits to master the Nature and use it. The manner we coordinate objects in space and time takes its roots in the most ancient civilisations. A deep understanding of present space-time reference system cannot be restricted to the present technical achievement brought by atomic clocks and space geodesy, but has also to consider the long term maturation of time-space measurements in conjunction with the discoveries and physical theories they led.

A picture speaks better than words. Of the very rich history underlying the development of space-time references, we offer the synthetic representation in chronological order in the figure hereafter. It can be seen how the conceptual representation of space and time references is associated with the development of clocks and astrometry. If many discoveries and physical theories have resulted from technical advances or have been confirmed by them, the inverse is also true: the search for tiny celestial motions (parallaxes, aberration, proper motion,...), Earth shape (flattening, geoid, topography), and ground displacement (tides, continental drift,...) hinted by theoretical considerations has motivated many technical progresses, especially in optics and time keeping. The tremendous advances of these last 50 years are mostly due to the invention of atomic clocks, their improvement, and their introduction in space geodesy for determining angles and distances, so that in their practical realisation time and space references become totally entangled, as described by Relativity theory.

REFERENCES

Guinot, B., Audoin, C., 1998, "Les fondements de la mesure du temps. Comment les fréquences atomiques règlent le monde", Ed. Elsevier Masson

Kovalesvky, J., Mueller, I.I., Kolaczek, B., 1989, "Reference frames in astronomy and geophysics", Kluwer Academic Publishers, 474 p.

OMIM is an interdisciplinary Group of SYRTE Department

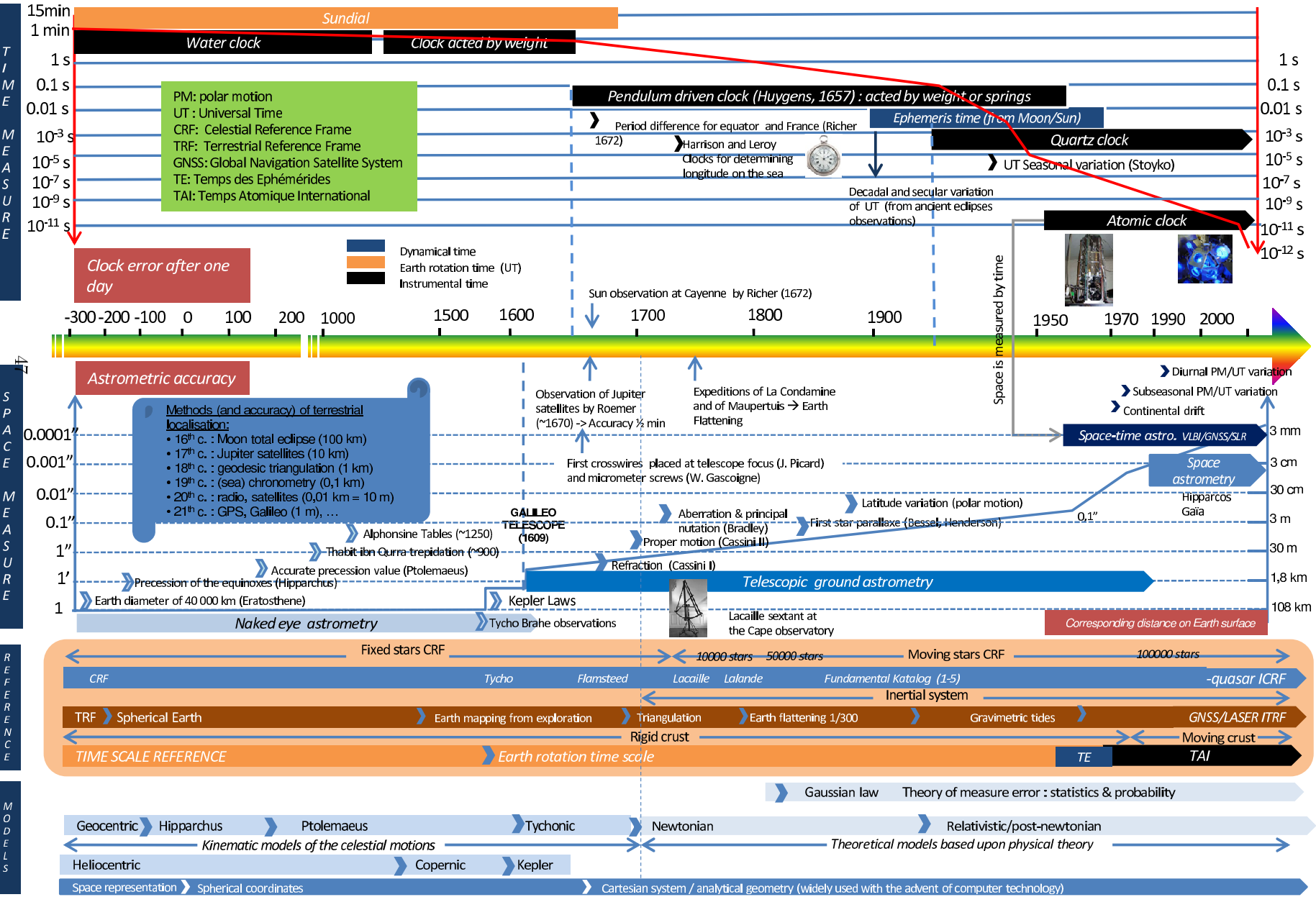
TIME MEASURE
SPACE MEASURE
REFERENCE
MODELS
Δt
15min
1 min
1 s
0.1 s
0.01 s
10-3 s
10-5 s
10-7 s
10-9 s
10-11 s
10-12 s
Sundial
Water clock
Clock acted by weight
PM: polar motion
UT : Universal Time
CRF: Celestial Reference Frame
TRF: Terrestrial Reference Frame
GNSS: Global Navigation Satellite System
TE: Temps des Ephémérides
TAI: Temps Atomique International
Pendulum driven clock (Huygens, 1657) : acted by weight or springs
Period difference for equator and France (Richer 1672)
Harrison and Leroy Clocks for determining longitude on the sea
Ephemeris time (from Moon/Sun)
Quartz clock
UT Seasonal variation (Stoyko)
Decadal and secular variation of UT (from ancient eclipses observations)
Atomic clock
Clock error after one day
Dynamical time
Earth rotation time (UT)
Instrumental time
Sun observation at Cayenne by Richer (1672)
-300 -200 -100 0 100 200 1000 1500 1600 1700 1800 1900 1950 1970 1990 2000
Space is measured by time
Astrometric accuracy
Methods (and accuracy) of terrestrial localisation:
• 16th c. : Moon total eclipse (100 km)
• 17th c. : Jupiter satellites (10 km)
• 18th c. : geodesic triangulation (1 km)
• 19th c. : (sea) chronometry (0,1 km)
• 20th c. : radio, satellites (0,01 km = 10 m)
• 21th c. : GPS, Galileo (1 m), …
Observation of Jupiter satellites by Roemer (~1670) -> Accuracy ½ min
Expeditions of La Condamine and of Maupertuis → Earth Flattening
Diurnal PM/UT variation
Subseasonal PM/UT variation
Continental drift
Space-time astro. VLBI/GNSS/SLR
0.0001″
0.001″
0.01″
0.1″
1″
1′
1
3 mm
3 cm
30 cm
3 m
30 m
1,8 km
108 km
First crosswires placed at telescope focus (J. Picard) and micrometer screws (W. Gascoigne)
Space astrometry
Hipparcos
Gaïa
0.1″
GALILEO TELESCOPE (1609)
Aberration & principal nutation (Bradley)
Latitude variation (polar motion)
First star parallaxe (Bessel, Henderson)
Alphonsine Tables (~1250)
Thabit ibn Qurra trepidation (~900)
Proper motion (Cassini II)
Accurate precession value (Ptolemaeus)
Refraction (Cassini I)
Precession of the equinoxes (Hipparchus)
Telescopic ground astrometry
Earth diameter of 40 000 km (Eratosthene)
Kepler Laws
Tycho Brahe observations
Lacaille sextant at the Cape observatory
Naked eye astrometry
Corresponding distance on Earth surface
Fixed stars CRF
10000 stars
50000 stars
Moving stars CRF
100000 stars
CRF
Tycho
Flamsteed
Lacaille
Lalande
Fundamental Katalog (1-5)
-quasar ICRF
Inertial system
TRF
Spherical Earth
Earth mapping from exploration
Triangulation
Earth flattening 1/300
Gravimetric tides
GNSS/LASER ITRF
Rigid crust
Moving crust
TIME SCALE REFERENCE
Earth rotation time scale
TE
TAI
Gaussian law
Theory of measure error : statistics & probability
Geocentric
Hipparchus
Ptolemaeus
Tychonic
Newtonian
Relativistic/post-newtonian
Kinematic models of the celestial motions
Theoretical models based upon physical theory
Heliocentric
Copernic
Kepler
Space representation
Spherical coordinates
Cartesian system / analytical geometry (widely used with the advent of computer technology)

Session 2.

THE NEXT ICRF - PROGRESS AND DEVELOPMENTS

LE PROCHAIN ICRF - PROGRÈS ET DÉVELOPPEMENTS

ICRF-3: ROADMAP TO THE NEXT GENERATION ICRF

C.S. JACOBS[1], F. ARIAS[2], D. BOBOLTZ[3], J. BOEHM[4], S. BOLOTIN[5], G. BOURDA[6,7], P. CHARLOT[6,7], A. DE WITT[8], A. FEY[9], R. GAUME[9], D. GORDON[5], R. HEINKELMANN[10], S. LAMBERT[11], C. MA[12], Z. MALKIN[13], A. NOTHNAGEL[14], M. SEITZ[15], E. SKURIKHINA[16], J. SOUCHAY[11], O. TITOV[17]

[1] Jet Propulsion Laboratory, California Institute of Technology/NASA
4800 Oak Grove Dr., Pasadena CA, USA
e-mail: Christopher.S.Jacobs@jpl.nasa.gov
[2] Bureau International des Poids et Mesures (BIPM), Paris, France
[3] Astronomical Sciences, National Science Foundation, Arlington, VA
[4] Technical University of Vienna, Austria
[5] NVI, Inc.,/NASA Goddard Space Flight Center, Greenbelt, MD
[6] Univ. Bordeaux, LAB, UMR 5804, F-33270, Floirac, France
[7] CNRS, LAB, UMR 5804, F-33270, Floirac, France
[8] Hartebeesthoek Radio Astronomy Observatory, South Africa
[9] U.S. Naval Observatory, Washington D.C.
[10] Deutsches GeoForschungsZentrum (GFZ), Potsdam, Germany
[11] Paris Observatory, France
[12] NASA Goddard Space Flight Center, Greenbelt, MD
[13] Pulkovo Observatory, St. Petersburg, Russia
[14] Institute of Geodesy and Geoinformation, University Bonn, Germany
[15] Deutsches Geodätisches Forschungsinstitut (DGFI), Munich, Germany
[16] Institute of Applied Astronomy, St. Petersburg, Russia
[17] Geoscience Australia, Canberra Australia

ABSTRACT. We propose a 3rd generation radio-based International Celestial Reference Frame (ICRF-3) to improve upon the highly successful ICRF-2. Our goals are to improve the precision as well as the spatial and frequency coverages relative to the ICRF-2 by 2018. This date is driven by the desire to create radio frames early enough to test the Gaia optical frame during its construction. Several specific actions are underway. A collaboration has been started to improve S/X-band precision of the ∼2200 VLBA Calibrator Survey sources which are typically 5 times less precise than the rest of the ICRF-2. S/X-band southern precision improvements are planned from observations with southern antennas such as the AuScope and HartRAO, S. Africa. We seek to improve radio frequency coverage with X/Ka and K-band work. An X/Ka frame of 631 sources now has full sky coverage from the addition of a 2nd southern station in Argentina which should strengthen the southern hemisphere in general. A K-band collaboration has formed with similar coverage and southern hemisphere precision goals. On the analysis front, special attention will be given to combination techniques both of VLBI catalogs and of multiple data types (e.g. VLBI+GPS). Finally, work is underway to identify and pinpoint sources bright enough in both radio and optical to allow for a robust frame tie between VLBI and Gaia optical frames.

1. INTRODUCTION

Since the adoption of the ICRF-1 (Ma *et al*, 1998) on 1998 Jan 01, the IAU has defined angular coordinates on the sky using axes defined from VLBI observations at S/X-bands (2.3/8.4 GHz) of a few hundred Active Galactic Nuclei (AGN). The current standard, ICRF-2 (Ma *et al*, 2009), uses 295 fiducials to define the axes and then densifies the frame with additional AGN for a total of 3414 sources (Fig. 1). The axes are claimed to be stable at the 10 μas level. The noise floor of individual coordinates is estimated to be 40 μas.

About 2/3 of the sources are from the VCS survey (Fig. 2; Beasley *et al*, 2002) which have about 5 times worse precision than the remaining 1/3 of the sources. Both the VCS and the ICRF-2, in general, are weak south of declination -30°, the approximate limit of the reach of northern arrays. To remedy these weaknesses, southern antenna arrays are being coordinated for VLBI observations (Fig. 3).

2. ASSESSMENT OF NEEDS for ICRF-3

A review of the needs for a next generation celestial frame revealed the following areas of concern:

1. More uniform precision: VLBA Calibrator Survey (VCS) is ∼2/3 of the ICRF-2 but VCS positions are 5 times worse than the rest of ICRF-2.
2. Weak southern hemisphere: The ICRF-2 and all VLBI frames are weak in the south due to a lack of southern stations and observations.
3. Reduction of source structure and core shift effects: Many sources at the standard S/X-bands have systematic errors due to non-pointlike nature of sources.
4. Extend reference frame to higher frequencies: High frequency frames at K (22–24 GHz) and Ka-band (32 GHz) have more point-like structure, but also fewer sources at present. Also, as with S/X, high frequency celestial frames are weak in the south.

3. ICRF-3 GOALS

Having reviewed the needs for the proposed ICRF-3, we set goals to address these needs within estimated resources constraints:

1. Date: Complete a radio-based candidate catalog for ratification by IAU as ICRF-3 by 2018 to be ready for comparisons before Gaia optical frame release 2021.
2. Accuracy: 70 μas or better (1-σ RA, Dec) to match Gaia's precision.
3. Uniform precision for all sources: 2nd generation VLBA Cal Survey (8 x 24 hr) now approved for VLBA observations will help to solve precision uniformity problems.
4. Uniform spatial coverage: Implies improving southern observations.
   S/X: increase number of observations between Australia and South Africa (e.g. Titov *et al*, 2013)
   K: Observations amongst South Africa, Australia, and Korea (Bertarini *et al*, 2013)
   X/Ka: Baselines from Malargüe, Argentina to Australia, California & Spain
5. High Frequency Frames: K (22–24 GHz), Ka (32 GHz)
   Increase number of sources to more than 500 at K-band and more than 700 at X/Ka-band.
   Accuracy: better than 70 μas
   Southern coverage: make southern accuracy comparable to northern accuracy.
6. Optical-radio frame tie: add more than 100 optically bright sources to radio frame to improve the frame tie to the Gaia optical frame (Bourda *et al*, 2011)

4. HIGH FREQUENCY RADIO FRAMES

As radio frequencies increase, sources tend to become more core dominated as the extended structure in the jets tends to fade away with increasing frequency. Also the spatial offset of the radio emissions from the AGN's central black hole due to opacity effects ("core shift") is reduced with increasing observing frequency. For applications lacking dual frequency observations for plasma calibrations, moving to higher frequencies quickly reduces charged particle effects. All these factors motivate the creation of celestial frames above the standard 8.4 GHz frequency.

While the astrophysics is better at higher frequencies, the presence of a rotational water line at 22 GHz makes observations at K and Ka-bands more weather sensitive and combined with the shorter wavelengths leads to shorter coherence times. Furthermore, sources are often weaker and antenna pointing is more difficult. The combined effect is lower sensitivity, but advances in recording technology are rapidly compensating with higher data rates. For example, both the VLBA and JPL's Deep Space Network are moving to 2 Gbps operations.

Lanyi *et al* (2010) and Charlot *et al* (2010) did pioneering work to develop a high precision celestial frame at 24 GHz. They used the VLBA to observe about 270 sources (Fig. 4) with precision better than 200 μas. This work showed that there were a sufficient number of compact sources with sufficient flux density for creating a celestial frame at 24 GHz.

Since 2005, the two baselines of NASA's Deep Space Network have been making observations at X/Ka-band of about 500 sources down to $-45°$ south. Recently they have been joined by ESA's DSA03

station in Malargüe, Argentina resulting in full sky coverage at Ka-band (Horiuchi *et al*, 2013). The X/Ka work now includes 630 sources (Fig. 5).

We also note that work is underway to explore combinations of S/X and X/Ka catalogs using the full parameter covariances in an effort to create a strengthened catalog product.

5. GAIA OPTICAL-RADIO FRAME TIE and ACCURACY VERIFICATION

Background: Launched in Dec. 2013, ESA's Gaia mission is designed to make state-of-the-art astrometric measurements (positions, proper motions and parallaxes) of a billion objects as well as photometric and radial velocity measurements (Lindegren, 2008; Mignard, 2013). Gaia's observations will include approximately 500 000 AGN of which ∼20 000 will be optically bright (V $<$ 18 mag), thus enabling very high precisions: 70 μas at V = 18 mag and 25 μas at V = 16 mag.

Tie sources: Bourda *et al* (2011) estimate that over 300 AGNs should be both bright in the optical and bright and compact in the radio thus enabling both Gaia and VLBI to make very precise position measurements of a common set of sources which should allow the Gaia Optical and VLBI radio frames to be rotationally aligned to better than 10 μas precision (1-σ, per 3-D component, [Horiuchi *et al*, 2013]). After making the optical-radio alignment, position offsets between the two techniques can be studied to characterize systematic errors. Having multiple radio frames (S/X, K, X/Ka) should be of great value in characterizing frequency dependent effects e.g. core shift.

6. CONCLUSIONS

The great success of the ICRF-1 and ICRF-2 in providing the IAU with a standard celestial reference frame has encouraged us to pursue improvements to enable a 3rd generation ICRF, the ICRF-3. We believe that further significant progress is achievable by 2018 by leveraging sensitivity improvements from higher data rates, improved geometry including greater use of southern hemisphere stations, and quantifying frequency dependent astrophysical effects from higher radio frequency observations at K and Ka-bands which in turn are expected to benefit tying the radio-based frames to a future optical frame based on the Gaia mission. Accordingly, we have begun a program of observations to create a candidate ICRF-3.

Acknowledgements. Thanks to the International VLBI Service for Geodesy and Astrometry (IVS) and its members for decades of dedication to the collection of the data used in this research (Schuh & Behrend, 2012). This research is done in part under NASA contract. Sponsorship by U.S. Government, our respective institutes and funding agencies is acknowledged.

7. REFERENCES

Beasley, *et al*, VLBA Calibrator Survey, ApJS, 141, 1, 2002.
http://adsabs.harvard.edu/abs/2002ApJS..141...13B

Bertarini *et al*, 'Extending the K-CRF with Emphasis on the S. Hemisphere,' Journees, 2013.
http://adsabs.harvard.edu/abs/2013jsrs.confE...3B

Bourda *et al*, 'VLBI observations of optically-bright extragalactic radio sources for alignment of radio frame with Gaia frame., A&A, 526, 2011.
http://adsabs.harvard.edu/abs/2011A%26A...526A.102B

Charlot, *et al*, 'The Celestial Reference Frame at 24 and 43 GHz. II. Imaging,' AJ, 139, 5, 2010.
http://adsabs.harvard.edu/abs/2010AJ....139.1713C

Horiuchi, S., *et al*, 'The X/Ka CRF: Results from combined NASA-ESA baselines,' AP-RSAC, 2013.
http://adsabs.harvard.edu/abs/2013apra.confE...1H

Lanyi, *et al*, 'The Celestial Reference Frame at 24 and 43 GHz. I. Astrometry,' AJ, 139, 5, 2010.
http://adsabs.harvard.edu/abs/2010AJ....139.1695L

Lindegren *et al*, 'The Gaia Mission: Science, Organization and Present Status,' IAU, 248, 2008.
http://adsabs.harvard.edu/abs/2008IAUS..248..217L

Ma, *et al*, ' The ICRF as realized by VLBI,' AJ, 116, 1, 1998.
http://adsabs.harvard.edu/abs/1998AJ....116..516M

Ma, *et al*, IERS Technical Note No. 35: '2^{nd} Realization of ICRF by VLBI,' Eds. A. Fey, D. Gordon, and C.S. Jacobs, IERS, BKG, Frankfurt am Main, Germany, 2009.
www.iers.org/documents/publications/tn/tn35/tn35.pdf
Mignard, Gaia Status & Early Release Plan, Journees, 2013.
http://syrte.obspm.fr/journees2013/powerpoint/mignard_jsr13.pdf
Schuh & Behrend, 'VLBI: fascinating technique for geodesy & astrometry,' J. Geodynam., 61, 68–80, 2012.
http://www.sciencedirect.com/science/article/pii/S0264370712001159
Titov, *et al*, 'International collaboration for improvement of the CRF in the S. Hemisphere,' IAG, 2013.
http://www.iag2013.org/IAG_2013/Info_files/Abstracts_iag_2013.pdf

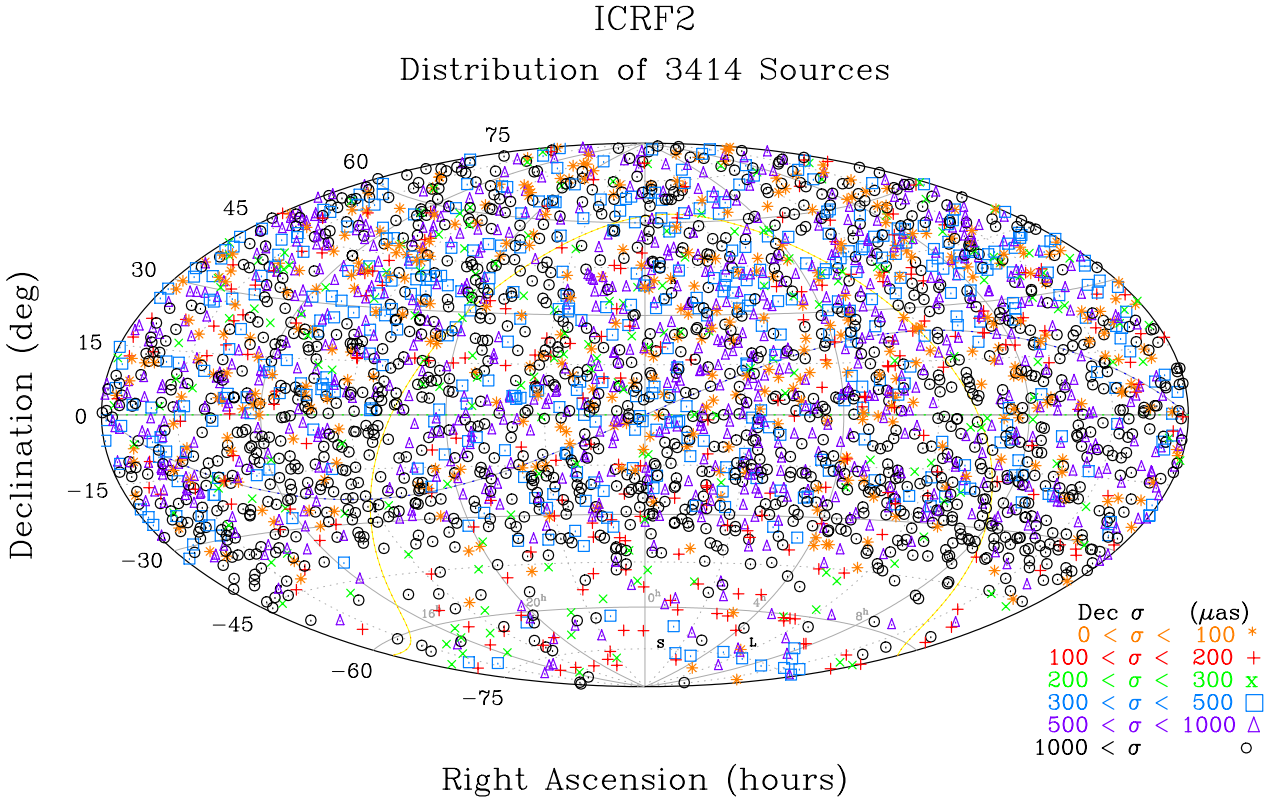

Figure 1: ICRF-2: the current IAU standard frame consists of 3414 sources (Ma *et al*, 2009). Note the lower spatial density of sources south of −30°. About 2/3 of the sources, originating from the VCS survey have 5 times lower precision than the well observed sources.

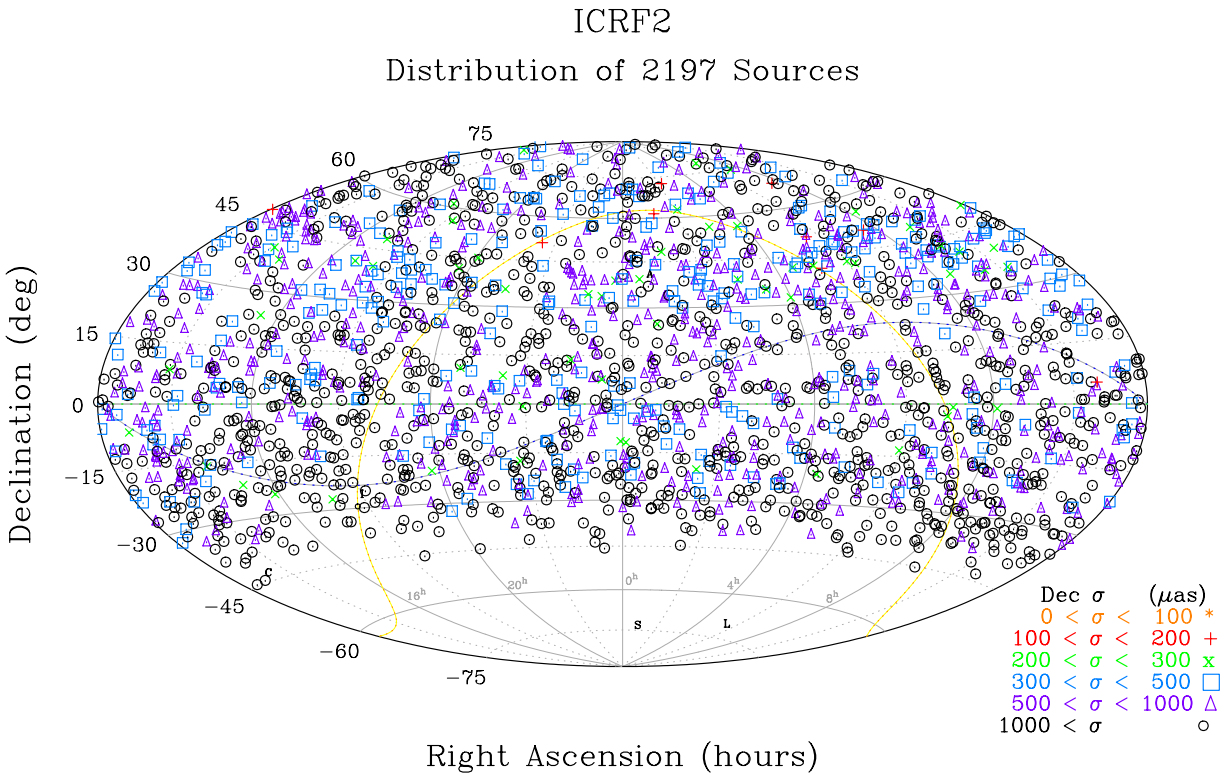

Figure 2: ICRF-2 survey sources. These 2197 sources are typically observed in only 1 or 2 sessions resulting in a median precision of $\sim$ 1 mas—5 times lower precision than non-VCS sources (Beasley *et al*, 2002). The lack of sources south of $-45°$ is due to the geometric limits of the all-northern VLBA. No comparable mas-level survey was available in the south at the time the ICRF2 was constructed. The LBA Calibrator Survey work now underway will help to rectify this gap.

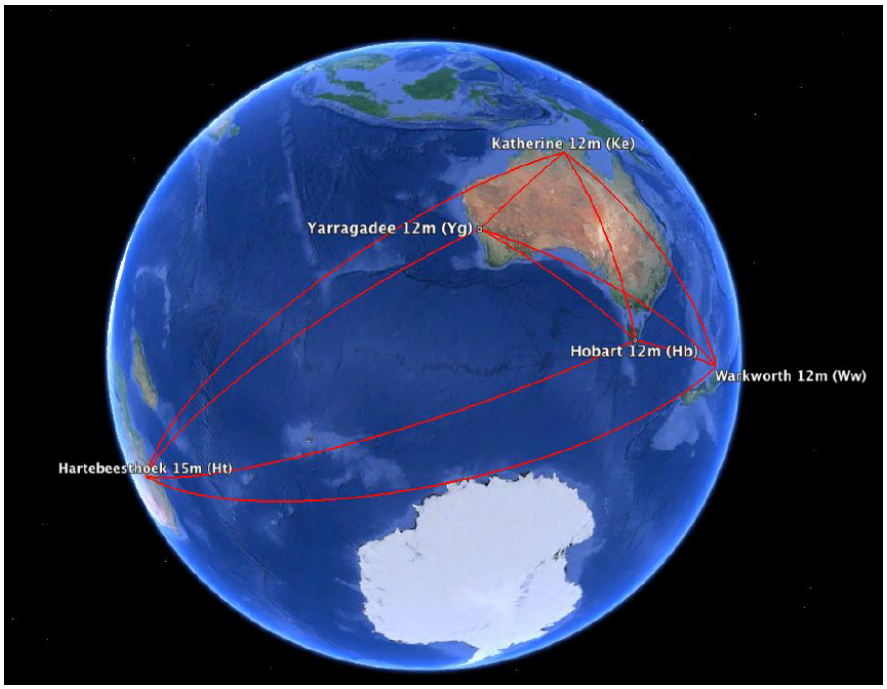

Figure 3: Southern stations: These new, fast southern stations are expected to improve the ICRF in the south. Because the newer stations are 12–15 meters in diameter, larger antennas such as Parkes, DSS45, Hobart-26m, and Hart-26m will need to be added in order to detect weaker sources (Titov *et al*, 2013).

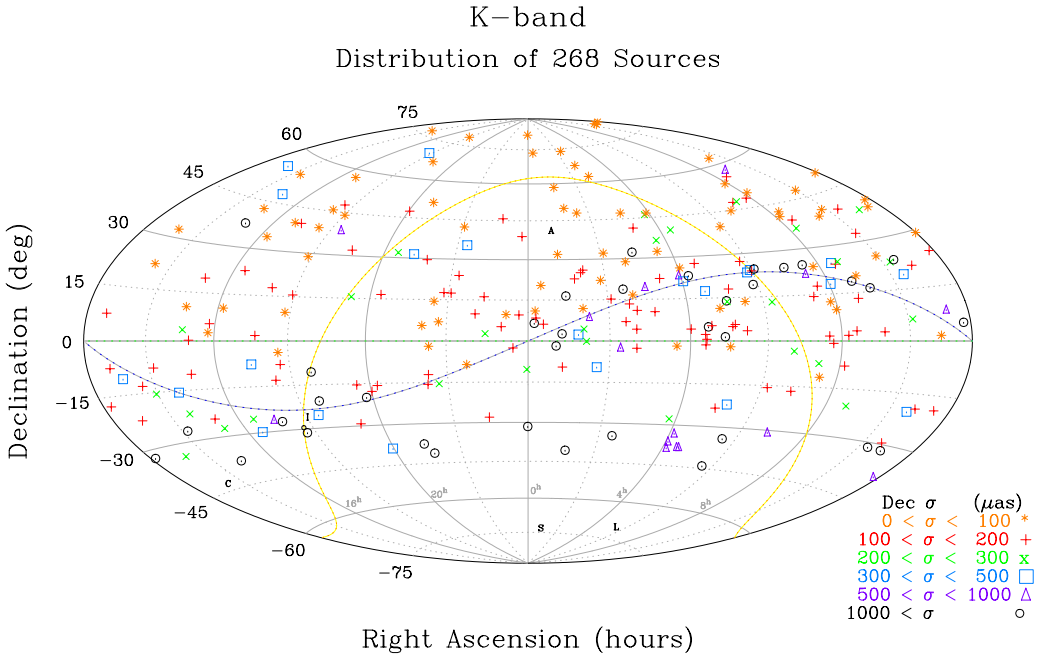

Figure 4: K-band Frame: Positions of 268 sources at 24 GHz were measured with the VLBA (Lanyi *et al*, 2010 and Charlot *et al*, 2010). Most with a precision better than 200 μas. The work of Bertarini *et al* is seeking to fill in the far south.

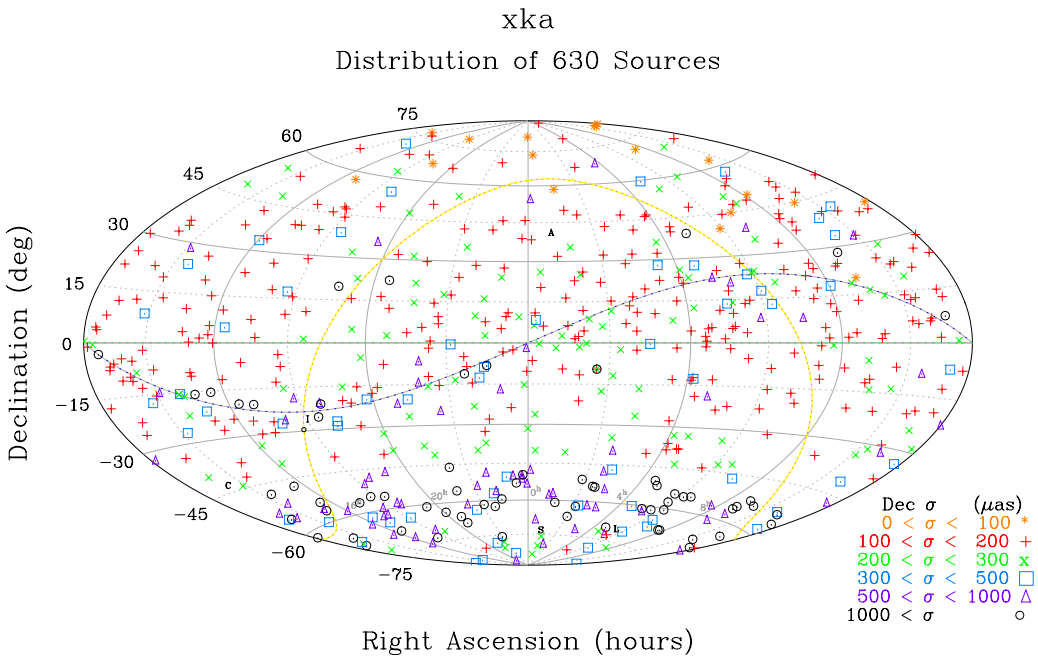

Figure 5: X/Ka Frame: Positions of 630 sources have been measured at 8.4/32 GHz using the combined NASA and ESA Deep Space Networks (Horiuchi *et al*, 2013).

GAIA STATUS AND EARLY MISSION

F. MIGNARD
University of Nice Sophia-Antipolis, CNRS, UMR Lagrange
Observatoire de la Côte d'Azur
bd de l'Observatoire, CS 34229 , 06304 Nice cedex 4
e-mail: francois.mignard@oca.eu

ABSTRACT.

After about 15 years of design and manufacturing the Gaia spacecraft was launched at the end of 2013. A nearly 6-month long in-orbit qualification and verification phase followed which formally ended in July 2014. This marked also the real start of the scientific mission with the regular observation taking. I report on this early mission phase and on the major findings made during the commissioning, allowing to give more realistic figures for the expected science performances.

1. GAIA LAUNCH AND EARLY OPERATIONS

The long awaited ESA space astrometry mission was successfully launched on 19 December 2013 at 09:12:18 UTC from the Europe's Spaceport in Kourou. Gaia was brought to space by a Soyuz ST-B launch vehicle equipped with a Fregat-MT upperstage. This Soyuz is the most recent version of this highly reliable rocket crowned with more than 1700 successful launches. It is, and by an enormous margin, the most used launcher since the beginning of the space era in 1957.

On January 7 the flight dynamic group at ESOC in Darmstadt sent a command to fire five of the eight thrusters attached to the chemical propulsion system to bring naturally Gaia onto its planned orbit around L2. This took place at 18:58 UTC and the burn lasted about two hours. The operation was very successful and completed as expected, with even a lower consumption of chemical due the accurate launch from Kourou. One week later a very small correction was applied to complete the insertion. From this day Gaia was on a pathway leading the spacecraft to reach its Lissajous orbit about L2 without further action. Later on, orbit manoeuvres are planned about every month to maintain the orbit within about 7000 km of this predicted path. The orbit reconstruction itself will reach a staggering accuracy of 100 m in position and 2.5mm/s in speed with the combination of the radio and optical tracking of Gaia.

During the few days after launch, several critical operations and tests have been completed:

- launch on 19th December 2013 from Kourou
- Sunshield successfully deployed within 90 mn of lift-off
- first reliable target orbit released by ESOC on 30 December
- focal plane video switched on on January 3, 2014 with all the 103 CCDs responding
- first image acquisition with a very bright star (α Aquarii)
- early scan in test mode starting on January 8, 2014
- injection to L2 done on 7 and 14 January, 2014 to near perfection
- service module in-flight test completed by mid-January without incident

The orbit, including the cruise phase to L2 is plotted in Fig. 1 for the whole 2014. The following years the same set of loops around L2 will repeat.

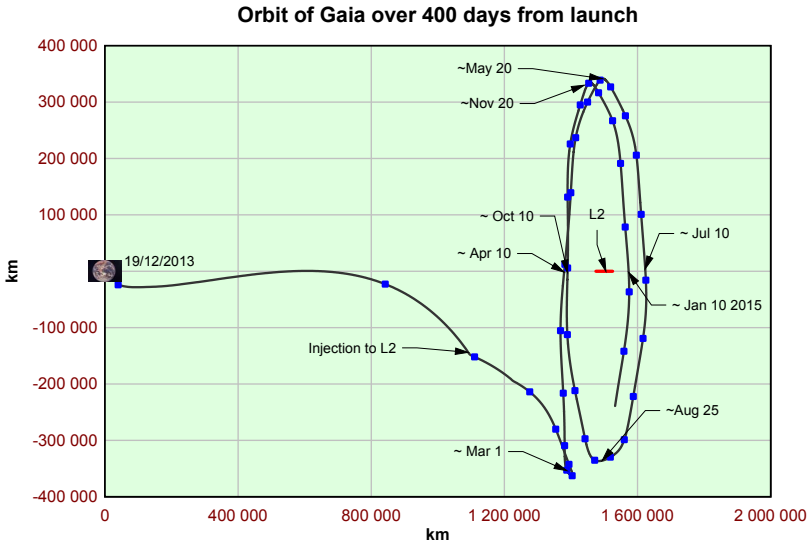

Figure 1: The orbit of Gaia in 2014. The orbit is plotted in a rotating frame and is referred to the Earth barycenter. The L2 point is not fixed in this frame, as the result of the elliptical orbit of the Earth-Moon barycenter about the Sun. The cruise phase is well visible on the left part of the plot.

The on-flight payload commissioning started early January after the completion of the Service Module qualification. All Gaia subsystems were tested during commissioning and can now be used in the routine phase of the mission. In particular:

- all 106 CCDs and associated electronics modules are working and are collecting data
- the data collection hardware is fully operational and the software has been tuned to match the in-orbit performances
- the science data from the CCDs is correctly transferred into the mass memory with an assigned priority
- the priority scheme on board is working correctly with low-priority data being overwritten in case of mass-memory overflow and high-priority data getting precedence in the downlink
- the telescopes have been aligned and focused for the full focal plane
- the attitude feed-back loop with the actuation of the micropropulsion system is operating normally
- the spacecraft spin rate has been matched to the clocking speed of the CCDs
- the phased-array antenna has a good link margin allowing high throughput of data to ground
- the power budget on board is very healthy
- the launch and all orbit corrections have been very accurate and efficient leaving a good margin of chemical propellant for all future orbit manoeuvres
- the science-mode attitude control is working very well, including the determination of the spin rate from the stars observed with the payload and the continuous adjustment of the spin rate with the micro-propulsion system
- the rubidium atomic clock on-board and the time-correlation procedure on ground provide the necessary accuracy for Gaia's science

2. UNEXPECTED PROBLEMS

While the overall functioning of all Gaia units is truly satisfactory, three significant departures from nominal were detected during the commissioning phase and are still under investigation.

- Undesired stray-light falling on the focal plane was detected early January and fully characterised the weeks after. It shows up as a periodic illumination of about 50% of the CCDs, with a period of 6h, equal to Gaia revolution period, and a phase indicating without ambiguity a geometry related to the direction of the Sun. The effect is smaller when the FOVs are at the largest angular distance from the Sun (135 deg) and increases gradually when the Sun is the closest (45 deg). The amount of light is large compared to the requirements, but still small in the absolute sense. The consequences are negligible for the bright stars, but the impact increases toward the smaller fluxes. The Radial Velocity instrument is the most affected by the effect and this will lead to a revision of the observation procedure to optimise the science return. There are apparently two distinct sources of parasitic light: one due the diffraction of the sunlight at the edge of the sunshield and the other from the Milky Way average brightness. Internal and hard to model reflections within the payload lead a small fraction of this light onto the focal plane.

- The angle between the two pointing directions of Gaia must be very stable over the spin period of 6h. For longer periods this is less critical and the angle is calibrated by the astrometric solution [1]. Given the importance of this issue, stringent design and manufacturing requirements were set by ESA to the Gaia industry main contractor. To control this stability Gaia is fitted with a metrological instrument (BAM: the Basic Angle Monitoring) to monitor passively the slightest high-frequency variations of this angle with few μas accuracy. It was expected that the natural variations would be below 10μas at the spin period thanks to a good thermal insulation. However the actual variations are much larger and close to 1 mas at the 6h-period. There is not yet a satisfactory explanation, but it has been demonstrated now that the BAM system does measure real variations. Its performance are good enough to calibrate the Basic Angle close to the required accuracy. A possible remaining calibration bias would affect the zero-point of the parallax and astronomical sources will be used at the mission end to assess and possibly correct this bias.

- The third anomaly seen during commissioning deals with the contamination of the mirror surfaces by water ice. Some water vapour has probably been stored into the Service Module during handling and is now released, enters the payload module before condensing on the cold surfaces. This impacts the overall optical throughput at a rate of a 10% efficiency loss per 50 to 100 days. The optical efficiency is regularly monitored and the contamination is removed by a periodic heating of optical parts. This is not a major inconvenient except for the increase of dead time, since after each heating one must wait the return to thermal stability at nominal temperature before collecting meaningful observations.

3. EXPECTED ASTROMETRIC PERFORMANCES

The astrometric standard-error is evaluated with the parallax according to general principles described in [2]. Calculation includes all known instrumental effects, including the straylight levels as measured during the commissioning phase. For instrument-related residual calibration errors at ground-processing level, an appropriate calibration error is included. So-called residual "scientific calibration errors" (e.g., mismatch of the model point spread function, sky-background estimation errors, etc.), all of which result from the on-ground data processing, are not included. These latter errors are assumed to be covered by a 20% margin. The post-commissioning values are given in Table 1. Compared to the pre-launch estimates, the degradation is limited to the faint stars, starting at about $V = 16$ in astrometry and is really significant for the mission faintest sources, which are also the most numerous. One must also notice that more bright stars will be eventually observable, since the conservative pre-launch detection limit was set at $V = 5.7$ instead of $V = 3$ for the current level. Even with this faint-end degradation, Gaia remains an unrivaled astrometry mission with its intrinsic performance and its survey mode with a single

instrument. Nothing better can be envisioned at the moment at least for two decades. For solar system objects, only the single-observation astrometric accuracy makes sense, but due to the scanning mode used by Gaia this accuracy is essentially 1-dimensional. Applying a typical degradation by a factor between 4 and 5 from the performances, one has a good measure of the individual epoch astrometry applicable to asteroids. This will be further degraded for planets with large apparent diameters (say above 100 mas) and fast moving (typically the NEOs with displacement > 100 mas/s). The vast majority of the asteroids are outside these ranges.

Table 1: Expected science performance after commissioning given as end-of-mission parallax standard errors averaged over the sky with uniform distribution.

	B1V μas	G2V μas	M6V μas
Bright stars	$3 < V < 12$ 5–14	$3 < V < 12$ 5–14	$5 < V < 14$ 5–14
V = 15	26	24	9
V = 20	600	540	130

4. CONCLUSION

On July 18, 2014 the commissioning phase was formally terminated and the Gaia in-orbit commissioning review (IOCR) took place. The IOCR board has endorsed all the recommended actions to mitigate the problems detected during the qualification. The mission has been formally handed from the ESA Project Manager (G. Sarri) to the ESA Mission Manager (W. O'Mullane). The nominal science mission has then started with about four weeks on an ecliptic pole scanning mode, before drifting continuously to the nominal scanning mode in September 2014. The scanning parameters will be selected and fixed for the next five years. During the commissioning phase nearly 30 billion astrometric images has been collected together with 2 billion spectra by the RVS instrument. The first public data release is now planned for mid-2016, nine months later than the pre-launch schedule. This is due partly to the much longer commissioning phase and to the need for the data processing to cope with a more difficult instrument calibration than foreseen during the preparatory phase.

References

[1] Lindegren, L., Lammers, U. et al., 2012, The astrometric core solution for the Gaia mission. Overview of models, algorithms, and software implementation, A&A vol. 538.

[2] De Bruijne, J. et al., 2005, Gaia astrometric,photometric,and radial-velocity performance assessment methodologies, Gaia Tecnical Note, Gaia-JDB-022.

EXTENDING THE K-BAND CELESTIAL FRAME EMPHASIZING SOUTHERN HEMISPHERE

A. DE WITT[1], A. BERTARINI[2], S. HORIUCHI[3], C. S. JACOBS[4], T. JUNG[5], J. E. J. LOVELL[6], J. N. MCCALLUM[6], J. F. H. QUICK[1], B. W. SOHN[5], R. OJHA[7]

[1] Hartebeesthoek Radio Astronomy Observatory
Farm 502 JQ, Hartebeesthoek, Broederstroom Road, Krugersdorp District, South Africa
e-mail: alet@hartrao.ac.za
[2] Max Planck Institut für Radioastronomie, Bonn, Germany
[3] C.S.I.R.O/Canberra Deep Space Communications Complex, Australia
[4] Jet Propulsion Laboratory, California Institute of Technology/NASA, Pasadena, CA, US
[5] Korea Astronomy & Space Science Institute, Daejeon, Republic of Korea
[6] University of Tasmania, Hobart, Australia
[7] Goddard Space Flight Centre/NASA, Greenbelt, MD, US

ABSTRACT. K-band radio observations have the potential to form the basis for the most accurate celestial reference frame (CRF) ever constructed. We present a new collaboration to observe southern hemisphere extra-galactic radio sources at 22 GHz (K-band). The aim of this project is to densify the ICRF at that frequency and to provide calibrators for astronomy. Relative to the standard S/X observing bands, at K-band sources are expected to exhibit more compact source morphology and reduced core shift. This reduction of astrophysical systematics should be advantageous in tying the VLBI radio frame to the Gaia optical frame. Initial fringe demonstrations were carried out on 23 August 2013 between telescopes in Australia, Korea and South Africa. The Korea to South Africa baselines will extend K-band CRF coverage down to about $-45°$ declination. Observations between Australia and South Africa will extend coverage to the south polar cap and thus gain full sky coverage for the K-band CRF. The second phase of our plan includes more extensive astrometric observations to complete sky coverage at K-band as well as observations using a larger network of telescopes in an effort to image source structure.

1. INTRODUCTION

Very long baseline measurements of positions of extragalactic radio sources define and maintain the current International Celestial Reference Frame (ICRF-2, Ma et al., 2009), which forms the underlying basis for positional astronomy. The ICRF-2 is based on dual frequency 2.3 GHz (S-band) and 8.4 GHz (X-band) Very Long Baseline Interferometric (VLBI) observations of 3414 reference sources, including 295 "defining' sources which determine the orientation of the frame's axes. Quasars being at great distances do not exhibit any measurable proper motion or parallax, making them ideal reference sources. VLBI observations of weaker sources, VLBI astrometry, spacecraft tracking, navigation and geodetic VLBI all rely on having reference sources which are compact, have strong VLBI detections, and have accurate, stable positions at the sub-milliasrcsecond level.

Unfortunately, at the standard S/X frequencies, many radio sources exhibit spatially extended structure that may vary in both time and frequency. Such structure can introduce significant errors in the VLBI measurements thereby degrading the accuracy of the estimated source positions. Our solution is to observe at higher radio frequencies such as K-band where on VLBI scales (milliarcsecond) sources tend to be more compact (e.g. Bietenholz et al., 2004; Charlot et al., 2010). VLBI observations of extragalactic radio sources have also shown that the location of the peak brightness point often varies with observing frequency due to opacity effects, a phenomenon sometimes called "core-shift". In particular, VLBI images of active galactic nuclei (AGN) show that the observed position of the peak brightness point moves closer to the central black hole as the frequency increases (e.g. Sokolovsky et al., 2011). Thus by observing at frequencies higher than the standard S/X bands we can expect to see more compact structure and also reduce the effect of core shift (Kovalev et al., 2008). This reduction in astrophysical systematics should allow for a more accurate and stable reference frame at higher frequencies and be particularly

advantageous in tying the VLBI reference frame to future optical reference frames such as Gaia.

2. HIGH FREQUENCY RADIO FRAMES

At present there are far fewer observations of extra-galactic radio reference sources at high radio frequencies compared to the standard S/X observing bands and many efforts are currently underway to improve the radio frequency coverage. Astrometric VLBI observations at 32 GHz (Ka-band) from NASA's Deep Space Network has already developed a catalogue of ~ 631 observable sources (134 south of $-45°$ declination) with highly accurate positions for improved deep-space navigation (Jacobs, 2013), showing that there are sufficient strong sources at higher frequencies. However, the Ka-band effort involved only a small number of telescopes and no source images were made. Astrometric and imaging observations by Lanyi et al., (2010) and Charlot et al., (2010), provided a foundation for the development of a reference frame at K-band. The current K-band frame consists of only 279 sources with weak coverage in the southern hemisphere, showing a rapid drop in source density at declinations south of $-30°$ (see Figure 1).

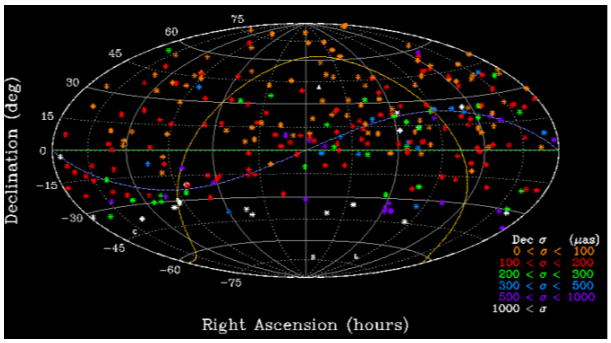

Figure 1: The distribution of celestial reference frame sources at 24 GHz (Lanyi et. al., 2010).

Because many stations across the globe have K-band receivers there is now an opportunity to create a worldwide K-band network with potential for high resolution imaging and astrometry. The advantage of observing at K-band is that radio observatories typically have K-band receivers, while Ka-band receivers are typically only available at tracking stations which are very few in number. The network of telescopes that can observe at K-band is therefore much bigger. For very long baseline observations at K-band, calibrator reference sources are also needed, in particular for trigonometric parallax distances to H_2O (22 GHz) masers as well as phase referenced observations to image the sub-milliarcsecond structure of the most compact regions of emission in AGN. High-resolution K-band observations would be of much value to study wavelength dependent systematic errors due to the core-shift effect.

3. WHY OBSERVE IN THE SOUTHERN HEMISPHERE ?

VLBI observations in the southern celestial hemisphere have always been more difficult both because there are fewer radio telescopes in the south than in the north, and because there are fewer known reference sources in the south. There have been many efforts in recent years to increase the number of known calibrator reference sources in the south, in particular the LBA calibrator survey (LCS), which has already produced a significant improvement at X-band (Petrov et al., 2011). There have also been a few observations at S-band, for example, Hungwe et al. (2011), and southern observations are planned at 1.6 GHz (L-band), to improve the number of calibrator sources for phase-referencing at low frequencies. In 2012 an International Astronomical Union (IAU) working group was formed with the goal of the realisation of the next generation International Celestial Reference Frame (ICRF-3), with specific emphasis on improving the accuracy and coverage in the southern hemisphere. Dedicated astrometric observations to improve the southern celestial reference frame at S/X band are currently underway, as proposed in Lovell et al. (2013). However, at present there are virtually no VLBI observations of reference sources at 22 GHz (K-band). All these low frequency programs thus invite complementary work at K-band.

4. VLBI OBSERVATIONAL PLAN AND NETWORK GEOMETRY

Observations to complete the sky coverage at K-band are under way and preliminary astrometric observations were carried out on 23 August 2013 between telescopes in Australia (Hobart 26m), Korea (Tamna 21m) and South Africa (HartRAO 26m). The Korea to South Africa baselines will extend K-band CRF coverage down to about $-45°$ declination, and observations between Australia and South Africa will extend coverage to the south polar cap and thus gain full sky coverage for the K-band celestial reference frame. Observations between Tamna and HartRAO are limited to about $\pm 45°$ declination and less than 4 hours of mutual visibility. More extensive astrometric observations are planned for the 21st of December 2013 that will also include the Tidbinbilla 70m DSN antenna in Australia.

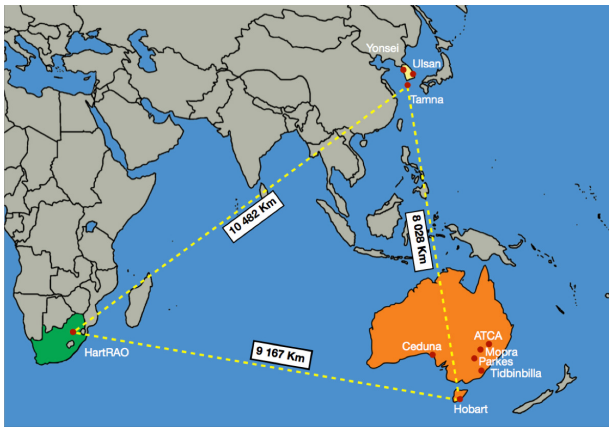

Figure 2: A map showing the proposed telescopes for the southern hemisphere K-band observations.

However, for imaging of source structure, as oppose to astrometry, a larger network of telescopes that provide a variety of baseline lengths and orientations is needed. For this purpose we have also submitted a proposal to observe and image a set of potential K-band reference sources at declinations below $-30°$. We will use the full Australian Large Baseline Array (AT-LBA), that will additionally also include the ATCA (6 x 22m), Ceduna (30m), Mopra (22m) and Parkes (64m) telescopes in Australia (see Figure 2). It should be noted, however, that although the AT-LBA provide a large network of antennas, we are still missing intermediate baseline lengths of a few 1000 km.

5. PRELIMINARY OBSERVATIONS AND RESULTS

In this study we tested the capability of the antennas to generate fringes, given the chosen setup. The observation ran for 4 hours on August 23rd, 2013, and about 20 sources from the LCS catalogue were observed. The frequency range that we selected serves to optimise the delay resolution function given all the constraints. Table 1 shows the selected frequencies for our observations and Figure 2 shows the obtained multi-band delay (MBD) resolution function.

BBC 1	BBC 2	BBC 3	BBC 4	BBC 5	BBC 6	BBC 7	BBC 8
22120.49	22152.49	22184.49	22232.49	22360.49	22424.49	22456.49	22488.49

Table 1: Centre sky frequency in MHz (channels are ± 16 MHz wide).

The standard deviation in the estimate of the MBD function derived from bandwidth synthesis is given by

$$\sigma_\tau = \frac{1}{2\pi \cdot SNR \cdot \Delta\nu_{rms}} \tag{1}$$

where the $\Delta\nu_{rms} = \sqrt{\frac{\sum(\nu_{BBC}-\bar{\nu})^2}{N-1}}$ with ν_{BBC} equal to the frequency of the baseband converter (BBC) channels, $\bar{\nu} = \frac{\sum \nu_{BBC}}{N}$ is the mean frequency and N is the number of BBCs (Clark et al., 1985). From Equation 1, the integration time and bandwidth are the only parameters that can be adjusted to improve

the precision of the group delay measurements. However, the integration time should be kept short to permit collecting observations at as many different geometries as possible for a good estimate of the atmospheric delay at the radio telescopes. Short integrations are also desirable because at higher radio frequencies the coherence time is short (often only $1-2$ minutes). As example, if we consider a source giving an SNR of 70, the uncertainty on the source position is about 0.1 mas, a typical value for astrometric VLBI. For historical reasons, astrometric data are taken using only the right circular polarisation (RCP) channel of the receiver. For consistency we also adopted this convention.

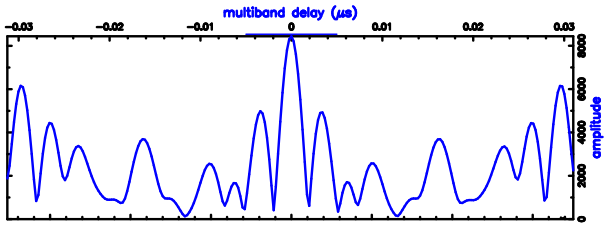

Figure 3: Measured delay resolution function using frequencies from Table 1.

We found fringes although the weather has been bad at all the sites. Figure 3 shows, as an example, the detection of ICRF J1427-4206 between HartRAO and Hobart (SNR = 70). Given the positive results of the test, we will proceed with a 24 hour observation, planned for the 21st of December 2013 .

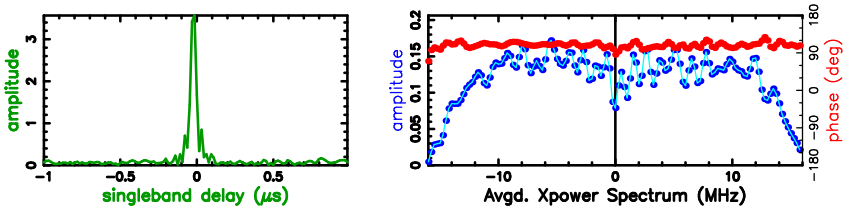

Figure 4: HOPS fourfit plot, showing the single-band delay (left) and the averaged power spectrum between HartRAO and Hobart26 for ICRF J1427-4206.

6. REFERENCES

Bietenholz, M. F., Bartel, N. & Rupen, M. P., 2004, "The Location of the Core in M81", ApJ, 615, pp. 173

Charlot, P. et al., 2010, "The Celestial Reference Frame at 24 and 43 GHz. II. Imaging", AJ, 139, pp. 1713

Clark, T. A. et al., 1985, "Precision Geodesy Using the Mark-III Very-Long-Baseline Interferometer System", IEEE TGRS, GE-23, no. 4, doi: 10.1109/TGRS.1985.289433

Hungwe, F. et al., 2011, "Characterization of long baseline calibrators at 2.3 GHz", MNRAS, 418, pp. 2113

Jacobs, C. S., 2013, "Proposed Roadmap for the ICRF-3", in Proceedings of the Journées 2013

Kovalev, Y. Y., et al., 2008, "Opacity in compact extragalactic radio sources and its effect on astrophysical and astrometric studies", A&A, 483, pp. 759

Lanyi, G. E., et al., 2010, "The Celestial Reference Frame at 24 and 43 GHz. I. Astrometry", AJ, 139, pp. 1695

Lovell, J. E. J., et al., 2013, "The AuScope geodetic VLBI array", Journal of Geodesy, 87, pp. 527

Ma, C. et al., 2009, "The Second Realization of the International Celestial Reference Frame by Very Long Baseline Interferometry", IERS Technical Note, 35, pp. 1

Petrov, L., et al., 2011, "The LBA Calibrator Survey of southern compact extragalactic radio sources - LCS1", MNRAS, 414, pp. 2528

Sokolovsky, K. V. et al., 2011, "A VLBA survey of the core shift effect in AGN jets. I. Evidence of dominating synchrotron opacity", A&A, 532, pp. A38

IMPACT OF SEASONAL STATION DISPLACEMENT MODELS ON RADIO SOURCE POSITIONS

H. KRÁSNÁ[1], Z. MALKIN[2,3], J.BÖHM[1]
[1] Vienna University of Technology
Department of Geodesy and Geoinformation E120/4
Gußhausstraße 27-29, A-1040 Vienna, Austria
e-mail: hana.krasna@tuwien.ac.at and johannes.boehm@tuwien.ac.at
[2] Pulkovo Observatory
Pulkovskoe Sh. 65, St. Petersburg 196140, Russia
e-mail: malkin@gao.spb.ru
[3] St. Petersburg State University
Universitetskii Pr. 28, St. Petersburg 198504, Russia

ABSTRACT. The International Terrestrial Reference Frame considers the position at a reference epoch plus a linear velocity term for station coordinates. However, the determination of the actual station position requires several other corrections partially recommended by the IERS Conventions (e.g., solid Earth tides, ocean tidal loading) as well as other non-linear displacements. In this study we focus on the impact of the seasonal station motions on the Celestial Reference Frame (CRF). The increasing accuracy of Very Long Baseline Interferometry (VLBI) observations and the growing time span of available data allow the determination of seasonal signals in station positions which still remain unmodelled in the conventional analysis approach. For that purpose, we create empirical harmonic models for selected stations within a global solution of all suitable VLBI sessions at annual and semi-annual periods. Furthermore, we introduce average annual models created by stacking yearly time series of station positions. The celestial reference frames estimated simultaneously with terrestrial reference frames are compared to each other. We find that seasonal station movements do not yield any significant systematic effect on the CRF but can cause significant changes in positions of radio sources observed only in a small number of sessions non-evenly distributed over the year.

1. INTRODUCTION

The analysis of measurements from space geodetic techniques requires the use of the best available models describing the deformation of Earth surface. The goal is to have a set of models which realistically describe changes in the station positions on the Earth surface during the time when the observations are carried out. As reported, e.g., by Collilieux et al. (2007), van Dam et al. (2007), Tesmer et al. (2009) or Malkin (2013) there are still deficiencies in the modelling of station movements over longer periods and systematic long-period signals are present in the station position time series. Malkin (2013) investigated the impact of the seasonal station movements on the estimated Universal Time (UT1) from the single-baseline intensive sessions. In this paper we consider the impact of the unmodelled effects on the VLBI results obtained from the 24-hour multi-baseline VLBI sessions. In particular we focus on the propagation of the seasonal station movements to the radio source positions building the celestial reference frame (CRF). Two treatment approaches of the unmodelled seasonal station displacement are introduced. First we model the surface deformation as a periodic movement with annual and semi-annual periods, in the second approach we create average annual models.

2. SEASONAL STATION DISPLACEMENT MODELS

About 5.6 million VLBI observations from 1984.0 to 2013.3 were analysed with geodetic VLBI analysis software VieVS (Böhm et al., 2012). The usual analysis strategy was applied, i.e. solid Earth tides, ocean tide loading, pole and ocean pole tide loading were modelled a priori according to the International Earth Rotation and Reference Systems Service (IERS) Conventions 2010 (Petit and Luzum, 2010). Additionally, we corrected a priori for tidal and non-tidal atmosphere loading (Petrov and Boy, 2004) as well as for

thermal deformation (Nothnagel, 2009). VieTRF13b and VieCRF13b, the reference frames estimated at the Vienna University of Technology, were used as priori terrestrial (TRF) and celestial reference frames. For each session a normal equation system was set up which included station coordinates and velocities, source coordinates, Earth orientation parameters (one offset), zenith wet delays (constrained with 1.5 cm after 60 minutes), tropospheric gradients (constrained with 0.05 cm after 6 hours), and clock parameters. In the reference solution, where source coordinates were fixed to their a priori values and station coordinates were estimated session-wise with no-net-translation (NNT) and no-net-rotation (NNR) conditions w.r.t. the VieTRF13b, a clear seasonal signal in the station position time series was visible. Therefore, we introduce two empirical models which describe the remaining long-period signal in the station coordinate time series. The first one is a harmonic model for annual and semi-annual periods, and the second one is an averaged model over a year. The average annual models were determined from the reference solution following the approach of Tesmer et al. (2009). First, an offset in each year of the estimated session-wise station coordinates was removed from the time series, then the time series were stacked into one mean year and a smoothing of the position estimates into a mean annual signal was done. For the smoothing a predefined smoothing spline function in the software MatLab was used, as weights the formal errors of the estimated coordinates were applied.

The study of seasonal station displacement was done for all stations which participated in more than 50 sessions and with observations evenly distributed over the yearly period. Consequently, we excluded the station O'Higgins from the study, which - due to its location in Antarctica - only observes during southern hemisphere summer months. Furthermore, with the afore-described parameterisation a global solution (S1G) was run where terrestrial and celestial reference frame were estimated simultaneously. The TRF was aligned to the a priori reference frame with the NNT+NNR condition on a set of 22 core stations, and for the CRF the NNR condition on 285 radio sources was applied. Tropospheric parameters (i.e., zenith wet delay and gradients), clock parameters, and Earth orientation parameters were reduced from the normal equations and estimated as arc parameters, i.e. from single session adjustment.

Thereafter, a second analysis of VLBI data was performed (solution S2G) in which sine and cosine amplitudes belonging to the annual and semi-annual periods were estimated as global parameters in a common adjustment of VLBI sessions together with terrestrial and celestial reference frames. Figure 1 shows the stacked time series of the height, east and north components for the ten most observing stations during the analysed time period. In light red colour the obtained model gained by adding the

http://vievs.geo.tuwien.ac.at/results

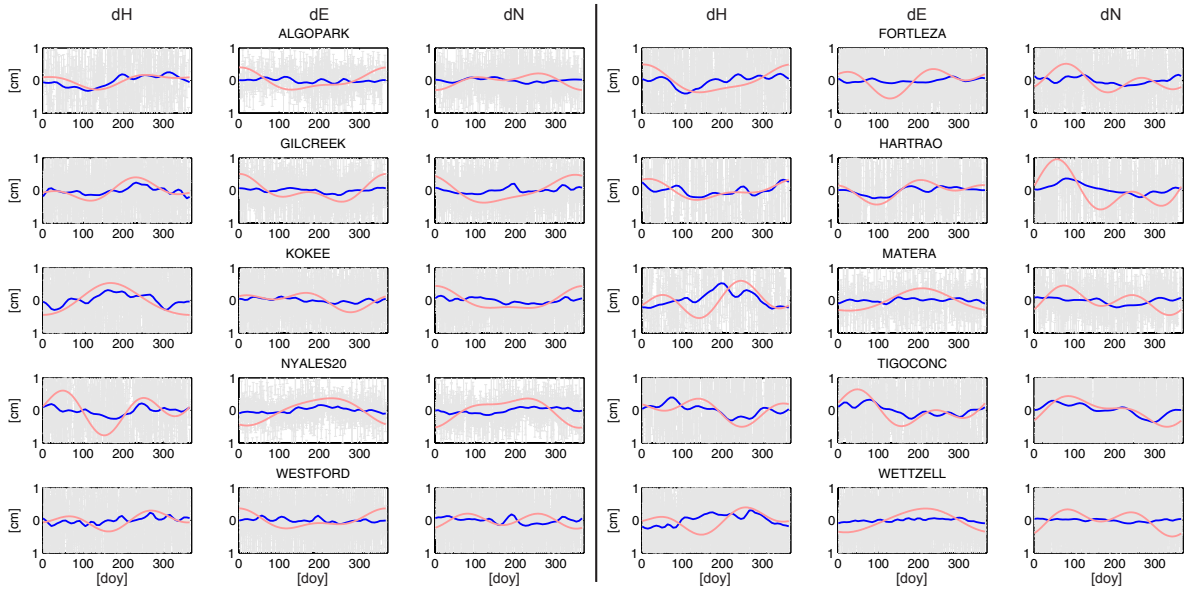

Figure 1: Seasonal station displacement models for ten stations which observed in most of the VLBI sessions. In light red the harmonic model and in blue the mean annual models are shown.

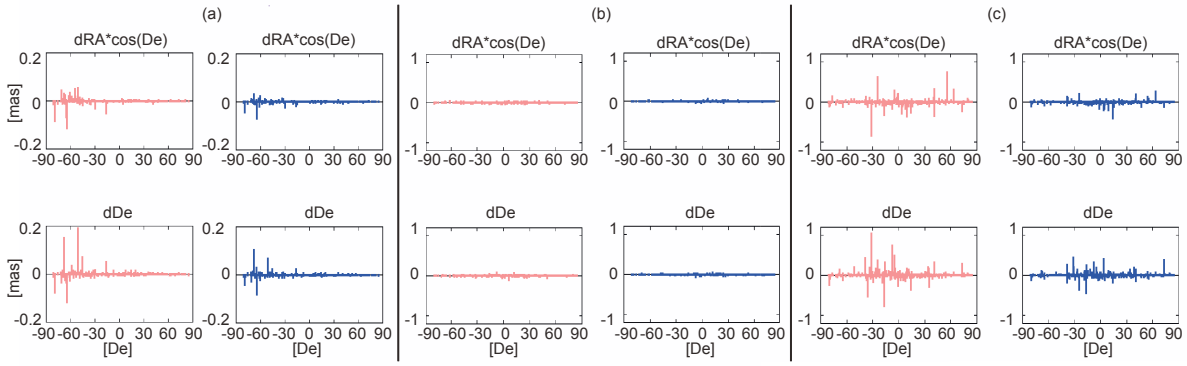

Figure 2: Differences between estimated radio source coordinates in right ascension (upper plots) and declination (lower plots). In light red the differences between solutions 1 and 2 (S1G-S2G) and in blue between solutions 1 and 3 (S1G-S3G) are plotted. The left-hand side plots "(a)" show datum sources, middle plots "(b)" contain only sources observed in at least two sessions with more than 20 observations, and right-hand side plots "(c)" depict all radio sources in the estimated CRF.

two harmonic components with annual and semi-annual periods is plotted. In blue colour the average annual model for the station displacement is shown which was applied a priori on the station coordinates in addition to the standard modelling in the third global solution (S3G). In this way a third pair of celestial and terrestrial reference frames from a global solution was obtained.

3. COMPARISON OF CELESTIAL REFERENCE FRAMES

The three global solutions described above yielded three celestial reference frames. The differences between the CRF where the harmonic signals in the station position were taken into account (S2G) and the standard solution (S1G) are plotted in light red colour in Figure 2. In blue colour the comparison between the CRF with reduced mean annual signal from the station coordinates (S3G) and the standard solution (S1G) is shown. In the upper plots the comparison in right ascension ($dRA \cdot \cos(De)$) and in the lower plots the differences in declination (dDe) are illustrated. The first two columns on the left-hand side designated as "(a)" display the comparison between the datum sources only, in the middle "(b)" differences between sources which participated in at least two sessions and were observed more than 20 times are shown, and the two last columns "(c)" depict the differences between all sources in

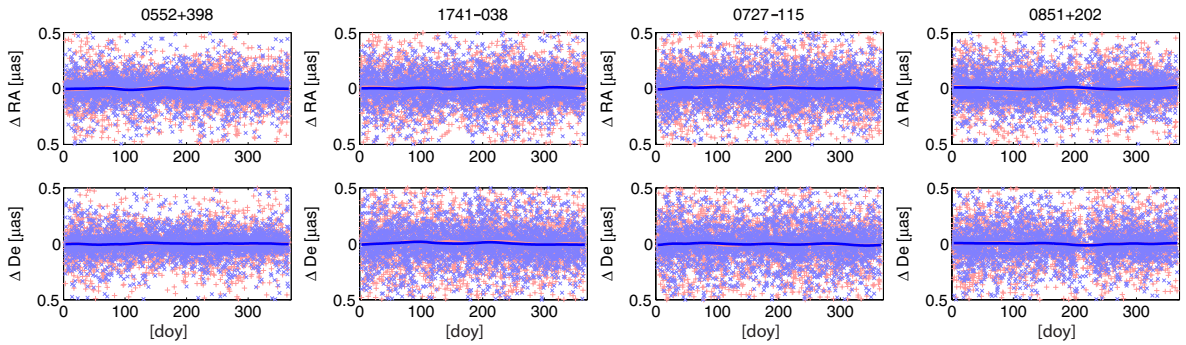

Figure 3: Differences in session-wise estimated coordinates for four most observed sources in right ascension (upper plots) and declination (lower plot) are shown. The light red "+" depict the differences between S2 w.r.t. S1 and the blue "x" show the differences between S3 w.r.t. S1. The lines are smoothed mean annual signal.

the estimated CRF. From the plots it is obvious that the application of seasonal station models does not cause any systematic effect in the estimated source coordinates. However, significant changes in the individual source position appear if the source is observed only in a small number of sessions distributed non-evenly over the year. This happens for the datum sources in the southern hemisphere, where the difference between the solutions reaches up to 0.2 mas. For the other sources observed only in one session with very few observations the difference in the estimated coordinates reaches up to 1 mas (Figure 2 (c)). In the middle plots which contain only sources with more than 20 observations these large differences vanish.

Beside the comparison of celestial reference frames, we also focused on a comparison between estimated time series of the source coordinates. We run again all three global solutions but excluded the four most observed sources from the celestial reference frame and estimated them session-wise as reduced parameters. Figure 3 shows the estimated positions of these most observed sources in our analysis with respect to the solution S1 . The light red "+" show the differences between the session-wise radio source coordinates from solutions S2 and S1, and differences between solutions S3 and S1 are plotted as blue "x". The lines depict the smoothed average annual signal. There is no significant propagation of the neglected seasonal signal from the station coordinates into the radio source positions. The differences between the solutions lie in the sub-microarcsecond range.

4. CONCLUSIONS

Two kinds of models for unmodelled long-period signals in station coordinates were created. One of them being the harmonic model at annual and semi-annual periods, the second one a non-harmonic mean annual model. Seasonal station movements do not yield any significant systematic effect on the CRF but can cause a significant change in position of radio sources with a small number of sessions non-evenly distributed over the year.

Acknowledgements. The authors acknowledge the International VLBI Service for Geodesy and Astrometry (IVS) and all its components for providing VLBI data. Hana Krásná is supported by the Austrian Science Fund within the FWF-Project P23143-N21 (Integrated VLBI).

5. REFERENCES

Böhm, J., Böhm, S., Nilsson, T., Pany, A., Plank, L., Spicakova, H., Teke, K., Schuh, H., 2012, "The new Vienna VLBI Software VieVS", IAG Symposium Series 136, Kenyon, S., Pacino, M.C., Marti, U. (eds.), pp. 1007–1011.

Collilieux, X., Altamimi, Z., Coulot, D., Ray, J., Sillard, P., 2007, "Comparison of very long baseline interferometry, GPS, and satellite laser ranging height residuals from ITRF2005 using spectral and correlation methods", J. Geophys. Res.112(B12403), pp. 1–18.

Malkin, Z., 2013, "Impact of seasonal station motion on VLBI UT1 intensives results", J. Geod. 87, pp. 505–514.

Nothnagel, A., 2009, "Conventions on thermal expansion modelling of radio telescopes for geodetic and astrometric VLBI", J. Geod. 83, pp. 787-792.

Petit, G., Luzum, B., 2010, "IERS Conventions 2010", IERS Technical Note No. 36, p. 179.

Petrov, L., Boy J.-P., 2004, "Study of the atmospheric pressure loading signal in very long baseline interferometry observations", J. Geophys. Res.109(B03405), pp. 1–14.

Tesmer, V., Steigenberger, P., Rothacher, M., Boehm, J., Meisel, B., 2009, "Annual deformation signals from homogeneously reprocessed VLBI and GPS height time series", J. Geod. 83, pp. 973–988.

van Dam, T., Wahr, J., Lavallée, D., 2007, "A comparison of annual vertical crustal displacements from GPS and Gravity Recovery and Climate Experiment (GRACE) over Europe", J. Geophys. Res.112(B03404), pp. 1–11.

ON ERRORS OF RADIO SOURCE POSITION CATALOGS

Z. MALKIN
Pulkovo Observatory, St. Petersburg, Russia
St. Petersburg State University, St. Petersburg, Russia
e-mail: malkin@gao.spb.ru

ABSTRACT. In this paper, a new method of investigation of the external radio source position catalogs RSPCs stochastic errors is presented. Using this method the stochastic errors of nine recently published RSPCs were evaluated. It has been shown that the result can be affected by the systematic differences between catalogs if the latter are not accounted for. It was also found that the formal uncertainties of the source position in the RSPCs correlate with the external errors. We also investigated several topics related to the formal uncertainties and systematic errors of RSPC.

1. INTRODUCTION

VLBI is currently the primary technique for maintening International Celestial Reference Frame (ICRF, Ma et al. 2009). The latter is realized as a catalog of radio source coordinates derived from processing of VLBI observations. Assessing the systematic and stochastic errors of radio source position catalogs (RSPCs) plays an important role in improvement of the ICRF. The internal stochastic error of the RSPCs is determined by the source position uncertainties given in the catalog. The external stochastic error can be assessed only from mutual comparison of several RSPCs.

In this work, we present a new approach to computation of the external stochastic errors of RSPCs. It allows to simultaneously analyze an unlimited number of RSPCs, the more the better, in fact. A key point is a new method of estimation of the correlation between catalogs. Another development is a new concept of weighted correlation coefficient, which is important for analysis of unevenly weighted data. The third improvement is accounting for systematic differences between catalogs. With this method, we obtained errors of nine recently published RSPCs. See Malkin (2013) for detailed description of the method and results.

We also investigated several other topics related to the formal uncertainties of the ICRF2 sources and a correspondence between the formal and external errors in source position.

2. METHOD OF THE ASSESSMENT OF EXTERNAL CATALOG ERRORS

We base our analysis at the 3-cornered hat method (TCH) originally developed for investigation of the clock frequency instability. In its original formulation, the TCH method was applied to three series of measurements, however it can be generalized to N-cornered-hat (NCH) method. If we analyze N catalogs, we have to solve the following system:

$$\sigma_{ij}^2 = \sigma_i^2 + \sigma_j^2 - 2\rho_{ij}\sigma_i\sigma_j, \quad i = 1 \ldots N-1,\ j = i+1 \ldots N\,, \tag{1}$$

where σ_{ij} are variances of paired differences between catalogs, ρ_{ij} are correlation coefficients between catalogs, σ_i, σ_j are unknown external errors of catalogs. For N catalogs, we have $N(N-1)$ equations.

The key point of the method is to find reliable estimates of the correlation coefficients ρ_{ij}. We propose the following strategy to estimate ρ_{ij}. Let us have N catalogs. First we select sources in common in all the catalogs, which are used for the analysis.

Now we consider the i-th and j-th catalogs. At the first step we computed the differences between these catalogs with all k-th catalogs, $k = 1, ..., N,\ k \neq i,\ k \neq j$. After that, we computed the correlation ρ_{ij}^k between catalog differences $\Delta_{ik} = Cat_i - Cat_k$ and $\Delta_{jk} = Cat_j - Cat_k$ for each k, where Cat_i, Cat_j, and Cat_k are vectors of the source positions in common. Computations were made separately for right ascension (RA) and declination (DE). RA differences were multiplied by $\cos(DE)$. The average value of ρ_{ij}^k over all k was considered an approximation to the correlation ρ_{ij} between i-th and k-th catalogs.

To estimate the correlation coefficient between two RSPCs we used a weighted correlation coefficient defined as

$$\rho^w_{xy} = \frac{\sum\limits_i \sqrt{p_{x,i}p_{y,i}}(x_i - \bar{x})(y_i - \bar{y})}{\sqrt{\sum\limits_i p_{x,i}(x_i - \bar{x})^2 \sum\limits_i p_{y,i}(y_i - \bar{y})^2}}, \qquad (2)$$

where x_i and y_i are input data, $s_{x,i}$ and $s_{y,i}$ are their standard errors, $p_{x,i} = 1/s^2_{x,i}, p_{y,i} = 1/s^2_{y,i}$, $\bar{x}$ and $\bar{y}$ are weighted mean of x_i and y_i. Figure 1 shows an example of computation of the standard (ρ_{xy}) and weighted (ρ^w_{xy}) correlation coefficient for an artificial set consisting of five measurements with two outliers. In this example, the standard correlation coefficient is equal to zero, whereas the weighted correlation coefficient is about unity.

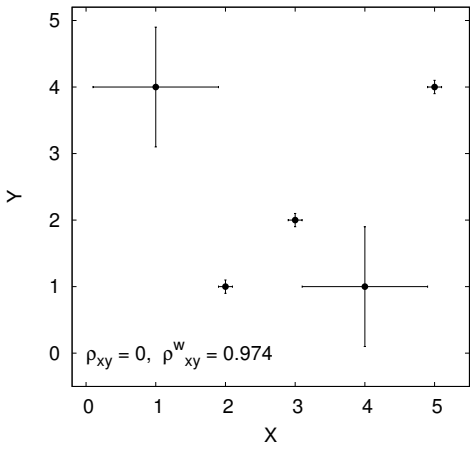

Figure 1: Standard (ρ) and weighted (ρ^w) correlation coefficient.

3. RESULTS OF ANALYSIS

We investigated nine recently published RSPCs: aus2012b, bkg2012a, cgs2012a, gsf2012a, igg2012b, opa2013a, rfc2013a, sha2012b, and usn2012a. They have 703 sources in common, which were used in subsequent computations.

The systematic differences between catalogs may have a substantial impact on the determination of their stochastic errors. Two examples of the systematic differences are depicted in Fig 2. Note larger differences in declination as compared with the differences in right ascension. One can see that the systematic differences between catalogs have a complicated structure, which cannot be described in terms of rotation and a few supplement low-frequency terms.

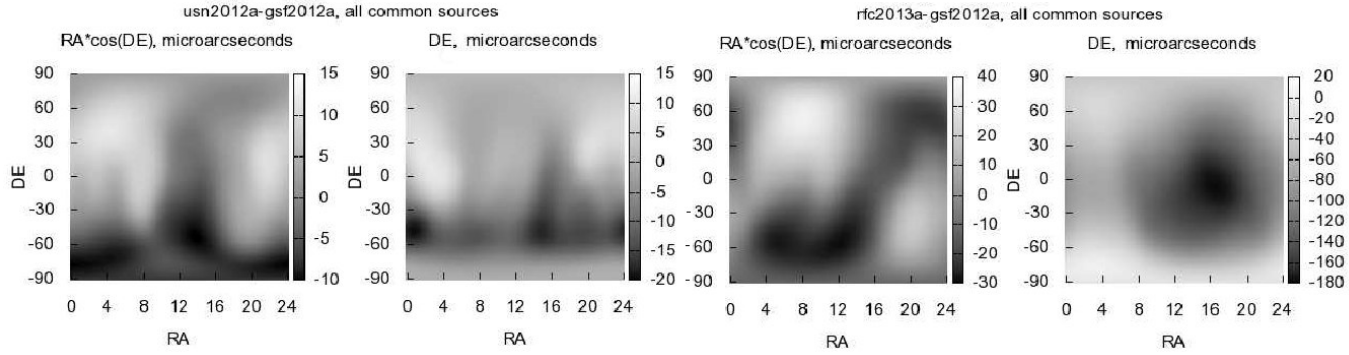

Figure 2: Systematic differences between catalogs: two examples of small (on the left) and large (on the right) differences. Unit: μas. See (Malkin 2013) for more plots.

The variances of the paired differences and correlation coefficients between catalogs were computed both for the original differences and the differences corrected for the systematic differences. It was found that both the variances of paired differences and the correlation coefficients between catalogs are substantially affected by the systematics (Malkin 2013) . The effect is especially significant for the pairs of catalogs with large systematic differences.

Table 1 shows the standard and weighted correlation coefficient between GSF and other catalogs. One can see that the correlations in RA and DE are very similar, and there is no clear dependence on the software. It is also noticeable that catalogs obtained at the same AC more closely correlate with each other than catalogs obtained in different ACs (Fig 3).

Finally, we computed the stochastic errors of the nine RSPCs in two ways: with and without correcting for the systematic differences between catalogs. The weighted correlation coefficients were used in both cases. The results are presented in Table 2. A comparison of the two variants shows that the systematic differences significantly affect the determination of their stochastic accuracy. The numbers in the last

Catalogs	ρ	ρ^w
	α / δ	α / δ
AUS – GSF	$+0.1861$ / $+0.2032$	$+0.1125$ / $+0.1129$
BKG – GSF	$+0.5082$ / $+0.6095$	$+0.4794$ / $+0.5038$
CGS – GSF	$+0.7711$ / $+0.7746$	$+0.6395$ / $+0.6348$
GSF – IGG	-0.0193 / $+0.2334$	$+0.3732$ / $+0.3693$
GSF – OPA	$+0.5210$ / $+0.4823$	$+0.4711$ / $+0.4931$
GSF – RFC	-0.2497 / -0.0311	$+0.2184$ / $+0.2582$
GSF – SHA	$+0.1528$ / $+0.1270$	$+0.1218$ / $+0.1195$
GSF – USN	-0.0268 / -0.0832	$+0.0099$ / $+0.0346$

Table 1: Standard (ρ) and weighted (ρ^w) correlation coefficients between GSF and other catalogs.

Catalog	B09	B10	B11	B12	G09	G10	G11	G12	O09	O10	O11	O12	O13
IF2	0.458	0.227	0.128	0.065	0.315	0.077	0.009	-0.052	-0.244	-0.295	-0.276	-0.283	-0.258
B09		**0.784**	**0.676**	**0.586**	0.220	0.187	0.152	0.130	-0.078	-0.085	-0.017	-0.009	0.003
B10			**0.929**	**0.808**	0.136	0.281	0.256	0.229	-0.016	-0.054	-0.051	-0.057	-0.039
B11				**0.923**	0.105	0.272	0.284	0.274	0.012	-0.024	-0.051	-0.074	-0.069
B12					0.091	0.260	0.275	0.327	0.033	-0.003	-0.047	-0.087	-0.119
G09						**0.639**	**0.519**	**0.335**	0.404	0.268	0.224	0.183	0.172
G10							**0.909**	**0.648**	0.295	0.309	0.298	0.248	0.225
G11								**0.777**	0.266	0.271	0.331	0.285	0.250
G12									0.189	0.206	0.269	0.289	0.276
O09										**0.738**	**0.503**	**0.394**	**0.320**
O10											**0.730**	**0.519**	**0.427**
O11												**0.857**	**0.732**
O12													**0.901**

Figure 3: Correlation coefficients between input catalogs. The catalog designation is formed from the first letter of the AC name (B for BKG, G for GSFC, O for OPA) and two last digits of year of publication; IF2 stands for ICRF2. The values related to catalogs obtained at the same AC are highlighted.

column of Table 2 are considered as the final result of our work. For comparison, the median source position uncertainty as reported in the catalog is given in the second column of Table 2. Figure 4 shows that the external stochastic errors correlate with formal (reported) uncertainties for catalogs with relatively large errors. For catalogs with higher accuracy, such a dependence is mush smaller.

Figure 5 shows the dependence of the position uncertainty in the ICRF2 catalog 2012a on the number of sessions and the number of observations (delays). Although the number of delays closely correlates with the number of sessions, the former seems to be the better argument for description of the dependence of the position uncertainty on the observational history of the source.

During computation of ICRF2, positions and position uncertainties of 39 sources were not solved as global parameters like positions and position errors of other *global* sources, but was derived from a special analysis of source position time series (Ma et al. 2009). For this reason, these sources were referred to as special handling sources (a.k.a. *arc* sources). As one can see in Fig. 5, formal errors in position of *arc* sources (marked with squares) do not correspond to general law. This problem was earlier addressed in the IERS/IVS ICRF2 Working Group discussions, but has not been satisfactory solved until now. Evidently, a special procedure to compute the position errors of these sources should be developed. On the other hand, a necessity for including *arc* sources in the ICRF may be worth further discussion.

4. CONCLUSION

1. A new approach to assess the external stochastic errors of radio source position catalogs has been developed. The new features of this method are: simultaneous processing of all catalogs, implementing a new strategy for estimating the correlations between RSPCs, using weighted correlation coefficients, accounting for systematic differences between RSPCs. Using this approach, we obtained independent estimates of the stochastic errors of the nine recently published catalogs, some of them for the first time.

Catalog	ME	Original differences	Corrected differences
	α / δ	α / δ	α / δ
AUS	76 / 86	49 / 56	46 / 51
BKG	28 / 40	23 / 27	21 / 27
CGS	26 / 38	27 / 46	25 / 27
GSF	24 / 36	15 / 21	14 / 17
IGG	49 / 62	48 / 59	42 / 44
OPA	27 / 37	15 / 23	14 / 18
RFC	105 / 110	63 / 93	60 / 74
SHA	27 / 38	13 / 17	12 / 17
USN	29 / 41	10 / 12	10 / 10

Table 2: Median reported uncertainties (ME) and external stochastic errors computed using original differences and differences corrected for the systematics. Unit: μas

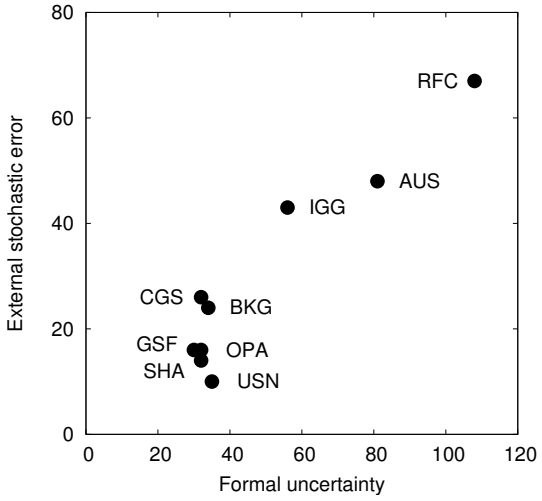

Figure 4: Correlation between reported and external errors.

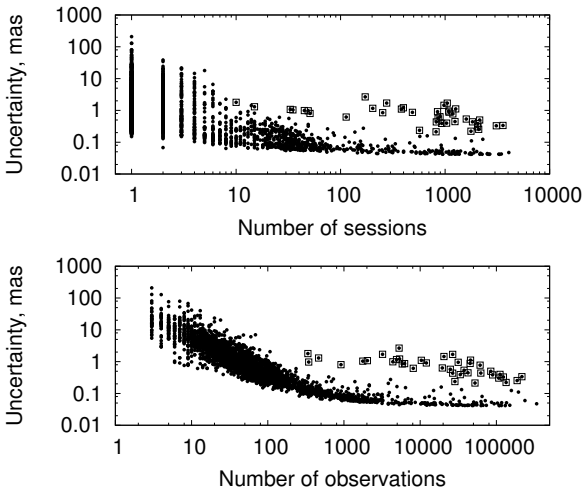

Figure 5: Dependence of the source position uncertainty on the observational history.

2. Modern radio source position catalogs show significant and complicated systematic differences at a level of tens μas, which must be accounted for during accuracy assessment and combination.

3. Catalogs obtained at the same AC are in close correlation with each other. This may evidence the presence of AC-specific systematic errors caused by specific modeling and analysis options traditionally used at different ACs.

4. The external catalog stochastic errors closely correlate with the formal source position uncertainty, most probably because of quality of the software used and analysis strategy details such as modelling and parameterization.

5. The ICRF2 source position uncertainties are not homogeneous for *global* and *arc* sources, which should be addressed during preparation of next ICRF versions.

Acknowledgements. The author is grateful to all the authors of the RSPCs, who made them available to us either via public access (AUS, BKG, CGS, GSF, OPA, RFC) or via personal contact (IGG, SHA, USN). The travel support from the organizers of the conference is highly appreciated.

5. REFERENCES

Ma, C., Arias, E.F., Bianko, G., et al., 2009, "The Second Realization of the International Celestial Reference Frame by Very Long Baseline Interferometry",
IERS Technical Note No. 35, A. Fey, D. Gordon, C.S. Jacobs (eds.). Frankfurt am Main: Verlag des Bundesamts für Kartographie und Geodäsie.

Malkin, Z., 2013, "A new approach to the assessment of stochastic errors of radio source position catalogues". A&A , 558, A29.

ANALYSIS OF TIME SERIES OF THE EOP AND THE ICRF SOURCE COORDINATES

V.E. ZHAROV[1,2], N.A. VORONKOV[2], N.V. SHMELEVA[1]
[1] Lomonosov Moscow State University, Faculty of Physics
Vorobjevi Gory, Moscow 119991, Russia
e-mail: vladzh2007@yandex.ru
[2] Lomonosov Moscow State University, Sternberg Astronomical Institute
Universitetskij prospekt, 13, Moscow 119991, Russia
e-mail: nvoronkov@mail.ru

ABSTRACT. Software ARIADNA was used for estimation of the Earth orientation parameters (EOP) for period 1984–2012. Simultaneously the time series of the coordinates of the ICRF radio sources were calculated. The least-squares method with constraints is applied. It is shown that most radio sources (including defining sources) are characterized by significant apparent motions.

1. INTRODUCTION

Very Long Baseline Interferometry (VLBI) technique is used by the International Earth Rotation Service and Reference System Service (IERS) for production of the Earth orientation parameters (EOP). They are required to study Earth orientation variations. Besides they are necessary to link the International Celestial Reference System (ICRS) and the International Terrestrial Reference System (ITRS).

The first of them is realized by the precise coordinates of extragalactic radio sources. A catalog of coordinates for 608 radio sources (Ma et al., 1998) was compiled using VLBI observations from 1975 to 1995 and is the first realization of the International Celestial Reference Frame (ICRF). In accordance with resolution B3 of the 27th General IAU Assembly, the new realization of the frame (ICRF-2) is based on two catalogs (Ma et al., 2009). The first one is the main catalog, while the second is supplementary. In total, both catalogs include 3414 sources, and 2197 objects were observed only one–two times.

The rotational stability of the frame is based on the assumption that some chosen sources have no proper motion and it means that there is no global rotation of the universe. One assumes that coordinates of them are known as precise as possible. These sources are unresolved with VLBI baselines comparable to the Earth diameter, and it was assumed that variations of their coordinates are negligible. The ICRF catalog contains 212 so called “defining” radio sources, while the ICRF-2 catalog contains 295 defining sources.

But analysis of time series of coordinates of the ICRF radio sources shows that many of them including the defining sources have significant apparent motion (Zharov et al., 2009). It is explained by motion of an emission region that is called by the ICRF source inside the jet of a quasar.

Software ARIADNA was used for estimation of the Earth orientation parameters (EOP) for period 1984–2012. In our previous work (Zharov et al., 2009) solution (EOP and the sources positions and velocities) was obtained for the first catalog of the ICRF sources (Ma et al.,1998).

New solution (EOP and the sources positions and velocities) was obtained for catalog ICRF-2 (Ma et al.,2009).

We show that

- many of new defining sources show significant apparent motion;
- small rotation of ICRF is transformed into long-term variations of the EOP.

To obtain the time series of the EOP and the ICRF sources coordinates the ARIADNA software was used. Solution ”sai2013a.eops” was based on accepted positions of the sources ICRF2, precession-nutation model IAU2006. The terrestrial reference frame was fixed by the VTRF2008 coordinates and velocities of stations. Solution ”sai2013b.eops” differs from previous one by adding the velocities of sources.

Secular variations of the EOP can be calculated by subtracting of two solutions "a" and "b".

2. SOLUTION DESCRIPTION

In the linear regression model under consideration, the estimated parameters can be subdivided into two different groups containing global and local parameters (Voronkov, Zharov, 2013). The former one includes the coordinates and velocities of telescopes, as well as the coordinates and apparent motions of radio sources that are estimated during the entire period of observation. Local parameters, including the Earths rotation, the dry and wet tropospheric delays of the signal, and the station clocks model, are calculated individually for each session.

Station clocks are estimated w.r.t. combined clock by a 2^{nd} order polynomial according equation:

$$\sum_j [C_0^j + C_1^j t + C_2^j t^2] = 0.$$

The zenith wet delay is parameterized by polynomial function too but order of it can be chosen as 3 or more in 2 h intervals.

In addition, the coordinates and apparent motions of the sources should satisfy the condition of the absence of the global rotation of the celestial frame of reference (no net rotation – NNR). As well, this condition is applied for the coordinates of telescopes (in the terrestrial frame of reference).

For all of these solutions a priori EOP are taken from IERS final products. Displacement of reference points, tidal variations in the Earth's rotation, transformation between the ITRF and ICRF are calculated according the IERS Conventions (2010) (IERS TN35, 2010). Atmospheric pressure loading have been applied according model developed in paper (Zharov, 2004).

3. RESULTS

The proposed method was applied for estimating the apparent motions of extragalactic radio sources. We processed more than 3200 daily sessions of the VLBI observations from 1984 to 2012. The solution was obtained with allowance for restrictions in corrections to the coordinates and apparent motions of the sources, and corrections to the coordinates and velocities of telescopes. The coordinates and apparent motions of the sources satisfy the condition of the no-net-rotation of the celestial frame of reference.

Figure 1 shows the distribution of the apparent motions of radio sources. In the southern hemisphere, the number of the sources is considerably lower than in the northern hemisphere. This is due to the insufficient number of observation stations in the southern part of the planet.

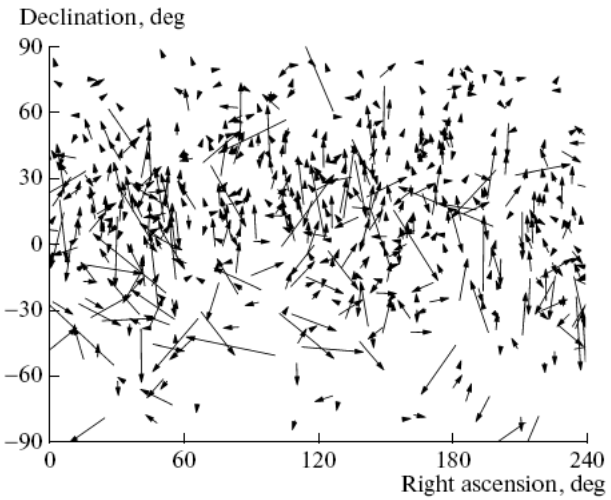

Figure 1: The apparent motions of radio sources depending in right ascension and declination.

As we can see from the histograms (Fig. 2 and Fig. 3), a great number of the sources have considerable apparent motions. More than half of them have apparent motions exceeding 50 microarcsecond per year.

Thus, we can assume that this phenomenon is not accidental and confirms previous conclusions based on the analysis of temporal series (Zharov et al., 2009). As was said, the main purpose in selecting defining sources is the creation of a stable frame of reference with fixed coordinate axes in space. Since the direction of the axes is determined by the coordinates of defining sources, the lack of apparent motions of these sources determines the stability of the system.

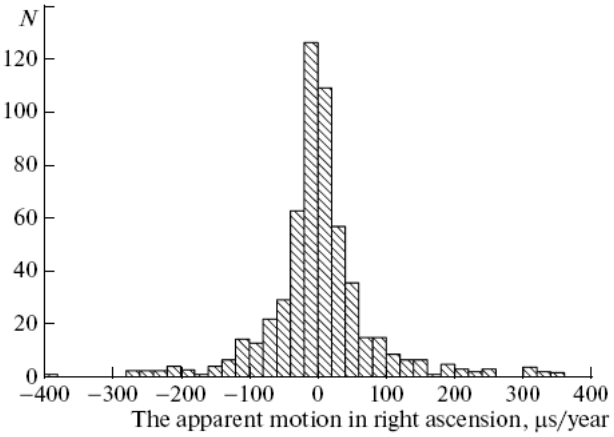

Figure 2: The apparent motion distribution histogram in right ascension.

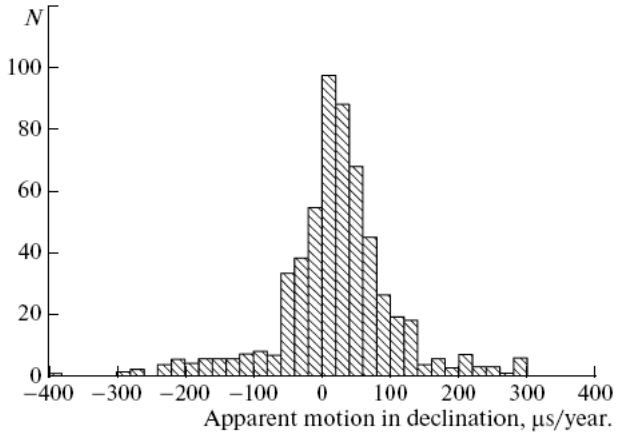

Figure 3: The apparent motion distribution histogram in declination.

The values of velocities of defining sources can reach a few microarcseconds per year. The variation of the ICRF source coordinates leads to small rotation of reference frame. To estimate the stability of the frame three small angles θ_1, θ_2, θ_3, which describe small rotation were calculated:

$$\mathbf{s}(t) = \begin{pmatrix} 1 & -\theta_3 & \theta_2 \\ \theta_3 & 1 & -\theta_1 \\ -\theta_2 & \theta_1 & 1 \end{pmatrix} \mathbf{s}(t_0)$$

where $\mathbf{s}(t)$, $\mathbf{s}(t_0)$ are unit vectors of a defining source at moments t and $t_0 = J2000.0$. Obviously, that variations of angles θ_1, θ_2, θ_3 are connected with motion of the defining sources and NNR condition. Stability of the ICRF (or constancy of θ_1, θ_2, θ_3) can be improved by correct choice of the defining source or extension of their number.

Rotation of the ICRF is due to the motions of sources. Variations of angles θ_1, θ_2, θ_3 are connected with the EOP or the effect of the source apparent motion has an impact on the determination of the EOP.

To calculate this effect two solutions "sai2013a.eops" and "sai2013b.eops" were obtained. From difference of solutions linear trend in x-coordinate of pole equal to $-2.77 \pm 0.22\,\mu$as/year, in y-coordinate of pole equal to $1.60 \pm 0.15\,\mu$as/year were found. Variations of nutation in longitude and obliquity are $0.47 \pm 0.46\,\mu$as/year, $-0.54 \pm 0.15\,\mu$as/year respectively, and UT is $0.144 \pm 0.007\,\mu$s/year.

Motion of extragalatic radio source can be decomposed on systematic and stochastic parts. The first of them can be explained by secular aberration drift of the extragalatic radio source motions caused by the rotation of the Solar System barycenter around the Galactic center (Titov et al., 2011). The dipole component of the velocity field is defined by the velocity of the Solar System barycenter and galactic coordinates of the radio source and can be estimated. Other regular part of the extragalatic radio source motions can be caused by the errors of the precession constants. It is planned to estimate this effect from our solutions.

4. CONCLUSIONS

New time series of the EOP and the ICRF sources coordinates were obtained. The ARIADNA software was used for this. Solutions were based on accepted positions of the sources ICRF2, precession-nutation model IAU2006.

It was shown that small rotation of the ICRF is due to the motions of sources. The effect of the source apparent motion has an impact on the determination of the EOP.

Acknowledgements. This work was supported by the RFBR grant 14-02-00735.

5. REFERENCES

Ma C., Arias E.F., Eubanks T.M., et al., 1998, "The International Celestial Reference Frame as Realized by Very Long Baseline Interferometry", Astronomical Journal, 116, pp. 516–546.

Ma C., Arias E.F., Bianco G., et al., 2009, "The Second Realization of the International Celestial Reference Frame by Very Long Baseline Interferometry", IERS Technical Note No. 35, A. Fey, D. Gordon, and C.S. Jacobs (eds.), Frankfurt am Main, Germany: Verlag des Bundesamtes für Kartographie und Geodäsie.

IERS Conventions (2010). G. Petit and B. Luzum (eds.), International Earth Rotation and Reference Systems Service (IERS). IERS Technical Note, No. 36, Frankfurt am Main, Germany: Verlag des Bundesamtes für Kartographie und Geodäsie, 179 pp., 2010.

Titov O., Lambert S.B., Gontier A.-M., 2011, "VLBI measurement of the secular aberration drift", A&A , doi: 10.1051/0004-6361/201015718.

Voronkov N.A., Zharov V.E., 2013, "Estimating the Apparent Motions of Extragalactic Radio Sources", Moscow University Physics Bulletin, 68, pp. 235–240.

Zharov V.E., 2004, "New models for reduction of the VLBI data", In Proceedings of the "Journees 2003 Systemes de Reference Spatio-Temporels", A. Finkelstein and N. Capitaine, (eds.), Institute of Applied Astronomy, St.Petersburg, pp. 231–235.

Zharov V.E., Sazhin M.V., Sementsov V.N., Kuimov K.V., Sazhina O.S., 2009, "Physical origins for variations in the apparent positions of quasars", Astr. Rep., 53, pp. 579–589.

SOURCE POSITIONS FROM VLBI COMBINED SOLUTION

S. BACHMANN, D. THALLER, G. ENGELHARDT
Federal Agency for Cartography and Geodesy
Richard-Strauss-Allee 11, 60598 Frankfurt am Main, Germany
e-mail: sabine.bachmann@bkg.bund.de

ABSTRACT. The IVS Combination Center at BKG is primarily responsible for combined Earth Orientation Parameter (EOP) products and the generation of a terrestrial reference frame based on VLBI observations (VTRF). The procedure is based on the combination of normal equations provided by six IVS Analysis Centers (AC). Since more and more ACs also provide source positions in the normal equations - beside EOPs and station coordinates - an estimation of these parameters is possible and should be investigated. In the past, the International Celestial Reference Frame (ICRF) was not generated as a combined solution from several individual solutions, but was based on a single solution provided by one AC. The presentation will give an overview on the combination strategy and the possibilities for combined source position determination. This includes comparisons with existing catalogs, quality estimation and possibilities of rigorous combination of EOP, TRF and CRF in one combination process.

1. INTRODUCTION

More and more IVS Analysis Centers (AC) are providing source positions in their Sinex files, beside EOPs and station coordinates. The task of the IVS Combination Center is to combine regular 24h-sessions of VLBI observations in a routine process. Currently, six IVS ACs are contributing to the combined solutions, among them 4 also provide source positions. Two different products are regularly submitted to the IVS data center: the rapid combination twice per week comprises EOP series and the quarterly solution every three month comprises EOP series and additionally station positions and a VTRF (terrestrial reference frame based on combined VLBI observations). Until now source positions have not been included in the routine combination process. With regard to the upcoming ITRF2013, where the IVS is highly encouraged to provide quasar coordinates, the combination procedure has been extended for these parameters. With regard to the upcoming ICRF3, the generation of a combined VLBI catalog with combined quasar coordinates based on based on combined VLBI data (VCRF) are investigated.

2. COMBINATION APPROACH

For the combination of source positions, all available VLBI 24h-sessions between 1984 and 2013 have been combined. Figure 1 shows a histogram which shows the distribution of the number of observations of sources. It can be seen (without going into details), that there is a large number of sources with very few observations and few number of sources which are regularly observed.

The combination is done on the level of datum free normal equations. The general combination approach for source positions is the same as for EOPs and station coordinates (ref. Böckmann et al. 2010). Thus, the additional implementations which are necessary for the combination of the source parameters can be embedded into the existing software, which allows to use approved modules for outlier test and weighting strategies (ref. Bachmann and Lösler 2012). The source parameters - right ascension (RA) and declination (DE) - of the individual ACs are transformed into equal apriori values, which are taken from the ICRF2. The general model of VLBI observations is based on the hypothesis, that the observed quasars and radio galaxies are situated very distant in space that they seem to be fixed observation targets. As a consequence, the ICRF does not contain velocities for source positions and no source velocities are estimated within the combination process. For the computation of equal apriori values, the common formula for apriori value transformation is applied (ref. Seitz 2009). Given two observations equations 1 and 2 the transformation can be formulated as follows:

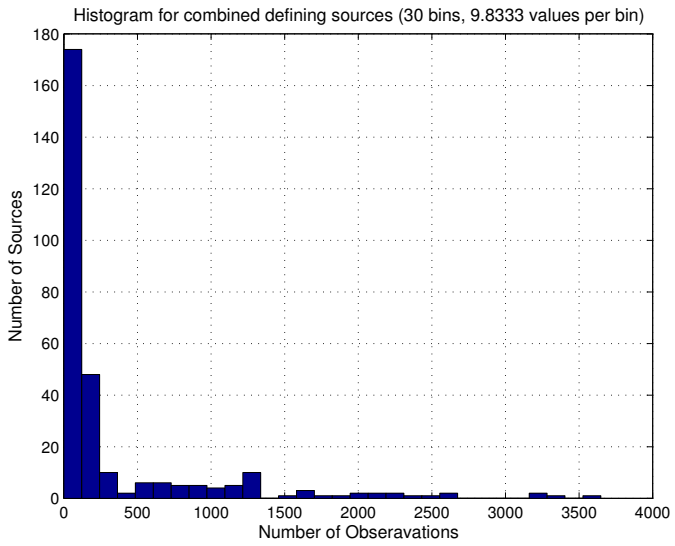

Figure 1: Observations of sources.

$$A_i x_i = b_i + v_i \quad \text{with} \quad x_i = p - p_{0i} \quad (i = 1, 2)$$
$$x_2 = p - p_{01} + p_{01} + p_{02} = x_1 + (p_{01} - p_{02}).$$

Where A_i denotes the design matrix (or coefficient matrix) of observations i, x_i denotes the vector of variables of observation i, b_i the expected value and v_i the correction of observation i.

As the source positions are supposed to be time-independent, a shift of the epoch is not applied.

For the estimation of the individual solution of each AC, source positions are estimated applying No-Net-Rotation (NNR) constraints to the parameters of the "Defining sources", which are assigned to be reliable sources of radiation due to their position stability and their source structure index (ref. Fey et al. 2009 (IERS TN 35)). Applying NNR conditions on spherical coordinates contains no rotation with respect to a reference and no change in the orientation with respect to a reference frame is carried out $(r_0 \times dr)$. Practice showed that applying NNR conditions for station source positions and does not suffice to solve the datum problematic of the normal equations system. Additionally, station coordinates are kept fixed when source coordinates are estimated.

The classification of sources also comprises "Special handling sources". These sources have been identified as unstable sources. Within the ICRF2 determination, they have been identified by applying various statistics on their parameters (right ascension RA and declination DE) like weighted root mean square (WRMS) variation about the mean and χ^2 tests per degree of freedom. Within the combination of source positions, special handling sources are threaten as free parameters without applying any constraints (thus no NNR condition). Within the ICRF2 determination, 39 special handling sources have been defined overall.

After the generation of individual solutions, outlier tests are applied on the parameter. The outlier test for source positions is similar to the outlier test of EOP and station coordinates. A Least Median of Squares (LMS) estimation is applied. The median is equal to the observation where the square residual is minimal ($med(v_i^2) \rightarrow \min$). The variance factor is than estimated by

$$\sigma_{LMS} = 1.4826 \left(1 + \frac{5}{n-u}\right) \sqrt{\min\ med(v_i^2)}$$

following Rousseeuw/Leroy 2003. An outlier (∇_i) is detected, if the test value is larger than a given threshold k within the data set. Supposed $k = 3$ - according to the three-sigma-rule - this is leading to

$$\nabla_i = \begin{cases} \text{false, if } |v_i| \leq k\sigma_{LMS} \\ \text{true, else.} \end{cases}$$

An outlier is identified if the difference of the value and the median is bigger than three times the standard deviation of the LMS estimator.

The combined solution is estimated by stacking the individual normal equations with equal apriori source positions. The individual weight of the contributing solutions is determined by a variance component estimation (VCE). Within the VCE, observation groups are composed and variance factors for each group are introduced. In order to compensate an over-weighting of individual contributions which are all using the same software package, the groups within the VCE are arranged by software packages (one package per group). The resulting weighting factors are then used to scale the individual normal equations before they are stacked to generate the combined solution. The stacked NGL is solved by fixing station coordinates and EOPs and applying NNR conditions on defining sources.

Figure 2 shows the individual solutions and the combined solution for session 13OCT24XE (R4608).

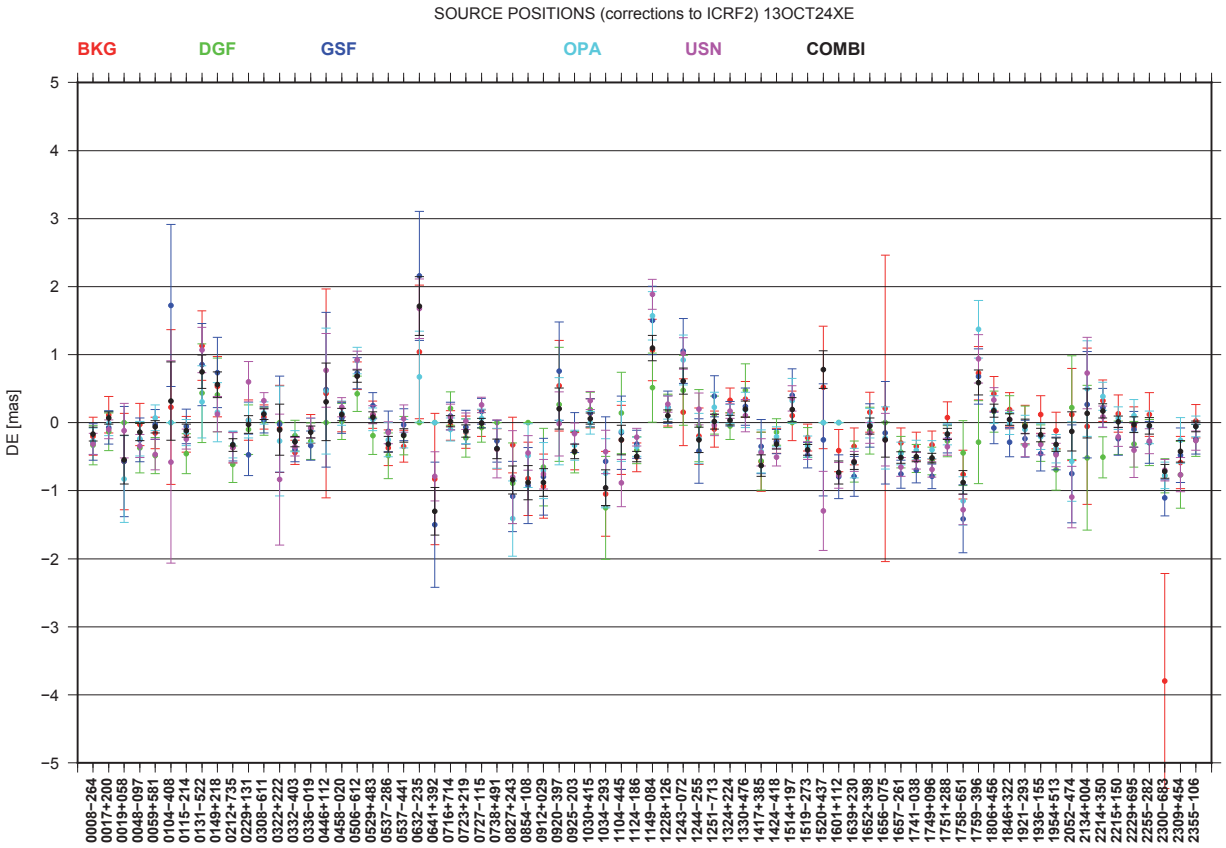

Figure 2: Source positions in declination for session 13OCT24XE

The figure shows, that the residuals for most sources are within a range of $\pm 1 mas$ for this session.

Beside the generation of time series composed of combined VLBI observations, first steps of a combined celestial reference frame as a global solution have been implemented. For this purpose, the sessions of the CONT08 campaign have been used to compile a first (very) small catalog of combined source positions. 15 24h VLBI sessions have been combined to one "celestial reference frame" containing 78 sources. Figure 3 shows the results of the combined catalog in declination and right ascension for 78 sources, which have been observed during the CONT08 campaign with respect to ICRF2. The comparison shows an agreement of the positions of ≈ 0.2 mas, which corresponds to a mean absolute difference of 0.12 mas in right ascension and 0.16 mas in declination.

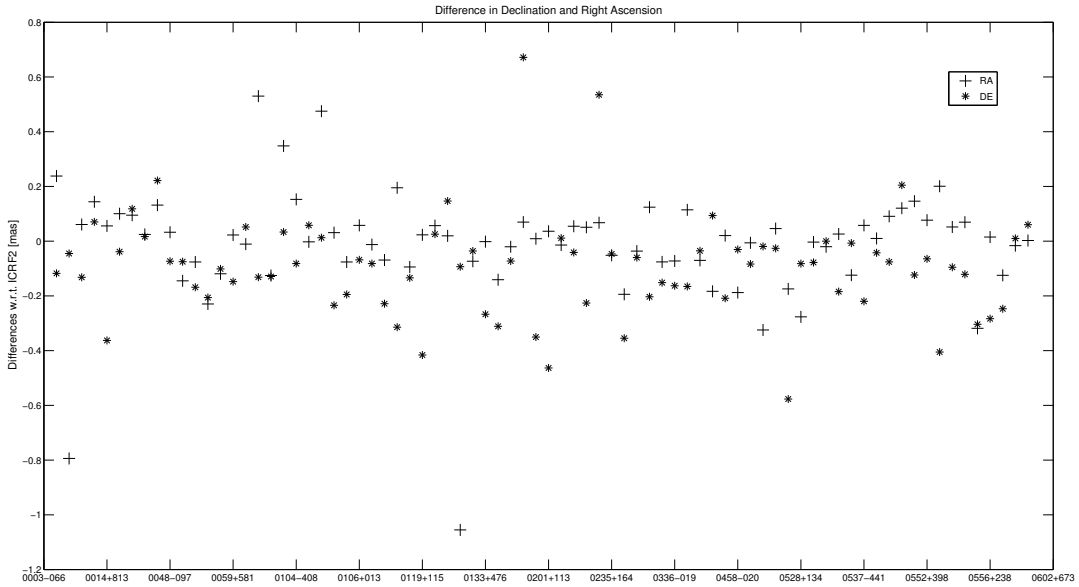

Figure 3: Differences in declination and right ascension for 78 sources of a first combined CRF.

3. SUMMARY AND OUTLOOK

The integration of sources within the routine combination process has been done successfully and first analyses look promising, for individual session combination as well as for a combined "global solution". In the near future, more Analysis Centers will provide source positions in the regular sinex contribution to the combined solution, which will be integrated into the combination process as soon as they are available. The next steps will be the analysis of the combined time series of source coordinates, to refine the combination procedure and to increase the number of sessions and sources within the combined solution. Furthermore, the number of sessions for a combined source catalog will be increased in order to include the hole time span of VLBI observations into a VCRF. Also the resulting source position stability with a complete VCRF will be studied and the results will be compared to the results of the ICRF2 generation and other catalogs.

4. REFERENCES

Böckmann, S. and Artz, T. and Nothnagel, A. and Tesmer, V., 2010, "International VLBI Service for Geodesy and Astrometry: Earth orientation parameter combination methodology and quality of the combined products", Journal of Geophysical Research, 115, doi: 10.1029/2009JB006465

Bachmann, S. and Lösler, M., 2012, "IVS combination center at BKG - Robust outlier detection and weighting strategies", IVS 2012 General Meeting Proceedings, NASA/CP-2012-217504.

Seitz, M., 2009, "Kombination geodtischer Raumbeobachtungsverfahren zur Realisierung eines terrestrischen Referenzsystems", Fakultät für Forst-, Geo- und Hydrowissenschaften der Technischen Universität Dresden.

Fey, Alan L. and Gordon, D. and Jacobs, Christopher S., 2009, "The Second Realization of the International Celestial Reference Frame by Very Long Baseline Interferometry (IERS Technical Note No.35)".

Rousseeuw, P.J. and Leroy, M., 2003, "Robust Regression and Outlier Detection", ISBN: 978-0471488552.

RIGOROUS VLBI INTRA-TECHNIQUE COMBINATION FOR UPCOMING CRF REALIZATIONS

A. IDDINK, A. NOTHNAGEL, T. ARTZ
Institute of Geodesy and Geoinformation, University of Bonn
Nußallee 17, 53115 Bonn, Germany
e-mail: aiddink@uni-bonn.de
nothnagel@uni-bonn.de
artz@igg.uni-bonn.de

ABSTRACT. The current realizations of the International Celestial Reference System (ICRS), the International Celestial Reference Frame 1 (ICRF1) and ICRF2, are based on solutions estimated by a single VLBI group. In contrast, the International Terrestrial Reference Frame (ITRF) is based on a multi-technique combination with contributions from different geodetic space techniques. These independent technique-specific solutions are again generated in intra-technique combinations of various analysis centers with all the benefits of combined solutions. To overcome the deficiencies of the past ICRF, one of the main objectives for the upcoming realizations of the fundamental frames should be a completely consistent and simultaneous determination of both frames. This involves inter- as well as intra-technique combinations. In multiple studies it has already been pointed out that the use of the intra-technique combination related to TRF and EOP estimations improves the stability and robustness of the results in comparison to individual solutions. This improvement should also be exploited for the CRF determination. In this work we focus on the consistency within the VLBI intra-technique combination. The main features and crucial steps of the developed CRF intra-technique combination strategy are explained and highlighted.

1. FEATURES OF THE EXISTING ICRF AND ITRF

Currently, the two existing fundamental frames, the International Celestial Reference Frame (ICRF) and the International Terrestrial Reference Frame (ITRF), are produced by different institutions and are based on various input data. The ICRF1 and ICRF2 (e.g., IERS 2009), both previous realizations of the ICRS, are single big monolithic solutions generated by the VLBI group at the NASA Goddard Space Flight Center (GSFC) using the Calc/Solve software package. Thus, the currently existing ICRF2, based on only one institution and one software package, is solely consistent to the GSFC specific TRF, which is aligned with the VLBI Terrestrial Reference Frame 2008 (VTRF2008) (Böckmann et al. 2010), and corresponding Earth Orientation Parameters (EOPs).

In contrast, the ITRF is based on contributions from four different geodetic space techniques [Global Navigation Satellite Systems (GNSS), Satellite Laser Ranging (SLR), Doppler Orbitography and Radio-positioning Integrated by Satellite (DORIS), Very Long Baseline Interferometry (VLBI)] and is computed in an inter-technique combination. This is done to benefit from the advantages of the individual solutions and to overcome technique-specific problems. Furthermore, these individual solutions are generated in an intra-technique combination of different analysis centers (ACs)(e.g., Böckmann et al. 2010).

Consequently, the current fundamental frames, the ICRF2 and the ITRF2008, as well as their related EOP series are not entirely consistent. To overcome this deficiency, both frames should be computed simultaneously and fully consistent in the upcoming realizations. Due to the fact that the EOPs are the direct link between both frames, this also comprises a simultaneous estimation of the EOP series.

In order to achieve these objectives and because of the fact that VLBI is the unique geodetic space technique which supplies source parameters for the CRF determination, it is necessary to focus on the consistency within the VLBI intra-technique combination. This is a first step towards a consistent realization of the upcoming ICRF3 and the respective ITRF version. At the present time, only the TRF and the related EOP series are regularly generated in a rigorous VLBI intra-technique combination by the International VLBI Service for Geodesy and Astrometry (IVS). By adding source positions to the rigorous VLBI intra-technique combination, the generation of a fully consistent VLBI output becomes possible. This innovation then links station coordinates, EOPs and source positions in a fully consistent

way. The benefits of an intra-technique combination, which have already been shown for TRF and EOPs determinations in several studies (Böckmann 2010), will be exploited for the CRF combination as well.

2. COMBINATION STRATEGY

In order to guarantee that the contributions of the combination are not distored by any constraints before combining them, the rigorous combination is performed at the level of datum-free normal equation systems. Furthermore, it is ensured that the full variance-covariance information of all parameters and all input contributions is rigorously transferred. The underlying datum for the TRF and CRF can be applied during the combination, to ensure an identical datum for all input series in the whole process. Considering the goal, that we want to achieve consistency within the VLBI intra-technique combination, it is crucial that all contributing normal equation systems contain the whole set of parameters, including station coordinates, source positions and EOPs. For that reason, only four out of the official six IVS contributing ACs can presently be used for initial CRF investigations.

The proposed combination strategy can be divided into several sections illustrated in Fig. 1. First of all, VLBI solutions in the form of datum-free normal equation systems containing source positions, station coordinates and EOPs need to be stored together from all contributing ACs. The delivery and exchange of these solutions is based on the Solution Independent Exchange Format (SINEX). Since high precision geodetic VLBI has started in late 1979, over 5000 sessions were observered and analysed by each of the contributing ACs. These session-wise datum-free VLBI normal equation systems are combined in a first VLBI intra-technique combination step. The interim results are combined single session normal equation systems. In general, this intra-technique combination step leads to several substantial positive effects compared to using a single independent solution. The combination enables the analysis of differences, the uncovering of systematic effects and the detection of outliers. The stability and robustness of the final combined products is improved and the analyst's noise is reduced (Böckmann 2010). The combination step itself contains a couple of preprocessing steps, transformations and tests, to achieve sensible and reliable combined results.

Based on the combined single session normal equation systems, we are able to generate one monolithic datum-free normal equation,which is a completely consistent VLBI output, containing all CRF, EOP and TRF components. Even more important is that this combination strategy generates an ample scope of possibilities building a global VLBI output.

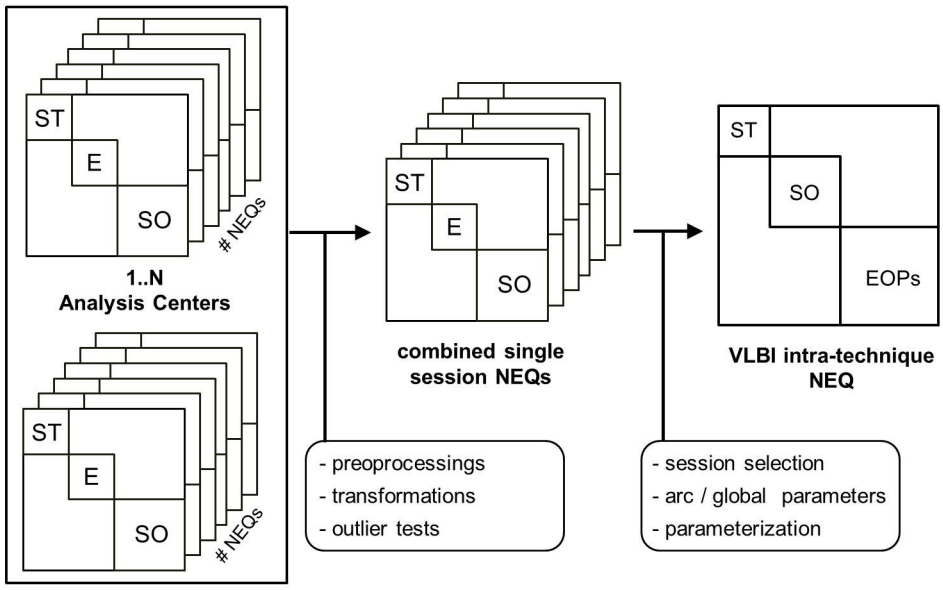

Figure 1: Combination strategy at the level of datum-free normal equations (NEQs). Parameter types: ST = station coordinates, E = EOPs, SO = source positions

Not all of the combined sessions are suitable for the determination of the desired parameters, therefore affected sessions can already be excluded in this intermediate step and will not influence the final products. Furthermore, the final parameterization of the CRF, TRF and EOP series can be freely chosen. Each parameter can be set up as an arc or a global parameter, i.e., being valid for either a single session only or the total time span, respectively. This offers the possibility to design the parameterization more appropriately than done in previous realizations of the fundamental frames. For example, the positions of special handling sources could be parameterized with continous piecewise linear functions or other suitable functions. In the previous realizations of the ITRS, station positions are represented with station coordinates and station velocities related to one explicit epoch. Considering the presented combination strategy it is imaginable and possible to represent motions of station coordinates with a different parameterization as well. Subsequently, the complete VLBI intra-technique normal equation system can contribute to the inter-technique combination. This enables an entirely consistent and simultaneous computation of the upcoming fundamental frames and their corresponding EOP series. It should be emphasized again that the full variance-covariance matrix of all sources is carried forward from each observing session and each AC to the final catalogue. The basic structure of the intra-technique combination strategy illustrated here is already realized in our software environment called BonnSolutionCombination (BoSC).

3. SUMMARY AND OUTLOOK

In this paper, a combination strategy for CRF determination has been presented. In order to generate a consistent CRF and TRF, investigations concerning the features and properties of a CRF combined from various VLBI solutions have to be made in upcoming studies. Individual CRFs based on solutions generated by different ACs are planned to be compared among themselves and to the official ICRF2. In this context, the impact of the additional data, which became available after the ICRF2 was published, can be examined as well. Based on comparisons between combined and individual CRFs we expect that a combined CRF provides improvements in terms of stability and robustness. Finally, we also plan to provide the mechanics for an inclusion of stand-alone catalogs, like K- and Ka-band reference frames, if full variance-covariance information is provided.

4. REFERENCES

Böckmann S., Artz T., Nothnagel A. (2010). VLBI terrestrial reference frame contributions to ITRF2008. Journal of Geodesy, 84, 201-219. doi: 10.1007/s00190-009-0357-7

Böckmann S., Artz T., Nothnagel A., Tesmer V. (2010). International VLBI Service for Geodesy and Astrometry: Earth orientation parameter combination methodology and quality of the combined products. Journal of Geophysical Research, 115, B04404, doi: 10.1029/2009JB006465

Böckmann S., Artz T., Nothnagel A., Tesmer V. (2007). Comparison and combination of consistent VLBI solutions. In: J. Böhm, A. Pany, H. Schuh (Eds.): Proceedings of the 18th European VLBI for Geodesy and Astrometry Working Meeting 2007, Geowissenschaftliche Mitteilungen, Heft Nr. 79, Technische Universität Wien, ISSN 1811-8330, pp 82-87

Böhm J., Böhm S., Nilsson T., Pany A., Plank L., Spicakova H., Teke K. and Schuh H. (2012). The New Vienna VLBI Software VieVS. In: S. Kenyon, M.C. Pacino, U. Marti (Eds.): Proceedings of IAG Scientific Assembly 2009, International Association of Geodesy Symposia Series Vol. 136, pp 1007-1011, doi:10.1007/978-3-642-20338-1-126

IERS (2009). The second realization of the international celestial reference frame by very long baseline interferometry. In: A.L. Fey, D. Gordon, and C.S. Jacobs (Eds.): IERS Technical Note 35, presented on behalf of the IERS/IVS Working Group, Verlag des Bundesamtes fr Geodäsie und Kartographie, Frankfurt am Main

THE GAIA INITIAL QUASAR CATALOGUE

A.H. ANDREI[1,2,3,4], S. ANTÓN[5], F. TARIS[3], G. BOURDA[6], J. SOUCHAY[3], S. BOUQUILLON[3], C. BARACHE[3], J.J. PEREIRA OSÓRIO[5], P. CHARLOT[6], R. VIEIRA MARTINS[1], S. LAMBERT[3], J.I.B. CAMARGO[1], D.N. da SILVA NETO[7], M. ASSAFIN[4], J.-F. LE CAMPION[6]

[1] ON/MCTI-BR; [2] CAR/U.H.-UK; [3] SYRTE/O.P.-FR; [4] OV/UFRJ-BR; [5] CICGE/FCUP; [6] LAB/U.B.1-FR; [7] UEZO/RJ-BR

[2] CAR-University of Hertfordshire, Hatfield (Herts), College Lane AL10 9AB, UK
e-mail: oat1@on.br

ABSTRACT. We present the latest, updated, and fully corrected version of the Gaia Initial QSO Catalog (GIQC), produced by the CU3 GWP-S-335-13000. It contains 1 248 372 objects, of which 191 802 are considered and marked as Defining ones, because of their observational history and existence of spectroscopic redshift. Also objects with strong, calibrator-like radio emission are included in this category. The Defining objects represent a clean sample of quasars. The remaining objects aim to bring completeness to the GIQC at the time of its compilation. For the whole GIQC the average density is 30.3 sources per sq.deg., practically all sources have an indication of magnitude and of morphological indexes, and 90% of the sources have an indication of redshift and of variability indexes.

1. MOTIVATION

Gaia will operate in survey mode, recordng transits of compact objects in the G magnitude range 6-20, to produce an unbiased census of the stars in the galaxy, but also of solar system constituents and extragalactic objects. Among the latter, there will be about 500 000 QSOs, if not much more (Andrei et al., 2008). The satellite observations imply in proper, in the relativistic sense, reference systems to which the measurements are initially referred. These are the ones described by Bastian (2007), but the final catalogue will comply to the IAU-sanctioned Barycentric Celestial Reference System (BCRS), resulting in the Gaia Celestial Reference Frame (GCRF) materialized by a dense mesh of fiducial QSOs. Notwithstanding, it is also worth to mention that two other quite robust extensions of the GCRF will be produced, to brighter regimens. The one formed by the unresolved galaxies (some 10 million of objects) and the QSOs that did not make it to be in the GCRF (presumably containing several radio-loud quasars). And the one formed the approximately half a billion of stars with highly accurate position and proper motions.

QSOs thus will define the GCRF, and accordingly Gaia own results are capable of classifying them. The QSO classification contains three major orientations: getting a zero-contaminants QSO sample to determine the GCRF; deriving the most complete QSO sample based on the full Gaia data; and determining astrophysical parameters for each QSO. The determination itself of a Gaia source as a QSO is planned to rely primarily on comparison of the photometric output against a template of spectral energy distributions (SED), ands secondarily on astrometric observables, variability analysis and a reliable initial list of known QSOs. Based on the end-of-mission color information, supervised Artificial Neural Networks (ANN) can virtually reject all contaminating stars (including white dwarfs), although the completeness drops to about 20% at G 20th (Bailer Jones et al., 2008). It can deliver the sample of 10 0000 quasars which can stabilize the GCRF to a residual rotation of less than 0.5 μas per year, provided they are well distributed over the sky (Mignard, 2012).

The relatively small number of points actually required to constitute a robust GCRF brings particular relevance for an initial list of known QSOs. This is exactly the purpose of the Gaia work package Initial QSO Catalogue for Gaia (GIQC), under the CU3, Core Processing Coordination (Andrei, 2007). It aims to obtain a clean sample of at least 10 000 quasars, distributed allsky off |20deg| of galactic latitude, with magnitude brighter than V=20 and point-like PSF. This bona fide initial clean sample is useful both for the actual orientation of the GCRF and to enlarge the templates of the recognition scheme. On the other hand, to attain completeness, the GIQC also brings, in separate categories, all objects reckoned as

quasars or point like AGNs, even if there is not spectroscopic redshift available. The latest version of the GIQC is considerably enlarged, chiefly for candidates and other quasars. Those have only photometric redshift and occupy mostly the SDSS region. Nevertheless their confirmation, either by Gaia or others, can add importantly to the recognition template library.

2. THE CATALOG

There is no optical type of observation that can deliver quasar's astrometry comparable to Gaia, but this is not required from the GIQC. Its purpose is to provide positions, and to an extent magnitudes, to enable unmistakable matching to Gaia own observations on allsky basis. Therefore the development of a Celestial Reference Frame is not in the scope of the GIQC, but rather it is tackled elsewhere (Souchay et al., 2009, 2012; Andrei et al., 2009). On the other hand, variability and morphology are important when selecting the quasars to form the fundamental Gaia astrometric frame. Since during the Gaia mission each quasar will me measured on average 80 times, with intervals from hours to months, along different directions, those indexes can give a head start or warning for the combination of the observations and understanding of the individual errors.

On forming the catalog, we started from the LQAC2 list (Souchay et al., 2012 - 187 504 objects). Then complemented with the SDSS DR10 (Schneider et al, 2010 - 116 105 objects), the 2dF/2qZ (Croom et al, 2004 - 22 835 objects), and the BOSS selection (Paris et al, 2012 - 87 822 objects). The VLBI QSRs are all important for the GCRF, thus they have been all introduced in the GIQC, naturally without duplicating the already existing entries. Thus entered the ICRF2 (Fey et al., 2010), the VLBA-6th supp calibrator list (Petrov et al., 2008), the VLA-2009 update calibrator list (NRAO, 2012), plus the list of candidates for the future reconciliation between the GCRF and the ICRF (Bourda et al., 2010), amounting to 4 925 objects. Redshift and optical magnitudes were searched in various catalogs and in the available literature, in special searching for matches in the GSC2.3 (Lasker et al., 2008) and the USNO B1.0 (Monet et al., 2003). Finally, were considered the SDSS photometrically selected quasar candidates (Richards et al, 2009 - 887 406 objects). For the remaining QSOs, which come from smaller catalogues, the analysis was made catalog by catalog, up to case by case.

Tables 1 and 2 present the GIQC main features.

Table 1 - Main features of the GIQC positions, magnitudes, and redshifts.

Number of sources	1 248 372
Sources with magnitude	1 246 512
Sources with redshift	1 157 285
Sources brighter than G=20	371 098
Sources fainter than G=21	690 507
Sources with redshift smaller than 1	250 405
Sources with redshift greater than 2	383 487
Astrometry precision	1 arcsec
Magnitude precision	0.5
Redshift precision	0.01
Average density	30.3 sources/deg^2
Average neighbor distance	3.7 arcmin (σ 4.9 arcmin)
Maximum distance to neighbor	5.2 deg
Maximum distance to neighbor (average of 100 larger values)	3.0 deg (σ 0.6 deg)

The GIQC goes beyond the columns appearing in the IGSL (Initial Gaia Source List), which provides the initial identification to the Gaia observed objects. In the GIQC much more information is given, to enable the assessment of the aptitude of a given QSO to form in the core Gaia reference frame. This focus on the reliability of origin catalogues, on the optical pointlikeness, and on the possibility of astrometric jitter. Such aspects, if unaccounted for, give rise to larger astrometric errors than would be expected on basis of the object magnitude, in special when combining measures taken at different times during the mission and at different directions of the Astro line spread function (LSF) over the source. By the same token, when those aspects are warned for and accounted for, they become a useful tool to bring back to the core Gaia quasar frame objects apparently troublesome, or to reject objects to this end using an objective criterion, and finally to postsign thus affected objects as revealed by Gaia observations as interesting astrophysics objects.

Following the magnitudes and redshifts (see Figure 1), there appear morphological indexes based on the comparison of the PSFs of the QSO and of the surrounding stars. There are three indexes, for Skewness, Roundness, and Normalness, referred to the B, R, and I images of the DSS (Digitized Sky Survey). Next, an estimation of the size of the accretion disk and dust regions are presented. These values behave as variability indexes. They indicate the maximum jitter or astrometric variation that can be expected for each QSO. Both the morphological indexes and the variability indexes have been previously presented (Andrei et al., 2012) and are fully discussed elsewhere in these proceedings (Coelho et al., 2013).

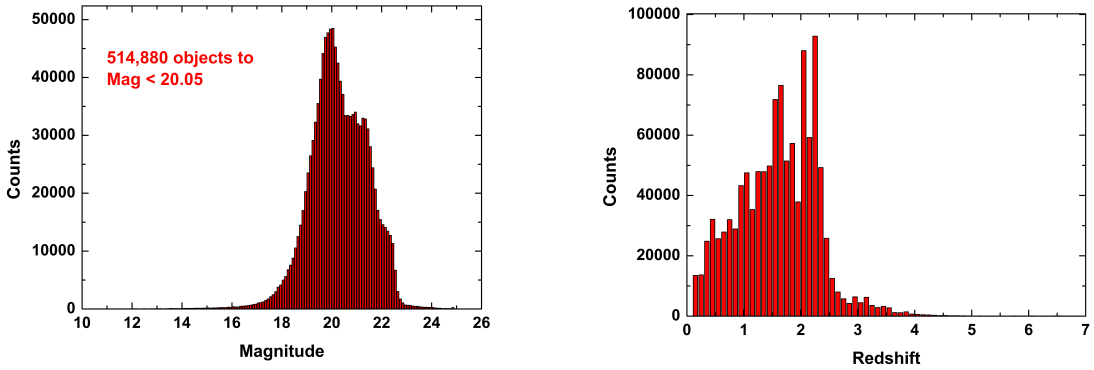

Figure 1: Histogram for the magnitude and redshift contents of the GIQC. Notice that more than half of the sources are beyond magnitude 20. Although this is nominal limit of Gaia, the actual observations may reach probably fainter, and also variability can bring QSOs to brighter magnitudes at times. The redshifts indicate the largest number of QSOs as being nearby ones, which is good in the astrometric sense, but also can result in a considerable number of objects for which the host galaxy is seen.

The Classification scheme follows in two columns. The first column brings the main classification, Defining, Candidate, and Other sources, given by the letters D, C, and O. The second column brings one-letter comments either on the original catalog, radio-loudness, or reliability of the detection. Table 2 summarizes the meaning of the flags.

The Candidate sources share the assuredness of the defining sources, but lack spectroscopic redshift and/or have magnitude fainter than 21. The Other sources are the remaining ones. The Other sources are mostly those which only photometric redshift, plus sources for which the redshift (or even the position) are less precise.

Table 2 - Classification flags in the GIQC.

Flag	**Column**	**Quantity**	**Description**
D	1	191 802	Defining - spectroscopic redshift
C	1	52 954	Candidates - reliable but only photometric redshift
O	1	1 003 616	Other - either magnitude and/or redshift issues
S	2	208 298	SDSS lists belonging
V	2	4 866	VLBI (or long base interferometry) position
L	2	599	Link candidate source, optimal magnitude and radio position
A	2	14 527	AGN, pointlike or core dominated
B	2	512	Bulge dominated extragalactic source
R	2	38 699	Radio position available, although of lower precision
P	2	1 026	Poor observational history, otherwise no issues
U tex	2	960 173	Unreliable detection (for this catalogue purposes)
F	2	5 208	Faint source
E	2	957	Empty field in the optical domain
G	2	13 507	no outstanding characteristic

The catalog presently contains 1 248 372 sources, being 191 802 defining (99.5% with magnitude, and 99.0% with spectroscopic redshift), 52 954 candidate, and 1 003 616 other quasars. Special programs are

being developed, mostly as association to LAMOST groups to densify the galactic plane content. Figure 2 bring the spatial distribution.

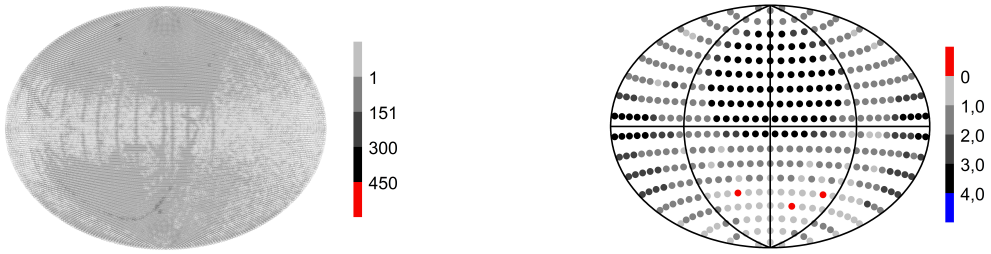

Figure 2: Sky density distribution of the GIQC on equatorial coordinates and logarithm scale. On the left, the contents of the whole catalog in equal area cells of radius 1 deg. On the right, the defining sources only, in equal area cells of radius 10 deg, In both plots the galactic plane is not devoid of points, emphasizing the efforts to densify that region.

3. FUTURE DEVELOPMENTS AND UPDATES

The GIQC is planned to be updated on yearly basis up to the end of the observational part of the mission, that is at least for other 5 years. This is because the last treatment for all the sources, QSOs and the GCRF in special, will reach the best results when all the passages are combined. Therefore there is scope to continue to feed the ANN with new QSOs and mainly with objects coming from different selection criteria. Another important point is to increase the number of objects by the galactic plane, and to obtain good redshifts for the VLBI link objects.

4. REFERENCES

Andrei, A.H.; 2007; Gaia Technical Note GAIA-C3-SP-GPA-AA-001

Andrei, A.H., Bouquillon, S., Camargo, J.I.B., Penna, J.L., Taris, F., Souchay, J., Silva Neto, da D.N., Vieira Martins, R., Assafin, M., 2009, Proc. of Journes vol. 2008, ed. N. Capitaine; 199.

Andrei, A.H., Souchay, J., Zacharias, N., Smart, R.L., VieiraMartins, R., da Silva Neto, D.N., Camargo, J.I.B., Assafin, M., Barache, C.; 2009; A&A, 505, 385

Bastian, U.; 2007; GAIA-CA-SP-ARI-BAS-003-06, Version 6.0.

Bourda, G., Charlot, P., Porcas, R.W., Garrington, S.T.; 2010; A&A 520, 113.

Croom, S.M., Smith, R.J. , Boyle, B.J. , Shanks, T.,, Miller, L., Outram, P.J. , Loaring, N.S.; 2004; MNRAS, 349, 1397.

Fey, A.L., Gordon, D., Jacobs, C.S.; 2010, IERS Technical Note No. 35.

Lasker, B.M. and 25 co-authors; 2008; AJ 136, 735.

Mignard, F.; 2012; Mem. S.A.It. Vol. 83, 918.

Monet, D.G. and 28 co-authors; 2003; AJ 125, 984.

Páris, I. and 75 co-authors; 2012; A&A 548, 66

Petrov, L., Kovelev, Y.Y., Fomalont, E.B., Gordon, D.; 2008; AJ 136, 580.

Richards, G.T., Deo, R.P., Lacy, M., Myers, A.D., Nichol, R.C., Zakamska, N.L., Brunner, R.J., Brandt, W.N., Gray, A.G., Parejko, J.K., Ptak, A., Schneider, D.P., Storrie-Lombardi, L.J., Szalay, A.S.; 2009; AJ 137, 3884.

Schneider and 47 co-authors; 2010; AJ 139, 2360.

Souchay, J., Andrei, A.H., Barache, C., Bouquillon, S., Gontier, A.-M., Lambert, S.B., Le Poncin-Lafitte, C., Taris, F., Arias, E.F., Suchet, D., Baudin, M.; 2009; A&A, 494, 799

Souchay, J., Andrei, A.H., Barache, C., Bouquillon, S., Suchet, D., Taris, F., Peralta, R.; 2012; A&A 537, 99

THE UPDATE OF THE LARGE QUASAR ASTROMETRIC CATALOG (LQAC)

J. SOUCHAY[1], A.H. ANDREI[2], C. BARACHE[1], F TARIS[1], S. BOUQUILLON[1], C. GATTANO[1]
[1] SYRTE, Observatoire de Paris, CNRS, UPMC
61 avenue de l'Observatoire, 75014 Paris, France
e-mail: Jean.Souchay@obspm.fr
[2] Observatorio Nacional/MCT, Rio de Janeiro /Observatorio de Valongo; UFRJ
Rio de Janeiro, Brazil
e-mail: oat1@ov.ufrj.br

ABSTRACT. We present the characteristics of the Large Quasar Astrometric Catalog which gathers more than 180 000 objects in its second up-date (LQAC-2), insisting on its advantages: improved accuracy of the equatorial coordinates of the sources, extensive photometry, calculation of the absolute magnitudes, morphology indexes.

1. INTRODUCTION

Quasars a priori materialize quasi-inertial directions in space. For this reason they represent ideal objects for modern astrometry. As they are supposed to undergo no detectable proper motion on contrast to stars, they constitute the basis of a primary reference frame, as is the case of the ICRF2(Ma et al. 2009; Boboltz et al. 2010) from VLBI observations. Since the identification of the first quasar 3C273 by Maarten Schmidt in 1962 as an extragalactic radiosource with high redshift and the construction of the first quasars catalog by De Veny et al. (1971) containing 202 objects, the number of known quasars has steadily increased, in particular in the past decade, thanks to huge surveys like the 2dF QSOs survey (Croom et al. 2004) and for a large part to the Sloan Digital Sky Survey (Fan et al. 1999; Adelman-McCarthy et al. 2007). Nowadays the number of recorded quasars that can be compiled reach more than 180 000 objects. Considering this dramatic increase, once in a while one needs to gather all the quasars into a single catalog that is as homogeneous as possible. This has been done for a long time through several releases by Véron-Cetty and Véron from 1984 to 2010.

In parallel, Souchay et al. (2009) have constructed what they call the LQAC (Large Quasar Astrometric Catalogue), which can be considered as an alternative catalog to the one from Véron-Cetty & Véron (2006, 2010). Some interesting points can be found in the LQAC. First, it is oriented towards astrometric reliability and performance as its name shows it. For the sake of homogeneity, it systematically privileges large surveys over small catalogs. Second it is based on a compilation strategy related to the astrometric level of the constituent catalogs; in other words, when an object is available in two or more catalogs, only the positions (in terms of celestial coordinates) provided by the most accurate catalog are retained. Third the LQAC contains exhaustive information on the photometry of the objects, thanks to crossidentifications between the constituent catalogs as well as between large surveys such as the 2MASS catalog (Cutri et al. 2003), the USNO B1.0 catalog (Monet et al. 2003) or the GSC2.3 catalog (Lasker et al. 2008). Finally the LQAC determines the absolute magnitudes of quasars in both bands i and r, by using up-to-date models of galactic extinction and recent values of cosmological parameters.

2. THE LQAC-2 : AN IMPROVED VERSION OF THE LQAC

Several reasons led us to construct a new version of the LQAC, called the LQAC-2 (Souchay et al., 2012). At first we considered a significant amount of new data from different origins, such as the ICRF2 (Ma et al. 2009; Boboltz et al. 2010) and the VCS (Petrov et al. 2008) at radio wavelengths, as well as the 8th release (DR8) of the Sloan Digital Sky Survey at optical wavelengths (Aihara et al. 2011). A second important reason is the inclusion of equatorial coordinates of the quasars as determined from the LQRF (Large Quasar Reference Frame), which a priori gives a more accurate optical determination of

Catalog Name	Flag	Nature	Nbs of quasars (LQAC2)	Nbs. of quasars (LQAC)
ICRF	A	radio	3 414	717
VLBA	B	radio	5 198	3 357
VLA	C	radio	1 858	1 857
JVAS	D	radio	2 118	2 118
SDSS	E	optical	126 577	74 868
2QZ	F	optical	23 660	22 971
2df-SDSS LRG	G	optical	9 058	0
FIRST	H	radio	969	969
HB	I	opt. & radio	6 721	7 245
2MASS	J	infrared	25 252	13 647
GSC2.3	K	optical	154 900	91 061
B1.0	L	optical	148 894	81 662
V&V (-SDSS)	M	optic. & radio	80 667	85 189

Table 1: Characteristics of the catalogs participating to our compilation of quasars both for the LQAC-2 and the LQAC. From Souchay et al. (2012)

	VV2010	A-L	LQAC-2	%
QSO's	168941	165065	187504	100.00
z	168324	160399	183652	97.94
u	152624	156178	167983	89.58
b	32085	156799	164721	87.84
v	131934	75713	102774	54.81
g	0	134881	134881	71.93
r	3939	162910	166033	88.54
i	551	149735	150278	80.15
z	0	134884	134884	71.93
J	0	25252	25252	13.46
K	0	25252	25252	13.46
1.4 Ghz	18111	1814	11797	6.29
2.3 Ghz	0	3482	3482	1.85
5.0 Ghz	5809	863	5358	2.86
8.4 Ghz	0	4551	4551	2.43
24 Ghz	0	61	61	0.03

Table 2: Comparison of the number of entries for each data item between the VV2010 catalog, the compilation of the catalogues A-L of the LQAC-2 and the final LQAC-2 catalog. From Souchay et al. (2012)

celestial coordinates with respect to the ICRF, compared with those given by original catalogs, for a large percentage of objects (except of course those, a minority, observed with the VLBI technique). Finally another reason comes from a decision to densify the data compared to the first LQAC catalog. One of the adding items is a LQAC identification number based on the celestial coordinates of the objects. Another significant additional information is the determination of three kinds of indexes, there by allowing a morphological classification. These indexes are obtained by comparison to the average morphology of the surrounding stars, thus freed of image aberrations. They are obtained from B, R, I images and their first interpretation is to point out the signature of the host galaxy.

As mentioned above one of the important qualitative improvements of the LQAC-2 with respect to the LQAC is due to the inclusion for a large part of the sample of LQRF coordinates. This inclusion deserves some further explanations : the Large Quasar Reference Frame (LQRF) was built by Andrei et al.(2009) in order to give the positions of the LQAC quasars with an optimized accuracy with respect to the original catalogs, the care of avoiding incorrect matches of its constituents quasars, the homogenization of the astrometry from different catalogs and the aim of obtaining a milli-arcsecond global alignment with the ICRF, as well as typical individual source position accuracies higher than 100 mas (milliarcseconds).

The methodology for building the LQRF is the following one : starting from the updated and presumably complete Large Quasar Astrometric Catalog (LQAC) list of QSOs, the initial optical positions of the quasars were taken from the USNO B1.0 catalog (Monet et al. 2003), the GSC2.3 catalog(Lasker et al. 2008), and from the SDSS Data Release 5 (Adelman-McCarthy et al. 2007). Then, the initial positions were placed onto UCAC2-based reference frames (Zacharias et al.,2004), followed by an alignment with the ICRF, to which were added the most precise sources from the VLBA calibrator list and the VLA calibrator list (when reliable optical counterparts exist). Finally, the LQRF axes were inspected through spherical harmonics, to define right ascension, declination and magnitude terms. In its first version (Andrei et al.,2009) the LQRF contains 100.165 quasars, represented with a rather homogeneous spatial density across the sky, from -83° to +88.5° in declination. For these reasons it can be considered as a good densificiation of the ICRF, the average angular distance between adjacent elements being roughly 10 arcmins.

In Table 1 we show the comparison of the number of objects included in the LQAC-2 release with respect to the initial LQAC for each constituent catalog, represented by a flag, whose the meaning can

be found in Souchay et al. (2012) The ICRF referenced catalog is the ICRF2 (Ma et al.,2009) with 3414 radiosources instead of the 717 ones of the ICRF-Ext.2 (Fey et al.,2004). The largest contribution is by far the SDSS with 126 577 quasars to be compared with the 187 504 objects of the whole LQAC-2, that is to say roughly 67.5 %. Notice that the 2MASS, GSC2.3, and B1.0 catalogs do not add any quasar to the sample, but contribute significantly to the addition of photometric information for cross-identified quasars.

In Table 2,we show the comparative number of entries per item. The last column indicates the corresponding percentage of entries in the LQAC-2 compilation. For instance we can notice that 97.94 % of the recorded objects have an information concerning their redshift, but that the radio flux information does not exceed 6.3 % (at 1.4 Ghz). This small value is not surprising. We must remind that it is generally considered that roughly only 10 % of QSO's have a significant radio emission.

3. FUTURE PROSPECTS AND CONCLUSION

A compilation of all the known quasars as the LQAC(Souchay et al., 2009) and its new release, the LQAC-2 (Souchay et al., 2012) looks like a useful and fundamental tool given the importance of QSO's in astrometry in general. One of the important points in the LQAC compilations concerns the optimization of the determination of coordinates through the LQRF catalog, and also degree of completeness of the photometry through a systematic cross-identification between the constituents of the various catalogs belonging to the compilation.

A new release including a significant proportion of new objects is scheduled in 2014, in particular by including the DR9 up-date of the SDSS quasars catalog.

4. REFERENCES

Adelman-McCarthy, J. K., Ageros, M. A., Allam, S. S., et al. 2007, ApJS, 172, 634
Aihara, H., Prieto, C. A.., An, D., et al. 2011, ApJS, 193, 29
Andrei,A.H., Souchay, J., Zacharias, N. et al.,2009, AA 505,385A
Boboltz, D. A., Gaume, R. A., Fey, A. L., et al. 2010, BAAS, 42, 512
Croom, S.M., Smith, R.J., Boyle, B.J., et al. 2004, MNRAS, 349, 1397
Cutri, R.M., Skrutskie, M.F., van Dyk, S., et al. 2003, NASA/IPAC Infrared Science Archive, http://irsa.ipac.caltech.edu/applications/Gator/=20
De Veny, J. B., Osborn, W. H., =Janes, K. 1971, PASP, 83, 611
Fan, X., Strauss, M. A., Schneider, D. P., et al. 1999, AJ, 118, 1
Fey, A.L., Ma, C., Arias, E.F., et al. 2004, AJ, 127, 3587
Lasker, B. M., Lattanzi, M. G., McLean, B. J., et al. 2008, AJ, 136, 735
Ma, C., Arias, E. F., Bianco, G., et al. 2009, IERS Technical Note No. 35
Monet, D.G., Levine, S.E., Canzian, B., et al. 2003, AJ, 125, 984
Petrov, L., Kovalev, Y. Y., Fomalont, E., Gordon, D. 2008, AJ, 136, 580
Souchay, J.,Andrei, A.H., Barache, C. et al., 2009, AA 494,799
Souchay J., Andrei,A.H., Barache,C. et al., 2012, AA537,A99
Véron-Cetty, M.-P., & Véron, P. 2006, A&A, 455, 773
Vron-Cetty, M. P., Vron, P. 2010, AA, 518, A10
Zacharias, N., Urban, S. E., Zacharias, M. I., et al. 2004, AJ, 127, 3043

OPTICAL DATA OF ERS OBTAINED AT 60 cm ASV AND 2 m ROZHEN TELESCOPES USEFUL FOR THE LINK OF ICRF – GAIA CRF

G. DAMLJANOVIĆ[1], F. TARIS[2], S. BOEVA[3], G. LATEV[3]
[1] Astronomical Observatory, Volgina 7, 11060 Belgrade 38, Serbia
e-mail: gdamljanovic@aob.bg.ac.rs
[2] SYRTE, Observatoire de Paris, CNRS, UPMC, Paris, France
e-mail: francois.taris@obspm.fr
[3] Institute of Astronomy and NAO, Sofia, Bulgaria
e-mail: sboeva@astro.bas.bg, glatev@astro.bas.bg

ABSTRACT. After the GAIA observations (ESA mission) a new optical celestial reference frame (CRF) will be provided which will replace the Hipparcos one. CRF will be dense and based on QSOs (quasi stellar objects). The plan for Gaia is to survey stars and QSOs brighter than 20 mag; it means, about 500 000 extragalactic sources (ERS) and billion stars of our galaxy. Till now, only nearly 10% of the International Celestial Reference Frame (ICRF) objects (about 70 common sources) are useful for the link between VLBI (radio) and future Gaia (optical) frames with the highest accuracy. It is because some sources are not optically bright enough, and some of them are not point-like ones but extended sources; the extended sources are not suitable for Gaia astrometric accuracy. So, it is necessary to detect, observe and determine the astrometric positions of common sources in both (optical and radio) domains. For the purpose of mentioned aligning the radio and optical frames, we need as much as possible additional optically bright QSOs (with magnitudes up to 18 and compact structures). The morphology and photometry variations of common QSOs make displacement of their optical photocenters. That displacement could be critical for this link. For morphology investigations, we also included the observations of QSOs made during the period 2011-2013 at the RCC telescope (of Rozhen National Astronomical Observatory, Bulgarian Academy of Sciences); the CCD camera VersArray 1300B was used, and $D/F = 2/16$. For photometry investigations, we use, among others, the 60 cm ASV telescope (Astronomical Station Vidojevica of Astronomical Observatory in Belgrade, Serbia); the CCD is Apogee U42, and $D/F = 0.6/6$. We present particularly some data obtained at these telescopes.

1. INTRODUCTION

The active galactic nuclei (AGN) objects (quasars, blazars, Seyfert galaxies, etc.), as extragalactic sources (ERS) at cosmological distances, have been treated as stable and point-like objects. Because of it, in 1997 (during XXIII GA of IAU in Kyoto) the realization of a quasi-inertial celestial reference frame was done by a set of positions of these objects; the International Celestial Reference Frame (ICRF) was established. ICRF is the first realization of the International Celestial Reference System (ICRS) via the positions of 608 ERS (and 109 added ones) estimated through Very Long Baseline Interferometry (VLBI) observations at S/X radio wavelengths (or frequencies of 2.3 GHz and 8.4 GHz). Out of these objects 212 are defining ones. ICRF2 appears as the second realization of ICRS (Fey et al., 2009). It was adopted on line with the IAU resolution in 2009 (XXVII GA of IAU in Rio de Janeiro). In ICRF2 there are the VLBI precise positions for 3414 compact radio astronomical sources, and 295 ones are defining sources.

Recently, it was noted that ERS objects are not point-like ones, and their morphology and photometry are changing with time. These effects with their evolution make displacement of optical photocenters and position instabilities of the radio center of ERS, and they are the limiting factors for defining ICRF. The position stabilities of ERS are very important for ICRF, and it is necessary to monitor the ICRF sources at both optical (Aslan et al., 2010) and radio wavelengths. Optically bright sources without extended VLBI features are good for the alignment between the VLBI and Gaia frames; one third of the ICRF sources are with an optical counterpart (brighter than 18 mag), and only 10 % of the ICRF sources (70 ones) are compact enough on VLBI scales and with mentioned optical counterparts. So, it is necessary to identify more suitable objects (Bourda et al., 2010, 2011).

Based on data collected with 2 m RCC telescope at Rozhen National Astronomical Observatory.

Unlike Hipparcos (ESA, 1997; van Leeuwen, 2007), the Gaia CRF will cover directly the optical domain. It will be based on bright QSOs with the most accurate coordinates. For good aligning ICRF2 (VLBI frame) – future Gaia CRF and the highest accuracy of targets we need consistency between radio and optical coordinates. It is necessary to pinpoint the relative position of the radio and optical emission in AGN with accuracy until a few tens of μas, but for now we see that the optical – radio shift (150 μas at X-band) is nearly ten times larger than VLBI and Gaia position accuracies (a few tens of μas at magnitudes 15-18); that shift is the problem for the link between the two frames. To average out the mentioned effects we need a large number of objects. Also, the gravitational microlensing could make a long – term optical variability in AGN. Other limiting factors for linking the reference frames are: the presence of a host galaxy (around the nucleus of the object), the distance of the AGN, the optical magnitude variation, the size of the emission region, structural modifications in the optical domain, etc. (Taris et al., 2013). Among others, using the 2 m Rozhen telescope we observe the objects for morphology and with the 60 cm ASV one for photometry investigations (Damljanović and Milić, 2012). We present particularly the main properties of these telescopes and some data in the next section.

2. OBSERVATIONS AND RESULTS

The optical observations of QSOs were carried out with telescopes located at different sites. Figure 1 shows the distribution of instruments. These telescopes are suitable for observations of QSOs which are interesting for morphology and photometry investigations. On line with Serbian – Bulgarian cooperation and the follow-up network for the Gaia photometric alerts we established the local mini-network of five telescopes at three sites (Rozhen and Belogradchik in Bulgaria, and Vidojevica in Serbia). According to the mentioned ICRF – Gaia CRF link and up to now, we have used three telescopes (which are in the list presented in Figure 1): the 60 cm ASV telescope (Astronomical Station Vidojevica of Astronomical Observatory in Belgrade), the 2 m RCC telescope at Rozhen National Astronomical Observatory (Bulgarian Academy of Sciences), and the 60 cm Rozhen one. We have mostly used the 2 m Rozhen instrument and the 60 cm ASV one (the 60 cm Rozhen just for a few objects), but it could be useful to include also the 60 cm instrument (the Belogradchik Astronomical Observatory) and the 50/70 cm Schmidt – camera.

The 2 m Rozhen telescope ($D/F = 2/16$, long.=24.7^o, lat.=41.7^o, h=1730 m) is useful for morphology investigation of QSOs. There are the observations from 2011 until now. The detector is the CCD camera VersArray 1300B: 1340x1300 pixels, pixel size is 20x20 μm, scale is 0.26 arcsec per pixel, FoV=5.6x5.6 arcmin. The seeing is from 1.5 arcsec to 3.5 arcsec, but during our observations in October 2013 it was very good (around 1 arcsec). The filters are Johnson UBV and Cousins RI. At Figure 2, as an example of morphology investigation using GALFIT analysis and data of 2m Rozhen telescope, a total of 4 optical counterparts of ERS were presented: 1144+402, 1219+044, 1252+119, and 1800+440.

The 60 cm ASV telescope ($D/F = 0.6/6$, long.=21.5^o, lat.=43.1^o, h=1150 m) is suitable for photometry investigation of QSOs. It has been in operation since mid-2011. In 2012 we started to collect the data with this instrument. The CCD is Apogee Alta U42: 2048x2048 pixels, pixel size is 13.5x13.5 μm, scale is 0.46 arcsec per pixel, FoV=15.8x15.8 arcmin. The seeing is in general about 1.5 arcsec, but during our observations in July and September 2013 it was better than 1 arcsec. The filters are the same as at the 2 m Rozhen telescope. By using the 2 m Rozhen telescope it is possible to catch a target brighter than 20 mag, and until about 18 mag with the 60 cm ASV telescope. During our observations in September 2013, with the 60 cm ASV we used the CCD SBIG-ST-10 XME (2184x1472 pixels, 6.8x6.8 μm, 0.23 arcsec per pixel, FoV=8.4x5.7 arcmin, and an adaptive optics – AO) successfully because that camera is for high resolution imaging. At the 60 cm Belogradchik telescope (long.=22.7^o, lat.=43.6^o, h=650 m) it is the CCD FLI PL09000, at the 50/70 cm Schmidt – camera (Rozhen) it is the CCD FLI PL16803, and at the 60 cm Rozhen instrument it is the CCD FLI PL9000.

During observations, we made 3 frames per filter, and used B, V, and R filters per object. The corrections for apparent displacements did not applied (Aslan et al., 2010; Kiselev, 1989) because of small field of view (FoV of 2 m Rozhen telescope is 5.6x5.6 arcmin and of 60 cm ASV it is 15.8x15.8 arcmin). All frames were reduced individually (dark, bias, flat, hot/death pixels) and after that the stacking (of 3 frames) was applied. The temperature of CCD VersArray was -110^o C and because of it the dark was not applied.

The MAXIM DL and IRAF image processing packages were used for photometry, relative to the available reference stars. As photometry example, we present the results (magnitudes of B, V and R filters) of the object 1101+384 (Mkn 421) observed with the 60 cm and 2 m Rozhen telescopes during

the same night (at April 2013):

- B filter (60 cm Rozhen), 12.330±0.057 at JD2456397.26922, 12.496±0.028 at JD2456397.27996, 12.618±0.035 at JD2456397.34190, 12.445±0.017 at JD2456397.43249, 12.570±0.089 at JD2456397.52857,
- B filter (2 m Rozhen), 12.530±0.006 at JD2456397.32750, 12.548±0.016 at JD2456397.45614,
- V filter (60 cm Rozhen), 12.033±0.031 at JD2456397.27155, 12.065±0.010 at JD2456397.28437, 12.152±0.013 at JD2456397.34631, 12.056±0.005 at JD2456397.43690, 12.135±0.060 at JD2456397.53006,
- V filter (2 m Rozhen), 12.172±0.005 at JD2456397.32969, 12.170±0.005 at JD2456397.45854,
- R filter (60 cm Rozhen), 11.786±0.005 at JD2456397.27388, 11.789±0.007 at JD2456397.28878, 11.851±0.016 at JD2456397.35072, 11.780±0.005 at JD2456397.44131, 11.848±0.025 at JD2456397.53154,
- R filter (2 m Rozhen), 11.801±0.005 at JD2456397.32235, 11.801±0.005 at JD2456397.46106.

Both set of presented results (made with 60 cm and 2 m Rozhen telescopes) are consistent between each other. During April 2013, the similar results were calculated using data done with 60 cm ASV telescope. We sent these data to the international center of WEBT program (Whole Earth Blazar Telescope) because that object is also on the WEBT list and it was very active during April 2013.

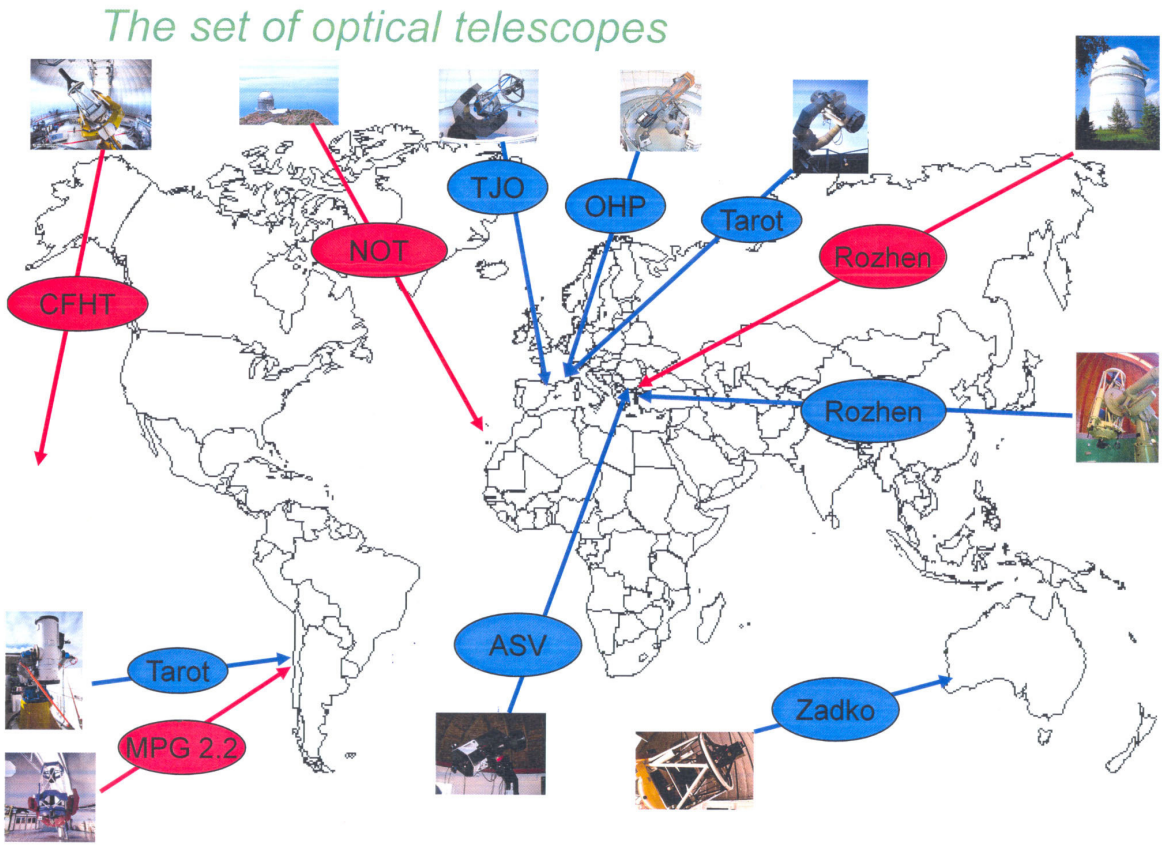

Figure 1: The optical telescopes for observations of QSOs (in line with morphology and photometry investigations of QSOs).

3. CONCLUSION

The optical observations of QSOs are possible by using 2 m Rozhen telescope and a good CCD camera, and useful for morphology investigations. Also, the data made with the 60 cm ASV telescope are good for photometry investigations. So, with both instruments we could produce the data which are good enough for the link between ICRF (radio) and Gaia CRF (optical) frames. Some problems (during observations and reductions of ERS visible in optical domain) can be caused by: faintness of the optical counterparts to ERS, atmospheric influences, technical problems, etc.

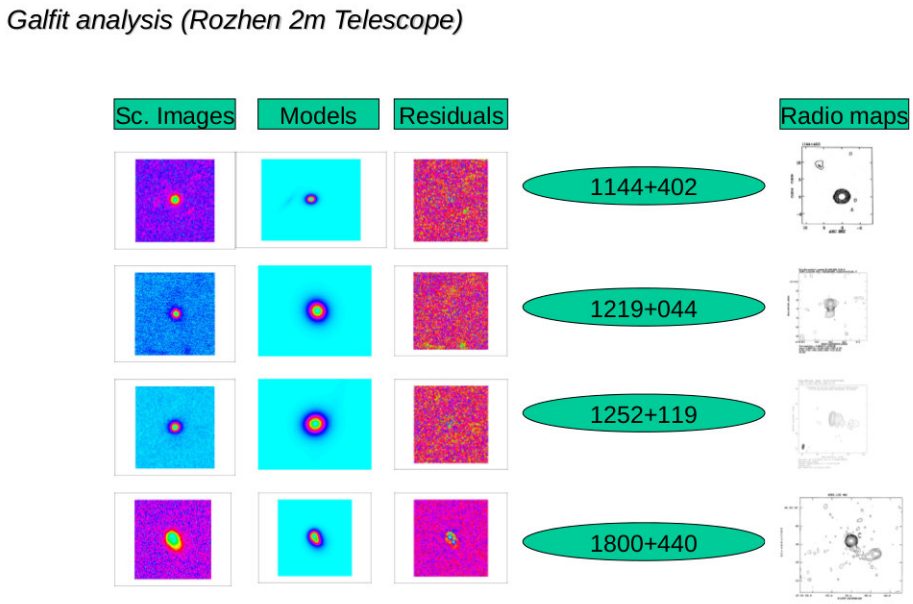

Figure 2: Some morphology results obtained by using GALFIT analysis (the objects 1144+402, 1219+044, 1252+119 and 1800+440 were observed with 2m Rozhen telescope).

Acknowledgements. G. Damljanović performed this work as a part of Project No 176011 "Dynamics and kinematics of celestial bodies and systems" supported by the Ministry of Education, Science and Technological Development of the Republic of Serbia. Also, G. Damljanović gratefully acknowledges the observing grant support from the Institute of Astronomy and Rozhen National Astronomical Observatory, Bulgarian Academy of Sciences.

4. REFERENCES

Aslan, Z., Gumerov, R., Jin, W., Khamitov, I., Maigurova, N., Pinigin, G., Tang, Z., Wang, S., 2010, "Optical counterpart positions of extragalactic radio sources and connecting optical and radio reference frame", A&A, 510, A10.

Bourda, G., Charlot, P., Porcas, R.W., Garrington, S.T., 2010, "VLBI observations of optically-bright extragalactic radio sources for the alignment of the radio frame with the future Gaia frame I. Source detection", A&A, 520, A113.

Bourda, G., Collioud, A., Charlot, P., Porcas, R., Garrington, S., 2011, "VLBI observations of optically-bright extragalactic radio sources for the alignment of the radio frame with the future Gaia frame II. Imaging candidate sources", A&A, 526, A102.

Damljanović, G., Milić, I.S., 2012, "CCD measurements in optical domain and astrometric positions of ICRF2 radio sources", Proc. of the Journées 2011, Earth rotation reference systems and celestial mechanics: Synergies of geodesy and astronomy, eds. H.Schuh, S.Boehm, T.Nilsson and N.Capitaine, Vienna University of Technology and l'Observatoire de Paris, 92.

ESA, 1997, "The Hipparcos and Tycho Catalogues", ESA SP-1200,ESA Publications Division,Noordwijk.

Fey, A.L., Gordon, D., Jacobs, C.S., 2009, "IERS Technical Note" No. 35.

Kiselev, A. A., 1989, "Theoretical foundations of photographic astrometry", Nauka, Moskva.

van Leeuwen, F., 2007, "Hipparcos, the new reduction of the raw data", Dordrecht: Springer.

Taris, F., Andrei, A., Klotz, A., Vachier, F., Cote, R., Bouquillon, S., Souchay, J., Lambert, S., Anton, S., Bourda, G., Coward, D., 2013, "Optical monitoring of extragalactic sources for linking of the ICRF and the future Gaia celestial reference frame I. Variability of ICRF sources", A&A, 552, A98.

THE SDSS QUASARS AS A TESTBENCH FOR THE GAIA FUNDAMENTAL REFERENCE FRAME GRID-POINTS

B. COELHO[1], A. H. ANDREI[1,2,3,4], S. ANTÓN[5,6]
[1] Observatório do Valongo - UFRJ
Ladeira Pedro Antônio 43, CEP 20080-090, Rio de Janeiro - RJ - Brazil
e-mail: bcoelho@astro.ufrj.br
[2] ON/MCTI-BR; [3] SYRTE/OP-FR; [4] CAR/UH-UK; [5] CICGE/FCUP-PT; [6] SIM/FCUL-PT

ABSTRACT. The ESA mission Gaia will furnish a complete census of the Milky Way, delivering astrometry, dynamics, and astrophysics information for 1 billion stars. Operating in all-sky repeated survey mode, Gaia will also provide measurements of extra-galactic objects. Among the later there will be about 500 000 quasars that will be used to build the reference frame upon which the several independent observations will be combined and interpreted. Not all the quasars are equally suited to fulfill this role of fundamental, fiducial grid-points. Brightness, morphology, and variability define the astrometric error budget for each object. The quasars spectroscopically certified from the SDSS catalog offer an optimum sample to discuss the future Gaia quasar population. We present a new method, based on the Gaia quasar database, to derive absolute magnitudes, on the SDSS filters domain. The method can be extrapolated all over the optical window, including the Gaia filters.

1. THE PROBLEM & HOW TO MINIMIZE IT

Quasars live in galaxies, which are extended objects. The later, if detectable, may influence the accuracy of the centroid position of the AGN. In terms of Gaia, considering pixel size, and assuming typical angular sizes of the host galaxy, the uncertainty in position can reach 60 μas, and that can not be ignored in an astrometric mission as Gaia. To warn on the likeness of such problem for a given QSO, we developed a method to reveal the presence of the host galaxy [1], [2]. We make use of 3 morphological parameters which measure the skewness (SHARP), the circularity (SROUND), and normalness (GROUND) of the PSF. It relies on comparing the QSO profile against the average PSF of nearby stars. The differences are interpreted as host galaxy tracers. We are testing this method using the 105 783 QSOs (spectroscopically confirmed) sample of the SDSS DR7 [3], which have 0.065< redshift(z) <5.46.

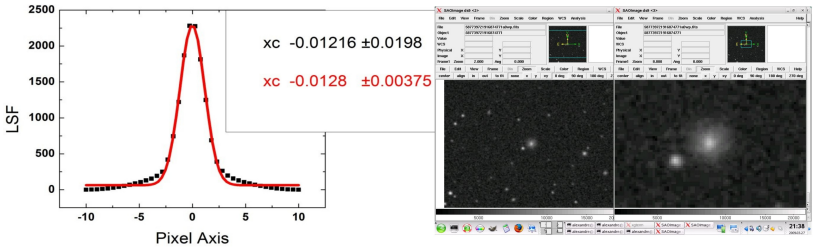

Figure 1: Simulation of the effect of a host galaxy component in the determination of the centroid position. One can see a variation in the measured position and an increment of the error.

2. FIRST RESULTS

We obtained frames in *ugriz* bands for all SDSS DR7 QSOs, this means: 528 915 frames with 2048x1489 pixels (0.39"/pix) totaling ∼2TB of data. We run an IRAF pipeline on all frames to derive the 3 PSF parameters. When a QSO has any of the 3 parameters $> 2\sigma$ from the mean PSF, that difference is interpreted as due to the presence of an extended component, i.e. the host galaxy. Schneider

et al.[3] found ∼4% of extended objects ($psfmag - modelmag > 0.2$ mag). As one can see in table 1 we found a higher fraction of extended objects. In figure 2 is noticeable that redder bands tend to be more sensitive to the presence of a host galaxy component, as expected.

	u	g	r	i	z
Objects classified	80.86%	89.34%	83.15%	75.74%	60.83%
Extended objects	15.07%	11.23%	13.26%	15.00%	19.21%

Table 1: QSOs for which we obtained morphological indices and percentage of extended objects relative to the total (105 783).

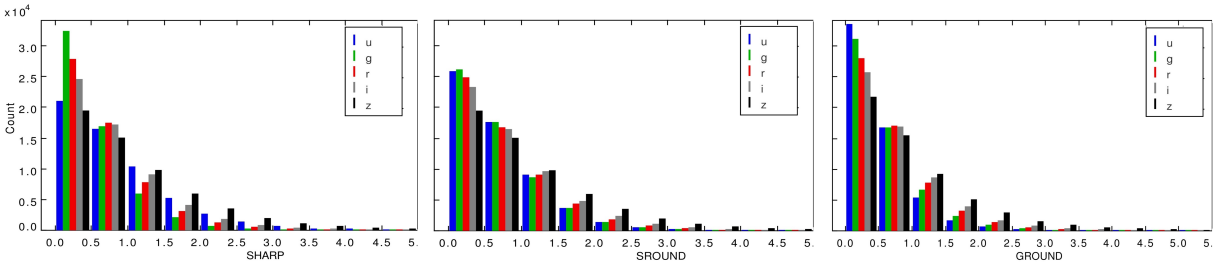

Figure 2: Distribution of the morphological indices for the 57 893 objects for which we obtained morphological classification in the 5 bands. From left-right:SHARP, SROUND, GROUND.

3. OBTAINING ABSOLUTE MAGNITUDES

Considering the redshift range of the objects, it is necessary to apply k-corrections to compute the absolute magnitudes, the correction is a function of redshift, filter used, and SED of the source. The SED continuum of QSOs is usually approached by a power law were the flux is proportional to $\nu^{-\alpha}$, being α the spectral index. It is common to use for QSOs α=0.5. An important fraction of QSOs emission arrives us as emission lines [4], so an additional correction for that becomes necessary. We are developing a new method to compute absolute magnitudes in the 5 bands (*ugriz*) of SDSS that also takes into account corrections for both Lymanα-forest and extragalactic dust effects. We make use of the Gaia spectral library[5], which contains synthetic spectra built with the modified template technique. We adopted α=0.5, to take advantage of the calibration from the available absolute magnitude Mi [3], but in principle different spectral indexes can be used.

4. STUDYING THE HOST GALAXY POPULATION

It is in general accepted a relationship between the AGN and the host galaxy, involving masses, sizes, brightness, morphological types, and star formation. however the particulars are far from being known or agreed upon. In our investigation we seek how the *ugriz* absolute magnitudes and morphological indexes differences can inform about those characteristics, and what they may reveal about the story of host/AGN co-evolution. Besides, simply from the observational point of view such relationships must be worked out because, due to the size of the spectrometers fibers and the smallness of the QSO emitting regions, there is always a large fraction of light from the host when the core is studied.

5. REFERENCES

[1]Andrei, A. et al., 2009, Gaia CU3 Plenary Meeting, Turin, Italy
[2]Andrei, A. et al., 2010, Journées 2010, Paris, France
[3] Schneider et al., 2010, AJ, 139, 2360
[4] Richards et al.,2006, AJ, 131, 2766
[5] Claeskens et al., 2006, MNRAS, 367, 879

VLBI REALIZATIONS OF THE CELESTIAL REFERENCE FRAME

S. LAMBERT[1], E. F. ARIAS[1,2], J. SOUCHAY[1]
[1] SYRTE, Observatoire de Paris, CNRS, UPMC & GRGS
e-mail: sebastien.lambert@obspm.fr; jean.souchay@obspm.fr
[2] Bureau International des Poids et Mesures
e-mail: farias@bipm.org

ABSTRACT. We validate four recent VLBI astrometric catalogs submitted to the International VLBI Service for Geodesy and Astrometry (IVS) data center by various IVS analysis centers. We compare these catalogs to the most recent realization of the International Celestial Reference System (ICRF2). The catalogs are found consistent with the ICRF2 at less than 15 μas for two of them, and at the level of 20 to 30 μas for the other two.

1. DATA

We considered four recent catalogs submitted to the International VLBI Service for Geodesy and Astrometry (IVS; Schuh & Behrend 2010). They were established at Geoscience Australia, Canberra (aus2012b), the Federal Agency for Cartography and Geodesy, Leipzig, Germany, and Institute of Geodesy and Geoinformation of the University of Bonn, Germany (bkg2012a), the NASA Goddard Space Flight Center (GSFC), Greenbelt, Maryland, (gsf2012a), and the Paris Observatory, Paris, France (opa2012a).

All catalogs were obtained by a single inversion of ionosphere-free VLBI delays accumulated between 1979 and mid-2012. Extensive technical descriptions of the solutions are available at the IVS data center. These solutions used state-of-the-art analysis methods. In addition to source coordinates, all centers estimated session-wise Earth orientation parameters and rates, together with a global terrestrial reference frame (station coordinates and velocities), and a number of nuisance parameters relevant to clocks and troposphere. The Australian analysis center used the OCCAM 6.2 geodetic VLBI analysis software package. Other centers used the latest release of the SOLVE geodetic VLBI analysis software package, developed and maintained at NASA/GSFC. At the level of accuracy reached nowadays, the small variants in the analysis options from one analysis centers to another can have significant consequences on the final VLBI products.

2. ANALYSIS AND RESULTS

Table 1 summarizes the characteristics of each catalogs. It is worth noting that none of the catalogs estimated coordinates for all the 3414 ICRF2 sources. Same situation arises for the ICRF2 295 defining sources. Such a point should be fixed by analysis centers in the future by including in their session list all the sessions which were used for the generation of the ICRF2 catalog.

The source coordinate offsets to ICRF2 are displayed in Figure 2. The extension of the patterns reflect the WRMS of Table 1. Figure 1 was obtained by averaging errors within declination bands of 5°. The error worsens significantly between 20°S and 50°S. This effect likely results from a miscorrected troposphere delay for southern observations (see Fey et al. 2010 for more details). The inclusion of more southern sources in the IVS schedule and the enforcement of baselines covering the southern hemisphere will help in fixing this problem in the future.

The source coordinate difference between catalogs can be modeled by a coordinate transformation that expresses a global rotation between catalogs together with other types of deformations. The coordinate transformation recommended by the IERS reads (IERS 1996)

$$\begin{aligned} \Delta\alpha &= A_1 \cos\alpha \sin\delta + A_2 \sin\alpha \sin\delta - A_3 + D_\alpha(\delta - \delta_0), \\ \Delta\delta &= -A_1 \sin\alpha + A_2 \cos\alpha + D_\delta(\delta - \delta_0) + B_\delta, \end{aligned}$$

wherein A_1, A_2, and A_3 are rotation angles around the X, Y, and Z axes, respectively, D_α and D_δ drifts in right ascension and declination as a function of the declination, and B_δ a bias in declination.

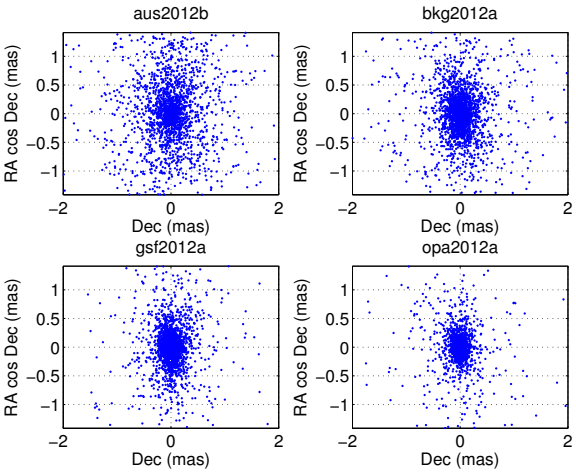

Figure 1: Offsets to ICRF2.

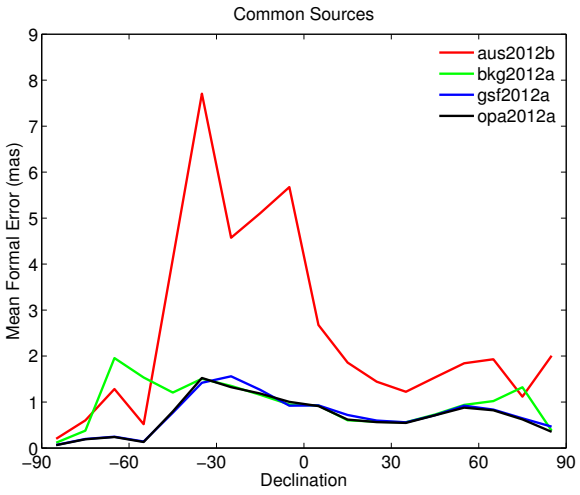

Figure 2: Mean formal error vs. declination for common sources.

Parameters were fitted to the coordinate differences of the defining sources by weighted least squares and reported in Table 2. Most of the catalogs are in agreement with the ICRF2 within 20 μas. The significant biases in declination observed in all catalogs reflect the dissymmetry between the two hemispheres. The small but significant departure in A_1 and A_2 should be further investigated by analysis centers.

	No. Sources			Right Ascension		Declination	
	Total	ICRF2	Defining	Mean	WRMS	Mean	WRMS
aus2012b	2895	2879	288	3.1	94.2	−7.2	83.6
bkg2012a	3253	3091	287	0.2	60.5	21.6	65.5
gsf2012a	3708	3407	294	3.5	55.6	−8.3	54.1
opa2012a	3526	3355	295	8.6	51.5	10.2	51.9

Table 1: Characteristics of the catalogs. Means and WRMS are expressed in μas.

	A_1	$\pm$	A_2	$\pm$	A_3	$\pm$	D_α	$\pm$	D_δ	$\pm$	B_δ	$\pm$
aus2012b	−23.4	*4.9*	3.6	*5.0*	2.8	*4.7*	0.6	*0.2*	0.4	*0.1*	−13.6	*4.7*
bkg2012a	6.7	*4.6*	15.2	*4.7*	0.6	*4.3*	0.1	*0.2*	0.3	*0.1*	17.6	*4.4*
gsf2012a	−2.6	*4.5*	6.8	*4.6*	−2.9	*4.2*	0.0	*0.2*	0.3	*0.1*	−13.7	*4.3*
opa2012a	−4.1	*4.6*	12.3	*4.7*	−6.7	*4.2*	0.2	*0.2*	0.1	*0.1*	9.7	*4.3*

Table 2: Transformation parameters to the ICRF2. Unit is μas.

3. REFERENCES

Fey, A. L., Gordon, D. G., Jacobs, C. S., et al. 2010, International Earth Rotation and Reference Systems Service (IERS) Technical Note 35, Bundesamts für Kartographie und Geodäsie, Frankfurt am Main

IERS 1996, International Earth Rotation Service (IERS) Annual Report 1995 (Observatoire de Paris, Paris), II–19

Schuh, H., & Behrend, D. 2012, J. Geodyn., 61, 68

AN ACCURATE AND STABLE MIXED METHOD TO OBTAIN COEFFICIENTS IN VSH DEVELOPMENTS OF RESIDUALS FROM ICRF2- CATALOG DIFFERENCES

F.J. MARCO[1], M.J. MARTINEZ[2], J.A. LOPEZ[1]
[1] Universidad Jaume I.
IMAC. Dept. Matematiques. Campus de Riu Sec. 12071 Castellon. Spain
e-mail: marco@mat.uji.es, lopez@mat.uji.es
[2] Universidad Politecnica de Valencia.
IUMPA. Dept. Matemetica Aplicada. Camino de Vera S/N. 46022 Valencia. Spain.
e-mail: mjmartin@mat.upv.es

ABSTRACT. Gaia catalog contains positions of quasars and positions and proper motions of stars in visible wavelengths. The update of methods which are useful in the treatment of systematic errors in the celestial sphere is pertinent. The study of the residuals in positions and proper motions was carried out by several authors, such as [3] and [6], through the use of a model of adjustment using infinitesimal rotations. Further, in [1] the adjustment using vectorial spherical harmonics (VSH henceforth) for the global differences was introduced. An exposition about VSH may be seen in [5]. VSH were already used by Wahr in his doctoral thesis [9] about nutation for a non rigid Earth model.
To study the global differences, we proceed in two different ways:

1. Direct computation of the coefficients of the considered model with a wide and selected number of common stars to both catalogues and calculation of the coefficients of the model, using the discrete least squares method. The presence of bias in the data suggests the use of an alternative procedure: The previous computation of a residual adjustment over the whole sphere by means of a kernel non parametric adjustment (KNP henceforth).
2. The hypothesis that the function of adjustment is square integrable over the sphere, allows the application of the method of least squares in its continuous version: The function is replaced by a KNP intermediate adjustment to obtain the coefficients for a selected parametrical model whose coefficients we want to estimate. This procedure was used in [1] for the comparison Hipparcos-FK5 obtaining, for the first time, a value of $d_{1,0}$ that must be taken into account, and in [2] for the determination of the spin between FK5 and Hipparcos, obtaining results fully compatible to those of [3] and [9]).

Mignard & Klioner [3] have made a detailed study of VSH in positions and proper motions, providing interesting theoretical and practical results. The authors emphasize the importance of considering, in the adjustment of the residuals of the positions, a particular term of the adjustment in declination, comparable to the one obtained in [1] by us.
The discrete least squares method may lead to instability and inaccuracy. In contrast, a greater accuracy and efficiency may be reached using the continuous least squared formulation discretized using our proposed Mixed Method. The power that has not been recovered is due to numerical truncations or discretizations.
The case of the vectorial spherical harmonics developments up to first order is shown in detail in [1]. Following the continuous line of work, it is necessary to perform certain mathematical hypothesis of regularity, regarding the type of function that we want to find. With the usual method (VSH(1)) we get coupled equations, which is not relevant for first order (see numerical result in VSH(1) in table 1). Nevertheless, we implement the problem more directly.
Let us consider the vectorial field $\Delta\mathbf{X} \equiv \mathbf{V}(\alpha,\delta) = V^{\alpha}(\alpha,\delta)\mathbf{e}_{\alpha} + V^{\delta}(\alpha,\delta)\mathbf{e}_{\delta} = (\Delta\alpha\cos\delta)\mathbf{e}_{\alpha} + \Delta\delta\mathbf{e}_{\delta}$ being $V^{\alpha}(\alpha,\delta)$, $V^{\delta}(\alpha,\delta)$ the scalar fields of the residuals and $\mathbf{e}_{\alpha}$, $\mathbf{e}_{\delta}$ the unitary vectors in the tangent plane and in the directions of the right ascension and declination, respectively.
On the other hand, and provided that we are in the surface of the unitary sphere, the only vectorial spherical harmonics involved are the spheroidal spherical harmonics $\mathbf{S}_{l,m}$ and the spherical toroidal har-

monics $\mathbf{T}_{l,m}$. We suppose that the field $\mathbf{V}$ accepts a development in toroidal and spherical harmonics. For the calculation of $\mathbf{V}$, in points regularly spaced over the sphere, we can use the kernel regression method [7] or a polynomial kernel regression. The first one is more economic computationally and it is accurate enough for the problem that we are dealing to. It is important to emphasize that, once the adjustment has been established for $\mathbf{V}$ over the set of points, this same set can be used in the numerical integration of the numerators. Thus we can easily calculate the estimations for higher orders of harmonics. The results up to order one are listed in Table 1 in the VSH(2) line and are only slightly different from the VSH(1) results.

The Mixed Method does not need to fix a priori an order for the adjustment. The stop criterion is to retrieve a % of the power (96% as is the case, it seems sufficient), so it is a non-linear adjustment Greedy method. On the contrary, the discrete least squares method is highly inefficient, and with each addition of a new order of the adjustment, all the coefficients must be recalculated again. Finally, the power theoretically recovered is false. There is no indication of a relationship between the recovered power of the function and the obtained coefficients.

In conclusion, the Mixed Method proposed is better in efficiency and stability, which also involves an accurate recovery of the function and, as a complement, an estimate of the noise in the data that is perfectly determined.

	ε_x	ε_y	ε_z	$d_{1,0}$	$d_{1,1}$	$d_{1,-1}$
[4]	-18.1	-14.6	-18.5	-64	-1.3	-18.3
[1]	-21.4	-18.6	-20.4	-10.1	-0.9	-25.7
VSH(1)	-20.2	-20	-18.5	-61.8	-6.3	-15.2
VSH(2)	-18.5	-13.6	-18.2	-61.8	-2.0	-18.9

Table 1: Global orientation and glide between the FK5 and the Hipparcos catalog, in mas, (1991.25). Results for [4] and [1] were obtained using the common stars and VSH have been obtained using a Mixed Method over the whole sphere. Coupled equations in VSH(1) line and decoupled in VSH(2).

REFERENCES

1. Marco F. et al. ,2004, A&A. 418
2. Marco F. et al. 2009. Pub. of the Astron. Soc. Pacific. 121.
3. Mignard, F.,& Froeschle, M. 2000, A & A, 354, 732
4. Mignard, F.,& Klioner, S. 2012, A & A, 547, A59
5. Morse P.H., Feshbach H. Methods of theoretical physics 2 vols. (McGraw-Hill, New York, 1953).
6. Schwan, H. 2001, A&A, 367, 1078
7. Simonoff J.S. 1996, "Smoothing Methods in Statistics", Springer-Verlag
8. Wahr J.M. The tidal motions of a rotating, elliptical, elastic and oceanless Earth. Ph. D. Thesis. University of Colorado, 216 pp.
9. Wand M. P. & M. C. Jones. Kernel Smoothing. Monographs on Statistics and Applied Probability. Chapman & Hall.

ABOUT HOMOGENEITY IN COMBINED CATALOGS

F.J. MARCO[1], M.J. MARTINEZ[2], J.A. LOPEZ[1]
[1] Universidad Jaume I.
IMAC. Dept. Matematiques. Campus de Riu Sec. 12071 Castellon. Spain
e-mail: marco@mat.uji.es, lopez@mat.uji.es
[2] Universidad Politecnica de Valencia.
IUMPA. Dept. Matematica Aplicada. Camino de Vera S/N. 46022 Valencia. Spain.
e-mail: mjmartin@mat.upv.es

ABSTRACT. The IAU recommendations regarding the ICRF realizations require the construction of radio sources catalogs obtained using very-long-baseline interferometry (VLBI) methods. The improvement of these catalogs is a necessary procedure for the further densification of the ICRF over the celestial sphere. [1], [2].
The different positions obtained from several catalogs using common sources to the ICRF make it necessary to critically revise the different methods employed in improving the ICRF from several radio sources catalogs. In this sense, a revision of the analytical and the statistical methods is necessary in line with their advantages and disadvantages.
We define homogeneity as applied to our problem in a dual sense: the first deals with the spatial distribution of the data over the celestial sphere. The second has a statistical meaning, as we consider that homogeneity exists when the residual between a given catalog and the ICRF behaves as a unimodal pure Gaussian. We use a nonparametrical method, which enables us to homogeneously extend the statistical properties of the residual over the entire sphere.
A combination of catalogs can only be homogeneous if we configure the weights carefully. In addition, we provide a procedure to detect inhomogeneities, which could introduce deformities, in these combined catalogs.
An inappropriate use of analytical adjustment methods provides erroneous results. Analogously, it is not possible to obtain homogeneous-combined catalogs unless we use the adequate weights.
In this study, we considered only the sources which have at least 15 observations in two sessions. We have not included some reference sources in our calculus that present oddly high residuals. All values are given in mas.
With respect to the study of the residuals, we have chosen to carry out a preliminary kernel nonparametric adjustment [7] (KNP henceforth) for the $\Delta\alpha cos\delta$ and $\Delta\delta$ in both catalogs and a vectorial spherical harmonics (VSH henceforth) of first order for the adjustment model. Then, we apply our mixed method [4], [5]. The existence of deformations has required the use of a correction for each catalog given by

$$\min_{C^i} \int_{S^2} \left\{ \left[(\Delta\alpha \cos\delta)^{(i)} - m_\alpha^{[i]}(\alpha,\delta) \right]^2 + \left[(\Delta\delta)^{(i)} - m_\delta^{[i]}(\alpha,\delta) \right]^2 \right\} dS \tag{1}$$

where C^i are the coefficients of the models $m_\alpha^{[i]}$ and $m_\delta^{[i]}$ with $i = 1$ (USNO) and $i = 2$ (JPL). The results for the coefficients of the VSH of first order may be seen in [5]. This must be considered in future studies.
Next, we consider only the rotations. We subtract the corrections provided by the rotations to the initial position to obtain the intermediate catalogs $USNO^1$ and JPL^1 $Cat^1 = Cat - correction$, where these corrections depend only on the rotations. The adjustment itself is given by $cat_i^1 - (ICRF - Ext2) = m^{[i,1]} + e^{[i,1]}, i = 1, 2$.
Now, we use the term WRMS that denotes weighted root mean squared. In our case, the function uses the weights assigned by the KNP adjustment. With regard to the WRMS in the entire sphere where we have used numerical integration and a KNP adjustment, the results may be visually checked for the USNO in figures 1 and 2.
For further details see [5].

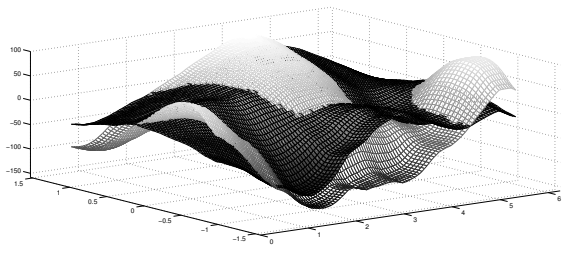

Figure 1: Differences in (ICRF-Ext2)-USNO for $\Delta\alpha cos\delta$ (in mas). The clear surface represents the initial differences, the dark surface represents the differences after the correction given by the rotations.

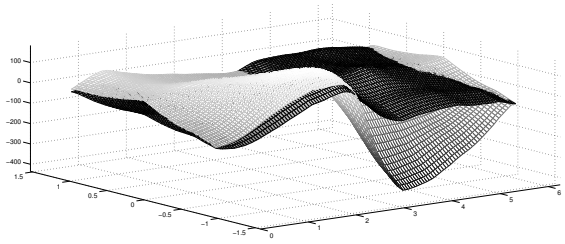

Figure 2: Differences in (ICRF-Ext2)-USNO for $\Delta\delta$ (in mas). The clear surface represents the initial differences, the dark surface represents the differences after the correction given by the rotations

REFERENCES

1. Arias, E.F., Charlot, P., Feissel, M., Lestrade, J.F., 1995, A&A, 303,604
2. Feissel, M.,& Mignard, F. 1998, A&A, 331, L33
3. Fey A., Gordon D., Jacobs C., eds, 2009, IERS Technical Note 35, The Second realization of the International Celestial Reference Frame by Very Long Baseline Interferometry, Frankfurt am Main 2010: Verlag des Bundesamts fr Kartographie und Geodasie
4. Marco F. et al. 2004, A & A. 418
5. Marco F. et al. 2013, A & A. 558, A98
6. Sokolova Ju., Malkin Z. A & A, 2007, 474, 2, 665
7. Wand, M. P., and Jones, M. C. 1995. Kernel Smoothing. London: Chapman and Hall.

PROBLEMS CAUSED BY BIASED DATA IN MODELS OF CATALOG ADJUSTMENT

M.J. MARTINEZ[1], F.J. MARCO[2], J.A. LOPEZ[2]
[1] Universidad Politecnica de Valencia.
IUMPA. Dept. Matematica Aplicada. Camino de Vera S/N. 46022 Valencia. Spain.
e-mail: mjmartin@mat.upv.es
[2] Universidad Jaume I.
IMAC. Dept. Matematiques. Campus de Riu Sec. 12071 Castellon. Spain
e-mail: marco@mat.uji.es

ABSTRACT. Working with catalogues requires an increasing precision. A powerful tool has been the comparison between different catalogues. To this aim contribute both the sophistication/refinement of the models of adjustment and the more careful treatment of the data.
We introduced a mixed method for the study of the relative orientation between the catalogues Hipparcos and FK5 [2], obtaining results comparable to those of other authors. We also introduced the VSH model of first order (rotation+ deformation), but the coefficients were obtained by a simple least squares adjustment because we were interested only in the relative rotation between the catalogues (The corresponding calculations for the spin were published in [3]).
The good distribution of the data (density and homogeneity), makes reliable the coefficients even applying a simple least square method. In particular, the value of $d_{1,0}$ was high enough as to be taken into account in later studies.
Very recently, Mignard and Klioner [5] have published a paper to introduce the use of VSH (of arbitrary order) in the comparison of catalogues. After reading it, we verified that their $d_{1,0}$ value was practically the same that the one obtained by us. We considered, then, to carry out the calculations again, with our method [2] (and [3]), being the results corroborated. We can affirm that our method is compatible with the developments in VSH given by Mignard et al. [5] and it makes useful contributions when the catalogues are not homogeneous. Some questions arise regarding with the advantages of our technique, the orthogonality or the choice of the kernel. Due to reasons of space, we will only highlight some of these points:

1. We have considered the meaning of functional orthogonality that allows the calculation of coefficients of a development on the basis of the calculation of determined integrals.
2. The mathematical methods must be used in particular problems and its utility is given related not only to a consistent theory, but also to contrastable numerical results.
3. The method VSH handles vectors in 2D in its theoretical formulation. We also consider vector fields (it is true, though, that the method is also applicable to scalar fields and, therefore, more general than the VSH) and, in fact, after having compared the coefficients calculated by us in [2], with those of Mignard et al [3] and with ours again [4], they coincide.
4. There are scalar and vectorial kernels (see [1]). Kernels and methods of kernel regression do exist for several dimensions. Nevertheless, the low technical difficulty from a mathematical point of view, makes not necessary their use. Provided that we work on the surface of a unitary sphere, the only vectorial spherical involved are the spheroidal and toroidal and the vector field can be developed using them. For the calculation of the components of the vector field over points regularly distributed over the sphere we can use the simple method of kernel regression or a method of local kernel polynomial regression. Computationally, the first is more economic and, in addition, it is sufficient for the problem that we are studying. We can easily carry out the estimations up to high orders estimations.
5. The choice of the kernel has very little impact [6].
6. It is not mathematically adequate the use of the method of the least squares with biased data and an unbiased model.

REFERENCES

1. M. Carbon, C. Francq, L.T. Tran. 1997. "Kernel Regression Estimation for Random Fields". Statistics and Probability Letters, 36, 115-125.
2. Marco F. et al. ,2004, A&A. 418
3. Marco F. et al. 2009. Pub. of the Astron. Soc. Pacific. 121.
4. Marco F. et al. 2013, A & A. 558, A98
5. Mignard, F. & Klioner, S. 2012, A & A, 547, A59
6. Simonoff J.S. 1996, "Smoothing Methods in Statistics", Springer-Verlag

EFFECTS OF THE DATUM CONFIGURATION OF RADIO SOURCES ON EOP DETERMINED BY VLBI

V. RAPOSO-PULIDO[1,2], R. HEINKELMANN[1], T. NILSSON[1], M. KARBON[1], B. SOJA[1], E. TANIR KAYIKCI[3], C. LU[1], J. MORA-DIAZ[1], H. SCHUH[1], J. GOMEZ-GONZALEZ[2]
[1] Helmholtz Centre Potsdam, GFZ German Research Centre for Geosciences
Department 1: Geodesy and Remote Sensing, 14473 Potsdam, Germany
raposo@gfz-potsdam.de
[2] IGN, National Geographic Institute Madrid, Spain
[3] Karadeniz Technical University, Department of Geomatics Engineering, Trabzon, Turkey

ABSTRACT. The Earth Orientation Parameters (EOP) provide the orientation of the International Terrestrial Reference System (ITRS) relative to the Geocentric Celestial Reference System (GCRS) as a function of time. How many and which radio sources are taken into account for the datum definition has a significant effect on the EOP determined by Very Long Baseline Interferometry (VLBI). In this work, using different options for the Celestial Reference Frame (CRF) datum definition, we show how the accuracy of the EOP and the radio source positions can be improved increasing the number of radio sources in the southern hemisphere.

1. INTRODUCTION

The special 24-hour session IYA09 (09NOV18XA) was conducted in the International Year of Astronomy (IYA) in order to observe as many of the 295 ICRF2 (Fey et al. 2009) defining sources as possible in a single session. A typical modern session contains 50-70 sources with a terrestrial network of seven to eleven stations, while the IYA09 includes 237 radio sources and 32 stations. This provides a much stronger geometry to study the impact of the datum definition on the EOP.

2. DATA ANALYSIS: RADIO SOURCE AND EOP ADJUSTMENTS

The data were analyzed with the Vienna VLBI Software (VieVS, Böhm et al. 2012) under consideration of the IERS Conventions (Petit and Luzum, 2010). The celestial datum was realized by applying NNR+dz conditions including different subsets of radio sources, where dz means that the sum of corrections in declination is constrained to zero. Radio sources with less than three observations were excluded from the analysis to avoid singularity problems. Datum A is the reference approach (ICRF2 defining sources, 229 sources), and B ($\delta \geq 0°$, 161), D ($-30° \leq \delta \leq 30°$, 135), E ($0h \leq \alpha \leq 12h$, 127), G ($12h \leq \alpha \leq 24h$, 102) and H ($\delta \leq 0°$, 68) are geometrical subsets. Subset C ($SI \leq 3$, 157) takes into account the structure index (SI), that describes the expected magnitude of the effects of intrinsic radio source structure on VLBI delay observations (Fey & Charlot, 1999). For subset F (F-V sources, 103) the radio sources were selected by statistical tests on the time-varying behavior of radio source coordinates (M. Feissel-Vernier, 2003). The overall formal error (d) was compared with the reference datum A (see Fig. 1). To estimate d we used the equation: $\mathrm{d}=\sqrt{\sigma^2_{\alpha cos\delta} + \sigma^2_\delta + \sigma_{\alpha cos\delta}\sigma_\delta C(\alpha,\delta)}$ with $\mathrm{C}(\alpha,\delta)=\frac{Cov(\alpha,\delta)}{\sigma_\alpha \sigma_\delta}$. Larger variations were found for radio sources of the southern hemisphere. C and F cover almost the same declination and right ascension ranges compared to A and thus showed the smallest differences. Comparing datum configurations B and H with E and G, the impact of the geometrical restriction in declination direction was much larger than in right ascension. For $dUT1$ the formal errors increased when the right ascension range was limited. A good right ascension range is necessary to accurately determine the origin given by the x-axis. Concerning the celestial pole offsets dX and dY, the maximal formal errors appeared for approach H, where the low number of radio sources and the restriction of the datum to the southern hemisphere introduced a defect. For the pole coordinates x_p and y_p the values were stable on the level of a few μas (see Table 1).

3. DATA ANALYSIS: CELESTIAL REFERENCE FRAME

The relative orientations of two 3D frames (e.g. CRF) can be modeled by three rotation angles ($A1$, A_2, A_3) around the x, y, z axes. In addition, systematic frame deformations, such as shearing (D_α, D_δ) and the bias in declination (dz) can be modeled at the same time: $\{d\alpha = A_1 tan\delta_1 cos\alpha_1 + A_2 tan\delta_1 sin\alpha_1 - A_3 + D_\alpha\delta_1$; $d\delta = -A_1 sin\alpha_1 + A_2 cos\alpha_1 + D_\delta\delta_1 + dz\}$ These equations were weighted by using the inverse of the variance of the offsets ($\sigma^2_{d\alpha}, \sigma^2_{d\delta}$) and then inverted. We compared the individual VLBI frames (A to H) with ICRF2 based on the corresponding radio sources. When all the defining sources were included (A), the formal uncertainties of the six parameters were smallest. Approach H showed the largest rotations and deformations with an absolute value of about 120 μas for A_3. Approach C with good geometry but only 157 radio sources showed results comparable to A, but with slightly higher uncertainties. Although the distribution of the radio sources of approach F is comparable to A and C, this approach contains only 103 radio sources and the shearing parameter D_α increased to about -1.5 μas/deg. When the geometry is restricted, i.e., the right ascension or declination range are not covered, the number of radio sources did not seem to play a significant role.

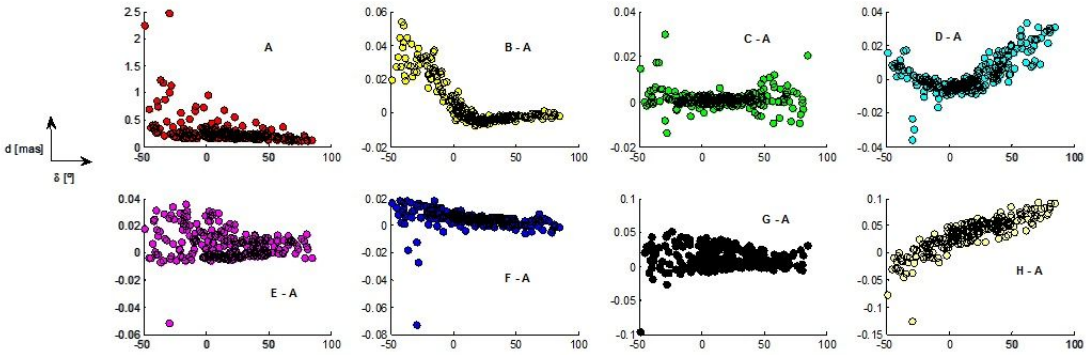

Figure 1: Formal errors of the radio source positions with datum A (upper left plot) and differences of formal errors w.r.t. those of the other subsets

	B-A	C-A	D-A	E-A	F-A	G-A	H-A
$\bigtriangleup\,\sigma_{dUT1}[\mu s]$	-0.14	-0.7	-0.9	0.88	0.28	1.74	2.08
$\bigtriangleup\,\sigma_{x_p}[\mu as]$	0.79	0.02	0.08	0.29	0.14	0.48	-0.38
$\bigtriangleup\,\sigma_{y_p}[\mu as]$	-0.006	-0.003	-0.04	-0.03	0.001	-0.11	-0.005
$\bigtriangleup\,\sigma_{dX}[\mu as]$	8.68	5.07	5.42	4.30	9.99	7.44	46.33
$\bigtriangleup\,\sigma_{dY}\ [\mu as]$	5.92	1.50	3.33	11.01	6.71	18.62	58.18

Table 1: Differences of the formal errors relative to the reference solution (see text)

Acknowledgements. We acknowledge IGN for its support and IVS for providing the data analyzed in this study, in particular all stations which took part at the IYA09 session.

4. REFERENCES

Böhm, J., Böhm, S., Nilsson, T., Pany, A., Plank, L., Spicakova, H., Teke, K., and Schuh, H., 2012, The New Vienna VLBI Software VieVS, doi: 10.1007/978-3-642-20338-1_126.

Feissel-Vernier, M., 2003, Selecting stable extragalactic compact radio sources from the permanent astro-geodetic VLBI program, doi: 10.1051/0004-6361:20030348.

Fey, A.L., Gordon, D., Jacobs, C.S., 2009, The Second Realization of the International Celestial Reference Frame by Very Long Baseline Interferometry, IERS Technical Note No. 35, ISBN: 3-89888-918-6.

Fey, A.L. and Charlot, P., 1999, VLBA Observations of radio reference frame sources. III. Astrometric suitability of an additional 225 sources, doi: 10.1086/313382.

Petit, G. and Luzum, B., 2010, IERS Conventions (2010), IERS Technical Note No. 36, ISBN: 3-89888-989-6.

Session 3

ATOMIC AND PULSAR-BASED TIMESCALES - PROGRESS AND DEVELOPMENTS

ÉCHELLES DE TEMPS ATOMIQUES ET ÉCHELLES DE TEMPS BASEÉES SUR LES PULSARS - PROGRÈS ET DÉVELOPPEMENTS

MULTI-GNSS TIME TRANSFER

P. DEFRAIGNE
Royal Observatory of Belgium
Avenue Circulaire, 3, 1180-Brussels
e-mail: p.defraigne@oma.be

ABSTRACT. Measurements from Global Navigation Satellite Systems (GNSS) are used since the eighties to perform precise and accurate Time Transfer. Only the GPS constellation was used during the last 25 years, with some experiments based on GLONASS measurements. The GLONASS constellation is presently completed, the first four GALILEO satellites are already operational, and the BEIDOU system also provides signals that can be additionally used for time transfer. Increasing the number of satellites, and hence the number of observations, will reduce the noise level of the solution. However, such a combination requires the knowledge of some inter-system biases in the receivers and the existence of satellite clock products which can be expressed with respect to a common reference. This paper will propose recent advances in these combinations, focusing on GPS, GLONASS and GALILEO.

1. INTRODUCTION

The International Atomic Time is computed by the BIPM from an ensemble time scale algorithm combining about 400 atomic clocks distributed in about 60 laboratories in the world. The data used are actually the differences between the clock readings, i.e. time intervals between the time pulses given by two clocks. It is therefore necessary to be able to compare the clocks, whatever the distance between them. One current technique for remote clock comparison (or time transfer) is based on the analysis of GNSS signals arriving in two GNSS stations where the clocks to be compared are each connected to the receiver. Measurements from GPS are used since the eighties (Allan & Weiss, 1980) to that goal. In its classical version, the GPS time transfer is performed using clock offsets collected in a fixed format, called CGGTTS (Common GPS GLONASS Time Transfer Standard), as described in (Allan &Thomas, 1994; Azoubib & Lewandowski,1998). These clock offsets represent the differences $(clock - REF)$ between the local clock and the reference timescale of the GNSS. They are obtained from the pseudorange measurements, corrected for the signal travel time (satellite-station), for the troposphere and ionosphere delays, and for the relativistic effects. A smoothing is then performed over 13 minute observation tracks, and the results are then corrected for the instrumental hardware delays. These hardware delays correspond to the electric delays accumulated by the signal between the antenna phase center and the internal timing reference of the receiver (or receiver clock). They are function of the frequency so that the combination of measurements from satellites of different constellations requires taking into account the inter-system and inter-frequency biases.

Starting with C/A code receivers, the method was then upgraded to take advantage of the dual-frequency receivers measuring codes on both frequencies, which allows to remove the ionosphere delays at the first order (i.e. 99.9 percent of the effect), thanks to the ionosphere-free dual-frequency combination. This led to a factor 2 improvement in the stability of the intercontinental time links up to averaging times of 10 days (e.g. Defraigne & Petit, 2003). In the present study, all the time transfer results will be obtained with the All in View (AV hereafter) approach (Petit & Jiang, 2008), i.e. the results $(clock - REF)$ for each station are first computed as a weighted average of the solutions provided by each satellite in view. The difference between the solutions obtained in the two stations gives then the time transfer solution between the two station clocks. Note that in parallel, the time-transfer technique based on Precise Point Positioning (PPP) has proven to be a very effective technique allowing the comparison of atomic clocks with a precision at the level of a hundred picoseconds, (e.g. Defraigne et al., 2008). PPP (Kouba & Héroux, 2001) is based on a consistent modeling and analysis of GPS (and possibly GLONASS) dual-frequency code and carrier-phase measurements. This technique is widely recognized for its high resolution (1 pt/30 s) and high frequency stability, reaching 10^{-15} at an averaging time of one day, thanks to the very low noise level of the carrier phases (see for instance Larson et al., 2000),

enabling time transfer with a statistical uncertainty of 0.1 ns, when ignoring the uncertainty on the instrumental hardware delays. This paper however concerns only the code-only analysis as a first step in the combination of different systems for time transfer. Furthermore, the introduction of inter-system biases is requested only for code-measurements, so that the same procedure will be applied to PPP afterwards.

The first section of the paper describes a method presented in (Defraigne et al., 2013) to combine GPS and GLONASS measurements for time transfer in All-in-View, using calibration data for both GPS and GLONASS. This method is based on a least square approach where the clock solutions for both stations are computed in the same process, and constrained by the difference between the calibration data of the two stations. The method was tested on the link Brussels-Paris for which a calibration was performed for GPS and GLONASS. After describing the methodology, the paper will present an estimation of the impact of using or not the GLONASS calibration results for that link using 6 weeks of data. The second section of the paper will provide some first results of the Galileo time transfer using a link between Brussels (Belgium) and Torino (Italy).

2. COMBINED GPS+GLONASS TIME TRANSFER

2.1. Theory

The AV clock solutions determined from GNSS signals refer to the receiver clock; these must be combined with the measurements of station hardware delays to get the de-synchronization of the clock with respect to the reference time scale REF of the GNSS:

$$clock - REF =< (t_{rec} - REF)_{sat} - \delta_a - \delta_c - \delta_r > +(clock - t_{rec}) \quad (1)$$

where $< >$ means averaging, $(t_{rec} - REF)_{sat}$ is the clock solution obtained from measurements on a given satellite, δ_a, δ_c and δ_r are the GNSS signal delays inside the antenna, cable and receiver, and $(clock - t_{rec})$ is the synchronization difference between the receiver clock and the external clock, which contains the cable delay between the clock and the receiver, and the delay between the connector and the receiver clock. This delay or the way to measure it is given by the manufacturer, while δ_a, δ_c and δ_r must be determined by experimental calibration.

The antenna and the receiver delay depend on the frequency of the GNSS signal. As all the GPS satellites emit the same frequencies L1 and L2, the hardware delays are the same for all the satellites and can be easily corrected for after the averaging procedure. Equation (1) for GPS can be simplified as:

$$clock - REF =< (t_{rec} - REF)_{sat} > -\Delta(rec) + (clock - t_{rec}) \quad (2)$$

It is however not the case with GLONASS as different satellites transmit on a different frequency pair, so that the antenna and receiver delays are different for each satellite, with inter-frequency biases (ISB) up to 25 ns in the code measurements. Equation (1) then becomes for GLONASS:

$$clock - REF =< (t_{rec} - REF)_{sat} - ISB(rec, sat, day) > +(clock - t_{rec}) \quad (3)$$

These ISBs must therefore be corrected for before the averaging when GLONASS data are used for time transfer. To get a time transfer solution from combined GPS and GLONASS measurements, we use the ESOC products in which the satellite clocks from both constellations are given with respect to the same reference time scale (Springer, 2009). However, due to the existence of the station-satellite biases, some ISBs are also present in the satellite clock products. As these are determined on a daily basis, it is necessary to determine also daily ISBs for time transfer, while physically these ISBs should be constant (if the temperature around the receiver is constant). One solution is to determine the ISBs present in the GLONASS measurements, with respect to the calibrated GPS solution, as proposed in (Harmegnies et al., 2013). However, the final solution is then based only on GPS calibration. We propose therefore an alternative which is to introduce the GLONASS calibration data for a link between two stations. This requires determining the ISBs of both stations at the same time in the time transfer computation.

Indeed, the ISBs can be separated into two components: $D(rec, sat)$ the physical station (receiver+antenna) hardware delay for the frequencies of the GLONASS satellite, which is constant over time, and $B(day, sat)$ a satellite bias which varies from day to day, associated with the GLONASS satellite clocks, and which is the same for all the GNSS stations. This reads:

$$ISB(rec, sat, day) = B(day, sat) + D(rec, f_{sat}) \quad (4)$$

where f_{sat} is the satellite frequency. Therefore, the difference between the ISBs of two stations is equal to

$$\begin{aligned} ISB(rec_1, sat, day) - ISB(rec_2, sat, day) &= D(rec_1, f_{sat}) - D(rec_2, f_{sat}) \quad (5) \\ &= \Delta_{12}(f_{sat}) \quad (6) \end{aligned}$$

and should be constant over time. The difference $\Delta_{12}(f_{sat})$ can be determined by relative calibration of the two stations, for each GLONASS frequency.

In order to use these differential delays in All in View (AV) and similarly in the future for PPP, the determination of the AV (or PPP) solution must be done at the same time for both stations. The reason is that for each station the biases $ISB(rec, sat, day)$ must be determined with respect to the GPS AV solution of the station, while verifying the relation

$$ISB(rec_1, sat, day) - ISB(rec_2, sat, day) = \Delta_{12}(f_{sat}) \quad (7)$$

We propose therefore, to first determine a GPS-only AV solution, and then to use a constrained least square approach to determine the ISBs of both stations (see Defraigne et al., 2013, for a full description).

2.2 Validation with the link ORB-OP

An experimental GLONASS+GPS calibration has been realized in June 2013, between two time laboratories: OP (Paris Observatory) and ORB (Royal Observatory of Belgium). Both stations are equipped with a Septentrio PolaRx4TR-PRO receiver connected to a H-maser, while a cesium is used in the second part at ORB. The corresponding station names are OPM8 and BRUX. The link calibration was realized using a traveling GNSS station, containing a Septentrio PolaRx4TR-PRO receiver, a 30 m antenna cable, and a Choke Ring Trimble Antenna. The scheme of the calibration follows the procedure proposed in (Esteban et al., 2010). The differential hardware delays in the GLONASS P3 band for the link OMP8-BRUX are shown in Figure 1.

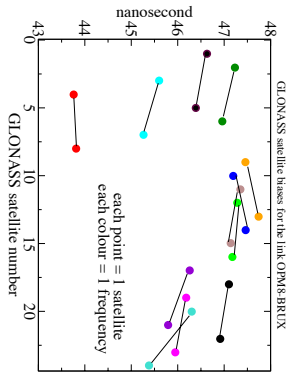

Figure 1: Differential GLONASS hardware delays of the P3 link OPM8-BRUX, computed for each satellite separately; two satellites transmitting the same frequencies are joined by a segment.

We can observe that except for satellites 20 and 24, which are on the frequency channel +2, i.e. on the border of the frequency band, the satellite pairs corresponding to a given frequency channel have differential hardware delays with a difference smaller than half a nanosecond.

Figure 2 presents the difference between the combined GPS+GLONASS solutions using or not the GLONASS calibration constraint to determine the ISBs of BRUX and OPM8. The global impact of using or not the GLONASS calibration constraint on the combined AV solution is, for this six week period and this particular baseline, between -1.2 and +1.2 nanosecond. Finally, Figure 3 shows the smoothed time transfer solution (median of a 1 day sliding window) over six weeks for BRUX-OPM8, based on the AV solution using GPS-only, and using GPS+GLONASS with and without taking the GLONASS calibration into account. We clearly see the impact of using the GLONASS calibration, while using only the GPS Calibration provides a solution very similar to the GPS-only solution.

The differences between the ISBs obtained with and without GLONASS calibration constraint are depicted in Figure 4 for BRUX and OPM8. These differences range between -2 and +2 nanosecond, and

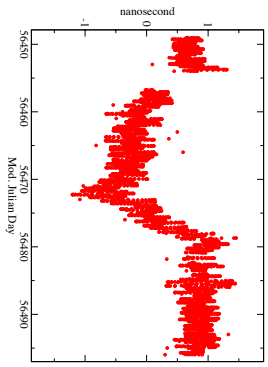

Figure 2: Differences between the time transfer solution OPM8-BRUX computed with AV in both stations with ISBs determined with and without the calibration constraint.

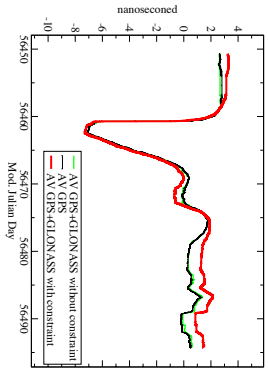

Figure 3: Comparisons between the time transfer solution for OPM8-BRUX computed with AV in both stations using GPS-only (black), GPS+GLONASS with (green) and without (red) the GLONASS calibration data.

are not constant over the one month period analyzed. The large peaks for OPM8 at mjd 56456 are due to an incomplete daily RINEX file, reducing the number of observations used to determine the ISBs; in that case the constraint is very useful to keep the correct calibration in the analysis.

3. FIRST RESULTS WITH GALILEO

Some first data analysis has been done using Galileo code measurements collected in two time laboratories equipped with a H-maser: the Royal Observatory of Belgium (Brussels), where two GNSS stations are equipped with a PolaRx4 receiver, and one in Torino, Italy, at the INRIM. While the existence of new signals could lead to new analysis strategies (see e.g. Martinez et al., 2013, or Panek, 2012), the present results are based on the same approach as used with GPS data, i.e. the ionosphere-free combination of Galileo codes E1 and E5 (E5a or E5b or E5-AltBoc) in a CGGTTS-like computation of the receiver clock solutions. The satellite tracks were however limited to 5 minutes rather than the conventional 13 minutes of the CGGTTS. The satellite positions and clocks were deduced from the IGS-MGEX products delivered by the Munich analysis center TUM. A first picture (Figure 5) shows the results of a 100 meter baseline, using the two stations in Brussels, BRUX and ZTB3, and compares them with the corresponding results obtained with GPS satellites and the ionosphere-free combination P3. Note that not the same clock is connected to BRUX and ZTB3; one is the free maser, while the second one is the steered maser. A linear drift was removed from the results.

From this first result, it can be concluded that the quality of the time transfer based on the ionosphere-free combination, directly related to the noise of the pseudoranges, is at least as good for Galileo as for GPS. A more precise comparison of the statistics of both solutions will be possible only when a larger

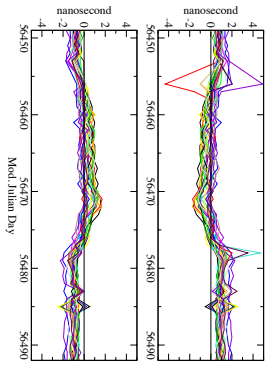

Figure 4: Differences between the GLONASS ISBs determined with and without GLONASS calibration data for OPM8 (top) and BRUX (bottom); each colour is for one given satellite

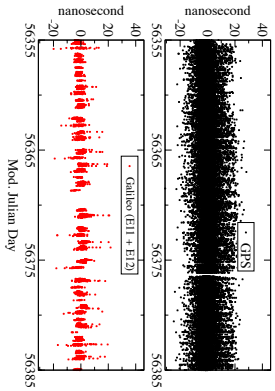

Figure 5: First results of time transfer on a zero-baseline using the ionosphere-free combination of Galileo E1 and E5.

number of Galileo satellites will be available. In order to determine if there is an optimal choice of signal in the E5 band, the time transfer link between Brussels and Torino was computed using the ionosphere-free combinations E1,E5A / E1,E5b / E1,E5. We could expect a smaller noise when using the combination E5, i.e. the AltBOC signal, as this one is characterized by a significantly reduced multipath (Simsky et al., 2008), but as seen in Figure 6, this is not the case, due to the combination with E1, and the considerable increase of the noise and multipath from the coefficient 2.26 appearing before E1 in the ionosphere-free combination with E5. The main conclusion from these preliminary results of Galileo time transfer is that using the ionosphere-free combination of E1 with one other code in the E5 frequency band provides a solution with a noise level at least similar to the one of GPS.

4. CONCLUSIONS

This paper summarized a method to combine GPS and GLONASS measurements for time transfer in All-in-View, using calibration data for both GPS and GLONASS. A more detailed presentation of the method can be found in (Defraigne et al EFTF 2013). GLONASS calibration data can only be introduced in the computation of a LINK, i.e. a difference of 2 AV solutions. Our proposed method introduces the calibration as constraints in the determination of inter-satellite biases and request that the AV solutions for both stations are computed together. The same method can also be applied to combined GPS+GLONASS PPP. This method was validated on a time transfer experiment between Brussels and Paris. The difference during six weeks between the time transfer solutions based on a combined GPS+GLONASS AV, obtained with and without GLONASS calibration results is in this case smaller than 2.5 ns peak to peak. This study will be extended to more baselines, and the uncertainty budget will be further evaluated. It will then be applied to Precise Point Positioning. The second part of the paper presented some first results of time transfer using Galileo measurements, using the ionosphere-

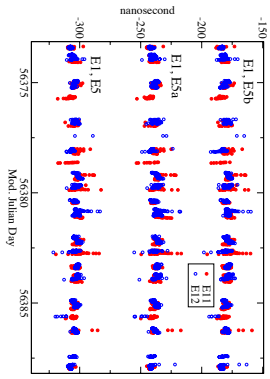

Figure 6: Comparison between the 3 iono-free combinations: E1+E5 / E1+E5a / E1+E5b; CGGTTS-like results, over 5 minutes tracks.

free combination of E1 with one other code in the E5 frequency band. It was shown that the noise level of the solutions is at the same level as when using GPS measurements.

Acknowledgements. The author thank Tim Springer and the ESOC for helpful discussions and availability of orbits and clock products.

5. REFERENCES

Allan, D.W., Weiss, M., 1980, Accurate time and frequency transfer during common-view of a GPS satellite, Proc. IEEE Freq. Contr. Symp., Philadelphia, PA, pp. 334-356.

Allan, D.W., Thomas, C., 1994, Technical directives for standardization of GPS time receiver software, Metrologia 31, pp. 69-79.

Azoubib, J., Lewandowski, W., 1998, CGGTTS GPS/GLONASS data format Version 02, 7th CGGTTS meeting.

Defraigne, P., Petit, G., 2003, Time transfer to TAI using geodetic receivers, Metrologia, 40, pp. 184-188.

Defraigne, P., Guyennon, N., Bruyninx, C., 2008, GPS Time and Frequency Transfer: PPP and Phase-Only Analysis, Int. J. of Nav. and Obs., vol. 2008, Article ID 175468, 7 pages, doi: 10.1155/2008/175468.

Defraigne, P., Aerts, W., Harmegnies, A. Petit, G., Rovera, D., Uhrich, P., 2013, "'Advances in multi-GNSS time transfer"', in Proc. EFTF-IFCS, Prague.

Esteban, H., Palacio, . J. , Galindo, F.J., Feldmann, T., . Bauch, A. , Piester, D., 2010, "'Improved GPS based time link calibration involving ROA and PTB"', IEEE Transactions on Ultrasonics, Ferroelectrics, and Frequency Control, UFFC-57, pp. 714-720.

Harmegnies, A., Defraigne, P., Petit, G., 2013, Combining GPS and GLONASS in all in view for time transfer, Metrologia 50, pp. 111.

Kouba, J., Heroux, P., 2001, GPS Precise Point Positioning using GPS orbit products, GPS solutions, vol. 5, pp. 12-28.

Larson, K., Levine, J., Nelson, L., Parker, T., 2000, Assessment of GPS carrier-phase stability for time-transfer applications, IEEE Trans. Ultrason., Ferroelect., Freq. Contr., vol. 47(2), pp. 484-494.

Martinez, M.C., Defraigne, P. Bruyninx, C., 2013, On the Potential of Galileo E5 for Time Transfer, IEEE Trans. Ultrason., Ferroelect., Freq. Contr., 60(1), pp. 121-131.

Panek, P., 2012, Time scales comparisons using simultaneous measurements in three frequency channels, Proc. of the 44th PTTI, Reston.

Petit G., Jiang, Z., 2008, GPS All in view time transfer for TAI computation, Metrologia 45, pp. 35-45.

Simsky, A., Sleewaegen, J.-M., Hollreise, M., Crisci, M., 2008, Experimental results for the multipath performance of Galileo signals transmitted by GIOVE-A satellite, Int. J. of Nav. and Obs., vol. 2008, Article ID 416380, 13 pages, doi: 10.1155/2008/416380.

Springer, T., 2009, NAPEOS mathematical models and algorithms, DOPSSYS-TN-0100-OPS-GN, 1.0.

DEVELOPMENT OF A PULSAR-BASED TIMESCALE

G. HOBBS
CSIRO Astronomy and Space Science
PO Box 76, Epping, NSW 1710, Australia
george.hobbs@csiro.au

ABSTRACT. In this paper we summarise how pulsar observations have been used to create a highly stable timescale. We review recent work from the Parkes Pulsar Timing Array team to create a timescale that has a stability comparable to existing atomic timescales. We discuss how this timescale will improve by combining data from more telescopes. We conclude by considering the long-term possibilities for pulsar-based timescales.

1. INTRODUCTION

In this review paper we describe how the regular rotation of millisecond pulsars can be used to create a highly stable timescale. Numerous observatories worldwide now carry out regular observations of such pulsars with the primary aim of searching for ultra-low-frequency gravitational waves formed from merging supermassive, binary black holes. Pulse times-of-arrival (ToAs) from the pulsars are measured. A model of each pulsar, that describes its rotation, position and orbit, is used to predict the ToAs for that pulsar. Discrepancies between the observed and predicted ToAs are known as the pulsar timing residuals. As gravitational waves are not included in the model for the pulsar, any such waves will induce timing residuals. Theoretical estimates predict timing residuals at the $<$100 ns level for a data set spanning $\sim$5 yr.

The observatory clock, to which the pulse ToAs are referenced, is normally based on a maser to provide a stable frequency standard and a system, now usually based on the Global Positioning Satellites, to provide absolute time. Using techniques such as the common view time transfer, the observatory timescale can be transferred to a realisation of Terrestrial Time, TT. For high precision timing, TT as realised by the Bureau International des Poids et Mesures is used, TT(BIPM).

Atomic time standards are becoming more and more stable. However, the stability over many years or decades is not well known. It is therefore possible that current terrestrial timescales are not sufficient for measuring pulse ToAs at the $<$100 ns level over many years. All pulsar observations referred to a given timescale will be affected by irregularities in that timescale. This provides the possibility that identical residuals in the data sets for different pulsars could be identified. Only recently have enough pulsars been observed with sufficient sensitivity to search for the timing residuals induced by irregularities in the terrestrial timescales. The Parkes Pulsar Timing Array (PPTA) project began during the year 2004 (Manchester et al. 2013). The PPTA currently observes 23 pulsars using the 64-m diameter Parkes radio telescope in Australia. The North American PTA (NANOGrav), described in McLaughlin (2013), formed in October 2007 and carries out observations with the Arecibo and Green Bank telescopes. The European PTA (EPTA; Kramer & Champion 2013) was established in 2004/2005 and includes telescopes in England, France, Germany, the Netherlands and Italy. In 2008 an agreement was made to share data sets between the three major PTAs. This led to the formation of the International Pulsar Timing Array (IPTA; see Manchester 2013 and references therein).

The basic methods for extracting a pulsar timescale have been known for many years (Guinot & Petit 1991, Petit & Tavella 1996, Rodin 2008, Rodin & Chen 2011, Hobbs et al. 2012). In brief, an ensemble of pulsars provides an Ensemble Pulsar Scale (EPS) that is analogous to the free atomic timescale Échelle Atomique Libre (EAL). The EPS can detect fluctuations in atomic timescales through the process of pulsar timing; the timing residuals for every pulsar in the sample will be affected by the timescale fluctuations in the same way. Identifying the signal common to all pulsars therefore allows the timescale fluctuations to be identified and corrected.

In this paper we initially describe an initial pulsar timescale produced using observations from the PPTA project. We then discuss a timescale likely to be produced using data from the IPTA. Finally, we

discuss possibilities that arise from new telescopes that will begin observations in the near future.

2. CURRENT STATUS

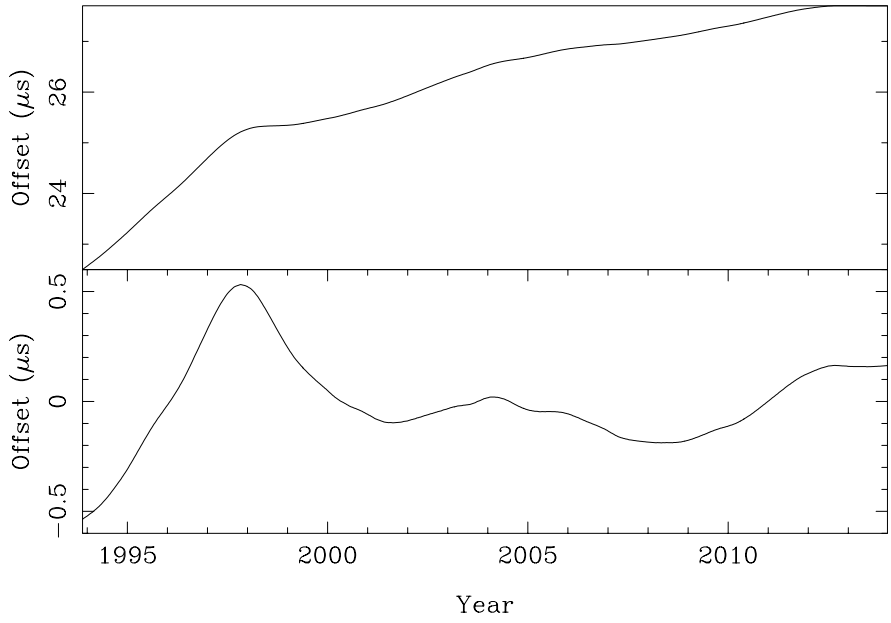

Figure 1: (top panel) The difference between the TT(TAI) and TT(BIPM2013). (bottom panel) The same, but after a quadratic polynomial has been fitted and removed.

The most stable and precise realisation of terrestrial time currently available is TT(BIPM2013). This timescale is obtained by retroactively applying a set of corrections to International Atomic Time, TT(TAI). For high precision pulsar timing it is usual to refer the pulsar ToAs to the best available realisation of TT, such as TT(BIPM2013). However, for our recent work we specifically chose to refer the ToAs to TT(TAI). The main reason for doing this was to confirm that we could recover the known irregularities in TT(TAI), i.e., could we recover TT(BIPM2013) from TT(TAI).

All attempts to use pulsars to search for irregularities in a terrestrial timescale are limited as we do not know the intrinsic pulsar pulse periods. Many phenomena, such as the pulsar slowing down, having a radial velocity from Earth, gravitational waves and drifts in the terrestrial timescale will also lead to an apparent change in that period. Hence, as part of the pulsar timing procedure it is necessary to fit for the pulse period and its first time derivative, i.e., to fit a quadratic polynomial to the timing residuals. The fitted parameters lead to new estimates of the pulsar's period and its time derivative. Post-fit timing residuals derived from the new parameters will not contain a quadratic polynomial and therefore, any errors in a timescale that induce residuals which follow a quadratic polynomial would be absorbed into the parameter fit and hence undetectable.

In the top panel of Figure 1 we show the expected signal TT(TAI)-TT(BIPM2013) before removing a quadratic polynomial. In the bottom panel we show the same, but after a quadratic polynomial has been fitted and removed. For observations spanning the years 1994 to 2014 and referred to TT(TAI) we would expect residuals at the < 500 ns level induced by errors in the time standard.

In Hobbs et al. (2012) we used observations from the PPTA project. The sampling for each pulsar is shown in the top panel of Figure 2. All the pulsars are different. For some pulsars, observations exist since the year 1994. These pulsars have wide-ranging properties. They have different data spans,

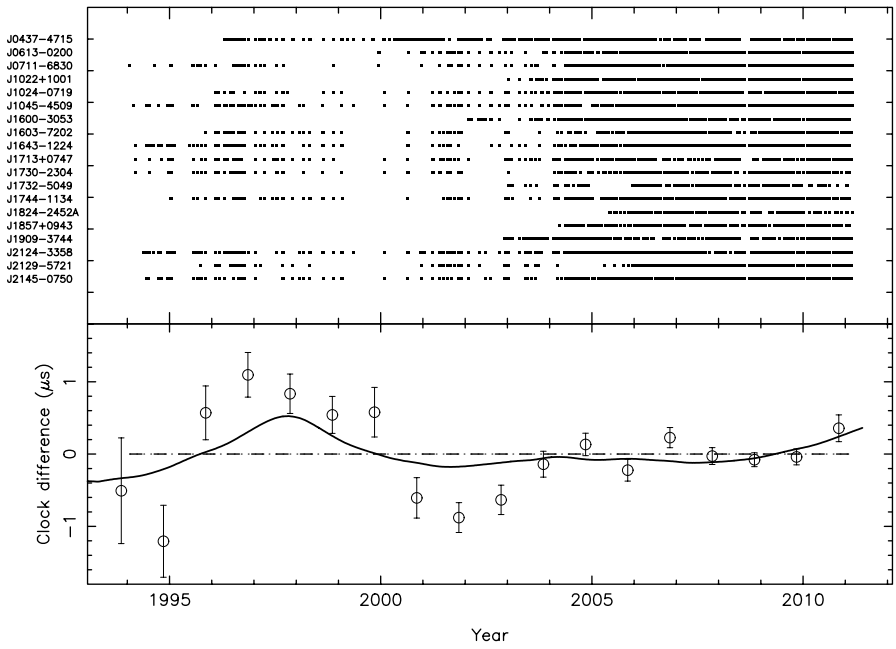

Figure 2: This figure is reproduced from Hobbs et al. (2012). The top panel shows the observing cadence for each of the pulsars in our sample. The lower panel shows the difference between the pulsar timescale and TT(TAI) as points with error bars. The solid line indicates the difference between TT(TAI) and TT(BIPM11) after a quadratic polynomial has been fitted and removed. Full details are available in Hobbs et al. (2012).

timing precision and sampling. Some pulsars are significantly affected by noise processes that induce low-frequency noise into the timing residuals. It was therefore necessary to develop a method for extracting the common signal that accounts for all these effects. The resulting algorithm is described in section 4 of Hobbs et al. (2012) and the result from applying the algorithm to the data is shown in the lower panel of Figure 2. We refer to the pulsar timescale as TT(PPTA2011). The difference between TT(PPTA2011) and TT(TAI) is shown in the figure as points with error bars. The expected signal, the difference between TT(BIPM2011) and TT(TAI) is shown as the solid line. In general there is good agreement between TT(PPTA2011)-TT(TAI) and TT(BIPM2011)-TT(TAI).

The largest deviation occurs between the years 1995 and 2003. During this time deliberate corrections were made to steer the TAI frequency to correct for changes in the primary frequency standards (Petit 2004). There is therefore a possibility that slight inaccuracies were introduced around this time. The PPTA data set has sparse sampling around this time and so it is also possible that these discrepancies come from the determination of the pulsar timescale. As shown below the use of data sets from the International Pulsar Timing Array project should be able to identify the reasons for the discrepancy.

3. THE INTERNATIONAL PULSAR TIMING ARRAY

The International Pulsar Timing Array (IPTA) team are in the process of combining data sets from the three current PTAs. The final data sets are not complete, but the pulsar names and their expected data spans have been published in Manchester (2013). For some of these pulsars it is possible to determine ToAs with < 50 ns precision. However, other pulsars are more poorly timed and may only achieve ~ 1 μs timing precision. Some pulsar data sets will be dominated by jitter noise and other pulsars by timing noise. It is therefore currently not trivial to predict how sensitive the IPTA data set will be to clock errors. In order to provide an initial prediction we have simulated data sets with the expected data spans,

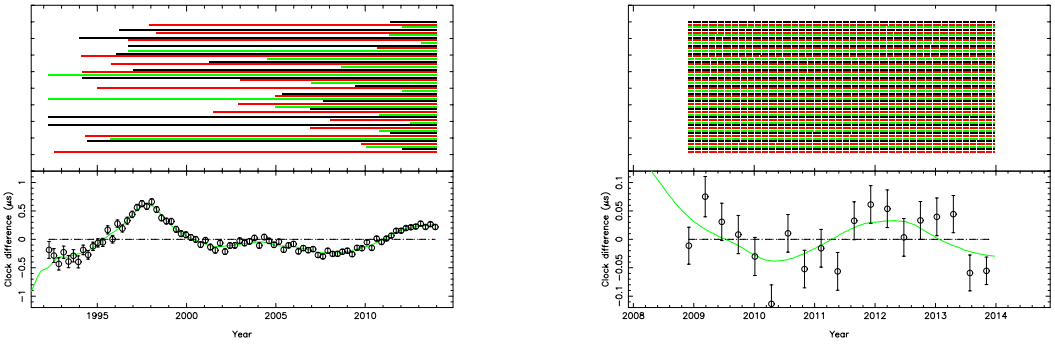

Figure 3: As in Figure 2, but using simulated data of the 50 pulsars being observed as part of the IPTA. In all cases the pulsars were assumed to be regularly sampled with a ToA precision of 500 ns. In the left hand panel the true data spans are used. In the right-hand panel only the last five years of data are simulated. For legibility the pulsar names, given in Figure 2, are not provided here. The pulsars simulated are listed in Manchester (2013).

but assume that all pulsars have a timing precision of 500 ns and are observed every 14 days. No low frequency noise processes are included in the simulation. The result is shown in the left-hand panel of Figure 3. With such a data set the expected discrepancies between TT(TAI) and TT(BIPM2013) can easily be identified.

As clocks improve, TT(TAI) is becoming more stable. In order to determine whether recent errors in TT(TAI) could be determined we have simulated IPTA data covering the last five years (all pulsars are simulated to have the same rms timing residual of 500 ns, same data span and same sampling). The result is shown in the right-hand panel of Figure 3. With such a short data span the clock errors are small, with a peak to peak amplitude of $\sim$ 100 ns. As seen in the Figure, it would be possible to detect the expected variation with the IPTA data sets, but it is unlikely that any smaller errors in TT(BIPM2013) could be identified.

The major purpose of the upcoming IPTA data sets will therefore be to 1) improve the pulsar-based timescale in the years before 2000 in order to confirm or deny the possible discrepancies seen using the PPTA data and 2) provide a long-term baseline for future, more precise data sets.

4. THE FUTURE

New telescopes are currently being designed and built. With its massive collecting area, the Five-hundred-meter Aperture Spherical Telescope (FAST) in China will provide high quality pulsar data sets on a large number of pulsars (see Nan et al. 2011). In the Southern Hemisphere the Square Kilometre Array (and its precursor telescopes such as MeerKAT) will also carry out large-scale pulsar timing array projects. Already existing telescopes are also being upgraded to provide more sensitive receivers covering much wider bandwidths. It is likely that the data sets from the larger telescopes will become limited by noise processes such as jitter noise on short time scales (see e.g., Shannon & Cordes 2012) and timing noise on longer time scales (e.g., Hobbs et al. 2010). However, with a careful choice of pulsars it seems likely that these telescopes would be able to provide combined data sets for at least 50 pulsars with an rms timing residual of $\sim$50 ns over a five year observing span. In Figure 4, we show the result that would be obtained if such telescopes had been observing for the last five years. The clock signal could be determined at the $\sim$ 10 ns level easily allowing the differences between TT(TAI) and TT(BIPM2013) to be identified.

Determining the pulsar time scale at this precision will lead to a long-term time standard that is competitive with the world's best atomic timescales. Combining the atomic time standards with the pulsar time standard will enable the development of a new timescale that is stable over decades. As emphasised in Hobbs et al. (2012) a pulsar-based timescale provides 1) an independent check on terrestrial time scales using astrophysical objects, 2) a timescale based on macroscopic objects of stellar mass instead

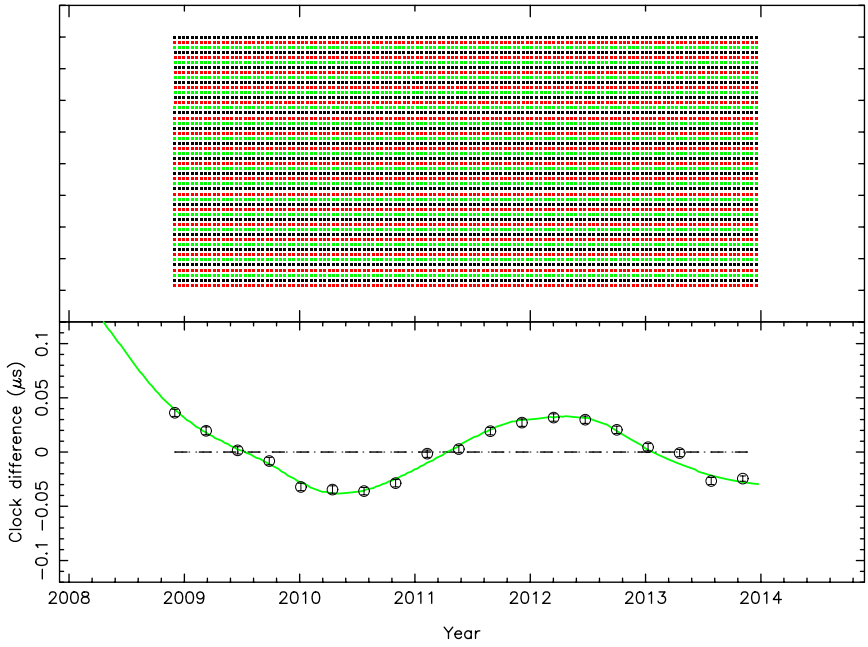

Figure 4: As in the right-hand panel of Figure 3, but using simulated data in which 50 pulsars are timed with a timing precision of 50 ns.

of atomic clocks and 3) a timescale that is continuous and will remain valid for millions of years.

Acknowledgements. The Parkes radio telescope is part of the Australia Telescope which is funded by the Commonwealth of Australia for operation as a National Facility managed by CSIRO. GH thanks for R. Manchester for comments on the manuscript.

5. REFERENCES

Guinot, B., Petit, G., 1991, "Atomic time and the rotation of pulsars", A&A, 248, 292

Hobbs, G., Lyne, A., Kramer, M., 2010, "An analysis of the timing irregularities for 366 pulsars", MNRAS, 402, 1027

Hobbs, G., et al., 2012, "Development of a pulsar-based time-scale", MNRAS, 427, 2780

Kramer, M., Champion, D., 2013, "The European Pulsar Timing Array and the Large European Array for Pulsars", CQGra, 30, 4009

Manchester, R., et al., 2013, "The International Pulsar Timing Array", CQGra, 30, 4010

McLaughlin, M., 2013, "The North American Nanohertz Observatory for Gravitational Waves", CQGra, 30, 4008

Nan, R., et al., 2011, "The Five-Hundred Aperture Spherical Radio Telescope (fast) Project", IJMPD, 20, 989

Petit, G., Tavella, P., 1996, "Pulsars and time scales", A&A, 308, 290

Rodin, A., 2008, "Optimal filters for the construction of the ensemble pulsar time", MNRAS, 387, 1583

Rodin, A., Chen, D., 2011, "Optimal filtration and a pulsar time scale", ARep, 55, 622

Shannon, R., Cordes, J., 2012, "Pulse Intensity Modulation and the Timing Stability of Millisecond Pulsars: A Case Study of PSR J1713+0747", ApJ, 761, 64

ATOMIC TIMESCALES AND PULSARS

G. PETIT

Time Department
BIPM, 92312 Sèvres France
email: gpetit@bipm.org

ABSTRACT. I review the atomic time scales generated by the BIPM, International Atomic Time TAI and the realization of Terrestrial Time TT(BIPM). TT(BIPM) is shown to be now accurate to within a few 10^{-16} in relative frequency and the performances of TAI and TT(BIPM) are compared. Millisecond pulsars have a very regular period of rotation and data from several pulsars may be used to realize an ensemble pulsar timescale. It is shown that a pulsar timescale may detect past instabilities in TAI. However TT(BIPM) is much more stable than TAI and should be used as a reference in pulsar analysis. Since the beginning of regular millisecond pulsar observations in the 1980s, primary standards and atomic time have gained one order of magnitude in accuracy every $\sim$ 12 years, and this trend should continue for some time.

1. BIPM ATOMIC TIMESCALES

Since decades, International Atomic Time TAI gets its stability from a large number of atomic clocks spread worldwide that generate the free atomic scale EAL and its accuracy from a small number of primary frequency standards (PFS) which frequency measurements are used to steer the EAL frequency: f(TAI) = f(EAL) + frequency steering, where the steering frequency is chosen so that the TAI scale unit is close to the SI second. Evolutions in the number and the type of clocks and primary standards and in the algorithms have progressively brought the 1-month stability of TAI in the low 10^{-16} and its frequency is known to the same level of accuracy.

The 1-month instability of EAL is estimated to be 3×10^{-16} in 2012-2013 following the estimation technique presented in [1]. It had been noticed for many years that EAL had a systematic drift with respect to the primary standards, a situation which prompted to a change in the prediction algorithm: Since August 2011 a quadratic model is used for frequency prediction [2] and the secular drift has disappeared. A consequence is that, since end September 2012, no new steering is needed and TAI differs from EAL by a constant rate.

Complementary to the TAI computation which is performed "in real-time" every month, the BIPM also computes every year (or whenever needed) another 'post-processed' timescale, TT(BIPM) [3], which is based on all available PFS data. Each new version TT(BIPMxx) updates and replaces the previous one, the latest official realization being TT(BIPM13), released in January 2014.

2. PERFORMANCE OF ATOMIC TIME AND PRIMARY STANDARDS BETWEEN THE 1980S AND NOW

We cover the progress of atomic clocks and time scales since the beginning of regular observations of millisecond pulsars. We distinguish two main periods which are delimited by the arrival of Cs fountains in the end of the 1990s.

In the first part, from the 1980s to end 1990s, the stability of TAI has notably improved.

- End 1980s - early 1990s: TAI is obtained from 150-170 clocks, and instability at a level above 1×10^{-14} is possible over several months to years; A major feature was then the introduction of a new type of commercial Cs clocks in 1993, providing a factor of 2-3 improvement in stability over previous clocks;
- At the end 1990s, TAI is obtained from more than 200 clocks, most of them of the new type, and its stability has improved to the level of a few parts in 10^{15} up to an averaging time of 1-2 years.

Concurrently, laboratory Cs standards (PFS) attain 1×10^{-14} accuracy at the end of the 1980s / early 1990s: PTB Cs1 (accuracy $\sim 3 \times 10^{-14}$) was operated continuously over 1978-1995; PTB Cs2 (accuracy

$\sim 1.5\times10^{-14}$) started continuous operation in 1986; NIST7 (accuracy $\sim 1\times10^{-14}$) started (discontinuous operation) in 1995. Moreover, a few other standards are also available from other time laboratories (CRL, NRC, SU). This drove the development of the post-processed time scale TT(BIPM), first computed in 1988 as TT(BIPM87) and yearly after 1992. Its accuracy (or instability over a few years) is estimated at $\sim 1 \times 10^{-14}$ in the end 1980s-early 1990s and at $\sim 3 \times 10^{-15}$ in the end 1990s.

In the second part, since the end-1990s, frequency standards have dramatically improved:

- The first Cs fountain PFS was reported to the BIPM in 1995, and regular submissions of fountain data started in 1999 with the number of reported evaluations steadily increasing over the years. Since 2004, the Consultative Committee for Time and Frequency (CCTF) [4] has regularly recommended the development and report of primary and secondary standards. Since 2009, more than four fountain evaluations are reported each month on average and this number will continue to increase as several new Cs fountains are currently under development.
- In addition a Secondary Frequency Standard (SFS) based on the 87Rb transition was reported for the first time in 2012: SYRTE-FO2(Rb) has a stated uncertainty $u_B = 3.3 \times 10^{-16}$ [5] and 30 evaluations, going back to end 2009, have been reported as of October 2013. On the other hand, the US Naval Observatory started in December 2011 to report data from 4 Rb fountains operated as clocks (not as SFS).
- Finally a very large number of frequency standards based on a number of different atomic transitions are in development. Some claim performance in the $\sim 10^{-17}$ or 10^{-18}. However they are not reporting to the BIPM yet.

On the other hand, industrial clocks have not very much changed but TAI has been based on more clocks with the years: about 200 in 2000, about 300 in 2005, more than 400 in recent years. In addition, the algorithm has been improved several times: new weighting schemes in 2001 and 2003; use of clock drift in the frequency prediction (2011); new weighting scheme (2014). The 1-month instability of TAI is estimated at $\sim 3 \times 10^{-16}$ in 2012-2013 and should somewhat improve with the recent changes. Its long-term (years) instability may reach $1 - 2 \times 10^{-15}$ until 2011, but should now remain well below 1×10^{-15} since the recent changes in the algorithm.

A new version of TT(BIPM) has been computed each year since 1999 and monthly estimates have been made available since 2009. Its accuracy / long-term instability was 6×10^{-15} in 1993-1994, reached 1×10^{-15} in the early 2000s with the arrival of Cs fountains and is now about $2 - 3 \times 10^{-16}$ since 2011.

3. LONG TERM COMPARISON OF TAI VS. TT(BIPM)

Figure 1 displays the comparison (in rate) of TAI and TT(BIPM12) over the period 1985-2013. We note the following:

- Before 1993, large instabilities are seen, of amplitude several 10^{-14}. This is probably due to the sensitivity of TAI clocks and time transfer techniques to the environment. After 1993, the stability improves with the introduction of new commercial clocks and of GPS time links.
- 1996-1998: An intentional frequency change of $\sim 2\times10^{-14}$ was introduced in TAI over the course of two years to account for the new practical realization of the second: as decided by the CCTF in 1996 [4], a frequency correction for the black-body frequency shift, which is typically of order 2×10^{-14} for Cs standards operated at room-temperature, must be applied to all frequency standards.
- 1999-2012: The behavior is more or less "random walk", but remains bounded by the steering of TAI. The instability is of order $1 - 2 \times 10^{-15}$ @ years.
- 2013 onwards (not shown): The EAL drift has been removed and no steering is needed; we still expect a bounded Random walk behavior for TAI-TT(BIPM), but with a much reduced amplitude, well below 1×10^{-15}.

As a summary, it is natural that, over any period, TAI is not as accurate / stable as TT(BIPM). Therefore the most recent realization of TT(BIPM) should be used for any analysis that is post-processed and demands stability or accuracy over long periods, as is the case for pulsar timing.

4. WHAT PULSARS MAY SAY ON TAI / TT(BIPM)

As indicated above, the difference in rate between TAI and TT(BIPM) over nearly three decades shows quite significant features, of amplitude much larger than the uncertainty in the frequency of TT(BIPM)

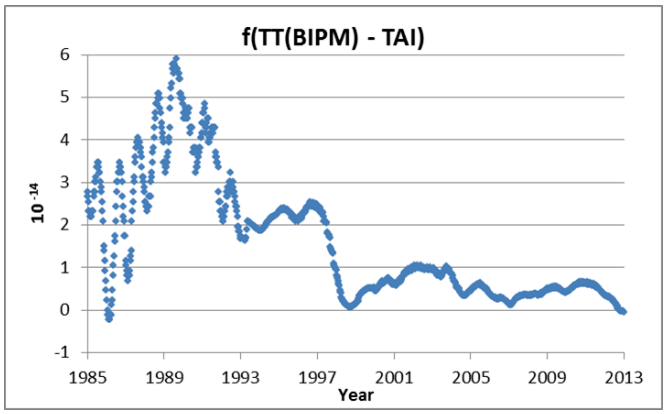

Figure 1: Difference in rate of TT(BIPM) and TAI; see text for details.

at the same epoch. Indeed, at any time, we estimate the uncertainty of TT(BIPM) to be the best achievable for an atomic timescale. If the rotation rate of a pulsar is more regular that TAI, we anticipate that an analysis of pulsar timing data that encompasses a long period could discriminate between TAI and TT(BIPM). The evidence would be that the pulsar timing data fit better a model of the pulsar parameters when TT(BIPM) is used as a reference than when TAI is the reference. Because programs of pulsar observation generally cannot cover such long periods without interruptions or other events that perturb the continuity, it has been proposed to generate ensemble pulsar time [6, 7]. Similarly to what is done for atomic time, an ensemble pulsar time ensures continuity and provides a better performance than any single participating pulsar.

Recently, Hobbs et al. (2012) [8] have used about 18 years of observations of 19 pulsars to solve for a "pulsar-based timescale" that they name TT(PPTA11). When using TAI as a reference, they show (see Figure 2) that TT(PPTA11) - TAI has very significant features and that these features are similar to those seen in TT(BIPM) - TAI after a quadratic adjustment. This is an evidence that TT(PPTA11) can reveal the main long-term instability in TAI over the studied period, which is due to the 1996-1998 TAI frequency change. As can be seen in Figure 2 and as concluded by Hobbs et al. (2012), there

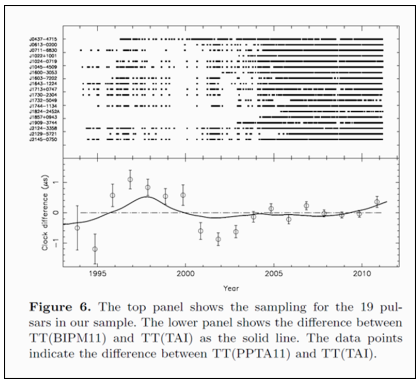

Figure 6. The top panel shows the sampling for the 19 pulsars in our sample. The lower panel shows the difference between TT(BIPM11) and TT(TAI) as the solid line. The data points indicate the difference between TT(PPTA11) and TT(TAI).

Figure 2: Reproduced from Figure 6 of Hobbs et al. (2012); cf. Hobbs 2014, this Volume page 117

still remain "marginal discrepancies between 1995 and 2003" between TT(PPTA11) and TT(BIPM11). These correspond in Figure 2 to the difference between the data points and the solid line.

To allow better comparison between TT(PPTA11), available as time data once a year, and TT(BIPM), available as frequency data, the data points for TT(PPTA11)-TAI in Figure 2 have been differentiated and the resulting yearly frequency points are reported in Figure 3, with the corresponding uncertainties obtained from Figure 2. One can see that the yearly points for TT(PPTA11) indeed show discrepancies with TT(BIPM11) but the values of the discrepancies as well as the uncertainties on f(TT(PPTA11)) are much larger than the estimated uncertainties of TT(BIPM11). Because there are correlations in both

series (the yearly TT(PPTA11) points and the monthly TT(BIPM11) points), it is not obvious to draw firm conclusions. Nevertheless there is about one order of magnitude difference in the uncertainties of the two series so the discrepancies between TT(PPTA11) and TT(BIPM11) are more likely to be due to TT(PPTA11) than to TT(BIPM11). If the uncertainty in the pulsar based time scale can be reduced, e.g. by solving for fewer points for the pulsar time scale or with more data from more stable and continuously observed pulsars, a similar analysis could provide uncertainties in the pulsar-based time scale quite close to the TT(BIPM) uncertainties over the 1990s. This would be a valuable source of information on atomic time before the Cs fountains.

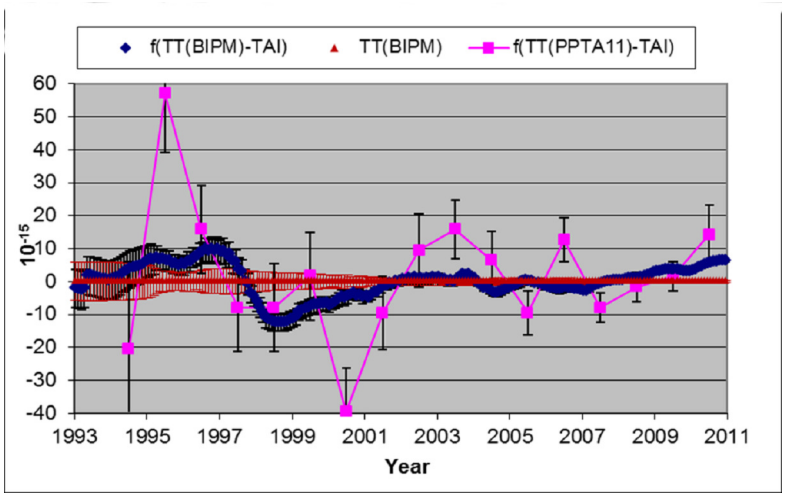

Figure 3: Frequency of TT(BIPM)-TAI (linear removed, dark blue) and estimated frequency uncertainty of TT(BIPM) (red), shown as monthly values. The frequency of TT(PPTA11)-TAI obtained by differencing the data points in Figure 2, is shown as yearly values (magenta).

5. CONCLUSIONS

Atomic timescales have gained one order of magnitude in long-term stability and accuracy every $\sim$ 12 years, and this trend should continue for some time. Present realizations of a pulsar-based timescale show frequency uncertainties that are significantly higher than those of atomic timescales. Future pulsar observations may overcome most limitations of the present pulsar data sets however it is not clear if these improvements will match those of the atomic timescales. Nevertheless a pulsar timescale may be used as a flywheel to transfer the accuracy of atomic time between epochs. In all cases, it is recommended that the latest realization of TT(BIPM) be used as a time reference for pulsar analysis.

6. REFERENCES

[1] Petit G 2007 The long-term stability of EAL and TAI (revisited) Proc. Joint Meeting of the European Time and Frequency Forum (EFTF) and the IEEE International Frequency Control Symposium (IEEE-FCS), Geneva(Switzerland) 391-394.

[2] Panfilo G, Harmegnies A, Tisserand L 2012 A new prediction algorithm for the generation of International Atomic Time Metrologia 49(1) 49-56.

[3] Petit G 2003 A new realization of Terrestrial Time Proc. 35th Precise Time and Time Interval (PTTI) Meeting (San Diego, CA) 307-316.

[4] Consultative Committee for Time and Frequency (CCTF): Reports of the CCTF meetings may be found at http://www.bipm.org/en/committees/cc/cctf/publications_cc.html

[5] Guéna, J. Abgrall, M., Rovera, D., Laurent, P., Chupin, B., Lours, M., Santarelli, G., Rosenbusch, P., Tobar, M.E., Li, R.X., Gibble, K., Clairon, A., Bize, S. 2012 Progress in Atomic Fountains at LNE-SYRTE. IEEE Trans. UFFC, 59, 391-410.

[6] Petit G., Tavella P., 1996, Pulsars and time scales, AA, 308, 290

[7] Rodin A.E., 2008, Optimal filters for the construction of the ensemble pulsar time, MNRAS, 387, 1583

[8] Hobbs, G., et al., 2012, Development of a pulsar-based time-scale, MNRAS, 427, 2780

TIME AND FREQUENCY COMPARISONS WITH OPTICAL FIBER LINKS

P.-E. POTTIE[1], O. LOPEZ[2], A. KANJ[1], D. ROVERA[1], J. ACHKAR[1], C. CHARDONNET[2]
A. AMY-KLEIN[2], and G. SANTARELLI[3]
[1] LNE-SYRTE, Observatoire de Paris, CNRS, UMPC
Observatoire de Paris, 61 Avenue de l'Observatoire, 75014 Paris, France
[2] Laboratoire de Physique des Lasers
Université Paris 13, Sorbonne Paris Cité, CNRS, 99 Avenue Jean-Baptiste Clément, 93430 Villetaneuse, France
[3] Laboratoire Photonique, Numérique et Nanosciences,
Université de Bordeaux 1, Institut d'Optique and CNRS, 351 cours de la Libération, 33405 Talence, France
e-mail: paul-eric.pottie@obspm.fr

ABSTRACT. For the last 5 years, ultra-stable optical fiber links have been successfully developed in order to enable ultra-stable and accurate frequency transfer between the best modern atomic clocks whose accuracy are below 10^{-15}. Optical fiber links exhibit fractional frequency stability in the range of 10^{-18} after only 3 h of measurement and frequency accuracy of a few 10^{-19}, with a range of a few 100 km up to 1800 km [12]. Recently, time transfer through optical fiber link was demonstrated, simultaneously with frequency transfer by the LPL-SYRTE group. Time deviation of the time transfer is below 20 ps, and the accuracy of the link is below 250 ps. These results overcome the capabilities of satellite based comparisons and could play a key role for geodesy, high-resolution radio-astronomy, and modern particle physics.

1. INTRODUCTION

Frequency metrology community witnesses for 20 years the impressive improvements of frequency standards, their accuracy being dropped down by 2 order of magnitude within 2 decades [1,2]. The stability and uncertainty of primary frequency standard are even surpassed by the optical lattice clocks, where the clock frequency does not belong anymore to the microwave domain but to the optical domain. Indeed, given the same interrogation time, and neglecting the noise of the local oscillator, the ratio of the line-width of the atomic fringes to the clock laser frequency is much smaller. These optical clocks demonstrate frequency stability as low as a few 10^{-16} at 1 second integration time. Systematic effects are much better controlled and the uncertainty budgets are in the low 10^{-17} range [3,4,5]. Their performances are even more interesting that they are operated with a variety of atom species, that make their comparisons a stringent test of the temporal variation of fundamental constants [6]. Moreover the gravitational shift is about 10^{-16}/m, so that an accurate knowledge of the geodetic potential is required for accurate remote comparisons of optical lattice clock. As prerequisite to these exciting prospects is the ability to compare 2 or more distant clocks at this level of precision.

In this paper we will briefly describe the technical limitations of coherent link and the state-of-the art frequency transfer abilities. We will present the REFIMEVE+ network for frequency standard dissemination in France and its connection at the borders. In a second part, a novel method to simultaneously disseminate an ultra-stable optical frequency and accurate timing over a public telecommunication network will be shown.

2. FREQUENCY TRANSFER

Actually clocks are compared with satellite based methods using a carrier in the microwave domain, as Global Navigation Satellite Systems (GNSS) and 2-way satellite time and frequency transfer (TWSTFT). The resolution of such means of comparisons is about 10^{-11} at one second and about 10^{-15} at 1 day integration time [7,8]. In order to reach better stability and uncertainty, one idea is to increase the carrier

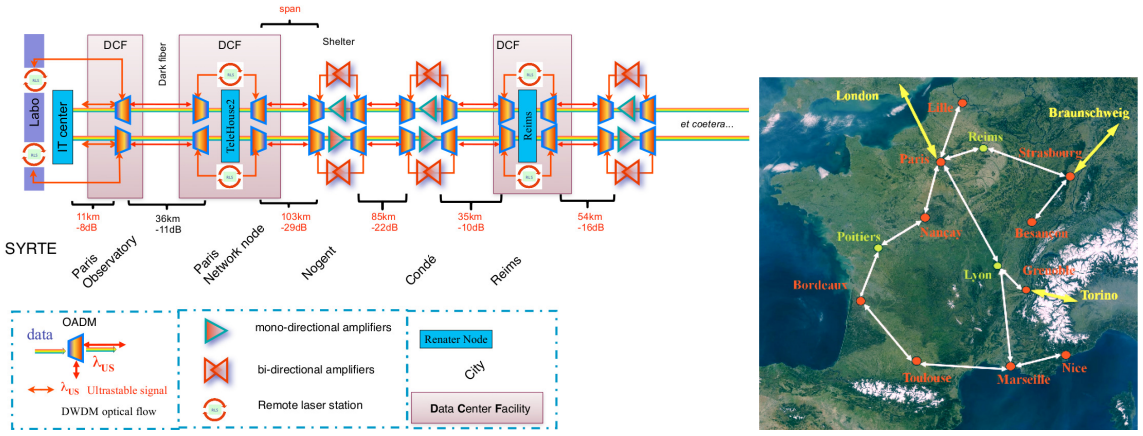

Figure 1: Left : Topology of coherent long haul link with parallel data traffic. OADM are inserted to bypass the uni-directionnal amplifiers. Bi-directional amplifiers are used instead of. After a number of spans, the metrological signal is regenerated to keep a large enough bandwidth of correction and to clean up the optical signal to noise ratio. Right : Map of the spots connected by the REFIMEVE+ project. The green and red dots corresponds to the places where at least 2 remote laser stations will be set up. The users of REFIMEVE will be connected to the red dots. Bi-directionnal amplifiers are omitted. The yellow arrows show the cross boarder links envisioned to connect to Germany, Italy, and UK.

frequency up to the optical domain, using an optical fiber as the medium of propagation.

The best optical frequency transfer is achieved so far by injecting a low phase noise laser into a single mode fiber. The frequency signal consists then of the frequency of the carrier laser. The fiber propagation noise is detected by an optical interferometer comparing the phase of the local laser with the one of the light that travelled forth and back through the same fiber [9]. In the case of fully bi-directional operation, one assumes that the accumulated phase noise is equal forth and back, and one can actively compensate the fiber noise.

There is mainly 3 technical challenges to overcome. First comes the attenuation, about 0.25 dB/km in average. This is partially compensated by the use of bi-directional amplifiers. As they are not isolated from back and stray reflections, the experimental gain must be set below about 15 dB to prevent it from self oscillations. With typical span length of 100 km, the losses are most often not compensated. As the input power must be below 5 mW, in order to avoid stimulated Brillouin scattering, the detected power in the interferometer is low (as low as 1 nW for the link described in [10]). In addition the detected noise power is very high, due to spontaneous emission, scattering processes and stray reflections. The necessary high signal to noise ratio needed by the phase lock loops is obtained by narrow filters and delicate signal treatment. The second technical challenge is to use a laser with a coherent length longer than the double length of the link. Typically a line width equal to 1 kHz is just enough for a 25 km long link only. The third and most severe limitation comes from the propagation delay and the finite velocity of light in the medium. Typically a 1000 km link will have a round trip delay of 5 ms. This limits the bandwidth of the correction to 25 Hz, which means that the acoustic noise is left almost uncompressed. It determines also the residual noise power at Fourier frequency lower than the cut off frequency [11]. In order to overcome all these limitations, we developed remote laser stations, that are able to transmit the metrological signal in a cascaded way (see figure 1).

The last, but not least, difficulty is actually to access the fiber. The rental cost of a fiber is quite prohibitive for most of the research institute. The alternative strategy we developed is to benefit from the existing telecommunication networks to broadcast the metrological signal. We use Optical Add-Drop Multiplexers (OADMs) to extract and insert the science signal into the telecommunication fibers. The price to pay is to use techniques compatible with data traffic, and additional losses penalty that arise from the insertion losses of the OADMs. Fiber Brillouin amplifiers as such used in Germany are prohibited in such networks for instance [12]. Despite these technical challenges, we successfully transfer an optical frequency over telecommunication network in parallel with data traffic over a link made of 5 spans with a total length of 540 km [10]. In this long haul link, the total end-to-end attenuation is in excess of 165 dB. With the help of six bidirectional EDFAs and a total amplification of about 100 dB, the net optical

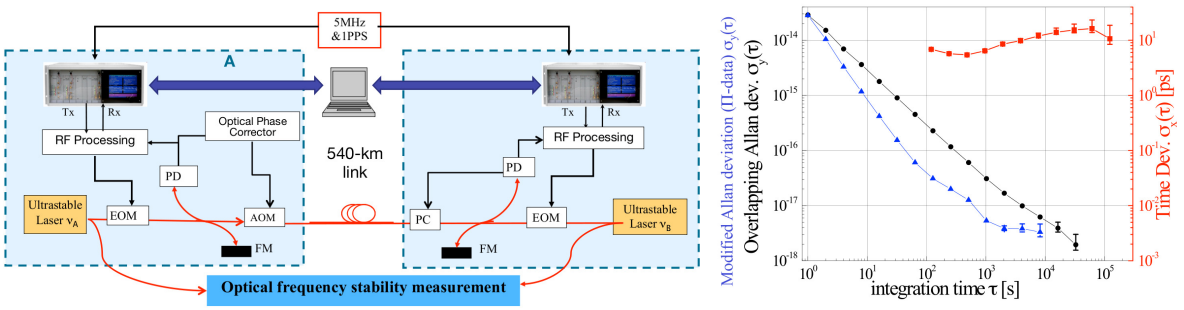

Figure 2: Left : Sketch of the experimental set up. Right : Relative frequency stability and time stability, represented in overlapping, modified and time deviation recorded versus 30 000 s integration time, for a simultaneous time and frequency transfer.

losses exceed 65 dB. Many technical details are given in [10]. We recorded a relative frequency stability of 4×10^{-14} at one second integration time, scaling down as τ^{-1} down to 10^{-18} after 40,000 s integration time. This excellent results give birth to the the REFIMEVE+ project, aiming at broadcasting the optical reference elaborated at SYRTE to 20 laboratories in France on the RENATER network, thanks to 85 bi-directional amplifiers and 48 remote laser stations (see fig. 1). The technologies are now being transferred to an industrial partner, IDIL [14]. The metrological network is expected to be built in 2016.

3. TIME TRANSFER

The upcoming challenge is to transfer not only frequency but also time. Time transfer and accurate timing is also important for numerous applications, from modern particle physics to communication network's synchronization. Long distance accurate time dissemination is usually based on GNSS signals, or geostationary telecommunication satellites, with an accuracy about 1 ns, and time deviation of few 100th of ps after one day averaging at best [7,8,13].

We introduced recently a novel method to transfer time simultaneously with frequency. We followed the general approach of satellite 2-way comparison that we transposed as phase modulation of an optical carrier [15]. The experimental set up is sketch in Fig. 2. A detailed description is reported in [17]. The method consists of relating the phase of a pseudorandom noise modulation carried on a radio frequency intermediate carrier signal (50-80 MHz) to the one-pulse-per-second (1PPS) and a 10 MHz reference signal from a common clock. The SATRE modem correlates the received signal and the local replica, and measures the time of arrival of the received signal with respect to the local clock. The time of arrival of both modems are afterwards collected, and the differential time delay is computed. At each link end the time signal is encoded on the laser as phase modulation with a fiber pigtailed electro optical modulator. A low modulation depth of 1% is used in order to keep the frequency transfer without degradation. The time signals are detected by an optical heterodyne beat-note of the local laser with the incoming signal. After several stage of delicate filtering and frequency mixing (parasitic signals due to stray reflections are 40 dB larger than the useful signals), the time signals are processed by the modems and sent to the computer. The frequency transfer stability and the timing stability/jitter are simultaneously measured and are plotted in Fig. 2. The frequency stability of the link reaches a resolution of 10^{-18} at 30 000 s averaging time, which is almost identical to the one reported in [10]. The timing stability shows a noise of less than 20 ps for all measurement time. We perform in addition a preliminary calibration campaign, in order to estimate the uncertainty of the time link, following standard calibration procedure in time and frequency metrology [16]. We vary the length of the link by setting "shortcuts" in the accessible places along the long-haul optical link, while keeping the overall link attenuation constant within ±2 dB. We vary therefore the link length from 10 m to 94 km, 400 km to the total of 540 km. The measured differential time delay variation is smaller than 50 ps. The sensitivity to power fluctuation was checked by changing the power of the signals from the optical detection up to the modem input. We found a coefficient below 15 ps/dB. Fiber chromatic dispersion is also very low, as the signals are quite narrow, and was estimated below 25 ps. Polarization mode dispersion plays also a minor role with contribution to the error budget below 20 ps. As both time measurements are collocated in this experiment the Sagnac

effect is zero. The preliminary conservative accuracy budget of 250 ps is actually mainly dominated by scarce phase jumps of about 50-80 ps that we believe to be due to technical imperfections. The system is quite robust and operates over many days with time variations below the above stated accuracy.

4. CONCLUSIONS AND OUTLOOK

We have presented the REFIMEVE+ metrological network that aims at transferring optical frequency standard at the French scale. We have shown that simultaneous time transfer was also possible on telecommunication network with an excellent level of stability, competitive with the satellite-based methods, and much better at short integration time. The accuracy of the time transfer is now limited by our calibration capability of all instrumental delays. In a near future, we hope to perform comparisons of means of comparison, in order to check the consistency of the methods and the stability of the calibration campaigns. These tests could also be used to measure Sagnac effect, and probe general relativity on giant Sagnac loops.

5. REFERENCES

[1] J. Guéna, *et al.*, "Demonstration of a Dual Alkali Rb/Cs Atomic Fountain Clock" IEEE Trans. on UFFC 57, 647 (2010)

[2] K. Dorenwendt, B. Fischer andT. Heindorff , "The PTB's Primary Time and Frequency Standards - Performance and Uncertainty" Physica Scripta. 41, 712-716 (1990)

[3] R. Le Targat *et al.*, "Experimental realization of an optical second with strontium lattice clocks" Nat. Commun 4, 2109 (2013)

[4] S. Falke *et al.*, "The 87Sr optical frequency standard at PTB", Metrologia 48, 5 (2011), 399

[5] B. J. Bloom *et al.*, "An optical lattice clock with accuracy and stability at the 10^{-18} level", Nature 506 71-75 (2014)

[6] V. V. Flambaum and E. V. Shuryak, "Dependence of hadronic properties on quark masses and constraints on their cosmological variation" Phys. Rev. D 67, 083507 (2003)

[7] D. Piester *et al.*, "Time transfer with nanosecond accuracy for the realization of International Atomic Time", Metrologia, 45,185, (2008)

[8] F. Nakagawa *et al.*, "Carrier phase TWSTFT experiments using the ETS-VIII satellite", Metrologia 50, (2013), 200-207

[9] L-S Ma *et al.*, " Delivering the same optical frequency at two places: accurate cancellation of phase noise introduced by an optical fiber or other time-varying path", Opt. Lett., 19, 21(1994), 1777-1779

[10] O. Lopez *et al.*, "Ultra-stable long distance optical frequency distribution using the Internet fiber network", Opt. Express 20, 23518 (2012)

[11] Newburry *et al.*, "Coherent transfer of an optical carrier over 251 km", Opt. Lett., 32, 21, (2007) 3056-3058

[12] S. Droste *et al.*, "Optical-frequency transfer over a single-span 1840 km fiber link.", Phys Rev Lett. 111(11) (2013)

[13] D. Piester, *et al.*, "Remote atomic clock synchronization via satellites and optical fibers", Adv. Radio Sci., 9, 1-7, doi:10.5194/ars-9-1-2011, (2011).

[14] IDIL Fibres optiques, 21 rue Louis de Broglie, 22300 Lannion, France

[15] D. W. Hanson, "Fundamentals of Two-Way Time Transfer by Satellite", 43rd Annual Frequency Control Symposium, pp. 174-178, 1989;

[16] A. Bauch, D. Piester, M. Fujieda, and W. Lewandowski, "Directive for operational use and data handling in two-way satellite time and frequency transfer (TWSTFT)", Rapport BIPM2011/01 (2011)

[17] O. Lopez *et al.*, "Simultaneous remote transfer of accurate timing and optical frequency over a public fiber network", Appl. Phys. B, **1** 10 (2013) 3-6

SOME ASTROMETRIC DISCUSSIONS ON PULSAR PARAMETERS BY TIMING AND VLBI

L. GUO[1], L. LI[1,2], M. ZHAO[1]
[1] Shanghai Astronomical Observatory, Chinese Academy of Sciences
[2] University of Chinese Academy of Sciences
80 Nandan Road, Shanghai 200030, China
e-mail:lguo@shao.ac.cn

ABSTRACT. The errors in solar system ephemeris are one of the systematic errors for pulsar timing. We will discuss how the errors in the ephemeris affect the pulsar parameters. The quasi-long period variations in ephemeris errors can accurately be determined by simulations. MSPs are the powerful tools to link ICRF and dynamical planetary reference frame at mas-level, both with timing and VLBI observations with the same accuracy. The primary results we present show the limited link precision due to so few common MSPs by two methods. We also obtained the position parameter of MSP J1939+2134 based on the Chinese VLBI Network. And we plan to carry on the pulsar timing observations with Shanghai 65m radio antenna by the end of this year. It will contribute to establish the pulsar catalogue more precisely in China and to link the ICRF and dynamical planetary frames with better accuracy.

1. INTRODUCTION

The precision of pulsar timing of arrival (TOAs) can arrive at scores of nanosecond, and the timing models used in TEMPO2 package are accurate in its description of predictable systematic timing effects to better than 1 ns at present. Besides the pulsar timing measurement errors, the largest remaining sources of potential errors also include the interstellar scattering, solar system ephemeris errors, atomic clock instability and gravitational waves(Edwards, Hobbs & Manchester 2006). The latter 3 items are the systematic errors. We will discuss the relation between the ephemeris errors and the pulsar parameters in section 2.

The astrometric parameters of pulsars can be obtained both by timing and VLBI phase reference methods. The millisecond pulsars (MSPs) are more stable than canonical pulsars (CP) and the TOA precisions of MSPs are also much better. The MSPs timing gives the positions in the Earth reference frame at milli-arcsecond (mas) level. And the VLBI method also gets the positions close to mas level, which are described in ICRF frame. When we observe the MSPs both with two techniques, we can get the Earth (dynamical) reference frame tie to the ICRF frame. The primary frame tie results based on the published pulsar parameters are in section 3.

In addition, Shanghai 65 m telescope was successfully put into use in Chinese lunar project this year and the pulsar timing is one of the main projects. Besides, the Chinese VLBI Network (CVN) has been developed consisting of a correlation center in Shanghai and another four antennas, including two 25 m telescopes at Shanghai(SH) and Urumqi(UR), 40 m at Kunming(KM) and 50 m at Beijing(BJ)(Li, Guo & Zhang 2007). We observed MSP J1939+2134 with CVN, and the results are in section 4. At last section 5 concludes all of our results.

2. EPHEMERIS AND PULSAR PARAMETERS

The pulsar parameters are referenced to the solar system barycenter (SSB). In high-precision pulsar timing, TOAs of pulses at an observatory are converted to timing of barycenter (TOBs) based on the solar system ephemeris. Errors in the ephemeris could cause the systematic variations in observed TOAs residuals(Champion et al. 2010). The observed TOBs associate with the TOBs at reference time t_0 by pulsar period P_0 and period derivative P_1 if we neglect the variations caused by the second derivative of pulsar period, which is expressed by $T^c_{ob} = T_0 + nP_0 + \frac{1}{2}n^2P_1$. Where n is the n^{th} pulse accounted from the pulse at t_0.

Supported by the National Natural Science Foundation of China (Grant Nos. 11003039), the Natural Science Foundation of Shanghai,China(Grant No.10ZR1435700)

At the same time, compared with the real SSB, SSB in the ephemeris has different variations, shown by equation 1. where $\Delta\vec{r}_{ssb}(n)$ on the left side of the means the total differences between two SSBs, and $\delta\vec{r}_{ssb}(n)$, $\delta\dot{\vec{r}}_{ssb}(n)$, $\delta\ddot{\vec{r}}_{ssb}(n)$ respectively stand for the quasi-long period, time derivatives and second derivatives of the differences. Compared equation 1 with the above expression of T^c_{ob}, $\delta\dot{\vec{r}}_{ssb}(n)$ and $\delta\ddot{\vec{r}}_{ssb}(n)$ can't be separated from P_0 and P_1. However, the quasi-long period term in the form of $\delta = \frac{1}{c}(\vec{r}\cdot\delta\vec{r}_{ssb})+\sigma$, will remain in the residuals, which could lead to a predominantly sinusoidal variation with quasi-long period and phase associated with planet's orbital motion about the Sun. If we neglect physical errors in timing residuals and σ only consists of white noises, the period variations can be solved by quasi-simultaneously timing data of about more than 6 uniform distributed MSPs. It is simulated based on TEMPO2 package. In the simulation, SSB of DE421 ephemeris can be taken as the real SSB, while observed TOA data of the MSPs, including MSP J0437-4715, J0613-0200, J1022+1001, J1713+0437, J1744-1134, J1909-3744, J1939+2134, with interval of two weeks and 32 years time span are produced with ephemeris DE200. The TOAs errors are several μs based on the actual observation accuracy. The simulation result is shown by figure 1. The position offsets are respectively on X- Y- Z- axis from the top to the bottom. The red line is the real differences between these two ephemerides, while the blue one is the simulation results. Such quasi-long period term between two ephemerides is well determined. The annual differences between ephemerides are absorbed by pulsar positions, which should be one type of red noises in TOAs residuals at observation data reductions.

$$\Delta\vec{r}_{ssb}(n) = \delta\vec{r}_{ssb}(n) + \Delta\dot{\vec{r}}_{ssb}(n)P_0 + \Delta\ddot{\vec{r}}_{ssb}(n)n^2P_1 \quad (1)$$

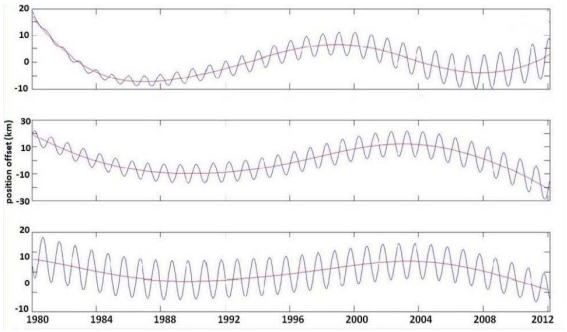

Figure 1: Comparison of the deduced differences by pulsar timing simulations and the real differences between the ephemerides DE421 and DE200

The ephemeris errors determined by observation timing data will be presented in our near future work. The evaluated parameters are usually determined after fitting a polynomial to 'whiten' the residuals of individual pulsar(Champion et al. 2010; Hobbs, Coles & Manchester 2012). Pulsar timing is the potential method to improve the precision of ephemeris SSB with the improvement of observation accuracy and longer observation span, while other spacecraft measurements are only sensitive to the individual planet.

3. REFERENCES FRAME TIE BASED ON MSPs

The link between the planet dynamical reference frame (DRF) and the radio source frame is usually derived from spacecraft delta VLBI observations. The pulsar parameters by timing are deduced referenced to SSB with the Earth ephemeris, which embodies the DRF, while the positions by VLBI is in the ICRF. By comparison with the pulsar positions deduced by VLBI observation, the Earth ephemeris is aligned to the radio frame (or ICRF), which is the unique method to directly link these two reference frames.

Considering timing accuracy of MSPs is far better than that of canonical pulsars, we select five MSPs, J0437-4715, J0737-3039, J1713+0747, J1939+2134, J2145-0750, both with timing and VLBI with the accuracy generally arrives at 1 mas. The astrometric parameters of the MSPs are listed by table 1. The 'T' and 'V' in the first column of table 1 means the positions by timing and VLBI. The right ascension and declination are briefly listed in second and arc-second. Firstly the pulsar positions by two methods are deduced to the identical epoch based on parallax and proper motion (Brisken 2001). The MSPs positions at the same epoch by two methods are respectively $\vec{X}_{DE405}$ and $\vec{X}_{ICRF}$. The relation between them is shown by $\vec{X}_{ICRF} = A^{ICRF}_{DE405}\vec{X}_{DE405}$, where A^{ICRF}_{DE405} is the transfer matrix from the Earth frame to

ICRF(Sekido 2001). In table 2, 5MSPs, 4MSPs and 3MPSs respectively means the transfer results from all five pulsars, without J1713+0747 and without J1713+0747 and J1939+2134. The position difference of J1713+0747 is larger than 20 mas in right ascension, which causes significant differences of results. The parameters of J1939+2134 were determined more earlier with limited precision. From the results shown by table 2, the frame tie results change a lot with the MSPs number due to so few common MSPs both observed by VLBI and timing. However, it is still prospective because a large VLBA pulsar astrometry program is under way. A sample of 60 pulsars will be observed this year as scheduled, and a program of 200 pulsars would be expanded for the next step(Deller et al. 2011), which will greatly expand the common MSPs sample and improve the reference frame link accuracy.

Table 1 MSPs astrometric parameters by timing and VLBI

MSP	MJD (days)	α (ss)	δ (ss)	μ_α (mas/yr)	μ_δ (mas/yr)	PX (mas)	Ref
T1	52005	15.8147635(3)	08.624170(3)	121.453(1)	-71.457(1)	6.65	[6]
V1	54100	15.883250(3)	09.031863(3.7)	121.679(5)	-71.820(9)	6.396(54)	[7]
T2	52870	51.24795(2)	40.7247(6)	-	-	-	[8]
V2	54100	51.2484119(26)	40.714310(99)	-3.82(62)	2.13(23)	0.87(14)	[7]
T3	54312	49.532628(2)	37.50165(6)	4.924(10)	-3.85(2)	0.94(10)	[8]
V3	52275	49.5306(1)	37.519(2)	4.75(10)	-3.67(15)	0.95(5)	[7]
V4	47892	38.56120(18)	59.1316(24)	1.4	-0.6	-	[9]
T4	52601	38.561286(7)	59.12913(15)	0.13(3)	-0.25(5)	0.4(4)	[10]
V5	54100	50.461901(98)	18.462388(558)	-15.43(207)	-7.67(81)	-	[8]
T5	53040	50.46412(3)	18.4399(14)	-9.66(15)	-8.9(4)	1.6(5)	[7]

Table 2 Rotation angles between the Earth frame and ICRF

	θ_x(mas)	θ_y(mas)	θ_z(mas)
DE405→ICRF(5MSPs)	-0.2±0.5	27.2±1.4	-23.3±1.6
DE405→ICRF(4MSPs)	-8.9±1.6	4.1±4.2	3.4±4.9
DE405→ICRF(3MSPs)	-8.4±0.5	5.4±0.3	1.9±0.2

4. MSP OBSERVATIONS WITH CVN

CVN has been put into work since Chang'E-1 lunar project in 2007(Li, Guo & Zhang 2007). The first successful CVN phase referencing observations of pulsar B0329+54 was in 2008(Guo et al. 2010). With the improvement of hardware and software of CVN, the network sensitivity has also been improved. We also pursue the observations of weaker MSPs. The MSP J1939+2134 is one of the best candidates of frame link and in deep space auto-navigation application, whose flux is 5 mJy at S band. And the parallax parameter by VLBI was published in 1995, whose precision was limited and its proper motion parameter is determined by timing. However, the red noise in the TOAresiduals reach scores of macro-second(Hobbs, Coles & Manchester 2012). Therefore it is the first MSP target with CVN.

The experiment of MSP J1939+2134 with CVN 3 antennas, SH 25 m, UR 25 m and KM 40 m, was on April 8, 2012. The calibrator in our observation is J1935+2031 with 1.5^o separation from the pulsar, whose position precision is 0.1 mas. The CVN observation mode is fast-switching between the pulsar and calibrator with a cycle time of 180 s on pulsar and 80 s on calibrator and the total record rate reaches 1024 Mbps. We used the Distributed FX (DiFX) software to correlate the data and AIPS to reduce the data (Deller et al. 2011; Deller, 2009). In the data reduction, we have considered updating the EOP parameters, correction of clock errors and clock rates, ionospheric errors by GPS data, the phase and delay corrections and so on. At last, we used the AIPS task 'JMFIT' to get the pulsar position shown by figure 2. Table 3 shows the best-fit position of the pulsar with CVN and the timing position reduced from parameters (Verbiest et al. 2009) at the observations epoch. From the comparison, the offsets between them are only 1.5 mas and 2.3 mas in right ascension and declination. And such little difference may be caused by the observation errors or link errors between ICRF and Earth ephemeris. To get further astrometric parameters of MSP J1939+2134, we will arrange another 4-5 observations with CVN next year. Besides J1939+2134, we will plan to observe more MSP at L, S and C band with 65 m antenna in the following year, which will contribute to improving the accuracy of the frame tie and the ephemeris, detecting the gravitational waves and so on.

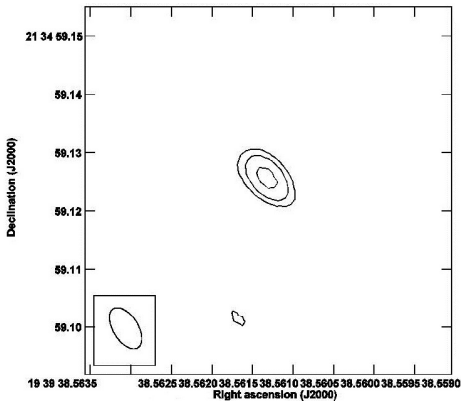

Figure 2: Image of MSP J1939+2134 observed with CVN at 2.2 GHz.

Table 3 The comparison of position parameters of MSP J1939+2134

	$\alpha(J2000.0)$	$\delta(J2000.0)$	$Obsfreq$
	h m s	^{o} ' "	GHz
1^a	19 39 38.5613	21 34 59.1267	2.2
2^b	19 39 38.5614	21 34 59.1244	1.4

^{ab} Results are respectively reduced from CVN in S band and timing observations by Pakes in L band.

5. CONCLUSION

The quasi-long period term of ephemeris errors can be deduced based on the simulations. But the annual errors of ephemeris are absorbed into pulsar position parameters. In addition, it is still difficult to get precise frame tie between ICRF and the earth ephemeris based on MSPs by timing and VLBI. The main cause is so few common MSP both by VLBI and timing. But it is promising in the near future with more results from the VLBA PI pulsar project and CVN observations.

At the same time, MSP J1939+2134 was successfully observed with CVN last year. To obtain the proper motion and parallax parameters more precisely, more observations will be carried on in 2014. Besides the CVN pulsar observation plan, Shanghai 65 m antenna will also concentrate on scores of MSPs timing topics. The results in the paper are primary, and they will be improved with more precise observations in the future.

6. REFERENCES

Edwards R. T., Hobbs G. B., Manchester R. N., 2006, TEMPO2, a new pulsar timing packages- II. The timing model and precision estimates, MNRAS, 372, 1549.

Deller A. T., et al, 2011, PSRπ: A large VLBA pulsar astrometry program, arXiv:1110.1979v2.

Li J. L., Guo L., Zhang B. 2007, The Chinese VLBI network and its astrometric role, IAU Symposium 248, 182-183.

Champion D.J., et al, 2010, Measuring the Mass of Solar System Planets Using Pulsar Timing, ApJL, 720, 201.

Hobbs G., Coles W., Manchester R. N. et al, 2012, Development of a pulsar-based timescale, MNRAS, 427,2783.

Verbiest, J. P. W., et al, 2008, Precision Timing of PSR J0437-4715: An Accurate Pulsar Distance, a High Pulsar Mass, and a Limit on the Variation of Newton's Gravitational Constant, ApJ, 679, 675.

Deller, A. T., et al, 2009, Precision Southern Hemisphere VLBI Pulsar Astrometry. II. Measurement of Seven Parallaxes, ApJ, 701, 1243.

Burgay, M. et al, 2006,The Double Pulsar System J0737-3039, MSAIS, 9, 345.

Dewey, R. J., et al, 1996, VLBI Astrometry of the Millisecond Pulsar B1937+21, AJ, 111, 315.

Bartel, N., et al, 1996, Frame-tie via Millisecond Pulsar VLBI, AJ, 112, 1690.

Sekido, M., 2001, Pulsar Astrometry by VLBI, PHD Thesis, Pushchino Radio Astronomy Observatory of the Lebedev Physical Institute.

Brisken W.F., 2001, High-precision pulsar astrometry using the VLA and VLBA interferometers, PHD Thesis. New Jersey: Princeton University.

Guo L., Zheng X. W., Zhang B., et al, 2010, New Determination of the position of the Pulsar B0329+54 with Chinese VLBI Network, Sci China Physc Mech Astro, 53, 8, 1560.

Verbiest J. P. W., Bailes M., Coles W. A., et al, 2009, Timing stability of millisecond pulsars and prospects for gravitational-wave detection, MNRAS, 400, 957.

REALIZATION OF THE NEW UTC(OP) BASED ON LNE-SYRTE ATOMIC FOUNTAINS

B. CHUPIN, S. BIZE, J. GUÉNA, Ph. LAURENT, P. ROSENBUSH, P. UHRICH, M. ABGRALL and G.D. ROVERA
LNE-SYRTE, Observatoire de Paris, CNRS, UPMC, France
e-mail: baptiste.chupin@obspm.fr

1. INTRODUCTION

For many years, UTC(OP), the real-time approximation of UTC built in LNE-SYRTE, Observatoire de Paris (OP), Paris, France, had been based on industrial Cesium (Cs) standards [1]. Since October 2012, new algorithm for the generation of UTC(OP) has been put in operation. It is based on the steering of a H-maser signal on the LNE-SYRTE Primary Frequency Standards. The current OP atomic fountain ensemble [2] comprises a Cs fountain called FO1, a dual fountain working with Cs and Rubidium (Rb) atoms called FO2, and a mobile Cs fountain called FOM. All fountains share the same cryogenic oscillator which is phase locked to a H-maser, so that all fountains measure the frequency of the same H-maser. Automatic fountain data processing provides hourly preliminary data corrected of all systematic frequency shifts. The steering of the H-maser frequency is calculated daily by a fit to the fountain data. First we describe the implementation of all the instruments used for the generation of UTC(OP) together with the current version of the algorithm. The choice of this algorithm has been oriented to obtain robustness of the system instead of the ultimate optimization of performances. We then present the results obtained during the first year of operation.

2. UTC(OP) IMPLEMENTATION

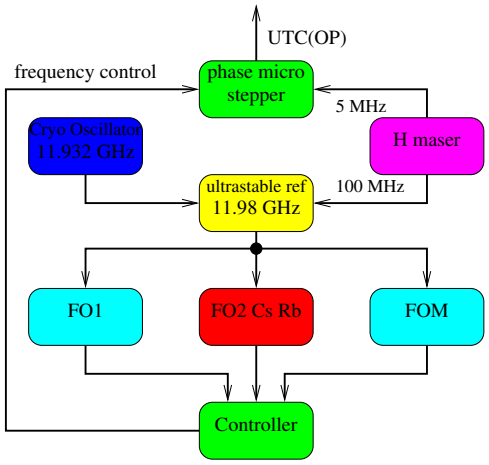

Table 1: Simplified block diagram of UTC(OP) generation.

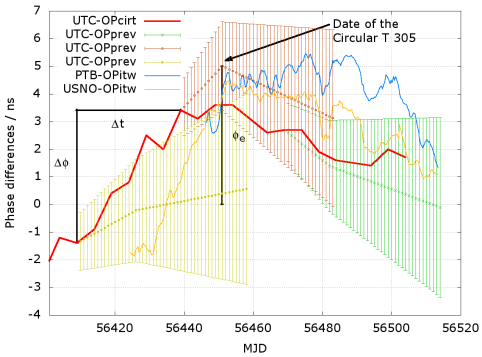

Table 2: The red lines show UTC − UTC(OP) as reported in Circular T. The colored dots with error bars are the predictions and prediction error propagation.

Figure 1 shows a simplified block diagram of the current hardware set-up used for the generation of UTC(OP). In normal operation the cryogenic oscillator that drives the three LNE-SYRTE atomic fountains is locked to the 100 MHz output of the free-running H-maser generating UTC(OP). Currently, the 5 MHz commercial phase micro stepper, historically used to steer commercial Cs standards, is still generating UTC(OP). A detailed description of the H-maser frequency distribution, filtered by the cryogenic oscillator can be found in [2].

A sophisticated automated post-processing allows for a quasi real time monitoring of the fountain

operations. A more careful manual processing is performed to provide data to BIPM for the monthly steering of TAI. But for the daily steering of the H-maser the quasi real time data are largely sufficient as they are to guarantee a stability at the 10^{-16} level for the time scale generation.

The frequency of the H-maser is measured simultaneously by all the fountains available in LNE-SYRTE. But in practice only data from one fountain are used for the automated steering. The choice of the selected fountain depends on the planning of operations.

In the normal data post-processing of LNE-SYRTE fountains all the systematic shifts are corrected every one cycle. For routine fountain comparison, and UTC(OP) generation, the original data files are converted in quasi real time to files with a reduced set of data averaged over 0.1 d. These pack files contain ten frequency values per day dated at pre-established epochs, namely 0.05 d, 0.15 d, etc.. Each point is obtained after filtering out some periods of the original file due to possible problems either in the fiber links or in the lock of the cryogenic oscillator. An additional cleaning is performed by fitting linearly the resulting data over each 0.1 d period and removing possible outliers exceeding the 5 sigma limit. The value of the linear fit at the middle of the interval is used to generate the pack file. The steering software predicts once a day the H-maser frequency for the next day by extrapolating the linear fit of pack files spanning the last 20 d.

The correction to be applied to the phase micro stepper for the next day is the sum of the predicted H-maser frequency and of an additional term updated monthly, that finely adjust the phase and the frequency of UTC(OP) to UTC, using data published by the BIPM in the Circular T. This fine adjustment is the sum of 2 terms. The first one is the average frequency difference, $\nu_p = \frac{\Delta\phi}{\Delta t}$, between UTC(OP) and UTC calculated over the Circular T period. The second term, $\nu_e = \frac{\phi_e}{60\times 86400}$, is calculated to compensate the last known time offset, ϕ_e, between UTC(OP) and UTC within 60 days. One can see on figure 2 these terms, the prediction and prediction error propagation.

3. RESULTS

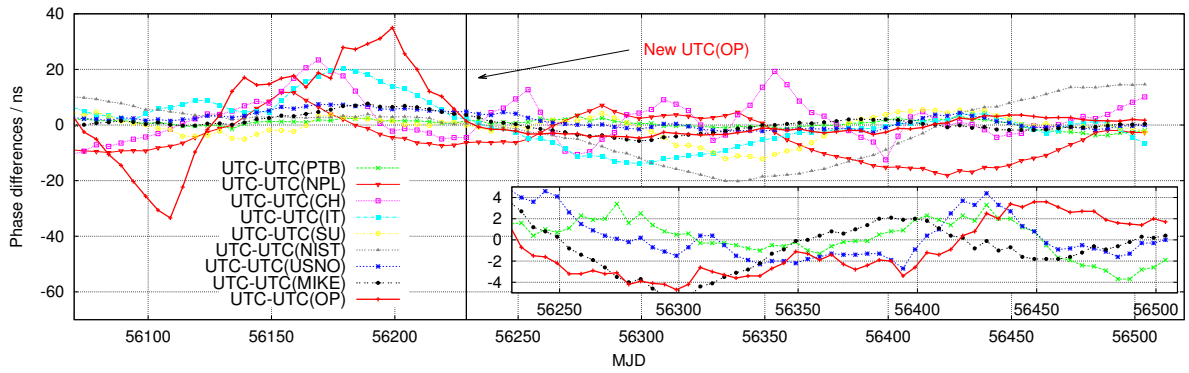

Figure 1: Comparison in ns of UTC − UTC(k) [from BIPM Circular T].

Figure 1 shows the differences between UTC − UTC(k) with the values extracted from the BIPM Circular T. Since the effective start of operations in October 2012, the departure of UTC(OP) from UTC has remained well below 10 ns. We expect that these performances might be kept on the long term with the current system.

Acknowledgements. The authors would like to thank the technical staff of SYRTE Références Nationales de Temps for the continuous support and monitoring. We also acknowledge the precious support of SYRTE Service d'Électronique for improving the reliability of the frequency distribution and measurement systems.

4. REFERENCES

[1] P. Uhrich *et al.*, 2005, Proc. of the 19$^{\text{th}}$ European Frequency and Time Forum.
[2] J. Guéna *et al.*, 2012, IEEE Transactions on UFFC, vol. 59, pp. 391–409.

ACES MICROWAVE LINK DATA ANALYSIS : STATUS UPDATE

F. MEYNADIER[1], P. DELVA[1], C. LE PONCIN-LAFITTE[1], C. GUERLIN[1,2], P. LAURENT[1], P. WOLF[1]
[1] LNE-SYRTE, Observatoire de Paris, CNRS, UMPC
F-75005, Paris, France
e-mail: Frederic.Meynadier@obspm.fr
[2] Laboratoire Kastler-Brossel, ENS, CNRS, UPMC
24 rue Lohmond, 75005 Paris, France

ABSTRACT. The Atomic Clocks Ensemble in Space (ACES-PHARAO mission [1]), which will be installed on board the International Space Station in 2016, will realize in space a time scale of very high stability and accuracy. This time scale will be compared to a ground clock network thanks to a dedicated two-way MicroWave Link (MWL). For that purpose our team is developing advanced time and frequency transfer algorithms.

The altitude difference between the ACES-PHARAO clock and ground clocks will allow to measure the gravitational redshift with unprecedented accuracy, as well as looking for a violation of Lorentz local invariance. Several ground clocks based on different atomic transitions will be compared to look for a drift of fundamental constants. Moreover, the mission will pave the way to a new type of geodetic measurement: the gravitational redshift will be used to measure gravitational potential differences between distant clocks, with an accuracy around 10 cm.

1. THE ACES MISSION AND ITS MICROWAVE LINK

The ACES payload includes : a cesium atomic clock (PHARAO), an active hydrogen maser (SHM), a GNSS receiver for precise orbit determination, a Frequency Comparison and Distribution Package (FCDP) for local comparison of the onboard clocks and generation of the onboard timescale, a MicroWave Link (MWL) using both code-phase and carrier-phase measurement.

The MicroWave Link (MWL) will be used for space-ground time and frequency transfer. A time transfer is the ability to synchronize distant clocks, i.e. determine the difference of their displayed time for a given coordinate time. The choice of time coordinate defines the notion of simultaneity, which is only conventional. A frequency transfer is the ability to syntonize distant clocks, i.e. determine the difference of clock frequencies for a given coordinate time.

2. TWO-WAY MEASUREMENT PRINCIPLE

The MicroWave Link is composed of three signals of different frequencies: one uplink at frequency $f_1 \simeq 13.5$ GHz, and two downlinks at $f_2 \simeq 14.7$ GHz and $f_3 = 2.2$ GHz. Measurements are done on the carrier itself and on a code which modulates the carrier. The link is asynchronous : a configuration can be chosen by interpolating observables. The so-called Λ-configuration minimizes the impact of the space clock orbit error on the determination of the desynchronisation [2].

We define the observables used by the Syrte Team (ST observables) by $\Delta\tau(\tau_e) = \tau_e - \tau_r$, where τ_e is the local time of emission of the signal and τ_r the local time of reception. It can be linked to desynchronisation :

$$\text{desynchronisation } (t_2) \equiv \tau^s(t_2) - \tau^g(t_2) = \frac{1}{2}\left(\Delta\tau^g_{\text{mo}}(\tau^g(t_4^0)) - \Delta\tau^s_{\text{mo}}(\tau^s(t_2^0)) + [T_{34} - T_{12}]^g\right) \qquad (1)$$

where t is coordinate time, $\Delta\tau_{\text{mo}}$ are the ST observables corrected for the delays in the cable between the clock and the antenna at transmission and at reception, s and g stand for *space* and *ground* respectively, $T_{ij} = t_j - t_i$ and $[.]^g$ is the coordinate time to the ground clock proper time transformation.

The time-of-flights T_{34} and T_{12} can be calculated from the known orbits of the clocks, accounting for the tropospheric, ionospheric and Shapiro delays.

The observables from the two downlinks can be used to determine the Total Electronic Content (TEC) of the atmosphere along the line-of-sight, in order to correct for the ionospheric delay. The two-way configuration cancels the tropospheric delay, which does not depend on the signal frequency at this level of accuracy.

3. DATA PROCESSING SOFTWARE

Our team is currently developing a prototype of the data processing software. It will be used as a guideline for Astrium who will implement the industrial-grade data processing in the ACES ground segment and also by our team, to achieve the highest possible accuracy in post-processing. The core algorithm has been largely inspired by Loïc Duchayne's PhD thesis [3].

4. SIMULATION AND ANALYSIS: FIRST RESULTS

The basic observables of the modem developed by TimeTech (TT observables) are different from the observables used by the Syrte Team (ST observables). The link between TT and ST observables is detailed in [4]. In order to test the data processing software, we wrote a simulation that generates TT observables as well as ST observables. The simulation is as much as possible independent from the data processing software.

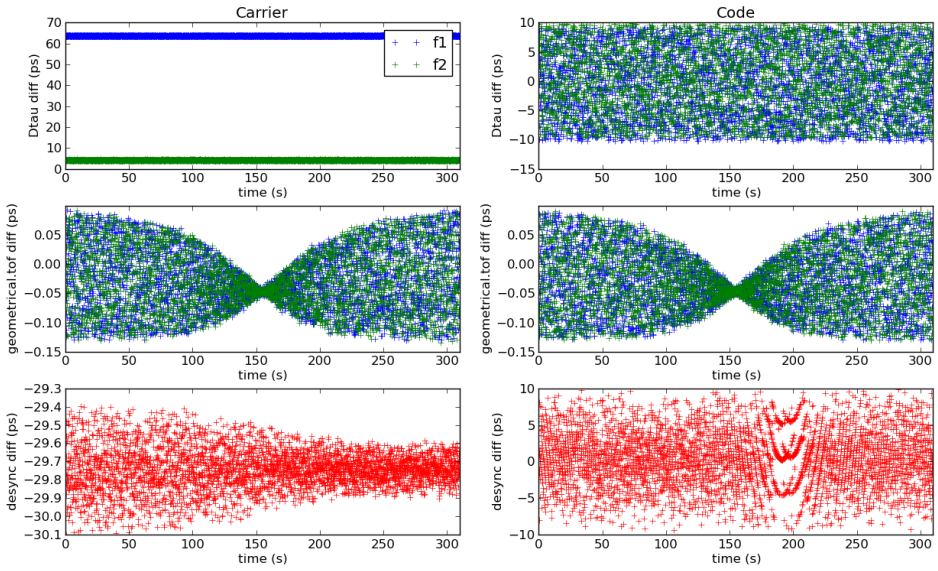

Figure 1: Here we plot the differences between simulated input quantities and quantities recovered by the data analysis software for: the ST observables recovered from the TT observables (Dtau diff), the time-of-flights and the desynchronisation, which is the final scientific product (see eq.(1)). Atmospheric delays and the lambda configuration are not yet implemented.

5. REFERENCES

[1] C. Salomon, L. Cacciapuoti, and N. Dimarcq., Atomic Clock Ensemble in Space:. An Update. In: International Journal of Modern Physics D 16 (2007), pp. 2511–2523

[2] L. Duchayne, F. Mercier, and P. Wolf. Orbit determination for next generation space clocks In: A&A 504 (2009), pp. 653–661.

[3] L. Duchayne., Transfert de temps de haute performance : le lien micro-onde de la mission ACES PhD thesis. Observatoire de Paris, 2008.

[4] P. Delva et al., Time and frequency transfer with a microwave link in the ACES/PHARAO mission In: Proceedings of the EFTF. 2012. eprint: 1206.6239.

Session 4a

EARTH ROTATION - THEORY

ROTATION DE LA TERRE - THÉORIE

THE GOAL OF THE IAU/IAG JOINT WORKING GROUP ON THE THEORY OF EARTH ROTATION

J.M. FERRÁNDIZ[1], R.S. GROSS[2]
[1] Dept. Applied Mathematics, University of Alicante
PO Box 99, E-03080 Alicante, Spain
e-mail: jm.ferrandiz@ua.es
[2] Jet Propulsion Laboratory, California Institute of Technology
Pasadena, USA
e-mail: richard.s.gross@jpl.nasa.gov

ABSTRACT. In 2012 the International Association of Geodesy (IAG) and the International Astronomical Union (IAU) initiated a process to establish a Joint Working Group (JWG) on Theory of Earth Rotation with the purpose of promoting the development of improved theories of the Earth rotation which reach the accuracy required to meet the needs of the near future as recommended by, e.g., GGOS, the Global Geodetic Observing System of the IAG. The JWG was approved by both organizations in April 2013 with the chairs being the two authors of this paper. Its structure comprises three Sub Working Groups (SWGs) addressing Precession/Nutation, Polar Motion and UT1, and Numerical Solutions and Validation, respectively. The SWGs should work in parallel for the sake of efficiency, but should keep consistency as an overall goal. This paper offers a view of the objectives and scope of the JWG and reports about its initial activities and plans.

1. INTRODUCTION

The International Association of Geodesy (IAG) and the International Astronomical Union (IAU) set up a new Joint Working Group on the Theory of Earth Rotation recently in 2013. A draft of a proposal to establish the JWG was initiated around the time of the IAU XXVIII General Assembly held in Beijing in August 2012 where the Joint Discussion 7 coordinated by IAU Division I and a business meeting of IAU Commission 19 took place. The draft was completed and opened to suggestions and discussions at the beginning of the next year and circulated among members of IAU C19 and IAG. Afterwards the revised document was put forward with the conformity of the proposed members, and the IAU C19 Organizing Committee, the IAU Division A Organizing Committee, and the IAG Executive Committee approved the final JWG proposal in April 2013.

According to the proposal, the purpose of the new JWG is to *"promote the development of theories of Earth rotation that are fully consistent and that agree with observations and provide predictions of the Earth Rotation Parameters (ERP) with the accuracy required to meet the needs of the near future as recommended by, e.g., GGOS, the Global Geodetic Observing System of the IAG"*.

Let us recall that IAG has organized all its observation activities under the umbrella of GGOS in order to respond to the scientific challenges associated with rapidly increasing requirements for geodetic observations (Plag et al 2009). Pursuing that end, GGOS 2020 demands improved consistency to all IAG products and accuracy of the order of 1 mm to the frames of reference, besides stability in time of 0.1 mm/y (Plag and Pearlman 2009). The former accuracy in position, measured on the Earth surface, corresponds roughly to an angle of 30 μas from the Earth's centre.

From the observational side, the accuracy and performance of the major techniques is increasing. A good example is provided by the new generation of VLBI. A number of stations compliant with the 2010 specifications are already in operation, are being deployed or have been approved by their respective funding institutions. Besides, the various IAG services are committed to reach GGOS goals. Therefore, it can be expected that series of more accurate Earth Orientation Parameters (EOPs) will be produced in a few years. In addition, it can also be expected that series of the whole set of EOPs at a sub-daily rate will also be produced in a few years, following the experience of continuous VLBI campaigns (Nilsson et al. 2010). That would be useful to overcome deficiencies in the models used to describe diurnal and sub-diurnal variations of EOPs (Böhm et al 2012).

Currently, series of EOPs are provided by several Analysis Centers and by the International Earth Rotation and Reference Systems Service (IERS), the international body in charge of both Earth rotation monitoring and prediction and of the realization and maintenance of the International Celestial Reference Frame and the International Terrestrial Reference Frame (ICRF and ITRF, respectively), with the assistance of other IAG services.

The set of EOPs currently in use was agreed upon following the recommendation of an IAU Working Group on Nutation (Seidelmann 1982) and comprises five angles used to transform station coordinates between ICRF and ITRF:

- Precession/nutation (dX, dY in the so-called *new* paradigm or $d\varepsilon$, $d\Psi$ in the *old* one)
- Earth Rotation Angle (ERA, formerly GMST or GAST - Greenwich Mean or Apparent Sidereal Times)
- Polar Motion (x, y)

Let us recall that the transformation is specified by five EOPs instead of the minimum of three parameters (which is the number of independent angles needed to specify the transformation from a given frame to another) because an intermediate reference system is used, corresponding to the Celestial Intermediate Pole (CIP), which nowadays replaces the former Celestial Ephemeris Pole (CEP).

Other interesting properties (Seidelmann 1982) that favored the adoption of five EOPs were that both sets of nutation angles and polar motion (PM) were free from diurnal components either in the "inertial" or the "body-fixed" reference systems, respectively. Besides, nutations are caused by mainly astronomically driven, predictable effects, while PM are caused by mainly geophysical, difficult to predict effects.

Precise definitions of the main and auxiliary parameters and frames can be found in the IERS Conventions 2010 (Petit and Luzum 2010), Supplement to the Nautical Almanac (Urban and Seidelmann 2013) or SOFA (Standards of Fundamental Astronomy) documentation (Hohenkerk et al 2010), for instance.

Let us further recall that IAU adopted a new nutation theory in 2000, based on MHB2000 (Mathews et al. 2002) as well as a new precession model in 2006 (Hilton et al. 2006), based on P03 by Capitaine et al. (2003). They are known as IAU 2000 nutation model and IAU 2006 precession model, or shortened names as IAU2000/2006.

The real accuracy of the series of EOP is difficult to assess. Recent estimates of accuracies of individual solutions corresponding to different techniques and analysis centers, when compared to combined solutions, can be found in the IERS Annual Report 2011 (Dick 2011, section 3.5.1). As for the current precession/nutation models, the most predictable component of Earth rotation, a reference value can be settled about 140 to 150 μas, in terms of wrms of the observation-model differences (Capitaine et al. 2009, 2012). Let us notice that the remarkable efforts made in the last years to improve the models have not been accompanied by a significant reduction of the residual wrms.

Given the values of those uncertainties/inaccuracies, we must conclude that the goal of the new JWG is really quite challenging.

2. TERMS OF REFERENCE

The terms of reference (ToR) of the JWG are:

1. A main objective of the Joint Working Group (JWG) is to assess and ensure the level of consistency of Earth Orientation Parameter (EOP) predictions derived from theories with the corresponding EOPs determined from analyses of the observational data provided by the various geodetic techniques. Consistency must be understood in its broader meaning, referring to models, processing standards, conventions etc.

2. Clearer definitions of polar motion and nutation are needed for both their separation in observational data analysis and for use in theoretical modeling.

3. Theoretical approaches must be consistent with IAU and IAG Resolutions concerning reference systems, frames and time scales.

4. Searching for potential sources of systematic differences between theory and observations is encouraged, including potential effects of differences in reference frame realization.

5. The derivation of comprehensive theories accounting for all relevant astronomical and geophysical effects and able to predict all EOPs is sought. In case more than one theory is needed to accomplish this, their consistency should be ensured.

6. There are no *a priori* preferred approaches or methods of solution, although solutions must be suitable for operational use and the simplicity of their adaptation to future improvements or changes in background models should be considered.

7. The incorporation into current models of corrections stemming from newly studied effects or improvements of existing models may be recommended by the JWG when they lead to significant accuracy enhancements.

3. DESIRED OUTCOMES

It is desired that the JWG:

1. Contribute to improving the accuracy of precession-nutation and EOP theoretical models by proposing both new models and additional corrections to existing models.

2. Clarify the issue of consistency among conventional EOPs, their definitions in various theoretical approaches, and their practical determination.

3. Establish guidelines or requirements for future theoretical developments with improved accuracy.

It is clear that the overall goals of the JWG cannot be achieved within only two years of activity, but the first term (until the next General Assembly of both IAU and IAG, i.e., mid 2015) should be used to develop a solid concept of how to reach its aims.

4. STRUCTURE AND OPERATION

The structure of the JWG is more complex than usual because its subject is quite broad and requires the participation of several fields of specialization covering the characteristics of the full set of current EOPs. On the other hand, the establishment of independent JWGs for the different sub-fields would imply a serious risk of obtaining results that would not be consistent with each other. Therefore, the JWG was structured as a whole JWG containing three Sub Working Groups (SWG).

The whole JWG has the following people in charge:

- **Chair**: José M. Ferrándiz (representing IAU)
- **Vice-Chair**: Richard Gross (representing IAG)

In their turn, the three SWGs forming the JWG are:

1. **Precession/Nutation** (Chair: Juan Getino)
2. **Polar Motion and UT1** (Chair: Aleksander Brzezinski)
3. **Numerical Solutions and Validation** (Chair: Robert Heinkelmann)

SWG 3 will be dedicated to numerical theories and solutions, relativity and new concepts and validation by comparisons among theories and observational series. The subjects of SWG 1 and 2 are self-explanatory.

These three SWGs should work in parallel for the sake of efficiency. To guarantee that the SWGs are linked together as closely as the needs of consistency demand, the Chair and Vice-chair of the JWG, Ferrándiz and Gross, will be involved in all SWGs as will the President of C19, Cheng-li Huang. In order to further improve the interaction of the SWGs, a number of people are members of more than one SWG. The up-to-date list of members by SWG can be seen in (Ferrándiz and Gross 2013).

5. ADDITIONAL INFORMATION

A dedicated web site of the WG is hosted by the institution of the Chair, the University of Alicante, Spain. It can be accessed directly at `http://web.ua.es/en/wgther/`.

After the closing of this edition of the *Journées* on September 18th, the Observatory of Paris kindly provided a time slot for working groups splinter meetings. A short meeting of the JWG on Theory of Earth rotation took place in the afternoon, open to all the attendees of JSR 2013. A brief report of the discussed topics is given in the Appendix.

Acknowledgements. JMF acknowledges partial support of Spanish government under grant AYA2010-22039-C02-01 from Ministerio de Economía y Competitividad (MINECO). The work of RSG described in this paper was performed at the Jet Propulsion Laboratory, California Institute of Technology, under contract with the National Aeronautics and Space Administration. Support for that work was provided by the Earth Surface and Interior Focus Area of NASA's Science Mission Directorate.

6. REFERENCES

Böhm, S., Brzeziński, A., Schuh, H., 2012, "Complex demodulation in VLBI estimation of high frequency Earth rotation components", J. Geodyn., 62, 56–58, doi:10.1016/j.jog.2011.10.002.

Capitaine, N., Wallace, P. T., Chapront, J., 2003, "Expressions for IAU2000 precession quantities", A&A, 412(2), pp. 567–586, doi: 10.1051/0004-6361:20031539.

Capitaine, N., Mathews, P. M., Dehant, V., Wallace, P. T., Lambert, S. B., 2009, "On the IAU 2000/2006 precession-nutation and comparison with other models and VLBI observations", Celest Mech Dyn Astron, 103, 179–190.

Capitaine, N., Lambert, S., Yao, K., Liu, J., 2012, "Evaluation of the accuracy of the IAU 2006/2000 precession-nutation", JD7 Space-time reference systems for future research, 28th IAU GA, Beijing (available at `http://www.referencesystems.info/uploads/3/0/3/0/3030024/capitaine_6.07.pdf`).

Dehant, V., 2002, "Report of the IAU Working Group on 'Non-rigid Earth Nutation Theory". In: Rickman H (ed) "Highlights of Astronomy", Vol. 12, pp 117–119.

Dick, W.R. (ed) ,2011, "IERS Annual Report 2011". Verlag des Bundesamts für Kartographie und Geodäsie, Frankfurt am Main (online version available at: http://www.iers.org/AR2011/).

Ferrándiz, J.M., Gross, R.S., 2013, "The New IAU/IAG Joint Working Group on Theory of Earth Rotation", IAG Symposia Series, Springer (submitted)

Hilton, J.L., Capitaine, N., Chapront, J., Ferrándiz, J.M., Fienga, A., Fukushima, T., Getino, J., Mathews, P., Simon, J.L., Soffel, M., Vondrak, J., Wallace, P., Williams, J., 2006, "Report of the International Astronomical Union Division I Working Group on Precession and the Ecliptic", Celest Mech Dyn Astron, 94(3), pp. 351–367. doi:10.1007/s10569-006-0001-2.

Hohenkerk, C. and the IAU SOFA board, 2010, "SOFA Tools for Earth Attitude". IAU (available at `http://www.iausofa.org`).

Mathews, P.M., Herring, T.A., Buffett, B.A., 2002, 'Modeling of nutation and precession: New nutation series for nonrigid Earth, and insights into the Earth's Interior. J Geophys Res, 107(B4). doi: 10.1029/2001JB000390.

Nilsson, T., Böhm, J., Schuh, H., 2010, "Sub-diurnal earth rotation variations observed by VLBI", Artificial Satellites, Vol. 45, No. 2 2010. doi: 10.2478/v10018-010-0005-8.

Petit, G., Luzum, B. (eds), 2010, "IERS Conventions 2010", IERS Technical Note No. 36. Verlag des Bundesamts für Kartographie und Geodäsie, Frankfurt am Main (online version available at: `http://www.iers.org/TN36/`).

Plag, H.-P., Gross, R., Rothacher, M., 2009, "Global Geodetic Observing System for Geohazards and Global Change". Geosciences, BRGM's journal for a sustainable Earth, 9, 96–103.

Plag, H.-P., Pearlman, M., eds., 2009. "Global Geodetic Observing System: Meeting the Requirements of a Global Society on a Changing Planet in 2020", Springer Berlin, 332 pages.

Seidelmann, P. K., 1982, "1980 IAU theory of nutation - the final report of the IAU Working Group on Nutation". Celest Mech, 27, 79–106.

Urban, S.E., Seidelmann, P.K. (eds), 2013, "Explanatory Supplement to the Astronomical Almanac", 3rd edn. University Science Books, Mill Valley.

APPENDIX

The following topics were discussed in the open JWG meeting held at the end of the conference, among others:

1. The need of agreeing on a common background among the three Sub-WG so that the main issue of consistency would not be lost as they develop their tasks.

2. The convenience of preparing a preliminary catalogue of potential sources of inconsistency among different parts of the theory and series of EOP from the various techniques. Inconsistencies may result from many causes: differences among reference systems used in theories and data analysis, realizations of frames, use of different geophysical models, etc. Estimation of magnitudes of their associated effects would help to ascertain which ones may be not negligible when pursuing the global accuracy level of GGOS, 1 mm or 30 μas.

3. Earth models used in different theoretical approaches to EOP also exhibit large variations. Some questions, as adopting triaxial models or taking into account other new geophysical effects, should be addressed in future as well as the possibility of working in terms of reference models/solutions and "anomalies" as done in other fields. Considering the role of theoretical predictions in a scenario in which observational accuracy goes ahead of theory was also pointed.

4. Several new effects on nutations have been proposed in the past few years. At short-medium term, it would be convenient to test them through analyses of observational data to ascertain the convenience of adopting some of them as new corrections.

5. Regarding future meetings of the WG and presentation of related activities:

   (a) A new splinter meeting of the WG can be held during the next AGU fall meeting in San Francisco. Abstract submission is closed.

   (b) The proposal of a session dedicated to earth rotation submitted to EGU 2014 has been modified to better include WG related presentations. A JWG (SWGx) splinter meeting(s) could be scheduled.

   (c) Another opportunity to meet will be in September 2014, during the Journées that will be held in St. Petersburg

   (d) The chance to meet more often by teleconferencing was also suggested.

   (e) The possibility of holding a dedicated workshop on the Working Group activities would be considered later.

NEXT STEP IN EARTH INTERIOR MODELING FOR NUTATION.

V. DEHANT[1], M. FOLGUEIRA[2], M. PUICA[2], L. KOOT[1], T. VAN HOOLST[1], A. TRINH[1]
[1] Royal Observatory of Belgium
avenue Circulaire 3, B1180 Brussels, Belgium
e-mail: v.dehant@oma.be
[2] Universidad Complutense de Madrid, Spain
e-mail: marta.folgueira@mat.ucm.es

ABSTRACT. Accurate reference systems are important for many geophysical applications and satellite observations. It is therefore necessary to know the Earth rotation and orientation with high precision. Interactions between the solid Earth and its fluid layers (liquid core, atmosphere, ocean) induce variations in the Earth's speed of rotation. In addition, because the Earth is not a perfect sphere, but rather an ellipsoid flattened at its poles, the combined gravitational forces acting upon it produce changes in the orientation of its spin axis. Precession describes the long-term trend in the orientation of the Earth, while nutation refers to shorter-term periodic variations. The nutations of the Earth are the prime focus of the present paper. Models are used to predict the real-time Earth rotation and orientation, based on past observations and theoretical considerations of geophysical processes. In particular, the coupling mechanisms at the internal boundaries have been shown to be important for rotation. We here address the coupling mechanisms at the core boundaries such as the topographic, electromagnetic and viscous couplings, and discuss improvements in their computation and observation. The study uses and compares numerical and semi-analytical approaches, with the objective of both improving the nutation model and the rotation, and better understanding the interior of the Earth.

1. RECENT ADVANCES IN OBSERVATION

Nutation observations are performed using Very Long Baseline Interferometry (VLBI). The performance of the VLBI antenna networks used for these observations has increased during the recent years. There are more stations used and more stable sources observed in each session, which has improved the definition and stability of the reference frame and therewith the observation of precession and nutations relating the celestial to the terrestrial reference frame. Moreover the time elapsed since the beginning of good observations has increased, allowing a higher precision determination of the long period nutations such as the 18.6 year nutation, than at the time of the previously adopted nutation model.

The nutation observations are compared with the theory as adopted by the IAU and IUGG in 2000 and 2003. The residuals are mainly due to the Free Core Nutation (FCN), a free mode excited by the atmosphere. The FCN amplitude cannot be precisely determined due to the poor knowledge of its excitation. We here subtract the effect of the FCN free mode contribution (as determined by the IERS) on the nutation in the time domain, and also the effects of the atmosphere and ocean on nutation, which has an important contribution on the prograde annual nutation. What remains is the nutation for the non-rigid Earth without ocean and atmosphere in the time domain, from which observed nutation amplitudes can be deduced with a precision at the ten microarcsecond level. These nutation amplitudes can be compared to theoretical ones computed for an ellipsoidal Earth, with a solid inner core, a liquid outer core, and an ellipsoidal inelastic mantle. Due to resonances in the response of the Earth with the FCN and FICN (Free Inner Core Nutation), one can deduce the "observed" coupling constants at the CMB (core-mantle boundary) and at the inner core boundary. This determination necessitates the knowledge of the forcing acting on the Earth. It is computed from a rigid Earth nutation theory accounting not only for the luni-solar direct effect on the Earth but as well for the direct and indirect of the planets.

2. COUPLING MECHANISMS AT CORE-MANTLE BOUNDARY

There are several coupling mechanisms that have to be considered to explain the observed coupling constant at the CMB: (1) the classical ellipsoidal pressure-gravitational torque, already considered in the MHB2000, the adopted nutation model, (2) the electromagnetic torque, also considered in the adopted

model, (3) the viscous torque, and (4) the topographic torque. In the adopted model, only the electromagnetic coupling is considered at the CMB. A revisite of this computation, together with the accounting of the viscous coupling does not lead to matching between theory and observation (coupling constants at the CMB from VLBI data). One explanation can be found by consideration of a thermal conductivity of liquid iron under the conditions in Earth's core is several times higher than previous estimates (Pozzo et al., 2012; Buffett, 2010, 2012).

Alternatively, inclusion of the topographic coupling may reduce the need of a large electromagnetic field. We know from seismology that there is a core-mantle boundary topography at the km level. The liquid pressure at the CMB on this topography induces a pressure torque able to transfer angular momentum from the core to the mantle. This phenomena is well known for the explanation of the decadal variations of Earth rotation (Hide 1977). At the nutation diurnal timescale, it is difficult and challenging to compute, but the topographic torque cannot be ruled out to explain the coupling constants determined from nutation observations. Wu and Wahr (1997) have used seismic value for the topography at the CMB and have computed the effect on nutations. They have shown that the effects on the retrograde annual nutation can be at the milliarcsecond level and that for some topography wavelength there are amplifications of the contributions. We shall examine the approach and equations and further study them. In particular we show that the amplifications can exist due to resonances with inertial waves in the rotating fluid core.

Aiming at obtaining the torque and the associated effects on nutation, we use the following strategy: (1) we establish the motion equations and boundary conditions in the fluid; (2) we compute analytically/numerically the solutions; (3) we obtain the dynamic pressure as a function of the physical parameters; and (4) we determine the topographic torque. Our results can then be compared with those of Wu and Wahr (1997) who used a numerical technique only.

The basic dynamical fluid motion equation is the linearized Navier-Stokes equation. If one considers that the equilibrium corresponds to the hydrostatic case, it can be expressed as

$$\frac{\partial \vec{V}}{\partial t} + 2\,\vec{\Omega} \times \vec{V} + \frac{1}{\rho_f}\,\nabla p - \nabla \phi_m + \Omega\,\frac{\partial \vec{m}}{\partial t} \times \vec{r} = 0 \tag{1}$$

where $\vec{\Omega}$ is the uniform equilibrium angular rotation of amplitude Ω, $\vec{m}$ is the scaled additional mantle angular velocity, $\vec{m} = \begin{pmatrix} m_1 \\ m_2 \\ m_3 \end{pmatrix}$, $\vec{r} = \begin{pmatrix} x \\ y \\ z \end{pmatrix}$ is the position of the fluid particle in the reference frame, $\vec{V}$ is the velocity of the fluid particle in the reference frame, ρ_f is the fluid density and p is the incremental effective pressure $p = P - P_0 - \rho_f \phi_1 - \rho_f \phi_e$ computed from the pressure P, the mass redistribution potential ϕ_1, and the external potential ϕ_e. Note that the angular velocity vector of the reference frame attached to the mantle $\vec{\omega} = \vec{\Omega} + \Omega \vec{m}$.

The boundary condition at the core-mantle boundary expresses that core material does not penetrate the mantle: $\vec{n} \cdot \vec{V} = 0$ ($\vec{n}$ is the normal to the surface). It depends on the boundary topography. We write the boundary surface (hydrostatic + non-hydrostatic parts) as

$$r = r_0 \left[1 + \sum_{n=1} \sum_{m=-n}^{n} \varepsilon_n^m Y_n^m(\theta, \lambda) \right] \tag{2}$$

where r_0 is the surface mean radius, $Y_n^m(\theta, \lambda)$ are the spherical harmonics of the colatitude θ and the longitude λ, and ε_n^m are small dimensionless numbers related to the existence of the topography. The largest contribution is ε_2^0 due to the flattening (hydrostatic + non-hydrostatic parts) of the CMB. It must be noted that the ϵ_2^0 in a topography development in spherical harmonics usually contains the hydrostatic part and the non-hydrostatic contribution to the topography; these must be separated. Here it is separated into a hydrostatic part ${\epsilon_2^0}^{hydr}$ and an additional one noted ϵ_2^0 for simplicity of writing.

We assume that the fluid is incompressible: $\nabla \cdot \vec{V} = 0$. We now decompose the velocity: $\vec{V} = \vec{v} + \vec{u} = \vec{v} + \Omega\, L\, \vec{q}$, where L is the maximum radius of the core and $\vec{q}$ is a non-dimensional velocity. One imposes that $\vec{u} << \vec{v}$. The philosophy for solving the equations is to separate the velocity into a global part ($\vec{v}$) and an additional part ($\vec{u}$ or $\vec{q}$ if normalized) and to separate the equation into two equations of which the solutions are $\vec{v}$ and $\vec{q}$ and can be computed analytically. The equation and condition for $\vec{v}$ are:

$$\begin{cases} \frac{\partial \vec{v}}{\partial t} + 2\,\vec{\Omega} \times \vec{v} + + \Omega\,\frac{\partial \vec{m}}{\partial t} \times \vec{r} - \nabla \phi_m = 0 \\ \nabla \cdot \vec{v} = 0 \end{cases} \tag{3}$$

The equation and condition for $\vec{q}$ are:

$$\left\{ \begin{array}{l} i\,\sigma_m\,\vec{q} + 2\,\vec{\hat{z}} \times \vec{q} + \nabla\Phi \;=\; 0 \\ \nabla \cdot \vec{q} \;=\; 0 \\ \vec{n} \cdot \vec{q} + \Omega^{-1}\,L^{-1}\vec{n} \cdot \vec{v} \;=\; 0 \end{array} \right. \tag{4}$$

where $\Phi = \frac{\phi}{\Omega^2\,L^2}$ and $\phi = \frac{p}{\rho_f}$, Φ being called the non-dimensional dynamic pressure, and where $\vec{\hat{z}}$ is the normalized vector in the direction of $\vec{\Omega}$. The time dependence of the variables is considered as $e^{i\sigma t}$ where σ is the nutation frequency in the reference frame attached to the mantle. When used in non-dimensional equations as above, the frequency to be used is σ_m instead of σ, where $\sigma = \Omega\sigma_m$.

After some algebra of the first equation of (4), one can obtain the following expression for $\vec{q}$ as a function of $\nabla\Phi$:

$$\vec{q} = \;\; \frac{-i\,\sigma_m}{4-\sigma_m^2}\left[\nabla\Phi \;-\; \frac{2}{i\,\sigma_m}\,\vec{\hat{z}} \times \nabla\Phi \;-\; \frac{4}{\sigma_m^2}\,(\vec{\hat{z}} \cdot \nabla\Phi)\,\vec{\hat{z}}\right] \tag{5}$$

Using the above equation for $\vec{q}$ and the incompressibility condition for this fluid velocity (second equation of (4)), one obtains the following equation for Φ:

$$\nabla^2\Phi \;-\; \frac{4}{\sigma_m^2}\,\frac{\partial^2\Phi}{\partial Z^2} \;=\; 0$$

where Z is a particular coordinate (related to the cylindrical coordinates involving the colatitude θ and used by Greenspan, 1969), which is equal to $\sqrt{\frac{\sigma_m}{2}}\cos\theta$. The factor $(1 - \frac{4}{\sigma_m^2})$ being negative, this mixed differential equation is an hyperbolic differential equation and has the typical form of a wave propagation equations. It expresses that small perturbations of an equilibrium configuration can propagate in the fluid in the form of waves which are the so-called inertial waves because they are controlled by the Coriolis force as a restoring force.

The solution of this equation for Φ must be proportional to the associated Legendre functions of the first kind; it has the following form:

$$\Phi \;=\; \sum_{l=1} a_l^k\,P_{lk}(\frac{\sigma_m}{2})\,Y_l^k(\theta,\lambda). \tag{6}$$

where $P_{lk}(\frac{\sigma_m}{2})$ are the fully normalized associated Legendre polynomials, and $Y_l^k(\theta,\lambda)$ the fully normalized spherical harmonics as introduced before. The a_l^k are coefficients that will be determined in the next step using the boundary conditions (third equation of (4)).

Using the boundary condition for $\vec{q}$ (third equation of (4)) and the expression of $\vec{q}$ as a function of Φ (Eq. (5)), substituting the above solution for Φ (Eq. (6)), after a lot of algebra, one obtains for the first order in the small quantities such as ϵ_n^m:

$$\begin{array}{rl} & \sin^2\vartheta \sum_{l,k} Y_l^k \left[kP_{lk}(\frac{\sigma_m}{2}) - \left(1 - \frac{\sigma_m^2}{4}\right) P'_{lk}(\frac{\sigma_m}{2})\right]\,a_l^k \\ + & \sin^2\vartheta \left[2\sqrt{\frac{2\pi}{15}}\left(1 + 3\sum_{n=0}\epsilon_n^m Y_n^m\right)\left(\frac{(\sigma_m^2+\sigma_m-2)}{2\sigma_m}Y_2^1 m_f^- + \frac{(-\sigma_m^2+\sigma_m+2)}{2\sigma_m}Y_2^{-1}m_f^+\right)\right. \\ & \left. +\sqrt{\frac{2\pi}{3}}\frac{(4-\sigma_m^2)}{2\sigma_m}\;\Psi\;\left(-Y_1^1 m_f^- \;+\; Y_1^{-1}m_f^+\right)\right] \\ + & \cos^2\vartheta\sqrt{\frac{2\pi}{3}}\;\Psi\;\left(-\frac{(\sigma_m+2)}{2}Y_1^1 m_f^- \;+\; \frac{(\sigma_m-2)}{2}Y_1^{-1}m_f^+\right) \\ + & \sqrt{\frac{2\pi}{15}}\sum_{n=1} m\epsilon_n^m Y_n^m\;\left(\frac{(\sigma_m+2)}{2}Y_2^1 m_f^- \;+\; \frac{(\sigma_m-2)}{2}Y_2^{-1}m_f^+\right) \\ = & \;0 \end{array} \tag{7}$$

where $Y_l^k \equiv Y_l^k(\vartheta,\lambda)$, $m_f^+ = m_1^f + im_2^f$, $m_f^- = m_1^f - im_2^f$, $P'_{lk}(x) = \frac{dP_{lk}(x)}{dx}$ and Ψ is given by:

$$\Psi = \sum_{n=1}\epsilon_n^m\left[\frac{n\sqrt{n-m+1}\sqrt{n+m+1}}{\sqrt{2n+1}\sqrt{2n+3}}Y_{n+1}^m \;-\; \frac{(n+1)\sqrt{n-m}\sqrt{n+m}}{\sqrt{2n+1}\sqrt{2n-1}}Y_{n-1}^m\right]. \tag{8}$$

Equation (7) allows us to solve for the a_l^k as a function of the ϵ_n^m and σ_m. Because we have only kept first order in ϵ_n^m, the a_l^k coefficients are linear functions of ϵ_n^m. It must be noted that this equation can be

considered component per component by projection on each $Y_{l'}^{m'}$ and that we can solve as well for each ϵ_n^m separately and then sum over all the contributions.

The boundary conditions at the CMB are imposed on the total velocity and yield thus a relation between $\vec{v}$ (and thus components of the relative global fluid rotation m_1^f and m_2^f), $\vec{q}$ (and thus the a_l^k coefficients), and the topography coefficients ϵ_n^m. This allows to solve for the a_l^k in terms of the relative global relative fluid rotation.

The total pressure torque on the whole topography can then be decomposed into two parts: $\Gamma^0 + \Gamma_{topo}^{\phi}$, where (1) Γ^0 is the constant classical part of the torque for an ellipsoidal topography at equilibrium, and (2) Γ_{topo}^{ϕ} is due to the inertial rotation pressure computed from the above solution. Only the second part of the torque is of importance when computing the effects of a perturbing potential related additional rotations of the core and the mantle on a topography different with respect to the ellipsoidal hydrostatic shape.

3. RESULTS

Substituting the solution for Φ, provided in Eq. (6) as a function of the coefficients a_l^k, in the expression for $\vec{q}$ provided by Eq. (5), and computing the contribution to the torque, one gets the $\vec{q}$-contribution to topographic torque $\vec{\Gamma}_{topo}^{\phi}$ as a function of a_l^k (or equivalently ϵ_n^m by means of Eq. (7)).

4. CONCLUSIONS

From our computation we see that some topography coefficients provide larger contributions to nutation than others. We have not yet solved some differences with respect to Wu and Wahr (1997), even when using the same CMB topography. But the main conclusion remains: it is possible to have topography coefficients that enhance the coupling at the core-mantle boundary.

With this computation, we have shown analytically that the degrees and orders of the nutation with significant amplifications depend on the degrees and orders of the excitation and of the topography expressed in spherical harmonics.

We must note however that the degrees and orders that come out of our computations/conclusions may change when the effect of an inner core is taken into account.

REFERENCES

Buffett B. and Christensen U., 2007, "Magnetic and viscous coupling at the core-mantle boundary: Inferences from observations of the Earths nutations."', Geophys. J. Int., 171(1), pp. 145-152, DOI: 10.1111/j.1365-246X.2007.03543.x.

Buffett B., 2010, "Chemical stratification at the top of Earth's core: Constraints from observations of nutations.", Earth and Planetary Science Letters, 296(3-4), pp. 367-372, DOI: 10.1016/j.epsl.2010.05.020.

Buffett B., 2012, "Geomagnetism under scrutiny.", Nature, 485(7398), pp. 319-320, DOI: 10.1038/485319a.

Pozzo, M., Davies, C., Gubbins, D. and Alfè, D., 2012, "Transport properties for liquid silicon-oxygen-iron mixtures at Earth's core conditions.", Physical Review B, 87(1), Id. 014110, DOI: 10.1103/PhysRevB.87.014110, and Nature 485, pp. 355358, DOI: 10.1038/nature11031.

Wu Xiaoping and Wahr J.M., 1997, "Effects of non-hydrostatic core-mantle boundary topography and core dynamics on Earth rotation", Geophys. J. Int., 128, pp. 18-42.

ON THE CHANGES OF IAU 2000 NUTATION THEORY STEMMING FROM IAU 2006 PRECESSION THEORY

A. ESCAPA[1], J. GETINO[2], J. M. FERRÁNDIZ[1], & T. BAENAS[1]
[1] Department of Applied Mathematics, University of Alicante
PO Box 99, E-03080 Alicante, Spain
e-mail: alberto.escapa@ua.es
[2] Department of Applied Mathematics, University of Valladolid
E-47011 Valladolid, Spain

ABSTRACT. The adoption of IAU 2006 precession theory (Capitaine et al. 2003) introduced some small changes in IAU 2000A nutation theory, relevant at the mircroarcsecond level. These adjustments were derived in Capitaine et al. (2005) and are currently considered in international standards like, for example, IERS Conventions (2010) or in the Explanatory Supplement to the Astronomical Almanac (2013). We reexamine the issue, working out the induced modifications due to a change in the value of the obliquity of the ecliptic and to the secular variation of the Earth dynamical flattening. In particular, within the framework of the Hamiltonian theory of the rotation of the Earth we derive analytical expressions of those changes for the motion of the figure axis. These expressions and their corresponding numerical contributions will be compared with those obtained in Capitaine et al. (2005).

1. INTRODUCTION

Precession–nutation motion is a basic ingredient to establish the transformation that relates celestial and terrestrial reference systems. It provides the evolution of a celestial pole with respect to the reference celestial system. From a dynamical perspective precession–nutation is a single entity, although it is conventionally separated into secular and long term parts, precession, and a non long term part, nutation (see, for example, IERS Conventions 2010, chapter 5 and references therein).

This motion is realized by International Astronomical Union (IAU) model for precession–nutation plus additional contributions provided by the International Earth Rotation Service (IERS) like, for example, the Free Core Nutation (FCN) caused by the interacting fluid outer core. That model reproduces the evolution of the Celestial Intermediate Pole (CIP) due to the external torques exerted by the Moon, the Sun, and the planets on the non–rigid, non–spherical Earth.

From a methodological point of view, last IAU models for precession–nutation have been constructed by considering two parts that comprise precession and nutation separately. For example, IAU 1980 nutation model was based on the works by Wahr (1981) and Kinoshita (1977), whereas its precession counterpart was given in Lieske et al. (1977). Later, by IAU Resolution B1.6, in XXIVth General Assembly (Manchester, 2000) the nutational part was replaced by the model developed in Mathews et al. (2002). The precessional component, however, was unchanged, keeping basically the theory of Lieske et al. (1977) with some corrections to precession rates.

In XXIVth General Assembly (Prague, 2006), Resolution B1 adopted the model by Capitaine et al. (2003) as the new IAU precession theory, which entered in forced on 1 January 2009. So, the current IAU model for precession–nutation is made up by two components: one for the nutation (Mathews et al. 2002) and other for the precession (Capitaine et al. 2003). To short, they are commonly referred as IAU 2000A nutation and IAU 2006 precession models.

At nowadays accuracy levels this two–component approach requires the introduction of some corrections in the nutation or the precessional part, ensuring in this way the compatibility and consistency between them, although as far as we know there is no explicit mention to this issue in IAU resolutions.

The corrections, or adjustments, of IAU 2000A nutation due to the adoption of IAU 2006 precession are mainly induced by the change in the value of the obliquity, with respect to IAU 1976 precession model (Lieske et al. 1977), and also by the introduction of a time rate of Earth J_2 parameter, not considered in previous models. The relevant values are

$$\epsilon_{A\ \mathrm{IAU\ 2006}} = 84381.40600 - 46.836769\,t + \cdots\,,\ \epsilon_{A\ \mathrm{IAU\ 1976}} = 84381.448 - 46.8150\,t + \cdots\,, \qquad (1)$$

where the obliquity is expressed in arcseconds and time is measured in Julian centuries since J2000.0; and by $\dot{J}_2 = -3 \times 10^{-9}\, cy^{-1}$ with $J_2 = 1.08263558 \times 10^{-3}$.

These modifications provide corrections to IAU 2000A nutation model (Capitaine et al. 2005), in such a way that the total nutation in longitude $\Delta\psi$ and in obliquity $\Delta\epsilon$ can be written as

$$\Delta\psi = \left(\frac{\sin \epsilon_{0\ \mathrm{IAU\ 2000}}}{\sin \epsilon_{0\ \mathrm{IAU\ 2006}}} + t\, \frac{\dot{J}_2}{J_2} \right) \Delta\psi_{\mathrm{IAU\ 2000A}},\ \Delta\epsilon = \left(1 + t\, \frac{\dot{J}_2}{J_2} \right) \Delta\epsilon_{\mathrm{IAU\ 2000A}}, \tag{2}$$

where ϵ_0 designates the value of the obliquity at J2000. They consist in a global rescaling of IAU 2000A nutation model, common for all the terms of the trigonometrical polynomial in which nutation is usually expanded. Besides, let us note that the nutations in obliquity are no affected by the change in ϵ_0 .

Numerically (Capitaine et al. 2005), the derived corrections greater than 1 microarcsecond (μas) are

$$d_{\epsilon_A} \Delta\psi = -8.1 \sin \Omega - 0.6 \sin (2F - 2D + 2\Omega)\,, \tag{3}$$

for the change in the value of the obliquity at J2000.0, and

$$\begin{array}{rcl} d_{j_2} \Delta\epsilon & = & -25.6\ t \cos \Omega - 1.6\ t \cos (2F - 2D + 2\Omega)\,, \\ d_{j_2} \Delta\psi & = & +47.8\ t \sin \Omega + 3.7\ t \sin (2F - 2D + 2\Omega) + 0.6\ t \sin (2F + 2\Omega) - 0.6\ t \sin (2\Omega)\,, \end{array} \tag{4}$$

due to the time rate of the J_2 parameter. In these expressions F denotes the mean argument of latitude of the Moon; D the mean elongation of the Moon from the Sun, and Ω the mean longitude of the Moon's mean ascending node, which in combination with the mean anomalies of the Moon, l, and the Sun, l' form the fundamental arguments of nutation. Usually (e.g., Kinoshita 1977), they are represented as

$$\Theta_i = m_{i1} l + m_{i2} l' + m_{i3} F + m_{i4} D + m_{i5} \Omega,\ m_{ij} \in \mathbb{Z}. \tag{5}$$

In spite of the smallness of corrections (3) and (4), they are considered in some relevant sources for Earth Rotation standards like IERS Conventions (2010), sec. 5.6.3; the Explanatory Supplement to the Astronomical Almanac (2013), p. 211; or Standards of Fundamental Astronomy (SOFA) routines (e.g., Hohenkerk 2012). When incorporated to IAU 2000A they give raise to the IAU $2006/2000\mathrm{A}_{\mathrm{R06}}$ precession–nutation model, although there is no official nomenclature to designate it (Urban & Kaplan 2012).

In this work we aim at providing an alternative, independent, and analytical derivation of the adjustments of nutation series induced by the obliquity value changes and the J_2 time rate. That is to say, our goal is to check the validity and scope of the adjustment nutation formulas given by Equations (2).

2. ANALYTICAL MODELING

The contributions to be discussed are very small, so, at this stage we will consider a first order theory and a rigid–like symmetrical Earth model, which incorporates the J_2 time rate.

To obtain their analytical expressions, we will make use of the Hamiltonian formalism of the rigid Earth (Kinoshita 1977). The Hamiltonian is given by the sum of the rotational kinetic energy and the first order term of the gravitational disturbing potential due to the Moon and the Sun, conveniently expressed in terms of the Andoyer canonical variables. Then, it is possible to construct an approximate analytical first order solution with the help of a canonical perturbation method. Following this procedure, with the proper modifications over Kinoshita's scheme, we have derived the nutation of the figure axis.

Our preliminary results show that at the μas level the adjustments can be modeled through the motion of the angular momentum axis (Poisson terms), whose expressions are much simpler than the figure axis ones and almost independent of the Earth model at the first order. In this way, the adjustments due to a change of the value in ϵ_A can be derived from the formulas

$$\Delta\psi = \frac{k}{\sin \epsilon_0} \sum_{i \neq 0} \frac{1}{\bar{n}_i} B_i' (\epsilon_0) \sin \Theta_i,\ \Delta\epsilon = -k \sum_{i \neq 0} \frac{m_{i5}}{\bar{n}_i} \frac{B_i (\epsilon_0)}{\sin \epsilon_0} \cos \Theta_i. \tag{6}$$

For the sake of conciseness we have just displayed the corrections of quasi–periodic nature, omitting mixed secular terms proportional to t that also must be considered. In Eqs. (6), k is a constant proportional

to the dynamical ellipticity of the Earth H_d (Kinoshita 1977), and $\bar{n}_i$ is approximately equal to the time derivative of Θ_i (Eq. 5). The functions $B_i(\epsilon_0)$ are defined as

$$B_i(\epsilon_0) = -\frac{1}{6}A_i^{(0)}\left(3\cos^2\epsilon_0 - 1\right) + \frac{1}{2}A_i^{(1)}\sin 2\epsilon_0 - \frac{1}{4}A_i^{(2)}\sin^2\epsilon_0, \tag{7}$$

the coefficients $A_i^{(0,1,2)}$ depending on the orbital motion of the external bodies. A list of the arguments Θ_i and the numerical value of $A_i^{(0,1,2)}$ are given in (Kinoshita 1977).

With respect to the modifications coming from the J_2 time rate, let us point out that it induces a time dependence in dynamical ellipticity of the Earth that, in turn, is translated to the constant k (Eqs. 6). In this way, we can write

$$k = k_0\left(1 + t\frac{\dot{H}_d}{H_d}\right) \simeq k_0\left(1 + t\ \frac{\dot{J}_2}{J_2}\right), \tag{8}$$

appearing in the nutations the following mixed secular terms

$$\Delta\psi = \frac{k_0}{\sin\epsilon_0}\left(1 + t\ \frac{\dot{J}_2}{J_2}\right)\sum_{i\neq 0}\frac{1}{\bar{n}_i}B_i'(\epsilon_0)\sin\Theta_i\ ,\ \Delta\epsilon = -k_0\left(1 + t\ \frac{\dot{J}_2}{J_2}\right)\sum_{i\neq 0}\frac{m_{i5}}{\bar{n}_i}\frac{B_i(\epsilon_0)}{\sin\epsilon_0}\cos\Theta_i. \tag{9}$$

However, the precise computation of this effect by means of the perturbation method also leads to the appearance of some quasi–periodic out of phase terms. They are given by

$$\Delta\psi = \frac{k_0}{\sin\epsilon_0}\frac{\dot{J}_2}{J_2}\sum_{i\neq 0}\frac{B_i'(\epsilon_0)}{\bar{n}_i^2}\cos\Theta_i,\ \Delta\epsilon = k_0\frac{\dot{J}_2}{J_2}\sum_{i\neq 0}\frac{m_{i5}}{\bar{n}_i^2}\frac{B_i(\epsilon_0)}{\sin\epsilon_0}\sin\Theta_i. \tag{10}$$

To be consistent in the development of the theory, the inclusion of the J_2 time rate forces one to consider also the time rate existing in the orbital coefficients $A_i^{(0,1,2)}$. This dependence is due to the secular variation of sun eccentricity (Kinoshita 1977). From a theoretical point of view, its treatment is quite similar to that of J_2 time rate, providing also out of phase nutations and mixed secular terms with analytical expressions similar to Equations (9) and (10).

3. DISCUSSION

Next, we will evaluate numerically the corrections to IAU 2000A nutations induced by the adoption of IAU 2006 precession model through the former analytical equations, and compare them with those derived in Capitaine et al. (2005). As regard to the adjustments due to the change in the ϵ_0 value, Equations (6) lead to a global rescaling in longitude arising from the denominator of the first factor $\sin\epsilon_0$. The obliquity is not affected, since for it the denominator is equal to 1. These results are equivalently to Equations (2), with $\dot{J}_2 = 0$, taken from Capitaine et al. (2005).

However, accordingly to Equations (6), this is not the only change, since all nutational terms in longitude and obliquity also depend on ϵ_0. In the case of the longitude this dependence just comes from $B_i'(\epsilon_0)$, whereas for the obliquity it is originated from the functions $B_i(\epsilon_0)$ and $\sin\epsilon_0$. Hence, a variation in the value of ϵ_0 will affect in a different way the amplitude of each argument Θ_i of the nutation series.

This new contribution has not only theoretical interest, but also a practical one, since the derived numerical values are of the same order of magnitude as those given in Eqs. (3). Namely, with a cutoff of 0.5 μas, we have found

$$d_{\epsilon_A}\Delta\epsilon = +0.8\cos\Omega,\ d_{\epsilon_A}\Delta\psi = -7.5\sin\Omega + 0.5\sin\left(2F - 2D + 2\Omega\right). \tag{11}$$

As we have mentioned Eqs. (6) are complemented with other providing mixed secular terms. These terms are not present in Capitaine et al. (2005), although one has an amplitude greater than 1 μas

$$d_{\epsilon_A}\Delta\psi = -8.1\ t\sin\Omega \tag{12}$$

In the case of the corrections induced by the J_2 rate, by comparing Eqs. (9) with Eqs. (6), it turns out that the modifications in the nutations are mixed secular terms proportional to $\dot{J}_2/J_2$ both in longitude and obliquity, in agreement with the results derived in Capitaine et al. (2005) given in Eqs. (2). We can

conclude that, strictly speaking, those formulas are only valid for the first order terms of the nutations, since some second order terms are proportional to k^2 and the rescaling factor to be considered would be different from $\dot{J}_2/J_2$ (see Eq. 8).

We have also derived that the inclusion of the J_2 time rate is responsible for some out of phase terms, not considered previously (Eqs. 10). Numerically, the terms relevant at the μas level are

$$d_{\dot{J}_2}\Delta\epsilon = -0.8\sin\Omega,\ d_{\dot{J}_2}\Delta\psi = -1.4\cos\Omega. \tag{13}$$

An analogous consideration must be done for consistency with respect to the time rate of the orbital coefficients $A_i^{(0,1,2)}$, what gives the correction

$$d_{\dot{A}}\Delta\psi = -0.5\cos l'. \tag{14}$$

4. SUMMARY

We have developed an analytical model that provides the adjustments of IAU 2000A nutation model (Mathews et al. 2002) stemming from the updating to IAU 2006 precession model (Capitaine et al. 2003). Our results present some differences with respect to the computed ones in Capitaine et al. (2005) that are included in IERS Conventions (2010) and SOFA routines (e.g., Hohenkerk 2012).

In the case of the variation due to the change in the obliquity value, it seems that the global rescale (Eqs. 2, with $\dot{J}_2 = 0$) must be supplemented with additional terms of similar magnitude that affect both longitude and obliquity (Eqs. 11). There are also new secular mixed terms not considered previously (Eqs. 12). Therefore, the total *new corrections* (in μas) to be considered for this variation are given by the sum of Eqs. (11) and (12), providing

$$d_{\epsilon_A}\Delta\epsilon = +0.8\cos\Omega,\ d_{\epsilon_A}\Delta\psi = -7.5\sin\Omega + 0.5\sin(2F - 2D + 2\Omega) - 8.1\ t\sin\Omega. \tag{15}$$

The secular mixed terms emerging from the time rate of J_2 are in agreement with those determined previously (Eqs. 4). However, we have found new out of phase terms (Eq. 13) that, in combination with those coming from the time rate of $A_i^{(0,1,2)}$ (Eq. 14), give the *new contributions* (in μas)

$$d_{\dot{J}_2+\dot{A}}\Delta\epsilon = -0.8\sin\Omega,\ d_{\dot{J}_2+\dot{A}}\Delta\psi = -1.4\cos\Omega - 0.5\cos l'. \tag{16}$$

The source of the discrepancies between our treatment and that of Capitaine et al. (2005) should be further investigated, introducing the corresponding modifications into the corrections considered in current standards and models.

Acknowledgements. This work has been partially supported by Generalitat Valenciana project GV/2014/072 and the Spanish MINECO projects AYA2010-22039-C02-01 and AYA2010-22039-C02-02.

5. REFERENCES

Capitaine, N., Wallace, P. T., & Chapront, J., 2003, Expressions for IAU 2000 precession quantities, A&A, 412, 567–586.

Capitaine, N., Wallace, P. T., & Chapront, J. 2005, Improvement of the IAU 2000 precession model, A&A, 432, 355–367.

Hohenkerk, C. Y., 2012, SOFA and the algorithms for transformations between time scales & between reference systems, Proceedings of the Journées 2011 "Systèmes de référence spatio-temporels", H. Schuh, S. Böhm, T. Nilsson, & N. Capitaine (eds.), Vienna University of Technology, 21–24.

IERS Conventions (2010), 2010, G. Petit & B. Luzum (eds.), IERS Technical Note 36.

Kinoshita, H., 1977, Theory of the rotation of the rigid earth, Celest. Mech., 15, 277–326.

Lieske, J. H., Lederle, T., Fricke, W., & Morando, B., 1977, Expressions for the precession quantities based upon the IAU 1976 system of astronomical constants, A&A, 58, 1–16.

Mathews, P. M., Buffet, B.A., & Herring T.A., 2002, Modeling of nutation and precession: New nutation series for nonrigid Earth and insights into the Earth's interior, J. Geophys. Res., 107, 10.1029

The Explanatory Supplement to the Astronomical Almanac, 3rd edition, 2013, S. E. Urban & P. K. Seidelmann (eds.), University Science Books.

Urban, S. E. & Kaplan, G. H., 2012, Nomenclature for the current precession and nutation models, Proceedings of the Journées 2011 "Systèmes de référence spatio-temporels", H. Schuh, S. Böhm, T. Nilsson, & N. Capitaine (eds.), Vienna University of Technology, 270–271.

Wahr, J. M., 1981, The forced nutations of an elliptical, rotating, elastic and oceanless earth, Geophys. J. R. Astron. Soc. , 64, 705–727.

ROTATIONAL-OSCILLATORY MOTIONS OF THE DEFORMABLE EARTH IN THE SHORT TIME INTERVALS

A.S. FILIPPOVA[1], Yu.G. MARKOV[1], L.V. RYKHLOVA [2]
[1] Moscow Aviation Institute
Volokolamskoe shosse, 4, Moscow, 125080, Russia
e-mail: filippova.alex@gmail.com
[2] Institute of Astronomy, Russian Academy of Sciences
ul. Pyatnitskaya, 48, Moscow, 109017, Russia

ABSTRACT. Based on the celestial mechanics' methods namely the spatial version of the problem of the Earth-Moon system in the gravitational field of the Sun a mathematical model of the rotary-oscillatory motion of the elastic Earth is developed. It is shown that the perturbing component of the gravitational-tidal forces normal to the lunar orbit's plane is responsible for some short-term perturbations in the Moon's motion. With the aid of the numerical-analytical approach a comparison between the constructed model and the high-frequency International Earth Rotation and Reference System Service (IERS) measurements is made.

1. INTRODUCTION

Mathematical models of rotary-oscillatory motion of the deformable Earth specify its rotational parameters using the observation data with a high degree of accuracy and provide their reliable prognosis. These models are an essential research tool for investigating a number of problems in astrometry, geodynamics, and navigation. The construction of theoretical models is accomplished through a compromise between the complexity of the model and the measuring accuracy. A meticulous analysis of the basis functions and their number, as well as the parameter settings, is required. A theoretical model should qualitatively and quantitatively correspond to astrometric data of IERS observations [1] and contain only a few essential unknown parameters (low-parametric model) subject to small variations due to nonstationary perturbing factors. These factors can be singled out and taken into account on short timescales.

2. MATHEMATICAL MODEL OF THE ROTARY-OSCILLATORY MOTION OF THE EARTH

We described the rotational motions of the deformable Earth and the oscillations of the Earth's pole using a simplified mechanical model for the viscoelastic rigid body of the Earth [2-4]. To take into account gravitational-tidal effects, we assumed the Earth to be axially symmetric ($(C-A)/B \approx 1/292$, $(B-A)/C \approx 2 \cdot 10^{-6}$) and two-layered, i.e., consisting of a rigid (spherical) core and a viscoelastic mantle. We could have used some more complex model. However, employing anymore complex figure for the Earth is not justified, since we cannot determine the geometrical and physical parameters of the Earth with the required accuracy and completeness via a statistical processing of indirect data from seismic measurements. We adhere to the idea that the complexity of a model must strictly correspond to the problem formulated and to the accuracy of the data used. To construct a model for the polar oscillations, we can determine a small number of some mean (integrated) characteristics of the inertia tensor. Comparison with measurements and further analysis indicate that our simplifications are justified [3, 4].

The proposed dynamical model contains relatively few parameters (it is a few-parameter model) that can be determined from observations; the model enables us to reliably interpret and the statistical characteristics of oscillations in the Earth orientation parameters (EOP), and also to forecast these [2, 3] over comparatively long time intervals (reaching several years). Using the dynamic Euler-Liouville equations with the varying inertia tensor and taking into account estimates of its terms in the harmonic composition of the variations in the tidal coefficients after averaging over the Earth's proper rotation, we obtain a set of differential equations for the EOP in the tied reference frame; i.e., for the quantities x_p,

y_p, $l.o.d.(t)$, $UT1-TAI$

$$
\begin{aligned}
&\dot{x_p} + Ny_p + \sigma_x x_p = \kappa_q r_0^2 + M_p^{S,L} + \\
&+ \varepsilon \left[2r_0 \delta r(t) \kappa_q + r_0^2 \sum_{i=1}^{N} A_i \cos(2\pi\vartheta_i \tau + \alpha_i) + \Delta M_p^{SL}(\Omega, I) \right], \\
&\dot{y_p} - Nx_p + \sigma_y y_p = -\kappa_p r_0^2 + M_q^{S,L} + \\
&+ \varepsilon \left[-2r_0 \delta r(t) \kappa_p + r_0^2 \sum_{i=1}^{N} B_i \cos(2\pi\vartheta_i \tau + \beta_i) + \Delta M_q^{SL}(\Omega, I) \right], \\
&\left[1 + \varepsilon \sum_{i=1}^{N} C_i \cos(2\pi\vartheta_i \tau + \gamma_i) \right] \frac{d}{dt} l.o.d.(t) = -\frac{D_0}{r_0} M_r^{S,L} + \\
&+ \varepsilon \left[\sum_{i=1}^{N} \frac{C_i}{2\pi\vartheta_i} \sin(2\pi\vartheta_i \tau + \gamma_i) l.o.d.(t) - \frac{D_0}{r_0} \Delta M_r^{SL}(\Omega, I) \right], \\
&\frac{d\left[UT1 - TAI\right](t)}{dt} = -D_0^{-1} l.o.d.(t), \quad D_0 = 86400.
\end{aligned}
\tag{1}
$$

Here, the unknown coefficients must be determined from a least-squarse fit to the IERS data; ϑ_j – are the frequencies of the variations of the inertia tensor (it is assumed that the frequencies ϑ_j can be corrected during the numerical modeling) [3]; the tidal coefficients $\kappa_{p,q}$ are periodic functions with the frequencies ϑ_j; $\Delta M_{p,q,r}^{SL}(\Omega, I)$ are additional terms of the specific lunar-solar gravitational-tidal moment in the spatial Earth-Moon system subject to the solar gravitation [3]; Ω is the longitude of the ascending node of the lunar orbit; I is the ecliptic inclination of the plane of the lunar orbit.

Let us present the results of our numerical simulations of the intrayear variations in the tidal irregularity of the Earth's axial rotation without taking the additional lunar perturbations into the account. Fig. 1 presents the theoretical curve for the interpolation (from September 1, 2010 to September 1, 2011)

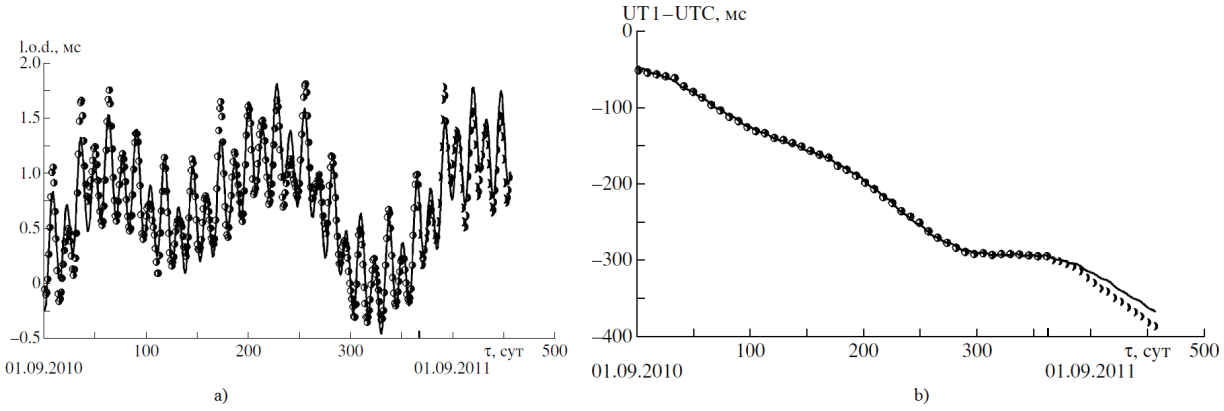

Figure 1: Interpolation (01.09.2010-01.09.2011)and forecast till 01.12.2011 in comparison between the observation data and (a) the variations of the length of the day $l.o.d.$ (b) time correlation $UT1-UTC$.

and forecast (from September 2, 2011 to December 1, 2011) of the variations (a) in the length of the day $l.o.d.$ and (b) in $UT1-UTC$. The solid curves show the theoretical model, while the points and half-moons show the IERS data compared to the model interpolation and forecast, respectively.

3. SPECIFIC FEATURES OF THE PROBLEM APPLIED TO SHORT-TERM FORECASTING OF THE EOP

Improving the coordinate-time support for satellite navigation requires high-precision forecasting of the Earth's rotation (the trajectory of the pole and UT1) over short time intervals. Extremely accurate forecasting for intervals lasting from 1 - 2 to 20 - 30 days could be of interest for various applications.

Constructing mechanical models capable of forecasting small-scale, high-frequency polar oscillations and irregularities in the Earth's rotation over short time intervals and explaining the observed irregularities encounter significant difficulties. Below, we consider some difficulties encountered in modeling the EOP (the polar oscillations and variations in the length of the day) using celestial mechanics; i.e., the spatial problem of the Earth-Moon system subject to the Sun's gravitation. The equations for the perturbed motion of the node of the lunar orbit Ω_M and the ecliptic inclination of the plane of the lunar orbit I take the form [3]:

$$\begin{aligned} \frac{d\Omega_M}{dt} &= -\frac{3}{4}\frac{n_S^2}{n_M}\left[1-\cos 2(l_M-\Omega_M)-\cos 2(l_S-\Omega_M)+\cos 2\lambda\right], \\ \frac{dI}{dt} &= \frac{3}{4}\frac{n_S^2}{n_M}\sin I\left[\sin 2(l_S-\Omega_M)-\sin 2(l_M-\Omega_M)+\sin 2\lambda\right]. \end{aligned} \tag{2}$$

Here, n_M and n_S are the sidereal mean motions of the Moon and the Sun; l_M, l_S are the mean longitudes of the Moon and Sun; $(l_M-\Omega_M)$ is the angle between the Moon and the ascending node of the lunar orbit, and $\lambda=(n_M-n_S)t+\lambda_0$ is the difference between the lunar and solar longitudes. The quantity λ is not a linear function of time, since the mean motion n_M is subject to at least periodic changes. The observational data can be used to determine the argument 2λ.

The right-hand sides of (2) contain both long-period and short-period terms, which contribute with fairly small amplitudes. Note that the period of the terms with the argument $2(\lambda-(l_M-\Omega_M))=-2(l_s-\Omega_M)$ reaches 173 days (the time between two successive solar passages across the line of nodes). The terms with the arguments 2λ and $2(l_M-\Omega_M)$ have periods of half the synodic ($T_M=29.53$ days) and zodiacal ($T_{\Omega_M}=27.21$ days) periods, respectively. The zodiacal lunar period mainly determines the variation in the lunar latitude.

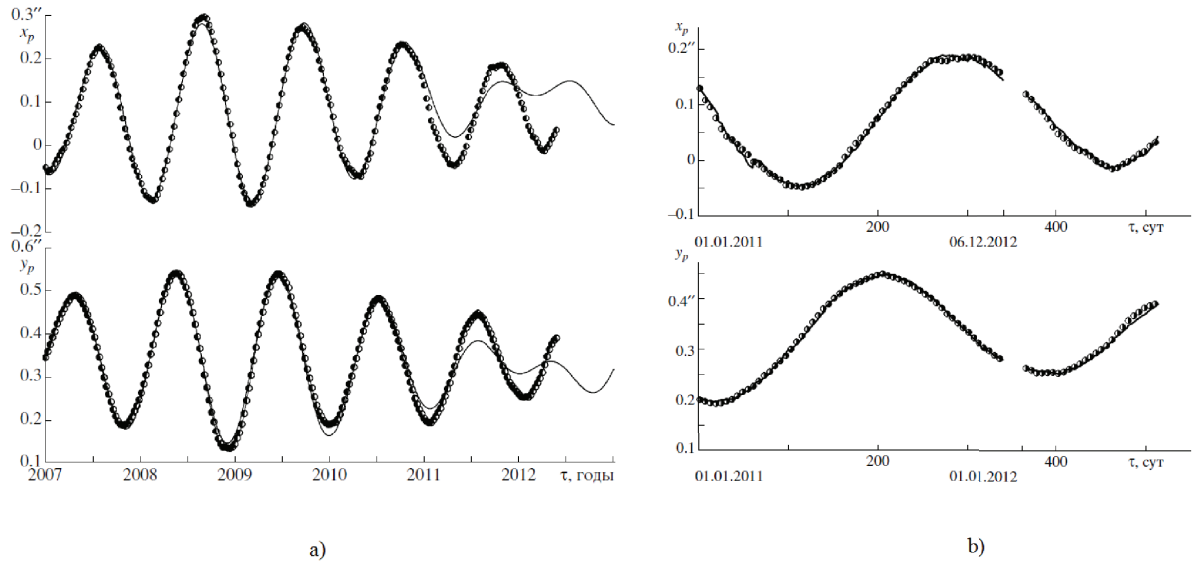

Figure 2: a) Interpolation (2007-2010) and forecast (01.01.2011-28.05.2012) of the oscillations of the Earth pole coordinates x_p, y_p without taking additional lunar perturbations into account; b) twenty-day forecasts for the coordinates of the Earth pole x_p, y_p corresponding to the time interval 01.01.2011–06.12.2011, and forecasts for the interval 01.01.2012–28.05.2012 considering the additional lunar harmonics.

Taking into account quasi-periodic lunar effects, analysis of the amplitude-frequency and amplitude-phase characteristics of the EOP reveals more complex small-scale features contained in the observations [1]. For that purpose we used refined equations for the oscillatory motions of the pole that include those terms on the righthand side of (1) containing the small parameter ε:

$$\begin{aligned}
&\Delta\dot{x}_p + N\Delta y_p = \varepsilon\left[2r_0\delta r(t)\kappa_q + r_0^2\sum_{i=1}^{N} A_i\cos(2\pi\vartheta_i\tau+\alpha_i) + \Delta M_p^{SL}(\Omega, I)\right],\\
&\Delta\dot{y}_p - N\Delta x_p = \varepsilon\left[-2r_0\delta r(t)\kappa_q + r_0^2\sum_{i=1}^{N} B_i\cos(2\pi\vartheta_i\tau+\beta_i) + \Delta M_q^{SL}(\Omega, I)\right],\\
&x_p = \bar{x}_p + \Delta x_p, \qquad y_p = \bar{y}_p + \Delta y_p.
\end{aligned} \tag{3}$$

Here, $\bar{x}_p$, $\bar{y}_p$ are the solutions for the equations (1) without taking into account the small parameter terms; Δx_p and Δy_p are additional terms for the coordinates of the Earth pole considering additional high-frequency lunar perturbations; A_i, B_i, α_i and β_i are unknown coefficients; and $\Delta M_{p,q}^{SL}$ are terms of higher orders of smallness in the expansion of the lunar-solar gravitational-tidal moment for the spatial problem considered.

The effect of the high-frequency model oscillations (3) is clearly seen in the beats (at the minimum amplitude of polar oscillations), when the irregular perturbations become clearer and comparatively stronger (fig. 2). The points show the IERS data while the solid curves show (a) a four-year interpolation and two-year forecast without taking additional lunar perturbations into account; (b) a twenty-day forecast for the Earth pole coordinates x_p, y_p considering high-frequency additional lunar harmonics. This approach requires a thorough analysis of the oscillations included in both the main and high-frequency models in the interpolation intervals. Our numerical simulations testify to the qualitative and quantitative improvement of the model.

4. REFERENCES

International Earth Rotation and Reference Systems Service - IERS Annual Reports http://www.iers.org/IERS/EN/Publications/AnnualReports/AnnualReports.html

L. D. Akulenko, Yu. G. Markov, V. V. Perepelkin, L. V. Rykhlova, A. S. Filippova, 2013, "Rotational-oscillatory variations in the Earth rotation parameters within short time intervals", Astron. Rep., 57(5), doi: 10.1134/S106377291304001X

L.D. Akulenko, S.S. Krylov, Yu.G. Markov, V.V. Perepelkin, 2012, "Modeling of the Earth's rotary-oscillatory motions in the three-body problem: interpolation and prognosis", Doklady Physics, 57(10), doi: 10.1134/S1028335812100059

L.D. Akulenko, Yu. G. Markov, V. V. Perepelkin, L. V. Rykhlova, 2008, "Intrayear Irregularities of the Earth's Rotation", Astron. Rep., 52(7), doi: 10.1134/S106377290807007X

A GENERALIZED THEORY OF THE FIGURE OF THE EARTH: APPLICATION TO THE MOMENT OF INERTIA AND GLOBAL DYNAMICAL FLATTENING

C.L. HUANG[1], C.J. LIU[1,2], Y. LIU[1]
[1]Key Laboratory of Planetary Sciences, Shanghai Astronomical Observatory, CAS
80 Nandan Road, Shanghai 200030, China
e-mail: clhuang@shao.ac.cn
[2] Univ. of Chinese Academy of Sciences, Beijing, China

ABSTRACT. A new integrated formula to obtain the equilibrium figures interior the earth to third-order accuracy is developed. In this formula, both the direct and indirect contribution of the anti-symmetric crust layer are included, as result, all the non-zero order and odd degree terms are included in the spherical harmonic expression of the equilibrium figures.

The moments of inertia (MoI: A,B,C) and global dynamic flattening (H) are important quantities in research of rotating Earth. Accurate precession and gravity observations give $H_{obs} \approx 1/305.5$, while its value from rotating symmetric PREM model and traditional theories of equilibrium figures, H_{PREM}, is about 1.1% less than H_{obs}.

Using our new potential theory and replacing the homogenous outermost crust and oceanic layers in PREM with CRUST2.0 model data, we recalculate the geometrical flattening profile of the Earth interior and finally get the values of MoI and H. Their consistencies with observations are significantly improved.

1. A GENERALIZED THEORY OF THE FIGURE OF THE EARTH

If the isotropic Earth is in hydro-static-equilibrium (HSE) and rotating constantly, the interior surfaces of equi-density, of equi-potential and of equi-pressure will coincide with each other. Let r denote the distance between a point in the Earth and the geocenter, and s is the mean equi-volumetric radii of the equi-potential surface cross this point. The traditional expression of r is:

$$r(s,\theta) = s\left[1 + \sum_{n=0}^{\infty} s_{2n}(s) P_{2n}(\cos\theta)\right] \tag{1}$$

The gravity (gravitational plus centrifugal) potential at this point can be expressed as:

$$W(s,\theta) = \frac{4}{3}\pi G\bar{\rho}s^2 \sum_{n=0}^{\infty} F_{2n}(s) P_{2n}(\cos\theta) \tag{2}$$

where $F_{2n}(s)$ is function of $s_{2n}(s)$, and $\bar{\rho}$ is the mean density of the whole Earth.
Because W is a constant and does not depend on the colatitude θ on any given level surface, then $F_{2n} = 0\,(n \neq 0)$. If truncated at $n = 1$, 2 or 3, it degenerates respectively to Clairaut equation (first-order accuracy), Darwin - de Sitter equation (second-order accuracy), and *Denis′* formula(*Denis*, 1989) (third-order accuracy). In eq(1), there is no term of longitude ϕ nor of odd degree P_{2n+1}, meaning that the equilibrium figures of the Earth must be rotational symmetric and equatorial (south-north) symmetric, and their details can be found in *Moritz (1990)*, *Denis (1989)* and *Denis et al. (1997)*. However, our real earth is not of so beautiful symmetric, instead, of topography and the geoid is also non-symmetric. In order to calculate, in more general, the figures of internal equi-potential surface and the geoid which are non-symmetric (Figure 1), we should replace eq.(1) by following equation:

$$r(s,\theta,\phi) = s\left[1 + \sum_{n=0}^{\infty}\sum_{m=-n}^{n} H_n^m(s) Y_n^m(\theta,\phi)\right], \tag{3}$$

All the non-zero order and odd degree terms are included in the above spherical harmonic expression of the equilibrium figures. N has to be truncated in practice and it takes 6 in this work.

From the figures of internal equi-density surfaces given by above, i.e., the density distribution inside the whole earth is known, the moments of inertia (MOI: A,B,C) and global dynamic flattening $H = \frac{(C-(A+B)/2)}{C}$ can then be calculated easily.

We consider the earth model that is the same of PREM (*Dziewonski & Anderson, 1981*), but the curst layer of depth of 71km in PREM is replaced by CRUST2.0 model (*Chulick et al., 2002*; *Mooney et al., 1998*) that consists of 7 different layers of depth up to 70.137 km and of $2^o * 2^o$ grid. One constrain is required here that the total mass of the earth be conserved. And the most part under the 71 km depth is still assumed to be in HSE. The inhomogeneous crust layer considered here is shown in following skeptical Figure 2.

Two effects of the loading of the anti-symmetric crust layer are considered here:

1) direct effect: the crust inhomogeneous mass change directly the gravitational potential for all mass points interior in different ways, therefore, the figures of equi-potential surfaces interior are changed without symmetries;

2) indirect effect: As the figures of equi-density surfaces (then the density distribution) interior are changed by the direct effect, the gravitational potential of other locations (outside/inside this surface) are changed, and the figures of equi-potential surfaces all through the earth are then changed again. This process is reciprocal and needs iteration, and will finally reach equilibrium. And all the figures can be gotten in more general, i.e., without any symmetry (Figure 3).

Incorporating both the direct effect and indirect effect, the gravity potential $W(s)$ crossing the point $r(s,\theta,\phi)$ becomes

$$\begin{aligned} W &= V_{in} + V_{out} + Z \\ &= GE_0(s) + G\bar{\rho}s^2 \sum_{n=0}^{\infty}\sum_{m=-n}^{n} Y_n^m \left[m_h p_{n,m} + \sum_{l=0}^{\infty} \frac{s^{l-2}}{\bar{\rho}} u_{l,n,m} + \sum_{l=1}^{\infty} g_{l,n,m} + \sum_{l=0}^{\infty} f_{l,n,m} \right] \\ &= GE_0(s) + G\bar{\rho}s^2 \sum_{n=0}^{\infty}\sum_{m=-n}^{n} Y_n^m(\theta,\phi)\Xi_n^m(s), \end{aligned} \tag{4}$$

where

$$\Xi_n^m = m_h p_{n,m} + \sum_{l=0}^{\infty} \frac{s^{l-2}}{\bar{\rho}} u_{l,n,m} + \sum_{l=1}^{\infty} g_{l,n,m} + \sum_{l=0}^{\infty} f_{l,n,m} \tag{5}$$

where, $p_{n,m}, u_{l,n,m}, g_{l,n,m}$ and $f_{l,n,m}$ are complex functions of all $H_n^m(s_i)$ (not only the figure coefficients of the surface of equivalent radii s, but also the figure coefficients of all other surfaces of equivalent radii s_i). And the final equations of the figure coefficients $H_n^m(s_i)$ can be expressed in following form, with the requirement that the gravity potential $W(s)$ on the equilibrium surface should be independent on the the colatitude θ and longitude ϕ,

$$\begin{cases} \Xi_n^m + (-1)^m \Xi_n^{-m*} = 0 \\ n = 1, \ldots, \infty \\ m = 0, \ldots, n \end{cases} \tag{6}$$

In eqs.(6), there are $\sum_{n=1}^{N}(n+1) = \frac{1}{2}N(N+3)$ equations for each surface (or layer), while do not forget that the earth model is discreted by K layers and K is usually bigger than several hundreds.

The detail derivation of the formula, the procedure to solve the complex equation system of the spherical harmonics of the figures, and its validation by comparisons with other results when we degenerate this theory to that of *Denis* by keeping only H_2^0, H_4^0 and H_6^0, will be presented in another paper, and we present here only the primary results.

2. APPLICATION TO THE CALCULATION OF THE MOMENT OF INERTIA AND GLOBAL DYNAMICAL FLATTENING

The moments of inertia (MoI: A, B, C) and global dynamic flattening (H) are important quantities in research of rotating Earth. Very accurate precession and gravity observations give $H_{obs} \approx 1/305.5$, while

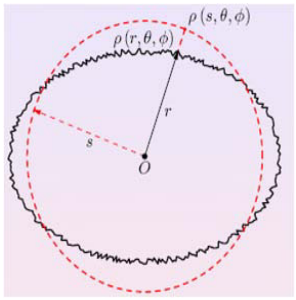

Figure 1: Expression of a general figure of equipotential surface interior the earth

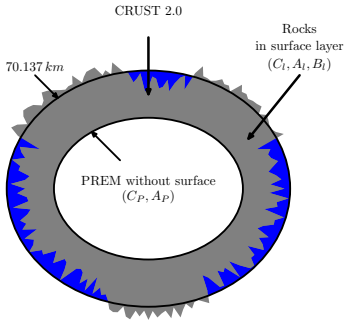

Figure 2: Skeptical earth model containing PREM and CRUST2.0

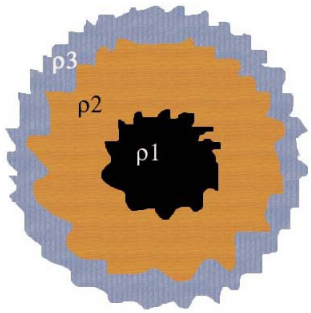

Figure 3: Skeptical plot of the change of all surfaces interior caused by both direct and indirect effects of the inhomogeneous crust

its value from rotating symmetric PREM model and traditional theories of equilibrium figures mentioned above, H_{PREM}, is about 1/308.5, approximately 1.1% less than H_{obs}. This phenemenoun and its possible interpretation have been discussed in several papers (e.g., *Defraigne (1997)*, *Dehant & Capitaine (1997)*, *Mound et al. (2003)*, etc.) with various kinds of assumptions, we will not discussed them here and readers are recommended to refer them for detail. In this paper, we skip these assumptions and tend to search reason from the theory of the earth figure itself.

The direct contribution of the crust layer to MoI and H are listed as following:

Table 1: Direct contribution of the crust layer to MoI and H

	A $10^{37}\ kg \cdot m^2$	B $10^{37}\ kg \cdot m^2$	C $10^{37}\ kg \cdot m^2$	1/H
PREM(-71km)	7.7087284	7.7087284	7.7336553	
CRUST2.0	0.2949340	0.2947971	0.2956929	
TOTAL	8.0036624	8.0035255	8.0293482	311.7674842

While, if considering both direct and indirect effect of the crust layer, the value of MoI and H are listed below:

Table 2: Direct & indirect contributions of the crust layer to MoI and H

	A $10^{37}\ kg \cdot m^2$	B $10^{37}\ kg \cdot m^2$	C $10^{37}\ kg \cdot m^2$	1/H
PREM(All)	8.0112987	8.0112987	8.0373506	308.5131401
PREM(-71km)	7.7164775	7.7164823	7.7418221	
CRUST2.0	0.2948918	0.2947790	0.2957497	
TOTAL	8.0113693	8.0112612	8.0375718	306.1164533

From above tables, if consider the direct effect of the curst layer only, H deviates from the H_{obs} more; but incorporating the indirect effect can reduce significantly the difference between H and H_{obs} from 1.1% to 0.2%, while we do not need any other assumptions in this work.

3. SHORT SUMMARY

In this short paper, the principle of a generalized theory to obtain the equilibrium figures interior the earth to fully third-order accuracy is presented. In this theory, both the direct and indirect contribution

of the anti-symmetric crust layer are included, as result, all the non-zero order and odd degree terms are included in the spherical harmonic expression of the equilibrium figures.

As a application (as well as a validation) of this new theory, we recalculate the moments of inertia (MoI) and global dynamic flattening (H), and it shows that the consistencies of H with observations H_{obs} are significantly improved from 1.1% to 0.2%, without any other assumption.

Acknowledgements. This work was supported by the National Natural Science Foundation of China (11073044/11373058/11133004) and Shanghai Key Laboratory of Space Navigation and Position Techniques.

References

[1] Chulick, G.S., Mooney, W.D., and Detweiler, S., 2002, Crust'02: A new global model. American Geophysical Union, Fall Meeting, S61A-1108

[2] Defraigne, P., 1997, Geophysical model of the dynamical flattening of the Earth in agreement with the precession constant, Geophys. J. Int., 130, 47–56.

[3] Dehant, V., and Capitaine, N., 1997, On the precession constant: values and constraints on the dynamical ellipticity; link with oppolzer terms and tilt-over-mode, Celest. Mech. Dyn. Astr. , 65, 439–458.

[4] Denis, C., 1989, Physics and Evolution of the Earth's Interior. Elsevier, 1989.

[5] Denis, C., Rogister, Y., Amalvict, M., Delire C., Denis A., and Munhoven, G., 1997, Hydrostatic flattening, core structure, and translational mode of the inner core. Phys. Earth Planet. Interior, pp. 195–206.

[6] Dziewonski, A.M., and Anderson, D.L., 1981, Preliminary reference earth model. Physics of the Earth and Planetary Interiors, pp 297–356

[7] Liu, Y., and Huang, C.L., 2008, Direct contribution of the surface layers to the Earth dynamical flattening. Proceedings IAU Symposium No.248, 2007, pp 403–404.

[8] Mooney, W.D., Laske, G., and Guy, M.T., 1998,, CRUST5.1: A global crustal model at $5^\circ \times 5^\circ$, J. Geophys. Res., 103, 727–746.

[9] Moritz, H., 1990, The figure of the earth: theoretical geodesy and the earth's interior, Karlsruhe: Wichmann

[10] Mound, J.E., Mitrovica, J.X., and Forte, A.M., 2003, The equilibrium form of a rotating earth with an elastic shell. Geophys. J. Int., 152, 237–241.

CONSTRUCTION OF THE NEW HIGH-PRECISION EARTH ROTATION SERIES AT LONG TIME INTERVALS

V.V. PASHKEVICH
Central (Pulkovo) Astronomical Observatory of RAS
Pulkovskoe shosse, 65/1, 196140, St.Petersburg, Russia
e-mail: pashvladvit@yandex.ru

ABSTRACT. In the previous investigation (Pashkevich, 2013) the high-precision Rigid Earth Rotation Series (designated RERS2012) dynamically adequate to the JPL DE406/LE406 (Standish, 1998) ephemeris over 2000 and 6000 years were constructed. The main aim of present research is improvement of the Rigid Earth Rotation Series RERS2012 by using the JPL DE422/LE422 (Folkner, 2011) ephemeris, and as a result of the construction of the new high-precision Rigid Earth Rotation Series dynamically adequate to the JPL DE422/LE422 ephemeris over 2000 and 6000 years. The discrepancies between the high-precision numerical solutions and the semi-analytical solutions of the rigid Earth rotation problem with respect to the fixed ecliptic of epoch J2000 are investigated by the least-squares method and by the spectral analysis methods. The problem is solved only for the relativistic (Kinematical) case in which the geodetic perturbations (the most essential relativistic perturbations) in the Earth rotation are taken into account.

1. INTRODUCTION

The present research is the continuation of the investigation of the rigid Earth rotation at long time intervals (Pashkevich, 2013). The purposes of this studies are construction of the new high-precision Rigid Earth Rotation Series RERS2013 dynamically adequate to the JPL DE422/LE422 ephemeris over 2000 and 6000 years and comparison of new solution RERS2013 with the previous solution RERS2012 (Pashkevich, 2013). The dynamics of the rotational motion of the rigid Earth is studied numerically by using Rodrigues-Hamilton parameters over 2000 and 6000 years. The numerical solution of the problem is obtained by solving the Lagrange differential equations of the second kind for the rigid Earth rotation with respect to the fixed ecliptic and equinox of epoch J2000 (Pashkevich, 2013). The orbital motions of the disturbing celestial bodies are defined by the DE422/LE422 ephemeris. These investigation is carried out for the relativistic (Kinematical) case, in which the geodetic perturbations (the most essential relativistic perturbations) in the Earth rotation are taken into account. The mathematical model of the problem is described in detail in the paper (Pashkevich, 2013).

2. ALGORITHMS AND RESULTS

The results of the numerical solutions of the problem are compared with the semi-analytical solutions of the rigid Earth rotation RERS2012. The residuals of these comparison are studied by means the iterative algorithm:

1. Numerical solution of the rigid Earth rotation is implemented with the quadruple precision of calculations. The initial conditions are computed by the semi-analytical solution of the rigid Earth rotation (RERS2012). Discrepancies between the numerical solution and the semi-analytical solution are obtained in Euler angles over all investigation time interval with one-day spacing (presented in Figure 1). The expressions for these discrepancies are as follows

$$\left.\begin{aligned}
\Delta\psi &= \sum_{k=0}^{6}\psi_k t^k + \sum_j\sum_{k=0}^{4}[\psi_{Sjk}\sin(\nu_{j0}+\nu_{j1}t) + \psi_{Cjk}\cos(\nu_{j0}+\nu_{j1}t)]t^k \\
\Delta\theta &= \sum_{k=0}^{6}\theta_k t^k + \sum_j\sum_{k=0}^{4}[\theta_{Sjk}\sin(\nu_{j0}+\nu_{j1}t) + \theta_{Cjk}\cos(\nu_{j0}+\nu_{j1}t)]t^k \\
\Delta\phi &= \sum_{k=0}^{6}\phi_k t^k + \sum_j\sum_{k=0}^{4}[\phi_{Sjk}\sin(\nu_{j0}+\nu_{j1}t) + \phi_{Cjk}\cos(\nu_{j0}+\nu_{j1}t)]t^k
\end{aligned}\right\}, \quad (1)$$

where ψ is the longitude of the ascending node of the Earth's dynamical equator on the fixed ecliptic J2000; θ is the angle of the inclination of the Earth's dynamical equator to the fixed ecliptic J2000; ϕ is the proper rotation angle of the Earth between the ascending node of the Earth's dynamical equator and the principal axis of the minimum moment of inertia; ν_{j0}, ν_{j1} are the phases and the frequencies of the corresponding semi-analytical solutions, respectively; $j = 1, ..., 4113$; t is the time in the Julian days; ψ_k, θ_k, ϕ_k are the coefficients of the secular terms; $\psi_{Sjk}, \theta_{Sjk}, \phi_{Sjk}, \psi_{Cjk}, \theta_{Cjk}, \phi_{Cjk}$ are the coefficients of the periodic and Poisson terms.

2. Investigation of the discrepancies is carried out by the least squares method and by the spectral analysis method (Pashkevich and Eroshkin, 2005). The set of the frequencies of the semi-analytical solution is used without change. Only the coefficients of the periodical terms and the coefficients of the Poisson terms are improved. The secular, periodic and Poisson terms representing the new high-precision rigid Earth rotation series $\mathrm{RERS2013}_i$ (where i is the number of iteration) are determined:

$$\left.\begin{aligned}
\psi_{\mathrm{RERS2013}_i} &= \Delta\psi_{i-1} + \psi_{\mathrm{RERS2013}_{i-1}} \\
\theta_{\mathrm{RERS2013}_i} &= \Delta\theta_{i-1} + \theta_{\mathrm{RERS2013}_{i-1}} \\
\phi_{\mathrm{RERS2013}_i} &= \Delta\phi_{i-1} + \phi_{\mathrm{RERS2013}_{i-1}}
\end{aligned}\right\}, \quad (2)$$

where $\psi_{\mathrm{RERS2013}_0} = \psi_{\mathrm{RERS2012}}$, $\theta_{\mathrm{RERS2013}_0} = \theta_{\mathrm{RERS2012}}$ and $\phi_{\mathrm{RERS2013}_0} = \phi_{\mathrm{RERS2012}}$.

3. Numerical solution of the rigid Earth rotation is constructed anew with the new initial conditions, which are calculated by $\mathrm{RERS2013}_i$.

4. Steps 2 and 3 are repeated till the assumed convergence level has been achieved.

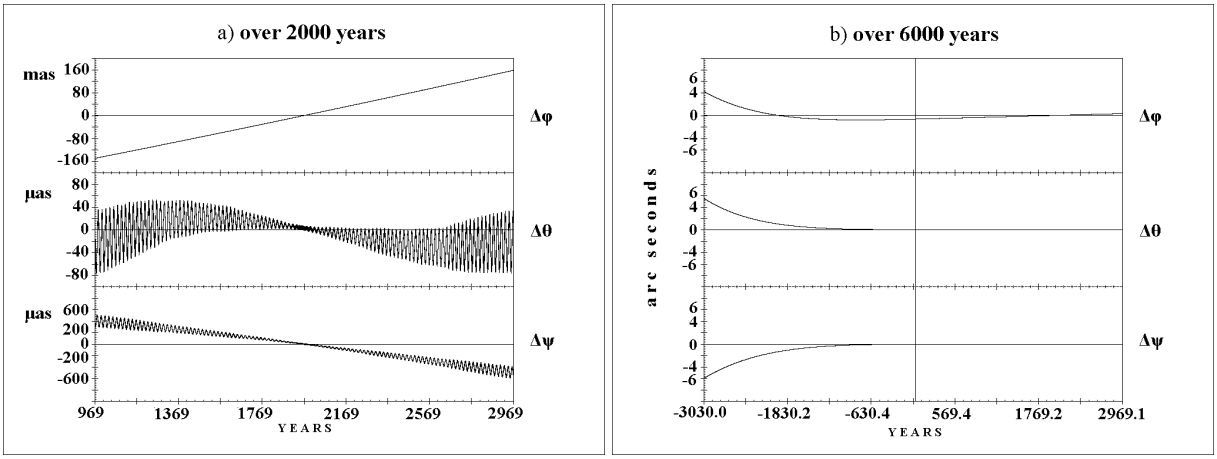

Figure 1: Discrepancies between the numerical and RERS2012 semi-analytical solutions of the Earth rotation (dynamically adequate to the DE406/LE406 ephemeris)

At first this investigation is carried out on 2000 years time interval. In Figure 1a the discrepancies are depicted between the numerical and RERS2012 over 2000 years. The secular trend does not surpass 600 μas over 2000 years for ψ and 160 mas over 2000 years for ϕ. The behavior of $\Delta\theta$ residuals are only periodic character and do not exceed 80 μas over 2000 years. The convergence level was achieved after

application of the third iteration of the iterative algorithm. So, the process of the iterative algorithm was finished at this step. As a result, the Rigid Earth Rotation Series (RERS2013) was constructed, which is dynamically adequate to the DE422/LE422 ephemeris over 2000 years. The discrepancies between the new numerical solutions and the semi-analytical solutions of RERS2013 do not surpass 4 μas over 2000 year time interval (presented in Figure 2).

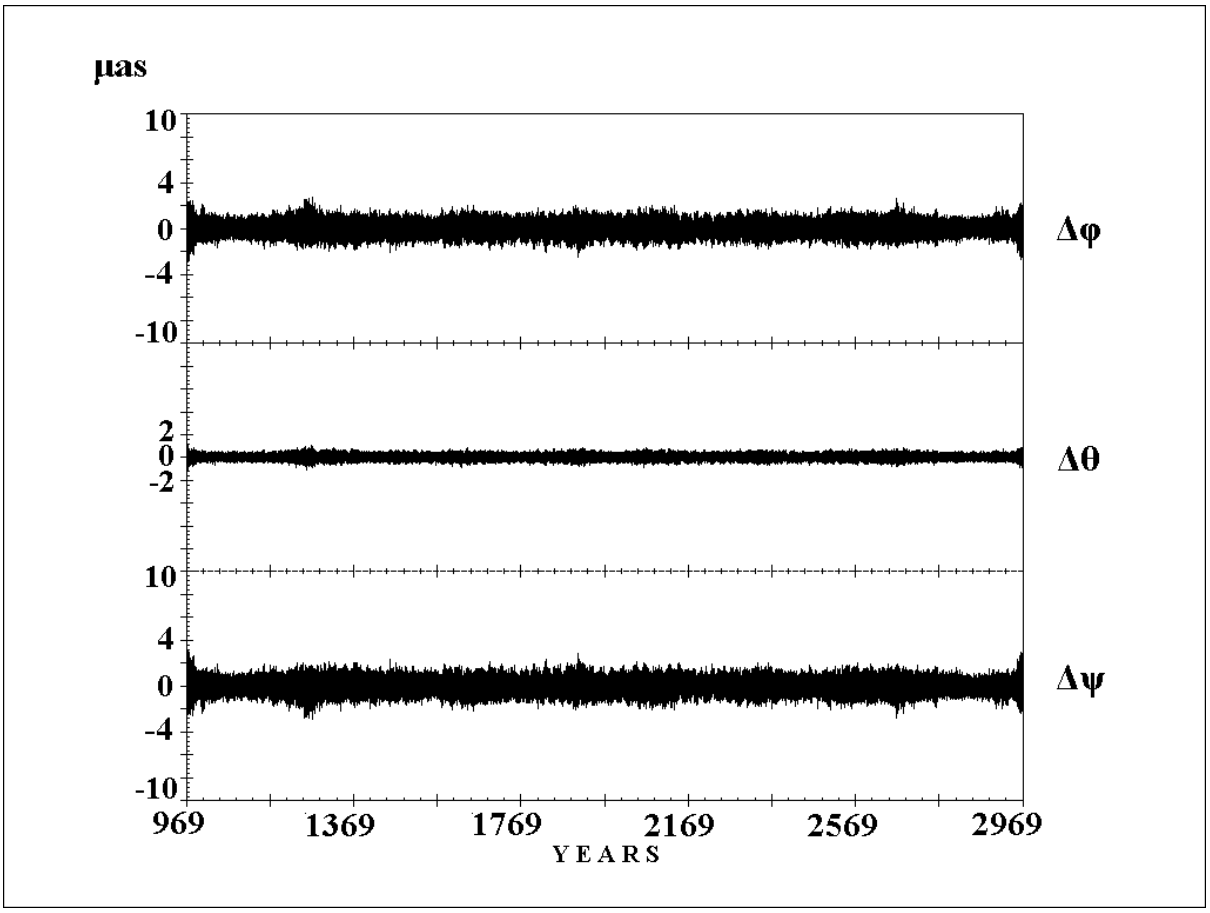

Figure 2: Discrepancies between the numerical and RERS2013 semi-analytical solutions of the Earth rotation (dynamically adequate to the DE422/LE422 ephemeris) over 2000 years after applied 3rd iterations of the iterative algorithm

This investigation is finished at 6000 years time interval. In Figure 1b the discrepancies are depicted between the numerical and RERS2012 over 6000 years. The secular trend in all Euler angles does not surpass 6 arc seconds over 6000 years. After application of the third iteration of the iterative algorithm, the convergence level was achieved and the process of the iterative algorithm was finished at this step. As a result, the Rigid Earth Rotation Series (RERS2013) was constructed, which is dynamically adequate to the DE422/LE422 ephemeris over 6000 years. The discrepancies between the new numerical solutions and the semi-analytical solutions of RERS2013 do not surpass 1 mas over 6000 year time interval (presented in Figure 3).

Thus, the result of the comparison on 2000 and 6000 years demonstrates a good consistency of RERS2013 series with the DE422/LE422 ephemeris.

3. CONCLUSION

As the results of this investigation, the new improved high-precision Rigid Earth Rotation Series RERS2013 dynamically adequate to the DE422/LE422 ephemeris over 2000 and 6000 years have been constructed. The series RERS2013 include about 4113 periodical and Poisson terms terms (without attempt to estimate new sub-diurnal and diurnal periodical and Poisson terms). The sub-diurnal and diurnal periodical and Poisson terms have not been investigated in this study. Therefore, they entered

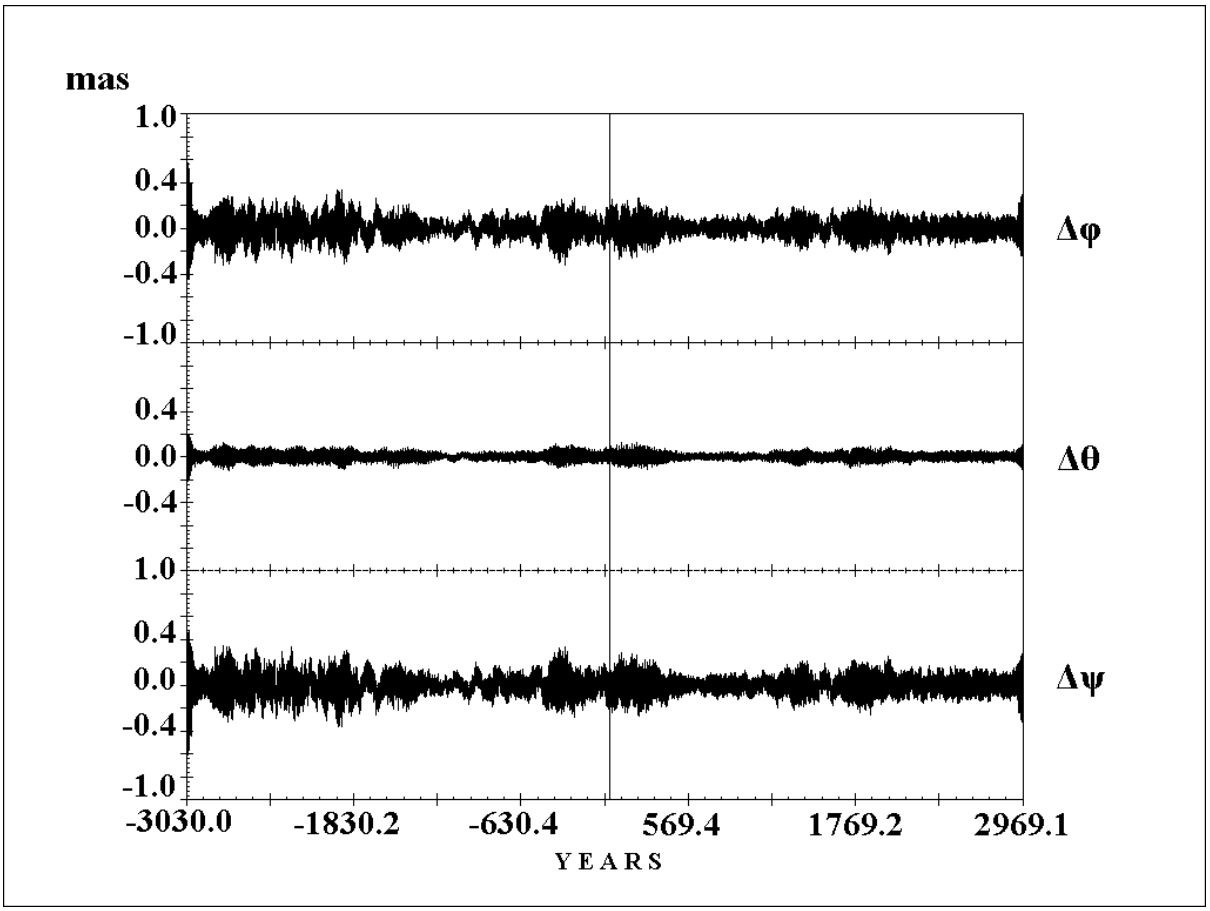

Figure 3: Discrepancies between the numerical and RERS2013 semi-analytical solutions of the Earth rotation (dynamically adequate to the DE422/LE422 ephemeris) over 6000 years after applied 3rd iterations of the iterative algorithm

into new solutions RERS2013 without change from RERS2012. The discrepancies between the numerical solution and RERS2013 do not surpass: 4 μas over 2000 years, 1 mas over 6000 years. It means a good consistency of the RERS2013 series with the DE422/LE422 ephemeris. The RERS2013 series is more accurate than the RERS2012 series, which is dynamically adequate to the DE406/LE406 ephemeris.

Acknowledgements. The investigation was carried out at the Central (Pulkovo) Astronomical Observatory of the Russian Academy of Science and the Space Research Centre of the Polish Academy of Science, under a financial support of the Cooperation between the Polish and Russian Academies of Sciences, Theme No 34. For the participation in the Journées 2013 was received the Grant of the Paris Observatory from French Ministry of Research (MESR), in the framework of the programme ACCES.

4. REFERENCES

Standish, E.M., 1998, "JPL Planetary and Lunar Ephemerides, DE405/LE405",JPL IOM 312.F-98-048.

Pashkevich, V.V. and Eroshkin, G.I., 2005, "Choice of the optimal spectral analysis scheme for the investigation of the Earth rotation problem", in Proc. of Journés 2005: Earth dynamics and reference systems: five years after the adoption of the IAU 2000 Resolutions (Space Research Centre of Polish Academy of Sciences, Warsaw, Poland, 19-21 September 2005), pp. 105–109.

Folkner W.F., 2011, "JPL Planetary and Lunar Ephemerides : Export Information" http://iau-comm4.jpl.nasa.gov/README.html

Pashkevich V.V., 2013,"Construction of the numerical and semi-analytical solutions of the rigid Earth rotation at a long time intervals", *Artificial Satellites*, Warszawa, Vol. 48, No. 1, (DOI: 10.2478/arsa-2013-0003), pp. 25–37.

FREE CORE NUTATION – POSSIBLE CAUSES OF CHANGES OF ITS PHASE AND AMPLITUDE

C. RON[1], J. VONDRÁK[1], Y. CHAPANOV[2]
[1] Astronomical Institute, Academy of Sciences of Czech Republic
Boční II, 14100 Prague 4, Czech Republic
e-mail: ron@asu.cas.cz, vondrak@ig.cas.cz
[2] National Institute of Geophysics, Geodesy and Geography, Bulgarian Academy of Sciences
Acad. G. Bonchev Str. Bl. 3, Sofia 1113, Bulgaria
e-mail: astro@bas.bg

ABSTRACT. The comparison of the observed series of celestial pole offsets (CPO) and integrated atmospheric and oceanic excitation functions fitted on the different intervals corresponding with the epochs of geomagnetic jerks, major earthquakes in the last decade and natural or systematic jumps in the observed CPOs is performed.

1. INTRODUCTION

In our previous solutions, where we used integration of atmospheric and oceanic excitation function in the Celestial Reference System (Vondrák and Ron, 2010, Ron and Vondrák 2011), the comparison with the observed celestial pole offsets (CPO) became out-of-phase after some time. We suppose that other excitation could have effect and should be taken into account. Before studying the possible mechanism of the excitations of geomagnetic jerks, strong earthquakes and other events, we simply divide the integration into shorter intervals defined by these events to see possible improvements in the fit of the integrated series to the observed CPO.

2. THE METHOD USED

The excitations of the Earth rotation in celestial reference frame (nutation) by atmosphere and ocean are studied by using Brzeziński's broad-band Liouville equations (Brzeziński, 1994):

$$\ddot{P}-i(\sigma'_C+\sigma'_f)\dot{P}-\sigma'_C\sigma'_f P = -\sigma_C\left\{\sigma'_f(\chi'_p+\chi'_w)+\sigma'_C(a_p\chi'_p+a_w\chi'_w)+i[(1+a_p)\dot{\chi}'_p+(1+a_w)\dot{\chi}'_w]\right\}, \quad (1)$$

where $P = dX + idY$ is excited motion of Earth's spin axis in celestial frame (CRF), σ'_C, σ'_f are the complex Chandler and FCN frequencies in CRF, respectively, σ_C in terrestrial frame. The dimensionless constants are $a_{p,w}$ and χ'_p and χ'_w are the angular momentum excitation functions (presure and wind) in CRF. To solve the second order differential equation (1) we apply the substitution

$$y_1 = P, \quad \text{and} \quad y_2 = \dot{P} - i\sigma'_C P, \quad (2)$$

leading to the system of two ordinary differential equations for two complex functions y_1 and y_2:

$$\begin{aligned} \dot{y_1} &= i\sigma'_C y_1 + y_2 \\ \dot{y_2} &= i\sigma'_f y_2 - \sigma_C\left\{\sigma'_f(\chi'_p+\chi'_w)+\sigma'_C(a_p\chi'_p+a_w\chi'_w)+i[(1+a_p)\dot{\chi}'_p+(1+a_w)\dot{\chi}'_w]\right\}. \end{aligned} \quad (3)$$

To solve the system (3) we have to set up initial values

$$y_1(0) = P_0, \quad \text{and} \quad y_2(0) = i(\sigma'_f - \sigma'_C)P_0, \quad (4)$$

that are constrained so that the free Chandlerian motion disappears. The final choice of P_0 was done by repeating integration of (3) with different values P_0 to fit the integrated series to VLBI CPO observations so that it reaches a minimum rms difference. We applied 4-order Runge-Kutta numerical integration in

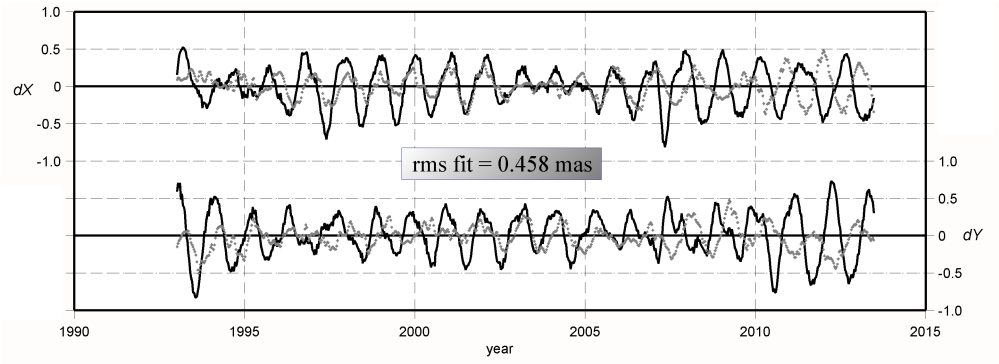

Figure 1: Observed and integrated celestial pole offsets with excitations based on ERA40 and operational model of atmosphere and ocean. The initial condition at 1993.0 only.

6-hour steps, using the procedure `rk4` from Numerical Recipes (Press et al., 1992), slightly modified for the complex domain.

3. THE DATA USED AND RESULTS

As series of observations we used the CPO from the IVS combined solution `ivs13q2X.eops` in the interval 1984.1–2013.5. The components of CPO dX and dY are given in unequally spaced intervals, (sometimes with outliers). We cleaned the data by removing CPO $>$ 1mas and cut the data before 1993.0. Then we added into the CPO the empirical Sun-synchronous correction that is applied in the MHB nutation theory to model the atmospheric and oceanic contribution (Mathews et al., 2002). Finally the series were interpolated to regular 10-day intervals using a filter to retain only periods between 180 and 6000 days (Vondrák, 1977).

As the geophysical excitations data we used the atmospheric angular momentum excitation function (AAM), both pressure and wind terms, of European Centre for Medium-Range Weather Forecasts (ECMWF) reanalysis ERA40. We used the reanalysis model before 2001 and operational model afterwards. The oceanic angular momentum excitation functions (OAMF), both matter and motion terms, of OMCT model in 1990.0–2013.5.0 (Dobslaw et al., 2010), driven by reanalysis atmospheric model ERA40 before 2001 and by operational model afterwards, were used. Both series were taken from Data Center of IERS and the data were cut before 1993.0.

Time series of AAM and OAM χ (in complex domain) were transformed from the terrestrial reference frame to the celestial one after Brzezinski et al. (2002) by using the complex decomposition at retrograde diurnal frequency $\chi' = -\chi e^{i\Phi}$, Φ is the Greenwich sidereal time. The long periodic behavior of the AAM and OAM functions become diurnal after applying the decomposition. Since we are interested in the long-periodic motion that is present in nutation, we applied the smoothing to remove periods shorter than 10 days and calculated their time derivatives needed for the integration.

We have done four solutions in total. First the solution with fixed initial values for the whole interval 1993–2013.5 was carried out. As seen in Fig. 1, the series become out-of-phase after 2007 and the rms fit reaches 0.46mas.

Geomagnetic jerks, which are observed as rapid changes in the geomagnetic field secular variations, are indicated as possible sources of Free Core Nutation excitation by Malkin (2013). We took the epochs of jerks from the paper at 1999.0, 2003.5 and 2007.5 to carry out the second solution. The resulting series are seen in Fig. 2. The agreement of the observed and integrated series is much better. The rms fit is equal to 0.25mas which is almost a half of that of the first solution.

The method of data and velocity jumps determination, based on the linear and parabolic trends in the integrated time series of CPO, is based on the method described in Chapanov et al. (this volume). It is sensitive to any impulse in the observed variations due to various geophysical processes or systematic data deviations. The method is very sensitive to small data jumps hidden inside the random noise and high frequency oscillations. The epochs of these jumps were found in 2004.3 and 2009.3. The solution is shown in Fig. 3.

In the last solution, shown in Fig. 4, we looked for the initial values in the epochs of major earthquakes

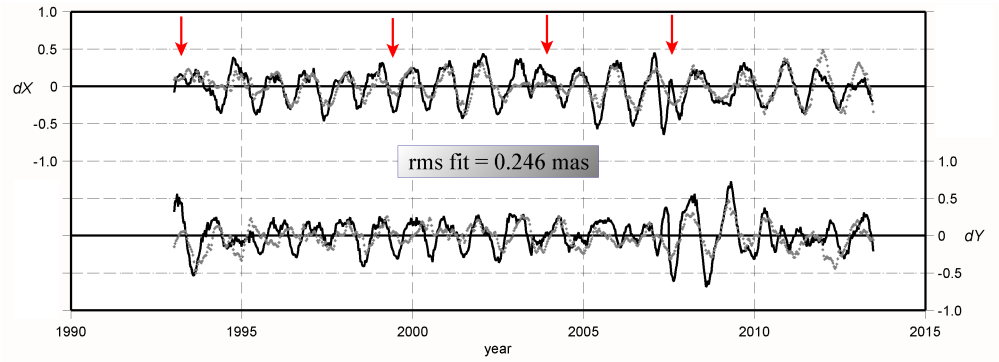

Figure 2: Observed and integrated celestial pole offsets with excitations based on ERA40 and operational model of atmosphere and ocean. The initial conditions at epochs of geomagnetic jerks after Malkin (2013).

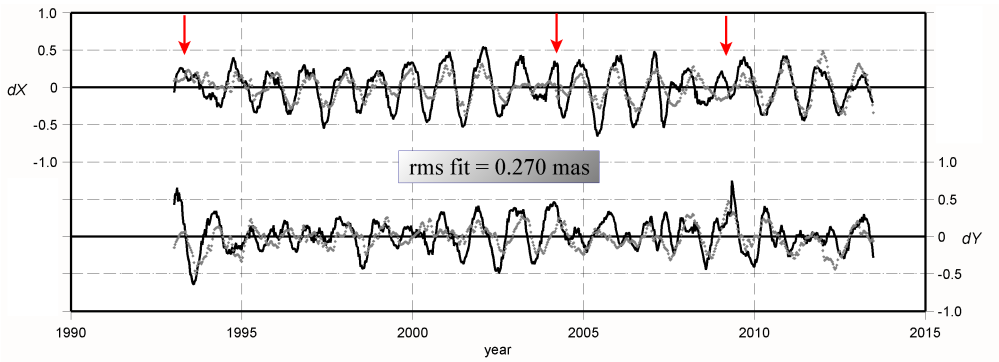

Figure 3: Observed and integrated celestial pole offsets with excitations based on ERA40 and operational model of atmosphere and ocean. The initial conditions at epochs of natural or systematic jumps in CPO derived after Chapanov et al. (this volume).

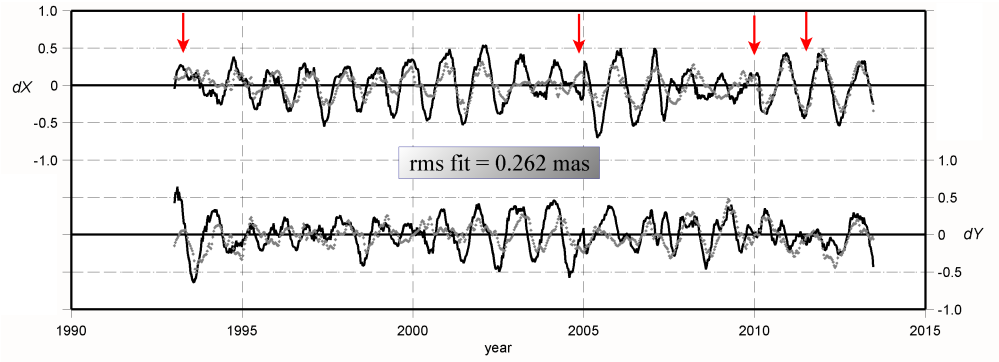

Figure 4: Observed and integrated celestial pole offsets with excitations based on ERA40 and operational model of atmosphere and ocean. The initial conditions at epochs of major earthquakes with $M_s > 8.8$.

larger than 8.8 magnitude scale during last decade. These are the Sumatra (2005.0), Chile (2010.2) and Japan (2011.9) earthquakes. The solutions are summarized in Table 1.

Table 1: Summarized results of all solutions; all values are in mas.

	interval	initial values	σ	$\overline{\sigma}$	shift
gm jerks	1993.0-1999.0	(-0.12; 0.41)	0.245	0.246	–
	1999.0-2003.5	(0.25; 0.26)	0.246		(0.09; 0.21)
	2003.5-2007.5	(0.02; 0.04)	0.248		(0.22; 0.29)
	2007.5-2013.5	(0.05;-0.32)	0.248		(0.19;-0.48)
jumps	1993.0-2004.3	(-0.12; 0.52)	0.279	0.270	–
	2004.3-2009.3	(-0.24; 0.19)	0.284		(-0.46;-0.19)
	2009.3-2013.5	(-0.18; 0.74)	0.228		(-0.03; 0.48)
earthquakes	1993.0-2005.0	(-0.10; 0.52)	0.286	0.262	–
	2005.0-2010.2	(0.33;-0.14)	0.276		(0.50;-0.20)
	2010.2-2011.9	(-0.28; 0.02)	0.158		(-0.35;-0.16)
	2011.9-2013.5	(0.35; 0.16)	0.189		(0.20; 0.07)

4. CONCLUSIONS

We detected considerable differences between ERA40 and ERAinterim in the wind term of AAM data (30% relative difference in amplitude of the semi-annual term of wind). Three different solutions were performed with the initial values valid in the intervals defined by consecutive dates of geomagnetic jerks, detected jumps in CPOs and large earthquakes. The solution with the geomagnetic jerks leads to the best agreement with observed CPO.

Acknowledgements. The paper was supported by grant No. 13-15943S awarded by the Grant Agency of the Czech Republic.

5. REFERENCES

Brzeziński, A., 1994, "Polar motion excitation by variations of the effective angular momentum function: II. Extended Model", Manuscripta Geodaetica, 19, pp. 157–171.

Brzeziński, A., Bizouard, C., Petrov, S., 2002, "Influence of the atmosphere on Earth rotation: what new can be learned from the recent atmospheric angular momentum estimates?", Surveys in Geophysics 23, pp. 33–69.

Chapanov, Y., Vondrák, J., Ron, C., Pachalieva, R., 2014, "Natural and systematic polar motion jumps", this volume.

Dobslaw, H., Dill, R., Grotzsch, A., Brzeziński, A., Thomas, M., 2010, "Seasonal polar motion excitation from numerical models of atmosphere, ocean, and continental hydrosphere", J. Geophys. Res.115, B10406, doi:10.1029/2009JB007127.

Malkin, Z., 2013, "Free Core Nutation and the geomagnetic jerks", J. Geodyn., in press, doi: 10.1016/ j.jog.2013.06.001

Mathews, P.M., Herring, T.A., Buffett, B.A., 2002, "Modeling of nutation and precession: New nutation series for nonrigid Earth and insights into the Earth's interior", J. Geophys. Res.(Solid Earth), 107(B4), doi:10.1029/2001JB000390.

Press, W.H., Teukolsky, S.A., Vetterling, W.T, Flannery, B.P, 1992, Numerical Recipes in Fortran 77. The Art of Scientific Computing, 2nd Edition, Cambridge University Press.

Ron, C., Vondrák, J., 2011, "Coherence between geophysical excitations and celestial pole offsets", Acta Geodyn. Geomater. Vol. 8, No. 3, pp. 243–247.

Vondrák, J., 1977, "Problem of smoothing of observational data II", Bull. Astron. Inst. Czechosl., 28, pp. 84–89.

Vondrák, J., Ron, C., 2010, "Study of atmospheric and oceanic excitations in the motion of Earth's spin axis in space", Acta Geodyn. Geomater. Vol. 7, No. 1, pp. 19–28.

STUDY OF THE PROGRADE AND RETROGRADE CHANDLER EXCITATION

L.V. ZOTOV[1,2], C. BIZOUARD[2],
[1] Sternberg Astronomical Institute of Moscow State University, Laboratory of Gravimetry
Universitetski pr., 13, Moscow, 119992, Russia
e-mail: tempus@sai.msu.ru
[2] SYRTE, Observatoire de Paris, CNRS, UPMC
61, Avenue de l'Observatoire, 75014, Paris, France
e-mail: christian.bizouard@obspm.fr

ABSTRACT. Observed motion of the Earth's rotation axis consists of components at both positive and negative frequencies. New generalized equations of Bizouard, which takes into account triaxiality of the Earth and asymmetry of the ocean tide, show that retrograde and prograde excitations are coupled. In this work using designed narrow-band filter and inversion we reconstruct geodetic excitation at the prograde and retrograde Chandler frequencies. Then we compare it with geophysical excitation, filtered out from the series of the oceanic angular momentum (OAM) and atmospheric angular momentum (AAM) for 1960-2000 yrs. Their sum coincides well with geodetic excitation only in the prograde Chandler band. The retrograde excitation coincides worse, probably in result of amplification of observational noises.

1. INTRODUCTION AND METHOD

Precise observations of Polar Motion (PM) require improvement of the theory, in particular, the introduction of triaxiality into the Euler-Liouville equations and considering the consequences for the ellipticity of the main wobbles, namely annual and Chandler (Gross, 2012). Despite Chandler excitation was found to be provided by the sum of AAM and OAM (Gross, 2000), the variability of the Chandler wobble amplitude over more then one century of PM observations still remains elusive. The Earth's PM is commonly modelled by the linear Liouville equation (Munk, MacDonald, 1960), (Lambeck, 1980)

$$\frac{i}{\sigma_c}\frac{dm(t)}{dt} + m(t) = \Psi(t), \tag{1}$$

where the complex Chandler angular frequency $\sigma_c = 2\pi f_c(1 + i/2Q)$ depends on real Chandler frequency $f_c = 0.8435$ yr^{-1} and quality factor $Q = 100$ (used below). In the dynamical system (1) the complex PM trajectory $m = m_1 + im_2$ is a filtered response to the input excitation $\Psi = \Psi_1 + i\Psi_2$. In (Bizouard, Zotov, 2013) new generalized version of Euler-Liouville equation was derived. The main equation has the form

$$(1-U)m + (1+eU)\frac{i}{\sigma_e}\frac{dm(t)}{dt} - Vm^* + eV\frac{i}{\sigma_e}\frac{dm^*(t)}{dt} = \Psi^{Pure}(t), \tag{2}$$

where parameter U depends on rheology, V characterises the asymmetric response, brought by triaxiality of the Earth and ocean pole tide, σ_e is the Euler frequency, asterisk $*$ means complex conjugation. The geophysical excitation free from rotational excitation stands in the left-hand side of (2), it is related to the effective excitation as $\Psi^{Pure}(t) = (1-U)\Psi(t)$.

Introducing the inverse symmetric transfer function

$$L^{-1}_{sym} = 1 + \frac{(1+eU)}{1-U}\frac{i}{\sigma_e}(i\omega) \approx 1 + \frac{i}{\sigma_c}(i\omega), \tag{3}$$

which coincides with the inverted transfer function of the classical equation (1), and asymmetric inverse transfer function

$$L^{-1}_{asym} = \frac{eV\frac{i}{\sigma_e}(i\omega) - V}{1-U}, \tag{4}$$

the equation (2) can be rewritten in the frequency domain as

$$L_{sym}^{-1}(\omega)\hat{m}(\omega) + L_{asym}^{-1}\hat{m}^*(-\omega) = \hat{\Psi}_{sym}(\omega) + \hat{\Psi}_{asym}(\omega) = \hat{\Psi}(\omega), \tag{5}$$

where $\hat{\cdot}$ is Fourier transform and the rule $\widehat{m^*}(\omega) = \hat{m}^*(-\omega)$ was applied. According to this rule, asymmetric operator (4) acts on the conjugated PM spectrum with inverted frequency $\hat{m}^*(-\omega)$.

In linear equation (1) the input at a particular frequency produces an output at the same frequency. In equation (2) the presence of both direct and conjugated variable m makes input at one frequency producing an output at both prograde and retrograde frequencies. Taking $\hat{m}$ at a particular frequency, we can reconstruct symmetric and asymmetric excitations for it (both of these excitations have prograde and retrograde components), using operators (3), (4), whose amplitude responses as function of ω are shown in Fig. 1, left.

In this work we shall use the new equation (5) to study Chandler wobble. In this framework the output at Chandler frequency is produced by input at prograde and retrograde frequencies. We will isolate the prograde and retrograde Chandler frequencies with the narrow-band Gauss filter modified according to the corrective filtering scheme proposed in (Zotov, Bizouard, 2012). The transfer function of the Gauss filter centered at prograde/retrograde Chandler frequency $\pm f_c$ is

$$L_h(f) = \exp\left(-\frac{(f \mp f_c)^2}{2f_0^2}\right). \tag{6}$$

The plots of these filters are also given in Fig. 1, left. The filter parameter (defining its width) was selected to be $f_0 = 0.04$ yr^{-1}. For the selected f_0 and f_c the filter (6) is narrow-band, not changing the phase of the signal. A time-window of more than 20 years extent corresponds to it. As the filtered signal undergo edge effects, it is not reliable for the first and last 10 years of the considered time interval. The trustful region is depicted by the red rectangle on the plots.

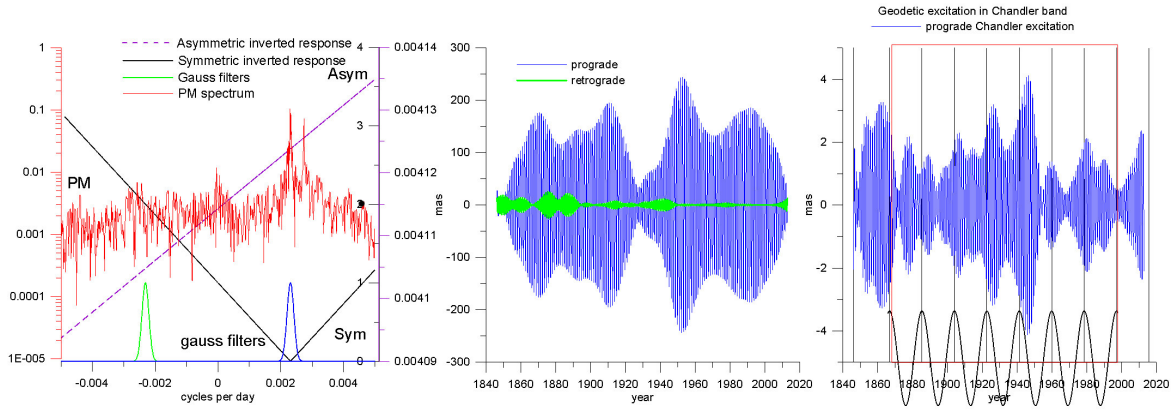

Figure 1: Amplitude responses of inverse operators $|L_{sym}^{-1}(\omega)|, |L_{asym}^{-1}(\omega)|$, prograde and retrograde Gauss filters, and PM spectrum (left). Filtered prograde and retrograde Chandler wobble (center). Prograde Chandler excitation obtained through classical inversion with $L_{sym}^{-1}(\omega)$ (right). Lunar 18.6-yr tide is shown along abscissa.

2. ANALYSIS AND COMPARISON OF RESULTS

Firstly, PM was filtered with Gaussian filter (6) in prograde and retrograde Chandler band (Fig. 1, center). Then the symmetric and asymmetric parts of geodetic excitation in prograde and retrograde Chandler band were obtained through multiplication by the symmetric (3) and asymmetric (4) inverse operators in frequency domain. The classical prograde Chandler excitation is shown in Fig. 1, right. As it was noted in (Zotov, Bizouard 2012), it has an amplitude modulation, often synchronous with the Lunar 18.6-yr tide.

The prograde and retrograde geodetic Chandler excitations are shown in Fig. 2, its classical (symmetric) part Ψ_{sym} is presented to the left, asymmetric part Ψ_{asym} is to the right. Asymmetric part of both prograde and retrograde component has an order of magnitude of 1 mas or less, and is thus

smaller than the symmetric contribution. Nevertheless, asymmetric part's contribution is significant at the contemporary level of observational precision (~ 0.05 mas). Retrograde asymmetric part with an amplitude up to 1 mas repeats the shape of the prograde Chandler wobble (Fig. 1, center), because it was obtained by multiplying this wobble by the linear function $L^{-1}_{asym}(\omega)$ (Fig. 1, left). It dominates in the total asymmetric excitation (sum of asymmetric prograde and retrograde parts) and is by far the most important innovation brought by the new equation (2).

On the contrary, the classical (symmetric) prograde Chandler excitation, as seen from Fig. 2, left, looks small over the background of retrograde part. The letter is especially large before 1900. It could be caused by the observational noise amplification at the retrograde Chandler frequency by the inverse operator $L^{-1}_{sym}(\omega)$, Fig. 1 left, where its amplitude response is quite large (if to compare with prograde). Then symmetric and asymmetric parts of geodetic excitation were added together and compared to the

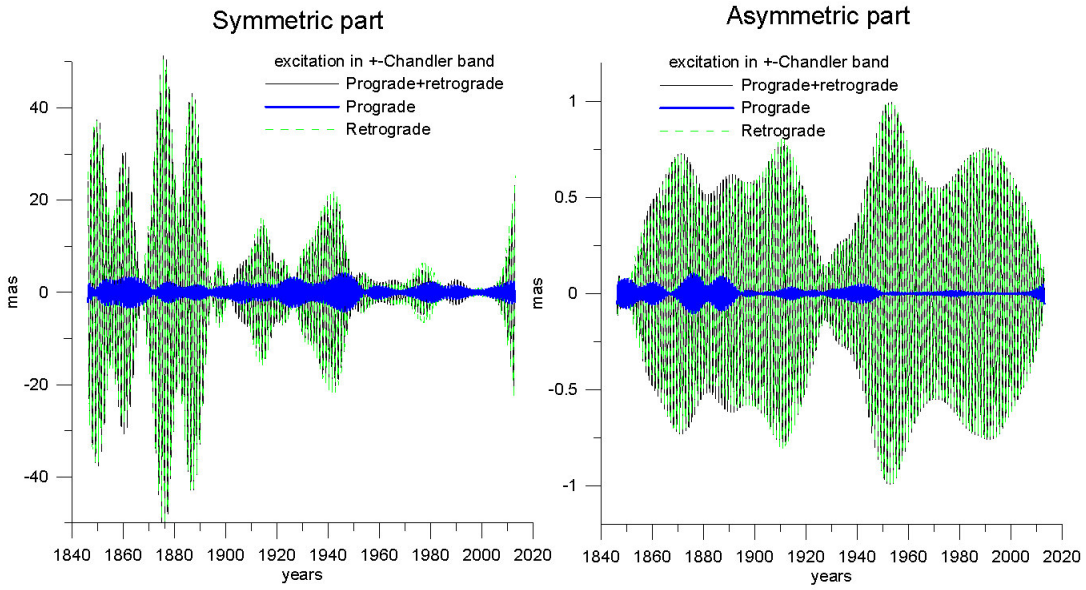

Figure 2: Symmetric Ψ_{sym} (left) and asymmetric Ψ_{asym} (right) components of the geodetic excitation at the prograde and retrograde Chandler frequencies.

geophysical excitation. The atmospheric contribution was obtained by filtering of NCEP/NCAR AAM combination of pressure (IB) and wind terms by the Gaussian filter (6) with parameters chosen above. Oceanic part of excitation was obtained in the same way from ECCO OAM time series, sum of bottom pressure and current terms. In Fig. 3 we plot geodetic and geophysical excitations in prograde (top) and retrograde (bottom) Chandler bands for AAM (left), OAM (center) and their sum (right). Despite the initial time series span is 1949-2010, we compare the results of filtering only for 1960-2000 (depicted with red rectangle) because of the edge effect. The agreement is good in the prograde band, while in the retrograde band OAM+AAM sum does not explain the geodetic excitation.

Table 1 presents the correlation coefficients between geodetic excitation and OAM, AAM, OAM+AAM geophysical excitations in prograde and retrograde Chandler bands. The misfit and worse correlation at the retrograde frequency could have several explanations. Firstly, as a result of observational noise amplifications during inversion. Secondly, by existence of some other factors, which excite the retrograde wobble. Finally, some defect could remain in the transfer function of dynamical equation (2), causing overestimation of the inverse amplitude response at this frequency. In any case, new equation (2) introduces an asymmetric part much smaller than the symmetric one, bringing the results presented in Fig. 3 and Table 1 in close agreement to what would have been obtained with classical modelling of Eq. (1).

3. CONCLUSION

We derived the geodetic excitation in prograde and retrograde Chandler band in the framework of generalised Euler-Liouville equation (2), accounting for asymmetry brought by ocean pole tide and triaxiality, and compared it to the geophysical excitation. Excitation at the retrograde Chandler frequency

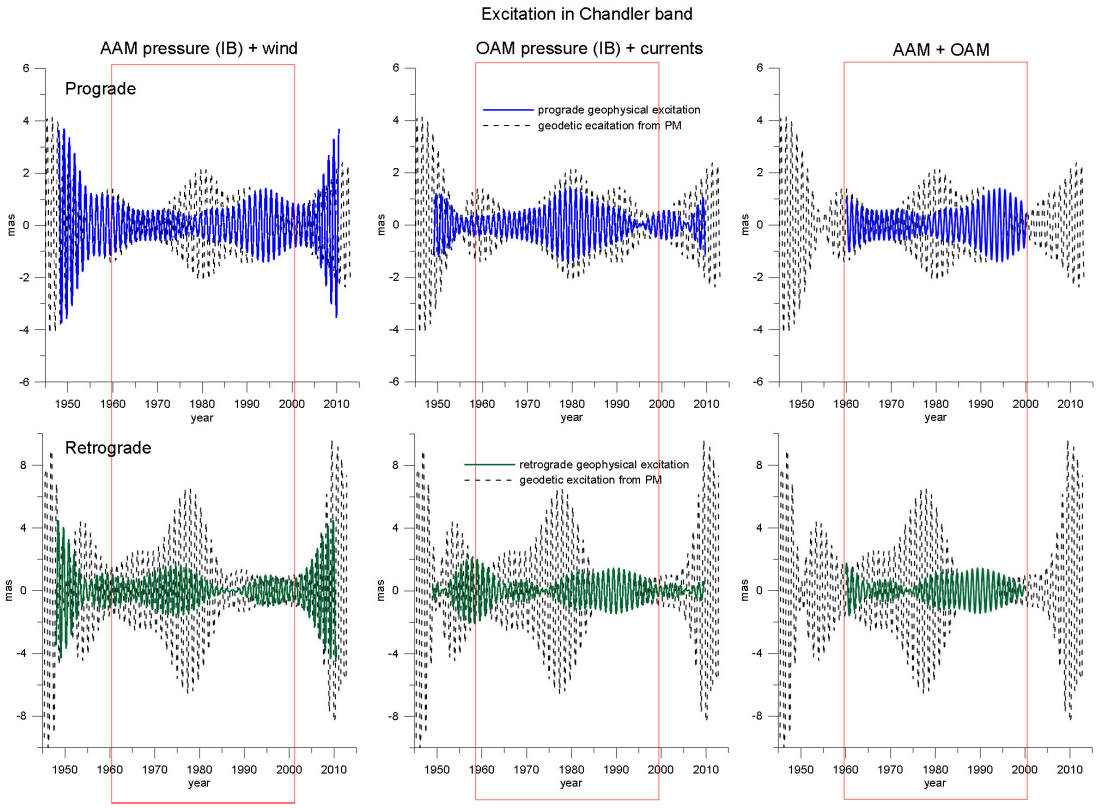

Figure 3: Comparison of geodetic excitation in prograde (top) and retrograde (bottom) Chandler frequency bands (sum of symmetric and asymmetric parts) with the geophysical excitation, related to AAM (left), OAM (center), AAM+OAM (right).

	AAM X	AAM Y	OAM X	OAM Y	AAM+OAM X	AAM+OAM Y
Prograde Chandler	0.598	0.596	0.896	0.897	0.920±0.010	0.920±0.011
Retrograde Chandler	0.428	0.430	0.123	0.126	0.438±0.056	0.439±0.056

Table 1: Correlation coefficients between geodetic and geophysical (AAM, OAM, their sum) excitations.

is found to be larger than at the prograde one. New formalism introduces the asymmetric input at the level of 1 mas, what is important at the contemporary level of observational precision, but does not sufficiently improve the geophysical budget of PM excitation. In particular, misfit between geodetic and geophysical excitation at the retrograde Chandler frequency remains questionable.

Acknowledgements. First author is indebted to Paris Observatory for supporting this work (2 month position). This work is also supported by the RFBI grant N 12-02-31184.

4. REFERENCES

Gross, R., 2000, The excitation of the Chandler wobble, Geophys. Res. Lett., 27(15), pp. 2329-2332.

Gross, R., 2012, Theory of Earth Rotation Variations, IAG Symposia, in press.

Bizouard C., L. Zotov, 2013, Asymmetric effects on polar motion, Celestial Mechanics and Dynamical Astronomy, Volume 116, Issue 2, pp. 195-212.

Lambeck K., 1980, The Earth's Variable Rotation; Geophysical Causes and Consequences, Cambridge University Press.

Munk W., MacDonald G., 1960, The rotation of the Earth, Cambridge Univ. Press.

Zotov L. V., Bizouard C., 2012, On modulations of the Chandler wobble excitation, Journal of Geodynamics, 62, pp. 30-34.

Session 4b

EARTH ROTATION - MODELLING AND OBSERVATIONS

ROTATION DE LA TERRE - MODÉLISATION ET OBSERVATIONS

THE IERS RETREAT: HOW TO IMPROVE EARTH ROTATION PRODUCTS?

D. THALLER, S. BACHMANN
Federal Agency for Cartography and Geodesy
Richard-Strauss-Allee 11, 60598 Frankfurt am Main, Germany
e-mail: daniela.thaller@bkg.bund.de

ABSTRACT. The IERS held a two-day retreat in Paris on May 23-24, 2013. The outcome of the discussions at the retreat are presented with respect to Earth Rotation studies. Special focus is given on the plans to improve the Earth rotation products of the IERS.

1. INTRODUCTION

The International Earth Rotation and Reference Systems Service (IERS) held its second retreat in Paris at the University Paris-Diderot from May 23-24, 2013. As the first IERS retreat took place in 2003, the second retreat aimed to revise the IERS activities during the past ten years. The main goal was to revise the products and developments of the IERS and to establish directions for the IERS over the next years to ensure that high accuracy products are generated regularly.

The IERS retreat was organized in seven sessions with the following conveners:

1. Move towards "real-time" products (H. Schuh, J. Wickert)
2. Rigorous combined products (Z. Altamimi, M. Seitz, R. Biancale)
3. Long-term stability and parameterization of the reference frame (X. Collilieux, D. Thaller)
4. Next generation of models and center-of-mass products (T. van Dam, R. Gross)
5. EOP prediction improvements (B. Luzum, C. Bizouard)
6. Unification of product formats (T. Herring, L. Soudarin)
7. Mechanism for IERS evolution (B. Richter, C. Ma)

The presentations given by the conveners and invited key persons are available at the IERS website: `http://www.iers.org/nn_10902/IERS/EN/Organization/Workshops/Retreat2013.html`. A summary of the discussions prepared by the IERS Analysis Coordinator can be found at this website, too.

The following chapters will summarize the major points of the IERS retreat related to the Earth rotation products.

2. TOWARDS REAL-TIME: UT FROM INTENSIVES

In Session 1 the current real time products of the IERS have been presented. One of the main "real-time" products are the VLBI Intensive sessions which are performed in order to determine UT with a low latency and at (nearly) daily intervals. Currently, three VLBI Intensive sessions are scheduled: INT1 (baseline Wettzell-Kokee), INT2 (baseline Wettzell-Tsukuba) and INT3 (baselines Wettzell-Tsukuba-NyÅlesund). Figure 1 shows the configuration and scheduling of the VLBI Intensive sessions. Daily dUT1 estimates based on these 1h observing sessions are derived.

The VLBI Intensive sessions aim to provide UT1 in "real-time" with the lowest latency possible. Table 2 shows the latency of VLBI Intensive sessions as it is achieved at the moment. In general the latency is a few hours only, but it may happen that the dUT1 estimates are provided with a latency > 1 day. The usage of eVLBI is a major step forward to reduce the latency.

As a consequence of the short observation interval (i.e., one hour only), there are only very few observations for the VLBI Intensive sessions. This situation causes problems for the parameter estimation:

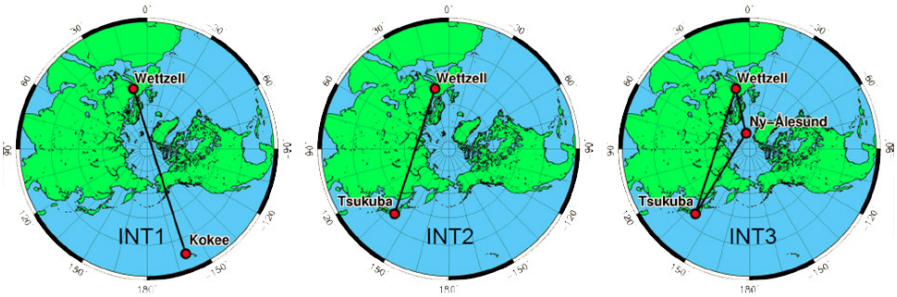

Figure 1: Configuration of the Intensive Sessions (from: Haas (2013))

Session name	Observing date/time	Correlation	Analysis	Latency correl. since end of observ.	Latency dUT1-res. since end of observ.
INT3 – 089	Apr 08, 07:00-08:00	Apr 08, 14:51	Apr 08, 18:26	06:51	10:26
INT1 – 089	Apr 08, 18:30-19:30	Apr 09, 04:54	Apr 09, 05:10	09:24	09:40
INT1 – 099	Apr 09, 18:30-19:30	Apr 10, 04:32	Apr 10, 17:45	09:02	22:15
INT1 – 100	Apr 10, 18:30-19:30	Apr 11, 02:15	Apr 11, 17:48	06:45	22:18
INT1 – 101	Apr 11, 18:30-19:30	Apr 12, 02:26	Apr 12, 03:19	06:56	07:49
INT1 – 102	Apr 12, 18:45-19:45	Apr 15, 15:10	Apr 15, 17:48	19:25	24:03
INT2 – 103	Apr 13, 07:30-08:30	Apr 15, 09:57	???	49:27	???
INT2 – 104	Apr 14, 07:30-08:30	Apr 15, 09:59	???	25:29	???

Figure 2: Latency of Intensive Sessions (from: Haas (2013)

1. Polar motion has to be kept fix; usually predicted values are available only;
2. Station coordinates have to be fixed on a priori;
3. Difficulties to estimate troposphere delay reliably;

Possible improvements are expected by combining with GNSS (Global Navigation Satellite Systems) solutions:

1. Polar motion determined by GNSS: use, e.g., IGS Ultra-Rapid or Rapid products
2. Troposphere determined by GNSS: combined VLBI-GNSS analysis including troposphere combination

Thaller et al. (2008) demonstrated that such type of VLBI-GNSS combination has the potential to improve the UT estimates derived from the Intensive sessions.

3. TOWARDS REAL-TIME: IGS EOP

The International GNSS Service (IGS) has launched its "Real-Time Service (RTS)" on April 1, 2013. Products of this service are at the moment only orbits and clocks, but it should be feasible to get also accurate EOPs in real time. The IGS will look into this aspect, but this requires a format allowing real-time dissemination of EOPs. A common product format has been discussed during the IERS retreat in Session 6 "Unification of product formats" (see below). Figure 3 shows the maximum and the mean latency as well as the outage periods of the IGS RTS. It can be seen, that an data outage is very seldom and that the latency is $< 1 - 4$ seconds in general.

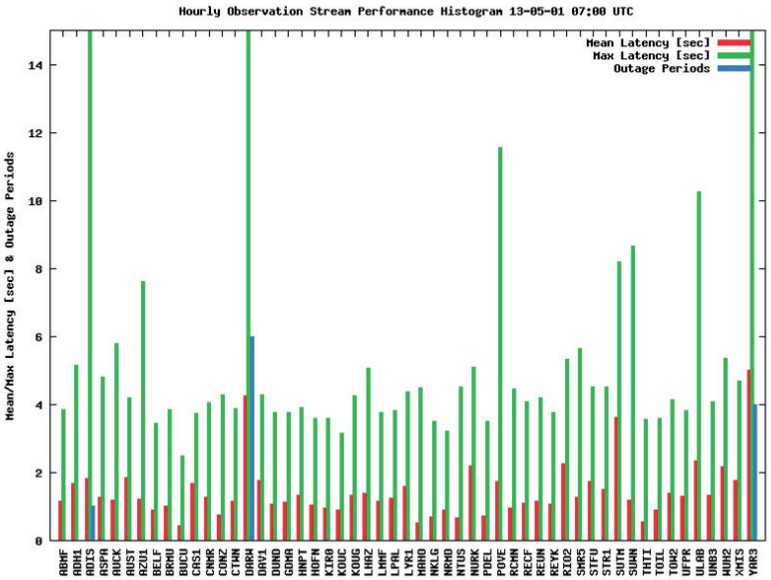

Figure 3: Latency of IGS RTS (from: Wickert (2013).

4. IERS RAPID SERVICE / PREDICTION CENTER

In Session 5 of the IERS retreat, possibilities for EOP prediction improvements have been presented and discussed. The IERS Rapid Service / Prediction Center provides multiple solutions of IERS EOP predictions per day: at 0310 UTC, 0910 UTC, 1710 UTC and 2110 UTC. The solutions are timed to take advantage of the latest IGS products. The solutions take approx. 10 minutes to complete, with a time split between data downloads and software run time.

Potential improvements of the products can be seen in the following fields:

- The data input is not optimized for 4 EOP solutions per day. A better temporal distribution is needed.
- The data combination algorithm is not optimal. Alternative methods have to be investigated.

EOP prediction can be improved by improving the input EOP data, the processing algorithm, the EOP modeling, and the geophysical analysis and forecast.

Figures 4 show how the EOP input data can be improved:

1. Reduce latency (left figure): reduce the time between the last observation and the epoch where the prediction is provided.
2. Improve accuracy (right figure): improve the accuracy of the input data.

Besides the improvements of the EOP, the analysis and forecast of the geophysical fluids also have to be improved. Four recommendations evolved from the discussions during the IERS retreat:

- Formal errors needed for data from AAM analysis (= internal validation).
- Inter-comparison between different sources of AAM data (= external validation).
- Request more frequent updates of AAM data (actually 6 hours).
- OAM should be provided operationally in real-time.

Figure 5 gives an overview on the current latency and accuracy of the IERS Rapid products.

Figure 6 shows the current latencies for rapid products and the expected latencies for the future: < 15 hours for the AAM, GPS (Ultras) from IGS RTS, < 24 hours for SLR, < 2 hours for VLBI Intensive sessions and < 2 days for VLBI 24-hour sessions.

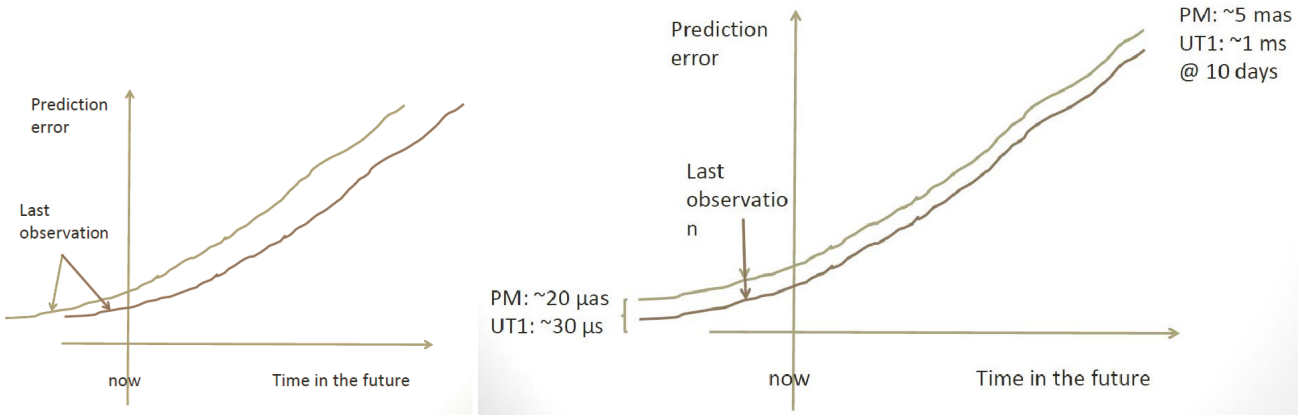

Figure 4: Impact on the quality of the prediction if: (1) the latency is reduced (left picture), or (2) the accuracy is improved (right picture). (from: Luzum (2013)).

Input	Latency	Refresh rate	PM Accuracy	UT1/LOD Accuracy
AAM	~18-42 hours	1/day		~60 µs/day
GPS (Ultras)	~15 hours	4/day	~20 µas	~15 µs/day
SLR	48-72 hours	1/day	~200 µas	
VLBI Intensives	~8-32 hours	1-2/day		~20 µs
VLBI 24-hour	10-17 days	2/week	~200 µas	~5 µs

Figure 5: Current latency and accuracy of IERS Rapid products (from: Luzum (2013))

5. REVISION OF THE IERS TERMS OF REFERENCE

The latest version of the IERS Terms of Reference (ToR) is dated October 10, 2010. As the IERS is a service, it should follow the needs of the users and review from time to time whether the ToR are still adequate to satisfy the needs of the users. The IERS retreat is a good opportunity to review the IERS ToR. In view of improving the Earth orientation products of the IERS, there are three Product Centers of interest:

- The Rapid Service / Prediction Center and the Earth orientation Center are responsible for Earth orientation parameters.
- The ITRS Center is responsible for the maintenance of the ITRS/ITRF.

The crucial point is that the ITRF computation does not concentrate solely on station positions anymore, but provides a consistent longterm solution for station positions **together with** Earth rotation parameters since the realization of ITRF2005 (Altamimi et al., 2007). Therefore, the question arises whether separated product centers for ITRF and Earth orientation are outdated, and whether a product center for rigorous combination on a "daily" (or weekly) basis would be much more adequate to provide the users with the best possible Earth orientation products? This question is, however, not that easy to answer as it would look at a first glance. Therefore, the decision on this subject will be adjourned until results from the IERS Working Group on "Combination at the observation level' (COL)" are available.

http://www.iers.org/ToR

Input	Latency	
AAM	~18-42 hours	< 15 hours
GPS (Ultras)	~15-21 hours	use from IGS Real-Time Service?
SLR	48-72 hours	< 24 hours
VLBI Intensives	~8-32 hours	< 2 hours
VLBI 24-hour	10-17 days	< 2 days

Figure 6: Expected latencies in future (from: Luzum (2013))

6. IMPROVEMENT OF PRODUCT FORMATS

In Session 6, die unification of IERS product formats have been investigated. The IERS provides diverse EOP products on its website. Figure 7 shows the IERS website with different EOP products. The critical point is that different formats are used for different product levels (Bulletin A, B and C04). In an ideal case, all important characteristics should be merged into one common format, and all IERS Earth orientation products should be provided in the common format.

In summary, the following issues have been identified to be improved:

- One common format for all Earth orientation products.
- EOP rates should be included in the files. Currently, only Length of Day (LOD) is given, but no polar motion rates.
- The leap second file (Bulletin C) is not machine readable.
- No format for Real-Time distribution of EOP currently available.

The IERS Analysis Coordinator works towards improvements of the format issues.

Rapid data and predictions

	Bulletin A	Plots	product metadata	latest version	available versions
Standard EOP data files	finals.all (IAU1980)	Plots	version metadata	latest version	
	finals.all (IAU2000)	Plots	version metadata	latest version	
	finals.data (IAU1980)	Plots	version metadata	latest version	
	finals.data (IAU2000)	Plots	version metadata	latest version	
	gpsrapid.out	Plots	version metadata	latest version	
Daily EOP data files	finals.daily (IAU1980)	Plots	version metadata	latest version	
	finals.daily (IAU2000)	Plots	version metadata	latest version	
	gpsrapid.daily	Plots	version metadata	latest version	

Figure 7: IERS EOP Data Website

http://www.iers.org/EOP

7. SUMMARY

In summery, all IERS retreat participants have passed a very good 2-day IERS retreat in Paris with many ideas and fruitful discussions. Several topics have been identified with potential for improving the IERS products and better satisfy the needs of the users. The main issues regarding EOPs have been formulated:

1. Move towards Real-Time,
2. Move towards combined EOP products (e.g. for Intensives),
3. Improvements for EOP prediction,
4. User-friendly common product formats.

Some of the innumerable activities are already ongoing - others will follow in the near future.

8. REFERENCES

Altamimi, Z., Collilieux, X., Legrand, J., Garayt, B., Boucher, C., 2007, "ITRF2005: A new release of the International Terrestrial Reference Frame based on time series of station positions and Earth Orientation Parameters", J. Geophys. Res.(Solid Earth), 112, B09401, doi:10.1029/2007JB004949.

Haas, R., 2013, "The IVS Intensive sessions on their way to near real-time", presented at the IERS Retreat 2013, held at Paris on May 23-24, 2013.

Luzum, B., 2013, "EOP Prediction Improvements", presented at the IERS Retreat 2013, held at Paris on May 23-24, 2013.

Wickert, J., 2013, "International GNSS Service New Products for Real-Time Applications", presented at the IERS Retreat 2013, held at Paris on May 23-24, 2013.

Thaller, D., Tesmer, V., Dach, R., Krügel, M., Rothacher, M., Steigenberger, P., 2008, "Combining VLBI intensive with GPS rapid solutions for deriving a stable UT time series", In: Finkelstein, Behrend (eds.) Proceedings of the 5th IVS General Meeting, held at St. Petersburg, March 3-6, 2008, pp. 8-13.

COMPARISON OF GEODETIC AND MODELLED EXCITATION FUNCTIONS BY ALLAN VARIANCE

C. BIZOUARD,
SYRTE, Observatoire de Paris, CNRS, UPMC
61, Avenue de l'Observatoire, 75014, Paris, France
e-mail: christian.bizouard@obspm.fr

ABSTRACT. Allan variance analysis allows to study the stability or the noise of a physical process at a given time scale. Whereas this statistical tool is widely used for quantifying the stability of the atomic clock, it can be applied to any time series. This is especially interesting for analysing Earth rotation excitation functions: in complement of the standard numerical methods (spectra, least-square adjustment, correlation and explained variance), it yields a stochastic comparison on observed excitation and the one derived from geophysical models. This permits to draw conclusions on the nature of the geophysical forcing of the Earth rotation in function of the considered time scale.

1. INTRODUCTION: THE ALLAN VARIANCE ANALYSIS

Allan variance analysis permits to quantify the stability of a time series at a given time scale. Moreover, as well as spectral density, its slope (in log-log scale) allows to characterise the noise at play. Widely used for time scale comparison, it is sometimes applied for analysing Earth Rotation Parameters (EOP) (see e.g. Malkin 2011) , especially for comparing statistical properties of EOP time series. Now we shall look its interest for characterising excitation of the Earth rotation.

First, in this introductory section, we shall briefly recall what is Allan variance analysis. Let x_i be a time signal equally sampled at instants $t_i = t_0 + i\tau$ $(i = 0, n)$ over the time interval $[t_0, t_n]$. We build the series y_k^T by averaging x_i over successive periods of length $T_m = m\tau$ with $m = 1, ..., \lfloor n/2 \rfloor$:

$$y_k^{(m\tau)} = \frac{1}{m} \sum_{i=0}^{m} x(t_0 + kT + i\tau) \text{ with } k = 0, ..., \lfloor n/m \rfloor \ . \tag{1}$$

The integer m indexes the length of the average, starting from τ to the mid of the sampled interval, that is $\lfloor n/2 \rfloor \tau$. The *Allan variance* series $\mathcal{AV}(m\tau)$ with $m = 1, ..., \lfloor n/2 \rfloor$ of x_i is composed of the variances of the $\lfloor n/2 \rfloor$ forward difference series (Allan 1987):

$$D_k^{(m\tau)} = \frac{y_{k+1}^{(m\tau)} - y_k^{(m\tau)}}{\sqrt{2}} \text{ with } k = 1, ..., \lfloor n/m \rfloor \tag{2}$$

that is :

$$\mathcal{AV}(m\tau) =< D^2(t) > \ . \tag{3}$$

As for the standard deviation relatively to the variance, the Allan deviation $\mathcal{AD}(m\tau)$ is defined by the square root of $\mathcal{AV}(m\tau)$. The more stable is the signal at $T_m = m\tau$ interval, the smaller are the forward differences of the corresponding averaged signal, and the smaller is the Allan variance for this time scale. So Allan variance series characterises the signal stability in function of the time scale. Developing the Allan variance, it can be easily shown that

$$\mathcal{AV}(m\tau) = R_{y^{(m\tau)}}(0) - R_{y^{(m\tau)}}(m\tau) \ , \tag{4}$$

where $R_{y^{(m\tau)}}$ is the discrete auto-correlation of time series $y_k^{(m\tau)}$. If the signal tends to repeat at time interval $m\tau$, then $\mathcal{A}(m\tau)$ tends to vanish as expected. Long period component (having more or less the period of the sampling), episodic jump or a discontinuity, as pointed out by Malkin (2011) do not affect much Allan deviation in contrast to standard deviation, and Fourier spectrum of the considered time series. So Allan deviation allows to eliminate systematic effect and to better characterise the pure

α	slope of the Allan Variance (AV) β	slope of the Allan Deviation (AD) $\beta/2$	stochastic process
0	-1	$-1/2$	white noise
-1	0	0	flicker noise
-2	1	1/2	red noise

Table 1: Correspondence between Allan variance slope β and slope α of the spectral density. Allan deviation slope is $\beta/2$.

random fluctuation of the studied signal at a given time scale. The value $AV(m\tau)$ are plotted in log-log scale. Then a slope β is related to a noise process of spectral density $K_\alpha f^\alpha$ with $\beta = -\alpha - 1$. Correspondence between α and β values is given in Tab. 1 for most common noises met in geodetic parameters.

2. METHOD AND DATA

From a few days to several decades, pole coordinates $p = x - iy$ and length of day variation ΔLOD are ruled by the linear differential equation fo first order:

$$p + i\frac{1}{\tilde{\sigma}_c}\,\dot{p} = \chi \qquad \frac{\Delta LOD}{LOD} = \chi_3\ , \tag{5}$$

where $\tilde{\sigma}_c \sim 2\pi/433(1+i/200)$ cycle/day is the complex Chandler frequency, χ and χ_3 are the effective Angular Momentum Functions (AMF) of any surface layer of the Earth (atmosphere, oceans, freshwater or combination of these ones), as far we do not consider other source of excitation (external torque,...). Common approach is to compare the first member of these equation χ_G, χ_3^G, namely the geodetic excitation G deduced from observed EOP, to the second member or effective AMF, reconstructed from Global Circulation Models (GCM) of the hydro-atmosphere. It is a well documented fact that hydro-atmosphere is the main source of excitation for periods below 10 years (see e.g. the excellent monography of Sidorenkov 2009), so that comparing time series G and AMF at this subdecadal time scale is meaningful. Geodetic

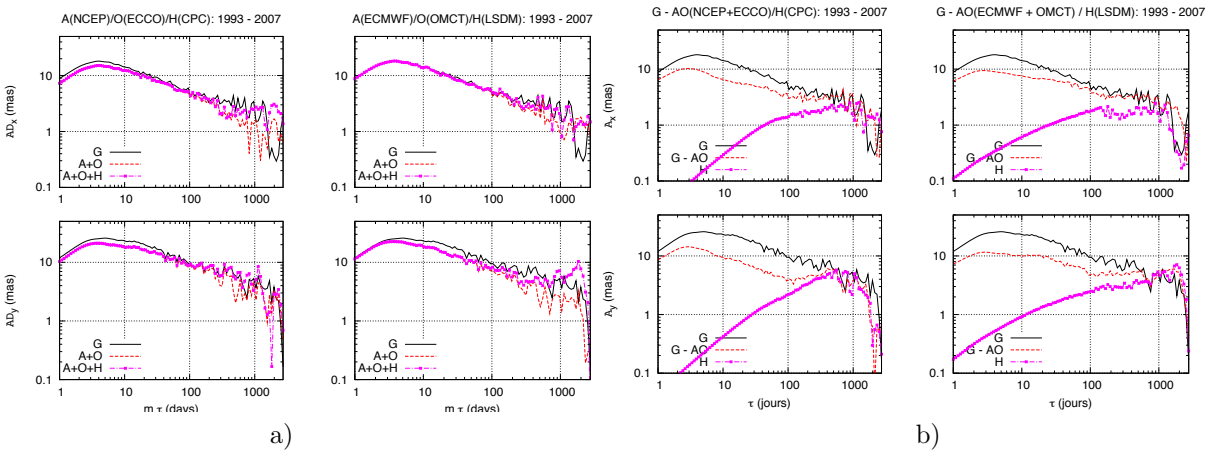

Figure 1: Comparative Allan deviation analysis of equatorial excitations: G, $A+O$, $A+O+H$ (left plot) and residual equatorial excitation $G-(A+O)$ and of hydrological contribution H (right plot)

excitation G is built from from C04 EOP time series according to Wilson (1985) digital filter, then is compared to the hydro-atmospheric angular momentum time series. When we add to atmospheric AMF time series (A) oceanic (O) or hydrological (H) ones, we consider consistent GCM, namely i) atmosphere: NCEP/NCAR (National Center for Environmental Prospect/National Center for Atmospheric Research); oceans: ECCO-MIT (Estimating the Circulation and Climate of the Oceans); fresh waters: CPC (Climate Prediction Center) (all series are supplied by the Global Geophysical fluid Center of the IERS http://geophy.uni.lu) ii) atmosphere: ECMWF (European Centre for Medium-Range Weather Forecasts); oceans: OMCT(Ocean Model for Circulation and Tides); freshwater: LSDM (Land Surface Discharge

Model) prepared by Geodetische Forschung Zentrum (ftp://ftp.gfz-potsdam.de/pub/home/ig/ops/). Before to perform Allan deviation analysis, the stable part of the signal (bias and seasonal harmonics), are removed by least-square fit over the considered time interval.

3. ALLAN DEVIATION ANALYSIS OF THE EQUATORIAL EXCITATION

First comparison will focus on the most most accurate pole coordinates, beginning with the advent of GNSS processing in 1993. Because hydrological time series CPC does not go beyond 2008, considered time interval is 1993-2007. On Fig. 1a we plot the Allan deviation of equatorial G along the ones of $A+O$ and $A+O+H$. We notice an overall good agreement, with $A+O$ and G presenting a slope of $\beta/2 = -0.5$ from 5 to 400 days, meaning a white noise process at stake (see Tab. 1). However combinations χ_{A+O} and χ_{A+O+H} presents a smaller Allan deviation than G below 100 days. Notice that y component is less stable than x one at seasonal period. Looking now at the residuals $G-(A+O)$ compared to H from 1 day to one year (Fig. 1b), we see that hydrological series, appearing as a red noise, do not account for the residual, which behave like a random process between white and Flicker noises. But, at longer period from one to several years, Allan deviation H comes in closer agreement with $G-A+O)$, pointing out the tremendous role of the freshwater redistribution in multi-annual polar motion (considering a time span from the 1960's this conclusion is reinforced). More generally, Allan deviation analysis permits to

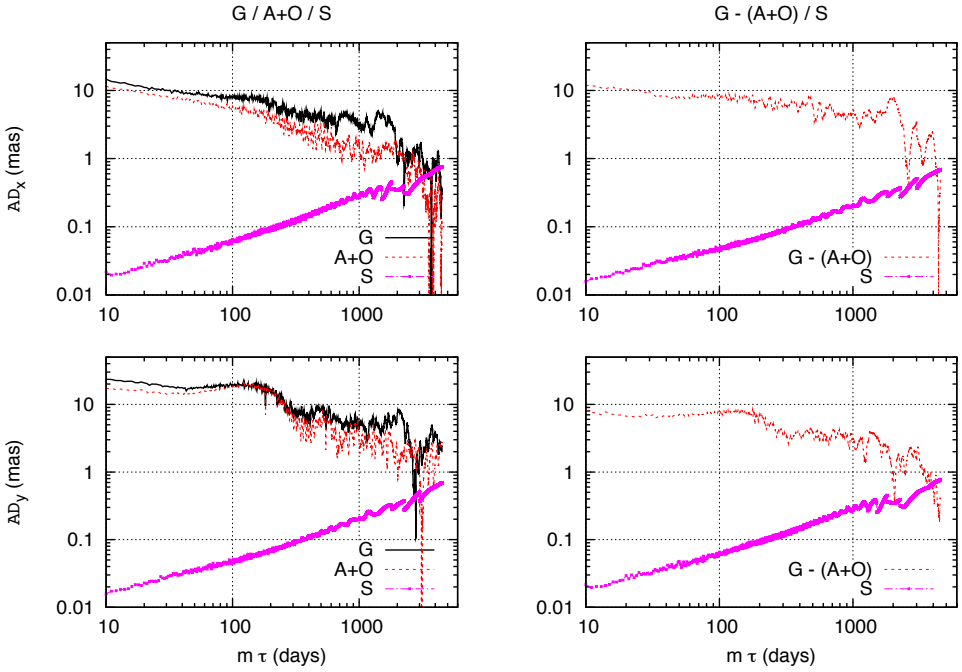

Figure 2: Comparative Allan deviation analysis of equatorial seismic excitation and of geodetic excitation and its residuals $G-AO$ over the period 1985-2011

know weather a geophysical process can excite Earth's rotation. For instance let us consider the seismic excitation S resulting from step wise mass redistribution estimated from 1985 to 2011 (Bizouard 2012). According to the slope of $AD(S)$, about 1/2 from Fig. 2, this is a random walk process (red noise), which cannot account for polar motion excitation below 3000 days (10 years).

4. ALLAN DEVIATION ANALYSIS OF THE AXIAL EXCITATION

As evidenced by Fig. 3, the axial geodetic excitation excitation G, namely offset of the length of day expressed in ms, fits the corresponding atmospheric excitation A (multiplied by 86400 s) SI up to time scale of 500 days. At short term time scale (below 50 days) hydrological contribution is negligible and residuals $G-A$ are explained by oceanic excitation, but only in the case of ECMWF/OMCT association. Above 50 days, neither ocean nor hydrological mass redistribution $G-A$ residuals can account for $G-A$

residuals. This probably points out a defect in hydrological or oceanic models at seasonal and longer periods.

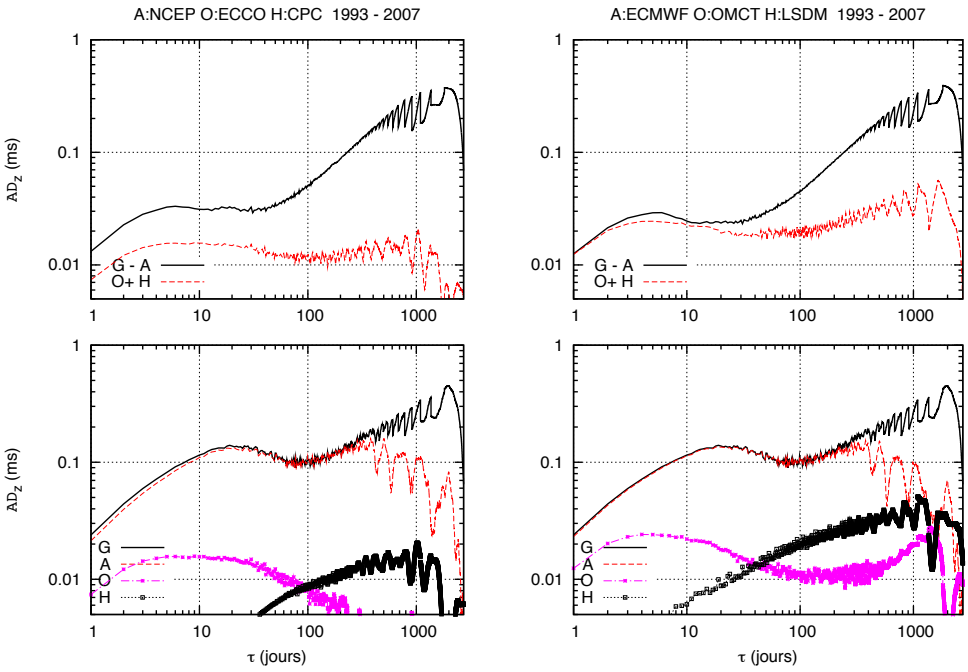

Figure 3: Comparative Allan deviation analysis of axial excitation. Bottom plots: geodetic G, atmospheric A and oceanic O. Upper plot: residuals $G - A$ compared with oceanic anf hydrological contributions $O + H$

5. CONCLUSION

Allan variance (or deviation) analysis is a powerful tool for analysing excitation time series of the Earth rotation, permitting at a given time scale to investigate underlying physical process. Indeed, from this single analysis, it can be concluded that i) equatorial excitation tends to be more stable at multi-year time scale ($\sim$ white noise) in contrast to axial excitation ($\sim$ red noise), meaning that physical processes at stake are different (surface redistribution versus fluid core) ii) over 400 days hydrological process are fundamental for explaining $G - AO$ residuals of the equatorial components iii) Earthquake do not influence polar motion below 10 years. The lack of compliance between Allan deviation can also point out defects in global circulation models. Thus, rapid equatorial fluctuations observed in $G - (A + O)$ residuals are not explained by hydrological contribution ; axial residuals $G - A$ over 50 days do not fit the corresponding excitation $O + H$.

6. REFERENCES

Allan D. (1987), Time and Frequency (Time-Domain) Characterisation, Estimation, and Prediction of Precision Clocks and Oscillators, IEEE Transactions on Ultrasonics, Ferroelectrics, and Frequency Control, UFFC-34: 647-654

Bizouard C. (2012), Interprétation géophysique du mouvement du pôle, Mémoire d'Habilitation à Diriger des Recherches, 245 p.

Malkin Z.M. (2011), Kinematics Phys.Celest. Bodies 27: 42-49

Sidorenkov N.S. (2009), The interaction between earth's rotation and geophysical processes, Wiley-VCH

Wilson C. (1985), Discrete polar motion equation, Geophys J. R. Astron. Soc. 80(2):551-554

ANALYSIS OF ATMOSPHERE-EXCITED INTRASEASONAL POLAR MOTION VIA THE TORQUE APPROACH

M. SCHINDELEGGER[1], J. BÖHM[1], D.A. SALSTEIN[2]
[1] Department of Geodesy and Geoinformation, Vienna University of Technology
27-29 Gußhausstraße, A-1040 Wien, Austria
e-mail: michael.schindelegger@tuwien.ac.at, johannes.boehm@tuwien.ac.at,
[2] Atmospheric and Environmental Research, Inc.
131, Hartwell Avenue, Lexington, MA 02421-3126, USA
e-mail: dsalstei@aer.com

ABSTRACT. Alongside the diagnosis of changes in fluid angular momentum, geophysically-driven perturbations of Earth rotation can be investigated by means of interaction torques arising at the boundary of the solid Earth. A recently published reassessment of this modeling route demonstrates the success of investigating torque quantities for the specific purpose of accounting for atmosphere-induced polar motion at intraseasonal periodicities. Here, we expand those considerations by a more detailed analysis of the well-known 10-day atmospheric normal mode signal in polar motion in terms of the underlying driving mechanisms provided by mountain, friction, and equatorial bulge torques. If a fully isostatic response of the sea surface to air pressure variations is implemented, mountain and bulge torque are shown to elicit wobbling motion in the 10-day band at roughly the same level, with the underlying local contributions being dominant over northern hemispheric landmasses. In combination with consistently calculated oceanic angular momentum estimates, atmospheric interaction torques provide a well-closed equatorial excitation budget across the frequency range of 1 to 2 weeks.

1. INTRODUCTION

Small irregularities in Earth rotation associated with motion and mass redistribution effects in the atmosphere, the oceans, the hydrosphere, etc. are preferably inferred from accurate quantifications of angular momentum changes within each of the geophysical fluids. This modeling route is generally viewed as robust and superior to its dynamic complement, the torque approach, which draws on global integrals of the mechanical forces acting on the solid portion of our planet. The strongest torque constituent by far, related to a degree 2/order 1 pressure pattern loading the equatorial bulge, is however common to both approaches in the form of either the ellipsoidal torque or the equatorial mass term of fluid angular momentum. Normal forces and tangential stresses occurring at sloping or along rough topography give rise to secondary but non-negligible mountain and friction torques, respectively, and the local character of these effects is usually cited as a major obstacle in deriving reliable torque-based Earth rotation predictions from global geophysical models. Contrary to this supposition, Schindelegger et al. (2013) recently showed that the quality of present-day atmospheric reanalysis systems has attained a level which renders equatorial torque estimates for the atmosphere as accurate as their AAM (atmospheric angular momentum) counterparts on seasonal and intraseasonal time scales. As a concise follow-up to this study, the present paper is devoted to polar motion variability at retrograde frequencies corresponding to 1–2 weeks, i.e. periodicities that accommodate the prominent atmospheric normal mode ψ_3^1. Feldstein (2008) studied this 10-day, westward propagating wave with regard to its dynamical origin in the atmosphere, concluding that the influence of local torques (mountain + friction) is about five times smaller than the driving provided by the ellipsoidal (equatorial bulge) torque. Here, Feldstein (2008)'s findings shall be complemented by inclusion of oceanic angular momentum (OAM) estimates, which have been corrected for the inverted barometer (IB) response of the oceans to atmospheric pressure fluctuations. This amendment gives a more complete account of the actually observed polar motion signal in the 10-day band.

The investigated daily AAM and torque time series cover the period 2007.0–2010.12 and correspond to those computed by Schindelegger et al. (2013) upon pressure level data (2° horizontal resolution) and surface fields (0.5° resolution) of ERA-Interim, the current reanalysis system of the ECMWF (European Centre for Medium-Range Weather Forecasts). Consistently calculated OAM in terms of non-dimensional

excitation functions were available from the Ocean Model for Circulation and Tides (OMCT) as residual values to an idealized IB ocean. Adhering to this convention, we derived ellipsoidal torque estimates (i.e. AAM mass signals) from an IB-corrected surface pressure field at each epoch.

2. EXCITATION FORMALISM

On time scales of a few days or longer, geophysical excitation embodied by either AAM or atmospheric torques relates to the reported position of the Celestial Intermediate Pole $\hat{p} = p_x - \mathrm{i}p_y$ via (Wahr, 1982)

$$\hat{p} + \frac{\mathrm{i}}{\hat{\sigma}_{cw}}\dot{\hat{p}} = \frac{1}{(C-A)\Omega}\left\{1.12\hat{H}^p + 1.61\hat{H}^w\right\} \tag{1}$$

$$\approx \frac{\mathrm{i}}{(C-A)\Omega^2}\left\{1.12\hat{L}^{e,(s)\to(a)} + 1.61\left(\hat{L}^{m,(s)\to(a)} + \hat{L}^{f,(s)\to(a)}\right)\right\} = \hat{\phi}^e + \hat{\phi}^m + \hat{\phi}^f, \tag{2}$$

where $\hat{\sigma}_{cw}$ is the complex-valued frequency of the Chandler Wobble, A and C denote mean equatorial and axial moments of inertia of the whole Earth which rotates with a nominal angular velocity described by Ω, and $\hat{H}^{p,w}$ represent the standard pressure and wind terms of AAM. Ellipsoidal, mountain and friction torques $\hat{L}^{e,m,f}$ of the atmosphere (a) are understood to act on the solid body (s), and their analytical expressions can be found in Schindelegger et al. (2013), albeit with a reversed sign. $\hat{\phi}^{e,m,f}$ designate the dimensionless excitation functions attributed to each torque component. The apparent equivalence between the pressure term and the ellipsoidal torque $\Omega\hat{H}^p = \mathrm{i}\hat{L}^e$ is exact, while that of the wind term and the cumulative local torque $\Omega\hat{H}^w \approx \mathrm{i}\hat{L}^m + \mathrm{i}\hat{L}^f$ is approximate. An accurate torque-based estimate of $\hat{H}^w$, that might be deployed in the well-established AAM formalism of Eq. (1), is however accessible through integration of the AAM budget equation in the frequency domain, see Schindelegger et al. (2013) for details. If applied to the 10-day band, the pure torque result (Eq. 2) suffers from considerable analytical inadequacies at the level of 10%, specifically due to equating the motion of the Celestial Intermediate Pole to that of the instantaneous rotation axis. It is thus primarily suited for obtaining a qualitative picture of the different torque terms' influence on polar motion.

3. INTRASEASONAL POLAR MOTION AND THE 10-DAY NORMAL MODE

The comparison of observed polar motion (C04-solution of the International Earth Rotation and Reference Systems Service for 2007.0–2010.12) to atmosphere-ocean excitation data was accomplished by aid of Eq. (1) for both angular momentum and torque quantities. After superimposing OAM functions on the right-hand side of the relationship and converting $\hat{L}^e$ to $\hat{H}^p$, the two types of excitation time series differ merely with regard to the wind term $\hat{H}^w$, which stems either from vertical integration of atmospheric fluxes (standard AAM case) or a frequency-dependent scaling of the three torque constituents in the

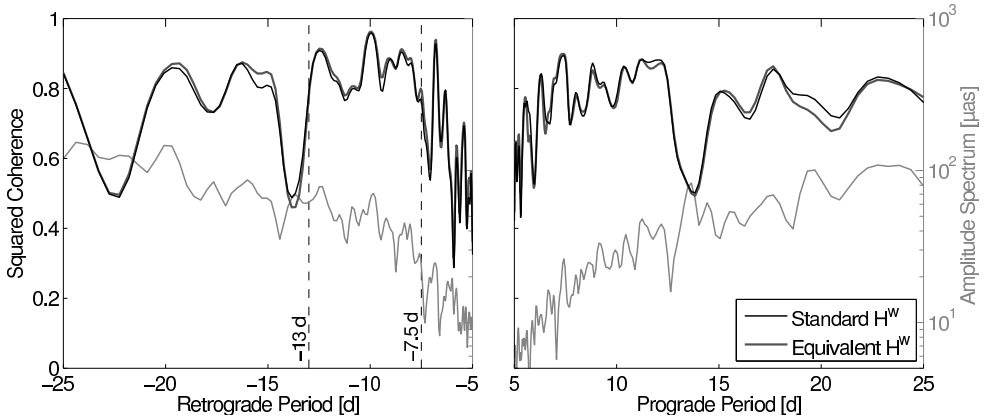

Figure 1: Amplitude spectrum of observed polar motion (*light gray curve*; scale on right) at periodicities from 5 to 25 d, and magnitude-squared coherence values (*black and dark gray curves*; scale on left) between the allocated geodetic excitation and the geophysical excitation as computed from OAM, IB-corrected AAM pressure term, and standard or equivalent AAM wind terms.

discrete spectral space followed by an appropriate inverse transform to the time domain, cf. Schindelegger et al. (2013). This torque-based version of $\hat{H}^w$ has been labeled as *equivalent wind term*. Figure 1 depicts the magnitude-squared coherence spectra between geophysical and geodetic excitation for each of the two approaches and places an amplitude estimate of the reported polar motion in the period range of 5 to 25 d underneath. (The built-in MATLAB functions *mscohere* and *pwelch* were deployed for this purpose.) Coherence values at about 0.7–0.8 on average indicate a close though not ideal match between observed and modeled wobble excitation throughout the probed frequencies, with remaining disparities primarily caused by model inconsistencies and unresolved dynamical processes. Within the 10-day band, whose boundaries were prescribed at -7.5 and -13 d following Feldstein (2008), the amplitude spectrum of up to 80 μas (smoothed value) is enhanced compared to its prograde equivalent. The combined atmosphere-ocean excitation function gives a proper account of the associated signal content as judged from an increased coherence level and generally small phase lag values in the range of $\pm 30^\circ$ (not depicted). Results from the torque-based approach perform marginally better in explaining the observed 10-day wobble and therefore positively warrant further examination of the interaction torques in the context of Earth rotation.

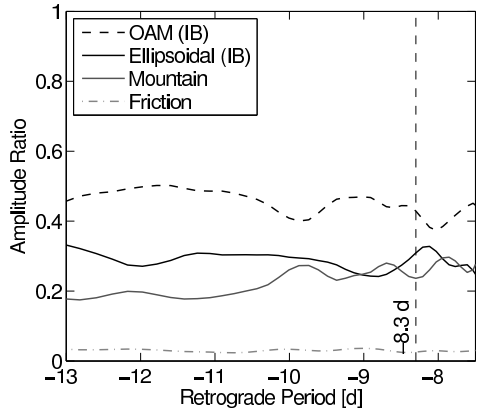

Figure 2: Frequency-dependent ratios of excitation functions for OAM (*black dashed curve*), IB-corrected ellipsoidal torque (*black solid curve*), mountain torque (*gray solid curve*), and friction torque (*gray dot-dashed curve*) relative to the sum of amplitudes of all four components.

Equation (2) is sufficient to qualitatively dissect the total excitation function $\hat{\phi}$ into its individual contributions provided by ellipsoidal, mountain, and friction torques (described by $\hat{\phi}^e$, $\hat{\phi}^m$, and $\hat{\phi}^f$) and the IB-corrected OAM functions as represented by $\hat{\phi}^o$. A smooth picture of the magnitude relationships within the interval (-13;-7.5) d was obtained by splitting the discrete Fourier transform (DFT) coefficients of each excitation component into overlapping spectral segments of distance 0.01 cpd (cycles per day) and bandwidth ± 0.05 cpd. For each sampling frequency σ_i, the DFT values were weighted by a Hanning window, condensed to mean amplitude values $\left|\hat{\phi}^{e,m,f,o}(\sigma_i)\right|$ within the segment, and finally expressed as *amplitude ratios* with respect to $\left|\hat{\phi}^e(\sigma_i)\right| + \left|\hat{\phi}^m(\sigma_i)\right| + \left|\hat{\phi}^f(\sigma_i)\right| + \left|\hat{\phi}^o(\sigma_i)\right|$ (the sum of all four ratios at σ_i amounts to 1, accordingly). Figure 2 displays the constellation of amplitude ratios within the 10-day band, where the usually cited theoretical period of ψ_3^1 at -8.3 d has been specifically marked. Noting that the utilized OAM values express departures from an ideal IB behavior, an approximate equipartition of power between atmospheric and oceanic dynamical processes in $\hat{\phi}$ is readily apparent. This magnitude relationship is in rough agreement with the findings of Ponte and Ali (2002) but probably more reliable in light of the improved geophysical fluid models used in the present study. Moreover, ellipsoidal and mountain torques elicit polar motion variability at approximately the same level (20–30% amplitude ratio each), which contrasts to Feldstein (2008)'s assessment of a much more dominant bulge effect. Both assertions are valid, though, since the IB-correction in the present study absorbs the majority of signal content in $\hat{\phi}^e$. The driving associated with friction torques does not exceed 4% in terms of amplitude ratios, but still constitutes a non-negligible quantity for high-accuracy polar motion considerations.

In a final processing step, the illustrative potential of the torque approach was exploited by a regional analysis of the Earth-atmosphere interaction signals that underlie the large ellipsoidal and mountain

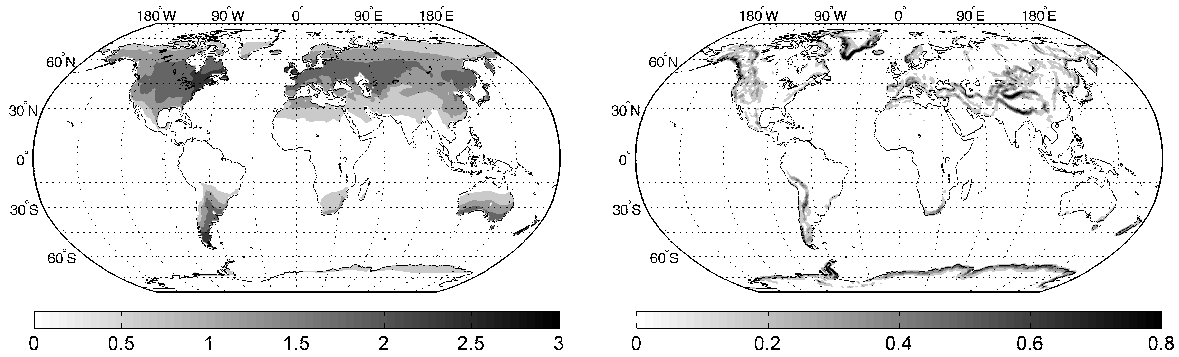

Figure 3: Mean amplitude maps of the grid point-wise contributions to ellipsoidal torque (left panel) and mountain torque (right panel) in the interval of (-13;-7.5) d in units of 10^{16} kgm^{2}s^{-2}.

torque influence on $\hat{\phi}^e$. Specifically, the complete 4-year records of IB and non-IB surface pressure fields from ERA-Interim were converted to grid point-wise contributions to $\hat{L}^e$ (IB) and $\hat{L}^m$ (non-IB, but restricted to land areas in any case) by evaluating their computational expressions (see Schindelegger et al., 2013) except for the double summation over latitude and longitude. The resulting complex-valued grids were subject to bandpass-filtering in the interval (-13;-7.5) d and averaged to mean amplitude values for each cell, leading to the global maps in Figure 3. Regions of angular momentum exchange are apparently confined to midlatitudes, which is intelligible given the spatial pattern of the 10-day normal mode (Feldstein, 2008) as well as the sensitivity areas of polar motion. The IB-correction effectively removes the contributions of pelagic points to $\hat{L}^e$, which is mostly affected by strong but possibly compensating surface pressure values over North America, Eurasia, and Patagonia. Mountain torque signals are of much more local character, with peak amplitudes being present at steep topographic gradients enclosing Greenland, the Tibetan Plateau, and the Antarctic Peninsula.

4. CONCLUSIONS

The dynamics of intraseasonal polar motion in the vicinity of the 10-day atmospheric normal mode have been reassessed on the basis of a recently produced 4-year set of Earth-atmosphere interaction torques and consistently calculated OAM functions. To derive accurate predictions of geophysically excited polar motion and simultaneously retain the torque terms' expressiveness in highlighting the underlying angular momentum exchange, a two-fold mathematical formalism has been compiled and successfully tested. The main findings comprise an equipartition of power between atmospheric and oceanic driving agents of retrograde 10-day wobbles as well as a comparable influence of equatorial bulge and mountain torques on the total atmospheric excitation function–both results of which have been deduced under the assumption of an isostatic oceanic response to air pressure variations. Examination of other prominent modes in both polar motion and changes in length-of-day represents a possible extension to this work.

Acknowledgements. This study was carried out within project P23143-N21 of the Austrian Science Fund. David Salstein was supported by the US National Science Foundation under Grant ATM-0913780.

5. REFERENCES

Feldstein S.B., 2008, "The dynamics of atmospherically driven intraseasonal polar motion", J. Atmos. Sci. 65(7), pp. 2290–2307, doi: 10.1175/2007JAS2640.1.

Ponte R.M., Ali A.H., 2002, "Rapid ocean signals in polar motion and length of day", Geophys. Res. Lett. 29(15), pp. 6-1–6-4, doi: 10.1029/2002GL015312.

Schindelegger M., Salstein D., Böhm J., 2013, "Recent estimates of Earth-atmosphere interaction torques and their use in studying polar motion variability", J. Geophys. Res.118(8), pp. 4586–4598.

Wahr J.M., 1982, "The effects of the atmosphere and the oceans on the Earth's wobble - I. Theory", Geophys. J. R. Astron. Soc. 70, pp. 349–372.

ESTIMATION OF THE CHANDLER WOBBLE PARAMETERS BY THE USE OF THE KALMAN DECONVOLUTION FILTER

A. BRZEZIŃSKI[1,2], M. RAJNER[1]
[1] Inst. of Geodesy and Geodetic Astronomy, Warsaw University of Technology, Warsaw, Poland
[2] Space Research Centre, Polish Academy of Sciences, Warsaw, Poland
e-mail: alek@cbk.waw.pl

ABSTRACT. We estimate the Chandler wobble (CW) parameters, the period T and the quality factor Q, based on the stochastic models of polar motion and geophysical excitation data. We apply the Kalman deconvolution filter developed by Brzeziński (1992). This filter can be used to analyze either the polar motion data alone, or simultaneously the polar motion and the excitation data, in order to estimate the unknown residual excitation. By imposing the minimum variance constraint upon the estimated unknown excitation we can find the best value of the resonant parameters T and Q. The CW parameters estimated from different sets of polar motion and geophysical excitation data are compared to each other as well as to the earlier results derived by the alternative algorithms.

1. INTRODUCTION

The parameters of the Chandler wobble, the frequency F (or, equivalently, the period T=1/F) and the quality factor Q, are important for studying global dynamics of the Earth because they define the equation describing geophysical excitation of polar motion (PM) and are closely related to various geophysical parameters. The first attempts to estimate the CW parameters started shortly after the establishment of the International Latitude Service in 1899. Several important results are shown in Table 1; for more complete review of the investigations concerning the Chandler wobble see (Plag et al., 2005).

An important contribution to modeling the observed Chandler wobble had been done by Jeffreys (1940, 1968). He assumed that the excitation function of the free wobble can be adequately modeled as a white noise process. After using the linear equation of polar motion he could arrive at the stochastic model of the Chandler wobble, which is the randomly excited harmonic oscillator with damping. Jeffreys (1940, 1968) used his model and the maximum likelihood method (MLM) scheme to analyze the ILS observations of polar motion. The corresponding estimates of T and Q are given in Table 1. The model of Jeffreys had been further developed by Ooe (1978), Wilson and Vicente (1980, 1990); see Table 1 for their results. The most frequently used estimate of T and Q is that by Wilson and Vicente (1990) based on the ARIMA model and the MLM algorithm: $T = 433.0 \pm 1.1$ days and $Q = 179$ $(74 - 789)$.

A new approach to the estimation of the CW parameters was proposed by Kuehne and Wilson (1996), and Furuya and Chao (1996). They adopted the optimization condition stating that the values of T and

Table 1: Selected estimates of the CW parameters with 1σ uncertainties, the period T_c in days and the quality factor Q_c.

Source	Method‡	F_c		Q_c	data (length in yr)
Jeffreys (1940)	AR	446.7 ± 6.8	46	(37–60)	ILS (42)
Jeffreys (1968)	AR	433.2 ± 3.4	61	(37–193)	ILS (68)
Ooe (1978)	MEM–AR	434.8 ± 2.0	96	(50–300)	ILS (76)
Wilson & Vicente (1980)	MLM–ARIMA	433.3 ± 3.6†	175	(48–1000)†	ILS (78)
Wilson & Vicente (1990)	MLM–ARIMA	433.0 ± 1.1	179	(74–789)	ILS+BIH (86)
Kuehne & Wilson (1996)	LSQ–PM/AAM	439.5 ± 1.2	72	(30–500)	Space93+AAM (9)
Furuya & Chao (1996)	OPT–PM/AAM	433.7 ± 1.8	49	(35–100)	Space94+AAM (11)

† These are not 1-σ but 90% uncertainties
‡ AR – autoregressive model, ARIMA – autoregressive integrated moving-average model, MEM – maximum entropy method, MLM – maximum likelihood method, LSQ – least squares method, OPT – optimization method, PM/AAM - simultaneous analysis of PM and AAM data

Q are such that the corresponding polar motion transfer function yields the best agreement between the observed polar motion and atmospheric angular momentum (AAM) series. This condition was then applied to the simultaneous analysis of the PM and AAM data, and the CW parameters were estimated by the least-squares (LSQ) or the optimization (OPT) procedure.

Here we follow the algorithm described by Brzeziński (2005) based on the Kalman deconvolution filter developed by Brzeziński (1992). This filter can be used to analyze either the polar motion data alone, or simultaneously the polar motion and the excitation data, in order to estimate the unknown residual excitation. By imposing the minimum variance constraint upon the estimated unknown excitation we can find the best value of the resonant parameters T and Q. We will apply this algorithm to different sets of polar motion and geophysical (atmospheric, oceanic and hydrological) excitation data. The estimated CW parameters will be compared to each other as well as to the earlier results given in Table 1.

2. DESCRIPTION OF THE MODEL

Geophysical excitation of the Chandler wobble is governed by the following first-order differential equation (e.g. Brzeziński, 1992)

$$\dot{p} - i\,\sigma_c p = -i\,\sigma_c \chi, \tag{1}$$

in which $i = \sqrt{-1}$ denotes the imaginary unit, $p = x_p - i\,y_p$ describes the change of the terrestrial direction of the Celestial Intermediate Pole, that is polar motion; and $\chi = \chi_1 + i\,\chi_2$ is the forcing (excitation) function of the geophysical fluid. The complex angular frequency of the Chandler resonance is $\sigma_c = 2\pi F_c\,(1 + i/2Q_c)$. The underlying terrestrial reference system is geocentric with its z-axis pointing towards the North pole, the x-axis towards the Greenwich meridian and the y-axis towards 90^o East longitude.

We assume for the rest of the paper that the excitation χ is a stochastic process with power spectral density (PSD) near F_c being approximately constant and equal to S_c.

As a next step we assume that the excitation of polar motion is a sum of the observed excitation χ_o (AAM, oceanic AM – OAM, hydrological AM – HAM) and the residual unknown excitation denoted χ_u

$$\chi = \chi_o + \chi_u. \tag{2}$$

These excitation functions are generated by the stochastic processes described by the following stochastic differential equations

$$\dot{\chi}_o = k_o \chi_o + w_o; \qquad \dot{\chi}_u = k_u \chi_u + w_u, \tag{3}$$

in which the coefficients k_o, k_u fulfill the stationarity condition $\Re k_o, \Re k_u \leq 0$ (with $\Re$ denoting the real part of a complex number) and $\{w_o\}, \{w_u\}$ are zero-mean, white Gaussian noises. In the following analysis we assumed $k_o = k_u = 0$, that is the random walk model for both χ_o and χ_u.

Having defined the state vector $[p\ \chi_o\ \chi_u]^T$ we can implement Kalman smoother for the linear system defined by equations (1), (2), (3), as described in details by Brzeziński (1992). By using simultaneous observations of p and χ_o as an input for the Kalman recursion we can smooth p and χ_o and estimate the unknown excitation χ_u. Several options of this algorithm are possible when applying to real data. First, we can use only the polar motion data. In this case the filtering becomes a pure deconvolution procedure. Second, it is possible to use either one or several observed excitation series (AAM and OAM, or AAM, OAM and HAM). In case of two or three excitation series we can treat them either as separate state variables or add them together prior to the analysis (we adopted this option here).

A straightforward approach to the CW parameters estimation is to find F_c, Q_c which minimize the mean squared value of the estimated unknown excitation χ_u. A more sophisticated algorithm, applied by Furuya and Chao (1996), is to compute the Fourier spectrum of the estimated residuals and minimize only the components from the vicinity of the Chandler frequency.

Below, we will proceed as follows. First we compute the mean-squared value V of the residual excitation and find its minimum with respect to F and Q by a 2-dimensional search procedure. Under certain assumptions, this procedure can be identified with the MLM algorithm and the confidence intervals defined by the cross-sections $V = V_{min}(1 + \varepsilon)$, for some $\varepsilon > 0$.

3. DATA ANALYSIS AND RESULTS

We use the following data sets in our analysis, PM data:

`POLE2010` – Kalman filter combination series (Ratcliff and Gross, 2011), 1900.0–2011.5;

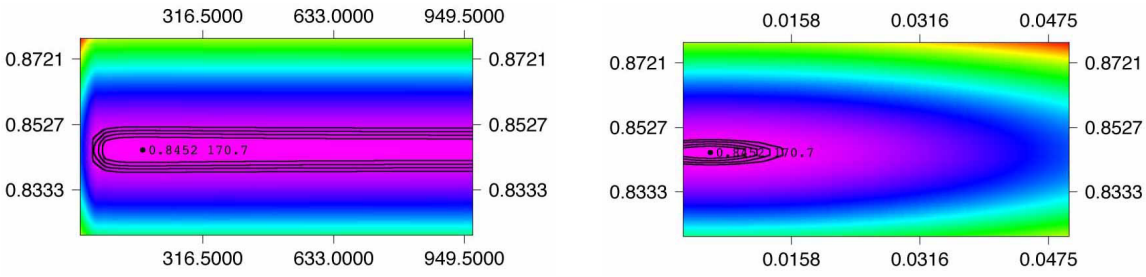

Figure 1: Chandler wobble parameters estimation from simultaneous analysis of PM and AAM data. The mean-squared value of residual excitation is shown as function of F and Q (left), and of F and 1/Q (right). Period of analysis: 1948-2010, input data PM – Pole 2010 and AAM – NCEP reanalysis.

`C01` – IERS combination of the optical astrometry observations (Vondrák *et al.*, 1995) with the BIH and IERS solutions, 1900.0–2012.0;

`C04` – IERS combined solution (Bizouard and Gambis, 2009), 1962.0–2009.6;

AAM data

`NCEP` – AAM series estimated from the output fields of the U.S. NCEP-NCAR reanalysis project (Kalnay et al., 1996), 1948–2012;

`ERA-int` – ERA Interim reanalysis from ECMWF (Uppala et al., 2008), 1989–2009;

Table 2: Chandler wobble parameters estimated from the simultaneous analysis of polar motion and AAM data: period T_c in days, quality factor Q_c and mean-squared value V_c of residuals (in mas^2).

Data sets	F_c	T_c	Q_c	V_c
(a) Period of analysis 1900.0–2011.5				
`C01`	0.8440	432.8	∞	1245
`POLE2010`	0.8435	433.0	2400	913
(b) Period of analysis 1948.0–2009.5				
`C01`	0.8449	432.3	235	1022
`C01/NCEP`	0.8459	431.8	111	1063
`POLE2010`	0.8434	433.1	128	678
`POLE2010/NCEP`	0.8459	431.8	90	708
(c) Period of analysis 1949.0–2002.9				
`C01/NCEP`	0.8498	429.8	230	1188
`C01/NCEP/ECCO1`	0.8492	430.1	380	1162
`POLE2010/NCEP`	0.8443	432.6	77	691
`POLE2010/NCEP/ECCO1`	0.8436	433.0	87	669
(d) Period of analysis 1980.0–2002.1				
`C01`	0.8418	433.9	∞	235
`C01/NCEP`	0.8439	432.8	125	269
`C01/NCEP/ECCO2`	0.8445	432.5	83	253
`POLE2010`	0.8417	433.9	∞	185
`POLE2010/NCEP`	0.8439	432.8	127	217
`POLE2010/NCEP/ECCO2`	0.8445	432.5	85	202
(e): Period of analysis 1989.0–2009.0				
`C04`	0.8423	433.6	269	186
`C04/ERA-interim`	0.8474	431.0	82	175
`C04/ERA-int/OMCT`	0.8472	431.1	64	144
`C04/ERA-int/OMCT/LSDM`	0.8491	430.2	53	163

OAM data

`ECCO` - OAM series based on the MIT global ocean model (Gross et al., 2003)

`ECCO1` - ECCO_50yr solution, 1949-2002;
`ECCO2` - c20010701 solution, 1980-2001;

`OMCT` - OAM series computed from the Ocean Model for Circulation and Tides (Dobslaw & Thomas, 2007), 1989-2009;

HAM data

`LSDM` - HAM series estimated from the output of the global hydrological model LSDM (Dill, 2008), 1989-2009.

We perform a consistent initial reduction of all the polar motion and geophysical excitation series. The purpose is to remove all deterministic signals which are not relevant to the problem considered. By an unweighed least squares fit, we estimate parameters of the model comprising the sum of complex sinusoids with periods ± 1, $\pm 1/2$, $\pm 1/3$ years, where the sign +/– indicates the prograde/retrograde motion, and the 4-th order polynomial accounting for low-frequency variation. This polynomial-harmonic model is then removed and the residual excitation series are simultaneously smoothed and interpolated at uniform 10-days intervals by the Gaussian low-pass filter with full width at a half of maximum equal to 20 days.

We estimate the Chandler wobble parameters for the following combinations of the data sets

1948.0 – 2009.5: C01/NCEP, POLE2010/NCEP;
1949.0 – 2003.0: C01/NCEP/ECCO1, POLE2010/NCEP/ECCO1;
1980.0 – 2002.3: C01/NCEP/ECCO2, POLE2010/NCEP/ECCO2;
1989.0 – 2009.0: C04/ERA-int/OMCT/LSDM.

Results of the analysis are shown in Figure 1 and Table 2.

4. CONCLUSIONS

Fig. 1 shows that the constant variance cross-sections are oriented along the F and Q axes which indicates the statistical independence of the estimates of the frequency F_c and the quality factor Q_c. Analysis of the polar motion data alone yields reliable estimates of the CW frequency F_c but exhibits some instability with respect to the quality factor Q_c. When taking into account the excitation series in the analysis, the estimated period becomes shorter, down to about 430 days which can be compared to the adopted reference value $T_c = 433.0 \pm 1.1$ day. At the same time, the estimated quality factor becomes lower, down to the factor of 3, with respect to the reference value $Q_c = 179$ $(74 - 789)$. The research reported here has to be continued. Particular problem which will be addressed in the next future are: 1) clarification of the problem of assigning the confidence intervals to the estimated parameters; 2) minimizing the variance in the vicinity of the Chandler frequency instead of that of the whole residual series.

Acknowledgments. The first author expresses his sincere thanks for the travel grant provided by the Local Organizing Committee of the Journées 2013. This work was supported by the Polish national science foundation NCN under grant No. DEC-2012/05/B/ST10/02132.

5. REFERENCES

Bizouard, C., and Gambis, D., 2009, "The combined solution C04 for Earth Orientation Parameters consistent with International Terrestrial Reference Frame 2005", in.: Geodetic Reference Frames, H. Drewes (ed.), IAG Symposia 134, Springer Verlag, Berlin Heidelberg, pp. 265–270.

Brzeziński, A., 1992, "Polar motion excitation by variations of the effective angular momentum function: Considerations concerning deconvolution problem", manuscripta geodaetica 17, pp. 3-20.

Brzeziski, A., 2005, "Review of the Chandler Wobble and its excitation", in.: Plag et al., 2005, pp. 109–120.

Dill, R., 2008, "Hydrological model LSDM for operational earth rotation and gravity field variations", Scientific Technical Report 08/09, Deutsches GeoForschungsZentrum GFZ, Potsdam, Germany, 37 pp.

Dobslaw, H., and Thomas, M., 2007, "Simulation and observation of global ocean mass anomaly", J. Geophys. Res.112, C05040, doi: 10.1029/2006JC004035.

Furuya M. and Chao B. F., 1996, "Estimation of period and Q of the Chandler wobble", Geophys. J. Int.127, pp. 693–702.

Gross, R. S., Fukumori, I., and Menemenlis, D., 2003, "Atmospheric and oceanic excitation of the Earth's wobble during 1980-2000", J. Geophys. Res.108 (B8), 2370, doi: 10.1029/2002JB002143.

Jeffreys H., 1940, "The variation of latitude", MNRAS 100(3), pp. 139–155.

Jeffreys H., 1968, "The variation of latitude", MNRAS 141(2), pp. 255–268.

Kalnay, E., et al., 1996, "The NMC/NCAR 40-year reanalysis project", Bull. Amer. Met. Soc. 77, pp. 437–471.

Kuehne J., Wilson C. R., and Johnson S., 1996, "Estimates of the Chandler wobble frequency and Q", J. Geophys. Res.101(B6), pp. 13573-13579.

Ooe M., 1978, "An optimal complex ARMA model of the Chandler wobble", Geophys. J. R. Astron. Soc. 53, pp. 445–457.

Plag, H.-P., Chao, B., Gross, R., and van Dam, T., (eds.), 2005, Proc. Workshop "Forcing of polar motion in the Chandler frequency band: a contribution to understanding interannual climate variations", Cahiers du Centre Européen de Géodynamique et de Séismologie, Vol. 24, Luxembourg.

Ratcliff, J. T., and Gross, R., 2011, "Combinations of Earth Orientation Measurements: SPACE2010, COMB2010, and POLE2010", JPL Publication 11-15, NASA JPL, California Inst. of Technology, Pasadena, Ca, USA.

Uppala, S., et al., 2008, "Towards a climate data assimilation system: status update of ERA Interim", ECMWF newsletter 115, pp. 12–18.

Vondrák, J., Ron, C., Pesek, I., and Cepek, A., 1995, "New global solution of Earth orientation parameters from optical astrometry in 19001990", A&A 297, pp. 899–906.

Wilson C. R., and Vicente R. O., 1980, "An analysis of the homogeneous ILS polar motion series", Geophys. J. R. Astron. Soc. 62, pp. 605–616.

Wilson C. R., and Vicente R. O., 1990, "Maximum likelihood estimates of polar motion parameters", in.: Variations in Earth Rotation, D. D. McCarthy and W. E. Carter (eds.), AGU Geophysical Monograph Series vol. 59, Washington, D.C., pp. 151-155.

NATURAL AND SYSTEMATIC POLAR MOTION JUMPS

Ya. CHAPANOV[1], J. VONDRÁK[2], C. RON[2], R. PACHALIEVA[1]
[1] National Institute of Geophysics, Geodesy and Geography of Bulgarian Academy of Sciences
Acad. G. Bonchev Str., Bl.3, Sofia 1113, Bulgaria,
e-mail: yavor.chapanov@gmail.com
[2] Astronomical Institute, Academy of Sciences of Czech Republic
Boční II, 14100 Prague, Czech Republic
email: vondrak@ig.cas.cz, ron@ig.cas.cz

ABSTRACT. Polar motion consists mainly of two harmonic oscillations with variable phases and amplitudes and small irregular variations. The small irregular variations may be due to various geophysical excitations and observation inaccuracy (mostly in the first half of the last century). A part of irregular polar motion variations consists of fast jumps of the mean values of polar motion coordinates. The direct determination of the polar motion jumps is difficult, because the jump values are very small relative to the seasonal and Chandler amplitudes. A useful high sensitive method of data jumps determination is proposed. The method consists of data integration and piecewise linear or parabolic trends determination. This method is applied to determine the natural and systematic polar motion jumps existing in pole coordinates from the solutions OA10 for the period 1899.7–1962.0 and C04 for the period 1962.0-2013.5. Only a few of the determined polar motion jumps can be interpreted as systematic biases due to observational errors. The major part of the detected polar motion jumps occurs almost regularly near the epochs of minimum amplitude (due to the beat of seasonal and Chandler wobbles), so the natural origin of these jumps is supposed.

1. INTRODUCTION

The modern knowledge uses time series of many years' permanent observations. The data contain some small residual systematic deviations due to instrument and station changes. Determination of the systematic deviations from the mean values was applied in (Chapanov et al., 2007, 2008; Gambis et al., 2011) by means of linear trends in integrated time series. This approach is used here in a method of data and velocity jumps detection by means of parabolic and linear trends in integrated time series.

2. A HIGHLY SENSITIVE METHOD OF IMPULSE DETECTION

The method of data jumps determination consists of several steps. The first step is a removal of linear trend from the original data, followed by the integration of the resulting time series. The new integrated time series consists of oscillations with the amplitudes smaller than those in the original data and of the parts with visible piecewise significant linear or parabolic trends. The parts with linear trends of integrated data correspond to the constant mean behavior of the original data, the sudden changes of the linear trends occur at the epochs of the jumps in the original data. The parts of integrated data with significant parabolic trends point out to the linear variations of the original data. The second step of the method is the creation of the table containing all the epochs of data jumps. The next step consists in calculating the mean values or trends in the original data parts, corresponding to the table of jump epochs, and the last step is the calculation of jump values between neighboring data parts.

The time series are integrated numerically by the well known trapezoid rule. Let consider function f of argument x, discretized into $N+1$ equidistant points $f(x_i)$, $i = 1, 2, \ldots, N+1$. Let the first argument $x_1 = a$, and last argument $x_{N+1} = b$. Then the grid spacing is $h = (b-a)/N$ and the trapezoid approximation to the integral is

$$\int_a^b f(x)dx = \frac{h}{2}\sum_{k=1}^{N}(f(x_{k+1}) + f(x_k)) = \frac{b-a}{2N}(f(x_1) + 2f(x_2) + \ldots + 2f(x_N) + f(x_{N+1})) \qquad (1)$$

To obtain the integral of a given time series $f(t_i)$, $i = 1, 2, \ldots, N + 1$ it is necessary to integrate N times the function f with boundaries $a = t_1$ and $b = t_i$, $i = 2,\ldots, N + 1$.

Any data jump of the original data will be expressed as a linear segment of the data after the jump epoch in the integrated time series. Any velocity jump of the original data will be expressed as a parabolic data behavior in the integrated time series.

3. POLAR MOTION JUMPS FOR THE PERIOD 1900-1962

Polar motion consists mainly of two harmonic oscillations with variable phases and amplitudes and small irregular variations. The small irregular variations may be due to various geophysical excitations and observation inaccuracy in the first half of the last century, too. A part of irregular polar motion variations consists of fast jumps of the mean values of polar motion coordinates. The direct determination of the polar motion jumps is difficult, because the jump values are very small relative to the seasonal and Chandler amplitudes.

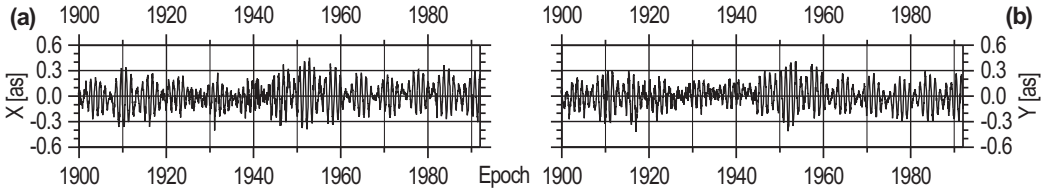

Figure 1: Detrended time series of polar motion coordinates from the solution OA10 of Vondrák et al. (2011).

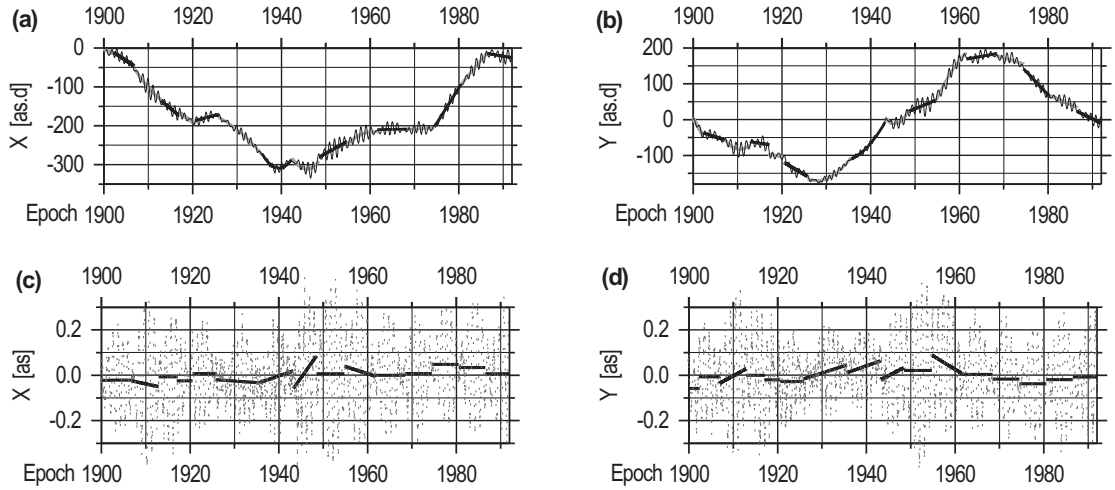

Figure 2: Integrated time series of detrended polar motion coordinates for the period 1900–1992 (thin lines) and their piecewise trends (bold lines) - (a), (b). Location of data and velocity jumps (bold segments) of polar motion coordinates (dashed lines) - (c), (d).

Fig. 1 presents the detrended time series of X and Y pole coordinates from the solution OA10 of Vondrák et al. (2011). The amplitude of polar motion beat is $0.2'' - 0.3''$. Significantly smaller jumps than the beat amplitude will be determined by the method described above. The integrated time series of X and Y pole coordinates from Fig. 1 are approximated by piecewise parabolic or linear trends (Fig. 2 a, b). The greatest part of the breaks between these trends occurs almost regularly in 6-year intervals during the time intervals with the least amplitude of seasonal and Chandler beat, so the natural origin of these jumps is supposed. The epochs of the trend breaks determine the epochs of data and velocity jumps, whose values for the period 1900-1962 are determined according the graphs in Fig. 2 b, c (Table 1). Only two jumps in 1902 and 1917.3 outside the polar motion minima are interpreted as systematic

biases due to observational errors.

4. POLAR MOTION JUMPS FOR THE PERIOD 1962-2013

Polar motion jumps for the period 1962–2013 are determined from the detrended C04 solution after removing all oscillations from annual-Chandler frequency band, determined by 16 harmonics of partial Fourier approximation with periods between 0.97a–1.36a (Fig. 3 a, b). The integrals of the filtered data better represent the existing linear and parabolic trends (Fig. 4 a,b). The RMS errors of polar motion data show significant changes in 1968.0, 1972.0, 1980.0, 1984.0 and 1993 (Fig. 3 c). The first three epochs of the error decrease are connected with data jumps, so they are associated with the systematic errors. Most of the detected data and velocity jumps occur during the polar motion minima and they are probably due to some natural impulse phenomena. The coordinate X has data jump in 1991.2 outside the polar motion minima and this jump is possible to associate with data systematics. Another significant jump outside the polar motion minima occur in 2008.8, whose source of excitation is among the geodynamical events in that time, because it is not possible that one and the same systematic error can occur in all space technique observations.

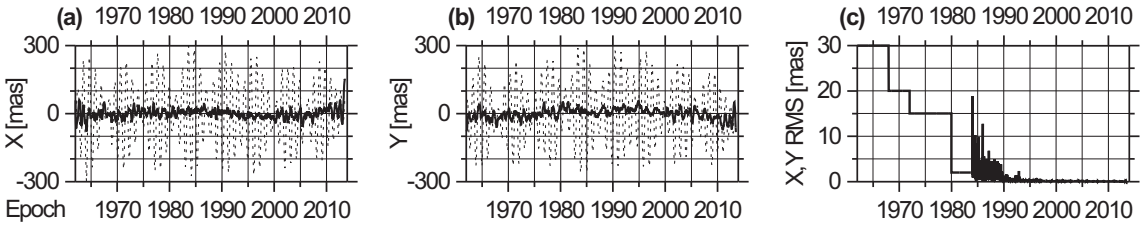

Figure 3: Polar motion detrended coordinates (dashed lines) and filtered data (bold lines) X (a) and Y (b) and their RMS errors (c) from the solution C04.

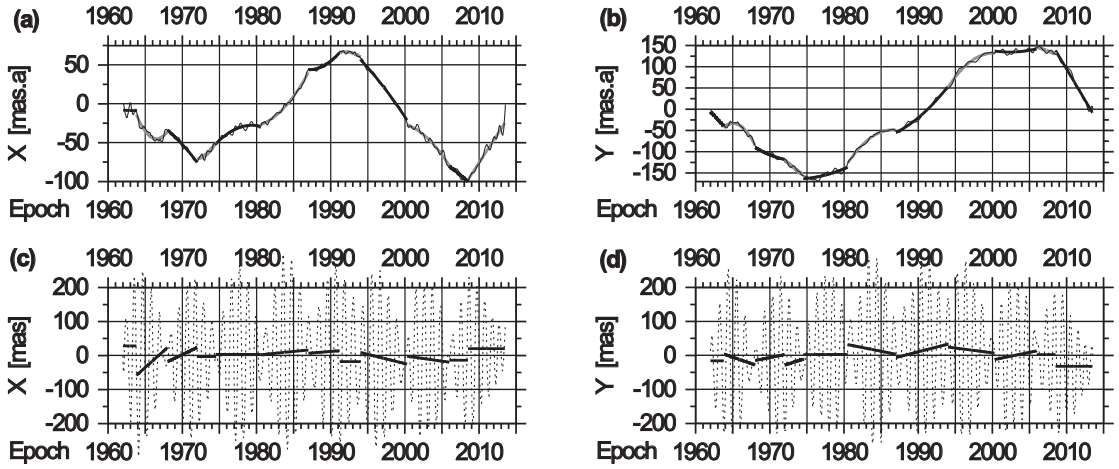

Figure 4: Integrated time series of detrended polar motion coordinates for the period 1962–2013 (thin lines) and their piecewise trends (bold lines) - (a), (b). Location of data and velocity jumps (bold segments) of polar motion coordinates (dashed lines) - (c), (d).

5. CONCLUSIONS

The method of data and velocity jumps determination based on the linear and parabolic trends in the integrated time series is highly sensitive to any impulse behavior of the observed variations due to various geophysical processes like earthquakes, tornadoes, hurricanes, geomagnetic jerks or to some systematic data deviations. The method is extremely sensitive to small data jumps hidden inside the level of random noise and high frequency oscillations of the data, because the integrated time series yield

Table 1: The epochs and values of data and velocity jumps of the coordinates X and Y of the polar motion for the period 1900–1962, determined from the solution OA10 and for the period 1962–2013, determined from the solution C04.

Epoch [years]	X Jumps [mas]	dX/dt Jumps [mas/a]	Y Jumps [mas]	dY/dt Jumps [mas/a]
1899.7	–22	0	–50	0
1902.0	–7	0	–7	0
1906.8	–7	-2.6	–10	+2.1
1912.8	+5	0	+5	0
1917.0	–16	0	–2	0
1920.5	+30	–6.8	–50	10.8
1925.8	–20	–0.8	–20	+6.5
1935.8	–50	+11.4	+15	+5.4
1942.8	–20	+8.8	+40	–12.9
1948.9	–16	0	–8	0
1955.2	+35	–6.5	0	–2.3
1962.0	+27 .3	0	–17.4	0
1963.8	–59.0	+20.0	+7.4	–9.0
1968.0	–18.0	+10.5	–14.6	+4.1
1972.0	–3.7	0	–28.8	+7.2
1974.5	+3.2	0	+2.6	0
1980.5	+1.8	+2.3	+31.7	–4.4
1987.0	+3.2	+3.8	–6.8	+5.7
1991.2	–8.5	–6.6	–	–
1994.1	+7.5	–5.2	+18.2	–2.0
2000.3	–2.1	–3.1	–4.9	+2.3
2006.0	–14.6	0	+1.9	0
2008.5	+8.4	0	–32.8	0

almost zero amplitude of high frequency terms, while the original data with mean linear or constant behavior yield magnitude in the integrated time series as large as the time intervals of these parts. The most of the detected data and velocity jumps occur almost regularly in 6-year intervals during the polar motion amplitude minima due to seasonal and Chandler beat, so the natural origin of these jumps can be supposed. Some systematics are connected with the error jumps in 1902, 1917.3, 1968, 1972, 1980, 1991.3. Anomalous polar motion jump occurs in 2008.5, when X increases by 8 mas and Y decreases by 33 mas, while during polar motion minima the jump magnitudes are less then 18 mas and less then 6 mas/a for the velocity. The 2008.5 anomaly probably prolongs the PM beat period up to 7–8 years.

Acknowledgements. The paper was supported by grant No. 13-15943S awarded by the Grant Agency of the Czech Republic.

REFERENCES

Chapanov, Ya., C. Ron, J. Vondrák, 2007, Estimation of the short-term zonal tides from UT1 observations; Proc. "Journees 2007 Systemes de Reference Spatio-Temporels", N. Capitaine (ed.), ISBN 978-2-901057-59-8, Observatoire de Paris, 2008, 208-209.

Chapanov, Ya., D. Gambis, 2008, Influence of AAM and OAM on the Universal time variations AIP. Conf. Proc. Vol. 1043 "Exploring the Solar system and the Universe", ISSN 0094-243X, ISBN 978-0-7354-0571-4, Melville, New York, 218-219.

Gambis, D., D. Salstein, Ya. Chapanov, 2011, Some systematic errors in AAM and OAM data, Abstr., Journees 2011, 19-21 Sept. 2011, Vienna.

Vondrák, J.; Ron, C.; Štefka, V.; Chapanov, Ya., 2011, New Solution of Earth Orientation Parameters 1900-1992 from Optical Astrometry, and its Linking to ICRF and ITRF, Publications of the Astronomical Society "Rudjer Boskovic", vol. 11, pp. 63-74

DETECTION OF THE 531-DAY-PERIOD WOBBLE FROM THE POLAR MOTION TIME SERIES

H. DING[1], W. SHEN[1,2]
[1] Department of Geophysics, School of Geodesy and Geomatics, Key Laboratory of Geospace Environment and Geodesy of the Ministry of Education, Wuhan University, Wuhan 430079, China
[2] State Key Laboratory of Information Engineering in Surveying, Mapping and Remote Sensing, China
corresponding author: e-mail: wbshen@sgg.whu.edu.cn

ABSTRACT. After Cater (1981, 1982) weakly detected a 530-day-period wobble (531dW) in the polar motion, only few studies were addressed to the observations of this wobble. In this report, based the EOP C04 polar motion time series by using the ensemble empirical mode decomposition method, the 531dW of the polar motion was clearly observed. Here, we present main results, and the details can be found in Ding & Shen (2014). Key words: Polar motion time series; EEMD; 531-day-period wobble.

1. INTRODUCTION

Due to the frequency modulation, the Chandler wobble (CW) has respectively periods 1 cpy (cycles per year) and 0.69 cpy when the beat frequency is 0.157 cpy (Carter 1981, 1982). Based on a 16-year time series of International Polar Motion Data, a 0.686 cpy component with its amplitude being around 10 to 17 mas (milliarcsecond) was weakly detected (Carter (1982). Morgan et al. (1982) found two spectral peaks at 532±10.8 days and 537±15.2 days, with their amplitudes around 8.6±2.0 mas and 7.4±2.2 mas, respectively. After confirming that a 500-day period component exists in the polar motion data with amplitude of 20 mas, Na et al. (2011) suggested that this phenomenon should be caused by resonance of an oscillating mode of the Earth. C. Bizouard (2013 personal communication) investigated this 530-day-period wobble without details released. This wobble (or referred to as an 18-month wobble) was also found in the analysis of the atmospheric angular momentum data by Wahr (1983) and Chen et al. (2010). In this report, using ensemble empirical mode decomposition (EEMD) as a filter, we demonstrated that the amplitude of the 531dW is about 40 mas (mean value). In another aspect, applying the frequency modulation of CW with a modulation index M=0.5 it was shown that there exists a 531dW signal with an amplitude of about 33 mas, but it has an opposite phase with the former. Hence, when the amplitude difference between them is below the background noise level, the 531dW could not be observed by conventional approach; otherwise it can be observed. In the sequel we present the main results. The details are referred to Ding & Shen (2014).

2. METHOD AND RESULTS

The EEMD (Huang & Wu 2008) is suitable for analyzing nonlinear and non-stationary time series (Wu & Huang 2009; Shen & Ding 2013). We chose the EOP C04 series (spanning from 1962 to 2013) to search for the target signals. In order to compare with the results of Carter (1981), we divided the series into three sub-series without overlap: 1962-1977 (16 yr), 1978-1994 (17 yr), and 1995-2013 (18.6 yr) series. For the 1962-1977 series, the data length is as same as that of Carter (1981), hence, we re-estimated the frequency and amplitude of the 531dW.

Based on the Fourier analysis, the target peak appeared only in the spectra of the 1962-1977 series, which is over their corresponding background noise level. This result is consistent with previous studies. The estimate values are listed in Table 1. For the x- and y-components of the 1962-1977 series, the corresponding amplitudes are 11.3 mas and 14.6 mas, while the estimates of both Carter (1981) and Morgan et al. (1982) are about 8 mas.

Carter (1981, 1982) considered that the modulation index M of the CW could be 0.23 or 0.38, where the modulation index M is defined as

$$e_t(x, y) = C_c \sin[\phi_0 + 2\pi f_c t + M. \sin(2\pi f_m t)] \quad (1)$$

		Target Wobble		Chandler Wobble		Annual Wobble	
		Frequency	Amplitude	Frequency	Amplitude	Frequency	Amplitude
1962-1977	x-Component	0.68751±3.2e-4	11.3±4.6	0.84381±2.4e-4	129.2±3.3	1.00023±2.6e-4	97.1±4.1
	y-Component	0.68753±3.4e-4	14.6±4.8	0.84383±2.7e-4	129.2±3.2	1.00028±3.1e-4	90.8±3.9
1978-1994	x-Component	–	–	0.84312±1.7e-4	180.1±2.1	1.00031±2.4e-4	90.6±3.4
	y-Component	–	–	0.84314±1.8e-4	180.1±2.2	1.00029±2.7e-4	84.1±3.5
1995-2013	x-Component	–	–	0.83892±2.5e-4	128.0±3.4	1.00030±3.6e-4	100.8±4.5
	y-Component	–	–	0.83893±2.4e-4	128.2±3.2	1.00027±3.8e-4	91.8±5.1

Table 1: The observed frequencies (cpy) and amplitudes (mas) of the CW, Annual wobble and the target wobble.

where $e_t(x, y)$ is the expected value of the x-component or x-component, f_m the frequency of the modulating signal, set as 0.157 cpy; f_c and C_c are the frequency and amplitude of the CW, and M is the modulation index, defined as $M = \dfrac{\Delta f}{f_m}$, where Δf is the maximum variation of f_m; Φ_0 is the starting phase, set as zero. However, our synthetic tests show that $M = 0.23$ and 0.38 cannot explain the results for the 1977-1994 and 1995-2013 series. Based on the results after using EEMD, when M=0.5, the results of synthetic tests are consistent with the observations of the three polar motion series. Here we only provide a simple explain, with the x-components of the 1962-1977 series being chosen; more details can be found in Ding & Shen (2014). Figure 1 shows the amplitudes of the IMF5 and IMF6 after using EEMD, where IMFs denote the intrinsic mode functions which compose the original data series; and Figure 2 shows the amplitude spectra of the synthetic series without using EEMD, and the modulation index M=0.5. The amplitude of the 531dW in the synthesis is 33.36 mas (Figure 2b), whereas the corresponding results of IMF 6 are 33.2. When M=0.5, the results from the frequency modulation of CW are consistent with the corresponding results from IMF6 very well.

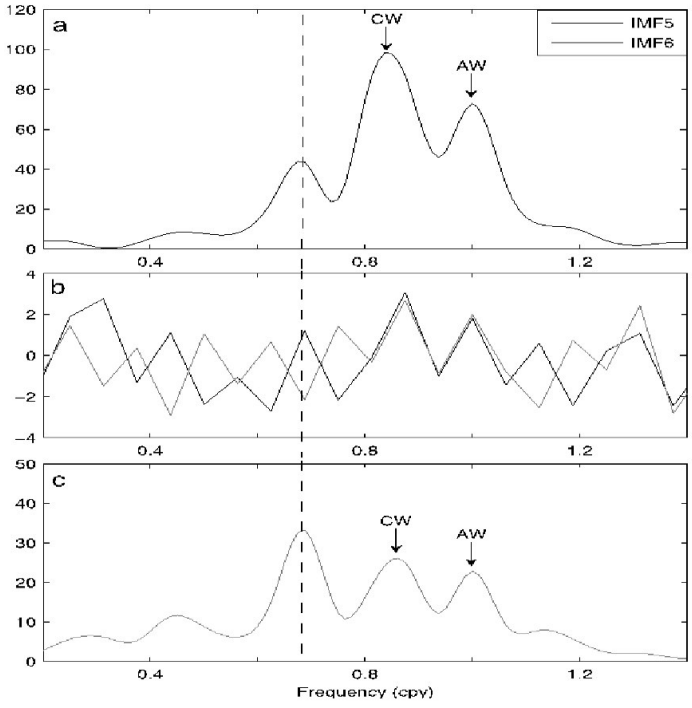

Figure 1: The amplitudes and phase spectra (middle slots) of the IMF 5 (top slots) and IMF 6 (bottom slots) of the x-components of the 1962-1977 series. CW and AW denote Chandler wobble and annual wobble respectively.

We considered that the 531dW in IMF5 might be caused by the atmospheric/oceanic excitation according to the results of Wahr (1983) and Chen et al. (2010) (some other excitations may also exist), whereas the 531dW in IMF6 might be caused by the frequency modulation of CW with a modulation index M=0.5; they have different phases. The relevant details are referred to Ding & Shen (2014).

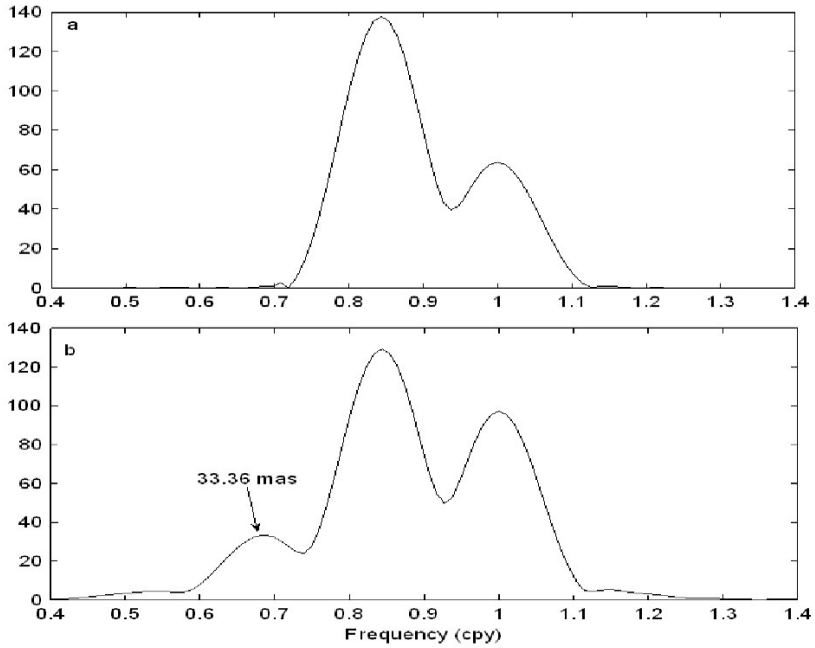

Figure 2: The amplitude spectra of the synthetic series for the x-component of the 1962-1977 series without using EEMD. (a) no frequency modulation; the input amplitudes of the Chandler wobble (CW) and annual wobble (AW) can make the corresponding amplitudes after considering frequency modulation of CW be equal to the observations. (b) The modulation index M=0.5.

3. DISCUSSION

As a suggestion, we consider that the 531dW is composed by two parts: one might be excited by the atmospheric/oceanic angular momentum and other by frequency modulation. Although our observed results can be appropriately explained by the suggested mechanism and the synthetic results, further confirmations are needed because until now the 531dW signal was poorly studied.

4. REFERENCES

Carter WE (1981) Frequency modulation of the Chandlerian component of polar motion. J Geophys Res 86:1653-1658. doi:10.1029/JB086iB03p01653

Carter WE (1982) Refinements of the polar motion frequency modulation hypothesis. J Geophys Res 87:7025-7028. doi:10.1029/JB087iB08p07025

Chen W, Shen WB, Dong XW (2010) Atmospheric Excitation of Polar Motion. Geo-spatial Information Science 13(2):130-136. doi:10.1007/s11806-010-0042-2

Ding H, Shen WB (2014). A 531-days-period wobble of the Polar motion. (submitted to Survey in Geophysics).

Huang NE, Wu Z (2008) A review on Hilbert-Huang transform: Method and its applications to geophysical studies. Rev Geophys 46 RG2006. doi:101029/2007RG000228

Morgan PJ, King RW, Shapiro II (1982) Spectral analysis of variation of latitude derived from lunar laser ranging and satellite Doppler observations (abstract). Eos Trans AGU 63:302

Na S, Cho J, Baek J, Kwak Y, Yoo S, Cho S, Lim H, Kwak Y, Park J, Park P 2011 500-day period component in the Earth's polar motion. American Geophysical Union Fall Meeting 2011 abstract #G53B-0910

Shen WB, Ding H (2013) Observation of spheroidal normal mode multiplets below 1-mHz using ensemble empirical mode decomposition. Geophys J Int, doi: 10.1093/gji/ggt468.

Wahr J (1983) The effects of the atmosphere and oceans on the Earth's wobble and on the seasonal variations in the length of day-II. Results. Geophys J R Astr Soc 74:451-487. doi:10.1111/j.1365-246X.1983.tb01885.x

Wu ZH, Huang NE (2009) Ensemble empirical mode decomposition: a noise-assisted data analysis method. Adv Adapt Data Anal 1:1-41. doi:10.1142/S1793536909000047.12

NUTATION DETERMINATION BY MEANS OF GNSS - COMPARISON WITH VLBI

N. CAPITAINE, K. YAO

SYRTE, Observatoire de Paris, CNRS, UPMC,
61, avenue de l'Observatoire, 75014 – Paris, France
e-mail: n.capitaine@obspm.fr

ABSTRACT. Space geodetic techniques cannot be used for a direct determination of the nutation offsets due to deficiencies in the modeling of the satellite orbits. However, as shown first by Rothacher et al. 1999 and then Weber & Rothacher (2001), GPS can be used to estimate the time derivatives of nutation quantities, similarly to what is done on a regular basis for UT1-UTC rates (or LOD) estimation. We have revisited the potential of GNSS observations for nutation estimation with the high precision currently achieved by this technique. The computations have been carried out by means of a new software, which has been developed in Matlab in the framework of K. Yao's PhD (2013), based on the GPS observations analysis strategy of CNES-GRGS GINS software, but with a few specific characteristics. The reference system for orbit computations is different from that generally used in order to minimize the influence of the a priori values of precession-nutation and UT1-UTC. The method is based on the determination of the time derivatives of the GCRS CIP coordinates (X, Y) with high temporal resolution. The observations used are 3 years of GPS measurements from 1 January 2009, obtained from a dense and globally distributed reference station network. The Xdot and Ydot time series so obtained are then analyzed in order to determine the corrections to the amplitudes of the short periodic terms of the IAU 2000 nutation model. The methodology, time series and results of this analysis are compared with those obtained from Very Long Baseline Interferometry (VLBI) observations of extragalactic radio sources.

1. INTRODUCTION

Space geodetic techniques cannot be used for a direct determination of the nutation offsets due to their correlations with the orbital elements of the satellite the computation of which is affected by the deficiencies in the modeling of the satellite orbits. However, as shown first by Rothacher et al. 1999, GPS can be used to estimate the nutation rates, similarly to what is done on a regular basis for LOD estimation; these authors computed a series of nutation rates covering 3.5 years, which was used for the estimation of the corrections to the IERS 1996 nutation model. Yet, nutation rates are not part of the IGS product and no other series of nutation rates have been provided since that time. The purpose of this study, done in the framework of K. Yao's PhD (2013), is to investigate the potential of GNSS observations for nutation estimation with the high precision that is currently achieved by this technique. We aim at developing the best use of GPS observations, independently of VLBI, for determining the nutation of the Earth's axis with the best possible accuracy.

2. ORBITAL ELEMENTS AND EARTH ORIENTATION PARAMETERS

The observed orbital elements of an artificial satellite referred to the GCRS (Geocentric celestial reference system) depend on the coordinates, X, Y of the CIP (Celestial Intermediate Pole) in the GCRS, and on the Earth Rotation Angle (ERA) at date t. Theoretically, these Earth Orientation Parameters (EOP) can be derived from the corresponding variations in the orbital elements of the satellite. However, due to strong correlations, their estimates are affected by the systematic errors in the orbital elements coming from deficiencies in the gravitational and non gravitational forces. In particular, absolute determination of the "celestial pole offsets" (dX, dY) or ERA are not possible from satellite observations. The systematic effects can be minimized for short term variations and with an appropriate choice of the reference system in which the orbit of the satellite is computed. The rates in X, Y and ERA can be estimated provided that the orbital perturbations are modeled with sufficient accuracy over the short time interval of the estimation.

Simplified relationships between the parameters rates can be expressed (at the 1st order of the offsets

and with Keplerian approximation) as follows (Capitaine & Wallace, 2007):

$$\begin{aligned} \dot{\mathrm{ERA}} &= -\dot{\Omega} - \cos i \cdot \dot{u}_0 \\ \dot{X} &= -\sin\Omega \cdot \dot{i} + \sin i \cos\Omega \cdot \dot{u}_0 \\ \dot{Y} &= \cos\Omega \cdot \dot{i} + \sin i \sin\Omega \cdot \dot{u}_0. \end{aligned} \tag{1}$$

Ω, i, being the right ascension of the ascending node and inclination of the orbital plane of the satellite and u_0 the argument of the latitude of the satellite at the osculating epoch.

3. MAIN CHARACTERISTICS OF THE STUDY

The method

The effect of the Earth Orientation Parameters (EOP) appears through the transformation between coordinates [ITRS] in the International Terrestrial Reference System and [GCRS] in the GCRS by the following equation:

$$[\mathrm{GCRS}] = Q(t) * R(t) * W(t) * [\mathrm{ITRS}], \tag{2}$$

where Q(t) is a matrix determined by the coordinates, X, Y, of the Celestial intermediate pole (CIP) in the GCRS, R(t) is the rotation matrix determined by the Earth rotation angle, ERA, and W(t) is a matrix determined by the the pole coordinates, x_P, y_P, i.e. the coordinates of the CIP in the ITRS.

The method used in this work is largely based on the GNSS observations analysis strategy of the CNES-GRGS GINS multi-technique software for orbit determination and Earth dynamics studies (Marty et al. 2011), but with the following specificities which take advantage of the specificity of the GNSS potential for estimation of the EOPs (cf. previous section):

(i) determination of the time derivatives of the GCRS CIP coordinates X, Y, and ERA, with high temporal resolution, along with x_P, y_P (pole coordinates),

(ii) computation of the satellite orbit in an inertial reference system that minimizes the influence of the a priori values for precession-nutation (i.e. X, Y) and UT1-UTC (i.e. ERA), that GPS cannot determine directly.

The new GPS analysis software

The computations are carried out by means of a new GPS analysis software, developed by K. Yao in Matlab environment and implementing the specificities (i) and (ii) described in the previous section.

The motivations are:

- To obtain long time series of time derivatives of the GCRS CIP coordinates (X, Y) and the ERA.
- To minimize the effect (on the computations) of the a priori values for (X, Y) and ERA.

The advantages of the Matlab environment are that codes are easy to understand, vectorial computation are easily programmed; many scientific algorithms functions are available and science programming library in C/FORTRAN can be re-used (i.e. SOFA library); Moreover, built-in tools are available for the visualization and the data analysis, graphical interface, etc.

The inertial system for orbit computation

The inertial reference system TIRS_0 that is used in this work for the satellite orbit computation is based on the Terrestrial Intermediate Reference System (TIRS) defined at date t_0 = 00 h of the beginning epoch of the arc under analysis (cf. Fig. 1). The realization of that reference system, which is not dependent on the X, Y and ERA quantities, minimizes the influence of the a priori values of precession-nutation and UT1-UTC on the computations. For more details on reference systems used for precession-nutation representations, see for example Capitaine & Wallace (2006).

Data set, calculations and estimations

The data set used in this work consists of 3 years of GPS measurements (double-differenced ionosphere-free phase observations) from 1 January 2009, performed every 300 s (315 360 observation epochs) by about 115 stations of IGS tracking network on the Earth on almost 32 satellites. The measurement models and corrections, as well as the models for orbit computations used in the analysis are compliant with the best up-to-date models and corrections.

The GPS observations are analyzed day by day with calculations that are largely based on the GPS analysis method of the GINS software:

- The first part of the calculations consists in the determination of the station clock biases using the GPS ionosphere-free combination, P_c, of the pseudo-range observations.

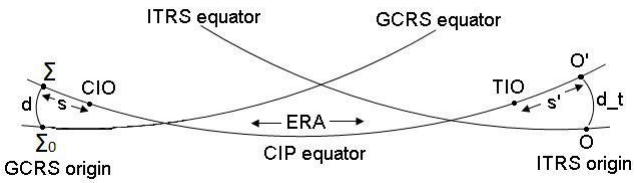

Figure 1: The reference system TIRS_0 is defined by the CIP equator and the origin O' on this equator. It is linked to the Terrestrial Intermediate Reference System, TIRS, defined by the CIP and the TIO (Terrestrial intermediate origin). The distance between O' and the TIO is the TIO locator, s'.

- The second part of the calculation consists of 11 successive steps, including the estimation of the parameters based on an iterative least-squares adjustment using the GPS double-differenced ionosphere-free phase observations, DDL_c. This provides time series of the parameters.

The a priori values for the EOPs are, for polar motion and LOD, the IERS C04 time series and for $\dot{X}, \dot{Y}$, the time derivatives of the IAU2006/2000A precession-nutation series.

The results obtained from the estimation process are composed of time series covering 3 years of (i) corrections to the time derivatives of the celestial pole offsets $d\dot{X}, d\dot{Y}$, every 6 h, i.e. corrections to the nutation rates (see Fig. 2), (ii) corrections to $E\dot{R}A$, i.e. dLOD, and (iii) polar motion corrections (i.e. dx_P, dy_P).

The computation has been successfully validated in several ways: computation of the residuals obtained by a fit to the DDLc observations available on the IGS FTP website (RMS≈ 8 mm), comparison of the zenith tropospheric delay with respect to the IGS product, evaluating the 3D orbit difference in the ITRF w.r.t. the IGS final orbit (typically ≈ 5 cm) and also by comparing the estimated pole coordinates to those obtained by GINS (typically ≈ 50 μas).

The correlations between the EOPs are included between 0.02 and 0.23 ($\dot{X}$ or $\dot{Y}$ and $E\dot{R}A$).

4. NUTATION ESTIMATION

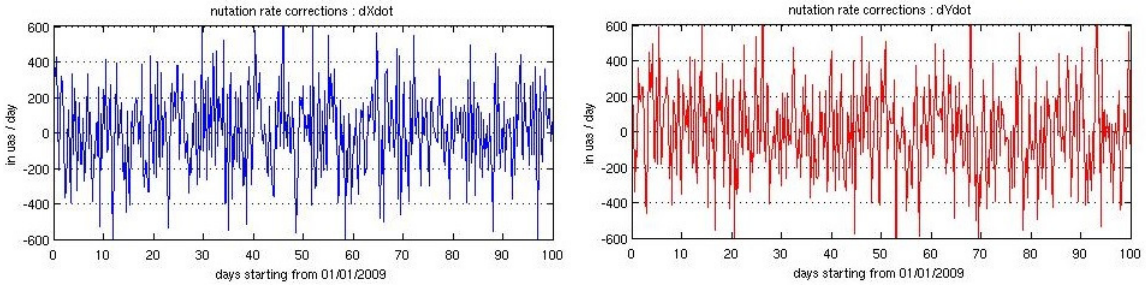

Figure 2: Time series (over a 100-day interval) of the estimated corrections ($\mathrm{d}\dot{X}$, $\mathrm{d}\dot{Y}$) to the time derivatives of the X (left) and Y (right) GCRS CIP coordinates; unit: μas/day.

We have used the 3-yr $\mathrm{d}\dot{X}$, $\mathrm{d}\dot{Y}$ time series as pseudo-observations to estimate corrections to the most important short-period terms of the nutation rates, using the following expressions, expressed as functions of the prograde and retrograde circular nutations:

$$d\dot{X}(t) = \sum_i [-a_{real,i}\sin(\alpha_i) - a_{imag,i}\cos(\alpha_i)]\dot{\alpha_i} \quad (3)$$

$$d\dot{Y}(t) = \sum_i [a_{real,i}\cos(\alpha_i) - a_{imag,i}\sin(\alpha_i)]\dot{\alpha_i}, \quad (4)$$

where where j is the unit of imaginary number, α_i is the argument of the IAU 2000 nutation term, i, and the coefficients $a_{real,i}, a_{imag,i}$ are the corrections to the coefficients of the nutation term with argument α_i.

The corrections estimates for the most important periodic terms are listed in Table 1. These discrepancies are expected to be due to geophysical causes, such as tidal or atmospheric perturbations. The

period (days)	$a_{real,i}$ μas	sigma μas	$a_{imag,i}$ μas	sigma μas
-15.39	6	9	-15	9
15.39	-5	9	-7	9
13.66	-14	8	-8	8
-12.66	2	7	19	7
-9.56	-10	5	-2	5

Table 1: GPS nutation estimation results (largest corrections)

accuracy obtained for the estimation of the corrections to the nutation terms is included between 2 to 14 microarcseconds according to the period of the term. It should be noted that such an accuracy is better than the accuracy which can be obtained by VLBI for the short periodic terms of nutation.

These nutation corrections derived from the 3-year (2009-2012) time series of corrections to the IAU 2006/2000 X and Y rates estimated by GPS have been compared to nutation corrections derived from the 22-year (1990-2012) time series of corrections to IAU 2006/2000 X, Y estimated by VLBI. The two set of corrections have been found to be of the same order of magnitude, but not perfectly consistent.

5. SUMMARY

GPS observations covering a 3-yr interval have been analyzed for estimating corrections to the short periodic terms of nutation. The computations have been carried out by means of a new GPS analysis software in Matlab environment, developed by K. Yao in the framework of his PhD (2013). In this analysis, the satellite orbit has been integrated in an appropriate inertial system which reduces the influence of the error in the a priori values for precession-nutation and the Earth rotation angle ERA.

This analysis has provided a 3-year time series of nutation rates corrections to the IAU2006/2000A a priori values along with corrections to the ERA rate and pole coordinates. These time series have been used to estimate corrections to the 28 largest nutation terms with period less than 20 days with an accuracy of about 10 μas.

This study proves that the GNSS technique alone (i.e. without any use of VLBI estimates) has the potential to determine the short-period terms of nutation. The corrections obtained by GPS for the short periodic terms of nutation has been compared with those obtained by VLBI. The two set of corrections are of the same order of magnitude, but they are not perfectly consistent. A better understanding of such discrepancies require further studies (Yao & Capitaine 2014).

6. REFERENCES

Capitaine N. & Wallace P.T., 2006, "High precision methods for locating the celestial intermediate pole and origin", A&A 450, 855

Capitaine N. & Wallace P.T., 2007, "The transformation between the Terrestrial and Celestial Reference Systems: Needs and potential of GPS and Galileo", Proceedings of the ESA 1st Colloquium Scientific and Fundamental Aspects of the Galileo Programme, ESA (ed.), on CD

Marty J.C., Loyer S., Perosanz F., Mercier F., Bracher G., Legresy, B. Portier L., Capdeville H., Fund F., Lemoine J.M. , Biancale R., 2011, "GINS: The CNES/GRGS GNSS scientific software", in Proceedings of the ESA 2011 Galileo scientific meeting

Rothacher M., Beutler G., Herring T. A., Weber R., 1999, "Estimation of nutation using the Global Positioning System", JGR 104, n^0B3, pp. 4835–4859

Weber, R., Rothacher M., 2001, "A Revised Set of Nutation Amplitudes Calculated From six Years of GPS Data", AGU Meeting 2001, abstract G51C-0252

Yao, K. 2013, "Nutation determination by VLBI and GPS techniques", Thèse de doctorat (PhD), Université Pierre et Marie Curie, 29 avril 2013

Yao K. & Capitaine N., 2014, in preparation

THE EARTH'S NUTATION: VLBI VERSUS IAU 2000A

S. LAMBERT[1], S. ROSAT[2], N. CAPITAINE[1], J. SOUCHAY[1]
[1] SYRTE, Observatoire de Paris, CNRS, UPMC
61, avenue de l'Observatoire, 75014 – Paris, France
e-mail: sebastien.lambert@obspm.fr
[2] Université de Strasbourg, EOST, IPGS, CNRS
5 rue René Descartes, 67084 – Strasbourg Cedex, France

ABSTRACT. The nutation measured by VLBI is compared with the IAU 2000A model. The differences are modeled empirically by adjusting the free core nutation and a number of tidal terms. The signal remaining in the residuals is discussed.

1. INTRODUCTION

Nutation time series obtained by very long baseline interferometry (VLBI) match the IAU 2000A model (Mathews et al. 2002) with differences of ∼200 microseconds of arc (μas) in rms. The main signal showing up in the residuals is due to the forced free motion associated with the retrograde free outer core nutation (FCN). It produces a quasi periodic signal of space-referred period about 430 days. The source of the excitation of the FCN is believed to be in the Earth's surface fluid layer pressure variations (e.g., Dehant et al. 2005) but remain unverified due to strong inconsistencies in the global circulation models at diurnal frequencies (de Viron et al. 2005), as well as the atmospheric contribution to the nutation (Bizouard et al. 1998, de Viron et al. 2005). In addition, several unmodeled or mismodeled tidal terms show up in the residuals at the level of a few tens of μas. The accurate determination of their amplitude is of importance to confirm the nutation theory, especially if they can constrain the geophysical parameters used in the non-rigid Earth theories. In this study, we fit corrections to IAU 2000A to VLBI data, including the FCN and several tidal terms.

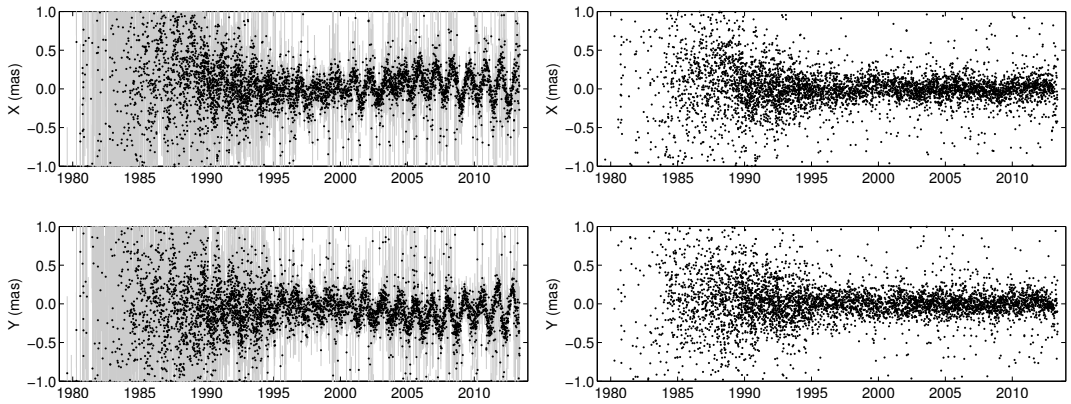

Figure 1: (*Left*) Nutation offsets to IAU 2000A as derived from VLBI observations. (*Right*) Residuals of the adjustment of the 21 tidal terms of Herring et al. (2002) (error bars were not reported).

2. ANALYSIS

We used nutation offsets to IAU 2000A as provided by the operational VLBI solution opa2013a made available by the Paris Observatory analysis center of the International VLBI Service for Geodesy and Astrometry (IVS; Schuh & Behrend 2010). To clean data from outliers, generally associated with unreliable networks or corrupted data, points whose distance to the mean is higher than 10 times the uncertainty were removed. This elimination is repeated until the χ^2 is reasonably close to unity. The

obtained nutation offsets to IAU 2000A are plotted in Fig. 1 (left).

Then, the complex-valued nutation offsets $\eta = \mathrm{d}X + \mathrm{i}\mathrm{d}Y$ were modeled by (i) a retrograde, 430-day signal with variable amplitude and phase to account for the FCN, and (ii) a number of tidal terms of fixed periods and phases of the form $\eta = A\mathrm{e}^{i\phi}$, where A is the complex amplitude, and ϕ the time-dependent astronomical phase given by linear combination of the Delaunay variables and mean longitudes of the planets (IERS 2010). The formal error associated with the observations was inflated by a scale factor of 1.3 and a noise floor of 60 μas. The values of the noise floor and the scale factor were determined over the period 1990–2013 by a method similar to Herring et al. (2002) and Lambert et al. (2008).

In a first step, 21 lunisolar terms used in Herring et al. (2002) and Mathews et al. (2002), were adjusted, leaving residuals displayed in Fig. 1 (right). The amplitudes are reported in Table **??**. These corrections, together with the fitted FCN signal, can be used to better predict the nutation for astro-geodetic applications. A visual inspection of the residuals in X reveals an interannual oscillation that reaches positive maxima around 2000 and 2006.

In a second step, we applied high resolution spectral methods in order to determine periods and phases of the remaining terms in the residuals. First, we used the frequency analysis mapping on unusual samplings (FAMOUS) software package developed by Mignard (2005) in a version modified by Collilieux (2008) that handles errors on observations. After first-guessing a number of spectral lines using a periodogram, FAMOUS uses nonlinear least-squares to refine the frequency of each spectral line. Alternatively, we developed a code (MIMOSA) that looks iteratively for spectral lines which minimize the χ^2 of the residuals. The frequency domain is scanned until the χ^2 is minimum. Then, the optimal frequency is fitted to the amplitude by a gaussian whose center and full width at half maximum give the central frequency and its uncertainty, respectively. The amplitudes and phase are finally adjusted by a global least-square inversion. Both FAMOUS and MIMOSA were applied to the data after 1990 and returned results in agreement within error bars (Table 2). Only three significant peaks were detected. We also check the results using the maximum of entropy method (MEM), which models the signal by an autoregressive (AR) process of order as large as the half number of samples. The power spectral density at any frequency in then deduced analytically using the set of AR coefficients. The MEM was applied to the signal preliminary regularized by taking averaged values every 15 days between 1990 and 2013, leaving about 570 points. The resulting spectrum exhibits peaks at 763 (7), 973 (28), and 2281 (199) days (the values between brackets indicate the full width at half maximum of the power spectral density peak obtained from an AR model of order 250), in agreement with the peaks detected by FAMOUS and MIMOSA.

The question comes now on giving a physical meaning to the peaks revealed by spectral methods. A methods is to compare periods and phases with those of IAU 2000A or the Rigid Earth Nutation (REN 2000; Souchay et al. 1999) tables. However, one cannot identify strictly each fitted term to one frequency. Each fitted term should rather be identified with a group of nutations whose frequencies are close each other around the relevant frequency. The shortest period could correspond to a group including the 727-day terms relevant to the interaction between Venus and the Earth ($4\mathrm{Ve} - 6\mathrm{Ea}$). The longest period could be associated with a group including the 2165-day term relevant to the interaction between the Earth and Jupiter ($F - D + \Omega - \mathrm{Ea} + \mathrm{Ju}$). Finally, the remaining period could correspond to the 943-day purely lunisolar period ($2l - 2F + \Omega$). The rigorous understanding of these terms is part of an ongoing research program.

3. REFERENCES

Bizouard, C., Brzeziński, A., & Petrov, S. D. 1998, J. Geod., 72, 561

Collilieux, X. 2008, Private communication

Dehant, V., Feissel-Vernier, M., de Viron, et al. 2003, J. Geophys. Res., 108, 10.1029/2002JB001763

Dehant, V., de Viron, O., & Greff-Lefftz, M. 2005, A&A, 438, 1149

Herring, T. A., Mathews, P. M., & Buffett, B. A. 2002, J. Geophys. Res., 107, 10.1029/2001JB000165

IERS 2010, International Earth Rotation Service (IERS) Technical Note 36, IERS Conventions 2010, Bundesamt für Kartorgraphie und Geodäsie, Frankfurt am Main, Germany, V–66

Mignard, F. 2005, Private communication

Mathews, P. M., Herring, T. A., & Buffett, B. A. 2002, J. Geophys. Res., 107, 10.1029/2001JB000390

Schuh, H., & Behrend, D. 2012, J. Geodyn., 61, 68

Souchay, J., Loysel, B., Kinoshita, H., & Folgueira, M. 1999, A&A Suppl. Ser., 135, 111

de Viron, O., Schwarzbaum, G., Lott, F., & Dehant, V. 2005, J. Geophys. Res., 110, 10.1029/2005JB003761

l	l'	F	D	Ω	Period	Re(A)	$\pm$	Im(A)	$\pm$
0	0	0	0	1	−6798.3837	41.8	2.3	−19.9	2.3
0	0	0	0	−1	6798.3837	24.3	2.3	−34.1	2.3
0	0	0	0	2	−3399.1919	3.2	2.2	−8.2	2.2
0	0	0	0	−2	3399.1919	10.9	2.2	−5.5	2.2
2	0	−2	0	−2	−1615.7478	−2.6	2.1	−7.6	2.1
−2	0	2	0	2	1615.7478	−2.0	2.1	−10.2	2.1
2	0	−2	0	−1	−1305.4792	−0.5	2.2	8.1	2.2
−2	0	2	0	1	1305.4792	1.7	2.2	5.2	2.2
2	0	−2	0	0	−1095.1750	0.6	2.1	0.4	2.1
−2	0	2	0	0	1095.1750	−5.2	2.1	−2.7	2.1
0	−1	0	0	−1	−385.9983	−1.8	2.1	0.7	2.1
0	1	0	0	1	385.9983	−6.2	2.1	0.6	2.1
0	−1	0	0	0	−365.2596	2.8	2.2	1.8	2.2
0	1	0	0	0	365.2596	−1.0	2.2	−1.3	2.2
0	−1	0	0	1	−346.6358	−1.1	2.3	−1.0	2.3
0	1	0	0	−1	346.6358	−1.4	2.3	−0.1	2.3
0	0	−2	2	−2	−182.6211	−11.9	2.1	4.8	2.1
0	0	2	−2	2	182.6211	6.5	2.1	−2.3	2.1
0	−1	−2	2	−2	−121.7493	0.1	2.1	2.4	2.1
0	1	2	−2	2	121.7493	2.4	2.1	2.2	2.1
1	0	0	−2	0	−31.8119	0.7	2.1	−1.9	2.1
−1	0	0	2	0	31.8119	−1.8	2.1	1.3	2.1
−1	0	0	0	0	−27.5545	−15.8	2.1	−7.3	2.1
1	0	0	0	0	27.5545	−1.0	2.1	0.3	2.1
−1	0	−2	2	−2	−23.9421	−1.0	2.1	0.7	2.1
1	0	2	−2	2	23.9421	−3.0	2.1	−1.8	2.1
0	0	0	−2	0	−14.7653	−2.7	2.0	4.1	2.0
0	0	0	2	0	14.7653	−1.7	2.0	0.4	2.0
−2	0	0	0	0	−13.7773	−1.0	2.1	0.7	2.1
2	0	0	0	0	13.7773	−0.6	2.1	−0.3	2.1
0	0	−2	0	−2	−13.6608	−10.1	2.1	−9.5	2.1
0	0	2	0	2	13.6608	−6.5	2.1	14.3	2.1
1	0	−2	−2	−2	−9.5569	0.5	2.1	−1.3	2.1
−1	0	2	2	2	9.5569	1.2	2.1	0.3	2.1
−1	0	−2	0	−2	−9.1329	−2.1	2.1	0.0	2.1
1	0	2	0	2	9.1329	−3.0	2.1	3.2	2.1
−1	0	−2	0	−1	−9.1207	2.1	2.1	2.6	2.1
1	0	2	0	1	9.1207	1.5	2.1	−2.1	2.1
0	0	−2	−2	−2	−7.0958	−4.3	2.1	−1.6	2.1
0	0	2	2	2	7.0958	−2.7	2.1	2.0	2.1
−2	0	−2	0	−2	−6.8594	−1.5	2.3	1.0	2.3
2	0	2	0	2	6.8594	0.3	2.3	−0.9	2.3

Table 1: Adjustment of the 21 tidal terms of Herring et al. (2002) to the nutation offsets to IAU 2000A. Uncertainties are formal errors corrected by the reduced χ^2 of the adjustment. Unit: μas.

Period (days)	±	Amplitude (μas)	±	Phase (°)	±
		FAMOUS			
2210	57	17	3	−93	11
764	9	13	4	−129	17
978	24	8	3	−173	24
		MIMOSA			
2222	378	16	3	−104	14
766	34	13	4	−121	19
962	65	8	4	173	20

Table 2: Terms detected by the FAMOUS and MIMOSA software packages. Units: amplitudes in μas, periods in days, and phases with respect to J2000.0 in degrees.

GRAVIMETRIC EXCITATION FUNCTION OF POLAR MOTION FROM THE GRACE RL05 SOLUTION

J. NASTULA
Space Research Centre of the PAS
Bartycka 18a, 00-716 Warsaw, Poland
e-mail: nastula@cbk.waw.pl

ABSTRACT.Impact of land hydrosphere on polar motion excitation is still not as well known as the impact of the angular momentum of the atmosphere and ocean. Satellite mission Gravity Recovery and Climate Experiment (GRACE) from 2002 provides additional information about mass distribution of the land hydrosphere. However, despite the use of similar computational procedures, the differences between GRACE data series made available by the various centers of computations are still considerable. In the paper we compare three series of gravimetric excitation functions of polar motion determined from Rl05 GRACE solution from the Center for Space Research (CSR), the Jet Propulsion Laboratory (JPL) and the GeoForschungsZentrum (GFZ). These data are used to determine the gravimetric polar motion excitation function. Gravimetric signal is compared also with the geodetic residuals computed by subtracting atmospheric and oceanic signals from geodetic excitation functions of polar motion. Gravimetric excitation functions obtained on the basis of JPL data differ significantly from the geodetic residuals while and the series obtained from CSR and GFZ are more compatible.

1. INTRODUCTION

Satellite mission Gravity Recovery and Climate Experiment (GRACE) is a source of data on temporal changes in Earth's gravity field. These data are available, in the form of changes in the coefficients C_{mn} S_{mn} - the so-called Level 2 gravity field product, include the GSM coefficients, estimated from satellite data, and the GAB, GAC, and GAD non tidal coefficients from atmosphere, atmosphere plus ocean, and ocean bottom pressure geopotential coefficients, respectively [Tapley et. al., 2004)]. Since 2002 there are have been a number of attempts to better process releases of these GRACE data. Here we use the most recently updated solution of Release 5 (Rl05) processed by three centers: Center for Space Research (CSR), the Jet Propulsion Laboratory (JPL) and the GeoforschungsZentrum (GFZ). The $\triangle C_{21} \triangle S_{21}$ coefficients of the newest Level 2 gravity field product are used here to compute gravimetric excitation functions of polar motion which reflect mainly the influence of the land-based hydrosphere (Hydrological Angular Momentum - HAM). We first explore the extent of agreement among the three Rl05 gravimetric excitation functions. We estimate also how well residual polar motion is explained with these newest gravimetric excitation functions.

2. DATA AND METHOD

The GSM coefficients reflect mainly the influence of the land-based hydrosphere, and to a lesser extent ice mass, and from seismic events, and do not include atmospheric and oceanic signals. This functions are also affected by errors of atmospheric and oceanic model approaches. To obtain information about the impact of all three geophysical fluids: land-based hydrosphere, atmosphere and oceans, the GAC coefficients should be added back to GSM. Atmospheric and oceanic model approaches however are certainly not error-free and the generation of the needed de-aliasing coefficients depends on several initial assumptions, as, e.g., a simplified two-year mean. The equatorial components of the polar motion excitation functions available for transfer of the fluid angular momentum to the solid Earth have been formalized as the χ_1 and χ_2, components, towards longitudes 0^o and 90^o E, respectively [Barnes, et al., 1983; Eubanks, 1993].

The equatorial components of the gravimetric polar motion excitation functions (χ_1 and χ_2) can be simply estimated directly from GRACE degree-2 and order-1 coefficients [Eubanks, 1993; Chen and

Wilson,2005;Chen et al.,2012; Nastula et al., 2007].

$$\chi_1 = -\sqrt{\frac{5}{3}}\frac{1.098 a_E^2 M}{C-A}\triangle C_{21}, \chi_2 = -\sqrt{\frac{5}{3}}\frac{1.098 a_E^2 M}{C-A}\triangle S_{21}$$

where M and a_E are the mass and mean radius of the Earth, respectively, C and A are the Earth's principal moments of inertia.

In the paper we use the following data:

1. GSM product - coefficients $\triangle C_{nm}$, $\triangle S_{nm}$ from RL05GRACE solutions developed by the CSR, JPL, and GFZ centers. The coefficients do not include the effects of atmosphere and ocean (http://icgem.gfz-potsdam.de/ICGEM/). The χ_1 and χ_2 components of gravimetric excitation functions computed from the GSM coefficients reflect mainly the influence of the land-based hydrosphere.

2. GAC de-aliasing product - coefficients $\triangle C_{nm}$ $\triangle S_{nm}$ of the gravitational field from atmospheric pressure (ECMWF) and from ocean bottom pressure (OMCT), prepared by CSR, JPL, and GFZ. (http://icgem.gfz-potsdam.de/ICGEM/). The χ_1 and χ_2 components of excitation functions computed from the GAC coefficients reflect mainly the matter term of the atmospheric and oceanic angular momentum in polar motion excitation.

3. GEOD - Geodetic polar motion excitation χ_1 and χ_2 function, computed from x, y pole coordinates from the IERS C04 combined solution [Gambis, 2004]. Additionally, the motion term including atmospheric winds (NCEP) and oceanic currents (ECCO) are removed from the series by the IERS (http://hpiers.obspm.fr/eop-pc/). The data are daily from 1963 to the present, and also averaged into monthly intervals. GEOD–AAM– OAM - χ_1 and χ_2 components of geodetic residuals GEOD–AAM–OAM containing the hydrological part of polar motion excitation obtained by removing from the geodetic excitation functions merged atmospheric and oceanic excitation computed from the GAC coefficients from the three centers. In this way we obtained three types of residuals GEOD–GACCSR, GEOD–GACJPL, GEOD–GACJPL.

3. RESULTS

Figure 1a compares the variability of χ_1 and χ_2 components (solid – lines)of gravimetric excitation function of polar motion computed from the GSM coefficients. Figure 1b shows similar comparisons after removal of trends and seasonal oscillations; these are estimated by a least–square fitting model, comprised of a 1st order polynomial and a sum of sinusoids with periods 1, $\frac{1}{2}$, $\frac{1}{3}$ years. We should emphasize significant differences between the series obtained from the same solution RL05 from the three data centers. Despite the use of similar procedures, differences among GRACE–related values from models processed by different data centers are still considerable, making their use in interpreting polar motion difficult. The series obtained from the GFZ data is the smoothest while the series received from JPL shows the largest variation (Fig. 1b).

Next, in order to verify which of computed gravimetric series, is compatible with geodetic excitation we compared gravimetric excitation series with geodetic residuals GEOD–AAM–OAM. Diagrams of these gravimetric residuals are also illustrated in Figure 1. As it can be seen from Figure 1a, all gravimetric functions calculated from gravity data show a trend that is not present in the geodetic residuals. From visual inspection of Figures 1 a,b one can see that relatively good agreement between gravimetric excitation functions and the geodetic residuals is obtained from the CSR data, especially for χ_2. This conclusion is confirmed by results shown in both parts of Table 1., which shows correlation coefficients and variances of differences between geodetic residuals and gravimetric excitations.

Comparison of the spectra of the analyzed excitation functions are presented in Figure 2 while Figure 3 shows the phasor diagrams of the most important oscillation which is the annual oscillation. As in Figure 1, one can see the large differences f the results obtained from the data of the three centers. The spectra confirm the largest degree of smoothing in the data from the GFZ, and the relatively best agreement between gravimetric excitation functions computed from the CSR data and the geodetic residuals. Comparing the amplitude of the annual oscillation vectors we can easily see the correspondence between

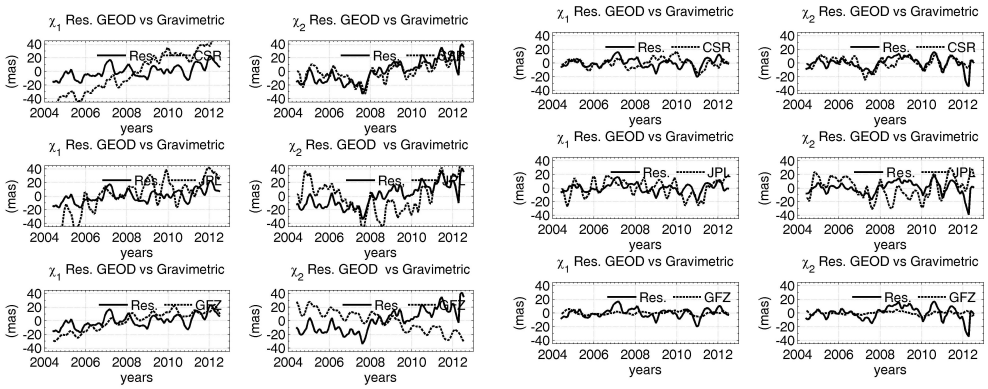

(a) (b)

Figure 1: a) Comparison of gravimetric excitation function computed from GSM coefficients from CSR, JPL, GFZ with geodetic residuals GEOD-GACCSR, GEOD-GACJPL, GEOD-GACGFZ , b) comparison of the series shows with trend and seasonal oscillations (annual, semi-annual, 120 days) removed.

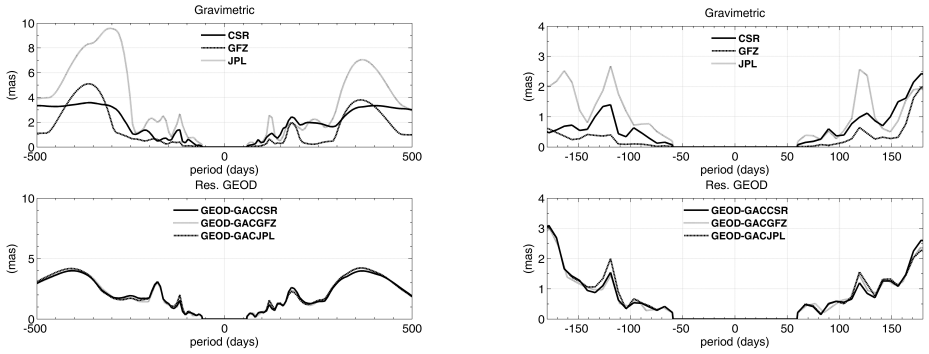

(a) (b)

Figure 2: Comparison of spectra of gravimetric excitation function computed from GSM coefficients (CSR, JPL,GFZ), with spectra of geodetic residuals GEOD-GACCSR, GEOD-GACJPL, GEOD-GACGFZ.

the values determined from the geodetic residuals and from the CSR data, in both prograde and retrograde parts of spectra. In terms of the direction the closest to the vectors of geodetic residuals is the CSR vector in the prograde part while the GFZ vector in the retrograde part.

4. CONCLUSIONS

GRACE data are a useful tool to determine time-variable geophysical mass fields, and in particular that of the changing land-based hydrology, which is estimated otherwise only with complex hydrological models. We found that these gravimetric–hydrological excitation functions, based on the most recent GRACE RL05 release, obtained by the three processing centers, JPL, GFZ, CSR, may differ significantly. One difference is that a greater degree of smoothness is exhibited by GFZ than the JPL and CSR ones. Analyses show that the use of these new data to compare with geodetic residuals, does not bring significant new results from to previous studies [Seoane et al., 2009, Jin et al.,2012, Chen and Wilson, 2005; Chen et al., 2012, Nastula, et al.,2007, 2011]. Overall, though, the best agreement between gravimetric–hydrological excitation functions and geodetic residuals was obtained for the CSR data series, and this may be due to some attributes in the processing.

Acknowledgements. The author expresses his sincere thanks for the travel grant provided by the Local Organizing Committee of the Journées 2013. This work was supported by the Polish national science foundation NCN under grant No. DEC-2012/05/B/ST10/02132.

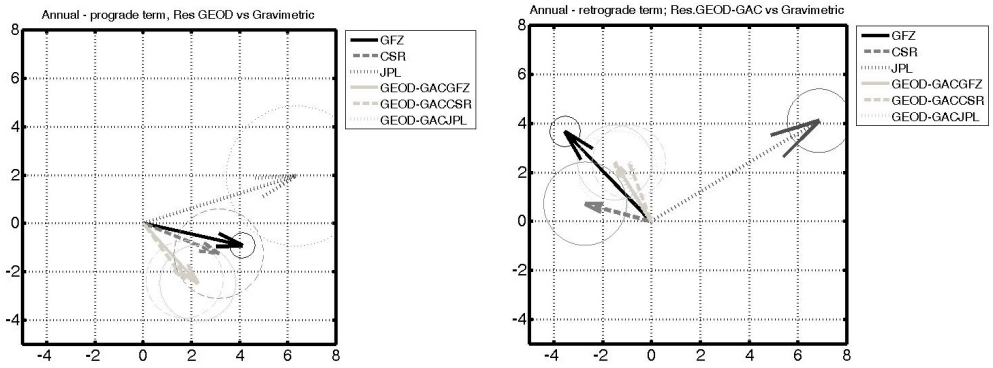

(a) (b)

Figure 3: Phasor of annual oscillations of gravimetric excitation functions (GFZ,JPL,CSR) and geodetic residuals(GEOD-GACJPL, GEOD-GACJPL, GEOD-GACCSR),(units are mas).

Table 1: Comparison of gravimetric excitation functions, with geodetic residuals in terms of correlation coefficients and variances of differences.

Data	Detrended				Non seasonal			
	Corr. Coeff		Variance Diff. (mas^2)		Corr. Coeff		Variance Diff. (mas^2)	
	χ_1	χ_2	χ_1	χ_2	χ_1	χ_2	χ_1	χ_2
Res. Geod vs JPL	0.31	0.53	256	398.2	0.32	0.23	62.7	256.7
Res. Geod vs GFZ	0.33	0.32	56.3	103.8	0.30	0.20	134.2	84.6
Res. Geod vs CSR	0.22	0.72	82.6	65.1	0.18	0.58	40	62.7

5. REFERENCES

Barnes, R.T.H., Hide R., White A.A., Wilson C.A., 1983, Atmospheric angular momentum fluctuations, length-of-day changes and polar motion. Proc. R. Soc. London, Ser. A 38731-73, doi:10.1098/rspa.1983.0050.

Chen, J.L., and Wilson C. R. ,2005, Hydrological excitation of polar motion, 1993-2002, Geophys. J. Int. 160, 833-839, doi:10.1111/j.1365-246X.2005.02522.

Chen, J.L., Wilson, C.R., Zhou, Y.H., 2012, Seasonal excitation of polar motion, J. Geodyn., 62, 8-15, doi: 10.1016/j.jog.2011.12.002.

Eubanks, T.M., 1993, Variations in the orientation of the earth. In: Smith, D.E., Turcotte, D.I., (Eds.), Contributions of Soace Geodesy to Geodynamics-Earth Dynamics, Geodyn. Ser., vol 24, AGU, Washington, D.C., pp. 1-54.

Gambis, D., 2004, Monitoring Earth orientation at the IERS using space-geodetic observations, J. Geod., 78, 295-3-2.

Jin, S.G., Hassan A.A., and Feng G.P. ,2012, Assessment of terrestrial water contributions to polar motion from GRACE and hydrological models, J. Geodyn., 62, 40-48, doi: 10.1016/j.jog.2012.01.009.

Nastula, J., R. M. Ponte, and D. A. Salstein , 2007, Comparison of polar motion excitation series derived from GRACE and from analyses of geophysical fluids, Geophys. Res. Lett., 34, L11306, doi:10.1029/2006GL028983.

Nastula, J., Pasnicka M., Kolaczek B. ,2011, Comparison of the geophysical excitations of polar motion from the period:1980.0-2009.0, Act Geophys, 59(3):561577.

Seoane, L., Nastula J., Bizourad C., Gambis D. ,2009, The use of gravimetric data from GRACE mission in the understanding of polar motion variations Geophys. J. Int. 178, 614-622.

Tapley, B.D., Bettadpur S., Ries J.C., et al. ,2004, GRACE measurements of mass variability in the Earth system. Science 3055683:503-505 doi:10.1126/science.1099192

EOP PREDICTION IMPROVEMENT BY WEAKENING THE EDGE EFFECT

X.Q. XU[1,2], Y.H. ZHOU[1], D.N. DONG[2]
[1] Shanghai Astronomical Observatory, Chinese Academy of Sciences
80 Nandan Road, Shanghai 200030, China
e-mail: xqxu@shao.ac.cn
[2] East China Normal University, Shanghai 200241, China

ABSTRACT. This study employs the LSTSA method to weakening the edge effect in Earth Orientation Parameters (EOP, length of day change ΔLOD and the polar motion PM) decomposed series. Comparing with predictions without any processing, EOP predictions after improving edge effect shows higher accuracy in short-term forecasting.

1. INTRODUCTION

Earth orientation parameters (EOP) are essential for transformation between the celestial and terrestrial coordinate systems. Due to the complex process of data processing, EOP are usually available with delay of hours to days. The growing demands of EOP in real-time and some period into the future by the spacecraft tracking and navigation have prompted greatly the researches on EOP predictions.

A number of techniques have been developed and applied in the EOP predictions, e.g., (a) the least Squares extrapolation of the harmonic model and the autoregressive (AR) prediction, (b) Spectral analysis and least Squares extrapolation, (c) Neural networks, (d) Kalman filter with atmospheric angular momentum forecast, (e) Wavelet decomposition and auto-covariance prediction, and (f) Adaptive transformation from the atmospheric angular momentum to length-of-day (LOD) change. And one major conclusion reached by the EOP prediction comparison campaign (EOP PCC) was that there is no particular prediction technique superior to the others for all EOP components and all prediction intervals. While the three techniques (a, b, c) work well in the polar motion prediction (PMX, PMY), the other three techniques (d, e, f) are preferred in the LOD and UT1-UTC forecast (Kalarus et al., 2010).

The edge effect in the end of EOP decomposition series is well known, but people pay little attention to its influence in EOP forecasting. Which will hampers the construction of an effective prediction model. For this problem, we extend the EOP sequence from both ends by a non-linear model namely the LSTSA (Leap-Step Time Series Analysis model), which mainly contains the deterministic part, stochastic part and white noise.

In this paper, we firstly describe the principles of the LSTSA model. Secondly, we employ the LSTSA method to extend the EOP series forward and backward, which can improve the edge effect in the both ends of the decomposed EOP data series. Finally we present an example of the EOP short-term predictions made by the AR method with the extended EOP series. Comparing with the predictions without any process, it is clearly that the predictions after improving edge effect performs generally better.

2. THE LSTSA MODEL AND EXTENDING THE EOP SERIES

The LSTSA model decomposes a time series into deterministic and stochastic components (Zheng et al., 2000). The stochastic component is further characterized by several stochastic models. Each stochastic model is valid within a sub-domain of the time series. The LSTSA model can be described as follows:

$$Z_n = D_n + S_n^{(p)} + E_n \quad Z_n \in U_p \quad p = 1, 2, \ldots, h \tag{1}$$

In Eq. (1), D_n represents a deterministic model, including bias, trend and stable periodic signals in the time series Z_n. S_n represents a stochastic model such as an autoregressive (AR), autoregressive moving average (ARMA) (Box and Jenkins 1970), or a nonlinear threshold autoregressive (TAR) model

(Tong 1990). U_p represents the P_{th} leap-step domain of time series Z_n. If the sample number $N = h \times m$, then Z_n is simply an additive white noise.

The D_n part in Eq. (1) is unrelated to the leap-step domain U_p. In our study we select annual, semiannual and a secular trend terms to characterize D_n in ΔLOD, and annual, semiannual and Chandler terms to characterize D_n in PM. After removing the D_n component, the following linear autoregressive (AR) model is selected to characterize $S_n^{(p)}$ for each residual series $Z_n^{(p)}$. In the leap-step domain U_p:

$$Z_n^{(p)} = \sum_{i=1}^{k} a_i Z_{n-i}^{(p)} + \varepsilon_n \tag{2}$$

Where k and a are the order and coefficient of the AR model of the residual time series. And the order and coefficient of each AR model can be identified and estimated according to the minimal information criteria AIC (Akaike 1971).

We now extend the time series by LSTSA extrapolation. In the process of the extrapolation, D_n in Eq. (1) (the red line at the top of Fig. 1 and Fig. 2) is estimated from the original 45-year EOP series (the black line at the top of Fig. 1 and Fig. 2) with the least square method. Using the stochastic model, the 45-year EOP series are extended forward and back-ward each for 2.5 years into a 50-year series. In the extended process, every EOP subseries in the leap-step domains are applied to $S_n^{(p)}$. The extended curve of residual series is plotted as the red dashed line at the bottom of Fig. 1 and Fig. 2.

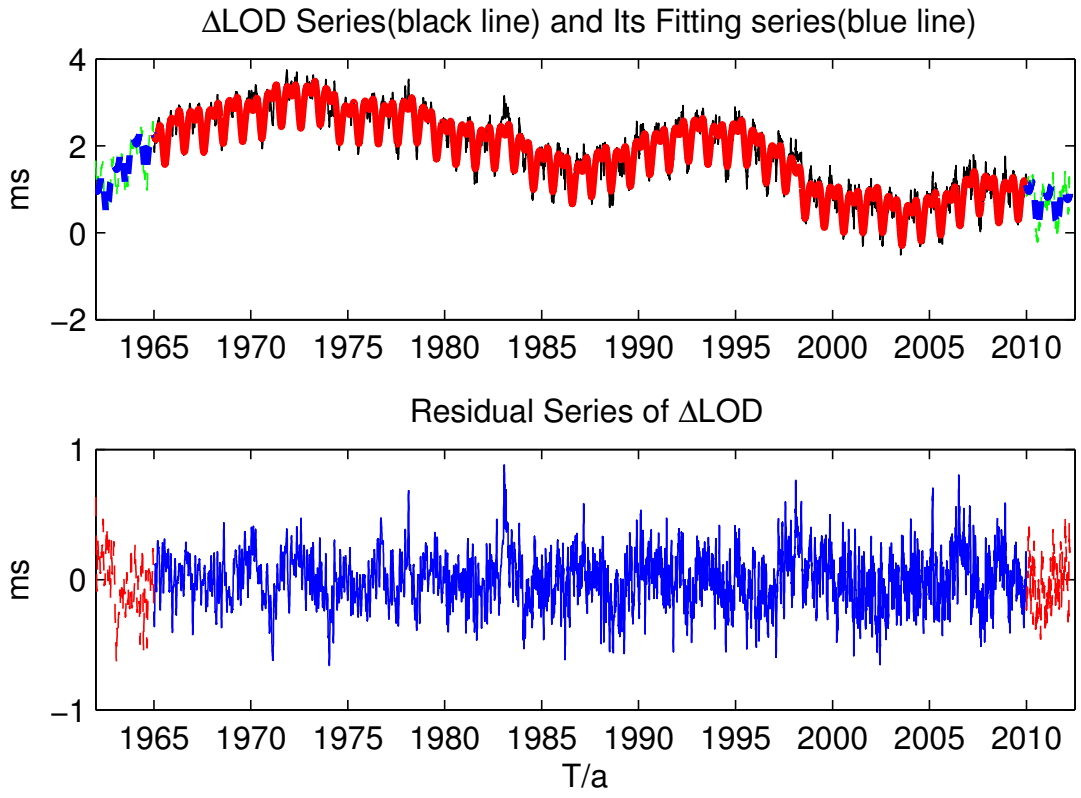

Figure 1: Extension series of ΔLOD sequence by LSTSA model.

3. RESULTS AND CONCLUSION

We first correct tidal terms in ΔLOD according to the IERS Conventions 2010 tidal models, then apply the LSAR model to extend the 45-year EOP series from the both ends, and get the 50-year extended EOP series. And then fit a linear term, annual and semiannual periodic terms to ΔLOD and a linear term, the Chandler term and annual term for the polar motion by the least square method. A small residual term is left after fitting (Xu et al., 2012). And chose the middle fitted 45 years ΔLOD and PMX series and residuals for prediction by AR model respectively, finally the 90 days ΔLOD and PMX

prediction sequences are obtained. For comparison, we also get the 90 days ΔLOD and PMX predictions by AR model without the LSTAR method.

The comparison results are given in Fig. 3. Which shows 90 days EOP observations and two predictions, the black dot line is EOP observation sequence, the blue dot line is predictions with the original 45-year EOP series, and the red dot line is predictions with the extended 50-year EOP series. It is clearly that the prediction after improving edge effect meets the observed values better.

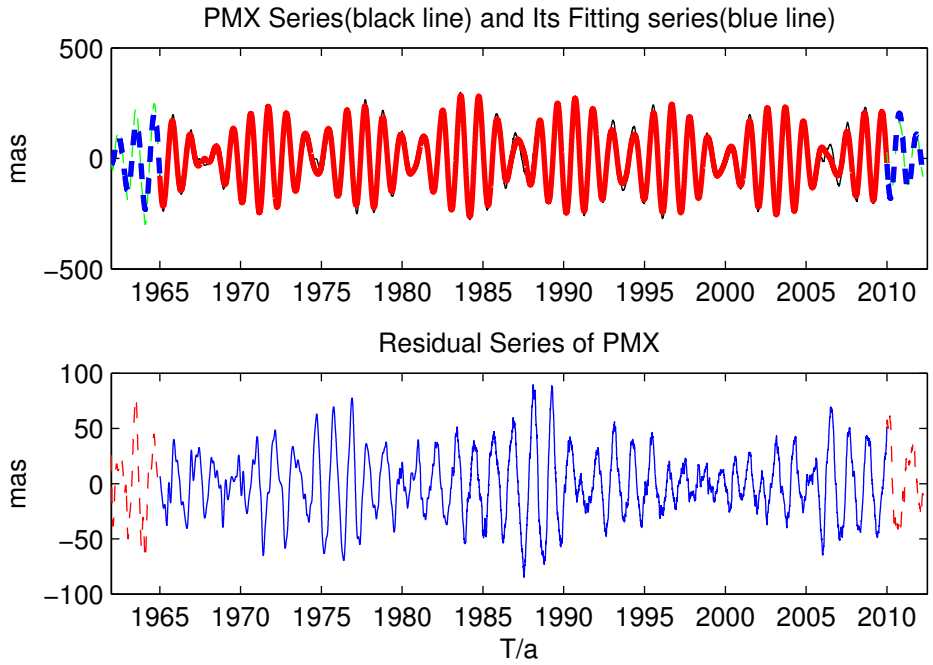

Figure 2: Extension series of PMX sequence by LSTSA model.

Acknowledgements. The research is supported by the NSFC grant (11303073, 11373017, 11373057, 11073045) and the 'International Postdoctoral Exchange Program' funding. We thank the International Earth Rotation and Reference System Service (IERS) for providing the EOP data.

4. REFERENCES

Akaike H., 1971, Autoregressive model fitting for control. Ann Inst Stat Math. pp. 163–180.

Box GEP, Jenkins GM., 1970, Time series analysis, forecasting and control. Holden-Day, San Francisco, pp.53–104.

Kalarus M., Schuh H., Kosek W., Akyilmaz O., Bizouard Ch., Gambis D., Gross R., Jovanovic B., Kumakshev S., Kutterer H., Mendes Cerveira P.J., Pasynok S., Zotov L., 2010 , Achievements of the Earth orientation parameters prediction comparison campaign. J Geod, 84, pp. 587–596.

Tong H., 1990, Non-linear time series: a dynamical system approach. Clarendon Press, Oxford, pp. 19–53.

Xu, X-Q, Zhou, Y-H, Liao X-H., 2012, Short-term earth orientation parameters predictions by combination of the least-squares, AR model and Kalman filter. J. Geodyn. 62:83–86.

Zheng D-W, Chao BF, Zhou Y-H, Yu N-H., 2000, Improvement of edge effect of the wavelet time–frequency spectrum: Application to the length-of-day series. Journal of Geodesy, 74(2), pp. 249–254.

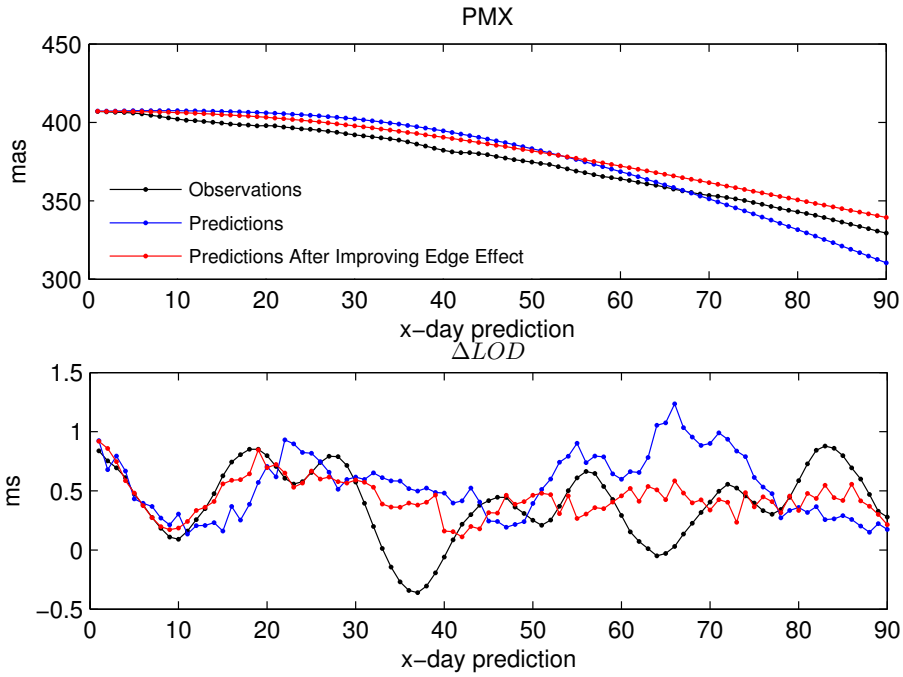

Figure 3: PMX and ΔLOD observations and predictions before and after improvement of edge effect.

THE "SIMEIZ-KATZIVELY" CO-LOCATION SITE OF SPACE GEODESY TECHNIQUES: CURRENT STATE AND FUTURE ACTIVITY

Ya. S. YATSKIV[1], P. S. ODYNETS[2], A. E. VOLVACH[3]
[1] Main Astronomical Observatory of National Academy of Sciences of Ukraine (MAO NASU)
27 Ak. Zabolotnogo str., 03680, Kyiv, Ukraine
e-mail: yatskiv@mao.kiev.ua
[2] Crimean Laser Ranging Observatory of MAO NASU (CLRO)
19 Ak. Shuleykina str., Katzively, 98688, Yalta, Crimea, Ukraine
[3] Crimean Astrophysical Observatory of Kyiv National University (CRAO)
98409, Nauchny, Crimea, Ukraine

ABSTRACT. Two Satellite Laser Ranging (SLR) stations, two Global Navigation Satellite System (GNSS) stations and Very Long Base Interferometry (VLBI) station are placed on the "Simeiz-Katzively" co-location site. The activity of these space geodesy techniques in 2010-2012 is presented. Special attention is paid on results of new local tie surveys at this co-location site.

1. CURRENT STATE OF ACTIVITY

Space geodetic techniques, such as SLR, VLBI, GNSS and traditional geodetic techniques observe the Earth system parameters at the "Simeiz-Katzively" co-location site (Crimea, Ukraine) since many years (see Figure **??**). In 80-ies of the XX century the second generation SLR systems named "KRYM" were used in the former USSR (see, e. g., Abalakin V. K. at al. 1985, Basov N. G. and Kokurin Yu. L., 1986). Two of these stations were placed at the Crimea, namely the Crimean scientific station of the Physical Institute of the USSR Academy of Sciences (at present the Crimean Laser Observatory of the Main Astronomical Observatory of the NAS of Ukraine, CLRO) and the Simeiz station of the Astronomical Council of the USSR Academy of Sciences (at present the Crimean Astrophysical Observatory of the Kyiv National University, CRAO). These stations participate in the ILRS under the names: Katzively (№1893) and Simeiz (№1873) since 1984 and 1998 respectively. The information of their activities in 2010-2012 is presented in Table 1.

Year	Location	Number of passes			Number of NP		
		LEO	Lageos	HEO	LEO	Lageos	HEO
2010	Katzively	1287	203	146	18183	1563	1079
2010	Simeiz	1105	332	8	14354	2688	44
2011	Katzively	1413	240	210	20156	1961	1455
2011	Simeiz	1108	296	10	14898	2309	75
2012	Katzively	1865	260	339	41194	3336	3946
2012	Simeiz	1007	244	80	11828	1740	488

Table 1: Operational compliance issues of the Katzively and the Simeiz SLR stations.

Based on the ILRS analysis one can state that these stations are less active as compared with operational activity of modern ILRS stations. Therefore as a first step we plane to improve a measurement precision (up to 10 mm) by using new guiding and recording systems. As a next step a new type of the SLR system will be installed at this co-located site.

In 1995 the VLBI observations were started by CRAO in cooperation with Goddard Space Flight Center (GSFC). At present the Simeiz VLBI station (IERS Number 123375008) is based on radiotelescope RT-22, recording system Mark-5A and Mark-5B+ and H-maser (time and frequency). RT-22 has steering parabolic mirror with diameter 22 m and focal length 9525 mm. Root mean square accuracy of surface is 0.25 mm and effective area 210 m^2 which does not depend on elevation angle at frequencies 2.3 and 8.4 GHz. The antenna has an azimuth-elevation mounting with axis offset -1.8±0.2 mm. Working range

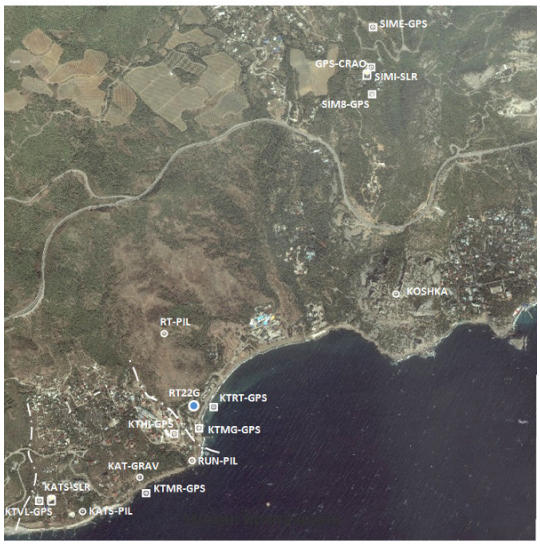

Figure 1: The "Simeiz-Katzively" co-location site

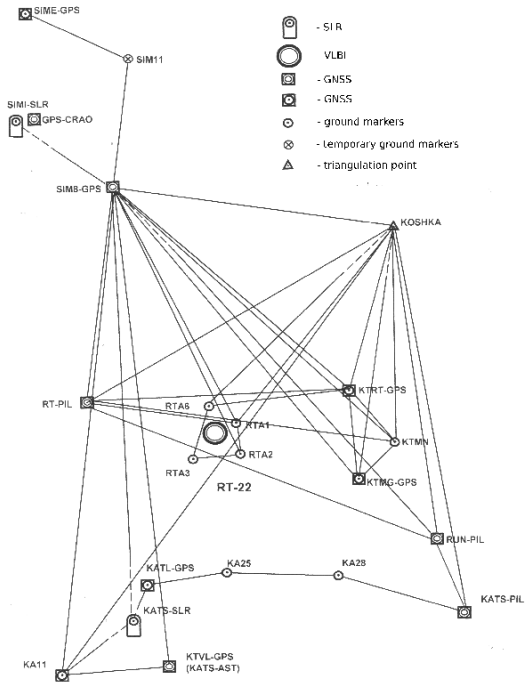

Figure 2: Set-up of the local survey at the "Simeiz-Katzively" co-location site

in azimuth is [-210°, 210°] (zero is to the south) and in elevation [-1°, 85°]. Maximum slewing rate is 1°.5/sec. The control system of the telescope provides an accuracy of pointing at the level of about 10″. The information on activity of the Simeiz VLBI station in 2010 – 2012 is given in Table 2.

Year	Number of sessions
2010	16
2011	17
2012	16

Table 2: Operational activity of the Simeiz VLBI station.

There are two GNSS station at this co-location site. The GNSS station CRAO was installed in 2004, the GNSS station KTLV was installed in2009. These stations receive the GPS signals (KTVL station observes the GLONASS also) with observation interval of 1 second.

2. NEW PRECISE LOCAL SURVEY TIES AT THE "SIMEIZ-KATZIVELY" CO-LOCATION SITE.

Study of the inter-technique discrepancies for ITRF and ERP realizations is one of new challenges for IERS. These discrepancies could be eliminated by careful combination of SLR, VLBI and GNSS data, along with precise local survey ties. Local survey at the "Simeiz-Katzively" co-location site was started in 1993 and several campaigns were undertaken in 1994, 2004, 2008 and 2011 (Samoylenko O. M., Odynets P. S. and Yatskiv Ya. S., in press).

As the result the coordinates of reference points of space-geodesy techniques and ground-based markers were derived with respect of the ITRF-2000 for the epoch 2004.6 and corresponding local ties for these reference points with respect to position of the RT-22 (see Appendix) were estimated.

Horizontal deformations δS, α and ν (in vectorial form) based on the data of local surveys were derived for different time intervals (see Table 3).

There are three zones of deformations at the "Simeiz-Katzively" co-location site, namely zone of intensive deformations (KATS Zone), zone of small deformations (SIMIRT Zone) and the SLR CRAO site which is relatively stable zone (see Figure 2).

Reference points	Time intervals								
	1994 – 2004			2004 – 2008			2008 – 2011		
	δS	α	ν	δS	α	ν	δS	α	ν
	mm	degree	mm/year	mm	degree	mm/year	mm	degree	mm/year
RT22G	0.0	0.0	0.0	0.0	0.0	0.0	0.0	0.0	0.0
KATS-SLR	33.8	185	3.4	38.2	168	9.6	11.2	236	3.7
KAVL-GPS	29.1	177	2.9	32.0	166	8.0	15.8	197	5.3
KATS-PIL	77.0	166	7.7	32.9	139	8.2	27.6	197	9.2
KAT-GRAV	-	-	-	184.0	132	46.0	33.0	125	11.0
KTMR-GPS	-	-	-	-	-	-	18.2	187	1.1
RUN-PIL	147.3	162	14.7	31.2	121	7.8	13.7	160	4.6
KTHI-GPS	52.3	114	5.2	31.3	132	7.8	-	-	-
KTRT-GPS	4.3	234	0.4	4.1	101	1.0	3.8	748	1.3
RT-PIL	2.6	157	0.3	4.1	101	1.0	4.5	80	1.5
KOSHKAC	12.7	333	1.3	12.7	90	3.2	27.8	300	9.3
SIMI-SLR	18.6	130	1.9	3.3	255	0.8	3.9	19	1.3
GPS-CRA	-	-	-	11.7	240	2.9	8.7	37	2.9
SIM8-GPS	-	-	-	3.1	322	0.8	4.7	298	1.6
SIMI-AST	0.0	0	0.0	3.4	2	0.9	4.4	55	1.5
SIME-GPS	24.8	188	2.5	6.8	126	1.7	25.1	96	8.4

Table 3: Horizontal deformations at the "Simeiz-Katzively" co-location site (credit: O. M. Samoylenko).

Velocities of horizontal displacements of markers in KATS Zone are from 3 mm/year to 15 mm/year (average value 8 mm/year). In SIMIRT Zone there are horizontal displacements of about 3 mm/year. Vertical displacements in these zones are three times less as compared with horizontal ones. Based on these results one can conclude that local deformations are very complicated at the "Simeiz-Katzively" co-location site. They have to be taken into account when combining the results of space geodesy observations and when new generation space geodesy techniques will be installed at this site.

3. FOLLOW-ON THE "SIMEIZ-KATZIVELY" OBSERVATION TECHNIQUES.

For consistent participation of the "Simeiz-Katzively" co-location site in International Space Geodesy Services (ILRS, IVS, IGS, etc.) it is necessary to undertake the following actions:

- modernizing the existing space geodesy techniques,
- improving the systematic of space geodesy observations and identifying their errors for excluding inter-techniques discrepancies,
- conducting the new local tie surveys,
- installing the new generation space geodesy techniques for SLR and VLBI observations.

We have started an implementation of the actions mentioned above.

4. REFERENCES

Abalakin V. K., Abele M. K., Artyukh Yu. N., et al., 1985, "Laser network designed for the Moon and artisicial Earth satellite ranging." Proc. of the Int. Conf. on Earth Rotation and the Terrestrial Reference Frames. Columbus, Ohio, USA. Vol. 1, pp. 246 – 256.

Basov N. G., Kokurin Yu. L., 1986, "Lasernaya lokatsiya Luny" in book "Nauka i Chelovechestvo" Moskow, pp. 263 — 278 (in Russian)

Samoylenko O. M., Odynets P. S. and Yatskiv Ya. S., (in press), "Issledovanie deformatsij Zemnoj poverhnosti i lokalna privyazka astronomo-geodezicheskikh priborov na Krimskom geodynamicheskom poligone "Simeiz-Katzively" " (in Russian)

APPENDIX.

RESULTS OF LOCAL TIE SURVEYS AT THE "SIMEIZ-KATZIVELY" CO-LOCATION SITE CURRIEDOUT IN 1994, 1999, 2008 and 2011.

Table 4: Excenters with respect to position of RT-22G at the epoch 2004.6 (local survey of 1994).

Station number	Station name	ΔX, m	$\sigma\Delta X$, mm	ΔY, m	$\sigma\Delta Y$, mm	ΔZ, m	$\sigma\Delta Z$, mm
1	2	3	4	5	6	7	8
12337S008	RT22G	0,0000	1,0	0,0000	2,0	0,0000	0,9
12337S006	KATS-SLR	713,4922	2,3	- 426,8797	1,5	- 335,0690	2,2
12337S003	SIMI-SLR	- 1328,631	0,2	197,4942	2,6	1461,0637	2,4
12337M001	SIME-GPS	- 1484,5990	5,2	155,2269	4,3	1648,7410	6,5
	KTRT-GPS	- 70,1277	-	54,7318	-	- 6,6172	-
	RT-PIL	- 10,7951	-	- 128,3651	-	191,5581	-
	KATS-PIL	650,2011	4,8	-259,1464	17,0	- 407,7329	1,0
	KTMR-GPS	389,2674	1,5	- 41,1734	8,9	- 334,2626	1,9

Note. 1) SIMI-SLR is point of mobile SLR station on which GPS receiver are centered;
2) Root mean square error of points does not include errors of GPS ground markers.

Table 5: Excenters with respect to position of RT-22G at the some epoch.

Excenters with respect to position of RT-22G at the epoch 2004.6 (local survey of 2004).

Station number	Method Method	Station name	ΔX, m	$\sigma\Delta X$, mm	ΔY, m	$\sigma\Delta Y$, mm	ΔZ, m	$\sigma\Delta Z$, mm
1	2	3	4	5	6	7	8	9
12337S008	VLBI	RT22G	0,0000	1,4	0,0000	1,2	0,0000	1,2
12337S006	SLR	KATS-SLR	713,5046	1,4	- 426,8749	5,5	- 335,1034	8,9
12337S003	SLR	SIMI-SLR	- 1328,6341	2,9	197,5098	3,1	1461,0536	5,8
12337M001	SLR GPS	SIME-GPS	- 1484,5782	3,7	155,2366	5,2	1648,7289	9,5
12337M002	GPS	GPS-CRAO	- 1333,7703	2,3	196,8987	3,7	1467,8380	6,5
	GPS	KTRT-GPS	- 70,1254	-	54,7290	-	- 6,6204	-
	GPS	RT-PIL	- 10,7927	-	- 128,3647	-	191,5636	-
	GPS	KATS-PIL	650,2201	1,1	- 259,1105	5,6	- 407,8023	7,1
	GPS	SIM8-GPS	- 1275,1947	2,4	261,8975	2,6	1392,7492	1,3
	GPS	KTMG-GPS	41,6859	2,3	68,1443	2,2	-106,0268	4,1

Excenters with respect to position of RT-22G at the epoch 2004.6 (local survey of 2008).

Station number	Method Method	Station name	ΔX, m	$\sigma\Delta X$, mm	ΔY, m	$\sigma\Delta Y$, mm	ΔZ, m	$\sigma\Delta Z$, mm
12337S008	VLBI	RT22G	0,0000	1,5	0,0000	1,7	0,0000	1,4
12337S006	SLR	KATS-SLR	713,5319	1,0	- 426,8470	6,8	- 335,1183	7,6
12337S003	SLR	SIMI-SLR	- 1328,6336	3,8	197,5062	4,9	1461,0508	6,5
12337M001	SLR GPS	SIME-GPS	- 1484,5820	5,5	155,2406	5,3	1648,7337	6,3
12337M002	GPS	GPS-CRAO	- 1333,7625	4,2	196,8918	4,5	1467,8324	5,2
	GPS	KTRT-GPS	- 70,1272	-	54,7326	-	- 6,6210	-
	GPS	RT-PIL	- 10,7946	-	- 128,3611	-	191,5630	-
	GPS	KATS-PIL	650,2372	1,2	- 259,0728	6,3	- 407,8022	6,4
	GPS	SIM8-GPS	- 1275,1951	4,6	261,8949	3,4	1392,7509	1,7
	GPS	KTMG-GPS	41,6765	1,7	68,1482	1,7	- 106,0303	2,5

Excenters with respect to position of RT-22G at the epoch 2004.6 (local survey of 2011).

Station number	Method Method	Station name	ΔX, m	$\sigma\Delta X$, mm	ΔY, m	$\sigma\Delta Y$, mm	ΔZ, m	$\sigma\Delta Z$, mm
12337S008	VLBI	RT22G	0,0000	1,5	0,0000	1,7	0,0000	1,4
12337S006	SLR	KATS-SLR	713,5449	1,0	- 426,8494	6,8	- 335,1179	7,6
12337S003	SLR	SIMI-SLR	- 1328,6322	3,8	197,5087	4,9	1461,0585	6,5
12337M001	SLR GPS	SIME-GPS	- 1484,5976	5,5	155,2603	5,3	1648,7281	6,3
12337M002	GPS	GPS-CRAO	- 1333,7676	4,2	196,8946	4,5	1467,8396	5,2
	GPS	KTRT-GPS	- 70,1191	-	54,7338	-	- 6,6158	-
	GPS	RT-PIL	- 10,7875	2,4	- 128,3510	2,4	191,5754	3,0
	GPS	KATS-PIL	650,2556	1,2	- 259,0703	6,3	- 407,8229	6,4
	GPS	SIM8-GPS	- 1275,1947	4,6	261,8902	3,4	1392,7517	1,7
	GPS	KTMG-GPS	41,6921	1,7	68,1430	1,7	- 106,0198	2,5
12337M003	GPS	KTVL-GPS	760,9140	4,0	- 458,5208	5,0	- 358,2345	6,7

ANOMALIES OF ASTRONOMICAL TIME-LATITUDE RESIDUALS AT YAO BEFORE WENCHUAN EARTHQUAKE

H. HU[1], J. VONDRÁK[2], Y.J. SU[3]
[1] Yunnan Observatory, Academia Sinica
Kunming 650011, P.R. China
e-mail: huhui@mail.ynao.ac.cn
[2] Astronomical Institute, Acad. Sci. Czech Rep.
Boční II 1401, 14100 Prague 4, Czech Republic
e-mail: vondrak@ig.cas.cz
[3] Seismological Bureau of Yunnan Province
Kunming 650224, P.R. China

ABSTRACT. Accurate optical astrometric observations of variations of the local vertical contain rich geophysical information. These may be used not only in the astronomical research, but also can provide important information for the earthquake forewarning (Li et al. 1978, Zhang 1981, Han et al. 1987, Hu et al. 1989, Hu et al. 2003, Han et al. 2007) . In the paper we analyze astronomical time-latitude residuals observed at Yunnan Astronomical Observatory in 2008–2009, and find that significant anomalies appeared before the earthquake of magnitude 8.0 that occurred in Wenchuan on May 12, 2008. The results obtained make us believe that the observed anomalies of time-latitude variations may provide an important warning sign before strong earthquakes and thus deserves further research.

1. DEFINITION OF THE ASTRONOMICAL TIME-LATITUDE RESIDUALS

Earth rotation parameters (ERP), Universal time ($UT1-UTC$) and polar motion (x, y), are obtained from worldwide observations processed by IERS. Astronomical time-latitude residuals (ATLR) for a specific astrometric instrument are obtained by removing the effects of ERP from the astronomically observed time ($UT0 - UTC$) and latitude ($\mathrm{d}\varphi$) variations, determined by the instrument. Time and latitude residuals RTj, RLj at j-th instrument are then expressed as:

$$\begin{aligned} RT_j &= (UT0 - UTC)_j + \frac{1}{15}(x \sin\lambda_j - y \cos\lambda_j) \tan\varphi - (UT1 - UTC) \\ RL_j &= \mathrm{d}\varphi_j - x \cos\lambda_j - y \sin\lambda_j, \end{aligned} \quad (1)$$

where φ_j, λ_j are geographic coordinates of the instrument. If these residuals are greater or equal to two times their standard deviation (2σ), we take them as warning signs before the occurrence of strong earthquakes.

2. ANOMALIES OF ATLR AT YUNNAN BEFORE WENCHUAN EARTHQUAKE

An earthquake $M_s = 8.0$ occurred in Wenchuan County (Sichuan province), China on May 12, 2008. It caused greatest heavy life and property losses in China's recent history. In March 2008 ATLR anomalies greater than 2σ appeared, both in RT and RL, at Yunnan Astronomical Observatory (YAO).

These are the first anomalies greater than 2σ that appeared after the earthquake of $M_s = 6.2$ in Dayao county of Yunnan province that occurred in 2003. No earthquake $M_s \geq 6.0$ occurred around YAO during the period from July 2003 to 2008.0. The epicenter of Wenchuan earthquake was about 670 km away from YAO. Although the distance is rather long, Wenchuan and YAO are both located on the same Xikang-Yunnan rhombic fault block.

Based on this fact, Long et al. (2006) rather precisely predicted that an earthquake of 8-th magnitude would occur in the Wenchuan region in 2008; they used the commensurable principle using historical earthquakes of Xikang-Yunnan rhombic fault block. Therefore the ATLR anomalies in March 2008 (see Fig. 1) may be a warning sign of Wenchuan earthquake. The anomalies observed in September 2008, also depicted in the figure, may be related to the earthquake of $M_s = 4.3$ that occurred at Kunming. Its

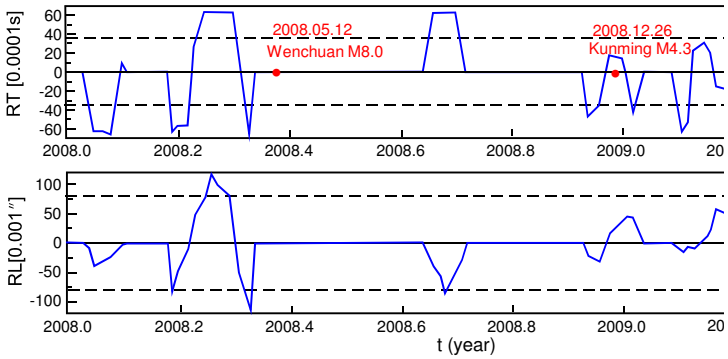

Figure 1: Astronomical time-latitude residuals observed at YAO

epicenter was only 24 km away from YAO.

3. POSSIBLE MECHANISM

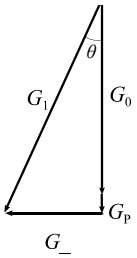

Figure 2: Disturbed gravity vector

The ATLR anomalies possibly originate from the motion of the underground masses before earthquakes. The change of the local plumb line direction reflects the changes in the horizontal component of the gravity, while its vertical component is directly measured with a gravimeter. Fig. 2 shows the gravitational acceleration of a local vertical G_0. Now, due to a disturbance of underground mass, the gravitational acceleration becomes G_1. Its disturbed part can be separated into G_p and G_-. Evidently G_p is measured by a gravimeter, and the horizontal component G_- can be derived from the angle θ, measured by the optical astrometric instrument, using the expression $G_- = \theta'' G_0/206265$.

Acknowledgements. This work was supported by the key project of the Ministry of Science and Technology of P.R. China (2012BAK19B01-07), the Chinese Astronomical Committee Foundation, and by the project RVO: 67985815, Czech Republic.

4. REFERENCES

Han, Y.B., Hu, H., Du, H.R., 1987, "Occurrence of short-period anomaly of residuals of astronomical time-latitude at Yunnan observatory preceding the Luquan earthquake ($M_L = 6.3$)", Kexue Tongbao, 32(17), pp. 1205–1207.

Han, Y.B., Ma, L., Hu, H., et al., 2007, "Application of astronomic time-latitude residuals in earthquake prediction", Earth, Moon, and Planets, 100, pp. 125–135.

Hu, H., Kan, R.J., Wang, R., et al., 1989, "A method for predicting a strong earthquake by means of astrometric observations", A&A 224, pp. 321–322.

Hu, H., Li, Z.X., Li, H., Fu, G., 2003, "Interannual variations of the vertical at Yunnan by astrometry and gravimetry techniques", Journal of Natural Disasters, 12(2), pp. 25–27.

Li, Zh., Zhang, G.D., Zhang, H., Liu X. 1978, "Correlation between the short anomalies of residuals of astronomical time and latitude and the major earthquakes around the observatories", Acta Geophysica Sinica (in Chinese), 4, pp. 278–291.

Long, X.X., Yan, J.P., Sun, H. and Wang, Z.Z., 2006, "Study on earthquake tendency in Sichuan-Yunnan Region based on commensurability", Journal of catastrophology (in Chinese), 21(3), pp. 81–84.

Zhang, G.D., 1981, "Deviation of the vertical caused by change of ground water level before a strong earthquake", Acta Seismologica Sinica (in Chinese), 3, pp. 152–158.

PREDICTION OF UNIVERSAL TIME USING THE ARTIFICIAL NEURAL NETWORK

J-Y. RICHARD[1], P. LOPES[1], C. BARACHE[1], C. BIZOUARD[1], D. GAMBIS[1]
[1] SYRTE, Observatoire de Paris, CNRS, UPMC,
61 av. de l'Observatoire, 75014 Paris, France
e-mail: Pedro.Lopes@obspm.fr

ABSTRACT. The monitoring of the Earth Orientation Parameters (EOP) variations is the main task of the Earth orientation Center of the IERS. In addition, for various applications linked in particular to navigation, precise orbit determination or leap seconds announcements, short and long term predictions are required. The method which is currently applied for predictions is based on deterministic processes, Least Square fitting, autoregressive filtering (Gambis and Luzum 2011). We present an alternative method, the Artificial Neural Networks (ANN) which has have already been successfully applied for pattern recognition. It has been tested as well by various authors for EOP predictions but with so far no real improvement compared to the current methods (Schuh et. al. 2002). New formalisms recently developed allow reconsidering the use of neural networks for EOP predictions. Series of simulations were performed for both short and long term predictions. Statistics and comparisons with the current methods are presented.

1. INTRODUCTION

The object of the project is to study the use of Artificial Neural Networks (ANN) (Hudson Beale et al. 2013), namely Multi-Layer Perceptron (MLP), to perform predictions of one of the Earths rotation parameters UT1 and to estimate the possibility to predict accurately the introduction of the Leap Second. ANN learns by training and can perform tasks such as function approximation, pattern recognition or prediction of events. A single neuron follow a simple mathematical equation, where the output is the result of the product between inputs and weights (Figure 1).

In the present study we have performed series of simulation to investigate the performances of the ANN prediction on both long term and short term intervals.

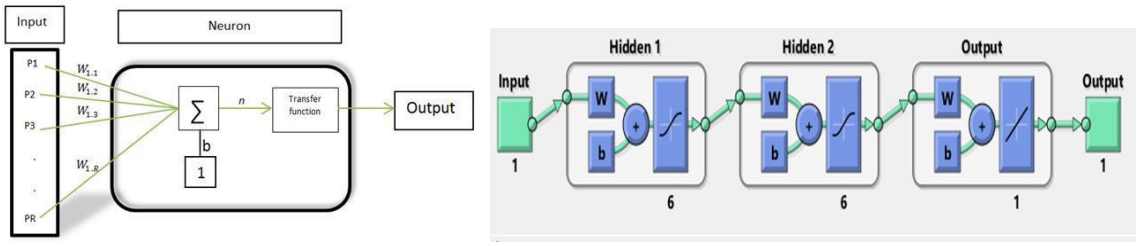

Figure 1: Single Neuron Diagram and Feed Forward Neural Network with connections between 2 hidden layers with 6 neurons each

2. LONG TERM PREDICTION OF UT1

This section aims to study the performance of a feed forward network when used with real data with a time step of 5 days, trying to approximate and predict UT1-TAI from 1962 to 2013, in order to estimate the maximal prediction horizon possible using ANN. Two kinds of networks have been simulated, NN1 (2 hidden layers with 6 neurons each) and NN2 (2 hidden layers with 12 neurons each). The procedure consists to train the network 10 times with the real data UT1-TAI and to select the best network based on the longest prediction horizon with an error smaller than 0.9s. Training sample is increased with one year of data and the procedure is iterative.

Figure 2 shows the long term prediction limit where |UT1-UTC| reaches 0.9s using neural networks NN1 and NN2 averaged and best network among the 10 trials each and the Least Squares Method (Gambis and Luzum 2011).

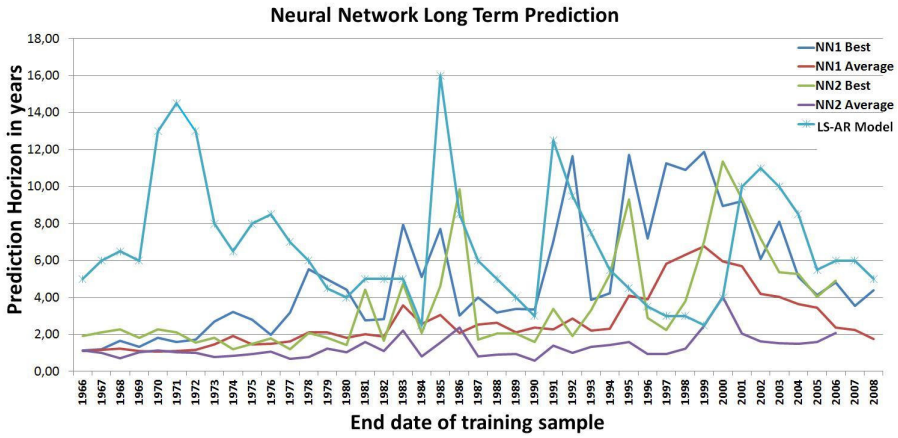

Figure 2: Long Term Prediction using neural networks NN1 and NN2 compared to the current method based on Least Squares processes

3. SHORT TERM PREDICTION OF UT1

The short prediction horizon simulated is ranging from 1 to 25 days using neural network with increasing training sample and number of neurons (2 hidden layers with neurons from 1 to 12, NN3), Increasing training sample size and constant number of neurons (2 hidden layers with 4 neurons each, NN4) and fixed neural network (2 hidden layers of 2 neurons each, NN5). We try to minimize the Root Mean Square Error by testing neural networks parameters such as training sample size and number of neurons (Figure 3).

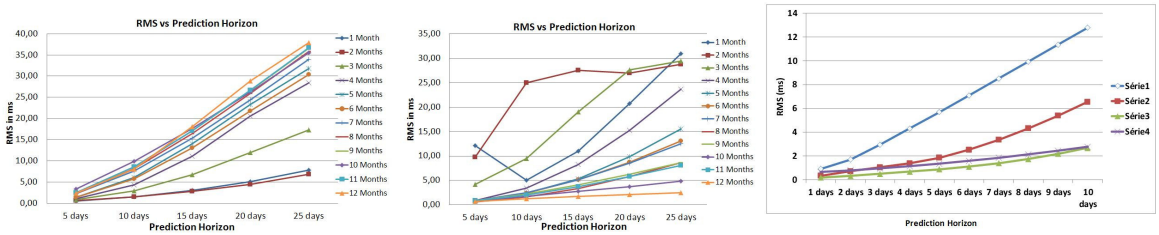

Figure 3: RMS using NN3 increasing sample and number of neurons / NN4 increasing sample and constant number of neurons / NN5 daily training with sizes ranging from 4, 10, 20 and 365 days

4. RESULTS AND CONCLUSION

For long term predictions of UT1-TAI, standard MLP appear to have a maximum prediction horizon of 2 years with 16 years of training before the predictions diverge too much from the real function (NN1), showing a lower performance than the current model (Gambis & Luzum 2011). For short term predictions, increasing the number of neurons requests longer training sample and the longer is the training, the lower is the RMS error for a constant number of neurons. With 20 days of training sample NN5 returns similar results than 1 year of training, about 2.7ms for UT1 forecast of 10 days and in comparable RMS error with NN3 requesting 1 month of training and NN4 with 12 months . Further developments concern the NARX modeling (Hudon Beale et al. 2013) applyed over UT1-TAI forecast.

5. REFERENCES

Hudson Beale M., Hagan M.T., Demuth H.B., M. T., 2013. Neural Network Toolbox User's Guide.

Gambis D. and Luzum B., 2011, Earth rotation monitoring, UT1 determination and prediction, Metrologia 48, S165-S170.

Schuh H., M. Ulrich, D. Egger, J.Muller, W. Schwegmann, 2002, Prediction of Earth orientation parameters by artificial neural networks, Journal of Geodesy 76: 247258

ON DETECTION OF THE FREE INNER CORE NUTATION FROM VLBI DATA

Z. MALKIN[1,2]
[1]Pulkovo Observatory, St. Petersburg, Russia
[2]St. Petersburg State University, St. Petersburg, Russia
e-mail: malkin@gao.spb.ru

ABSTRACT. Several attempts to discover the FICN signal in VLBI nutation series made during last years failed. In this paper, we present some results of our further steps in this direction, unfortunately not successful either. We investigated several VLBI CPO series by means of spectral and wavelet analysis. It has been shown that there are several periodic signals with close amplitude around the expected FICN period without any prevailing one that can be reliably associated with the FICN. The most interesting for further analysis is a relatively stable oscillation with period of about 750–800 days, which is, however, beyond the intervals predicted in other studies. It seems to be necessary to improve theoretical estimates of the FICN period to make its search in the observational data more promising.

1. INTRODUCTION

Free inner core nutation (FICN,) is one of the four free rotational modes of the Earth considered in the theory of the Earth's rotation. Detecting of this signal in the observational data is a very important scientific task allowing us to substantially improve our knowledge about the Earth's interior and dynamics.

According to Mathews et al. (2002) the FICN period is between 930 and 1140 days. Koot et al. (2010) estimated the FICN period from 904 ± 29 to 945 ± 30, i.e. between 875 and 975 days (1σ interval). Because of a small expected amplitude of the FICN signal its detection can be successful only from the most accurate nutation series obtained from the VLBI observations. It may be also possible that the FICN oscillation has the amplitude and phase variations like free core nutation (FCN).

Several attempts made during last years to find the FICN component in these series failed, see, e.g., Lambert et al. (2012) and papers cited therein. Moreover, the results depend on the celestial pole offset (CPO) series (dX, dY) used. In this work, we performed a new analysis of all available CPO series to investigate possible geophysical signals in expected FICN frequency band.

2. DATA ANALYSIS

We analyzed several CPO series obtained in IVS analysis centers by means of spectral and wavelet analysis. These series include the combined IVS series, as well as individual CPO series obtained in IVS Analysis Centers: AUS (Australia), BKG (Germany), CGS (Italy), GSF (USA), IAA (Russia), OPA (France), USN (USA).

As it was shown in many studies, the main components of CPO include long-term trend caused by the errors in modelling precession and low-frequency nutation terms, and free core nutation (FCN). The FCN signal was removed from the CPO time series prior to further analysis.

Firstly, the spectral analysis was applied to all CPO series in complex form $dX + idY$. Result of these computations is presented in Fig. 1. One can see from these spectra that the CPO variations in the FICN frequency band show several unstable harmonics of similar amplitude, and no prevailing signal is revealed that can be reliably associated with the FICN. Correlation between the spectra of different series is not very good. Properly speaking, agreement between the CPO series is, in fact, rather poor, which does not allow one to reliably obtain the signal pattern. Some correlation between series can be explained by both presence of real physical signal and using the same observational data and similar analysis options.

Figure 2 shows the result of wavelet analysis applied to the IVS combined CPO series after removing trend and FCN. One can see a complicated structure of the CPO variations without a clearly detected signal around the expected FICN period, except the signal with period about 800 days.

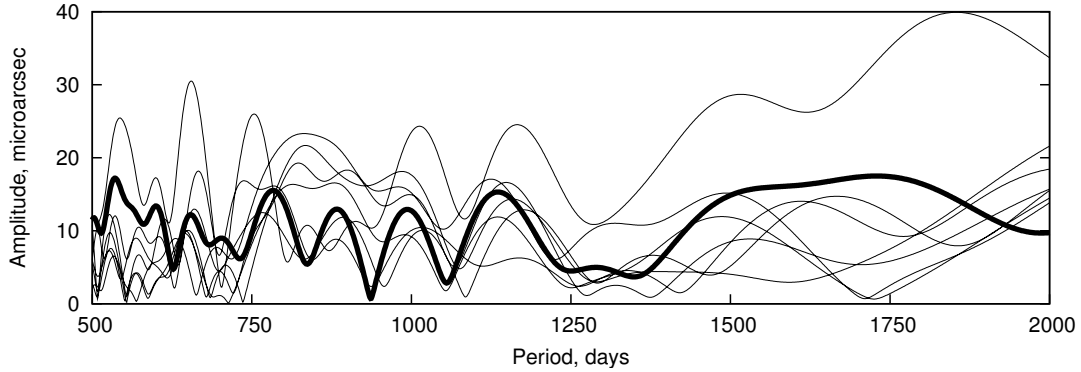

Figure 1: Periodogram of the individual (think line) and IVS combined (thick line) CPO series after removing FCN.

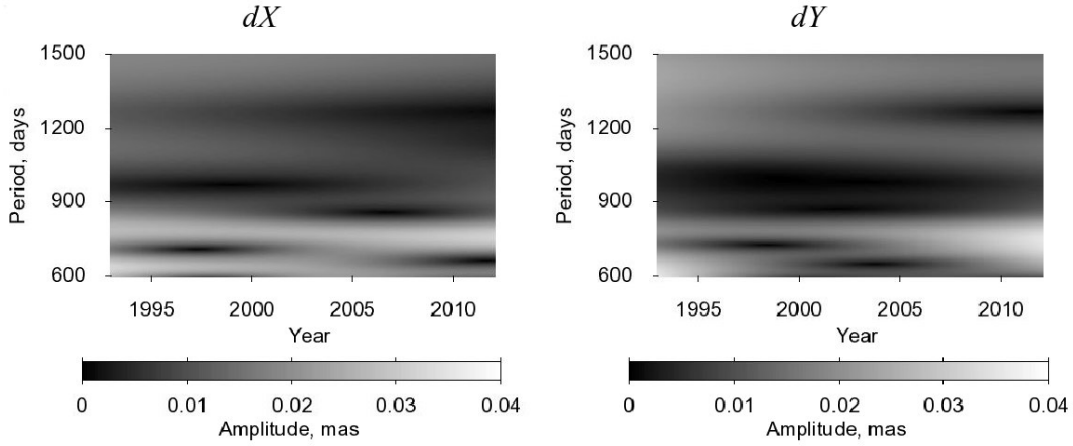

Figure 2: Wavelet scalograms for the IVS combined CPO series after removing FCN.

3. CONCLUSION

The results of this study presented above show that the CPO variations in the FICN frequency band have a complicated structure, as was already shown by Lambert et al. (2012). Several unstable harmonics of close amplitude are present in the spectra, and no prevailing signal can be reliably associated with the FICN. Wavelet analysis revealed relatively stable oscillation with period of about 750–800 days, which is, however, beyond the intervals found in other studies cited above. Unfortunately, the theoretical prediction of the FICN period is not sufficiently accurate to unambiguously connect one of the oscillations with FICN. Hence, it seems to be necessary to improve the theoretical estimates of the FICN period to make its search in the observational data more promising.

Acknowledgements. The author is grateful to the organizers of the conference for the travel support.

4. REFERENCES

Koot, L., Dumberry, M., Rivoldini, A., de Viron, O., Dehant, V., 2010, "Constraints on the coupling at the core-mantle and inner core boundaries inferred from nutation observations", Geophys. J. Int., 182, pp. 1279–1294.

Mathews, P.M., Herring, T.A., Buffett, B.A., 2002, "Modeling of nutation and precession: New nutation series for nonrigid Earth and insights into the Earth's interior", J. Geophys. Res., 107(B4), ID 2068.

Lambert, S., Rosat, S., Cui, X., Rogister, Y., Bizouard, C., 2012, "A Search for the Free Inner Core Nutation in VLBI Data", IVS 2012 General Meeting Proc., pp. 370–374.

ANALYSIS OF EWT MAPS FROM GRACE MISSION AND LAND HYDYDROLOGY DATA

T. NAGALSKI
Space Research Center Polish Academy of Sciences
ul. Bartycka 18A, 00-716 Warsaw
e-mail: tnagalski@cbk.waw.pl

EXTENDED ABSTRACT.

Using the Stokes coefficients from the Gravity Recovery and Climate Experiment (GRACE) gravimetric mission we can assess the Equivalent Water Thickness (EWT) maps showing the heterogeneity of the gravitational field. To obtain these maps we used the formula (1). Nevertheless the maps of EWT delivered from unfiltered data, present the well known characteristic stripes. To cut out the perturbation and to enhance the signal to noise ratio we need to use a filter to the raw data. Then we show the impact of the smoothing of the Stokes coefficients on the resulting EWT map distribution we used the Stokes coefficients made accessible and filtered by the International Centre for Global Earth Models (ICGEM) imported from three research centers GeoForschungsZentrum Potsdam (GFZ), Jet Propulsion Laboratory - NASA (JPL) and Center for Space Research (CSR) with the aid of an anisotropic method of smoothing of the geopotential coefficients from GRACE with three degrees of smoothing DDK3, DDK2 and DDK1 (Kusche 2009). The result of filtering may be seen on Figures 1b, 1c and 1d. Additionally we made some researches with NOAA Climate Prediction Center (CPC) land hydrosphere geophysical model. We obtained the Stokes coefficients from EWT map from January 2007, computing with formula (2). The resulting coefficients were subjected to filtration in the same way as the GRACE data. Next the EWT maps from the filtered coefficients were computed by formula (1). The result of filtered geophysical EWT maps can be seen in Figures 2b and 2c and compared to the unfiltered map seen in Figure 2a. Dividing the filtered by the original geophysical maps we got a scaling factor for the DDK filters. In Figures 3a to 3c we can see the scalling factor maps for DDK3, DDK2 and DDK1 filter respectively. After investigating scaling factor maps we came to some conclusions. Scaling factor reaches values close to unity for DDK3 filter, about 1.3 to 1.7 for DDK2 and up to 3 for DDK1, outside several areas in North Africa, Australia and some parts of Asia, where values exceed significantly value of 3.

COMPUTATIONAL PROCEDURE

D.P.Chambers 2006

$$\triangle q(\phi,\lambda,t) = \frac{R_{\oplus}\rho_{\oplus}}{3\rho_W}\sum_{n=0}^{40}\sum_{m=0}^{n}\frac{(2n+1)}{(1+k_n)}P_{nm}(\sin\phi)[\triangle C_{nm}(t)\cos m\lambda + \triangle S_{nm}(t)\sin m\lambda] \quad (1)$$

Wahr and Molenaar 1998

$$\begin{bmatrix} \triangle C_{nm} \\ \triangle S_{nm} \end{bmatrix} = \frac{3\rho_W}{4\pi\rho_E R_E}\frac{1+k_n}{2n+1}\int_0^{2\pi}\int_{-\frac{\pi}{2}}^{\frac{\pi}{2}}\triangle q(\phi,\lambda,t)P_{nm}(\sin(\phi))\begin{bmatrix} x\cos(m\lambda) \\ \sin(m\lambda) \end{bmatrix}\cos(\phi)d\phi d\lambda \quad (2)$$

$\triangle q(\phi,\lambda,t)$ – change in water storage in a unit area
$\triangle C_{nm}, S_{nm}$ – Stokes coefficients
ρ_W – density of fresh water($1000kg/m^3$)
ρ_E – mean density of the Earth($5517kg/m^3$)
R_E – mean equatorial radius of the Earth($6371km$)
ϕ – geographic latitude
λ – geographic longitude
$P_{nm}(\sin(\phi)))$ – fully normalized Associated Legendre Polynomials of degree n and order m
k_n – are Love number of degree n

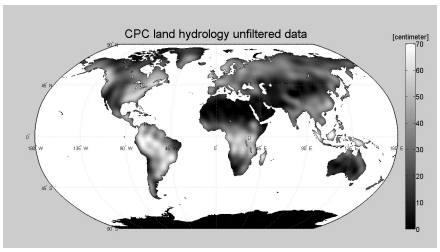

Figure 1: EWT map from CPC model from January 2007 without any filter

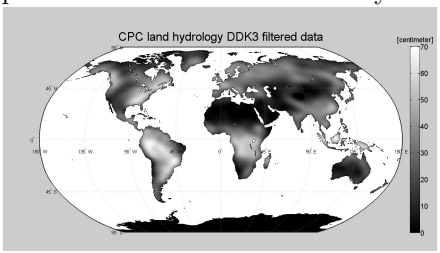

Figure 2: EWT map from CPC model from January 2007 with usage of DDK3 filter

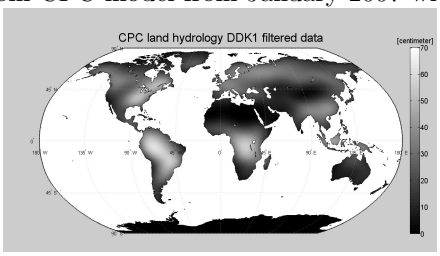

Figure 3: EWT map from CPC model from January 2007 with usage of DDK1 filter

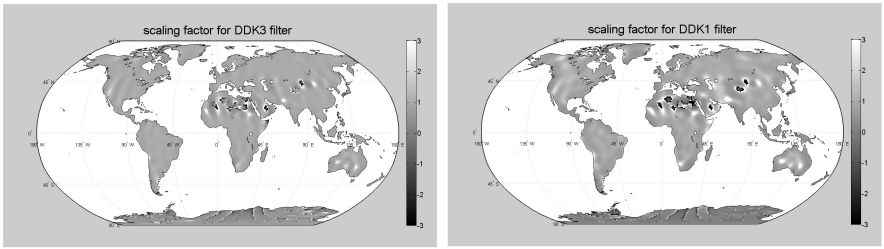

Figure 4: Map of scaling factor for the DDK3 (left) and DDK1(right) filter for January 2007

Acknowledgements. The research reported here was supervised by Dr hab. Jolanta Nastula and was supported by the Polish National Science Centre and Information Technology, through project number TT/142/13 and Paris Observatory

REFERENCES

Chambers D.P., 2006, Converting Release-04 Gravity Coefficient into Maps of Equivalent Water Thickness, Geophysical Research Letters

Kusche, Jürgen / Schmidt, Roland / Petrovic, Svetozar / Rietbroek, Roelof: Decorrelated GRACE time-variable gravity solutions by GFZ, and their validation using a hydrological modelIn: Journal of Geodesy, 83. Jg. 2009, Heft 10, S. 903-913

Wahr, J., M. Molenaar, and F. Bryan, 1998. Time- Variability of the Earths Gravity Field: Hydrological and Oceanic Effects and Their Possible Detection Using GRACE, J. Geophys. Res., 103, 30205-30230

AMPLITUDE-FREQUENCY ANALYSIS OF THE EARTH ORIENTATION PARAMETERS AND THE VARIATION OF THE SECOND ZONAL HARMONIC OF THE GEOPOTENTIAL

V.V. BONDARENKO, A. S. FILIPPOVA, Yu.G. MARKOV, V.V. PEREPELKIN
Moscow Aviation Institute
Volokolamskoe shosse, 4, Moscow, 125080, Russia
e-mail:vadimkin1@yandex.ru

ABSTRACT. An amplitude-frequency analysis of the rotary-oscillatory Earth motion under the action of gravitational-tidal perturbing torques from the Sun and the Moon is carried out using the classical mechanics' methods. The simulation results of the oscillatory process in the motion of the Earth pole and the variations of the second zonal harmonic δc_{20} of the geopotential are studied. Based on the dynamic Euler-Liouville equations expressions for amplitude and phase of the Earth pole oscillations are obtained. A comparison of the spectral power densities of the time series between the Earth pole coordinates and the δc_{20} variations of the gepotential is carried out. A functional dependence of the aforementioned component of the geopotential from the amplitude and phase of the Earth's pole oscillatory process is shown.

1. INTRODUCTION

The study of the time variations of the geopotential as a result of the rotary-oscillatory processes of the Earth motion is of a significant natural-sciences and practical interest. Oscillations of the Earth's inertia tensor components depend on many factors, among them the mechanical and physical parameters of the planet, the motions of tide-forming bodies, and the observed large-scale phenomena in nature. Time-dependent variations of these and other factors (regular and irregular oscillations, stochastic fluctuations, secular variations) affect the Earth rotary-oscillatory processes and the rotational parameters of the planet. The dynamic processes of the Earth orientation parameters (EOP) in turn have an effect on its figure and lead to the fluctuations of the gravitation field. Observed variations of the EOP, the variations of the Earth's gravitational field and oscillations in the large-scale geophysical events appear to be in a considerable correlation.

2. DYNAMIC PROCESSES OF EOP AND SECOND ZONAL HARMONIC OF THE GEOPOTENTIAL

From the SLR (Satellite Laser Ranging) observation data [1] of the zonal coefficient c_{20} main variations are divided out being caused by the quasi-periodic annual perturbation component. It is known [2–4], that the external perturbation also leads to the six-year modulations of the oscillatory process of the Earth pole. Thus, the annual variations in the moments of inertia and the Earth rotary-oscillatory motions occur in phase. Annual oscillations in the polar motion, if considered in terms of celestial mechanics [3, 4], are accounted for by the gravitational tidal torque and its combination structure dependent on the nutation angle. The annual components of the solar gravitational tidal torque constitute a vector rotating in a related coordinate system with the mean angular velocity of the Earth orbiting the Sun.

The correspondence between these perturbations can be found from the comparison of the spectral power densities of the time series between the Earth pole coordinates observations (e.g. y_p) [2] and the variations of the δc_{20} [1]. Based on the modelling of the Earth pole oscillations a division of the oscillatory process into the components is performed. Observation frequency spectrum δc_{20} and the $y_p^{\nu_t}$ series

$$y_p^{\nu_t} = \hat{y}_p - y_p^N, \tag{1}$$

which is obtained from the observations $\hat{y}_p$ [2] by subtracting the Chandler component y_p^N, are congruent in the two main frequency regions - in the frequency interval from 0.8 to 1.2 and less than 0.3 cycles per

year. It should be noted that here the Chandler component y_p^N is defined as a set of the oscillations with the main Chandler frequency N and close to it frequencies.

Assumed that $x_p = c_x + a\cos\psi$ and $y_p = c_y + a\sin\psi$, the equations for amplitude and phase variables of the Earth Pole modulation motion have the form $\dot{a} = \mu_t\cos(\psi - \nu_t)$, $\quad \dot{\psi} = N - a^{-1}\mu_t\sin(\psi - \nu_t)$, where $\mu_t = \mu(t)$, $\nu_t = \nu(t)$ are the function of time, which are expanded into a sum of periodical components; the values $\mu_t\cos\nu_t$, $\mu_t\sin\nu_t$ are perturbations which lead to the observed oscillations of the Earth pole and which have the dimensions of specific torque. The expression for δc_{20} is assumed in the form:

$$\begin{aligned} &\delta c_{20} = \lambda_t^c\cos\nu_t + \lambda_t^s\sin\nu_t + f(a(\nu_i,\xi_i,\alpha_i),\psi(\vartheta_j,\eta_j,\beta_j)),\\ &f(a,\psi) = \varepsilon a\int\frac{\mu_t\sin(\psi-\nu_t)}{a}dt. \end{aligned} \tag{2}$$

Here f is the function of amplitude and phase of the pole oscillation; dimensional coefficient ε is refined from SLR observations and has the order 10^{-3} (the amplitude a of the Earth pole oscillations is expressed in angular milliseconds).

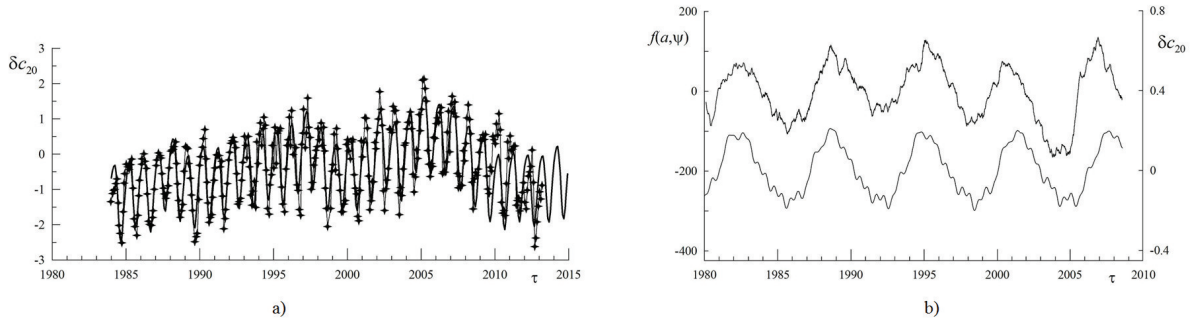

Figure 1: a) Interpolation of the variation of the second zonal harmonic δc_{20} of the geopotential from 1984 till 2008 and extrapolation for six years (2009–2014). b) A comparison of the function $f(a,\psi)$ from the amplitude and phase of the Earth pole oscillations (upper curve) that is built directly from the IERS observation data from 1980 till 2008 with the corresponding component divided out of the observations of the second zonal harmonic c_{20} of the geopotential (lower curve).

Fig. 1 a) shows the interpolation of expression (2) using the observation data of the SLR from 1984 till 2008 inclusive and extrapolation for six years with the forecast for two years. The contrast line on the figure is obtained theoretical curve, the connected by line asterisks are the measurements data. The component with oscillations corresponded to expansion of function $f(a,\psi)$ for harmonic components is divided out during interpolation. The observed curve is shown on fig. 1 b) with comparison of function $f(a,\psi)$ that built directly from observations of the Earth pole oscillations.

3. REFERENCES

Chen, J.L., C.R. Wilson, B.D. Tapley, J. Ries, 2004, "Low Degree Gravitational Changes from GRACE: Validation and Interpretation", J. Geophys. Res.(Letters), 31(22), doi: 10.1029/2004GL021670

International Earth Rotation and Reference Systems Service - IERS Annual Reports http://www.iers.org/IERS/EN/Publications/AnnualReports/AnnualReports.html

S. S. Krylov, Yu. G. Markov, V. V. Perepelkin, 2013, "Amplitude and frequency analysis of diurnal oscillations of the Earths pole", Doklady Physics, 58(4), doi: 10.1134/S1028335813040095

L. D. Akulenko, Yu. G. Markov, V. V. Perepelkin, L. V. Rykhlova, A. S. Filippova, 2013, "Rotational-oscillatory variations in the Earth rotation parameters within short time intervals", Astron. Rep., 57(5), doi: 10.1134/S106377291304001X

CONT11 - HIGH-FREQUENCY EARTH ROTATIONS VARIATIONS FROM VLBI OBSERVATIONS

E.A. SKURIKHINA, A.V. IPATOV, S.G. SMOLENTSEV, A.A. DIYAKOV, V.V. SCHPILEVSKY
Institute of Applied Astronomy of RAS
Kutuzov Quay 10, 191187 St.-Petersburg, Russia
e-mail: sea@ipa.nw.ru
e-mail: ipatov@ipa.nw.ru

ABSTRACT. Results of data processing of CONT11 (http://ivscc.gsfc.nasa.gov/program/cont11/) IVS 15 day campaign of continuous VLBI sessions with a network of 13 globally distributed stations in September 2011 with participation of two stations of Russian QUASAR network stations Badary and Zelenchukskaya are presented. Preliminary analysis results on EOP precision, baseline length precision are discussed. The observed intraday variations EOP are compared with a tidal model. Troposphere parameters are compared with ones obtained with GPS technique.

CONT11 is a campaign of continuous VLBI sessions was held from 15-th till 29-th of September 2011. At the global VLBI network from 13 stations with the goal to acquire state-of-the-art VLBI data and continuous to study high frequency (sub-daily) Earth Orientation Parameters (EOP).

Secondary treatment program CONT11 observation was carried out using a software package OCCAM / GROSS. In the calculation of diurnal EOP 15 daily sessions were combined into one 15-day session (consisting of 16 430 scans and 145 214 delays), which has been processed using a package OCCAM/GROSS using the forward run of the Kalman filter to estimate the stochastic parameters. As stochastic parameters are considered EOP (pole coordinates and universal time), the date, time, wet component of the tropospheric delay at the zenith (WZD). The behavior of stochastic parameters of simulated random walk process. Otherness from standard treatment regimen is shown in Table 1.

Solution type	Parametrization
EOP service solution (daily EOP)	constant parameters: X_{pol}, Y_{pol}, $dUT1$, X_c, Y_c stohastic parameters : WZD, $clock$ A-priory spectral density for EOP: 100 $m$as^2
Intraday EOP solution (X_{pol}, Y_{pol}, $dUT1$)	constant parameters: X_c, Y_c stohastic parameters : X_{pol}, Y_{pol}, $dUT1$, WZD, $clock$ A-priory variance for EOP: 1 $m$as^2 A-priory EOP spectral density : 1 $m$as^2 a day

Table 1: Distinction these solution from EOP service solution

As the evaluation accuracy can be used here and recurrence bases lengths. Repeatability lengths bases was 0.43 ppb, for comparison to CONT08 - 0.94 ppb, for CONT05 - 1.39 ppb.

Diurnal variation of X_{pol}, Y_{pol} and $dUT1$ were compared with the model of diurnal variations of EOP IERS Conventions 2010 (designed here as "model"), RMS ($X_{pol}-$ model = 167 μas, RMS ($Y_{pol}-$ model) = 164 μas, RMS ($dUT1-$ model) = 18 μs.

The value of Tropospheric Total Zenith Delay (TZD) obtained during CONT11 from VLBI are in a good agreement with date obtained from GPS observations. For example we show s here the picture for Badary station with TZD from VLBI and GPS data. The results of TZD comparison for all stations for CONT11 are in the Table 2. At the row 2 given Number of points, at the row 3 and 4 - RMS and bias for the differences of TZD from VLBI and GPS.

We are planning to continue the data analysis with QUASAR software and careful analysis of obtained series of intra day EOP and tropospheric parameters intra day variations.

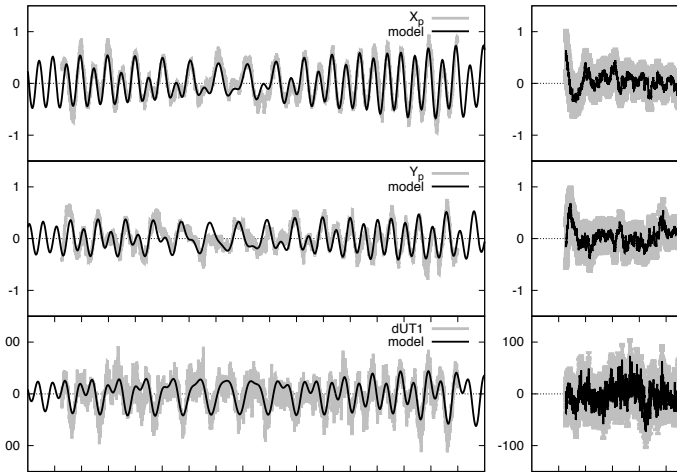

Figure 1: EOP intra-day variations from CONT11

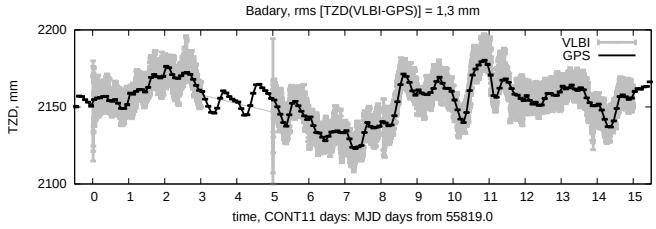

Figure 2: Example of TZD: TZD from VLBI and GPS observations during CONT11 company for Badary station

Station	Number if point	RMS	bias
Badary	621	1.3	0.1
Concepcion	472	4.4	-2.4
Hartrao	543	1.7	0.3
Hobart12	471	2.5	0.2
Forteleza	191	1.7	0.1
Kokee	778	2.7	-0.3
Ny Alezund	12346	4.6	-1.2
Onsala	634	4.7	-1.4
Tsukuba	848	5.6	-1.2
Westford	655	5.4	-2.0
Wettzell	699	4.6	-1.0
Zelenchukskaya	660	7.4	-3.3
Yebes	10516	5.5	-4.7

Table 2: Comparison of TZD from VLBI and GPS observations during CONT11 (for stations in Ny Alesund and Yebes used for comparison data of USNO GPS Analysis Center (AC), for other stations - CODE GPS AC

DISCUSSION ON THE TOPIC
Theory, modelling and observations of Earth Rotation

SHORT SUMMARY

A number of issues that were presented during Session 4a and 4b were put to the discussion:

- the next steps in Earth interior modelling (cf. V. Dehant's presentation in Session 4a, pp. 144–147),
- the importance of the studies on Earth rotation for geophysical interpretations (cf. C. Huang's presentation in Session 4a, pp. 156–159),
- the goals of the newly established, "IAU/IAG Joint Working group on the Theory of Earth Rotation" (cf. J. Ferrandiz presentation in Session 4a, pp. 139–143),
- the importance of the best possible accurate realization of the ICRF for Earth rotation studies (cf. presentations on the 3rd realization of the ICRF in Session 2),
- possible recommendations to the IVS about VLBI campaigns devoted to improvements in the Earth rotation model (submitted to A. Nothnagel, Chair of the IVS DB),
- The importance of using other kinds of observations than VLBI only for nutation studies (cf. N. Capitaine's presentation in Session 4b, pp. 200–203),
- etc.

For more details on issues related to the IAU/IAG Joint Working group on the "Theory of Earth Rotation", see `http://web.ua.es/es/wgther`,
and especially `http://web.ua.es/es/wgther/reports-of-jwg-meetings.html`.

Session 5

SOLAR SYSTEM DYNAMICS
- THEORY, MODELLING AND NUMERICAL STANDARDS

DYNAMIQUE DU SYSTÈME SOLAIRE
- THÉORIE, MODÉLISATION ET STANDARDS NUMÉRIQUES

ROTATIONAL AND LIBRATIONAL MOTION OF SOLAR SYSTEM BODIES

N. RAMBAUX[1,2]
[1] Université Pierre et Marie Curie
[2] IMCCE-Observatoire de Paris
e-mail: Nicolas.Rambaux@imcce.fr

ABSTRACT. Planetary exploration has revealed the great richness and diversity of the terrestrial planets and natural satellites. The mean rotational motion of planets was determined from ground-based telescopes since few centuries and nowadays the measurement resolution afforded by space telescopes and spacecraft allows the detection of small variations in the rotational motion that bear the signature of internal properties. The investigation of the interiors of planets and satellites is instrumental to understanding planetary processes operating on a global scale. Here, we will present the knowledge of the rotation and librations (for bodies in spin-orbit resonance) of some Solar system bodies that has been measured recently.

1. INTRODUCTION

The mean rotation of planets and natural satellites have been detected few centuries ago and today the improvement and accumulation of data allow astronomers to distinguish variations in the mean rotational motion. Such variations have been identified for the Earth since 2$^{\text{nd}}$ century B.C. when Hipparcus measured the precession and then in 1747 when Bradley determined the first nutation (see e.g. Souchay & Capitaine 2013). In 1839 Bessel revealed the lunar physical libration by using a heliometer (see e.g. Koziel 1985). The oscillations around uniform motion are called nutations for non-resonant rotator like the Earth and librations for bodies in spin-orbit resonance. These variations intrigued dynamisicists and geophysicists because they bear the signature of internal properties. The determination of the present core state reveals crucial information on our understanding of the thermal evolution and geophysical history of the bodies. In addition, the knowledge of the rotational state of bodies is useful for cartography and for the planning of space missions.

In this short review, we will focus on the recent determination of the librations of the Moon, Phobos, and on the first librational determination for Epimetheus, Enceladus, and Mimas. We will also mention the recent results on Mercury and Venus.

2. THE ROTATIONAL MOTION OF THE MOON

It is well known that our natural satellite is in spin-orbit synchronous resonance implying that the Moon shows on average the same face towards the Earth. The Moon's rotation is measured with a remarkable accuracy of few milli-arcseconds thanks to the Lunar Laser Ranging (LLR) experiment that has been active since 1969 (e.g. Dickey *et al.* 1994). This experiment consists in the measurement of the round-trip travel time of a short laser pulse between an Earth observatory and one of the five corner cube retroreflector arrays settled on the Moon. US astronauts established three corner cube arrays during Apollo-era missions (Apollo 11, 14, and 15) and two were added by the soviet robotic missions Lunakhod (Lunakhod 1 and 2). Echoes of the Lunakhod 1 have been obtained in April 2010 (Murphy *et al.* 2011) thanks to a new determination of the array position by Lunar Reconnaissance Orbiter. Earth observatories such as the Apollo station (Murphy 2009) and OCA station (Samain *et al.* 1998) regularly shoot the Moon in order to obtain echoes and carry on the collection of data. The LLR data processing is a very sophisticated and challenging task, even after more than 40 years of routine observational operation.

Due to the high accuracy of the LLR observations and the large amount of data, the lunar rotation is integrated numerically, for example in the DE ephemeris (Williams *et al.* 2001) and INPOP ephemeris (e.g. Fienga *et al.* 2009). These models are joint numerical integration of the orbits of the Moon, the

Earth, the planets and asteroids, and of the lunar rotation (Williams *et al.* 2001; Fienga *et al.* 2009). The dynamical partial derivatives of the orbits and lunar Euler angles with respect to solution parameters such as moment of inertia, gravity field, tides, dissipation, interaction with a fluid core and initial conditions are computed and the adjustment provides the determination of these geophysical parameters (for a complete description see Standish and Williams 2012).

The rotational motion of the Moon is mainly sensitive to the gravitational torque of the Earth acting on its dynamical figure. The rotational motion may be described through the Euler equation written in the Moon's reference frame

$$\frac{d[I]\vec{\omega}}{dt} + \vec{\omega} \wedge [\vec{I}]\vec{\omega} = \vec{\Gamma} \tag{1}$$

where $[I]$ is the inertia tensor of the Moon and $\vec{\omega}$ is the angular velocity vector. The external gravitational torque of the Earth that acts on the dynamical figure of the Moon is expressed as

$$\vec{\Gamma} = \frac{3GM}{r^3}\vec{u} \wedge I\vec{u} \tag{2}$$

where $\vec{u}$ is the unit vector toward the Earth, M the Earth's mass. In DE and INPOP models, there are also gravitational torques due to other bodies in Solar system (Sun, Venus, and Jupiter) and the gravitational field of the Moon is developed until degree 6 and the Earth at degree 2. The external gravitational torque (Eq. 2) depends on the relative distance between the Moon and the Earth. The response of the Moon to this external torque is called librational motion and corresponds to oscillatory motion of the Moon around a uniform rotational motion. The librational motion can be decomposed in a Fourier series where the forced frequencies arise from periods present in the lunar orbit from (1) Earth-Moon-Sun effects, with periods related to the Delaunay arguments of lunar theory, and (2) planetary effects. A second set of frequencies, called free frequencies are also present in the librational motion of the Moon and they correspond to the dynamical normal modes of the Moon in spin-orbit resonance when its spin is displaced from its dynamical equilibrium position (e.g. Williams *et al.* 2001; Rambaux and Williams 2011). The amplitudes of the periodic forced libration terms depend on both the strength of the torque applied to the aspherical Moon and how close the forcing period is to the resonant periods of the rotation, the free periods. The strength of a torque term can be variable in time, as for example due to the eccentricity of the Earth-Moon orbit around the Sun, which varies with time and alters the amplitude of the librations. In addition, if the tides are introduced, the tensor of inertia $[I]$ is variable with time and mixes some terms in the librational motion (see Williams *et al.* 2001).

To take into account the presence of the core an additional equation of motion of the form

$$\frac{d\vec{H}^c}{dt} + \vec{\omega} \wedge \vec{H}^c = \vec{\Gamma}_c \tag{3}$$

is introduced. The $\vec{\Gamma}_c$ represents the interaction between the core and the mantle. In Williams *et al.* (2001), the core is assumed to be spherical and the coupling is dissipative. That formulation has been supplemented in the DE model (e.g. Williams *et al.* 2013) to take into account the core oblateness.

A new vision of the interior of the Moon has emerged from the combination of the GRAIL data (Zuber *et al.* 2013), seismic lunar models (Weber *et al.* 2011; Garcia *et al.* 2011) and the LLR model (Williams *et al.* 2013). Notably, from the mean density, mean moment of inertia of the solid Moon, and the tidal potential love number, the lunar structure appears divided into a thin crust, a thick mantle layer, and a fluid outer core that probably contains an inner core. In addition, the LLR data is sensitive to oblateness of the core and to the dissipation through the detection of a shift of 0.26" in the pole direction and the determination of the amplitude of four librational terms. The dissipation factor can be described through a power law in frequency but the sign of the power law (negative) is still challenging for the geophysical models that predict a positive sign. In addition, since the free librations damp with time, the observational detection of free librations requires recent excitation or continuing stimulating mechanisms. The settlement of new laser retroreflectors or active transponders on the surface of Moon may improve significantly the understanding of the interior structure of the Moon (Dehant *et al.* 2012).

3. ENCELADUS AND OTHER SATELLITES

The detection of librations is not unique to the Moon. Today, we know four additional satellites that exhibit variations in their rotational motion: Phobos, Epimetheus, Enceladus, and Mimas. Their main

librational amplitude and periods are listed in Table 1. The reported detections are on the librations in longitude that correspond to the oscillations of the body principal axis projected onto the equatorial plane of the satellite. The amplitudes of these librations are generally larger than the amplitude of the libration in latitude, North-South oscillations. The librations in longitude can be expressed as (e.g. Rambaux *et al.* 2010)

$$\gamma = A_0 \sin(\omega_0 t + \phi_0) + \sum_i \frac{\omega_0^2 H_i}{\omega_0^2 - \omega_i^2} \sin(\omega_i t + \alpha_i) \quad (4)$$

where $\omega_0 = n\sqrt{3\sigma}$ is the resonant frequency of this spin-orbit problem and A_0, ϕ_0 are two constants of integration. The H_i, ω_i, and α_i are respectively the magnitude, the frequency and the phase of the orbital perturbations. For example, the libration in longitude is caused by the variations in the orbital velocity related to the non-ezro eccentricity. In this case, the magnitude of the perturbation is $H_i = 2e$ with e the eccentricity and the frequency is the orbital frequency. Then the amplitude of physical libration γ is equal to $6e\sigma/(3\sigma - 1)$. If the perturbed orbital motion implies a long period term, then the resulting amplitude of libration is almost equal to the magnitudes of the orbital perturbation because $\omega_i \ll \omega_0$. Comstock and Bills (2003) gave a large overview of the amplitude of the librations in longitude due to the non-zero eccentricity for rigid bodies. The presence of a fluid ocean modifies the resulting amplitude libration (see e.g. Van Hoolst *et al.* 2013) but the amplitude of librations for such bodies have not yet been observed.

The main libration of Phobos was determined 20 years ago by Duxbury and Callahan (1989). They used a digital control point network based on Viking images. The amplitude of librations have been confirmed and improved by MEX data (Willner *et al.* 2010) as well as from the orbital perturbation (Jacobson 2010). These new data and adjustment stimulated the elaboration of new models of Phobos librations in order to find evidence of possible origin of Phobos (Rambaux *et al.* 2012; Le Maistre *et al.* 2013).

The NASA-ESA space mission Cassini has orbited in the Saturnian system since 2004. The numerous flybys of Cassini over Saturnian satellites led to the discovery of the librational motion of three satellites: Epimetheus, Enceladus, and Mimas. The rotational motion of Epimetheus has been obtained as a by-product of the construction of the shape model (Tiscareno *et al.* 2009). This method works well for this satellite because it has a large librational amplitude, roughly 5.9° (see Table 1). Unfortunately, the same method applied to the companion Janus does not provide a clear detection ($0.33° \pm 0.66°$), Tiscareno *et al.* 2009). Following the detection of Epimetheus' librations, the rotational motions of Enceladus and Mimas were determined. In this case, the control point network method has been used by Giese *et al.* (2011) and Tajeddinne *et al.* (2013), respectively.

The horsechoe shaped orbital librations of Epimetheus and Janus leads to further investigation of their rotational responses by numerical (Noyelles 2010) and analytical studies (Robutel *et al.* 2010). A generalization of the rotational motion for co-orbital satellites in spin-orbit resonance has been formulated by Robutel *et al.* (2011) and applied to Telesto, Calypso, Helene, and Polydeuces in perspective of future detection. Thomas *et al.* (2013) investigated the librations of Helene based on the same approach that Tiscareno *et al.* (2009) used but did not detect librational motion. For Enceladus, the librational detection used the model developed by Rambaux *et al.* (2010) in order to discriminate between long and short period. The librations of Enceladus are dominated by the long-period librations resulting from its interaction with Dione. For Mimas, the comparison of the observed amplitude with the libration computed for a hydrostatic model developed by Noyelles *et al.* (2011) shows a large departure for the libration at the orbital period (0.944 days). The amplitude of the observed libration at the orbital period is twice the prediction whereas the five other detected librations have amplitudes in very good agreement. Such a large departure may be interpreted as the signature of an elongated core that can give information on the origin of Mimas (Tajeddinne *et al.* 2013).

Stiles *et al.* (2008, 2010) analyze the rotation of Titan from radar observations by assuming a non-constant angular velocity. Then Merigolla and Iess (2011) investigated the possibility to detect librations in the rotational motion of Titan. It appears that the amplitude of the librations is below the detection accuracy as confirmed by theoretical models (Van Hoolst *et al.* 2013).

4. MERCURY AND VENUS

The best illustration of the relationship between rotation and interior is certainly obtained for Mercury. Margot *et al.* (2007, 2012) performed Earth-based radar interferometry observations of Mercury. They

Satellite	Amplitude	Frequencies	References
The Moon(a)	90.706”	365.260	Rambaux and Williams (2011)
	16.799”	27.555	”
	16.762”	1095.220	”
Phobos	1.2° ± 0.15°	0.3190 days	Willner *et al.* (2010)
Epimetheus	5.9° ± 1.2°	0.692 days	Tiscareno *et al.* (2009)
Enceladus	0.056°	1.372 days	Giese *et al.* (2011)
Mimas(b)	43.78° ± 0.07°	25772.62 days	Tajeddine *et al.* (2013)
	42.1’ ± 1.8’	8590.87 days	”
	48.3’ ± 1.3’	0.944 days	”

Table 1: Determination of the librations in longitude for natural satellites. (a) For the Moon, the table lists only the three largest librations; for the rest of spectrum see Rambaux and Williams (2011). (b) For Mimas, Tajeddine *et al.* (2013) detected three more librations.

obtain the rotational motion of Mercury with a great accuracy and discovered the amplitude of forced libration at the orbital period equal to (38.5 ± 1.6 arcseconds) and an obliquity value of Mercury of (2.04 ± 0.08) arcminutes (Margot *et al.* 2012). The forced amplitude can be modeled as (e.g. Margot *et al.* 2007):

$$\gamma = \frac{3}{2}\frac{B-A}{C_m} f(e) \sin nt \tag{5}$$

where A and B are the equatorial moments of inertia of Mercury, C_m is the polar moment of inertia of the mantle, and $f(e)$ is a function depending on the eccentricity. Indeed C_m represents the inertia of the body, i.e. its resistance to the motion. If the core is solid, it is all the body that responds to the gravitational torque of the Sun and the denominator C_m must be replaced by C, if the core is fluid, only the mantle will respond by assuming that the interior is decoupled from the mantle because the inertial coupling is small (Rambaux *et al.* 2007). As the moment of inertia of the mantle C_m is smaller than the total moment of inertia C, the amplitude of libration is increased for Mercury with a fluid core.

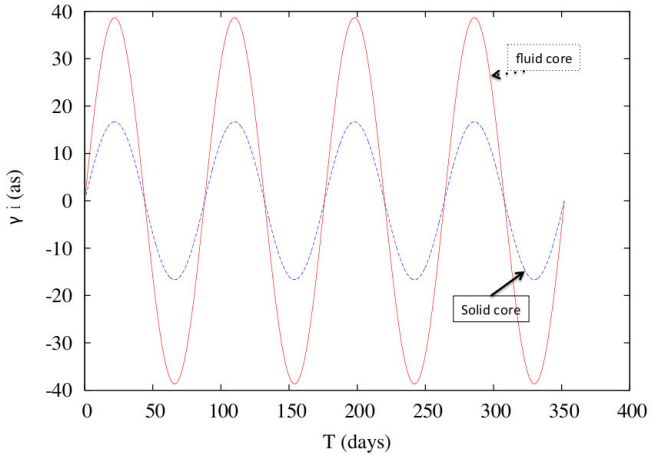

Figure 1: Amplitude of librations for Mercury for two different interiors structures (liquid and solid).

The residuals of the forced librations between the observations and the model show an additional libration of which the origin is still a mystery. Some hypotheses have been suggested and investigated: existence of a free libration, forced librations due to Jupiter, interior coupling (see the discussion and references in Margot *et al.* 2012). But no firm explanation on this additional libration has been provided. The identification of this forced libration would associate the interior properties more accurately with improving significantly the interior models (e.g. Rivoldini *et al.* 2009; Hauck *et al.* 2013).

The rotational motion of Venus is the least known among the four terrestrial planets. This is essentially due to the thick atmosphere that conceals the surface. The Magellan mission used radar images (Davies *et al.* 1992) and VEX followed thermal emissivity anomalies (Mueller *et al.* 2012) to track landmark features at the surface of the planet. The anomalous features appear to be slightly shifted when using the Davies et al. rotational model developed in 1992. Possible origins of this variation in the spin period is the exchange of angular momentum between the atmosphere and the solid body, the solar gravitational torque acting on the triaxial figure, or the presence of a fluid core (Cottereau *et al.* 2011). However, the peak-to-peak length-of-day variations induced by these mechanisms seem to be too small to explain the observational data. Understanding the mechanisms responsible for these two observations will bring crucial information on the nature of interior or atmospheric couplings in Venus.

5. CONCLUSION

The determination of the rotational motion has been improved during the last ten years by Earth-based observations and/or in-situ space missions visiting these bodies. The increase of the accuracy and accumulation of data allow a better vision of the interior of the Moon while the first measurement of the librational or rotational variations for Epimetheus, Enceladus, Mimas, Mercury, and Venus reveals extremely rich bodies. In parallel to these new measurements, the development of the modeling (analytical and numerical) including more and more physics allows a full exploration and exploitation of these observations that lifts the veil on the interior of Solar system bodies.

Acknowledgements. I thank J. Williams and J. Laskar for discussion and comments on this manuscript.

6. REFERENCES

Comstock R.L. & Bills B.G., 2003, J. Geophys. Res., 108(E09), 5100

Cottereau, L., Rambaux, N., Lebonnois, S., & Souchay, J. 2011, aap, 531, A45

Davies, M. E., Colvin, T. R., Rogers, P. G., Chodas, P. W., & Sjogren, W. L. 1992, LPI Contributions, 789, 27

Dickey, J.O., Bender, P.L., Faller, J.E., Newhall, X.X., Ricklefs, R.L., Ries, J.G., Shelus, P.J., Veillet, C., Whipple, A.L., Wiant, J.R., Williams, J.G., Yoder, C.F., 1994. Lunar laser ranging: a continuing legacy of the Apollo program. Science 265 (5171), 482–490. doi:10.1126/science.265.5171.482.

Duxbury T.C. and Callahan J.D., 1989,Phobos and Deimos Control Networks, Icarus 77, 275-286

Fienga, A. et al., 2009. INPOP08, a 4-D planetary ephemeris: From asteroid and time- scale computations to ESA Mars Express and Venus Express contributions. Astron. Astrophys. 507 (3), 1675–1686. http://dx.doi.org/10.1051/0004-6361/ 200911755.

Giese, B., Hussmann H., Roatsch T., Helfenstein P., Thomas P. C. , and Neukum G. 2011, Enceladus: Evidence for librations forced by Dione, EPSC-DPS Joint Meeting 2011, Vol. 6, EPSC-DPS2011-976

Hauck, S. A., Margot, J.-L., Solomon, S. C., *et al.* 2013, The curious case of Mercury's internal structure, Journal of Geophysical Research (Planets), 118, 1204

Garcia, R. F., J. Gagnepain-Beyneix, S. Chevrot, and P. Lognonne (2011), Very preliminary reference Moon model, Phys. Earth Planet. Inter., 188, 96–113, doi:10.1016/j.pepi.2011.06.015.

Jacobson, R. A., 2010,The orbits and masses of the martian satellites and the libration of Phobos, The Astronomical Journal, 139, 668

Koziel, K. 1985, Astrophysics and Space Science, 110, 193

Le Maistre, S., Rosenblatt, P., Rambaux, N., et al. 2013, Planetary and Space Science, 85, 106

Margot, J.-L., S. J. Peale, R. F. Jurgens, M. A. Slade, and I. V. Holin (2007), Large longitude libration of Mercury reveals a molten core, Sci- ence, 316, 710–714.

Meriggiola, R., Iess, L., 2012. A new rotational model of Titan from Cassini SAR data, in: EPSC Abstracts Vol. 7 EPSC2012-593.

Margot, J.-L., Peale, S.J., Solomon, S.C., et al. 2012, Journal of Geophysical Research (Planets), 117

Murphy T.W., 2009, Lunar Ranging, Gravitomagnetism, and APOLLO, Space Science Reviews, 148, 217

Murphy, T.W., Adelberger, E.G., Battat, J.B.R., Hoyle, C.D., Johnson, N.H., McMillan, R.J., Michelsen, E.L., Stubbs, C.W., Swanson, H.E., 2011. Laser ranging to the lost Lunokhod 1 reflector. Icarus 211 (2), 1103–1108. doi:10.1016/j.icarus. 2010.11.010.

Noyelles, B., 2010, Theory of the rotation of Janus and Epimetheus. Icarus, 207:887–902.

Noyelles, B., Karatekin, Ö., & Rambaux, N. 2011, Astronomy and Astrophysics, 536, A61
Rambaux, N., T. van Hoolst, V. Dehant, and E. Bois (2007), Inertial core-mantle coupling and libration of Mercury, Astron. Astrophys., 468, 711–719, doi:10.1051/0004-6361:20053974.
Rambaux, N., Castillo-Rogez, J., Williams, J., Karatekin, O., 2010. Librational response of Enceladus. Geophys. Res. Lett. 37, L04202. http://dx.doi.org/10.1029/ 2009GL041465.
Rambaux, N., Williams, J.G., 2011. The Moon's physical librations and determina- tion of their free modes. Celestial Mechanics and Dynamical Astronomy, 109 (1), 85-100. doi:10.1007/s10569-010-9314-2.
Rambaux, N., Castillo-Rogez, J.C., Le Maistre, S., Rosenblatt, P., 2012. Rotational motion of Phobos. Astronomy and Astrophysics 548 (December), A14,
Robutel, P., Rambaux, N., and Castillo-Rogez, J., 2011, Analytical description of physical librations of saturnian coorbital satellites Janus and Epimetheus. Icarus, 211:758–769.
Rivoldini, A., T. van Hoolst, and O. Verhoeven (2009), The interior structure of Mercury and its core sulfur content, Icarus, 201, 12–30.
Samain, E., Mangin, J. F., Veillet, C., et al. 1998, Millimetric Lunar Laser Ranging at OCA (Observatoire de la Cote d'Azur), Astronomy and Astrophysics Supplement, 130, 235
Souchay J., and Capitaine N., 2013, Precession and Nutation of the Earth,
Standish, E. M., and J. G. Williams (2012), Orbital ephemerides of the Sun, Moon, and planets, in Explanatory Supplement to the Astronomical Almanac, 3rd ed., edited by. S. Urban and P. K. Seidelmann, pp. 305–345, University Science Books, Mill Valley, Calif. http://iau- comm4.jpl.nasa.gov/XSChap8.pdf Stiles *et al.* (2008, 2010)
Tajeddinne, R., Rambaux, N., Lainey, V., Charnoz, S., and Noyelles B., 2013, Mimas: Strong forced longitudinal librations and constraints to its internal structure using Cassini ISS observations, European Planetary Science Congress 2013, Vol. 8, EPSC2013-391
Thomas, P. C., Burns, J. A., Hedman, M., et al., 2013, Icarus, 226, 999
Tiscareno, M. S., Thomas, P. C., and Burns, J. A., 2009, The rotation of Janus and Epimetheus. Icarus, 204:254–261.
Van Hoolst, T., Baland, R.M., Trinh, A., 2013. On the librations and tides of large icy satellites. Icarus 226, 299–315.
Weber, R. C., P.-Y. Lin, E. J. Garnero, Q. Williams, and P. Lognonne (2011), Seismic detection of the lunar core, Science, 331, 309–312, doi:10.1126/science.1199375.
Williams, J.G., Boggs, D.H., Yoder, C.F., Ratcliff, J.T., Dickey, J.O., 2001. Lunar rotational dissipation in solid body and molten core. Journal of Geophysical Research 106 (E11), 27933–27968. doi:10.1029/2000JE001396.
Williams, J. G., A. S. Konopliv, D. H. Boggs, *et al.* (2013), Lunar interior properties from the GRAIL mission, J. Geophys. Res., submitted.
Margot, J.-L., S. J. Peale, R. F. Jurgens, M. A. Slade, and I. V. Holin (2007), Large longitude libration of Mercury reveals a molten core, Sci- ence, 316, 710–714.
Zuber, M. T., D. E. Smith, M. M. Watkins, *et al.* (2013), Gravity field of the Moon from the Gravity Recovery and Interior Laboratory (GRAIL) mission, Science, 339, 668–671, doi:10.1126/Science.1231507.

TESTS OF GRAVITATION AT SOLAR SYSTEM SCALES BEYOND THE PPN FORMALISM

A. HEES[1], W. M. FOLKNER[1], R. A. JACOBSON[1], R. S. PARK[1], B. LAMINE[2],
C. LE PONCIN-LAFITTE[3], P. WOLF[3]
[1] Jet propulsion Laboratory - California Institute of technology
4800 Oak Grove Drive, Pasadena, CA, 91109, USA
e-mail:{Aurelien.D.Hees, William.D.Folkner, Robert.A.Jacobson, Ryan.S.Park}@jpl.nasa.gov
[2] IRAP, Université de Toulouse, CNRS, 31400 Toulouse, France
e-mail: brahim.lamine@irap.omp.eu
[3] Observatoire de Paris, SYRTE, CNRS/UMR 8630, UPMC
61 avenue de l'Observatoire, F-75014 Paris, France
e-mail: {christophe.leponcin,peter.wolf}@obspm.fr

ABSTRACT. In this communication, the current tests of gravitation available at Solar System scales are recalled. These tests rely mainly on two frameworks: the PPN framework and the search for a fifth force. Some motivations are given to look for deviations from General Relativity in other frameworks than the two extensively considered. A recent analysis of Cassini data in a MOND framework is presented. Furthermore, possibilities to constrain Standard Model Extension parameters using Solar System data are developed.

1. INTRODUCTION

The General theory of Relativity (GR) is not the ultimate theory of gravity. This assumption is motivated by theoretical developments like the search for a quantum theory of gravitation or the unification of the gravitation with the other fundamental interactions. From an observational point of view, puzzling galactic and cosmological observations can not be explained by GR and the standard model of particles. Accounting for these observations is usually done by introducing new types of matter: the so-called Dark Matter and Dark Energy fluids. Since these constituents have not been directly observed yet, they may be a hint of a deviation from GR. Therefore, searches for alternative theories of gravity is very important. Due to the very high accuracy measurements available, the Solar System is a very good laboratory to test GR. In Section 2, we will briefly recall what are the two formalisms widely used so far to test GR in the Solar System and what are the current constraints in these formalisms. In Section 3, we give some motivations to consider tests of gravitation beyond the standard formalisms. We also present a sensitivity analysis of Messenger and Cassini data to the Standard Model Extension. Finally, in Section 4, we present a new test of the MOND phenomenology done using Cassini data.

2. STANDARD TESTS OF GENERAL RELATIVITY

GR is built on two principles. The first one is called the Einstein Equivalence Principle. It implies that gravity can be identified to space-time geometry which is mathematically described by a space-time metric $g_{\mu\nu}$. In particular, test masses follow geodesics of this metric and ideal clocks measure the proper time of this metric. This principle is now very well tested through the Universality of Free Fall, tests of the Local Lorentz Invariance and tests of the Local Position Invariance. A review of the current tests of the Einstein Equivalence Principle can be found in Will (2006). Nevertheless, there exist strong theoretical motivations to improve the current constraints on the equivalence principle (see Damour, 2012) coming from string theories, from theories with variable fundamental constants, from the anthropic principle, ...

The second principle upon which GR is built is the Einstein field equations that determine the form of the metric tensor. In GR, the form of the metric tensor is directly influenced by the energy/matter

content of the space-time through the Einstein equations. Up to now, two formalisms have been widely used to test the form of the metric tensor: the Parametrized Post-Newtonian (PPN) formalism and the search for a fifth force.

The PPN formalism is a phenomenology making an interface between theoretical developments and experiments. In the PPN formalism (fully described in Will (1993)), the space-time metric is parametrized by 10 dimensionless coefficients that can be tested independently of any fundamental underlying theory. Forty years of precise experiments have constrained PPN parameters to be very close to those expected from GR (for a review, see Will (2006)). In particular, the two most famous PPN parameters γ and β (whose values are 1 in GR) are now constrained at the level of 10^{-5} with the measure of the Shapiro delay with the Cassini spacecraft (Bertotti et al. 2003) and with planetary ephemerides (Pitjeva and Pitjev, 2013 and Verma et al. 2013).

The fifth force formalism considers a modification of the Newtonian potential with a Yukawa potential parametrized by a range of interaction λ and a strength of interaction α (see Talmadge et al. 1988 and Adelberger et al. 2009). These parameters have been tested in a very wide range (see Adelberger et al. 2009 and Fig. 31 of Konopliv et al. 2011). In particular, α is constrained at a very high level of accuracy ($\alpha < 10^{-10}$) at Earth-Moon and Sun-Mars distances. It is also worth mentioning that windows remain opened at very short distances and at very large distances.

While the current constraints on these two formalisms are very impressive, there exist theoretical models that predict deviations smaller than the current accuracy. One good example of such a model is given by theories developing screening mechanism (see for example Brax et al. 2012). Upcoming space missions like Gaia or BepiColombo will improve the current limits in these formalisms.

3. BEYOND THE STANDARD FORMALISMS

Even if the PPN and the fifth force formalisms have been extensively used so far, there are motivations to consider alternative frameworks. Indeed, not all the alternative theories of gravity enter these formalisms. To illustrate this, we will give four examples of alternative theories of gravity considered in the literature that are not entering the standard formalisms.

First, the *Post-Einsteinian Gravity (PEG)* (Jaekel and Reynaud 2005, 2006) is an alternative theory of gravity based on a non local extension of Einstein field equations as suggested by radiative corrections. Phenomenologically in the Solar System, the space-time metric can be parametrized by two radial dependent potentials. This can be seen as an extension of the PPN formalism where the γ and β PPN parameters have been promoted to a function of the radial coordinate.

The second example is given by the *Standard Model Extension (SME)* framework. This phenomenology has been developed to systematically consider possible violations of the Lorentz symmetry. In the gravitational sector, the weak field space-time metric is parametrized by a symmetric trace-free tensor $\bar{s}_{\mu\nu}$ (Bailey and Kostelecký, 2006) different from the PPN parametrization.

Another example is given by the *Fab Four theory*, which is a tensor-scalar theory of gravitation developed in the cosmological context to solve the cosmological constant problem. It was shown that the Solar System metric derived from this theory is parametrized by four parameters and is not covered by the PPN parametrization (Bruneton et al. 2012).

Finally, it was shown that the *MOdified Newtonian Dynamic (MOND)* phenomenology produced an effect in the Solar System called the External Field Effect (EFE). It is due to the non-linearity of MOND equations in which the gravitational dynamics of a system are influenced by the external gravitational field (Blanchet and Novak, 2011). In the Solar System, it implies a quadrupolar correction to the Newtonian potential

$$\Phi = -\frac{GM}{r} - \frac{Q_2}{2} x^i x^j \left(e_i e_j - \frac{1}{3}\delta_{ij} \right) \tag{1}$$

where e_i is a unitary vector pointing towards the galactic center and Q_2 is a parameter related to the fundamental MOND theory.

The four examples given here are interesting alternative theories of gravity that do not enter the PPN or the fifth force formalism. For these kind of theories, only very few constraints at Solar System scales are available today and there is a strong interest to constrain these theories with Solar System data.

Recently, software aiming at simulating range, Doppler and astrometric observables directly from the space-time metric has been developed (Hees et al. 2012). The main advantage of this software is that it allows one to produce simulations in a wide class of alternative theories of gravitation very easily. In

particular, all the potential effects produced by a deviation from GR are automatically taken into account including the effect on the orbits of bodies, on clock behavior, effect on light propagation, ... This software also provides a fit of the initial conditions of the different bodies to identify the incompressible signature produced by a modification of gravity on observations. By incompressible signature, we refer to the signature that is not correlated with the initial conditions and that will not be absorbed in real data analysis. This signature is the one that would be observed in residuals of real data analysis (done in GR using standard procedure) while the correct gravitation theory is the considered alternative theory.

For example, we used the software described above to identify the incompressible signatures produced by SME on Messenger (around Mercury) and Cassini (around Saturn) spacecraft. The radioscience observations of these spacecraft depend on linear combinations of the fundamental parameters $\bar{s}_{\mu\nu}$. Figures representing the incompressible signatures produced by linear combinations of the SME parameters on Messenger and Cassini observations are given in Hees et al. (2013a). These signatures are characteristic of SME and can be searched in the residuals of real data analysis.

A comparison of the amplitude of these signatures with the accuracy of the measurements gives an estimate of the uncertainties on the SME coefficients that would be reachable in a real data analysis. Under the assumptions that no anomalous residuals have been observed during the data analysis, these uncertainties can be interpreted as an order of magnitude of an upper bound on the SME coefficients. The estimated uncertainties on SME coefficients reachable using Messenger and Cassini are given in Table 1. These values are very good compared to the current limit on SME parameters and this gives a strong motivation to consider a test of SME using Messenger and/or Cassini radio tracking data.

Coeff.	Uncertainties
$\bar{s}_A$	1.1×10^{-10}
$\bar{s}_{TX}$	3.1×10^{-8}
$\bar{s}_B$	1.4×10^{-8}
$\bar{s}_C$	3.2×10^{-11}

(a) : Messenger

Coeff.	Uncertainties
$\bar{s}_F$	8.6×10^{-11}
$\bar{s}_{TX}$	1.2×10^{-8}
$\bar{s}_G$	1.5×10^{-8}
$\bar{s}_H$	2.3×10^{-11}

(b) : Cassini

Table 1: Estimated reachable uncertainties on SME coefficients. The expression of the linear combinations are given in Hees et al. (2013a).

4. A TEST OF MOND WITH CASSINI DATA

As mentioned above, the main effect of the MOND phenomenology in the Solar System is called the External Field Effect (EFE) and is modeled by a quadrupolar correction to the Newtonian potential (1). This effect is parametrized by the MOND EFE parameter Q_2 that depends on the fundamental MOND theory (more precisely on the MOND interpolating function). The value of Q_2 for standard MOND interpolating functions has been computed by Blanchet and Novak (2011) and is framed by

$$2.1 \times 10^{-27}\ s^{-2} \leq Q_2 \leq 4.1 \times 10^{-26}\ s^{-2}. \tag{2}$$

In a recent study (Hees et al. 2013b), we have used 9 years of Cassini radio tracking to constrain Q_2. The analysis is done in two steps: first, the spacecraft trajectory around the Saturn barycenter is fitted and then the Saturn orbit is adjusted. The model used for the spacecraft data reduction is standard and can be found in Moyer (2000). With current models, the range and Doppler can be fit to their intrinsic noise level without any signature remaining (when using both range and Doppler). This is due to the number of free parameters that are estimated (in particular the numerous maneuvers). For this study, we have estimated spacecraft trajectories with only Doppler and satellite imaging data. Omitting the range data from the spacecraft trajectory estimates leads to larger range residuals since they are not absorbed in the spacecraft orbit parameters and this allows the range data to be used to estimate corrections to the Saturnian orbit.

The range measurements have been used to estimate corrections to the orbit of Saturn and the EFE parameter. A standard model for the adjustment has been considered and extended to take into account the EFE (see Hees et al. 2013b). The principal estimated parameters included in the fit are the orbits of the Earth and Saturn, the mass parameter of the Sun, the EFE parameter Q_2, a constant correction to the radio delay, a constant scale factor correction to the solar plasma modeling.

In order to have realistic uncertainties on the estimated parameters, it is important to consider observations that are independent in the adjustment. The range residuals when taking one range observations by tracking pass for the fit is presented on the left of Figure 1. As one can see, the residuals are clustered in groups of data corresponding to the same spacecraft orbit estimate. This means range measurements within a single spacecraft orbit segment are highly correlated since they share a common estimated spacecraft trajectory relative to Saturn. Therefore, we consider only one range observation per spacecraft segment and the corresponding residuals are presented on the right of Figure 1.

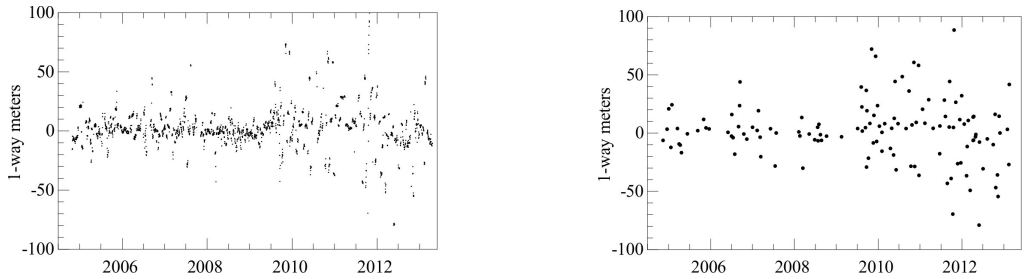

Figure 1: Range measurement residuals (left: one observation per tracking pass - right: one observation per orbit segment).

We obtain an estimate of the Q_2 parameter given by

$$Q_2 = (3 \pm 3) \times 10^{-27}\ s^{-2}. \tag{3}$$

The value $Q_2 = 0$ is included in the 1-σ confidence interval. This means the set of data used does not favor a MOND theory with respect to GR. Moreover, our result puts a very stringent constraint on the interval (2) computed theoretically. In particular, MOND theories characterized by standard MOND interpolating functions like $\mu_{1,2}$, $\mu_{\rm exp}$ or $\mu_{\rm TeVeS}$ (see Blanchet and Novak (2011) for a review of these MOND interpolating functions) are excluded by Cassini data.

Acknowledgements. The research described in this poster was partially carried out at the Jet Propulsion Laboratory, California Institute of Technology, under contract with the National Aeronautics and Space Administration A. Hees thanks the BAEF for financial support.

5. REFERENCES

Adelberger, E. G., Gundlach, J. H., Heckel, B. R. et al., 2009, Prog. in Particle and Nucl. Phys. 62, 102.
Bailey, Q., Kostelecký, V. A., 2006, Phys. Rev. D 74, 045001.
Bertotti, B., Iess, L., Tortora, P, 2003, Nature 425, 374.
Blanchet, L., Novak, J, 2011, MNRAS 412, 2530.
Brax, P., Davis, A.-C., Li, B., et al. 2012 Phys. Rev. D 86, 044015.
Bruneton, J.-P., Rinaldi, M., Kanfon, A. et al. 2012, Advances in Astronomy, 430694.
Damour, T., 2012, Class. and Quantum Grav. 29, 184001.
Hees, A., Lamine, B., Reynaud, S., 2012, Class. and Quantum Grav. 29, 235027.
Hees, A., Lamine, B., Le Poncin-Lafitte, C., Wolf, P., 2013a, Proceedings of CPT'13, arXiv:1308.0373.
Hees, A., Folkner, W. M., Jacobson, R. A., Park, R. S., 2013b, submitted to Phys. Rev. Letters.
Jaekel, M.-T., Reynaud, S., 2005, Class. and Quanum Grav. 22, 2135.
Jaekel, M.-T., Reynaud, S., 2006, Class. and Quanum Grav. 23, 777.
Konopliv, A. S., Asmar, S. W., Folkner, W. M., et al. 2011, Icarus211, 401.
Moyer, T. D., 2000, "Formulation of Observed and Computed Values of Deep Space Network Data types for Navigation", Ed. J.H. Yuen, JPL.
Pitjeva, E. V., Pitjev, N. P., 2013, MNRAS, 432, 4, 3431.
Talmadge, C., Berthias, J.-P., Hellings, R. W., Standish, E. M., 1988, Phys. Rev. Letters 61, 1159.
Verma, A., Fienga, A., Laskar, J., et al., 2013, arXiv:1306.5569.
Will, C., 1993, "Theory and Experiment in Gravitational Physics", Cambridge University Press.
Will, C., 2006, Living Rev. Relativity 9, 3.

NUMERICAL EPHEMERIDES OF PLANETS AND NATURAL SATELLITES OF IAA RAS AND THEIR USES FOR SCIENTIFIC RESEARCH

E.V. PITJEVA[1], G.A. KOSMODAMIANSKIY[1], D.A. PAVLOV[1], P. PITJEV[2],
A.L. POROSHINA[1], V.I.SKRIPNICHENKO[1]
[1] Institute of Applied astronomy RAS
Kutuzov Quay 10, 191187 St.-Petersburg, Russia
e-mail: evp@ipa.nw.ru
[2] St. Petersburg State University
Universitetski pr.28, 198504 Petrodvoretz, Russia
e-mail: ai@astro.spbu.ru

ABSTRACT. The dynamical model of the planetary part of the EPM2013 ephemerides of the IAA RAS has been fitted to about 800000 observations of different types (1913-2013). Their reference frame has been established with 321 ICRF-based VLBI measurements of spacecrafts near planets taken into account. EPM ephemerides serve as the basis for the Russian Astronomical and Nautical Astronomical Yearbooks, are planned to be used in the GLONASS and LUNA-RESOURCE programs, and are used for determination of physical parameters (asteroids masses, planet rotation, topography), $GM_\odot$ and its secular variation, the PPN parameters, the upper limit on mass of the dark matter in the Solar System. Moreover, numerical ephemerides of the 22 main planet satellites have been constructed; they also provide the basis for improving positions of the outer planets. Files containing polynomial approximation for EPM ephemerides (EPM2004, EPM2008, EPM2011) along with TT-TDB and ephemerides of Ceres, Pallas, Vesta, Eris, Haumea, Makemake, and Sedna are available from `ftp://quasar.ipa.nw.ru/incoming/EPM/`. The files are provided in IAA's binary and ASCII formats, as well as SPK and PCK formats.

1. THE DEVELOPMENT OF EPM2011 EPHEMERIDES

The EPM ephemerides (**E**phemerides of **P**lanets and the **M**oon) of the IAA RAS originated in the 1970's and are being improved since that time. These ephemerides are based upon relativistic equations of motion for celestial bodies and light rays, as well as relativistic time scales. EPM ephemerides are computed in the barycentric coordinate frame—BCRS, over more than 400-year interval (1787–2214).

Including into the process of simultaneous integration the 21 largest TNO (some of them are quite far, Eris which surpasses Pluto is an example) causes a significant change to the barycenter of the Solar System. The comparison of barycentric coordinates between EPM numerical theories and other ephemerides (DE, INPOOP) knowingly is nonsensical and gives large differences. Only the comparison of relative coordinates (heliocentric or geocentric) shows real differences between ephemerides.

Ephemerides EPM2011 were constructed (2011 – July 2012) before the B2 resolution of 28 GA IAU which fixed the value of the astronomical units of length (au) equal 149597870700 meters and proposed the determination of $GM_\odot$ in SI units. In EPM2011 the au value has been determined: $au_{EPM2011}$ = 149597870695.88 meters. Although following the B2 resolution does not increase the accuracy of constructed ephemerides, the next EPM ephemeris implementation will be made in accordance with the B2 resolution.

The dynamic model of the lunar motion was constructed by G. Krasinsky. Currently M. Vasiliev and E. Yagudina are developing the lunar part of the EPM ephemerides (one can find their publication in this issue). The tidal perturbation in the lunar orbital motion (due to tidal dissipation on the Earth body), as well as in rotational lunar motion (due to tidal dissipation on the Moon body) are computed using model with a delayed argument. The potential of the Moon is calculated up to 4-th order of the zonal index, the potential of the Earth includes the 5-th order harmonics.

During some time the planetary and lunar parts of the EPM2011 ephemerides were being improved separately. For EPM2011/m ephemerides, the parameters of the lunar and planetary parts of ephemerides have been in agreement with each other ("m" stands for "Moon"). The result of this agreement was a

moderate change in the lunar motion, whereas the planet positions of EPM2011 and EPM2011/m are practically equivalent. While earlier the lunar libration was being computed along with positions of planets and the Moon for EPM ephemerides, now for the first time it is available to public: `ftp://quasar.ipa.nw.ru/incoming/EPM/`.

EPM2011/m ephemerides contain coordinates and velocities of the Sun, the Moon, nine major planets, three largest asteroids (Ceres, Pallas, Vesta) and 4 TNO (Eris, Haumea, Makemake, Sedna) (in au, au/day) as well as lunar libration (in radians) and TT-TDB (in seconds).

Thanks to the effort done by the IAU Commission 4 Working Group on Standardizing Access to Ephemerides and File Format Specification, EPM2011/m ephemerides are now provided in the formats developed by the Navigation and Ancillary Information Facility of Jet Propulsion Laboratory at NASA. The formats are: Spacecraft and Planet Kernel (SPK) for the position ephemerides of the Sun, Moon, Earth, other planets, and asteroids; also for the so-called "time ephemerides" containing TT-TDB data. Planetary Constants Kernel (PCK) for lunar orientation (libration angles). It was decided to avoid any kind of recalculations during the conversion from IAA's formats to PCK/SPK formats. To achieve that goal, a new data type (Type 20) has been added to the SPK and PCK specifications to support "velocity-only" Chebyshev polynomials used in EPM. The originally available data types were Type 2 (position only) and Type 3 (position and velocity). With Type 20, the differences between EPM files provided in IAA's binary format and the ones provided in the SPK/PCK formats are only in technical data (file header, section headers, comments etc), while the Chebyshev coefficients are identical in both formats. The SPK and PCK files for the EPM2011/m theory are available on the IAA's FTP site, as well as the original text and binary formats (Pavlov, Skripnichenko, 2014).

2. THE DIFFERENCES BETWEEN EPM2011 AND EPM2013 EPHEMERIDES

Planetary parts of EPM2013 differ from those of EPM2011 in: improved dynamical model; updated database of asteroids (masses and orbits); upgraded database observations.

For constructing planetary ephemerides using the best modern observations, it is necessary to take into account all influencing factors.

The dynamical model of planet part EPM2013 takes into account the following:

- mutual perturbations from the major planets, the Sun, the Moon and 5 most massive asteroids;
- perturbations from the other 296 asteroids chosen due to their strong perturbations upon Mars and the Earth;
- perturbation from the massive two-dimensional asteroid ring ($R_1 = 2.06$ au, $R_2 = 3.27$ au) with the constant mass distribution;
- perturbations from the 30 largest Trans-Neptunean Objects (TNO);
- perturbation from a massive ring of TNO in the ecliptic plane with the radius of 43 au;
- the relativistic perturbations;
- perturbations due to the solar oblateness $J_2 = 2 \cdot 10^{-7}$.

The main improvement of EPM2013 is usage of a massive two-dimensional asteroid ring instead of a one-dimensional asteroid ring in the EPM2011 model, as well as the including of 30 individual TNO into the integration instead 21 TNO for the EPM2011 model.

The EPM2013 ephemerides have been fitted to 792327 observations of different types, spanning 1913-2012, from classical meridian observations to modern planetary and spacecraft ranging (see Table 1). 114657 new observations have been added since EPM2011 (677670) including the observations obtained in 2010–2012 for Odyssey, Mars Reconnaissance Orbiter (MRO), Mars Express (MEX) and Venus Express (VEX) spacecraft, the 108 VLBI data (2011–2013) for VEX, Odyssey, MRO, as well as 224 SSD observations obtained in 2012 at Flagstaff and TMO observatories. These new data were received by us due to the courtesy Dr. W.Folkner and Dr. A.Fienga. The ephemerides of the inner planets are based fully on radio-technical observations (mostly, measurements of time delays).

In addition to optical observations of outer planets, positional observations of their satellites are used for construction of planetary ephemerides, as these observations are more precise and practically free from the phase effect, which is difficult to take into account. Since the position of a satellite relatively to the stars is determined both by the planetary motion and the satellite's own motion around the planet, the measurements of the positions of satellites may be used to define the planetary orbits more accurately. Analytical theories of the motion of the satellites by Lieske, Vienn and Duriez, Lascar and Jacobson are

Planet	Radio		Optical	
	Interval of observations	Number of observations	Interval of observations	Number of observations
Mercury	1964–2009	951	—	—
Venus	1961–2013	53379	—	—
Mars	1965–2012	680030	—	—
Jupiter+4 sat.	1973–1997	51	1914–2012	13364
Saturn+9 sat.	1979–2009	126	1913–2012	15056
Uranus+4 sat.	1986	3	1914–2012	11861
Neptune+1 sat.	1989	3	1913–2012	11664
Pluto	—	—	1914–2012	5839
In total	1961–2013	734543	1913–2012	57784

Table 1: 792327 observations used for fitting of EPM2013

incorporated in the ERA software system. However there is no opportunity to correctly introduce to these analytical theories the parameters of the satellites' motion improved from observations. Therefore, the researchers at the IAA RAS construct their own numerical theories of the motion of the satellites of Mars and the outer planets (Poroshina et al., 2012). The dynamical models of satellites' motion include mutual perturbations of the satellites, perturbations from the Sun, major planets, and figure of the central planet. For the Phobos and Deimos motion, the tidal perturbations from Mars are also taken into account. The satellite ephemerides were improved to about 70 000 astrometric observations of different types: position, differential, observations of mutual events of Jupiterian and Saturnian satellites, spacecraft observations for Martian satellites. The obtained ephemerides have been compared to observations and ephemerides of other authors and are successfully used for improvement of orbital motion of satellites themselves as well as of their central planets.

EPM2013 have been oriented to ICRF with the accuracy better than 1 mas by including into the total solution 321 ICRF-based VLBI measurements of spacecraft 1989–2013 near Venus, Mars, and Saturn. in EPM2011, there were only 213 VLBI observations.

3. USAGE OF EPM FOR SCIENTIFIC RESEARCH

At present EPM ephemerides are used for astronavigation on the Earth and space: they are the basis for the Russian Astronomical and Nautical Astronomical Yearbooks since 2006, and are planned to be used in the GLONASS and LUNA-RESOURCE programs and for various other programs.

Masses of 21 of 301 largest asteroids have been estimated directly from spacecraft ranging; masses of the rest asteroids were obtained from their known diameters and the estimated densities for the three taxonomic types (C, S, M). The total mass of the asteroid main belt including the masses of all asteroids and the asteroid ring has been obtained: $M_{\rm belt} = (12.3 \pm 1.2) \cdot 10^{-10} M_\odot$ ($\approx 3\, M_{\rm Ceres}$). From the estimate of the mass of the TNO ring and the known masses of the 21 largest TNO and Pluto we obtained the mass of the whole set of TNO: $M_{\rm TNO} = 790 \cdot 10^{-10} M_\odot$ ($\approx 164\, M_{\rm Ceres}$ or $2\, M_{\rm Moon}$) (Pitjeva, 2013). Those estimates shed light on the dynamics of the Solar System now and at the time of its formation.

New estimations of PPN parameters have been obtained: $\beta - 1 = -0.00002 \pm 0.00003$, $\gamma - 1 = 0.00004 \pm 0.00006$. The good correspondence of the planetary motions and the propagation of light to the predictions of General Relativity narrows significantly the range of possibilities for alternative theories of gravitation (Pitjeva & Pitjev, 2013).

It has been found from planet observations that heliocentric gravitational constant $GM_\odot$ is decreasing with the rate $G\dot{M}_\odot/GM_\odot = (-6.3 \pm 4.3) \cdot 10^{-14}$ per year (2σ). The variation of $GM_\odot$ reflects the balance between the mass lost through radiation and solar wind and the material falling onto the Sun. Using the maximum limits for a possible change of $M_\odot$, it has been obtained that the annual change of the gravitation constant G must fall within the interval $-7.0 \cdot 10^{-14} < \dot{G}/G < +7.8 \cdot 10^{-14}$ with a 95% probability (Pitjeva & Pitjev, 2012; Pitjeva & Pitjev, 2013).

Using the estimates of the additional perihelion advances obtained from observation for different planets, it has been found that the density of dark matter $\rho_{\rm dm}$ must be less than $1.1 \cdot 10^{-20}$ gcm^{-3} at the distance of Saturn's orbit, and the mass of dark matter inside Saturn's orbit must be less than

$7.9 \cdot 10^{-11} M_\odot$, even if it is concentrated toward the center (Pitjev & Pitjeva.,2013; Pitjeva & Pitjev,2013).

4. RESULTS AND CONCLUSION

Improvement of the dynamical model of planet motion and increase of the number of high-precision spacecraft data have resulted in the following progress:

- the accuracy of estimation of the mass of the two-dimensional asteroid ring and the total mass of the asteroid belt increased by the order of magnitude: $M_{belt} = (12.242 \pm 0.106) \cdot 10^{-10}\ M_\odot$;
- orbits of all planets have changed and were improved distinctly. In particular, the formal uncertainties of the semi-major axes of the inner planets have halved
- the residuals also have been improved; the rms residuals of ranging for Odyssey, MRO, MEX spacecraft have decreased up to 1.1 m (see Figure 1).

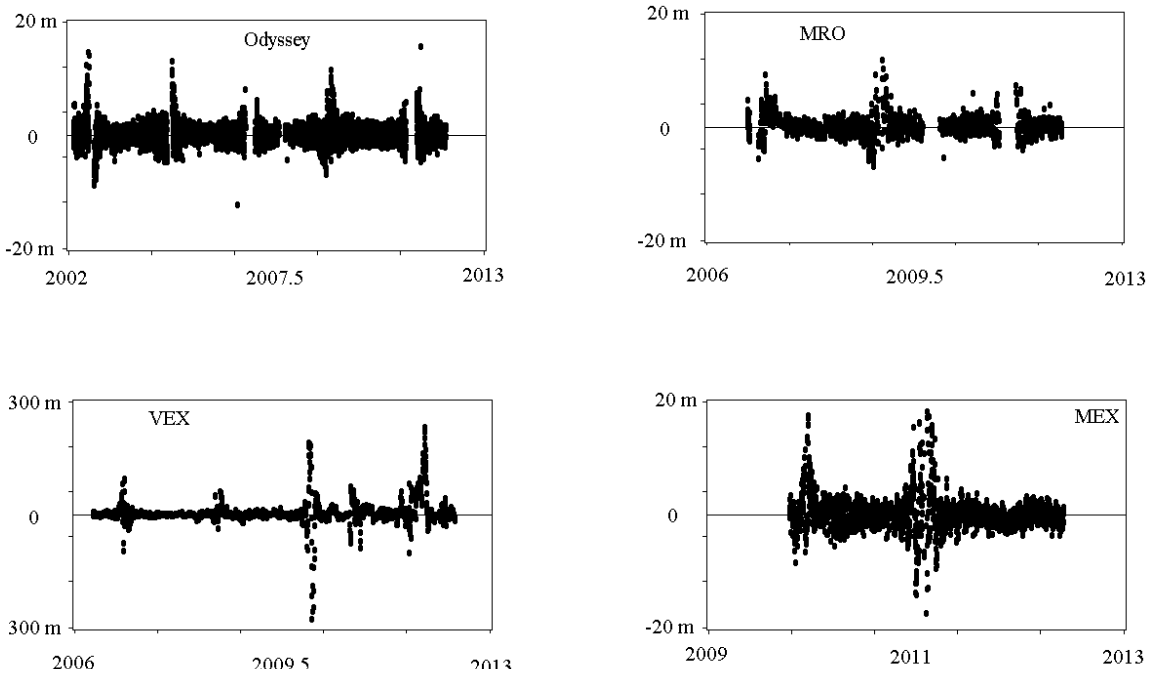

Figure 1: The rms ranging residuals for spacecraft Odyssey 1.1 m, MRO 1.1 m, MEX 1.4 m, VEX 3.1 m.

5. REFERENCES

Pavlov D.A., Skripnichenko V.I., 2014, "Preliminary results in implementation of a cross-platform version of the ERA software system" (in Russian), IAA RAS Transaction, Science, St.Petersburg, 28, 8 p.

Pitjev N.P., Pitjeva E.V., 2013, "Constraints on dark matter in the solar system", Ast. Lett., 39, pp. 141–149, doi: 10.1134/S1063773713020060.

Pitjeva E.V., 2013, "Updated IAA RAS Planetary Ephemerides-EPM2011 and Their Use in Scientific Research", Sol. Syst. Res., 47, pp. 386-402, doi: 10.1134/S0038094613040059.

Pitjeva E.V., Pitjev N.P., 2012, "Changes in the Sun's mass and gravitational constant estimated using modern observations of planets and spacecraft", Sol. Syst. Res., 46, pp. 78-87, doi: 10.1134/S0038094612010054.

Pitjeva E. V., Pitjev N. P., 2013, "Relativistic effects and dark matter in the Solar system from observations of planets and spacecraft", MNRAS , 432, pp. 3431-3437, doi: 10.1093/mnras/stt695.

Poroshina A., Kosmodamianskiy G., Zamarashkina M., 2012, "Construction of the numerical motion theories for the main satellites of Mars, Jupiter, Saturn and Uranus", IAA RAS Transaction, Science, St.Petersburg, 26, pp. 75–87.

INPOP13a AND ITS APPLICATIONS FOR TESTING GRAVITY

A. FIENGA[1,2], A.K. VERMA[3,4], J. LASKAR[2], M. GASTINEAU[2], H. MANCHE[2]
[1] Observatoire de la Côte d'Azur, GéoAzur CNRS UMR-7329, Valbonne, France
[2] IMCCE, Paris Observatory, UPMC, univ. Lille1, CNRS, Paris, France
[3] Observatoire de Besançon, UTINAM CNRS UMR CNRS-6213, Besançon, France
[4] Centre National d'Etudes Spatiales, Toulouse, France
e-mail: agnes.fienga@oca.eu

ABSTRACT. The new INPOP13a planetary ephemerides constructed in using Messenger raw data is introduced. Improvements over Mercury and Earth orbits are presented as well as new constraints obtained for the Sun oblateness J_2, the Sun gravitational mass and the deviations to General relativity through the PPN parameters β and γ. Preliminary results for acceptable time variations of the gravitational constant G are also given.

1. INPOP13a

A full description of the analysis of the Messenger spacecraft raw data can be found in Verma et al. (2013) as well as the detailed description of the construction of the INPOP13a planetary ephemerides. We stress particularly in this presentation the results obtained for the PPN parameters β and γ and the Sun oblateness J_2. As Messenger is orbiting Mercury, the closed planet to the sun, its orbit is very sensitive to the gravitational potential of the sun and to possible violations of general relativity. The tracking data of Messenger and the deduced estimation of the Earth-Mercury distances are then very efficient to estimate the oblateness of the sun and acceptable non-unity or non-zero values of PPN parameters. Table 1 gives an overview of the improvements obtained with INPOP13a such as a two order of magnitude improvement in the estimations of the geocentric distances of Mercury, a factor 3 improvement in the estimation of $GM_\odot$ and a reduction of 25% in the uncertainty of $J_2^\odot$.

Table 1: Most significant determinations of parameters done with INPOP13a in comparisons with INPOP10e (Fienga et al. 2013), DE423 (Folkner 2010) and DE430 (Williams et al. 2013). The $GM_\odot$ line gives values of $GM_\odot$ - 132712440000. The line labeled MSG range gives the residuals obtained by comparisons between the Mercury-Earth distances deduced from the raw tracking of Messenger and the one deduced from the corresponding ephemerides. Intervals of $\beta - 1$ and $\gamma - 1$ correspond to values inducing modifications of postfit residuals below 25% in comparison to INPOP13a residuals.

	INPOP13a	INPOP10e	DE423	DE430
	$\pm 1\sigma$	$\pm 1\sigma$	$\pm 1\sigma$	$\pm 1\sigma$
$J_2^\odot \times 10^{-7}$	(2.40 ± 0.20)	(1.80 ± 0.25)	1.80	(2.10 ± 0.70)
$GM_\odot$ [km^3. s^{-2}]	(48.063 ± 0.4)	(50.16 ± 1.3)	40.944	41.94
(EMRAT - 81.3)×10^4	5.770 ± 0.020	5.700 ± 0.020	5.694 ± 0.015	5.691 ± 0.024
MSG range [m]	-0.4 ± 8.4	6.2± 205	3.8 ± 106	-0.5 ± 41.9
	INPOP13a	INPOP10a	DE423	Cassini (Bertotti et al. 2003)
$(\beta - 1) \times 10^5$	0.2 ± 2.5	-6.2 ± 8.1	4 ± 24	
$(\gamma - 1) \times 10^5$	-0.3 ± 2.5	4.5 ± 7.5	18 ± 26	2.1 ± 2.3

The use of Messenger data allows also to improve drastically the quality of the estimations of acceptable intervals of values for PPN β and γ different from 1. Based on the method presented in [2] we obtained new maps of acceptable violations (cf. Fig 1 and Table 1) showing the reduction of one order of magnitude in the size of acceptable intervals in $\beta - 1$ and $\gamma - 1$ but also the better disentangling of the two determinations compared to the one obtained with INPOP10a. Table 1 gives the obtained acceptable intervals of β and γ for a 25% modification of the postfit residuals.

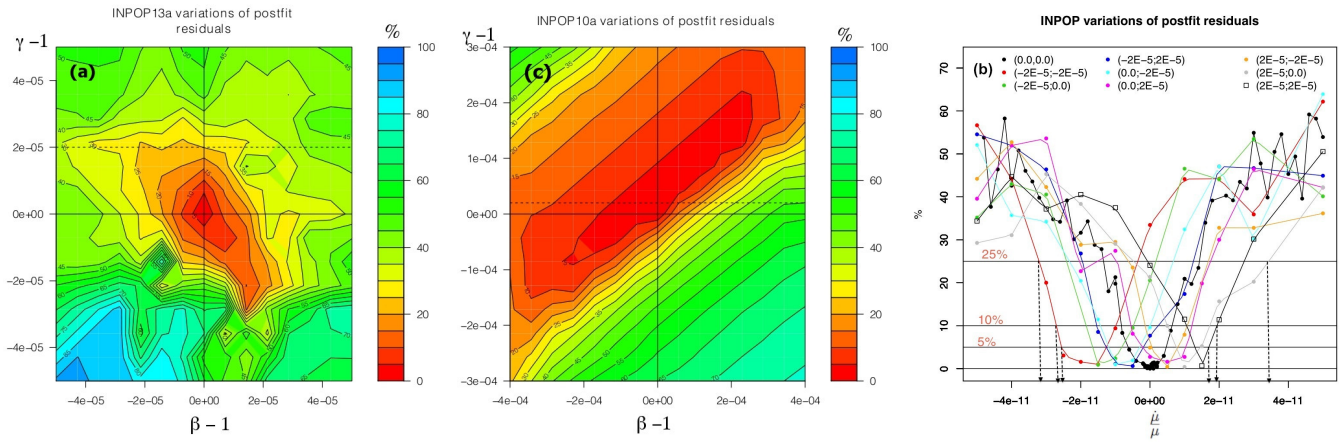

Figure 1: Panels a and c: Variations in postfit residuals obtained for different values of PPN β (x-axis) and γ (y-axis). Panel b: Variations in postfit residuals (% in y-axis) obtained for different values of $\dot{\mu}/\mu$.

Table 2: Comparisons of $\dot{G}$/G values found in the literature and values obtained with INPOP13a considering $\beta = \gamma = 1$ and $\beta \neq \gamma \neq 1$ with $\eta(= 4 \times \beta - \gamma - 3) = (1.05 \pm 12.55) \times 10^{-5}$.

Method	$\dot{G}$/G $\times 10^{13}$ yr^{-1}	Method	$\dot{G}$/G $\times 10^{13}$ yr^{-1}
LLR	(4 ± 9)	EMP (Pitjeva & Pitjev 2013)	$(0.166 \pm 0.724)^*$
Binary pulsar	(40 ± 50)	DE (Konopliv et al. 2011)	$(1.0 \pm 1.6)^{**}$
Helioseismology	(0 ± 16)	INPOP $\beta = \gamma = 1$	$(0.72 \pm 1.71)^*$
Big Bang nucleo.	(0 ± 4)	INPOP $\beta \neq \gamma \neq 1$	$(1.30 \pm 1.46)^*$
Planck +WP+BAO	(-1.42± 2.48)		

$^*\dot{M}_\odot/M_\odot = (-0.67 \pm 0.31) \times 10^{13}$ yr^{-1} $^{**}\dot{M}_\odot/M_\odot = -0.9 \times 10^{13}$ yr^{-1}

2. PRELIMINARY RESULTS FOR $\dot{G}/G$

The equations introducing possible time variations of the gravitational constant G have been introduced in the INPOP integration of the planetary equations of motion in considering :

$$\begin{aligned} \frac{\dot{\mu}}{\mu} &= \frac{\dot{G}}{G} + \frac{\dot{M}_\odot}{M_\odot} \\ M_\odot(t) &= M_\odot(t_0) + (t - t_0) \times \dot{M}_\odot \\ G(t) &= G(t_0) + (t - t_0) \times \dot{G} \\ \mu(t) &= G(t) \times M_\odot(t). \end{aligned}$$

Following the idea of the PPN β and γ estimations, several planetary ephemerides have been built and adjusted to observations considering different values for $\dot{G}/G$. A first step was to introduce the non-zero values of G with β and γ equal to unity. This approach is the one used by previous authors such as Pitjeva & Pitjev (2013) and Konopliv et al. (2011). Results and comparisons with the previous estimations can be found in Table 2. A second approach was to modify the values of the 3 parameters β, γ and $\dot{G}/G$ in the same time. For a seek of simplification, the changes of β and γ are given with the PPN parameter $\eta = 4 \times \beta - \gamma - 3$. Considered modifications of β and γ led to variations of η of about $(1.05 \pm 12.55) \times 10^{-5}$. New competitive constraints given in Table 2 were found but also new correlations between these parameters (Figure 1). Since then, deeper investigations based on Monte-Carlo simulations for β, γ, $J_2^\odot$ and $\dot{G}/G$ were investigated and will be intensified in using denser computations.

3. REFERENCES

Bertotti B., Iess L., and Tortora P., 2003, A test of general relativity using radio links with the Cassini spacecraft., Nature, 374–376.

Fienga A., Laskar J., Manche H., Kuchynka P., Desvignes G., Gastineau M, ., and Cognard I., 2011, The planetary ephemerides INPOP10a and its applications in fundamental physics., Celest. Mech. Dyn. Astr. 111, 363.

Fienga A., Manche H., Laskar J., Gastineau M., and Verma A.K., 2013, INPOP new release: INPOP10e. ArXiv e-prints 1301.1510.

Folkner W. M., 2010, Planetary ephemeris DE423 fit to Messenger encounters with Mercury., JPL interoffice memorandum IOM 343R-10-001 .

Konopliv A.S., Asmar S.W., Folkner W.M., Karatekin O.,Nunes D.C., Smrekar S.E., Yoder C.F., and Zuber M.T., 2011, Mars high resolution gravity fields from MRO, Mars seasonal gravity, and other dynamical parameters, Icarus 211, 401–428.

Pitjeva E. V., and Pitjev N. P., 2013, Relativistic effects and dark matter in the Solar system from observations of planets and spacecraft., MNRAS 432, 3431–3437.

Verma A.K., Fienga A., Laskar J., Manche H., and Gastineau M., 2013, Use of MESSENGER radioscience data to improve planetary ephemeris and to test general relativity, A&A 561, A115 (2014)

Williams J., Boggs D., and Folkner W., 2013, DE430 lunar orbit, physical librations, and surface coordinates., JPL JPL interoffice memorandum IOM 335-JW,DB,WF-20130722-016

APPROXIMATION OF ORBITAL ELEMENTS OF THE TELLURIC PLANETS BY COMPACT ANALYTICAL SERIES

S.M. KUDRYAVTSEV
Lomonosov Moscow State University, Sternberg Astronomical Institute
13, Universitetsky Pr., Moscow, 119992, RUSSIA
e-mail: ksm@sai.msu.ru

ABSTRACT. We take the long-term numerical ephemeris of the major planets DE424 (Folkner 2011) and approximate the orbital elements of the telluric planets from that ephemeris by trigonometric series. Amplitudes of the series' terms are the second- or third-degree polynomials of time, and arguments are the fourth-degree time polynomials. The resulting series are precise and compact; in particular the maximum deviation of the planetary mean longitude calculated by the analytical series from that given by DE-424 over [-3000; 3000], the total time span covered by the numerical ephemeris, is:

- for Mercury: 0.0016 arcsec (the series includes 767 terms);
- for Venus: 0.015 arcsec (648 terms);
- for the Earth-Moon barycenter: 0.019 arcsec (535 terms);
- for Mars: 0.056 arcsec (770 terms).

1. DEVELOPMENT METHOD

In order to approximate the orbital elements of the telluric planets by analytical series we used an author's modification of the spectral analysis method (Kudryavtsev 2004, 2007). According to this modification, the expansion of an arbitrary tabulated function F of time t is directly made to trigonometric series, where both arguments and amplitudes of the series' terms are high-degree polynomials of time. Therefore, the approximating function $f(t)$ has the following form

$$f(t) = \sum_{k=0}^{N} \Big[\big(A^c_{k0} + A^c_{k1} t + \cdots + A^c_{kh} t^h\big) \cos \omega_k(t) + \big(A^s_{k0} + A^s_{k1} t + \cdots + A^s_{kh} t^h\big) \sin \omega_k(t) \Big], \tag{1}$$

where $\omega_k(t)$ are some pre-defined arguments which are assumed to be q-degree polynomials of time

$$\omega_0(t) \equiv 0, \qquad \omega_k(t) = \nu_k t + \nu_{k2} t^2 + \cdots + \nu_{kq} t^q \quad \text{if } k > 0, \tag{2}$$

$A^c_{k0}, \cdots, A^s_{kh}, \nu_k, \cdots, \nu_{kq}$ are constants, and N is the number of terms in the expansion.

In the present study the polynomial arguments are various combinations of multipliers of the planetary mean mean longitudes, where the latter are defined by Simon et al. (1994). In order to obtain such an expansion, we first find the projections of $F(t)$ on a basis generated by the functions

$$\mathbf{c}_{kl}(t) \equiv t^l \cos \omega_k(t), \quad \mathbf{s}_{kl}(t) \equiv t^l \sin \omega_k(t); \quad k = 0, 1, \cdots, N;\ l = 0, 1, \cdots, h$$

through numerical computation of the following scalar products over a time span of $[-T; T]$

$$A^c_{kl} = < F, \mathbf{c}_{kl} > \equiv \frac{1}{2T} \int_{-T}^{T} F(t) t^l \cos \omega_k(t) \chi(t)\, dt, \tag{3}$$

$$A^s_{kl} = < F, \mathbf{s}_{kl} > \equiv \frac{1}{2T} \int_{-T}^{T} F(t) t^l \sin \omega_k(t) \chi(t)\, dt \tag{4}$$

where $\chi(t) = 1 + \cos \frac{\pi}{T} t$ is the Hanning filter chosen as the weight function.

However, the basis functions $\mathbf{c}_{kl}$, $\mathbf{s}_{kl}$ are usually not orthogonal. Therefore, at the second step we perform an orthogonalization process over the expansion coefficients in order to improve the quality of representation and avoid superfluous terms; the details are available in (Kudryavtsev 2004, 2007).

2. RESULTS

Following the above described procedure we have approximated Keplerian orbital elements of Mercury and mean orbital longitudes of all telluric planets by compact trigonometric series, where amplitudes are either the second- or third-degree polynomials of time, and arguments are the forth-degree time polynomials. The long-term numerical ephemeris DE424 (Folkner 2011) is used as a source. It covers the time span of [-3000; 3000]. The expansion is done over the complete time span covered by the ephemeris; the results are presented in Tables 1–2. The analytical series are denoted as DEA-424 there. Table 2 also includes the comparative characteristics of the VSOP2013 solution (Simon et al., 2013), the latest and most accurate analytical theory of motion of the telluric planets to date.

Keplerian element	Number of terms in DEA424, N	Maximum difference DEA424-DE424
a	479	2.1×10^{-9} AU
e	623	7.5×10^{-9}
i	282	0.0004”
Ω	569	0.0013”
π	900	0.0032”
λ	767	0.0016”

Table 1: Maximum difference between Keplerian orbital elements of Mercury given by the analytical series DEA424 and numerical ephemeris DE424 over the time span of [-3000; 3000].

Planet	DEA424,	DEA424-DE424		VSOP2013,	VSOP2013-INPOP10a(ext.)[1]	
	N	[1890; 2000]	[-3000; 3000]	Num. of terms[2]	[1890; 2000][3]	[900; 3100][4]
Mercury	767	0.0008”	0.0016”	272360	0.00003”	0.01”
Venus	648	0.0032”	0.015”	289647	0.00002”	0.002”
EMB	535	0.0046”	0.019”	294426	0.00001”	0.03”
Mars	770	0.0095”	0.056”	309140	0.00074”	0.70”

Table 2: Maximum difference between the mean longitudes of the telluric planets given by the analytical series DEA424, VSOP2013 and numerical ephemerides DE424, INPOP10a(ext.) over various time spans.
Notes:
[1] Hereafter INPOP10a(ext.) denotes the original planetary ephemeris INPOP10a by Fienga et al. (2011) extended by Manche (2012) over the time span of [-4000; 8000];
[2] The data are taken from Simon et al. (2013), Table 7;
[3] The data are taken from Simon et al. (2013), Table 8;
[4] The data are taken from Simon et al. (2013), Table 11.

While the work on developing the planetary ephemeris DE424 to analytical series was in progress, a new planetary ephemeris DE430 (Folkner, 2013) and its extension DE431 were released. The planetary ephemeris DE431 is valid over [-13000; 17000], an essentially longer time span than that of any numerical ephemeris developed before. Table 3 presents our first results in expansion of the mean longitude of Mercury from this extra long-term ephemeris to analytical series over the total time span of 30,000 years covered by DE431. The analytical development of the planetary ephemeris DE431 is denoted as DEA431 there. Table 3 also contains the comparison of the development characteristics with similar data provided by the analytical theory VSOP2013.

Difference in the mean	Time span		
longitude of Mercury	[0; 4000]	[-4000; 8000]	[-13000; 17000]
DEA431-DE431	0.0016”	0.0020”	0.030”
VSOP2013-INPOP10a(ext.)[1]	0.03”	0.12”	n/a

Table 3: Maximum difference between the mean longitude of Mercury given by the analytical series DEA431, VSOP2013 and numerical ephemerides DE431, INPOP10a(ext.) over various time spans.

Note [1] The data are taken from Simon et al. (2013), Table 11.

In Table 3 the number of terms N in series (1) used by the DE431 solution for calculating the mean longitude of Mercury is 909. The maximum degree h of polynomials for amplitudes of terms in these series is four.

Acknowledgements. Research supported in part by the Russian Foundation for Basic Research. A travel grant provided to the author by the LOC of the Journées 2013 and the French Ministry of Education and Research in the framework of the programme ACCES* is sincerely appreciated.

3. REFERENCES

Fienga, A., Laskar, J., Kuchynka, P., Manche, H., Desvignes, G., Gastineau, M., Cognard, I., Theureau, G., 2011, “The INPOP10a planetary ephemeris and its applications in fundamental physics”, Celest. Mech. Dyn. Astr. , 111, pp. 363–385, doi: 10.1007/s10569-011-9377-8.

Folkner, W.M., 2011, “Planetary ephemeris DE424 for Mars Science Laboratory early cruise navigation”, JPL IOM 343R-11-003.

Folkner, W. F., Boggs, D. H., Williams, J. G., 2013, Planetary ephemeris DE430, IOM 343R-, in preparation.

Kudryavtsev, S.M., 2004, “Improved harmonic development of the Earth tide generating potential”, J. Geodesy, 77, pp. 829–838, doi: 10.1007/s00190-003-0361-2.

Kudryavtsev, S.M., 2007, “Long-term harmonic development of lunar ephemeris”, A&A , 471, pp. 1069–1075, doi: 10.1051/0004-6361:20077568.

Manche, H. 2012, Private communication.

Simon, J.L., Bretagnon, P., Chapront, J., Chapront-Touzé, M., Francou, G., Laskar, J., 1994, “Numerical expressions for precession formulae and mean elements for the Moon and planets”, A&A , 282, pp. 663–683.

Simon, J.-L., Francou, G., Fienga, A., Manche, H., 2013, “New analytical planetary theories VSOP2013 and TOP2013”, A&A , 557, A49, 12pp. doi: 10.1051/0004-6361/201321843

EPM-ERA 2013 - THE NEW VERSION OF LUNAR EPHEMERIS DEVELOPED IN IAA RAS

M.V. VASILYEV, E.I. YAGUDINA
Institute of Applied Astronomy Acad. Sci.,Russia
10, Kutuzov quay, 191187, St.-Petersburg, Russia
e-mail: eiya@ipa.nw.ru; mvv@ipa.nw.ru

ABSTRACT. EPM-ERA 2013 is the newest version of the lunar ephemeris developed in IAA RAS after 2011. New Lunar ephemeris EPM-ERA 2013 was compared with USA DE405, DE421, DE423, DE430 and French INPOP10e lunar ephemerides. Comparison showed that EPM-ERA 2013 is still slightly worse than all of these ephemerides, suggesting the necessity of further improving the dynamical model of EPM-ERA. The fact that all modern lunar ephemerides evidently cannot adequately describe most accurate LLR observations makes this task especially pressing for authors. Several practical applications were also considered to estimate the impact of the using different lunar ephemerides on the orbit determination accuracy of such objects as GNSS satellites and Near-Earth asteroids.

1. INTRODUCTION

Modern Lunar ephemerides have been developed in JPL, USA: DE405, DE421, DE423, DE430; IMCCE: INPOP10e-Intégrateur Numérique Planétaire de Observatoire de Paris; IAA RAS, Russia: EPM-ERA2013. These ephemerides are being constantly improved, and their precision become higher with new measurable information such as modern LLR observations. High accuracy of LLR data requires dynamical theories of adequate precision. The analysis of 18700 LLR observations (1970-2013), which includes 105 measurements of newly discovered Lunokhod1, has been presented in the paper. The comparison with all listed ephemerides of the Moon is given.

2. MATHEMATICAL MODEL

The dynamical model EPM-ERA 2013 is constructed by simultaneous numerical integration of the equations of orbital motion of the Moon, major planets, asteroids, TNO (Trans-Neptunian Objects), rotational motion of the Moon (Krasinsky 1999; Krasinsky 2002) and taking into account perturbations from asteroid belt and TNO ring. Numerical integration, residuals calculations and LSM fitting are performed using ERA system developed in IAA RAS (Krasinsky & Vasilev 1996). The most important model updates are the following ones: numerical integration with retarded argument was realized; the potential of the Earth is calculated according to recommendations of IERS for artificial Earth's satellites; 80-bites instead of 64-bites floating point calculation was realized in the numerical integration; the interaction between Moon figure and the potential of point mass of Jupiter and Venus was added; the difference between receiving and transmitting stations at Haleakala were taken into account; weighting procedure was revised for most accurate Apache LLR observation; 4-sigma criterion was used for the observation rejection.

3. OBSERVATIONS AND PARAMETERS DETERMINED

In the present analysis 18700 LLR observations have been included in the processing. The station Apache was presented by new 1576 highest precision LLR measurements. The number of observations at each site is shown in Table 1.

The number of ranging to Apollo 11, Apollo 14, Apollo 15, Lunahod 2 are 1585, 1557, 12724 and 452 respectively. 105 LLR observations of Lunakhod 1 were also added into the fitting process. Before 1998 the observations were obtained by request from observatories, later on they have been retrieved from FTP server *ccdisa.gsfc.nasa.gov/pub/slr*, partly from *oca.eu/gemini/donnees/las_lune*, some of them were obtained by private correspondence. During the fitting process 65 parameters have been determined.

Station	Time interval	Number of LLR observations
McDonald	1970 Mar - 1985 Jun	3440
MLRS1	1985 Jan - 1988 Jan	275
MLRS2	1988 Aug - 2012 Jan	3114
HALEAKALA	1984 Nov - 1990 Aug	694
CERGA	1985 Jan - 2013 Feb	9599
Apache	2006 July - 2012 Aug	1576
TOTAL	1970 Mar- 2013 Feb	18700

Table 1: Distribution of LLR observations

The set of parameters includes the lunar initial coordinates and velocities, libration angles and their velocities, Stokes coefficients of the selenopotential, Lunar love numbers k_2,h_2, l_2, the angles of time delay, the coordinates of 5 reflectors, the coordinates of 6 observational stations etc. Since lunar rangings are invariant relatively to the rotation of the Earth-Moon system as a whole, all the set of orientation parameters of this system cannot be determined simultaneously. Due to this reason, longitude and latitude of the most often observable reflector Apollo 15 have been fixed. Values of these two parameters were obtained from a simplified solution made as the first step, in which lunar libration has not been improved. LLR observations are sensitive to the Earth's gravitational constant Gm_E. The investigation shows that the correction to Gm_E cannot be reliably separated from corrections to X coordinate of the reflectors. Thus the value Gm_E has not been included into the list of parameters.

4. ANALYSIS OF THE RESULTS

EPM-ERA2013 ephemeris has been obtained using 18700 LLR observation and adjusting the set of 65 parameters listed above. Residuals statistics depending on the observational station and the time interval of observations can be seen in table 2.

Residuals wrms (cm)	Number of observations	Observational stations	Interval of observations
26.8	3162	McDonald	19700415.0-19850630.0
11.6	191	MLRS1	19850301.0-19880127.1
18.8	1136	CERGA	19840407.2-19860612.2
7.4	3247	CERGA	19871012.2-19941213.2
4.2	5060	CERGA	19950107.2-20130219.2
10.9	538	Haleakala	19841113.1-19900830.1
5.8	989	MLRS2	19880229.0-19951228.0
6.1	1775	MLRS2	19960125.0-20120401.0
3.5	1564	Apache	20060407.1-20120828.1
4.9	17662	Total	19700415.0-20130202.2

Table 2: EPM-ERA ephemeris, statistics of residuals

It is known that the analysis of LLR data depends not only on the dynamical model but on partial derivatives relative to a number of parameters, many of which also require numerical integration. To compare our result with the results obtained using DE and INPOP10e ephemerides, residuals calculations have been made with the ephemerides mentioned using derivatives from EPM-ERA 2013. Statistics of post-fit residuals and the number of LLR observations used to calculate these residuals for DE405, DE421, DE423, DE430, INPOP10e and EPM-ERA 2013 ephemerides are presented in Table 3. The direct comparison of the post-fit residuals statistics obtained by using EPM-ERA2013 ephemeris and INPOP10e one are given in Table 4. For INPOP10e ephemeris, the statistics of residuals were taken from

the following website: arXiv1301.1510[astro-ph.EP].

Ephemerides	Wrms(cm) residuals	Number of observations	Number of deleted observations
DE 405	4.5	18121	579
DE 421	3.8	18154	546
DE 423	3.8	18141	559
DE 430	3.6	18144	556
INPOP10	4.4	18214	586
EPM-ERA 2013	4.9	17662	1038

Table 3: Statistics of residuals for EPM-ERA ephemeris, compared with DE and INPOP10 ephemerides

Station		INPOP10e			EPM-ERA 2013	
	Period	Std. dev.	N	Period	Std. dev.	N
Cerga	1984-1986	15.9	1158	1984-1986	18.8	1136
Cerga	1987-1995	6.4	3415	1987-1995	7.3	3247
Cerga	1995-2012	4.0	5058	1995-2013	4.2	5060
McDonald	1969-1986	31.3	3487	1970-1986	26.8	3162
MLRS1	1982-1985	73.4	405	1982-1985	-	-
MLRS1	1985-1988	7.4	163	1985-1988	11.6	191
MLRS2	1988-1996	4.7	1148	1988-1996	5.8	981
MLRS2	1996-2012	5.6	1972	1996-2012	6.1	1775
Haleakala	1984-1990	8.1	733	1984-1990	10.9	538
Apache	2006-2010	5.2	935	2006-2012	3.5	1564
Matera	2003-2012	29.5	33	2003-2012	-	-

Table 4: Comparison of results EPM-ERA2013 and INPOP10e ephemerides, statistics of residuals

All post-fit residuals of LLR observations processed in EPM-ERA2013 are presented in Fig.1. Fig.2 and Fig.3 demonstrate post-fit residuals for McDonald and Apache stations respectively.

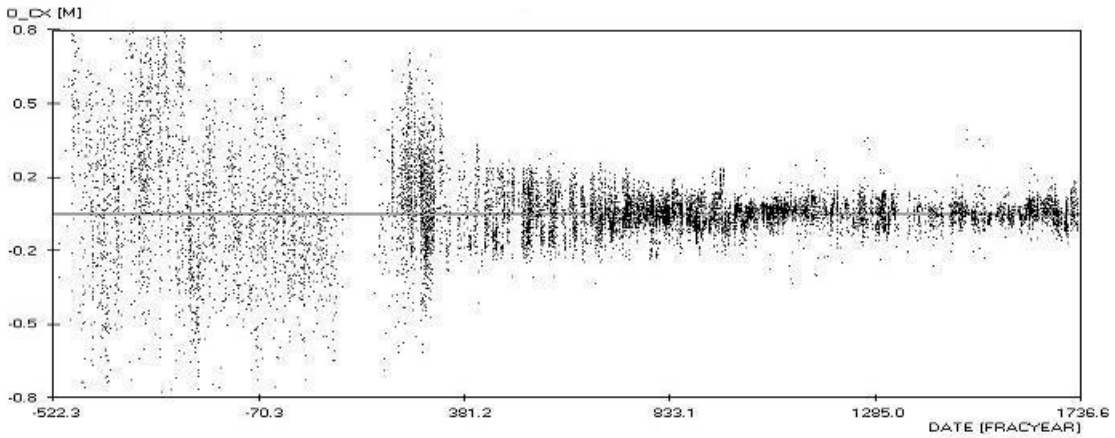

Figure 1: EPM-ERA2013, residuals (laser ranging)

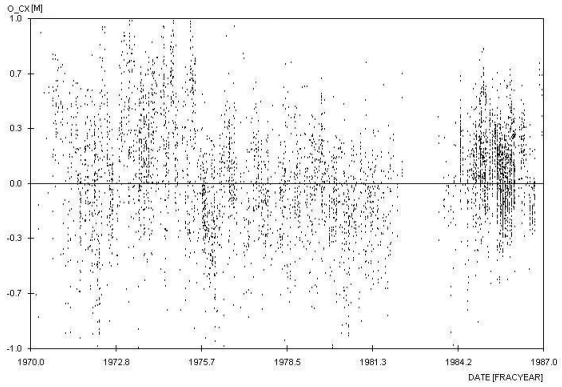

Figure 2: MacDonald station, 1970-1987

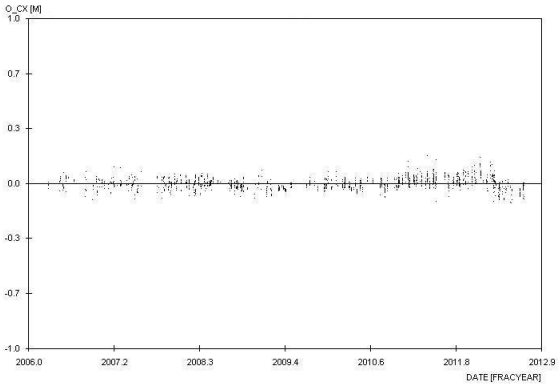

Figure 3: Apache station, 2006-2012

One can see the drastic improvement in the accuracy of LLR observations during the last decade which requires adequate improvement of the rotational motion model of the Moon.

5. CONCLUSION

The investigation shows that the inner accuracy of EPM-ERA 2013 was improved to 4.9 cm from 6.0 cm in the previous version. Most likely EPM-ERA 2013 provides the upper limit of accuracy in case when the model of lunar rotation described by Krasinsky is used. Nevertheless, Lunar rotation model requires further improvements and a more sophisticated model than the Krasinsky one. The work is in progress.

6. REFERENCES

Krasinsky G.A.,1999, "Tidal Effects in the Earth-Moon System and the Earth's Rotation", Cel. Mech., N 75/1, pp. 39-66.

Krasinsky G.A., 2002, "Selenodynamical parameters from analysis of LLR observations of 1970-2001", Communications of the IAA RAS, N 148, pp. 1-27.

Krasinsky G.A., Vasiliev M.V., 1996, "ERA: knowledge base for Ephemeris and dynamical astronomy", Proceedings of IAU Colloquium 165, Poznan, Poland, pp. 239-244.

SOLAR SYSTEM DYNAMICS WITH THE GAIA MISSION

D. HESTROFFER[1], J. BERTHIER[1], B. CARRY[1], P. DAVID[1], V. LAINEY[1], N. RAMBAUX[1], W. THUILLOT[1], J.-E. ARLOT[1], D. BANCELIN[1,2], F. COLAS[1], J. DESMARS[1,3], H. DEVILLEPOIX[1], M. FOUCHARD[1], A. IVANTSOV[1], I. KOVALENKO[1,4], V. ROBERT[1,5]

[1] IMCCE, Paris Observatory, UPMC, Univ. Lille1, CNRS
77 av. Denfert-Rochereau, F-75014 PARIS, France
e-mail: hestro@imcce.fr
[2] Institut für Astronomie der Universität Wien, Vienna, Austria
[3] Observatorio National, Rio de Janeiro, Brasil
[4] LESIA, Paris Observatory, CNRS, ESEP, France
[5] IPSA, 94200 Ivry-sur-Seine, France

ABSTRACT. The Gaia mission is to be launched on December 19$^{\text{th}}$, 2013 by the European Space Agency (ESA). Solar System science is well covered by the mission and has been included since the early stages of its concept and development. We present here some aspects on the astrometry and dynamics of Solar System Objects (SSO) – in particular asteroids, comets and satellites – as well as ground-based support. We also touch upon the future of SSO astrometry that will be achieved indirectly, after mission completion, from the Gaia astrometric catalogue.

1. INTRODUCTION

Gaia – "the billion star surveyor" – is the next cornerstone mission to be launched by ESA. At the time of writing this proceeding, Gaia launch is scheduled on December 19, 2013. Following on the success of Hipparcos, Gaia is an extremely high-accuracy astrometric European space mission. Gaia is much more than a second Hipparcos though, its main scientific objective being to obtain a new global picture of the Galaxy (Perryman et al., 2001). With a focal plane containing more than hundred CCD detectors, Gaia will map the whole sky down to 20$^{\text{th}}$ magnitude, providing unprecedented astrometric accuracy and multi-wavelength data. Where Hipparcos catalogued a little less than 120 000 stars with parallaxes at a precision of 1 mas (milli-arcsecond), Gaia promises to observe 1 billion of stars and celestial objects with parallaxes at better than 10 μas (micro-arcsecond), in several colours at visible wavelength, including radial velocity measurements. Thus Gaia by probing about 1% of the stars of the Milky Way will yield a 3-D – or even 6-D – picture of a good fraction of our Galaxy, and hence a big leap in our understanding of its origin, structure and evolution. Besides, the Gaia mission will cover several scientific objectives, stellar physics, quasar and galaxies, exoplanets, reference frames, fundamental physics, Solar System...

2. THE MISSION

Performing astrometry from space has many advantages as has already been proved by the Hipparcos/Tycho missions. For Gaia in particular, the thermo-mechanical stability of the spacecraft, combined with the selection of a station at L2 Sun-Earth Lagrangian point for operations, makes it a very stable environment for operations; the drawback being that the data downlink is less favorable. Gaia's instrumentation provides absolute astrometry, broad-band photometry, spectro-photometry from low resolution spectra, and modest imaging capabilities. Additionally, spectroscopic data with higher resolution $R = 11\,500$ will be obtained for the sources down to 17$^{\text{th}}$ magnitude, yielding measure of radial velocity at a 10 km/s level. The final catalogue will be published in 2022 soon after the mission completion, with nominal duration of five years and a possible one year extension. With the amount of data collected and later processed on ground, Gaia is a petabyte (10^{15}) mission.

Since Gaia is regularly scanning the whole sky – acquiring observations with no input catalogue – a very large number of Solar System Objects (SSO) will be observed by the telescope(s), with roughly 60 transits per source on average, at solar elongation in the range 45–135° (see Table 1). Given the present catalogued population in the Solar System, one can expect to observe about 300 000 SSO, mainly

main-belt asteroids, and mostly known. Nevertheless Gaia will observe some dwarf planets, Jupiter Trojans, Centaurs and trans-Neptunian objects (TNO) orbiting beyond Neptune (including Pluto), and closer to the Earth some near-Earth objects (NEO, including potentially hazardous asteroids, PHA). Additionally Gaia will observe about 200 Jupiter family comets (JFC) and a few long period comets, and about 20 planetary satellites, on either regular or irregular orbits, around Mars, Jupiter, Saturn, Uranus and Neptune. Besides, Gaia will indirectly detect the reflex motion due to exoplanets orbiting around their host star. Worth to notice, the detection algorithm implemented on board of the spacecraft yields additional limitation: Objects larger in size than an apparent diameter $\rho \gtrsim 0.7 - 0.9$ arcsecond will not be observed; thus no data is expected neither for planets, nor the Galilean satellites, and in some occasions no data for the dwarf planet Ceres. While performing well for SSOs, the satellite and mission has been optimally designed for its primary purpose: observations of stars. There are hence a few particular aspects, and numbers reported in Table 1, for SSOs observation by Gaia. The average number of observations (transits of one of the field-of-view) for bodies in the ecliptic is somewhat lower than for a typical star. The astrometric precision of use for SSO is the one of a transit, which is lower than the precision of stellar positions and parallaxes at the μarcsec level given in the literature, since the latter is derived at the end of the mission from the collection of all the transits for a given star.

Table 1: Gaia mission - general fact sheets for SSOs.

Launch	Dec. 19, 2013
Duration	5years +1year extension
Observing mode	CCD, TDI scanning
Solar elongation	45–135°
# of observations	60 obs./target
Limiting magnitude/size	20 (possibly 21)
Limiting upper size	0".7–0".9
Astrometric precision /CCD	0.2 – 3 mas
Photometric precision	0.001 mag
Catalogue release	≈ 2022

Gaia will provide big advances in the science of Solar system objects (Mignard et al. 2007, Hestroffer et al. 2010). The broad-band photometry and snapshot spectro-photometry enables the reconstruction of rotation properties (rotation period, spin direction, ellipsoidal shape). The CCD signal shall also provide size determination for approximately 1000 objects, and detection of binaries at separation larger than ≈100 mas. Last, the astrometry will provide some advances as described in the following.

3. SCIENCE IN THE SOLAR SYSTEM

There are two different pipelines for data reduction and analysis. The short-term pipeline of data reduction – performed on a daily basis – is processing the SSO identification, astrometric reduction, observations threading and initial orbit computation for unidentified objects, and science alert. The long-term pipeline – performed on a semester basis – treats all data for all objects together, and for SSOs it will derive the shape and spin of the asteroids, orbit adjustments, and analysis of global effects on the dynamics.

The identification. Source that has not been matched to stars from stellar catalogues at first look, will be cross-matched with a specific planetary ephemerides computation. A routine has been implemented in the data reduction pipeline to identify theses objects; it is based on the `SkyBot` engine of precomputed ephemerides (Berthier et al. 2006), regularly updated from the IAU Minor Planet Center (MPC) collection and the `astorb` database of orbital elements. Then, given the expected position and magnitude of all planetary bodies at the given date and in the direction of observations, one can identify known SSOs. Observations of moving objects that would not be identified by this way will next be thread together and an initial orbit is computed for newly discovered objects.

URL `http://vo.imcce.fr`

Gaia-FUN-SSO. Given the advance in present ground-based surveys (LINEAR, Catalina, Pan-Starrs, etc.), and the limiting magnitude of Gaia, most of the SSOs that Gaia will observe are already catalogued. Nevertheless, Gaia has the potential to discover new objects because it scans the whole sky in very good observing conditions, and goes down to low solar elongations (45°). Hence Gaia can be efficient at discovering quasi satellites of the Earth or Atiras (on inner Earth orbits). A support programme of ground-based observations has been set-up – Gaia-FUN-SSO – for science alerts; this network will perform follow-up observations in order not to loose a newly detected NEO. Several observatories worldwide, yet mostly in the Northern hemisphere, with telescopes in the range 0.4 – 2 m, including some Schmidt telescopes, participate to the network. The central node will validate and trigger the alerts, request ground-based observations providing dedicated ephemerides, and collect the final astrometry. Besides the Gaia astrometry as well as the ground-based one are systematically sent to the MPC, since – following the ESA and DPAC policy – all such science alert data has to be made public with no proprietary period.

Global effects on dynamic. On the long term, when astrometric data has been acquired over more that one year one can adjust the orbits of asteroids and comets. By using the Gaia data alone over 5 years, a general improvement of a factor of 30 is expected on the orbit determination (depending on the actual number of observations per target). Given the high astrometric accuracy, established in a high quality reference frame, one will be able to detect small effects and estimate both physical and dynamical parameters. Asteroid mass determination is expected from close encounter of several thousands targets asteroids with more massive one (Mouret et al. 2007), and from resolved binary asteroids. This will provide a revolution in the field that still suffers from low-number statistics (Carry et al. 2012). Detection of NEOs and orbit refinement for PHAs will provide better impact probability estimates. Astrometry of comets and small objects orbiting close enough to the Sun will provide detection and modelling of non gravitational effects, in particular the Yarkovsky effect. Long term astrometry of asteroids (essentially NEOs) will enable to derive simultaneously and directly the Solar quadrupole J_2 and the parameterised-post-Newtonian PPN parameter β, in addition to a measure of $d(G\,M_\odot)/dt$, providing hence an independent local test of General Relativity.

Several satellites will be observed by Gaia (excluding the large Galilean one as mentioned in Sect. 1), yielding again high accuracy astrometry. All these topics will benefit from a combination of Gaia data with high precision ground-based data. This is the case for the dynamics of planetary satellites that depends on long-period effects, larger than just the 5 to 6 years mission duration. When combined to all astrometric data available (including classical telescopic ones, radio science, mutual phenomenon, old photographic plates, etc.) dynamical models can be improved and subsequently models for the outer major planets, through derivation from their centre-of-mass pseudo-positions as given by their satellites (Morisson et al. 1997). Combination of high accuracy space+ground-based data, as provided by current radar observations programs (Margot & Giorgini 2010) is also advantageous for deriving secular drifts on NEOs or other SSOs orbit from relativistic acceleration. Similarly, a treatment for exoplanets is performed, combining all astrometric data together, and with a dedicated orbit computation. This will enable to confirm the presence of a planetary companion and if so the derive fundamental parameters of the system. In some cases complementary ground-based radial-velocity observations and data will advantageously improve the knowledge of the exoplanetary system.

Finally Gaia will valuably contribute to the Space Situational Awareness program of ESA through the detection capabilities of PHAs and high astrometry of near-Earth objects, since such observations dramatically reduce the uncertainty and error propagation of the ephemerides and yield better impact probabilities estimates (Bancelin et al. 2013). In contrast to the science alert data for critical SSO – such as newly discovered NEO, variable star, etc., any other data is not distributed automatically on the short-term reduction pipeline, but at final Gaia catalogue publication and also at intermediate releases. There will be several such intermediate releases starting twenty-two months after launch for the basic positions and magnitude.

4. PROSPECTIVE

In addition to the scientific results the mission will harvest by observing directly thousands of SSOs with high accuracy, Gaia – through the use of its stellar catalogue – will moreover have a big impact

URL `https://www.imcce.fr/gaia-fun-sso/`

on future (and past) astrometry of SSOs, changing considerably the science of the Solar System. Indeed current astrometry of asteroids is mainly limited by systematic effects. The Tycho catalogue has shown to be more advantageous in this respect than the Hipparcos catalogue, the latter having only 3 stars/deg^2, far from being enough for doing astrometric measurements. Nevertheless, even the Tycho catalogue is not dense enough in a typical field-of-view of 15'×15', and the USNO or UCAC catalogues – sometimes combined with 2MASS data – are mostly used in the community. USNO and UCAC catalogues however suffer from strong zonal errors, introducing bias in any analysis and orbit improvement. As shown by Chesley et al. 2010, these errors can be corrected to a certain amount; yet the Gaia catalogue of stars – being by essence an astrometric catalogue – will make that future astrometry precision will essentially reach the stochastic precision due to photon noise and centroiding (Desmars et al. 2013). Not only can this be applied to future CCD observations, but to past observations too – including old photographic plates – that can be re-reduced once the Gaia catalogue is available (e.g. NARRO, Arlot et al. 2013).

5. REFERENCES

Arlot, J.-E. 2013. A new reduction of old observations: a challenge for the next decade. Proc. of the NAROO-GAIA workshop "A new reduction of old observations in the Gaia era", Paris, June 2012, pp. 19–26.

Bancelin, D., Hestroffer, D., Thuillot, W. 2012. Dynamics of asteroids and near-Earth objects from Gaia astrometry. P&SS, 73, pp. 21–29.

Berthier, J., Vachier, F., Thuillot, W., Fernique, P., Ochsenbein, F., Genova, F., Lainey, V., Arlot, J.-E. 2006. SkyBoT, a new VO service to identify Solar System objects. Astronomical Data Analysis Software and Systems XV ASP Conf. Series, Vol. 351, pp. 367.

Carry, B. 2012. Density of asteroids. P&SS 73, 98–118

Chesley, S. R., Baer, J., Monet, D. G. 2010. Treatment of star catalog biases in asteroid astrometric observations. Icarus, 210, pp. 158–181.

Desmars, J., Bancelin, D., Thuillot, W., Hestroffer, D. 2013. Statistical and numerical study of asteroid orbital uncertainty. A&A , 554(A32), doi: 10.1051/0004-6361/201321090.

Hestroffer, D., Dell'Oro, A., Cellino, A., Tanga, P. 2010. The Gaia Mission and the Asteroids. LNP 790, pp. 251–340.

Margot, J.-L., Giorgini, J. D. 2010. Probing general relativity with radar astrometry in the inner solar system. IAU Symp., 261, pp. 183–188.

Mignard, F., Cellino, A., Muinonen, K. et al. 2007. The Gaia Mission: Expected Applications to Asteroid Science. EM&P, 101, pp. 97–125.

Morrison, L. V., Hestroffer, D., Taylor, D. B., van Leeuwen, F. 1997. Check on JPL DExxx using HIPPARCOS and TYCHO Observations. Proc. ESA Symp. SP-402 "Hipparcos-Venice'97", pp. 149–152.

Mouret, S., Hestroffer, D., Mignard, F. 2007. Asteroid masses and improvement with Gaia. A&A 472, 1017–1027.

Perryman, M. A. C., De Boer, K. S., Gilmore, G. et al. 2001. GAIA: Composition, formation and evolution of the Galaxy. A&A , 369, pp. 339–363.

LOCAL TESTS OF GENERAL RELATIVITY WITH SOLAR SYSTEM OBJECTS AND THE GAIA MISSION

D. HESTROFFER, P. DAVID, M. SAILLENFEST
IMCCE, Paris Observatory, UPMC, univ. Lille1, CNRS
77 av. Denfert-Rochereau, F-75014 PARIS
e-mail: hestro@imcce.fr

ABSTRACT. The Gaia mission to be launched by ESA in 2013 will observe, in addition to stars, a large number of solar system objects (SSO). Gaia will provide during its 5 years mission high precision astrometry in an absolute reference frame of about 300 000 asteroids, including many Near-Earth Objects. The very precise orbits will enable to determine simultaneously the solar J2 and the PPN parameter beta and other parameters for testing the GR. Improvement from combining Gaia and radar data are also expected.

1. INTRODUCTION

The Gaia space mission is an ESA astrometric mission of the Horizon 2000+ programme that will provide Europe a successor to Hipparcos/Tycho with many huge improvements. The number of stars observed and catalogued, in addition to the precision of the measures – astrometric, photometric, and spectroscopic – complemented by some imaging capabilities, make it more than a Hipparcos-two. In this respect, the Gaia satellite and telescope will observe a large number of Solar System Objects (SSO) during the 5 years mission duration, down to magnitude $V \approx G \leq 20$. As presented in Hestroffer et al. (2014, this issue) and Mignard et al. (2007).

Given the astrometric precision involved—at the sub-mas level—relativistic effects have to be taken into account in the data reduction and analysis. This was already the case in the Hipparcos mission, also for the Solar System objects (Hestroffer 1994, 1997), and is now also mandatory at all stages of the reduction pipeline within the Gaia mission. A group, REMAT, within the Gaia DPAC Data Processing and Analysis Consortium, is providing RElativity Models And Testings. In this framework tests of General Relativity (GR) can be performed by measuring the Parameterised Post-Newtonian (PPN) parameters, and more exactly their possible deviation from the canonical value of the GR theory. This is done for instance from the astrometry of stars and a measure of the light deflection through parameter γ (e.g. Mignard & Klioner 2010; Raison et al. 2010), but also by a test of the quadrupole effect around Jupiter and the GAREX experiment (Crosta & Mignard 2006; Le Poncin-Lafitte and Teyssandier 2008), and last, from the orbit of solar system objects. We will present in the following some aspects of the scientific outcome of Gaia within the Solar System for deriving the PPN β, together with the Solar quadrupole J_2 and other parameters, and prospective for testing GR or other alternative theory.

2. MISSION AND EXPECTED RESULTS

There are some obvious advantages to use astrometry from space, of high precision and accuracy, with a single instrument and data reduction performed directly in a fundamental stellar catalogue. All these are provided by the Gaia satellite, telescope and mission. On the other hand the programmatic of the Gaia observations is not adapted to SSO, but imposed by the scanning law of the satellite. Given the orbital elements and *absolute* magnitude of the asteroids (or comets) from e.g. the `astorb` database, one can compute the set of observations for any asteroid (or comet, similarly) and their *apparent* magnitude. Since most of Gaia asteroids are well known objects, we will be able to derive orbit improvements from ordinary least squares techniques involving only Gaia observations within the DPAC consortium. We can then perform a variance analysis of the system of equations' inversion and get the formal precisions of all unknown parameters estimation.

The astrometric precision is—depending on the target's magnitude—of the order of 1 mas and better. Given such unprecedented astrometric precision available for the observations of Solar System, big

improvements are expected in orbit refinement, so that small effects and perturbations on the orbits can be detected, dynamical or physical parameters estimated such as mass of asteroids (Mouret et al. 2007), and models tested. In particular, small additional acceleration due to GR is affecting all orbits of SSOs, and mostly this of eccentric orbits close to the Sun. Thus Near Earth Objects (asteroids and comets) are particularly good test particles for the purpose of testing the General Relativity in the Solar System. It is well known that both the Sun quadrupole J_2 and GR imply an advance of the perihelion of the orbit that can hardly be separated from the observation of one single target, such as Mercury, alone. Gaia will provide observations of bout 2000 NEOs and will yield a simultaneous determination of both J_2 and PPN β. The order of precision obtained 10^{-4} for β, 10^{-8} for J_2, are not much better than current estimates but completely independent of other modelling (Nordvedt, Sun interior, ...) or assumption on one of the parameters. Besides of these test of GR combined with the measure of Sun dynamical flattening, one will be able to test a possible variation of the gravitational constant. Moreover, since all SSO positions will be derived directly in the optical ICRF realised by the Gaia QSOs, a direct link between the *dynamical* and *kinematical* non-rotating frames will be established. This will put the ecliptic and equinox within the ICRF, and also test a possible rotation rate at the μas/year level (Hestroffer 2010).

3. PROSPECTIVE

All estimates so far consider only observations from Gaia alone over five years of SSOs brighter than magnitude 20 (and additionally with some conservative approach assuming only one CCD per transit instead of 9). Besides, other framework can be considered such as post-Einsteinian gravity, MOND, SME (Hees et al. 2014, and references therein). Some improvements can hence be expected in several ways:

- observing more objects down to magnitude $V \leq 21$. This is considered because the limitation in magnitude is not imposed by the telescope and instruments sensitivity, but by the data downlink to Earth. Going to fainter magnitude has his cost of operations but shows some benefits particularly for testing the GR.

- one year mission extension. Such extension can be decided by ESA at later stages of the mission. Increasing the time span has obvious advantages for deriving orbits' precession and their secular effects, making angles and longitudes on the orbit vary quadratically with time. Combined with the push in limiting magnitude, a gain of factor 2 can be expected.

- complementary ground-based observations for a few targets. Only measures of high precision and with high *accuracy* can be considered here, these are already obtained by radar techniques at Arecibo (Margot & Giorgini 2010) and will span about two decades.

4. REFERENCES

Crosta M-T and Mignard F. 2006. Microarcsecond light bending by Jupiter. Classical and Quantum Gravity 23, 4853–4871.

Hees et al. 2014. Tests of gravitation at Solar System scale beyond PPN formalismIn. Proc. of JSR 2013. This issue

Hestroffer et al. 2010. Gaia and the asteroids: Local test of GR. Proceedings of the International Astronomical Union, IAUs Vol. 261, 325.

Hestroffer et al. 2014. Solar System dynamics with the Gaia mission and beyond. In: Proc. of JSR 2013. This issue

Le Poncin-Lafitte, C., Teyssandier, P. 2008. Physical Review D 77, 044029.

Margot J.-L. & Giorgini J. D. 2010. Probing general relativity with radar astrometry in the inner solar system. Proceedings of the International Astronomical Union, IAUs Vol. 261, 183.

Mignard F. et al. 2007. The Gaia Mission: Expected Applications to Asteroid Science. EM&P 101, 97.

Mignard F. & Klioner S. 2010. Gaia: Relativistic modelling and testing. Proceedings of the International Astronomical Union, IAUs Vol. 261, 306.

Raison F. et al. 2010. Implementation of the Global Parameters Determination in Gaia's Astrometric Solution (AGIS). ASP Conf. series 434, 386.

REPORT OF THE IAU COMMISSION 4 WORKING GROUP ON STANDARDIZING ACCESS TO EPHEMERIDES AND FILE FORMAT SPECIFICATION

J. L. HILTON[1], C. ACTON[2], J.-E. ARLOT[2], S.A. BELL[2], N. CAPITAINE[2], A. FIENGA[2], W.M. FOLKNER[2], M. GASTINEAU[2], D. PAVLOV[2], E. V. PITJEVA[2], V. I. SKRIPNICHENKO[2], & P. WALLACE[2]
[1] U.S. Naval Observatory
3450 Massachusetts Ave. NW, Washington, DC 20392, USA
e-mail: james.hilton@usno.navy.mil
[2] Affiliations, addresses, and e-mail address of co-authors are available upon request.

ABSTRACT. The IAU Commission 4 Working Group on Standardizing Access to Ephemerides recommends the use of the Spacecraft and Planet Kernel (SPK) file format to provide a uniform format for the position ephemerides of planets and other natural solar system bodies, and the use of the binary Planetary Constants Kernel (PCK) format for the orientation of a body. It further recommends supporting data be stored in a text PCK. These formats are used by the SPICE system developed by the Jet Propulsion Laboratory. A new data type, Type 20: Chebyshev (Velocity Only) has been added. Other changes to the specification are new object identification numbers for coordinate time ephemerides, and a set of three new data types that uses the TCB rather than the TDB timescale.

1. RECOMMENDATIONS

To provide a uniform format for the position ephemerides of planets and other natural solar system bodies, the International Astronomical Union (IAU) Commission 4: Ephemerides Working Group on Standardizing Access to Ephemerides recommends:

1. The use of the Spacecraft and Planet Kernel (SPK) file format.
2. The use of the binary Planetary Constants Kernel (PCK) format ephemeris file for the orientation of a body.
3. Supporting data on the ephemerides, such as values of parameters, whether they are fixed or adjusted, and their uncertainties, are stored in a text PCK kernel.

2. INTRODUCTION

These file formats were developed for and are used by the SPICE system, developed by the Navigation and Ancillary Information Facility (NAIF) of NASA's Jet Propulsion Laboratory (JPL).

Most users will want to use either the SPICE libraries or CALCEPH, developed by the Institut de mécanique céleste de calcul des éphémérides (IMCCE), to access ephemerides stored in these formats.

SPICE is an information system to assist scientists in planning and interpreting scientific observations from space-based instruments. SPICE data and software may be used within many different computing environments. The software is available in FORTRAN 77, C, IDL and MATLAB from the NAIF web site.

CALCEPH is an ephemeris file reader developed by the IMCCE primarily to read its Intégrateur Numérique Planétaire de l'Observatoire de Paris (INPOP) planetary ephemerides. Starting with version 2.0, CALCEPH has the ability to read text PCK, binary PCK, and SPK kernels. It may be linked to programs written in C, FORTRAN 77, and Fortran 90/95/2003. It is available at the INPOP web site and will be made available at the IAU Commission 4: Ephemerides web site (http://iaucom4.org/index.html).

3. CHANGES MADE TO THE BINARY SPK AND PCK FORMATS

To meet the requirements of the wider community, NAIF has agreed to make some additions to the SPK format and adjustments to SPICE and its documentation.

1. A new data type, named Type 20: Chebyshev (Velocity Only).
2. The data types beginning with 101 have been reserved for ephemerides where the time argument is TCB rather than TDB.
3. Data types 901 through 910 have been reserved for the development of new ephemeris types by other groups.
4. Each solar system object is assigned a unique identification number. Ephemeris object numbers have also been reserved for coordinate time ephemerides. The value:
   - 1 000 000 001 indicates that $TT - TDB$ is stored in the X-coordinate.
   - 1 000 000 002 indicates that $TCG - TCB$ is stored in the Y-coordinate.
   - 1 000 000 003 indicates that $TT - TDB$ is stored in the X-coordinate and $TCG - TCB$ is stored in the Y-coordinate.

4. THE FULL SPECIFICATIONS OF THE SPK AND PCK FORMATS

Some users, such as ephemeris developers, may want to access the ephemeris files directly or construct ephemeris files in these formats using their own software. For those readers that require a detailed specification of the file formats, they will be made available in the full version of this report online at the IAU Commission 4: Ephemerides web site.

Acknowledgements. The working group acknowledges the participation and help of NAIF in adapting SPICE to meet the requirements of all the groups participating in this working group. Nat Bachman of NAIF is providing help in reviewing the full report to assure the specification of the file formats is correct.

SOFA: AUTHORITATIVE TOOLS & STANDARD MODELS

C.Y. HOHENKERK, Chair IAU SOFA Board
HM Nautical Almanac Office
UK Hydrographic Office, Taunton, TA1 2DN, United Kingdom
e-mail: Catherine.Hohenkerk@ukho.gov.uk

ABSTRACT. The International Astronomical Union's Standards of Fundamental Astronomy (SOFA) service has the task of establishing and maintaining an accessible and authoritative set of algorithms and procedures that implement standard models used in fundamental astronomy. This poster highlights the current tools, in particular those that address *Times Scales and Calendars* and *Earth Attitude*, and previews the upcoming set of *Astrometry Tools*.

1. INTRODUCTION

SOFA is an IAU Division A Working Group that provides a library of building blocks of fundamental astronomy routines in Fortran and ANSI C. The SOFA library is authoritative, constructed with great care, practical, supported and accessible via its website at http://www.iausofa.org. Each month the website typically receives over 1500 unique visitors. At present there are 687 registered users and the latest edition (9a), released in July 2012, has been downloaded 4497 times. There are currently 59 canonical routines delivering IAU Standards, such as IAU 2006 precession, IAU 2000A nutation and other IAU Resolutions.

This poster highlights SOFA's three "cookbooks" and the manual. The manual contains the terse descriptions consisting of detailed preamble comments in the individual routines as well as lists of the subroutine calls alphabetically and grouped into topics (e.g. time scales). The cookbooks on the other hand (see References) provide, for astronomers in particular, tutorial introduction into the topics. Short examples demonstrate how to call the routines to perform the types of conversions and transformations that may be needed in a particular application.

Note that the names of all Fortran routines have the form `iau_NAME` while for ANSI C the routine names are `iauName`. Here, for clarity, just `NAME` is used.

2. TOOLS FOR TIME SCALES AND CALENDARS

SOFA provides the standard routines for converting between civil and Julian dates and between Julian and Besselian epochs. Importantly SOFA includes conversion between time scales. In total there are 27 routines covering time scales and calendars.

SOFA recognizes seven time scales, namely TAI, UTC, UT1, TT, TCG, TDB and TCB. The strategy is to provide routines that link adjacent pairs of time scales (e.g. `UTCUT1` and `UTCTAI`). This is the simplest scheme that gives the user the most flexibility, needed because users provide the supplementary quantities such as ΔT and UT1−UTC, which either cannot be predicted or for which there are model choices. The routines use SOFA's two-argument Julian date convention, which enables rounding errors to be minimised. The routines `DTF2D` and `D2DTF` handle the conversion between civil date and time and Julian date (or, in the case of UTC, quasi-JD) and vice versa. In the case of UTC this deals with leap seconds, when it is correct to report $60.\cdots$ seconds. Importantly, the routines preserve precision by ensuring that the tiny differences are added to (or subtracted from) the smaller of the two date arguments.

3. TOOLS FOR EARTH ATTITUDE

SOFA's Earth Attitude tools comprise 89, comprising not only the canonical routines that implement the various IAU standards and resolutions but also a variety of support routines. All these routines thus give the user the full scope of transformations to enable their application to achieve the results required easily and correctly. Table 1 lists some of the the most useful IAU 2006/2000A routines.

Quantities	**Comments**	**SOFA Routine Names**
X, Y, s	CIP & CIO locator	`XYS06A, XY06, S06`
$\bar{\gamma}$, $\bar{\phi}$, $\bar{\psi}$, ϵ	precession (Fukushima-Williams)	`PFW06, FW2M`
ϵ, ζ, z, θ	precession (traditional)	`P06E`
$\Delta\psi$, $\Delta\epsilon$	nutation	`NUT06A, NUT00A`
ERA, EO	Earth rotation, equation of origins	`ERA00, EO06A, EORS`
GMST, GAST, EE	Greenwich sidereal time	`GMST06, GST06A, EE06A`
$\mathbf{M} = \mathbf{N}\,\mathbf{P}\,\mathbf{B}$	bias-precession-nutation	`PN06A, PNM06A`
$\mathbf{C} = \mathbf{C}(X+DX,\ Y+DY,\ s)$	Celestial to Intermediate	`C2IXYS`
$\mathbf{W} = \mathbf{R}_1(-y_p)\,\mathbf{R}_2(-x_p)\,\mathbf{R}_3(s')$	polar motion	`POM00`
$\mathbf{Q} = \mathbf{W}\,\mathbf{R}_3(\mathrm{GAST})\,\mathbf{M}$	Celestial to Terrestrial (equinox)	`C2TEQX`
$\mathbf{Q} = \mathbf{W}\,\mathbf{R}_3(\mathrm{ERA})\,\mathbf{C}$	Celestial to Terrestrial (CIO)	`C2T06A, C2TCIO, C2TXY`

Table 1: List of Earth orientation quantities and SOFA routine names. All routine names are preceded by `iau`. DX, DY, x_p, y_p (IERS) are supplied by the user. Use `TR` to calculate the inverse matrix.

4. ASTROMETRY TOOLS

These routines deal with the chain of astrometric transformations linking star data from a catalog and the observed direction of the incoming radiation. The core routines convert between the barycentric and geocentric reference systems and thus deal with the effects of space motion, parallax, light-deflection and aberration, as well as refraction (approximate). These fundamental routines together with the others from the time and Earth orientation sections of SOFA provide a collection of routines that may be used to transform between any of the following: a star's catalog position (ICRS), its astrometric position, its CIRS position, and its observed position (TIO position, ITRS position). This set of routines (32) will be made available in the next (10th) release.

Acknowledgements. The SOFA project is only possible due to the collaborative effort and hard work of the members of the Board, who with their institutes are listed in Table 2. Since the IAU General Assembly in 2012, Wen-Jing Jin of Shanghai Astronomical Observatory (an original Board member) retired and we welcome Jinling Li. George Hobbs (ATNF) stepped down to concentrate on other issues including Pulsar time scales, and we welcome Scott Ransom. The Board thank both Wen-Jing and George for their contributions.

Thanks are due to the Board for their oversight and in particular to Patrick Wallace, who in retirement continues to produce the source code, and Steven Bell who manages the website. Thanks are also due to the Institutes of Board members and to the United Kingdom Hydrographic Office for hosting the website.

John Bangert	United States Naval Observatory (retired)
Steven Bell	HM Nautical Almanac Office, UKHO, UK
Mark Calabretta	Australia Telescope National Facility (retired)
Nicole Capitaine	Paris Observatory, France
William Folkner	Jet Propulsion Laboratory, USA
Catherine Hohenkerk	HM Nautical Almanac Office (Chair), UK
Jinling Li	Shanghai Astronomical Observatory, China
Brian Luzum	United States Naval Observatory (IERS)
Zinovy Malkin	Pulkovo Observatory, St Petersburg, Russia
Jeffrey Percival	University of Wisconsin, USA
Scott Ransom	National Radio Astronomy Observatory, USA
Patrick Wallace	RAL Space (retired), UK

Table 2: SOFA Board Members, their institute and country

5. REFERENCES

SOFA Cookbooks downloadable from http://www.iausofa.org/cookbooks.html, including

SOFA Time Scales and Calendar Tools (Fortran sofa_ts_f.pdf and ANSI C sofa_ts_c.pdf versions),

SOFA Tools for Earth Attitude (sofa_pn.pdf).

ON SOLUTION OF SECULAR SYSTEM IN THE ANALYTICAL MOON'S THEORY

T.V. IVANOVA
Institute of Applied Astronomy of Russian Academy of Sciences
10, Kutuzov quay, St.-Petersburg, 191187, Russia
e-mail: itv@ipa.nw.ru

The theory of the orbital motion of the Moon in the frameworks of the general planetary theory GPT (Brumberg, 1995) enables to represent the lunar coordinates in a purely trigonometric form and valid, at least formally, for an indefinite interval of time. For that the Moon is considered to be an additional planet in the field of eight major planets. The trigonometric form of the coordinates is ensured by a special technique of the solution of the lunar equations that enables to separate the short–period and long–period terms arguments. The long–period terms form an autonomous secular system. The trigonometric solution of this system describes the secular motions of the lunar perigee and node with taking into account the secular planetary inequalities. The secular system in Laplace–type variables was constructed in (Ivanova, 2013). The aim of this paper is to solve this secular system by the normalizing Birkhoff transformation.

The basic series of the Moon's theory have the form

$$p = \sum_{m=0}^{\infty} \sum_{i+j+k+l=m} p_{i,j,k,l}(t) \prod_{n=1}^{9} a_n^{i_n} \overline{a}_n^{k_n} b_n^{l_n} \overline{b}_n^{m_n}, \quad w = \sum_{m=1}^{\infty} \sum_{i+j+k+l=m} w_{i,j,k,l}(t) \prod_{n=1}^{9} a_n^{i_n} \overline{a}_n^{k_n} b_n^{l_n} \overline{b}_n^{m_n} \qquad (1)$$

where the dimensionless complex conjugate variables p, q and real variable w representing small deviations from the planar circular motion are introduced instead of geocentric lunar rectangular coordinates. a_n, b_n are the complex Laplace–type variables proportional to the eccentricity and inclination of the body with number n. The coefficients in (1) are quasi–periodic functions of mean longitudes of the major planets $(\lambda_i, i = 1, 2, \ldots, 8)$ and the Moon (λ_9)

$$p_{i,j,k,l}(t) = \sum_{\gamma} p_{i,j,k,l,\gamma} \exp \sqrt{-1}\,(\gamma\lambda), \qquad w_{i,j,k,l}(t) = \sum_{\gamma} w_{i,j,k,l,\gamma} \exp \sqrt{-1}\,(\gamma\lambda), \qquad (2)$$

$$\gamma = (\gamma_1, \gamma_2, \ldots, \gamma_9), \quad (\gamma\lambda) = \sum_{i=1}^{9} \gamma_i \lambda_i, \quad \sum_{i=1}^{9} \gamma_i = 0.$$

The coefficients $p_{i,j,k,l,\gamma}$ and $w_{i,j,k,l,\gamma}$ are the functions of the semi–major axes, mean motions and masses of the bodies under consideration. It should be noted that the planetary theory is limited by the keplerian terms, the first–order with respect to the masses intermediary and linear theory. It is sufficient for constructing the theory of motion of the Moon. The terms with $m = 0$ in (1) represent an intermediate solution independent of eccentricities and inclinations of all the bodies. It is sought by iterations. In the previous papers (for instance, Ivanova, 2013) it had the form of the Poisson series due to the expansion of the frequency denominators with respect to the ratios of the mean motions of the planets and the Moon. In this paper the intermediate solution has the form of the echeloned series (Ivanova, 2001) without any expansion. The terms with $m > 0$ in (1) are obtained for non–zero values of the eccentricities and inclinations of all the bodies. The technique of Birkhoff normalization for separating fast and slowly changing variables is used here. The terms which do not enable to be integrated without secular terms correspond to critical combinations of multi–indices satisfying the relations

$$\sum_{n=1}^{9} i_n - j_n + k_n - l_n = 1, \qquad \gamma_n = \delta_{9,n} - i_n + j_n - k_n + l_n, \qquad (3)$$

$\delta_{i,n}$ being the Kronecker symbol. They are represented in the similar manner as the series (1) with (2). Such terms form an autonomous secular system

$$\dot{\alpha} = \sqrt{-1}\, N \left[A\alpha + \Phi(\alpha, \overline{\alpha}, \beta, \overline{\beta})\right] , \quad \dot{\beta} = \sqrt{-1}\, N \left[B\beta + \Psi(\alpha, \overline{\alpha}, \beta, \overline{\beta})\right] \tag{4}$$

in slowly changing variables $\alpha = (\alpha_1, \ldots, \alpha_9)$ $(\alpha_i = a_i \exp -\sqrt{-1}\lambda_i)$ and $\beta = (\beta_1, \ldots, \beta_9)$ $(\beta_i = b_i \exp -\sqrt{-1}\lambda_i)$. To complete this system one should add the corresponding conjugate equations. Here N is the diagonal matrix of mean motions of the planets and the Moon, A and B are 9×9 constant matrices of semi-major axes, mean motions and masses of all the bodies under consideration. 9–vectors Φ, Ψ are represented by the power series with quasi–periodic coefficients

$$\Phi = \sum\nolimits^{*} \Phi_{i,j,k,l,\gamma} \prod_{n=1}^{9} \alpha_n^{i_n} \overline{\alpha}_n^{k_n} \beta_n^{l_n} \overline{\beta}_n^{m_n} , \quad \Psi = \sum\nolimits^{*} \Psi_{i,j,k,l,\gamma} \prod_{n=1}^{9} \alpha_n^{i_n} \overline{\alpha}_n^{k_n} \beta_n^{l_n} \overline{\beta}_n^{m_n} . \tag{5}$$

Functions Φ, Ψ contain only forms of odd degree in slowly changing variables α, $\overline{\alpha}$, β, $\overline{\beta}$ starting with the third degree terms. The asterisk at the summation sign indicates that this summation is taken only over critical values (3). Let μ_j, $S_{\cdot j}$ and ν_j, $T_{\cdot j}$ $(j = 1, 2, \ldots, 9)$ be the eigenvalues and eigenvectors of the matrices NA and NB in (4), respectively. Then the first step to solve the secular system (4) is the construction of the linear transformations $\alpha = Sx\,, \quad \beta = Ty$ which transform (4) into the form

$$\dot{X} = \imath \big[PX + NR(X)\big] \tag{6}$$

with 9–vectors of new variables $X = (x, \overline{x}, y, \overline{y})$ ($x, \overline{x}, y, \overline{y}$ are 9–vectors) and new right–hand members presented by 9–vectors $R_1 = N^{-1}S^{-1}N\Phi\,, \quad R_2 = -\overline{R}_1\,, \quad R_3 = N^{-1}T^{-1}N\Psi\,, \quad R_4 = -\overline{R}_3\,.$ P is 9×9 diagonal matrix of the structure: $P = diag(\mu\,, -\mu\,, \nu\,, -\nu)$. The resulting secular system (6) is solved by Birkhoff normalization technique which consists of constructing the formal power series $X = Y + \Gamma(Y)$ with new variables $Y(u, \overline{u}, v, \overline{v})$ ($u, \overline{u}, v, \overline{v}$ are 9–vectors) reducing (6) to the system

$$\dot{Y} = \imath \big[PY + NF(Y)\big] \tag{7}$$

with the power series F admitting the straightforward integration of this system without t–secular terms. Functions Γ and F representing the series in powers of Y are found by iteration technique. Since the influence of the Moon on the major planets is not taken into account the system (7) splits into two secular systems for the Moon and for the planets. The last of them is determined in GPT. As a result, the equations (7) for the Moon are transformed into the system of linear equations

$$\dot{u}_9 = \sqrt{-1}\, u_9\, (\mu_9 + \delta\mu_9), \qquad \dot{v}_9 = \sqrt{-1}\, v_9\, (\nu_9 + \delta\nu_9)\,. \tag{8}$$

$\delta\mu_9$ and $\delta\nu_9$ are real constant corrections to corresponding eigenvalues for the Moon. Hence, these equations admit the straightforward integration and the solution has the form

$$u = \eta_{1,9} \exp \sqrt{-1}\, \varphi_{1,9}, \qquad v = \eta_{2,9} \exp \sqrt{-1}\, \varphi_{2,9}, \tag{9}$$

$$\begin{pmatrix} \varphi_{1,9} \\ \varphi_{2,9} \end{pmatrix} = \begin{pmatrix} \mu_9 + \delta\mu_9 \\ \nu_9 + \delta\nu_9 \end{pmatrix} t + \begin{pmatrix} \tau_{1,9} \\ \tau_{2,9} \end{pmatrix}, \qquad \begin{pmatrix} \delta\mu_9 \\ \delta\nu_9 \end{pmatrix} = n \sum\nolimits^{*} \begin{pmatrix} U^1_{km} \\ U^2_{km} \end{pmatrix} \prod_{i=1}^{9} \eta_{1,i}^{2k_i} \eta_{2,i}^{2m_i}$$

with real constants of integration $\eta_{j,i}$ and $\tau_{j,i}$ $(j = 1, 2\,;\, i = 1, \ldots, 9)$.

The resulting solution of the secular system for the Moon has the form

$$\begin{pmatrix} \alpha \\ \beta \end{pmatrix} = \sum \begin{pmatrix} \alpha_{klmn} \\ \beta_{klmn} \end{pmatrix} \prod_{i=1}^{9} \exp \sqrt{-1} \Big[(k_i - l_i)\, \varphi_{1,i} + (m_i - n_i)\, \varphi_{2,i} \Big] , \quad \sum_{i=1}^{9} (k_i - l_i + m_i - n_i) = 1\,. \tag{10}$$

The trigonometric solution of the secular system has the semi–analytical form with numerical coefficients α_{klmn} and β_{klmn}. It includes terms due to the secular evolution of the lunar perigee and node as well as of that of the major planets.

REFERENCES

Brumberg V., 1995, "Analytical Techniques of Celestial Mechanics", Springer, Heidelberg.

Ivanova T., 2001,"A new echeloned series processor (EPSP)", Celest. Mech. Dyn. Astr. 80, pp. 167–176.

Ivanova T., 2013,"Constructing the secular system in the analytical Moon's theory", Astron. vestn., V. 45, No.5, 2013 (in Russian).

ON FUTURE OPPORTUNITIES TO OBSERVE GRAVITATIONAL SCATTERING OF MAIN BELT ASTEROIDS INTO NEO SOURCE REGIONS

A. IVANTSOV, S. EGGL, D. HESTROFFER, W. THUILLOT
IMCCE, Paris Observatory, UPMC, univ. Lille1, CNRS
77 Avenue Denfert-Rochereau, 75014 Paris, France
e-mail: ivantsov@imcce.fr

1. INTRODUCTION

Physical and orbital properties of the current NEO population can be explained when one assumes that their primary origin lies in the asteroid main-belt and Jupiter-family comet (P<20 years) regions (Bottke et al., 2000a, 2002; Greenstreet et al., 2012; Mainzer et al., 2012). Orbital resonances with the Gas Giants within the main-belt which cause strong eccentricity-pumping are transport mechanisms that can carry main belt asteroids into the inner Solar System. Two well known resonances in this respect are the 2:1 and 3:1 mean-motion resonance with Jupiter as well as the ν_5 and ν_6 secular resonances. Since the average life-time of asteroids in resonances is much shorter than the age of the Solar System, a constant flux of asteroids into resonant regions is necessary in order to sustain the observed NEO population (Morbidelli et al., 2002).

Non-gravitational forces such as the Yarkovsky effect can cause a slow drift into resonance (Bottke et al., 2000b). Also, close encounters among asteroids lead to orbital migration (Delisle & Laskar, 2012; Carruba et al., 2012, 2013). Yet, the importance of gravitational interactions between asteroids with respect to further moving future NEOs towards resonances is not well understood. This is due to computational difficulties arising with the numerical solution of the gravitational N-body problem. Results of multiple scattering events, for instance, strongly depend on the number of interacting bodies considered. Using high precision orbit predictions over one hundred years, we identify main belt asteroids that are injected into - or stay in the vicinity of relevant resonant regions that might cause them to become NEOs in the far future. We, thus, intend to provide interesting targets for astrometric observation campaigns which may lead to a better understanding of the processes involved in the generation of NEOs.

2. METHOD

In a first step, we identified those asteroids that are likely candidates to be scattered into a resonance. For this purpose the analytically calculated proper element catalog from AstDys has been searched and asteroids that are close to secular and mean motion resonances have been identified. The mean motion resonances (MMR) considered are 3:1, 5:2, 2:1, and 7:3 between asteroids and Jupiter. Secular resonances were included up to second order in g and s (e.g. Machuca & Carruba, 2012). Our current sample encompasses asteroids with a distance of no more than 0.5 ["/yr] from the secular resonant frequencies and a maximum proper semi-major axis distance of 10^{-3} au from the locations of the four MMRs that are considered to be source regions for NEOs.

In order to determine, whether any of the sampled asteroids will be pushed into or at least closer to a resonance within the next century, we performed an exploratory numerical propagation of 1273 asteroids that where closest to the investigated secular resonances, and 52 asteroids that were close to the previously mentioned MMRs. Perturbations from all planets (DE431) as well as from the biggest 16 asteroids were considered. The equations of motion include all relevant post-Newtonian terms, as well as the J_2 form factor of the Sun. Initial conditions of the main belt objects (MBOs) were acquired from the HORIZONS for consistency. The proper elements of asteroids were computed using OrbFit 4.2 (Milani & Gronchi, 2010).

3. PRELIMINARY RESULTS

A comparison of analytical proper elements for all numbered asteroids once for J2000 and once a century later yields that, in fact, 18 out of the 52 near mean motion resonant asteroids stay in the

vicinity of their respective MMRs over 100 years, and 4 of them might even become resonance crossers during this time. For nearly secular resonant asteroids, 455 out of 1273 remained close to their resonance and 128 potential resonance crossing events were recorded. A shortened list of possible resonance crossing asteroids is given in Table 1.

MMR	
7:3	271956, 299835, 332810, 338943
SECULAR	
$\nu_6 + \nu_{16}$	11094, 112561, 112588, ...
$2\nu_5 + \nu_6$	103395, 127993, 13106, 132964,...
$2\nu_6 + \nu_5$	103774, 104624, 195280, 321328, ...
$2\nu_6 - \nu_5 - \nu_{16}$	108497, 148758, 177861, 203561, ...
$3\nu_6 - \nu_5$	146121, 176517
$2\nu_6 + \nu_{16}$	6234, 47790, 146664, 90239,...
$3\nu_6 - 2\nu_5$	54486, 367618
$\nu_6 + 2\nu_{16}$	164537
$2\nu_6 - \nu_5$	75399, 233930
$2\nu_6 + \nu_{16}$	24986, 252191, 234075

Table 1: Identified asteroids that may experience resonance crossing over the next century.

4. CONCLUSIONS

We have found considerable dynamical mixing close to investigated resonances since only roughly one-third of our asteroids' sample stayed close to the respective resonances within the next 100 years. About one-tenth of the investigated population was identified as potentially resonance crossing. A more detailed modeling of the gravitational scattering processes will provide information on the importance of asteroid-asteroid interaction around resonances relevant to NEO production.

5. REFERENCES

Bottke, W. F., Jedicke, R., Morbidelli, A., Gladman, B., Petit, J.-M. 2000a, "Understanding the distribution of Near-Earth Asteroids", Science, 288, pp. 2190-2194.

Bottke, W. F., Morbidelli, A., Jedicke, R., et al. 2002, "Debiased orbital and size distribution of the Near Earth Objects", Icarus, 156, pp. 399-433.

Bottke, W. F., Rubincam, D. F., Burns, J. A. 2000b, "Dynamical evolution of main belt meteoroids: Numerical simulations incorporating planetary perturbations and Yarkovsky thermal forces", Icarus, 145, pp. 301-331.

Carruba, V., Huaman, M., Domingos, R. C., Roig, F. 2013, "Chaotic diffusion caused by close encounters with several massive asteroids II. The regions of (10) Hygiea, (2) Pallas, and (31) Euphrosyne", A&A 550(A85), doi: 10.1051/0004-6361/201220448.

Carruba, V., Huaman, M., Douwens, S., Domingos, R. C. 2012, "Chaotic diffusion caused by close encounters with several massive asteroids. The (4) Vesta case", A&A 543(A105), doi: 10.1051/0004-6361/201218908.

Delisle, J.-B., Laskar, J., 2012, "Chaotic diffusion of the Vesta family induced by close encounters with massive asteroids", A&A 540(A118), doi: 10.1051/0004-6361/201118339.

Greenstreet, S., Ngo, H., Gladman, B. 2012, "The Orbital Distribution of Near-Earth Objects inside Earth's Orbit", Icarus, 217, pp. 355-366.

Machuca, J. F., Carruba, V. 2012, "Secular dynamics and family identification among highly inclined asteroids in the Euphrosyne region", MNRAS , 420, pp. 1779-1798.

Mainzer, A., Grav, T., Masiero, J. et al. 2012, "Characterizing Subpopulations within the near-Earth Objects with NEOWISE: Preliminary Results", ApJ, 752(110), doi: 10.1088/0004-637X/752/2/110.

Milani, A., Gronchi, G. F. 2009, Theory of Orbit Determination, Cambridge University Press.

Morbidelli, A., Bottke, W. F., Froeschlé, C., Michel, P. 2002, "Origin and evolution of Near Earth Asteroids", Asteroids III, University of Arizona Press, pp. 409-422.

COMPARISONS OF EPHEMERIDES

S.G. NELMES, C.Y. HOHENKERK
HM Nautical Almanac Office
UK Hydrographic Office, Taunton, TA1 2DN
e-mail: susan.nelmes@ukho.gov.uk, catherine.hohenkerk@ukho.gov.uk

ABSTRACT.

The objectives of IAU Division A Commission 4 - Ephemerides include

- Promote improvements to the usability and accuracy of astronomical ephemerides, and provide information comparing computational methods, models, and results to ensure the accuracy of data provided.
- Promote the development of explanatory material that fosters better understanding of the use and bases of ephemerides and related data.

As part of this remit work has been carried out to produce a new webpage that provides tools for comparing three ephemerides, in particular EPM2011/m, DE430/LE430 and INPOP10e. These ephemerides are from expert groups around the world; Russia's Institute for Applied Astronomy, USA's Jet Propulsion Laboratory and France's IMCCE and Paris Observatory. Here we describe some of the aspects of this webpage and the comparisons being carried out.

1. COMMISSION 4

Commission 4 - Ephemerides is an IAU commission under Division A and its aims are as follows

- Maintain cooperation and collaboration between the national offices providing ephemerides, prediction of phenomena, astronomical reference data, and navigational almanacs.
- Encourage agreement on the bases (reference systems, time scales, models, and constants) of astronomical ephemerides and reference data in the various countries. Promote improvements to the usability and accuracy of astronomical ephemerides, and provide information comparing computational methods, models, and results to ensure the accuracy of data provided.
- Maintain databases, available on the Internet to the national ephemeris offices and qualified researchers, containing observations of all types on which the ephemerides are based. Promote the continued importance of observations needed to improve the ephemerides, and encourage prompt availability of these observations, especially those from space missions, to the science community.
- Encourage the development of software and websites that provide astronomical ephemerides, prediction of phenomena, and astronomical reference data to the scientific community and public.
- Promote the development of explanatory material that fosters better understanding of the use and bases of ephemerides and related data.

2. THE COMMISSION 4 WEBPAGE FOR COMPARISON OF EPHEMERIDES

To help achieve the aims detailed above Commission 4 has produced a new webpage that provides various ways of comparing three ephemerides, in particular EPM2011/m (produced by Russia's Institute for Applied Astronomy), DE430/LE430 (produced by USA's Jet Propulsion Laboratory) and INPOP10e (produced by France's IMCCE and Paris Observatory). This webpage will allow users, who use ephemerides in a variety of ways and are faced with a choice of which one to use, to access a comparison that informs them of the strengths, weaknesses, similarities and differences of the available options.

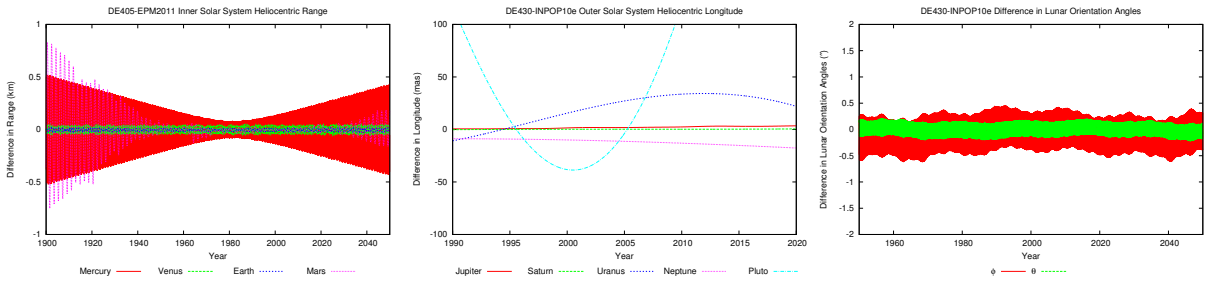

(a) (b) (c)

Figure 1: Examples of the visual comparisons available on the webpage.

The webpage makes no claim as to which ephemerides should be used in any particular circumstance. Instead it just provides some tools to help the user make an informed decision about their choice of ephemerides.

3. VISUAL COMPARISONS

One set of tools on the webpage is a series of plots that have been produced comparing the three ephemerides. Examples are shown in figure 1. The values compared are the differences between the ephemerides in

- The heliocentric longitude and latitude of the planets.
- The barycentric and heliocentric distances of the planets.
- The geocentric range, longitude, latitude, right ascension and declination of the Moon.
- The lunar orientation and rotation angles.

The plots are produced over both long (1900 or 1950 to 2050) and short (1990 to 2020) time periods.

4. INFORMATION

Another tool provided is a table of information about each of the ephemerides. Information has been requested from each of the ephemerides providers and a summary is shown on the webpage in an easy to compare format. The table includes, among other items, a comparison of which solar system objects are included, the type of coordinates and the reference system used, the dates covered and also details on the file structure of the ephemerides and how they may be read. There are various links to more detailed information and documentation located on the providers' websites, as well as download links.

5. STILL TO COME

More information is still to be added to the website to aid ephemerides comparisons including details on initial assumptions, how asteroids and TNOs are included and other parameters used.

Acknowledgements. Thank you to the Commission 4 organising committee for all their comments and helpful suggestions during the creation of the webpage, in particular Agnès Fienga, William Folkner and Elena Pitjeva along with their colleagues and institutions. Thanks also go to James Hilton of USNO for all his help. The UK Hydrographic Office is also thanked for hosting the Commission 4 website.

6. REFERENCES

Commission 4 Website http://www.iaucom4.org/

ON THE SPATIAL DISTRIBUTION OF MAIN BELT ASTEROIDS

D. SOUAMI[1,2,3], A. LEMAITRE[1], J. SOUCHAY[3]
[1] Namur Center for Complex Systems (NAXYS), UNamur, Belgium
[2] Université Pierre & Marie Curie, Paris, France
[3] SYRTE, Observatoire de Paris, CNRS, UPMC, France
e-mail: damya.souami@obspm.fr; anne.lemaitre@unamur.be; jean.souchay@obspm.fr

ABSTRACT. We investigate here the distribution of main belt asteroids in the (i: inclination, Ω: longitude of the ascending node) space with respect to the ecliptic-equinox J2000. We identify and confirm a sinusoidal behaviour of this distribution, which disappears when the inclination is given with respect to Jupiter's orbital plane, or with respect to the invariable plane (IP). This behaviour is explained by planetary secular effects, mainly due to Jupiter. Furthermore, we identify three different orbital behaviours that explain the density distribution in this space.

1. INTRODUCTION

We present here the analysis of a not so common distribution, the Main Belt Asteroid (MBA) population in the osculatory element domain defined by the inclination, and the longitude of the ascending node (i,Ω). We show (Fig.1(a)) that a particular sinusoidal aspect of the distribution is observed and that it is due to secular effects of the planets, mainly Jupiter.

2. MODEL AND ARGUMENTS

One should ask two questions: (i) is this distribution an artefact due to an observational bias? (ii) does the area of maximal density correspond to a particular dynamical grouping?

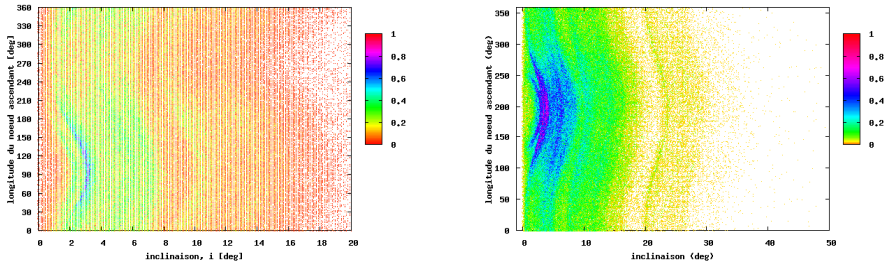

(a) (24) Themis, $i = 0°, 75$ (b) (24) Themis, $i = 0°, 75$

Figure 1: Density distribution of the asteroids (333.841 numbered MBAs) in term of orbital plans with respect to the ecliptic-equinox J2000 (Fig.1(a)), with respect to the Invariable Plane (IP) (Fig.1(b)).

The answer to both question is *"No"*. In fact, the "waves" (Fig.1(a)) are also observed in the distribution defined by mean i vs mean Ω. Though, when the elements are given with respect to the solar system's (IP) (Souami & Souchay, 2012) (Fig.1(b)) or with respect to Jupiter's or Saturn's orbital planes, this sinusoidal behaviour tends to disappear and the distribution is flattened.

Some people have looked into the problem, for example Michkovitch (1947) suggested the secular perturbations to be at the origin of a similar distribution for the longitude of the perihelium. Scheirich (2005) observed the distribution but did not provide an explanation. Here, using a simplified secular model following the approach of Murray & Dermott (1999; Chap. 7), we provide an answer to the problem. We consider the truncated Hamiltonian to the second order in both eccentricities and inclinations. For a massless asteroid, of semi-major axis a, and mean motion n; the perturbing function is written:

$$\mathcal{R} = na\Big[\frac{1}{2}A(h^2+k^2) + \frac{1}{2}B(p^2+q^2) + \sum_{j=1}^{2} A_j(hh_j + kk_j) + \sum_{j=1}^{2} B_j(pp_j + qq_j)\Big], \quad (1)$$

where p and q are the components of the inclination vector; h and k those of the eccentricity vector. The matrices A et B, which are function of the Laplace coefficients are given by their classical expressions (Murray & Dermott 1999). The indices $i = 1$, and $i = 2$ are used for Jupiter and Saturn, respectively.

The perturbing function given by Eq (1) is uncoupled in eccentricity and inclination, thus we can restrict ourselves to the secular terms in inclination. The solution is given by

$$p(t) = I_{free}\sin(Bt+\gamma) + p_0(t) \quad , \quad q(t) = I_{free}\cos(Bt+\gamma) + q_0(t) \tag{2}$$

It is written as the sum of the forced solution $(p_0(t), q_0(t))$ and the free one (which is periodic and has an amplitude I_{free}). The free motion depends upon the initial conditions of the inclination vector (of amplitude I_{free}, and phase γ). This is clearly observed for the asteroid (24) Themis (Fig.2(a)), and two fictitious Themis (Figs:2(b),2(c)) for which we vary the value (I_{free}).
$p_0(t) = -\sum_{i=1}^{2} \frac{\mu_i}{B-f_i}\sin(f_i t+\gamma_i)$, $q_0(t) = -\sum_{i=1}^{2} \frac{\mu_i}{B-f_i}\cos(f_i t+\gamma_i)$, where $\mu_i = \sum_{j=1}^{2} B_j I_{ji}$.
The forced motion is associated with a forced inclination $I_{\rm forced}$, and node $\Omega_{\rm forced}$

$$I_{\rm forced} = \sqrt{p_0^2+q_0^2} \quad , \quad \tan\Omega_{\rm forced} = \frac{p_0}{q_0}, \tag{3}$$

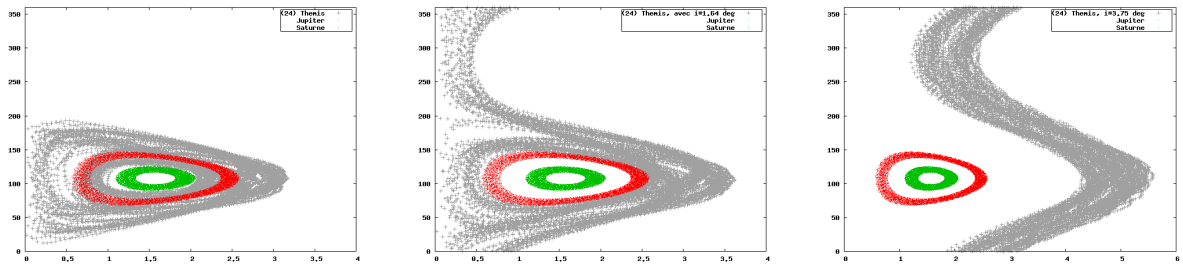

(a) (24) Themis, $i = 0°,75$ (b) $i = 1°,64$ (c) $i = 3°,75$

Figure 2: The secular motion in (i, Ω) plane over 10 000 years, for the asteroid (24) Themis (in grey): $a = 3,14$ au, $e = 0,13$ et $i = 0°,75$ (Fig. 2(a)). The other figures 2(b), 2(c) are for a fictitious Themis fictifs of inclination $1°,64$ et $3°,75$, respectively; green for Jupiter et red Saturn.

We have identified three different secular dynamics of the asteroids, depending on the initial conditions (I_{free}): *i*)- libration for small I_{free} values (Fig. 2(a)), *ii*)- homogenous or regular circulation (Fig 2(b)), *iii*)- heterogenous circulation for relatively high values of I_{free} (Fig. 2(b)).

3. CONCLUSIONS

We have explained with a simple secular model the observed distribution of minor planets in the (i, Ω) plane, with respect to the ecliptic-equinox J2000.0; proving by a simple analytical model that the distribution is mainly due to secular effects of Jupiter. The results are confirmed numerically considering a more complete model (see Souami 2012).

We were able to distinguish three different dynamical behaviours that depend on the initial inclination. The superposition of the three dynamics explains the observed distribution, though one question remains open: what are the initial conditions that would lead to the observed distribution?

4. REFERENCES

Michkovitch V.V., Publications de l'Institut Mathématique de l'Académie Serbe des Arts et Sciences, (S.S.)I(01): 62–70, 1947

Murray C. D., & Dermott S. F. 1999, Solar system dynamics by Murray, C. D., 1999

Scheirich P., 2005, *http://sajri.astronomy.cz/asteroidgroups/groups.htm*

Souami D. 2012, PhD thesis: Etude dynamique et observationnelle des astéroïdes de la ceinture principale, University Pierre & Marie Curie 2012

Souami D. & Souchay J. 2012, A&A, 543, A133

RECENT ACTIVITIES OF THE FP7-ESPaCE CONSORTIUM

W. THUILLOT[1], V. LAINEY[1], V. DEHANT[2], J.-E. ARLOT[1], L. GURVITS[3,7], H. HUSSMANN[4], J. OBERST[5], P. ROSENBLATT[2], J.-C. MARTY[6], B. VERMEERSEN[7], S. BAUER[4], J.-P. DE CUYPER[2], D. DIRKX[7], D. HESTROFFER[1], M. KUDRYASHOVA[2], L.-E. MEUNIER[1], A. PASEWALDT[4], N. RAMBAUX[1], V. ROBERT[1], R. TAJEDDINE[1], K. WILLNER[5]
[1] IMCCE, Paris Observatory, UPMC, Univ. Lille1, CNRS
77 avenue Denfert Rochereau 75014 Paris, France
e-mail: thuillot@imcce.fr
[2] ROB, Royal Observatory of Belgium, Brussels, Belgium
[3] JIVE, Joint Institute for VLBI in Europe, Dwingeloo, The Netherlands
[4] DLR, German aerospace center, Berlin, Germany
[5] TUB, Technical University Berlin, Germany
[6] CNES, French space agency, Toulouse, France
[7] TUD, Delft University of Technology, Delft, The Netherlands

ABSTRACT. The consortium ESPaCE (European Satellite Partnership for Computing Ephemerides) is composed of seven European institutes: IMCCE ((Institut de Mécanique Céleste et de Calcul des Ephémérides, Paris Obs.), ROB (Royal Observatory of Belgium), TUB (Technical University of Berlin), JIVE (Joint Institute for VLBI in Europe), TUD (Delft University of Technology), French space agency (CNES) in France and German Aerospace Center (DLR) in Germany. The objective of this FP7 European project is to provide new accurate ephemerides of natural satellites and spacecraft. For this goal many astrometric data issued from ground-based observations as well as from space observations have been analyzed and reduced. On the other hand new technologies applied to the positioning of spacecraft are also studied. The ESPaCE project addresses also data related to gravity and shape modeling, control point network and rotational parameters of natural satellites. The accuracy improvement of these ephemerides makes them a powerful tool for the analysis of space missions or the preparation of future missions, or for the determination of some physical parameters.

1. THE CONCEPT AND OBJECTIVES

The first purpose of the ESPaCE project is to explore and understand the physical phenomena, the physical structure and the dynamical processes of the Earth's Moon, the Martian moons Phobos and Deimos, as well as the numerous planetary moons of the Solar system, and of Jupiter and Saturn in particular, their origin, their dynamics and their evolution. The second purpose of this project is to link celestial mechanics, dynamics, space science, Radio Science, LLR (Lunar Laser Ranging), VLBI (Very Long Baseline Interferometry) and astrometry. The main outputs are the improvement of the ephemerides of the Martian, Jovian, Saturnian and Uranian satellites and of orbits of spacecraft, as well as constraints on the interior and dissipation processes associated with these planetary systems.

The main part of the activity is focused on the extraction and analysis of astrometric data from spacecraft measurements that have not yet been used in the orbit dynamic reconstruction and on the combination of these data with ground-based astrometric data. The project will also advance the European expertise in ultra-precise tracking of planetary probes. By these means, we intend to provide new dynamical models for several natural satellites, a characterization of their rotation properties, and improve spacecraft orbit determination methods for space science.

This four year project, which began on 2011 June 1st, is organized in 12 work-packages: management of the project, Radio Science (RS), Laser Ranging (LR), VLBI, digitized data handling, astrometry, definition of coordination reference frames and improvement of planetary coordinate knowledge, methods for determination of spacecraft and satellites ephemerides, set up of databases, data access and distribution methods, educational and outreach activities, and scientific management (Thuillot et al., 2013).

The project concentrates at achieving maximum synergy between all the work packages above in order to deliver to the professional communities and communities at large the best scientific products adequate

to the present day cutting edge space science and technology. For further information web pages are accessible at : http://espace.oma.be/

2. RECENT RESULTS

Astrometry from digitized photographic plates and telescopic observations

The new technology ROB Digitizer (Damian) was used to digitally disclose with unprecedented precision the astrometric data archived in photographic plates of the Martian ($\approx$ 500 plates), the Galilean ($\approx$ 550 plates) and the Saturnian ($\approx$ 1000 plates) satellites mostly taken with the 26" refractor at USNO and at the South African Yale Station. Almost 200 plates from different locations will also be considered. Other telescopic observations, mutual events of planetary satellite systems (Uranus 2007, Jupiter 2009), have been reduced.

Astrometry from RS and Space images

Precise determination of S/C orbit is done thanks to RS (MEX, Viking 1&2, Mariner 9 data) and will be used in a global astrometry solution of the satellite dynamical models. Besides, space imaging is used (Pasewaldt et al., 2012). 239 Phobos and 136 Deimos images have been studied and lead to observational accuracies between 0.5 and 3.6 km. Intersatellite measurements of the least distance during Martian moons encounters show also promising astrometry results.

Astrometry from LR and VLBI tracking

New technologies for providing high accurate astrometry of S/C through tracking or ranging data are studied. The combination of RS and VLBI observations during a flyby of spacecraft around a planet or moons is under study (Duev et al., 2012). Besides, we foresee to contribute to the positioning of Gaia using VLBI tracking techniques. Results using 1-Way LR to LRO have been obtained and show rms of 13.2cm. This may let us expecting a performance e <1 cm with a dedicated two-way system. Performance study of Phobos laser ranging concept for geodetic observables is currently in progress.

Shape modeling, reference system and rotation

ESPaCE intends to provide coordinate systems of several satellites and rotation parameters (Rambaux et al., 2012). A Phobos control point network is under development. A provisional version has been used for providing space astrometry but also for providing measures of rotation parameters. Potential applications to the libration study of the Saturnian and Jovian satellites are foreseen. The development of reference shape and reference system of icy satellites is also under study. Interior and dynamical parameters will be inferred.

New satellite and spacecraft ephemerides

New ephemerides of the Martian and the Uranian moons have been developed. Ground-based astrometry and space astrometry (MEX, Phobos2, Viking data) are used for Phobos and Deimos. Post-fit residuals show typical accuracy of 65 mas ($\approx$ 20 km). For the Uranian moons, residuals of micrometer observations, photographic plates and CCD frames covering 1870-2012 are obtained. Mutual events residuals of these satellites show very accurate results with rms of 20 mas (Arlot et al., 2013). The ephemerides are accessible at ftp.imcce.fr.

Acknowledgements. of support from the EC's 7th Framework Programme (FP7/2008-2017) under grant agreement n. 263466.

3. REFERENCES

Arlot J.-E. et al., 2013, Astrometric results of observations of mutual occultations and eclipses of the Uranian satellites in 2007, A&A 557, A4

Duev et al., 2012, Spacecraft VLBI and Doppler Tracking : algorithm and implementation, A&A 541, A43

Pasewaldt A., J. Oberst, K. Willner et al., 2012, New astrometric observations of Deimos with the SRC on Mars Express, A&A 545, A144

Rambaux N., J.C. CasilloRogez, S. Le Maistre, P. Rosenblatt, 2012, Rotational motion of Phobos, A&A 548, A14

Thuillot W. et al., 2012, ESPaCE: European Satellite Partnership for Computing Ephemerides, in Let's Embrace Space Vol. II , EU Entr. & Indust, Chap. 25, 287-292.

FINAL DISCUSSION

Meeting notes by Catherine Hohenkerk and Susan Nelmes (30 September 2013)

Discussion on the topic "The next ICRF - Progress and developments"

Procedure for the realisation of the next ICRF. International effort for observations and combinations. ICRF3 versus GAIA celestial frame

Co-Chairs: Francois Mignard (FM), Chris Jacobs (CJ)
Other contributors: Nicole Capitaine (NC), Yaroslav Yatskiv (YY), Axel Nothnagel (AN), AA (Alexandre Andrei), AB (Alessandra Bertarini), JK (Jean Kovalesky)

CJ, Chair of the IAU Working Group on ICRF3, started the discussion by talking about the ways to contribute. It was not necessary to have large VLBI networks single dish-telescopes were good. Lots of groups can contribute to research.

FM said that there were systematic problems in both the optical and radio but consistent in the aspect of using the IERS conventions. GAIA perhaps could help with systematic errors in VLBI. Currently we have two independent reference frames. How can these be combined? There are not many overlapping sources.

CJ confirmed the need for optical counterparts to the radio sources for identification.

YY asked how many of the radio source would be visible with GAIA?

FM confirmed that there would be 500 000 optical quasars observed by GAIA. FM also confirmed that there would be software that would allow the bad quasars/observations to be removed.

NC asked CJ what would be discussed by the Next ICRF WG?

CJ said that there was 2 phases, lasting until 2018. The current focus was the southern hemisphere observations, SX, SKA, and all the data combinations and comparisons, which would last until 2015.

AN said that solutions generated carry full covariance information. Combining catalogues into one reference frame is difficult due to the different covariances in the different systems. This is a big challenge for the WG.

CJ confirmed that the correlations are different between catalogues.

JK asked if separate catalogues were produced or just the combinations?

CJ said there were difficulties comparing catalogues from different frequencies, for example exactly where are the jets? Higher frequencies need more coverage. Also AN (who heads up International Very Long Baseline Interferometry Service (IVS)) is pushing for better comparisons between different frequency catalogues.

GH said it was hard to get time on large telescopes, so were smaller ones OK?

AB commented that more antennae would be good.

GH wondered if high frequency observations would be cut due to funding issues.

AB said they were hoping to get time on Parks before the funding was cut.

Audience asked how many sites so far?

CJ said that there was a small number at the moment but they were trying to increase the number. The Spanish or Portuguese may be able to purchase new antennae.

Audience: We recognise precision of the GAIA catalogue, but how do we connect with optical telescope observations? How do we use microarcsecond accuracy on the ground?

FM said that the GAIA (stellar) frame was very accuratethe best one yet. It would last a while, but it would degrade very slowly over time.

CJ said that the GAIA catalogue (frame) would be very useful, for example for adaptive optics.

AA Remember that star catalogues have zonal errors, but there will be no zonal errors in the GAIA catalogue. This is a big advantage. ICRF is only based on high frequencies, which is not accessible to lots of antennas.

CJ said that some parts were accessible, but it is a big issue.

AN said that change over of broad band will help the situation. Every telescope currently observing will be used for further work and may be improved to the KA band if suitable.

CJ suggested that the cost of research may come down due to cheaper data storage.

Discussion on the topic
"Atomic time and pulsar-based timescales - Progress and developments"

Pulsar time scale versus atomic time scale

Co-Chairs: Gérard Petit (GP), George Hobbs (GH)
Other contributors: Francois Mignard (FM), Nicole Capitaine (NC), Chris Jacobs (CJ), Yaroslav Yatskiv (YY)

GH, who is the Chair of the IAU Working Group on Pulsar Time Scale and Atomic Time, started the discussion by summarising the current status. He told the audience that the IAU WG was set up at the last IAU to bring together people working on pulsar and atomic time scales. Atomic time scales have always been more precise, but pulsar time scales (which started in the 1990 s) are improving all the time and now they are in the same ball park (1 order of magnitude out according to GP talk). Improvements are currently being made using the Parks 60 m dish, the compact array, and in the future with dishes in China and the Square Kilometre Array (SKA), all of which will all have an impact. The WG mission is to learn, talk, share data, i.e. in particular understand the basis and standards of the data, etc. Discussions have started on e-mail, mainly between GH, GP and Dick Manchester. Anybody who is interested is welcome to join in.

GP commented that long continuous sets of observations, including going back into the past was essential.

GH said that over the past 5 years there were good data sets. However, in the past the Pulsar community was not good at archiving their data. Some old data did exist. Parks had archived data back to the 1990s and efforts were being made to extract data from Arecibo and Greenbank, however some of it was not in a formal archive.

FM commented that pulsar timing is currently a matter of research and is showing quality, and asked if it could be turned into a service and what sort of effort would be needed to do this.

GH said that all the work on pulsars was on gravitational wave (GW) detection, for which there was much funding and hence funding for telescopes. Time scales were an easy side project, but it was only this WG that had a real interested in it.

GP commented that the GW community should be interested in Time Standards!

YY asked how accurate was the data?

GH: Pulsars were massive and complicated. Young pulsars are often funny with glitches/wobbles. Milliseconds pulsars are much more stable, but there are some irregularities. Parks telescope has picked up some rotational irregularities over 10-year timescales. More pulsars are needed. The longer the time spans requires more pulsars in order to find and discount irregularities. Errors in TAI dominate over periods ¡30 years, solar system ephemerides errors over periods ¿ 30 years. It is unclear where rotational irregularity errors fit in.

CJ asked what were these glitches?

GH said that the glitches were like star quakes. Dramatic increase in spin rate and within a short time the rate would then decay back to almost, but not quite, the original rate.

CJ pointed out it was always easier to get funding if there was an IAU resolution.

NC asked if a new time scale could be produced through a combination of BIPM with pulsars.

GP said that TT(BIPM) was produced by post-processing every year and it would be possible to add in extra information from pulsar analysis to give stability.

POSTFACE

JOURNÉES 2014 SYSTÈMES DE RÉFÉRENCE SPATIO-TEMPORELS

"Recent developments and prospects in ground-based and space astrometry"

organized by Pulkovo Observatory (Russia), 22-24 September 2014

Scientific Organizing Committee

N. Capitaine, France (Chair); Z. Malkin (Co-Chair), Russia; A. Brzeziński, Poland; V. Dehant, Belgium; A. Escapa, Spain; C. Hohenkerk, UK; C.Huang, China; I. Kumkova, Russia; D.D. McCarthy, USA; M. Soffel, Germany; J. Souchay, France; J. Vondrák, Czech R.; Ya. Yatskiv, Ukraine

Local Organizing Committee

A. Devyatkin (Chair), T. Borisevich, A. Vershkov, Z. Malkin, K. Maslennikov, N. Miller, V. Pashkevich, V. Pleshakov, I. Shevchenko

Conference location : Pulkovo Observatory, Pulkovskoe Shosse, 65, 196140, St. Petersburg, Russia

Scientific objectives

The Journées 2014 "Systèmes de référence spatio-temporels", with the sub-title "Recent developments and prospects in ground-based and space astrometry"', will be organized at Pulkovo Observatory, from 22 to 24 September 2014. It will be the twenty-third meeting in these Journées conference series which provide an international forum for advanced discussion in the fields of space and time reference systems, Earth rotation, dynamics of the solar system, astrometry and time. In 2014, the Journées will be focused on the issues related to the celestial reference frame and system, relativity and time scales, Earth rotation and geodynamics, numerical standards, ephemerides and dynamical models for planetary systems, future development of astronomical software, etc.

This will include special consideration of the progress of the ESA Gaia mission and of the VLBI2010 project, as well as of the realization of the next ICRF.

The Journées 2014 are sponsored by Pulkovo Observatory, Russian Academy of Sciences, Paris Observatory/SYRTE and are included in the program of celebrating the 175th anniversary of Pulkovo Observatory. They are co-sponsored by the International Astronomical Union (IAU) and the International Association of Geodesy (IAG).

Scientific programme

The scientific programme of the Journées 2014 includes the following sessions:

Session 1 - Celestial reference system and frame,
Session 2 - Relativity and time scales,
Session 3 - Solar and extrasolar systems dynamics,
Session 4 - Earth's rotation and geodynamics,
Session 5 - Astronomical almanacs and software,
as well as a sub-session on the'IAU/IAG Joint Working Group on Theory of Earth Rotation".

This also includes discussion related to IAU Division A Working Groups relevant to the topic of the Journées.

Contact

For information related to the scientific program, Nicole Capitaine: n.capitaine@obspm.fr,
for all requests related to the Conference organization, Zinovy Malkin: malkin@gao.spb.ru.

See also the web page at: `http://www.gao.spb.ru/english/as/j2014/home.htm` that is regularly updated, including the provisional programme, list of participants and information on the venue, accommodation, etc.